Universidad de Granada

Departamento de Física Teórica
y del Cosmos

Disk-Halo interaction: The molecular clouds in the Galactic center region

Denise E. Riquelme Vásquez
Instituto de Radio Astronomía Milimétrica - IRAM

Tesis Doctoral

Editor: Editorial de la Universidad de Granada
Autor: Denise E. Riquelme Vásquez
D.L.: GR 1734-2012
ISBN: 978-84-9028-091-1

Departamento de Física Teórica
y del Cosmos
Universidad de Granada

Instituto de Radio Astronomía Milimétrica - IRAM

Disk-Halo interaction: The molecular clouds in the Galactic center region

Memoria presentada por:

Denise E. Riquelme Vásquez

para optar al grado de

Doctora por la Universidad de Granada

Dirigida por:

Jesús Martín-Pintado
Rainer Mauersberger

Granada, 13 de Diciembre de 2011

Como director de la tesis titulada *Disk-Halo interaction: The molecular clouds in the Galactic center region*, presentada por **Denise E. Riquelme Vásquez**,

Dr. Jesús Martín-Pintado, Doctor en Ciencias Físicas.

Declara:

Que la presente memoria, titulada *Disk-Halo interaction: The molecular clouds in the Galactic center region* ha sido realizada por **Denise E. Riquelme Vásquez** bajo su direccíon en el Instituto de Radio Astronomía Milimétrica. Esta memoria constituye la tesis que **Denise E. Riquelme Vásquez** presenta para optar al grado de **Doctora por la Universidad de Granada**.

Granada, a 13 de Diciembre de 2011

Fdo:
Jesús Martín-Pintado

Declara:

Que la presente memoria, titulada *Disk-Halo interaction: The molecular clouds in the Galactic center region* ha sido realizada por **Denise E. Riquelme Vásquez** bajo su direccíon en el Instituto de Radio Astronomía Milimétrica. Esta memoria constituye la tesis que **Denise E. Riquelme Vásquez** presenta para optar al grado de **Doctora por la Universidad de Granada**.

Granada, a 13 de Diciembre de 2011

R. Mauersberger

Fdo:
Rainer Mauersberger

Denise E. Riquelme Vásquez, autora de la tesis *Disk-Halo interaction: The molecular clouds in the Galactic center region*, autoriza a que un ejemplar de la misma quede ubicada en la Biblioteca de la Escuela Superior de Física de Granada.

Fdo.: Denise E. Riquelme Vásquez
Granada, a 13 de Diciembre de 2011

Dedicado a Esteban

Contents

List of Figures

List of Tables

Agradecimientos

El periodo del doctorado ya se ha terminado, y además de todas las experiencias y aprendizajes reunidos, me ha dejado con un gran sentimiento de gratitud hacia todas las personas que han hecho este trabajo posible.

Quisiera agradecer a mis directores de tesis. A Jesús por transmitir su entusiasmo y motivación por la ciencia, las reuniones y largas conversaciones telefónicas, muchas de ellas muy fuera del horario laboral, que me daban entusiasmo para seguir adelante con este proyecto. A Rainer, por sus acertados comentarios y rápidas correcciones. Por su gran paciencia explicando y respondiendo mis preguntas. A ambos por escuchar, dirigir y dar sentido a mis ideas. Siempre escuchando lo que yo quería transmitir, ayudando a ponerlo en la forma correcta. Por la gran cercanía que han mostrado, haciendo las reuniones muy entretenidas, no solo científicamente con la gran cantidad de ideas que me daban, sino también con el agradable trato personal.

Quisiera agradecer a mi familia, en especial a mi papá y a mi mamá por el apoyo y comprensión que me han dado siempre. El amor que me mandaban día a día y la confianza que siempre pusieron en mi, fue fundamental para vivir esta experiencia y llegar a terminar el doctorado. A Felipe, Andrea, Benjamín y Martín, que me alegraban con las fotos de los niños. A mis abuelitas, tías, tíos, primos y amigas (María Luisa, Carina, Vicky y María Luz) que siempre estuvieron preocupados de mi, mandandome cariño a la distancia, en especial a Javiera, que aunque yo estuviera tan lejos, siempre me hacía partícipe de su vida. La persona fundamental en este proceso de doctorado, ha sido Esteban. Su infinita comprensión y apoyo, no solo en lo personal como novio, si no también en lo profesional, su estricta y constructiva crítica, siempre incentivandome a hacer las cosas bien, sus innumerables ayudas de IDL, sus correcciones de inglés, de matemática y física, y la enorme cantidad de noches de observación a las cuales me acompañó, han sido imprecindibles durante todos estos años. Su amor y cuidados en todo momento, en especial, por animarme cuando todo se ponía difícil y saber disfrutar conmigo los logros y felicidades.

Al Instituto de Radioastronomía Milimétrica, a sus directores Rainer y Carsten, que me ha dado la oportunidad de hacer la tesis doctoral. A todos mis compañeros que trabajan en la oficina del IRAM de los distintos grupos (backend, receptores, informática, etc), en especial a Esther que siempre ha estado dispuesta a ayudar en todo y a María. Parte importante de estos 4 años ha sido "la vida de telescopio". Quisiera agradecer a todos mis compañeros que trabajan en el radiotelescopio, a los operadores, ingenieros, técnicos, y a todo el personal, muy en especial a todas las cocineras quienes siempre se preocuparon de cocinar mis platos favoritos, y a Paco, con quien compartí muchas películas y conversaciones.

La vida no estaría completa sin los amigos y amigas que han formado mi familia en España. A Breezy y Rebeca, que han sido mis compañeras de oficina durante la mayor parte de mi doctorado, haciendo el día a día una constante fiesta. Ellas han sido un gran apoyo y compañía, con las cuales desarrollamos una gran complicidad, y de quienes, en lo personal y profesional aprendí muchísimo. A Cristina, siempre dispuesta a escucharme y tranquilizarme en todo momento (¡las extraño chicas!). La vida en la oficina no sería tan divertida sin Manu, que siempre nos contagia su alegría; a Jorge, a Christof, a Willy, a Maeva y a Sandra, por los excelentes momentos compartidos (huevos con aceite, ski, tapas, Caladero, Untoten, etc...). También quisiera agradecer a mis amigos que no pertenecen al IRAM; a mis amigos del grupo de Chilenos, cuya cercanía me trajo un pedazo de mi tierra que a veces es tan necesario, y a Trini y Ben, cuyas fondue de queso y las idas al Saint Germain me desconectaban y alegraban, y a Irene y a Gabriella. Gran parte de motivación se la debo a Arancha, con quien compartí muchos viajes a observar y muchas aventuras. Granada es una ciudad preciosa, en la cual practicamente estamos todos de paso... quisiera poder reencontrarme con cada uno de ustedes en un futuro. Quiero agraceder a mis amigos de Bonn, a Pablo, Laura, Felipe y Arturo por la buena acogida cuando iba de visita. Y a todos los astrónomos buena onda con los cuales coincidí en mis semanas de AoD. También quiero agradecer a Manu, Feña y Esteban por las correcciones ortográficas que pacientemente me ayudaron a hacer en esta tesis.

Quisiera agradecer a mis colaboradores, a Sergio Martín por su apoyo y comentarios; a Leo Bronfman y Jorge May (†), por su constante apoyo, y a Isabel Pérez por su buena disposición ayudándome en las observaciones.

Finalmente quiero agradecer al financiamiento recibido del proyecto AYA 2008-06181-C02-02.

Summary

The formation and evolution of galaxies is one of the hot topics in Astrophysics. In particular, processes like gas accretion through disk-halo interaction and bar potential, together with galactic winds and superwinds of massive star formation, are thought to play a key role in the evolution of galaxies.

The Milky Way, and in particular the Galactic center (GC), offers an excellent opportunity to explore in detail the chemical and physical processes associated to the accretion and ejection phenomena present in galactic nuclei. In this thesis, we study two kinds of phenomena which are presumably occurring in the GC region, and are believed to be partly responsible for the gas accretion toward the nuclear region of the Galaxy: the barred potential, and the Giant Molecular Loops (GMLs).

Binney et al. (1991) have shown that the large-scale gas kinematics in the central regions of the Galaxy can be accounted for by a barred galactic potential, in which there are two major families of orbits inside the bar: the X1 orbits parallel to the bar, and the inner X2 orbits, orthogonal to it. The gas falls from X1 to X2 orbits when it self-intersects in the X1-X2 orbits transition. The other phenomenon are the huge loop structures (GMLs) found by Fukui et al. (2006) and thought to be formed by a Parker instability. The gas of the loops is thought to flow down along the magnetic field lines, and join the Galactic plane, generating shock fronts at the "foot points" of the loops. However, so far there is no clear observational evidence of gas accretion from the X1 orbits and/or from high latitudes in the GMLs. In this thesis the high altitude clouds found in the GML will be referred as "halo" to differentiate from the molecular clouds in the Galactic plane.

In this thesis, we first performed a large-scale study of the GC region in SiO$(2-1)$, $HCO^+(1-0)$, and $H^{13}CO^+(1-0)$ (Riquelme et al 2010b ,A&A, 523, A45) using the 4 m-NANTEN telescope. We found an increased emission in SiO as compared to the HCO^+ line intensity at the foot points of the GMLs and toward the 1.3 complex, which indicates the presence of shocks (Martín-Pintado et al., 1992, 1997). From this study we selected 7 positions as places where the SiO emission shows an enhancement with respect to the HCO^+ emission. The positions are considered in this thesis as the "interaction regions", because they mark the places where gas in the GC could be interacting with gas coming from higher latitude ("disk-halo interaction") or from larger galactocentric radius, according to the GMLs scenario and the bar potential model, respectively. They were selected including five positions in the GMLs and two positions in the X1-X2 orbits interaction places. The positions placed in the GMLs were called "halo" as previously mentioned. Among them, 3 positions are placed where the gas in the GMLs joins the gas in the disk (foot points of the loops), and 2 positions are placed at the top of the loops. Each of the positions located at the X1-X2

orbits interaction places has two main kinematical components, one associated to the X1 orbits and the other to the X2 orbits. They were called as "disk X1", and "disk X2". Finally, we selected 2 additional positions close to $b = 0°$ that we called "disk" which are not associated to neither the GMLs nor the locations of the orbits interaction, and therefore they should trace the typical GC clouds.

To test if the GMLs scenario is correct, or if the gas is being ejected from the disk in the GC, we studied the $^{12}C/^{13}C$ isotopic ratio to trace gas accretion/ejection. Using the IRAM 30m-telescope, we observed the $J = 1 - 0$ rotational transition of HCO^+, HCN, HNC, and their ^{13}C isotopic substitutions toward the 9 selected positions. While ^{12}C is predicted to be formed in first-generation, massive stars on rapid timescales, ^{13}C is produced primarily via CNO processing of ^{12}C seeds from earlier stellar generations, on a longer timescale. The $^{12}C/^{13}C$ isotopic ratio shows, therefore, the relative degree of primary to secondary processing in stars. We found a systematically higher $^{12}C/^{13}C$ isotopic ratio (> 40) toward the halo and the X1 orbits than for the GC "standard" molecular clouds (20-25). The high isotopic ratios are consistent with the accretion of the gas from the halo and from the outskirts of the Galactic disk (Riquelme et al 2010a, A&A, 523, A51).

The next step was to study the physical conditions of the molecular gas in the interaction regions of the GC. Using the Effelsberg 100m-telescope, we measured the metastable inversion transitions of NH_3 from $(1,1)$ to $(6,6)$ in 6 positions that can be observed from this site. Using rotational diagrams and large velocity gradient calculations, we estimated for the first time, the kinetic temperatures of the molecular clouds in these regions. We derive two kinetic temperature regimes (one warm at $\sim$ 200 K and one cold at $\sim$ 40 K) for all the positions, except for the halo where only the warm component is present. Using the 30m-telescope, we also observed molecular tracers of different physical processes like SiO, HNCO, CS, $C^{18}O$, and ^{13}CO (shocks, photodissociation, dense gas). The fractional abundances derived from the different molecules support the shock origin of the heating mechanism in the GC (Riquelme et al 2012a, A&A, submitted).

Finally, we used the Mopra telescope to map one molecular cloud (M−3.8 + 0.9) at the foot points of the GMLs in 3mm lines. The maps reveal structures at small scales in the SiO emission, and large differences between the spatial distribution of the SiO and the HCO^+. The SiO emission in the M−3.8 + 0.9 cloud presents narrow profiles (20 km/s) in comparison with the HCO^+ profiles (50 km/s), thus, shocked gas is dynamically more confined than the HCO^+ emission (Riquelme et al 2012b, in prep.).

Overall, the results presented and discussed in this thesis give important clues to the undersanding of the nature of the molecular clouds in the Galactic center region. They evidence the presence of shocks and are consistent with the shock origin of the heating mechanisms. Furthermore, this work strongly supports the accretion of the gas towards the GC (through bar potential and GMLs) as the cause of such shocks.

This thesis is organized in eight chapters, and one appendix. Chapter 1 presents an introduction which covers the main characteristics and components of the GC, describing the kinematics and dynamics of the molecular gas, and the phenomena responsible of the gas accretion at Galactic scales. At the end of this chapter, we present the aims of this thesis. Chapter 2 gives the basic theoretical tools used throughout this work. Chapter 3 presents the large-scale study of the GC, which allowed the selection of

the positions and regions studied in detail in this thesis. Chapter 4 describes the isotopic study mentioned above. Chapter 5 presents the study of the physical conditions of the molecular gas in the disk-halo and X1-X2 interaction regions. Chapter 6 reports mapping of selected 3-mm lines of one molecular cloud. The conclusions are given in Chapter 7, and we present the perspectives and future projects triggered by this thesis in Chapter 8. Finally, we include one Appendix, which describes the calibration processes for the Effelsberg telescope. At the beginning of each chapter, we briefly introduce the fundamental concepts and theory needed for a better understanding of the science presented there.

Resumen

La formación y evolución de galaxias es uno de los temas actuales de gran interés en Astrofísica. En particular, procesos de acreción de gas a través de la interacción disco-halo y del potencial barrado, además de vientos galácticos y supervientos provenientes de la formación de estrellas masivas, se piensa que juegan un papel fundamental en la evolución de galaxias.

La Vía Láctea, y en particular, el centro Galáctico, nos ofrecen una excelente oportunidad para explorar en detalle los fenómenos presentes en los centros de las galaxias, tales como los procesos químicos y físicos asociados a la acreción y eyección de gas. En esta tesis se estudian dos tipos de fenómenos que supuestamente están ocurriendo en la región del centro Galáctico, y que se cree que serían responsables en parte de la acreción de gas hacia el núcleo de la Galaxia: el potencial barrado, y los bucles gigantes de gas molecular.

Binney et al. (1991) mostró que la cinemática a gran escala en el centro Galáctico puede ser explicada mediante un potencial barrado, en el cual hay dos familias principales de órbitas: las órbitas X1 que son paralelas a la barra, y las órbitas X2, que son ortogonales a ella. El gas cae de las órbitas X1 a las X2 cuando éste se autointersecta en los lugares de transición de las órbitas X1-X2. El otro fenómeno son las enormes estructuras con forma de bucles encontradas por Fukui et al. (2006), que se piensa que están formadas por una inestabilidad de Parker. El gas en los bucles fluye a lo largo de las líneas de campo magnético, y se junta con el plano Galáctico generando frentes de choques en unos lugares que se llamaron "pies de los bucles". Sin embargo, no hay evidencia observacional clara de acreción de gas desde las órbitas X1 o desde altas latitudes Galácticas en los bucles moleculares gigantes. En esta tesis, las nubes a alta latitud ubicadas en los bucles moleculares gigantes fueron llamadas "halo" para diferenciarlas de las nubes moleculares que se encuentran en el plano Galáctico.

En esta tesis, primero se realizó un estudio a gran escala de la región del centro Galáctico en las líneas de emisión molecular de SiO$(2-1)$, $HCO^+(1-0)$, y $H^{13}CO^+(1-0)$ (Riquelme et al 2010b ,A&A, 523, A45) usando el telescopio NANTEN de 4 metros. Se encontró un enriquecimiento de la emisión de SiO con respecto a la de HCO^+ en los pies de los bucles y también hacia un complejo molecular ubicado hacia la longitud Galáctica de $l = 1°.3$, lo que indica la presencia de choques (Martín-Pintado et al. 1992, 1997). De este estudio se seleccionaron 7 posiciones como lugares donde la emisión de SiO se muestra enriquecida con respecto a la de HCO^+. Estas posiciones fueron consideradas en esta tesis como "regiones de interacción", ya que ellas marcan las regiones donde el gas en el centro Galáctico podría estar interactuando con gas proveniente de latitudes mas altas ("interacción disco-halo") o desde mayores radios galactocéntricos, de acuerdo al escenario de los bucles gigantes de gas y del poten-

cial barrado. Las posiciones fueron seleccionadas incluyendo cinco posiciones en los bucles gigantes de gas molecular y dos posiciones en los lugares de interacción de las orbitas X1-X2. Las posiciones ubicadas en los bucles gigantes de gas molecular fueron llamadas "halo", como se mencionó anteriormente. De ellas, 3 posiciones están ubicadas en los lugares donde el gas en los bucles se junta con el gas del disco (pie de los bucles), y 2 posiciones están ubicadas en la parte alta de los bucles. Cada una de las posiciones ubicadas en la interacción de las órbitas X1-X2 tienen 2 principales componentes cinemáticos, uno asociado a las orbitas X1 y otro asociado a las órbitas X2. Ellos fueron llamados "disco X1" y "disco X2". Finalmente, se seleccionaron 2 posiciones adicionales cercanas a $b = 0°$ que fueron llamadas "disco", las cuales no están asociadas ni a los bucles gigantes de gas molecular, ni a los lugares de interacción de las órbitas, por lo que estarín trazando gas estándar del centro Galáctico.

Para probar si es correcto el escenario de los bucles gigantes de gas molecular, o si por el contrario, el gas estuviera siendo eyectado desde el disco del centro Galáctico, se estudió la razón isotópica $^{12}C/^{13}C$ para trazar la acreción/eyección del gas. Utilizando el telescopio de 30 metros de IRAM, se observaron las transiciones rotacionales $J = 1 - 0$ de HCO^+, HCN, HNC y de sus sustituciones isotópicas de ^{13}C en las 9 posiciones seleccionadas. Mientras se predice que el ^{12}C es formado en la primera generación de estrellas masivas en escala de tiempo cortas, se espera que el ^{13}C sea producido principalmente mediante procesamiento de carbon-nitrógeno-óxigeno de semillas de ^{12}C provenientes de generaciones de estrellas más tempranas, en una escala de tiempo más lenta. Entonces, la razon isotópica $^{12}C/^{13}C$ muestra el grado relativo de procesamiento primario-secundario en estrellas. Se encontró sistemáticamente una alta razón isotópica $^{12}C/^{13}C$ (> 40) hacia el halo y las órbitas X1 comparada con la razón normal de las nubes del centro Galáctico ($20 - 25$). La alta razón isotópica encontrada es consistente con acreción de gas desde el halo y desde las zonas más externas del disco de la Galaxia (Riquelme et al 2010a, A&A, 523, A51).

El paso siguiente fue el estudio de las condiciones físicas del gas molecular en las regiones de interacción en el centro Galáctico. Se utilizó el telescopio Effelsberg de 100 metros para observar las transiciones metaestables de inversión de la molécula NH_3 desde la (1,1) a la (6,6), en las 6 posiciones que eran visibles desde la ubicación geográfica del telescopio. Utilizando diagramas rotacionales y cálculos en la aproximación de grandes gradientes de velocidad, se estimaron, por primera vez, la temperatura cinética de las nubes moleculares en esas regiones. Se derivaron dos temperaturas cinéticas (una caliente de $\sim$ 200 K y otra mas fría de $\sim$ 40 K) para todas las posiciones, excepto para el halo, donde se encontró sólo la componente de temperatura caliente. Utilizando el telescopio de 30 metros de IRAM también se observaron diferentes trazadores moleculares de diferentes procesos físicos, tales como SiO, HNCO, CS, $C^{18}O$, y ^{13}CO (choques, fotodisociación, gas denso). Las abundancias fraccionales derivadas de las distintas moléculas apoyan la hipótesis de los choques como mecanismo de calentamiento del centro Galáctico (Riquelme et al 2012a, A&A, enviado).

Finalmente, se utilizó el telescopio Mopra de 22 metros para realizar cartografías en varias líneas moleculares de longitud de onda de 3 mm de una nube molecular ubicada en los pies de los bucles (M−3.8 + 0.9). Los mapas revelaron estructuras a pequeña escala en la emisión de SiO, y grandes diferencias entre la distribución espacial de las moléculas de SiO y de HCO^+. La emisión de SiO presenta perfiles más delgados en comparación con los de HCO^+, lo que se interpreta como que los choques estan

dinámicamente más confinados que el HCO^+ (Riquelme et al 2011b, en preparación).

En terminos generales, los resultados presentados y discutidos en esta tesis proporcionan importantes claves para la comprensión de la naturaleza de las nubes moleculares de la región del centro de la Galaxia. Ellos evidencian la presencia de choques y son consistentes con la hipótesis de los choques como mecanismo de calentamiento. Mas aún, este trabajo soporta fuertemente la idea de que la acreción del gas hacia el centro Galáctico es la causa de dichos choques.

Esta tesis está organizada en ocho capítulos y un apéndice. El capítulo 1 presenta una introducción que resume las principales características y componentes del centro Galáctico, describiendo la cinemática y dinámica del gas molecular, y los fenómenos responsables de la acreción del gas a escalas Galácticas. Al final de este capítulo se presentan los objetivos de esta tesis. El capítulo 2 entrega las herramientas teóricas básicas necesarias a lo largo de esta tesis. El capítulo 3 presenta el estudio a gran escala del centro Galáctico, que permitió la selección de posiciones y regiones utilizadas en esta tesis. El capítulo 4 describe el estudio de razones isotópicas mencionado anteriormente. El capítulo 5 presenta el estudio de las condiciones físicas del gas molecular en las regiones de interaccion disco-halo y en las regiones de interacción de las orbitas X1-X2. El capítulo 6 describe el mapa de las líneas de 3 mm de la nube molecular M$-3.8 + 0.9$. Las conclusiones son presentadas en el capítulo 7, y en el capítulo 8 se describen las perspectivas y trabajos futuros originados a partir de esta tesis. Finalmente, se incluye un apéndice que describe los procedimientos de calibración para el telescopio Effelsberg. Al comienzo de cada capítulo, se introducen la teoría y conceptos fundamentales, requeridos para un mejor entendimiento de la ciencia presentada a continuación.

Chapter 1

Introduction

1.1 Our Milky Way

The Milky Way, our Galaxy, is a barred spiral galaxy (SBc in the Hubble classification of galaxies) with a diameter of 30 kpc, with the Sun placed 2/3 away from the center, at a galactocentric radius of $\sim$ 8 kpc[1], between the Perseus and Sagittarius arms (in a feature known as the Orion arm or Orion spur). The Galaxy harbors about 10^{11} stars, and it is estimated that the oldest stars of the thin and thick disks (see below) are $\sim$ 8 and $\sim$ 10 Gyr respectively, and for the halo are $\sim$ 13 Gyr (see e.g., (Binney & Tremaine 2008; Carroll & Ostlie 2006)). The number of the spiral arms is still under debate. Splitting the Galaxy in the inner and outer part (taking the Sun position as reference), it is possible to discuss about them. In the inner part of the Galaxy, there is the "Expanding 3-kpc Arm", which was discovered in the neutral hydrogen 21 cm emission by van Woerden et al. (1957). There is robust evidence that the arm lies on the near side of the Galactic center and is expanding away from it at a velocity of -53 km s^{-1}at $l \sim 0^{\circ}$. The evidences come from the 21 cm emission, and from the CO (carbon monoxide) longitude-velocity diagrams and its absorption of continuum emission toward the Galactic center (see e.g., Bitran et al. 1997). The large noncircular motion of the arm has been attributed to explosive expulsion of gas from the center (van der Kruit 1971; Sanders & Prendergast 1974) and was one of the earliest arguments for the existence of a bar at the Galactic center (de Vaucouleurs 1964). Recently, Dame & Thaddeus (2008) found the far-side counterpart of this arm, the "Far 3-kpc Arm", from a reanalysis the Columbia-CfA-Chile CO survey (Dame et al. 2001) towards the Galactic center (Bitran et al. 1997). The far 3-kpc arm has a velocity of +56 km s^{-1}at $l \sim 0^{\circ}$, and give additional support to the bar. Outside the zone of influence of the bar, there is generally assumed that the Galaxy has four principal spiral arms: Norma, Sagittarius, Perseus, and Scutum-Centaurus (also knows as Scutum-Crux).

The most accurate picture of the face-on Milky Way was constructed in the 212^{th} American Astronomical Society Meeting (in St. Louis, MO, June 2008) using all avail-

[1]The standard IAU Galactic center distance is 8.5 kpc (Kerr & Lynden-Bell 1986), however there are several works which have obtained a more accurated value. For example, Reid (1993) estimated a distance of 8.0 ± 0.5 kpc. Recently, Genzel et al. (2010) averaging different direct measures give a distance of $8.23 \pm 0.20 \pm 0.19$ kpc, where the first error is the variance of the weighted mean and the second error the unbiased weighted sample variance.

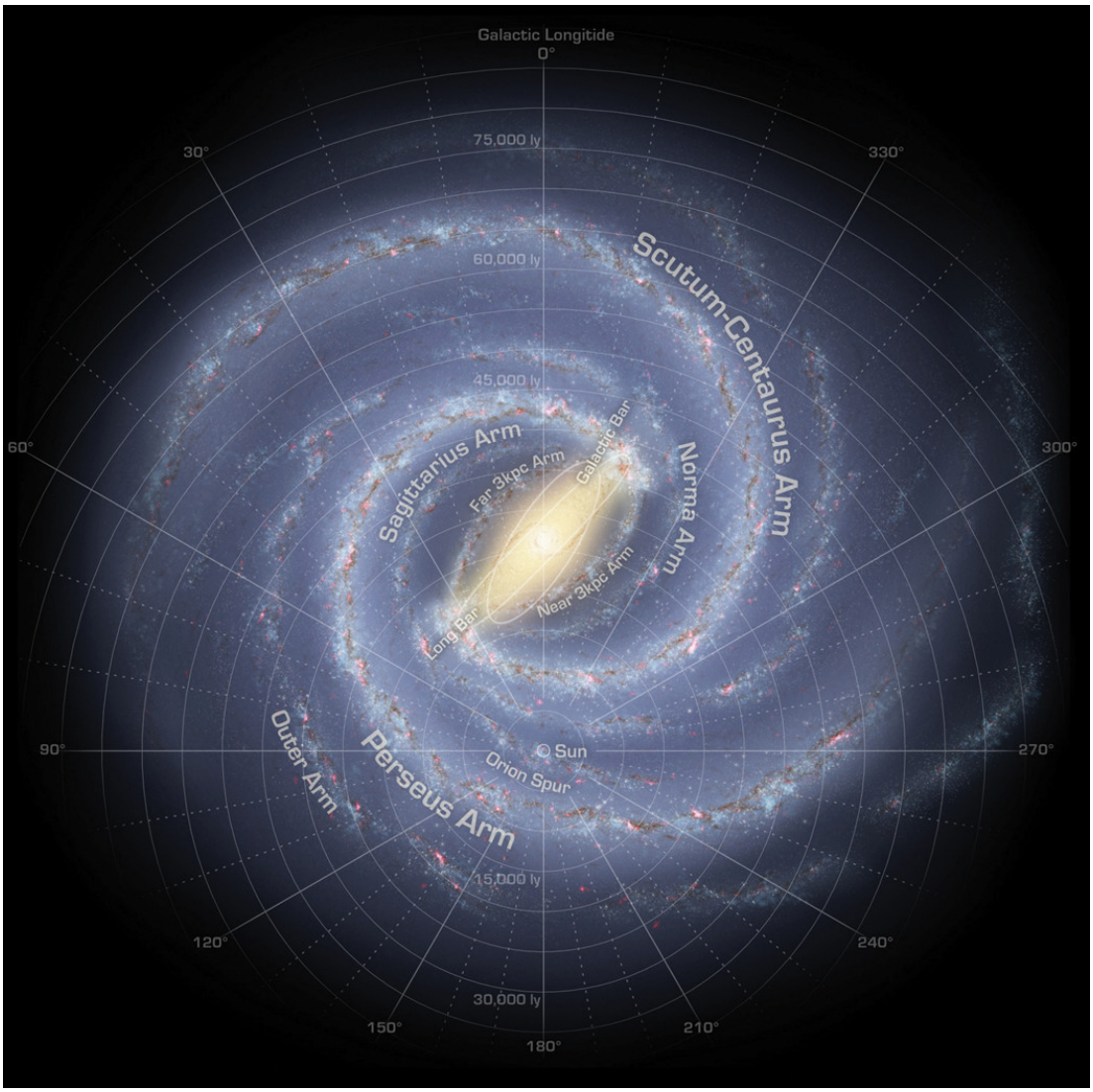

Figure 1.1: Milky Way face-on (Churchwell et al. 2009)

able observational data including the stellar data from GLIMPSE[2], the HI 21 cm Galactic Plane Surveys, and CO surveys (see, Fig. 1.1 from Churchwell et al. 2009). The image was constructed by R. Hurt of the Spitzer Space Science Center in consultation with R. Benjamin of the University of Wisconsin-Whitewater.

The stellar components of the Galaxy are the thin and the thick disks, the halo,

[2]GLIMPSE ("Galactic Legacy Infrared Mid-Plane Survey Extraordinaire") is a survey carried out using Spitzer telescope. The survey has 3 parts: GLIMPSE I fully imaged the Galactic plane covering an area of 220 deg^2 ($|l|$ = 10° to 65° , and $|b| \leq 1°$), with a spatial resolution < 2″ at wavelengths 3.6, 4.5, 5.8, and 8.0 μm using the Infrared Array Camera (IRAC). GLIMPSE II fully imaged the inner 20° of the Galactic plane with the same resolution and sensitivity as GLIMPSE I, increasing the latitude coverage at the inner part of the Galaxy. GLIMPSE III sampled the latitude distribution of the central bar by extending the GLIMPSE I & II latitude coverage to ±3° at nine selected latitudes and to ±4° within 2° of the Galactic center.

and the bulge. The thick disk was discovered by Gilmore & Reid (1983). It has a velocity dispersion of $v \sim 40\,\mathrm{km\,s^{-1}}$ and a height of about 1 kpc (see e.g., Freeman 2011). The thick disk is an important clue in the study of the Galaxy formation because it shows a kinematical and chemical relic of the early Galaxy. The stars in the halo have very different kinematics than those in the rotating thick and thin disks. The mean rotation of the stellar halo is $\sim 0\,\mathrm{km\,s^{-1}}$ and it is supported against gravity by its velocity dispersion. Metal poor RR Lyrae stars delimite a two component halo, a flattened inner component and a spherical outer component (Hartwick 1987). The halo is probably formed from the debris of small accreted galaxies, which continue at the present time. The disruption of the Sgr dwarf spheroidal galaxy (see §1.5.1) is an example of this phenomenon. The inner halo component could be formed in a dissipative way (Zolotov et al. 2009). The bulge is a triaxial structure that looks like a bar. The first evidence of the bar was given by Blitz & Spergel (1991), and Dwek et al. (1995) fitted the peanut-shaped bulge by boxy Gaussian functions. The bulge/bar has an aspect ratio of 10:4:3 (length:width:height), a half-length of $\sim 3.1 - 3.5$ kpc Gerhard (2002). The inclination of the bulge is still under debate, with a value ranging from $10° - 45°$ (see e.g., Rodriguez-Fernandez & Combes 2008, and references therein), but many works give a value of $15° - 30°$. In addition of the bar like boxy-bulge, there are evidences of a second bar (longer and thinner than the boxy-bulge bar) in the Galactic center region (Picaud et al. 2003; López-Corredoira et al. 2001, 2007; Benjamin et al. 2005).

The central region of our Galaxy harbors a large number of phenomena and structures. An overview of the Galactic center including radio continuum, millimeter, infrared, and X-ray observations suggests that the center of the Milky Way behaves as a mildly active starburst galaxy, delineated as a weak, Seyfert-type nucleus driven by a black hole coincident with the compact source Sgr A* (see e.g., Mezger et al. 1996; Morris & Serabyn 1996).

The 10% of the molecular gas of the Galaxy is located in the bulge. Large scale surveys of CO isotopomers (see e.g., Bally et al. 1987; Heiligman 1987; Jackson et al. 1996; Dahmen et al. 1997; Bitran et al. 1997) showed that the cloud and the intercloud medium in the gaseous bulge of the Milky Way are molecular. There are several surveys of molecular clouds in the center of the Galaxy (see Table 3.1 for a list of atomic and molecular surveys of the Galactic bulge), and all of these have shown a complex and rich morphology and characteristics (see §1.3)

1.2 Characteristic of the gas in the Galactic center region

It is well known that the molecular clouds in the Galactic center (GC) region, i.e., the central kpc of the Galaxy, have different characteristics than the molecular clouds in the disk. High temperatures (see e.g., Hüttemeister et al. 1993a) but without warm dust (Odenwald & Fazio 1984) , high supersonic internal velocity dispersions ($\sim 15 - 50$ km s^{-1}), high pressure, high density ($\sim 10^4$ cm^{-3}) (Morris & Serabyn 1996), extended SiO emission (Martín-Pintado et al. 1997) and strong magnetic fields (Morris & Serabyn 1996) are typical features throughout this region. The GC region is a very prolific source of complex molecular species, and it provides a chemical template for the understanding of the molecular composition of other galaxies. In this thesis, we

focus on the study of molecular clouds in the Galactic center. In order to depict a complete picture of the ISM in the GC, we briefly summarize the general characteristic of the gas in this striking region.

1.2.1 Phases of the interstellar medium in the Galactic center

The GC is totally obscured in the optical and ultraviolet wavelength by the Galactic plane dust, therefore, the GC is observed manly from radio and infrared frequencies and then at high energies (> 1 keV).

1.2.1.1 Hot plasma

The hot thin plasma of $10^7 - 10^8$ K is studied by X-ray and γ-ray emission. The GC is a prominent source in X-rays and γ-rays which present a very complex emission consisting of both thermal and non-thermal radiation, produced by compact and extended sources, sourrounded by more diffuse components. This region is seen in the continuum and line emission, mainly in the 6.7 keV Kα transition of He-like Fe, and 6.4 keV Kα transition of neutral Fe. The electron density average is $0.3 - 0.4$ electrons cm^{-3} in this component, and the total thermal energy of the electron is $5 \times 10^{52-53}$ erg. The total plasma mass is $2000 - 4000$ M$_\odot$ (Koyama et al. 1996).

The X-rays view: energies from 1 to 10 keV In this energy band, the GC is dominated by few bright, sometimes transient, X-ray binaries. We also found a large population of weak point-like persistent and transient sources, several components of diffuse emission, several sources of thermal and non-thermal radiation, and a weak central emission associate to Sgr A* (a strong compact source of nonthermal emission, where a supermassive black hole is located, see §1.3.1.1). Following Goldwurm (2011), we discuss the X-ray emission in the three sections:

- *Sgr A.* Towards Sgr A*, Chandra resolved the central Rosat source into several components and detected a weak source in the position of Sgr A*. In the 15'' radius, the surrounding diffuse emission shows a 6.55 keV Fe line indicating fluorescence from plasma in non equilibrium ionization, which is explained as due to the interaction of powerful stellar winds generated by massive stars of nearby young star cluster, which also provide the bulk of the material accreting in the supermassive black hole. Chandra also discovered X-ray flares from Sgr A*. Moving outwards, Sgr A East appears as a single, compact, mixed morphology supernova remnant (SNR), where the non-thermal radio shell surrounds a centrally peaked thermal X-ray emission of one component at 1 keV and another at 4 keV. The X-ray emission shows that Sgr A East is a typical SN II or SN Ia occurred about $\lesssim 10^4$ years ago

- *The discrete X-ray source population.* Over 9000 discrete sources spatially distributed as the stellar population were detected in the $2^\circ \times 0.8^\circ$ region around the GC with the Chandra monitoring of the GC in a total exposure time of 2.25 Ms (Muno et al. 2009). The bulk of the weak sources are probably cataclysmic variable with a fraction of hard magnetically-accreting white dwarfs.

- *The X-ray diffuse emission.* This emission consists of three components (Muno et al. 2004; Park et al. 2004; Koyama et al. 2009): an irregular soft component described by a low temperature ~ 1 keV plasma model, an uniform 6.7 keV line associated to a continuum emission described by a hot plasma, and a clumpy 6.4 keV Fe line component correlated with molecular material.

  The soft component is traced by the low energy K_α and K_β lines of He-like and H-like ions of Si, S, Ar, and Ca. It is explained by the interaction of SN remnants or stellar winds from young and massive stars with the interstellar matter of the region.

  The hot component, traced by the He-like and H-like ionized Fe lines (6.7 keV and 6.9 keV respectively) is uniformly distributed, concentrated along the Galactic plane with a peak towards the center. Such a hot gas (10^8 K) cannot be bound to the Galaxy at all (Yamauchi et al. 1990; Sunyaev et al. 1993), escaping from the center at a few thousand $\mathrm{km\,s^{-1}}$ in $< 10^5$ yr, therefore it is hard to explain this component. Different theories have been proposed to explain the hot component, such as gas dominated by helium rather than hydrogen, which could allow the gas be bound to the region; the motion of the molecular clouds through the strong magnetized medium, which produces a strong heating mechanism by dissipation of hydromagnetic wave energy; and finally, an unresolved population of weak discrete sources. Although there are some evidences which support the last hypothesis, the issue is still under debate (see Goldwurm 2011, and references therein).

  The last component is the 6.4 keV fluorescence line of neutral or weakly-ionized Fe, which present a clumpy morphology clearly correlated to the molecular material of the central molecular zone (CMZ, Morris & Serabyn 1996, corresponds to a region with a galactocentric radius od ~ 200 pc where the gas is mainly molecular, see §1.3.1). The fluorescence line at 6.4 keV is produced when an atom or ion of a heavy element (Fe) is left in an excited state following ejection from an inner K or L-shell by an incident X-ray photon. Then, the atom or ion may return to its lower energy state by emitting an electron from the higher shell or by radiative transition (Frank et al. 2002). The origin of the 6.4 keV line is non-thermal and must be associated either to irradiation by photons with energies > 7.1 keV (Thompson scattering) or interaction with low energy electrons (thermal bremsstrahlung). The line shows a clear correlation with Sgr B2, which was interpreted as fluorecent line due to scattering of hard X-ray emission, coming possibly from a strong outburst of X-rays from Sgr A* occurred ~ 300 yr ago which illuminates Sgr B2 generating the Fe line (X-ray reflection nebula model). The Fe K_α line also was detected in Sgr C, in $G0.1-0.1$ and non-thermal radio filaments. The recent striking discovery of variations in the 6.4 keV line flux in Sgr B2 by Terrier et al. (2009, 2010) and in Sgr A* by Ponti et al. (2010) supports the X-ray reflexion nebula scenario. These authors also show that the variations can be explained by one single outburst of Sgr A* which started 400 years ago and ended ~ 100 years ago.

The γ-rays view: energies > 20 keV. In the γ-rays regime, Diehl et al. (1993) report the detection of the ^{28}Al line at 1.8 MeV. This line is formed in nucleosynthesis sites

such as novae, SN, and the interior of massive stars, and has a lifetime of 10^6 years, which indicates that a recent episode of massive star formation took place in the GC. The EGRET telescope found a γ-ray flux towards the GC of $2 \times 10^{37} \mathrm{erg\,s^{-1}}$ for energies > 500 MeV in an error circle of 0.2° (Mayer-Hasselwander et al. 1998). Latter, with INTEGRAL (see below) the 511 keV line emission, produced by electron-positron annihilation, was mapped showing that the emission is extended and composed by both, a bulge and a weaker disk components.

In the last 10 years, the GC emission at energies > 20 keV has been explored in detail with INTEGRAL[3], HESS[4] and FERMI[5]. INTEGRAL obtained the 20-800 keV band image of the GC with an unprecedent precision (Fig. 1.2). The emission is dominated by bright and variable x-ray burst (XRB), but also a faint and persistent emission compatible with a source placed at 1'' of the Sgr A*, which would correspond to a diffuse emission concentrated in the inner central 10-20 pc or to the sum of the contribution of unresolved point-like sources (Bélanger et al. 2006; Krivonos et al. 2007). The spectrum at > 20 keV extending up to 150 keV shows a non-thermal component, which is still unexplained. From the very high energy γ-rays bands, HESS reported the presence of a bright TeV point like source centered within 1′ from Sgr A* Aharonian et al. (2004, 2009). Aharonian et al. (2006) reported the discovery (using HESS) of a TeV diffuse emission closely correlated with the molecular clouds in the CMZ. The source close to Sgr A* found previously by EGRET[6], was confirmed by the medium-high γ-rays energies covered by FERMI, and also found another excess which is compatible with Sgr B2 (which was not detected by EGRET previously). The γ-rays emission from the GC has been clearly detected, but its origin and nature is not fully understood.

1.2.1.2 Ionized warm gas

The ionized gas, which is traced by radio continuum and recombination lines, is characterized by an electron temperature of $5000 - 10000$ K and densities of $10^2 - 10^4 \mathrm{cm^{-3}}$. This component of the ISM is widely found throughout the GC region. From the 5 GHz continuum maps of Altenhoff et al. (1979), Mezger & Pauls (1979) state that 50% of this flux correspond to thermal radio continuum, where there is an extended low density (ELD) H II (of 500×300 pc^2) region, which corresponds to the 60% of the thermal emission, and a number of giant H II regions (most of them associated with Sgr A, B, C, D complexes), which contribute with the 40% of the ionized gas. Several works have shown that the distributions of both ionized gas and diffuse infrared emission in the CMZ (Altenhoff et al. 1979; Odenwald & Fazio 1984; Handa et al. 1987; Cox & Laureijs 1989) are distribuited much more symmetrically than the

[3]International Gamma-Ray Astrophysics Laboratory, is a satellite launched in Oct 2002 for detecting γ-rays.

[4]The High Energy Stereoscopic System (HESS), is a system of imaging atmospheric Cherenkov telescopes for to study very high energy (VHE) gamma-ray in the 100 GeV to 100 TeV energy range

[5]The Fermi Gamma-ray Space Telescope is a space observatory launched in 2008. It has two instruments: the Large Area Telescope (LAT) and the Gamma-ray Burst Monitor (GBM). The LAT is an imaging gamma-ray detector which detects photons with energy from 30 MeV to 300 GeV, with a field of view of about 20% of the sky. The GBM consists of 14 scintillation detectors can detect gamma-ray bursts in the energy range from 8 keV to 1 MeV and from 150 keV to 30 MeV

[6]Energetic Gamma Ray Experiment Telescope, was one of four instruments of the Compton Gamma Ray Observatory satellite, that detect γ-rays from 30 MeV to 30 GeV

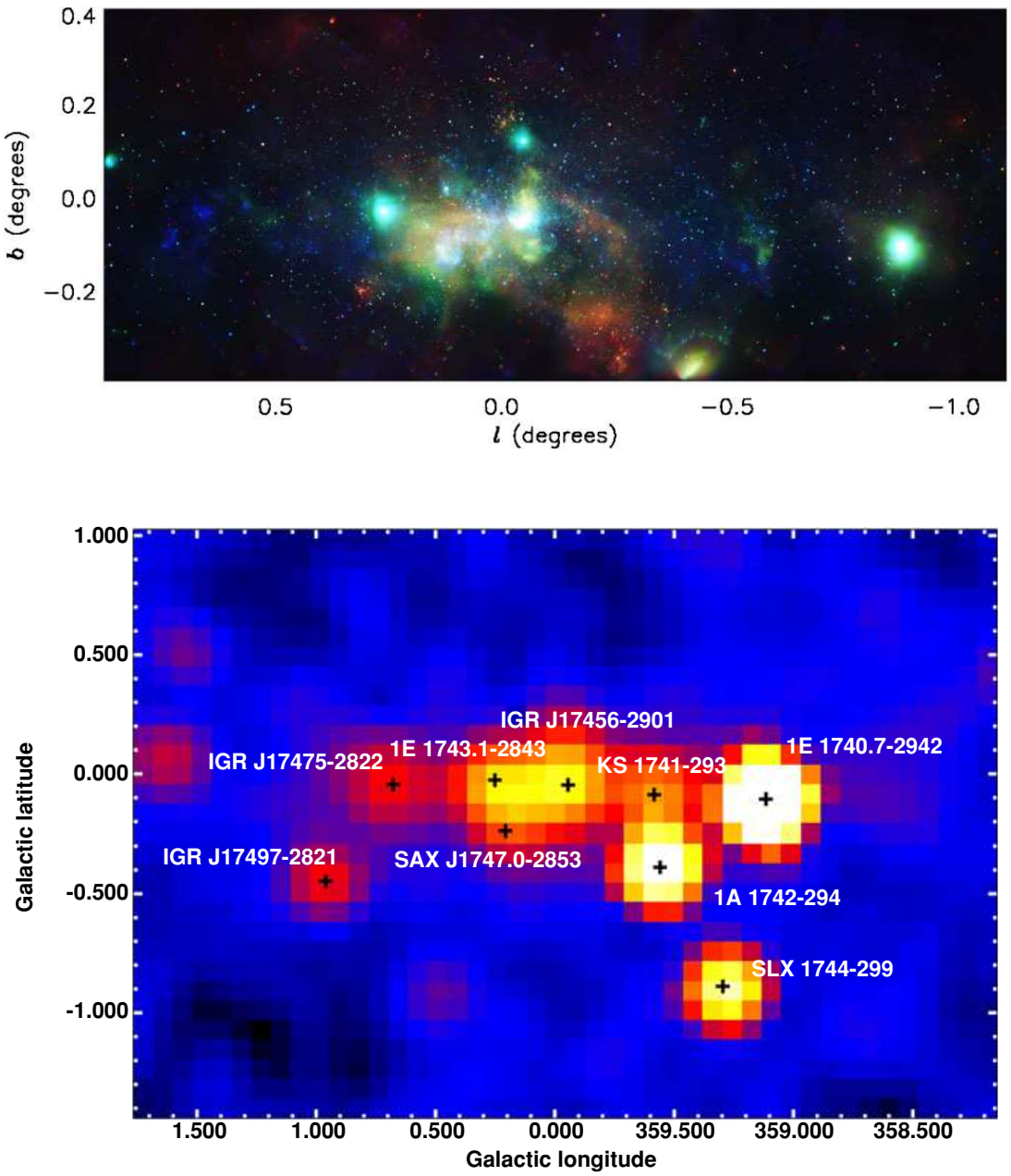

Figure 1.2: The GC seen at high energies. Top: three color X-ray image of the GC obtained with the deep survey of the Chandra observatory in the 1-8 keV range. Red is 1-3 keV, green is 3-5 keV, and blue is 5-8 keV Muno et al. (2009). Bottom: INTEGRAL image of the GC in the 20 – 40 keV band. The image was produced combining all the GC observations from 2003 to 2009 for 20 Ms of exposure time Terrier et al. (2010). The position of IGR 17475-2822 is compatible with Sgr B2 molecular cloud.

molecules (e.g, traced by CO), which suggests that the heating sources are more evenly distributed than are the discrete clouds. The dust temperature drops as r^{-3} from its central peak to its asymptotic value of 23 K near a radius of 200 pc. The ionized gas is also studied in fine structure lines (Rodríguez-Fernández & Martín-Pintado 2005). Many surveys with low angular resolution (Lockman & Gordon 1973; Pauls & Mezger 1975) have shown that the ionized gas rotates in the same direction of the neutral gas and shows large line widths of $50 - 100$ km s^{-1}, which indicates a high degree of turbulence. In the CMZ, the production rate of the Lyman continuum photons is $1 - 3 \times 10^{52} s^{-1}$, and the far-infrared luminosity is 10^9 $L_\odot$, which is typical for Galactic H II regions. The infrared excesses is roughly 10 and 30, as deduced for individual H II regions and the extended emission, which requires a later population of stars (see, Morris & Serabyn 1996, and references therein). Odenwald & Fazio (1984); Lis & Carlstrom (1994) considered star formation with an underabundance of O stars, but the abundant population of K and M giants in the GC is enough to heat the dust in the extended region to the observed levels (Cox & Laureijs 1989). Nakagawa et al. (1996) propose a soft interstellar radiation field from the underabundance of C^+ emission from the CMZ.

Studies of the recombination lines using centimeter interferometers (VLA) and single dish hydrogen recombination lines towards selected regions such as the most prominent H II regions (Sgr A, B, C, D) and ionized nebulae ("the Sickle"), have reveled the physical conditions for these regions: electron temperatures from $4000 - 8000$ K, and electron densities of $300 - 1000\,cm^{-3}$. The fine structure lines ratios are almost independent of the electron temperature and can be used to derive electron densities and the properties of the ionizing radiation. From the fine structure lines, Lacy et al. (1980) and Genzel et al. (1984) derived an electron density of $\sim 10^4$ cm^{-3} and an effective temperature of the ionizing radiation of < 35000 K in the central pc of the Galaxy. Towards the Sickle region, Simpson et al. (1997) found electron densities of $\sim 200\,cm^{-3}$ and an effective temperature of the ionizing radiation of 36000 K. Using fine structure and recombination lines observed with ISO, Rodríguez-Fernández & Martín-Pintado (2005) studied 18 sources within the CMZ which were selected as molecular clouds placed far from the thermal continuum sources. They derived electron densities of the ionized gas from 100 to < 30 cm^{-3} and a ionizing-radiation of $32000 - 37000$ K.

1.2.1.3 Neutral cold gas

As mentioned before, the molecular gas in the GC region shows different characteristics than the molecular clouds in the disk of the Galaxy. The molecular gas in this region has high kinetic temperatures, large line width and, extended SiO emission. In the following we briefly summarize its most striking properties, and some of them will be treated in deepth in this thesis.

Kinetic temperature and large linewidth The molecular clouds in the GC have higher kinetic temperatures (30-200 K, see e.g., Güsten et al. 1981; Morris et al. 1983; Hüttemeister et al. 1993a) than the clouds in the disk of the Galaxy. The dust temperature in the GC is low ($\lesssim 40$ K, Pierce-Price et al. 2000). Therefore a direct and widespread gas heating mechanism that heats directly the gas is required.

To account for the high kinetic temperatures, several heating mechanisms have been proposed, such as cosmic rays, magnetic ion-slipping, dissipation of mechanical turbulence, etc. This topic is discussed in §5, where we derive for the first time the kinetic temperature of high latitude clouds in the GC region.

High supersonic internal velocity dispersions ($\gtrsim$ 15 km s^{-1}) are present in the molecular clouds in the GC region. These linewidths are one order of magnitude higher than the ones found in the disk. This characteristic may be related to the heating of the gas by the dissipation of turbulence which still holds if the cloud velocity dispertions are due to magnetosonic disturbances. Fleck (1980) proposed the energy extraction of the tidal field as the origin of the large linewidth, Das & Jog (1995) conclude that this mechanism is efficient only for a central bar potential (Morris & Serabyn 1996).

Densities It is well known that molecular clouds in the GC have on average higher densities than in the disk, which are needed to withstand tidal shearing and disruption (Güsten & Downes 1980). Güsten (1989) provided an expression for the minimum density required to survive to tidal forces, $n(H_2) \geq 10^4 \left(\frac{75pc}{R_c}\right)^{1.8}$ cm^{-3} (where R_c is the galactocentric distances). The high density gas has been traced by different molecules, in particular with CS(2-1) (Tsuboi et al. 1999), HCN (Jackson et al. 1996), and CS(3-2), (2-1) (see §5.4.1)

Extended SiO emission and its relationship with large scale shocks SiO (silicon monoxide) traces shocks and high temperature chemistry in interstellar clouds. High temperature chemistry reactions and models including shocks or molecule formation in fast molecular outflows predict enhancements of the SiO abundances.

In the Galactic disk, quasithermal SiO emission is seen in very small regions, tightly correlated with high temperature regions, and it is associated mainly with energetic outflows powered by young stars (Downes et al. 1982), and shocked molecular clouds associated with the supernova remnant IC443 (Ziurys et al. 1989). The fractional abundances of SiO can change by more than six order of magnitude between quiescent cold gas and hot shocked dense gas (Ziurys et al. 1989; Martín-Pintado et al. 1992). This peculiar chemistry suggests that Si is highly depleted on grains in the molecular clouds and that SiO appears only in very small regions where shocks release Si or SiO into the gas phase (Martín-Pintado et al. 1992), although high temperature gas phase chemistry may still play a minor role (Langer & Glassgold 1990).

It is believed that the dust grains, which are formed by silicon and carbon, are partly destroyed by the shock waves and thus deliver Si into gas phase. Seab & Shull (1983) showed that shocks can produce significant grain destruction. Their model predicts that up to half of the Si and Fe can be delivered to the gas phase from shocks with velocities $>$ 50 km s^{-1} whitout a significant change of the C, O, and N abundances. Once the Si is in gas phase in the hot post-shock region, it can form SiO by shock chemistry (Iglesias & Silk 1978) and/or ion-molecule chemistry (Herbst et al. 1989). It is also possible that a significant fraction of SiO can be directly released in gas phase due to the silicate grain destruction.

The SiO emission is widely detected in the molecular clouds throughout the GC region (Martín-Pintado et al. 1997; Hüttemeister et al. 1998), which has been interpreted in terms of large scale shocks. Hüttemeister et al. (1998) argue that the bulk of the SiO

emission comes from a cold and dense component (20 – 30 K, 10^4 cm^{-3}), but it was likely formed under conditions of high kinetic temperature and grain erosion by shocks (Martín-Pintado et al. 1992). Hüttemeister et al. (1998) support their claim based on the large SiO abundance that they found in one hot and thin cloud, where the SiO formation processes should be ongoing. Within $\sim 10^6$ yr (Wilson et al. 2009a), the SiO molecule freezes out on the grain mantles and the clouds loses their chemical memory of the shock. In §3 I present a large scale survey of the GC region in the $J = 1 - 0$ rotational transition of HCO^+ and $H^{13}CO^+$ and the $J = 2 - 1$ transition of SiO. This is the largest SiO map of the GC region ever presented, and it shows clearly the widespread nature of the SiO emission throughout the GC region which is a clear signal of shocks.

Rich chemical complexity of the Galactic center The GC region has a very rich organic chemistry. Requena-Torres et al. (2008) have detected complex organic molecules in individual clouds throuhout the CMZ. Requena-Torres et al. (2006) argue that the chemistry in the CMZ is even richer to that in hot molecular cores and over a much larger scale.

1.2.1.4 Pressure Balance

The thermal (Sawada et al. 2001), non-thermal and magnetic pressure of the interstellar medium in the CMZ is very large, being at least two orders of magnitude higher compared to these of the Galactic disk (Spergel & Blitz 1992). Much of the volume of the GC is filled by hot diffuse gas ($T \sim 10^8$ K, $n \sim 0.04$ cm^{-3}), which has a pressure of 5.5×10^{-10} dynes cm^{-2}, and is in approximate pressure equilibrium with the warm molecular clouds (150 K) at densities of $\sim 10^4$ cm^{-2} ($p = n(H_2) \times T_K \times k \sim 2 \times 10^{-10}$ dynes cm^{-2}). In particular, Sawada et al. (2004) found a high-pressure region in the central $\sim$ 100 pc which is dominated by high-density gas and contains star-forming regions and coexists with the GC arms found by Sofue (1995). If the magnetic field has a strength of 0.1 – 1 mG (se §1.2.2), the magnetic pressure has an intensity of $\sim 0.4 - 4 \times 10^{-8}$ dynes cm^{-2} which is two orders of magnitude higher than the thermal pressure. Morris & Serabyn (1996) argue that this magnetic pressure would be linked to the turbulence pressure, which reaches a value of $\sim 10^{-8}$ dynes cm^{-2} in the cloud of the GC.

1.2.2 Magnetic field

The magnetic field is a key component of the Galactic center because its presence influences the physical properties of the ISM. There are several observational manifestations of the magnetic field in this region: non-thermal radio filaments (NTFs) and a large scale helically worm structure, polarized thermal emission of the dust from molecular clouds, and extended syncrotron emission from cosmic rays or SN (Morris 2006). The magnetic field in the intercloud medium occupying most of the volume of the GC is thought to be traced by the NTFs. The NTFs are magnetic flux tubes illuminated by syncrotron emission from relativistic electrons. The radio continuum emission is linearly polarized and is characterized by a spectral index consistent with synchrotron radiation. Occasionally they present a filamentary counterpart at X-rays,

of tens of parsecs long and only a fraction of a parsec wide (typically < 0.5 pc). Fig. 1.3 shows a schematic map of the radio filaments catalogued by Yusef-Zadeh et al. (2004) in their λ = 20 cm survey of the GC. They can be isolated (called threads Morris & Yusef-Zadeh 1985), or they can be found in bundles, such as those of the prominent Radio Arc (Yusef-Zadeh et al. 1984). They are uniform in brightness and curvature, and because most of they are roughly perpendicular to the Galactic plane, they reveal a poloidal large-scale geometry for the magnetic field. The slightly outward curvature indicates that the magnetic field does not remain vertical at large latitudes, but they turn to a more general poloidal geometry (Morris 1990). The strength of the magnetic field is still controversial, ranging from tens of microgauss to $\sim$ a milliGauss. It has been estimated by several methods, like e.g., assuming energy equipartition between the magnetic field and the energetic particles (Tsuboi et al. 1986, $\sim 10\,\mu$G), Faraday rotation (Tsuboi et al. 1985, $\sim 10\,\mu$G), dynamical arguments (Yusef-Zadeh & Morris 1987a, $\gtrsim$ 1 mG), Zeeman splitting measurements in dense neutral regions (Schwarz & Lasenby 1990; Marshall et al. 1995; Uchida & Guesten 1995; Crutcher et al. 1996, $\sim$ 1 mG). In general, the methods that assume equipartition or minimum-energy field strengths give an intensity of the magnetic field of $\sim 50 - 200\,\mu$G, which likely underestimates the true field strengths probably because the NTFs appear to be dominated by magnetic fields. The strength deduced by the dynamical condition of $P_{\rm mag} \gtrsim P_{\rm ram}$ gives a value of $\sim$ 1 mG. Another open question is whether the strong field is limited to the NTFs or is pervasive troughout the CMZ. LaRosa et al. (2005) image the GC at 74 MHz and 330 MHz revealing a source of $6^\circ \times 2^\circ$ of diffuse nonthermal synchrotron emission centered in the GC. A minimum-energy analysis of this emission yields a magnetic field strength of $6(\phi/f)^{2/7}\ \mu$G (where ϕ is the proton to electron energy ratio and f is the filling factor of the synchrotron emitting gas). They noted that even with extreme data combination ($\phi \simeq 100$, and $f \simeq 0.1$) any pervasive magnetic field must be of the order of 10 μG or weaker, at least at scales of 125″ ($\gtrsim$ 5pc), and does not prevent locally strong magnetic field at smaller sizes scales (See Ferrière 2009, for a review of the magnetic field in the GC region).

Interstellar dust grains tend to spin about their small axes and to align their axes along the local magnetic field. The dust grains emit polarized thermal radiation at far-IR and submm wavelengths. By observing the dust grain emission at these wavelengths it is inferred a magnetic field parallel to the galactic plane and perpendicular to the large scale intercloud field revealed by NTFs (Aitken et al. 1986, 1991; Davidson 1996; Novak et al. 2000; Chuss et al. 2003). The dust grains absorb starlight at optical and near-IR wavelengths. While the optical starlight is completely absorbed before reaching us, the NIR starlight suffers only partial extinction, and we can detect it linearly polarized in the direction of the magnetic field. Therefore this technique is used to trace the average magnetic field in the plane of the sky towards the GC. While FIR/submm observations indicate that the magnetic field direction depends on gas density (Chuss et al. 2003), the NIR results shows that the field appears to be everywhere horizontal, including in the diffuse ISM (Nishiyama et al. 2009, 2010, see Fig. 1.4).

The tidal shear and Galactic rotation deform the molecular clouds and therefore the magnetic field lines. This effect would explain the orthogonality of both magnetic field components. Because of the tidal shear, clouds envelopes tend to get stretched into tidal streams that may subtend a large angle at the GC. Therefore, the magnetic field

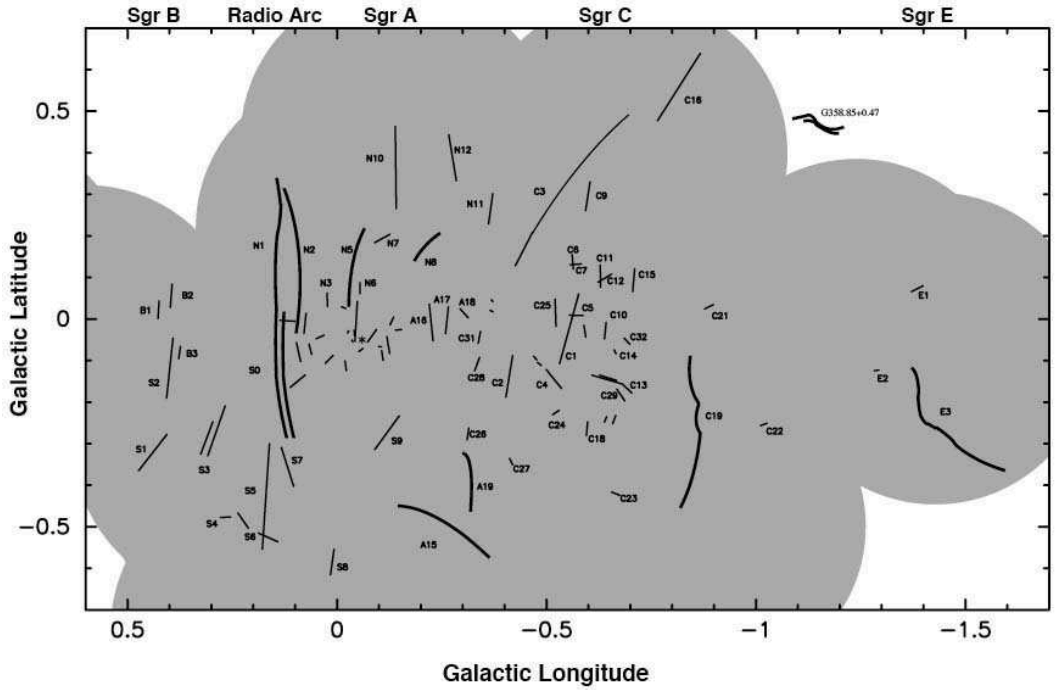

Figure 1.3: Schematic map of the NTFs (From Yusef-Zadeh et al. 2004)

in the molecular clouds, presumably "flux-frozen" to the partially ionized molecular clouds, will be deformed in an azimuthal configuration, with the field lines oriented along the direction of the shear (Tsuboi et al. 1999). So far there is little evidence that the cloud and intercloud environments are magnetically coupled to each other. The other option is that the cloud is "anchored" to the non-rotating Galactic halo, or it arcs back to the Galactic plane at large radii and is anchored there. In either case, the field lines do not rotate with the CMZ, and the molecular cloud move thought the field with a large velocity.

1.2.3 Star formation

The star formation in the GC occurs in the peculiar molecular environment described above (high density, high thermal pressure, strong gravitational tidal field). These physical properties, unique in the Galaxy, influence the characteristics of the star formation, which is also affected by the inflow of molecular material from further out in the Galaxy (Morris & Serabyn 1996; Figer 2009). The collapse of the molecular clouds by self-gravity is bothered by the strong tidal force near the nucleus, so that it is only possible for molecular clouds with densities $> 10^4(75\ \mathrm{pc}/\mathrm{R_{GC}})^{1.8}\ \mathrm{cm}^{-3}$, where R_{GC} is the galactocentric radius (Güsten & Downes 1980).

In spite of these conditions in the GC, stars are actually forming. The present-day star formation is strong in Sgr B2, which is the most intense star formation site in the Galaxy (see review from Figer 2009, and references therein), which in the next few Myrs will form a stellar cluster comparable in mass to the Arches cluster (see below).

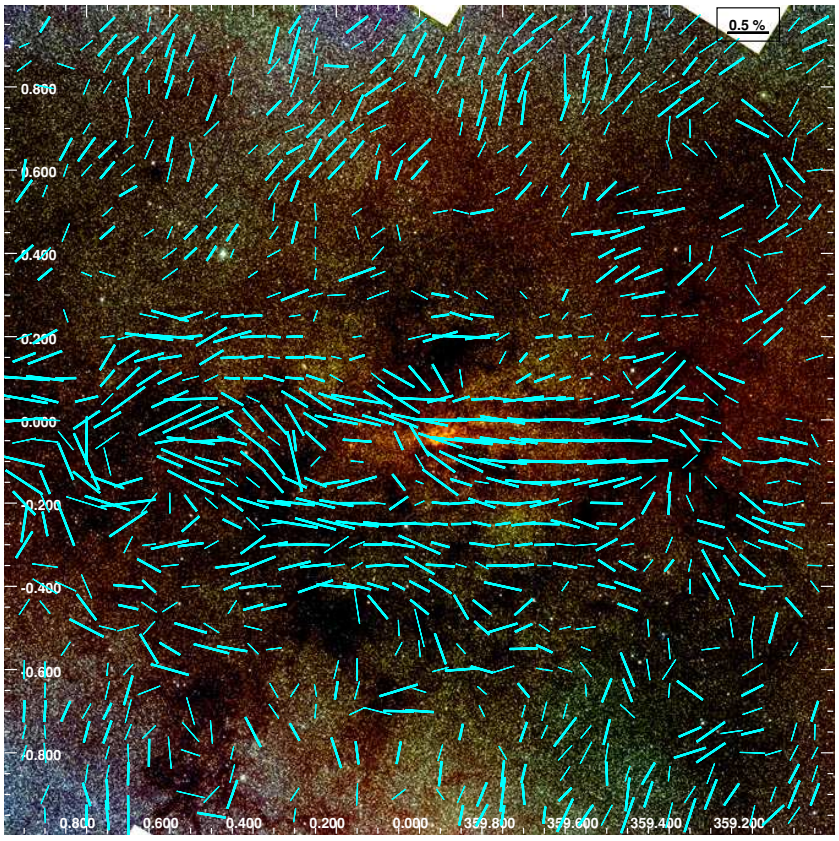

Figure 1.4: NIR mosaic image of the Galactic center region covering 2° ×2° in the GC region. The three NIR bands are J (blue, 1.25μm), H (green, 1.63μm), and K_S (red, 2.14μm). Observed E vectors of polarization for the Galactic center components in the K_S band are also plotted with cyan bars whose length indicates the degree of polarization (Fig. from Nishiyama et al. 2010)

Cloud-cloud collision may be the cause of the intense star formation in this region (Sato et al. 2000). On the contrary, towards the central 50 pc of the Galaxy, there are just a dozen of ultra-compact H II regions and O-stars still embedded in their natal environs. Also, there is evidence for a continuous and persistent star formation activity in the GC from the presence of asymptotic giant branch stars throughout the GC region, and the analysis of the photometry of the field population in the GC (see Fig. 1.5).

The star formation over the last 10 Myrs is dominated by the three outstanding massive stellar clusters: The Central, the Quintuplet, and the Arches (see Fig. 1.6). They are all young, but the Quintuplet and Central clusters are about twice the age of the Arches cluster. Each contains $\gtrsim 10^4$ $M_\odot$ in stars. They have very high central stellar mass densities, up to nearly 10^6 $M_\odot$ pc^{-3} (exceeding central densities in most globular clusters). They have luminosities of 10^{7-8} $L_\odot$, and are partly responsible for heating nearby molecular clouds. They also generate 10^{50-51} ionizing photons per second, which are enough to account for nearby giant H II regions.

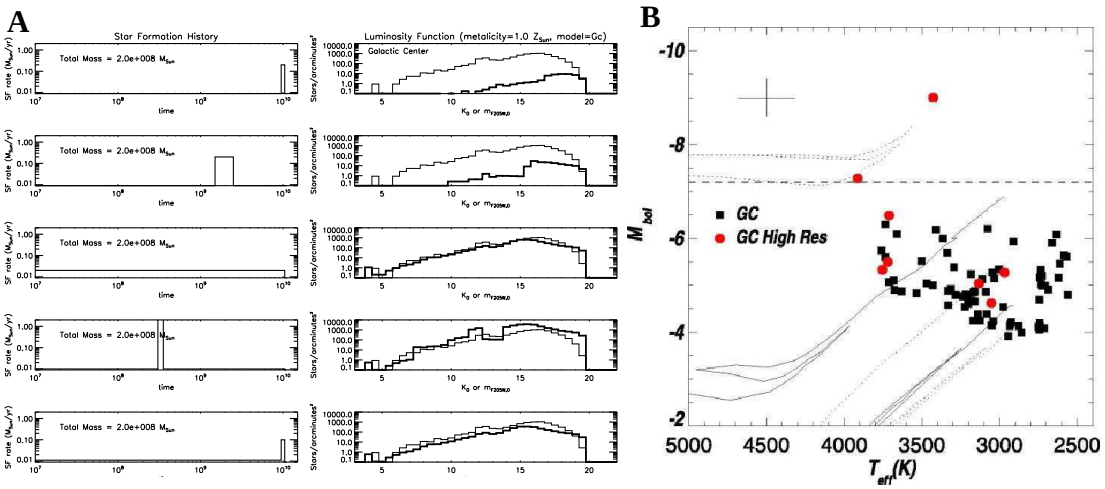

Figure 1.5: A. Figure from Figer (2009) showing various star formation scenarios (left), and resultant model luminosity functions (right, thick) compared to observed luminosity functions (right, thin) in the GC. The third panel from the top, i.e. continuous star formation, best fit the data. B. Estimates of absolute magnitude versus temperature for stars in the GC. The presence of supergiants (above the horizontal line) demonstrates intermediate age star formation of massive stars. Figure from Figer (2009) but original from Blum et al. (2003).

The Central cluster is formed by at least 80 massive stars, including $\sim$ 50 OB stars on the main sequence and $\sim$ 30 more evolved. In this cluster, there is a dense collection of stars known as "s-stars". Their proper motions are consistent with closed orbits surrounding a massive, and dark, object having $2 - 4 \times 10^6$ $M_\odot$ (Schödel et al. 2003; Ghez et al. 2005).

The Quintuplet, with an aye of 4 Myrs and an initial mass of $> 10^4$ $M_\odot$, contains more than 30 evolved stars. The Quintuplet heats and ionizes the nearby Sickle HII region. This cluster receives its name for its five very bright stars, which are called the Quintuplet Proper Members (QPM), which are yet spectroscopically featureless, making their spectral classification ambiguous. Tuthill et al. (2006) show that the QPMs are dusty Wolf-Rayet[7] stars and presumably binaries. This cluster also contains two Luminous Blue Variables, one is known as the Pistol star, and the other is FMM362. The Arches cluster is young (2 Myrs) and massive (10^4 $M_\odot$), and contains the richest collection of O-stars and Wolf-Rayet stars in any cluster in the Galaxy. The most massive dozen or so members of the cluster have strong emission lines at infrared wavelengths which are produced in strong stellar winds that are also detected at radio wavelengths and x-ray emission (Figer 2009).

The initial mass function (IMF) (the distribution of stellar masses at birth) in the GC presents a slope more flattened than the Salpeter value (Figer et al. 1999; Stolte et al. 2003), but some authors argue that this effect is due to dynamical evolution, i.e.,

[7]Wolf-Rayet stars are evolved, massive, very hot (50000 K) and very luminous ($10^5 - 10^6$ $L_\odot$) stars which undergo heavy mass loss

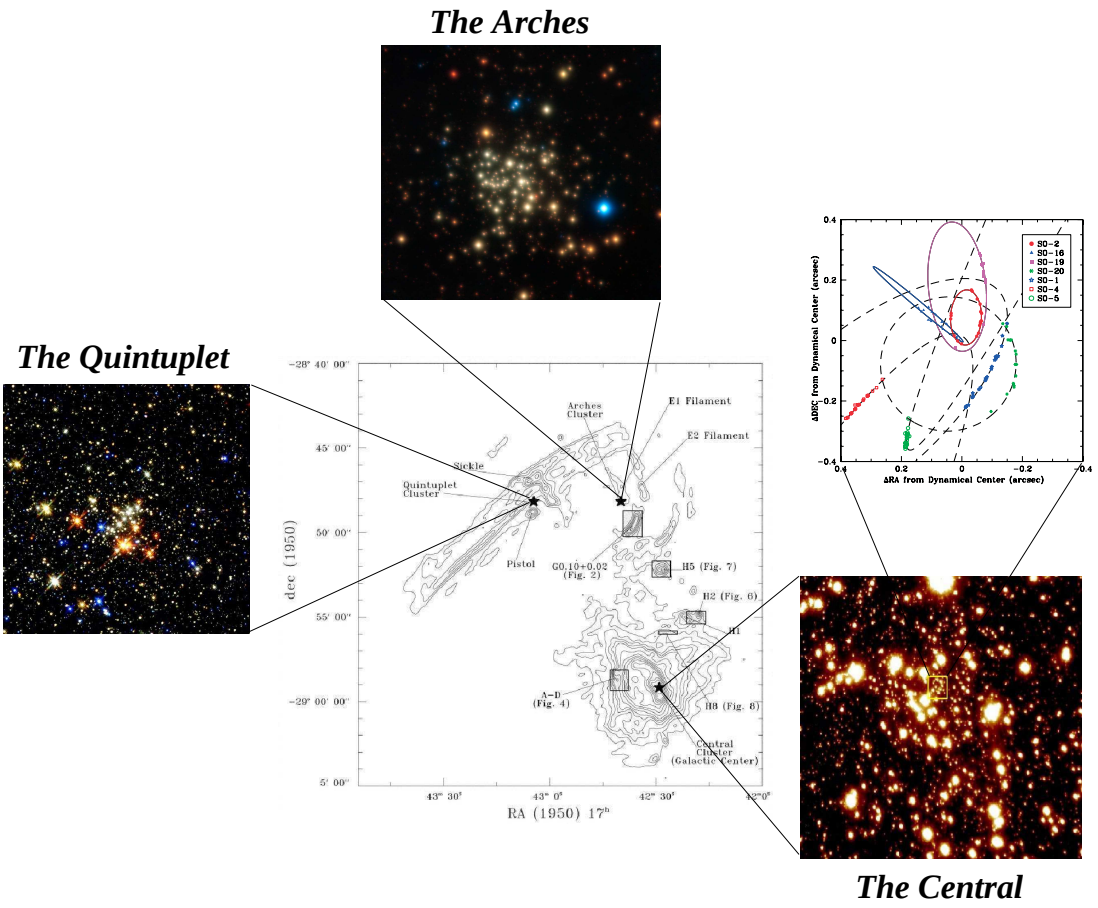

Figure 1.6: Stellar cluster of the GC. Central: Radio emission from the GC region at 6 cm (Yusef-Zadeh & Morris 1987a). Left: The Quintuplet cluster (Figer et al. 1999). Top: The Arches cluster (Figer et al. 1999). Right: The Central cluster Figer (2009). The upper figure shows the proper-motion measurements of the s-stars (see text for details) (Ghez et al. 2005).

the slope was the standard value at the beginning but flattened at the present-day (Portegies Zwart et al. 2003). The upper mass cutoff is 150 $M_\odot$ (Figer 2005), and the lower mass cutoff is 6 $M_\odot$ (Stolte et al. 2005). The star formation rate, which is obtained assuming a normal IMF, is about $0.3 - 0.6$ $M_\odot$ yr^{-1} (Güsten 1989), but if we consider that high mass stars are favored by the molecular environment, the star formation rate would be even lower. Güsten (1989) gives a lower limit which is 0.05 $M_\odot$ yr^{-1}. Yusef-Zadeh et al. (2009); An et al. (2011) published a range of values for the star formation rate in the CMZ from $0.07 - 0.15$ $M_\odot$ yr^{-1}, and recently Immer et al. (2011) obtain for the CMZ a star formation rate of 0.08 $M_\odot$ yr^{-1} which is based on a Kroupa IMF (Kroupa 2001).

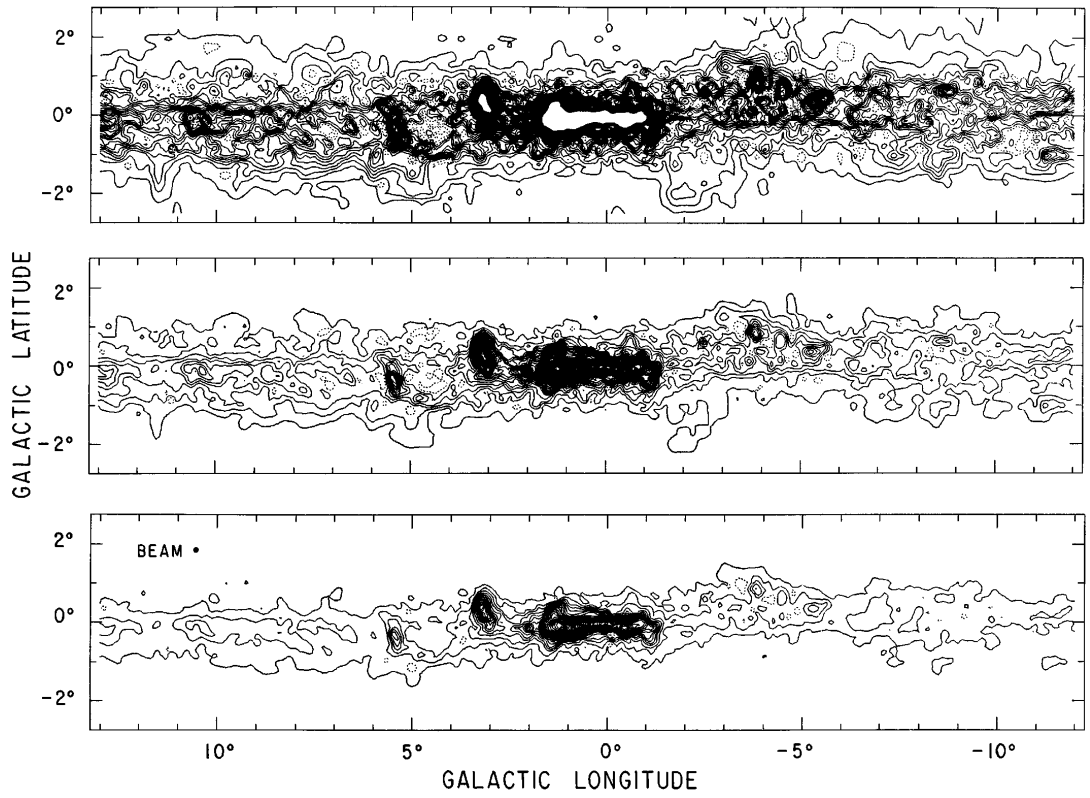

Figure 1.7: Spatial distribution of CO line intensity ($\int T_A^* dv$) integrated over the velocity range −320 to 320 km s^{-1}displayed in three different contour levels (at 13, 32.5, 65 K km s^{-1}, which correspond to 4σ, 10σ, and 20σ). The Galactic center region ranges from $l \sim -5°$ to $l \sim 5°$. Figure from Bitran et al. (1997)

1.3 Galactic Center Molecular Components

Throughout this thesis, we refer to the "Galactic center region", the ~ 1.5 central kpc of the Galaxy ($-5° \lesssim l \lesssim 5°$). Fig. 1.7 shows the spatial distribution of CO line intensity ($\int T_A^* dv$) integrated over the velocity range −320 to 320 km s^{-1}(Bitran et al. 1997). Inside this region, there is a large compact and luminous nuclear region, known as the "Central Molecular Zone" (CMZ, Morris & Serabyn 1996) which produces 5 – 10% of the infrared and Lyman continuum luminosities of the Galaxy and harbors ~ 10% of the molecular gas in our Galaxy.

Still in the central kpc but outside of the CMZ, there are several giant molecular clouds, which have received less attention than the CMZ in previous studies. Those molecular clouds were called by us as the "Peripheral Molecular Zone" (PMZ), and they correspond to the five molecular clouds with large CO luminosities and large linewidths observed by Bitran et al. (1997).

1.3.1 The Central Molecular Zone (CMZ)

The CMZ was defined by Morris & Serabyn (1996) and corresponds to the region placed in a radius of $\sim$ 200 pc from the center, where the gas is mainly molecular ($\sim$ 90%, Ferrière et al. 2007) with high densities of $n(H_2) \gtrsim 10^4\,cm^{-3}$, a high surface density (several hundred $M_\odot\ pc^{-2}$), H_2 molecular mass of $1.9 \times 10^7\ M_\odot$, H I mass of $1.7 \times 10^6\ M_\odot$ (Ferrière et al. 2007). The CMZ was modeled by Ferrière et al. (2007) as a 500 pc $\times$ 300 pc ellipse, centered on $(x_c, y_c) = (-50\,pc, 50\,pc)$ and inclined clockwise by 70° to the line of sight (see Fig. 1.9). The high densities are required to withstand tidal shearing. The high surface density and the high mass suggest mass concentration due to inflow from larger radii (see Morris & Serabyn 1996, and references therein). LaRosa et al. (2000) present a λ = 90 cm continuum image (see Fig. 1.8) of the CMZ obtained using the Very Large Array (VLA), which is sensitive to the thermal and non-thermal emission, giving us a perspective of the large scale radio structure of the CMZ.

The distribution of the molecular gas in the CMZ has the following characteristics: 3/4 of the dense molecular gas is located at positive longitudes, 3/4 is at positive velocities, and about 30% of the gas shows large radial and vertical motions (Bally et al. 1988). Fig 1.11 shows the kinematics of the molecular gas. It is possible to divide the kinematics (see §1.4) of the molecular gas in two components: a high velocity component ($130 - 200\ km\,s^{-1}$) and a lower velocity component ($< 100\ km\,s^{-1}$). In this second velocity component, there is a population of dense and massive molecular clouds close to the true Galactic plane, called the "Galactic center disk population" (Bally et al. 1988; Heiligman 1987), which includes the known Sgr A, B, C, E, D molecular complexes (the neutral counterparts of the continuum structures seen in Fig. 1.8) and filament-like clouds with coherent velocity gradients over scales of 30–100 pc, suggestive of dust lanes and tidally stretched arcs or arms of gas (see, e.g., Morris & Serabyn 1996, and references therein). The following molecular structures are identified in our large scale survey in SiO, HCO^+ and $H^{13}CO^+$ molecular lines emission (see §3).

1.3.1.1 Sgr A region

Placed at $l \sim 0°$, the Sgr A complex has been extensively studied in radio-continuum and molecular emission identifying several components. Fig. 1.10 shows a sketch of the 12 central pc of the Galaxy from the recent molecular study of this region by Amo-Baladrón et al. (2011). Sgr A is formed by three components: the ***Sgr A West*** H II region, with a minispiral morphology that seems to be feeding the nucleus (Lo & Claussen 1983; Roberts & Goss 1993), which is centered more or less on the central stellar cluster; the nonthermal shell source supernova remnant (SNR) ***Sgr A East***, which is offset from the center, but lies behind or contains Sgr A West; and a strong compact source of nonthermal emission ***Sgr A****, visible in the continuum map (Yusef-Zadeh & Morris 1987a), and where a supermassive ($4 \times 10^6\ M_\odot$, Ghez et al. 2005) black hole is present as deduced by the dynamical study of the orbiting stars (Genzel et al. 2000).

A ring of molecular gas and dust is surrounding Sgr A West, (kown as the Circunnuclear Disk, CND, Becklin et al. 1982; Guesten et al. 1987), whose inner edge suffers UV-photoionization (Roberts & Goss 1993) due to a dense stellar population of massive stars in the central cluster (Krabbe et al. 1995; Figer 2009) . The molecular

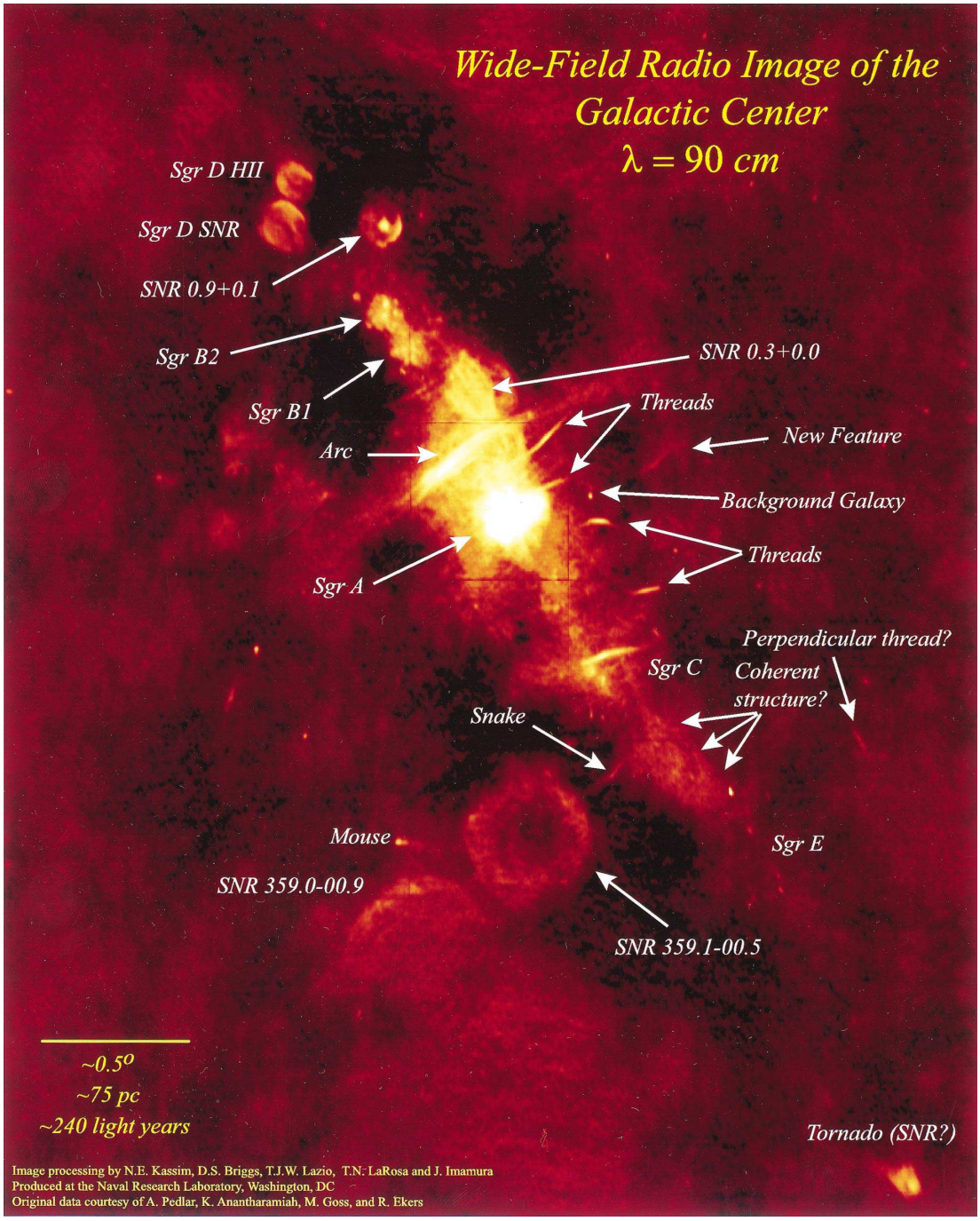

Figure 1.8: 90 cm continuum image of the GC region. The image is centered in Sgr A covering an area of $4° \times 5°$ with an angular resolution of 43″ (LaRosa et al. 2000)

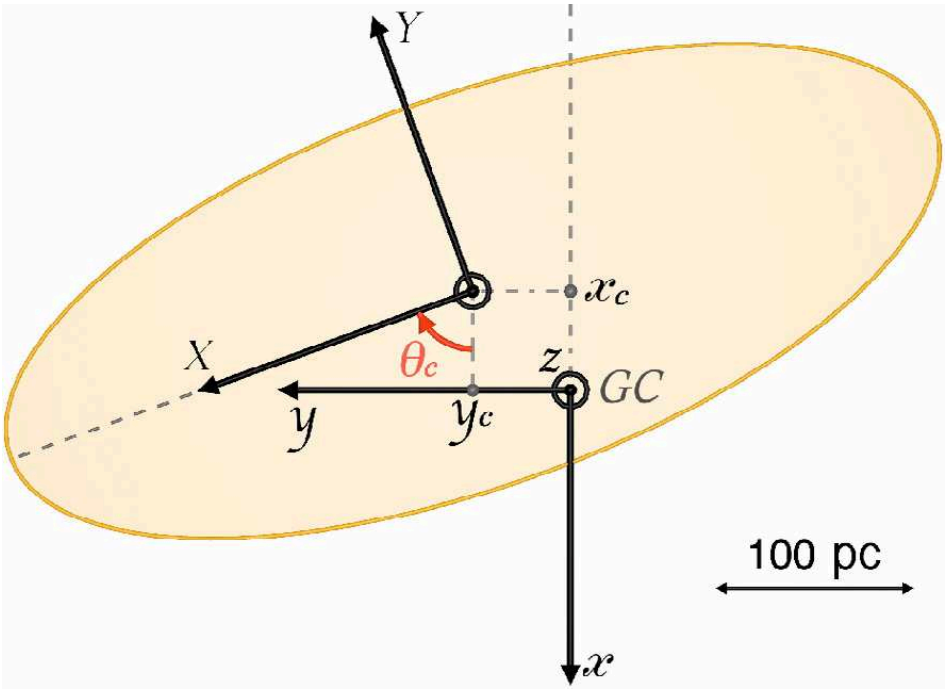

Figure 1.9: Face-on view of the model of the CMZ by (Ferrière et al. 2007). (x, y, z) are the Galactocentric coordinates and (X, Y) the CMZ horizontal coordinates. The CMZ is elliptical, 500 pc × 200 pc in size, centered on $(x_c, y_c) = (-50\text{pc}, 50\text{pc})$ and inclined by $\theta_c = 70°$ to the line of sight.

complexes M−0.13−0.08 and M−0.02−0.07 dominate the surrounding of Sgr A*, which correspond to the 20 km s^{-1} and 50 km s^{-1} clouds and are probably feeding the CND. Both clouds are connected by a ridge of compressed gas and dust that warps around SNR Sgr A East.

The Non Thermal Filament (The Arc) The Arc is the feature seen in Fig. 1.8 placed at ∼ 50 pc in projection from Sgr A perpendicular to the Galactic plane at $l \sim 0.17°$. This structure is resolved into a large number of narrow linear features by Yusef-Zadeh et al. (1984), which show strong polarization with no line emission and emitting strong nonthermal synchrotron radiation, most likely magnetic flux tubes filled with relativistic electrons. Several prominent H II regions cross and appear to interact with the Arc filaments, which suggests particle acceleration via magnetic reconnection between a large-scale magnetic field and molecular cloud magnetic fields (Serabyn & Morris 1994). The Arc seems to interact with a thermal continuum source called "The Sickle" (G0.18−0.04). Yusef-Zadeh & Morris (1987b) pointed out that most of the

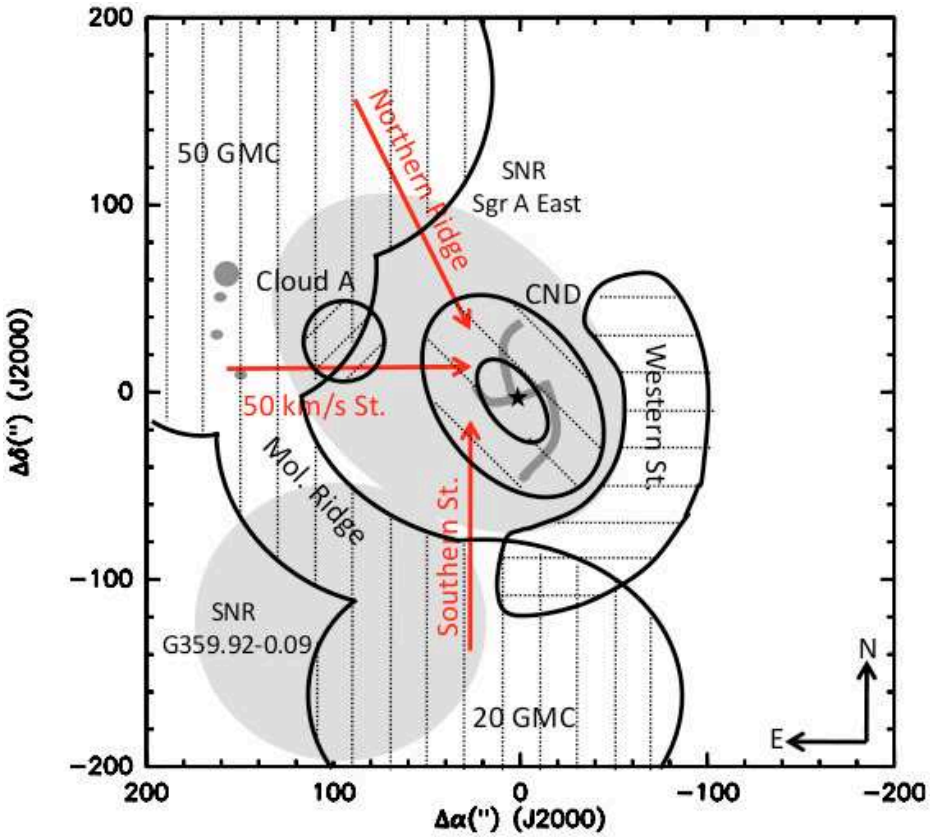

Figure 1.10: Sketch of the 12 central parsecs of the Galaxy. Gray regions represent radio continuum features. Big ellipses correspond to the SNRs Sgr A East and G359.92-0.09, the central minispiral to the HII region Sgr A West, and the four little circles to the Sgr A East compact H II regions. The central star represents Sgr A*. Molecular gas features are represented by stripped regions, whereas red arrows toward the center point out the possible connections between the CND (the elliptic disk) and the giant molecular clouds of this region (Amo-Baladrón et al. 2011)

nonthermal filaments of the Arc undergo abrupt discontinuities where they encounter the ionized ridge of G0.18−0.04, and Serabyn & Guesten (1991) demonstrated that this H II region lies at the surface of a relatively massive molecular cloud.

1.3.1.2 Sgr B region

Sgr B is the most massive molecular cloud in the Galaxy. It is placed at $l \sim 0.6°$ and it contains the complexes Sgr B1, Sgr B2, and G+0.6-0.0.

The Sgr B1 is a massive star forming region placed at $(l, b) = (0°.5, 0°.0)$. The emission from Sgr B1 arises from a wealth of extended bright rim and shell-like structures. One of these features is a bar of ionized gas approximately 6 pc in length. The presence of these large structures might be the result of individual compact HII regions that have expanded and coalesced over time, which suggests that Sgr B1 is evolved

(Mehringer et al. 1993a). The expansion of a molecular shell of 30×40 pc suggests an age of $\sim 10^6$ years (Sofue 1990). Sgr B1 also has four compact H II regions, which might suggest that although this complex is evolved, the process of star formation is ongoing. However, there is no evidence to ensure that Sgr B1 is young, because the maser emission found there is characteristic of evolved stars or low-mass star forming regions (Mehringer et al. 1993a).

Placed at about 100 pc from the center, Sgr B2 is a very massive ($> 5 \times 10^6$ $M_\odot$, H_2 column density $> 10^{24}$cm^{-2}, Lis & Goldsmith 1990) and well-studied molecular cloud complex which contains multiple centres of spectacular star formation activity, as indicated by a giant H II region with many compact and ultra-compact H II regions (Mehringer et al. 1993b; Gaume et al. 1995), and by the maser emission from water, hydroxyl, formaldehyde, and methanol (McGrath et al. 2004; Gaume & Claussen 1990; Mehringer et al. 1994; Caswell 1996; Mehringer & Menten 1997). Several O-type stars are needed to account for the high far-IR luminosity of $\gtrsim 10^7$ $L_\odot$. The main recent star formation complexes are, from north to south, Sgr B2(N), Sgr B2(M) and Sgr B2(S). All have prominent radio , millimeter and sub-millimeter (Gordon et al. 1993; Pierce-Price et al. 2000) and infrared (Goldsmith et al. 1992) continuum emission. Sgr B2(N) is extremely rich in complex molecules. The densest core emits at around $v_{\rm LSR} = 60 - 65$ km s^{-1}, but there is a "hole" in the CO and CS emission around $v_{\rm LSR} = 40 - 50$ km s^{-1} in this area, which has been attributed to a collision between the $v_{\rm LSR} = 40 - 50$ km s^{-1} cloud and a cloud at $v_{\rm LSR} = 70 - 80$ km s^{-1}, triggering the star formation activity. For a complete and recent map of Sgr B2 in multiple 3-mm molecular lines, see Jones et al. (2008).

The region G0.6 − 0.0 lies between Sgr B1 and Sgr B2 and contains at least four compact sources. Because its velocity is intermediate between Sgr B1 and Sgr B2, and an arc of emission to the east and south of these compact components seems to bridge both complexes, it is thought that these regions are physically related (Mehringer et al. 1995).

1.3.1.3 Sgr C region

Placed at $l \sim -5.5°$, Sgr C shows signs of current star formation traced by masers, and compact and evolved H II regions with stars of type B0 and earlier (Liszt & Spiker 1995). The molecular mass is $\sim 5 \times 10^5$ $M_\odot$ (Liszt & Spiker 1995; Lis & Carlstrom 1994), the average density n(H_2) $\sim 6 \times 10^3$ cm^{-3}, and the column density of H_2, N(H_2) $\sim 2 \times 10^{23}$ cm^{-2}.
This region also has bright non-thermal radio filaments (see §1.2.2). There is one large NTF that highlights from the others due to the similarity with the "Arc", where also it is found a thermal source perpendicular to the NTF (as in the Arc). It is though that the filament could be associated with a molecular cloud (Bally & Yusef-Zadeh 1989), which is observed in several molecules and in the 800 μm continuum (Lis & Carlstrom 1994).

1.3.1.4 Sgr D region

The radio continuum Sgr D complex is placed at $l \sim 1.1°$, and it is formed by two extended sources. As we can see in Fig.1.8 the northern source correspond to a compact

H II region sourrounded by an halo of diffuse emission (Liszt 1992; Mehringer et al. 1998), and the southern is a SNR. Close to Sgr D at $(l, b) = (0.9^\circ, 0.1^\circ)$ there is another SNR. The molecular emission associated with the Sgr D complex extends to $l \sim 1.6^\circ$ (Dahmen et al. 1997) or to $l \sim 1.9^\circ$ (Bally et al. 1988), but due to the wealth of this molecular emission we discuss it separately.

1.3.1.5 Sgr E region

Towards the negative longitude edge of the CMZ we found a radio continuum source called Sgr E ($l \sim -2.2^\circ$). Sgr E is a complex of molecular clouds and H II regions where the star formation is ongoing. The molecular gas has a velocity of $v \sim -210$ km s^{-1}. This region probably indicates the outer south boundary of the nuclear ring of star formation in the Galaxy (Liszt 2006). In this thesis, we observe up to $l \sim -1.5^\circ$, but the molecular gas at longitudes $-1 < l < -1.5$ has a velocity component of ~ -200 km s^{-1}, therefore we assume that this gas is associated to the Sgr E region.

1.3.1.6 l =1.3° Complex (also referred as l =1.5° complex Bally et al. 1988; Oka et al. 2001)

This unusual cloud complex belonging to the CMZ, shows broad velocity line widths and a large latitudinal scale height. It is rich in shells and arcs of dense molecular gas. In the survey of CO(3 − 2), CO(1 − 0), HCN(1 − 0), HCO$^+$(1 − 0), SiO(1 − 0) and (2 − 1) carried out with ASTE and Nobeyama 45m telescopes, Tanaka et al. (2007) found an enhancement in the CO (3-2)/CO(1-0), HCN/CO, HCO$^+$/CO intensity ratios in the gas with a LRS velocity higher than 110 km s^{-1}. Also they identified 9 expanding shells in HCN maps, and compact SiO features associated with the shells which are clearly seen in the high velocity range ($v_{\rm LSR} \geq 110$ km s^{-1}). They derive mass, kinetic energy and kinematical age of the turbulent gas traced by SiO, obtaining huge kinetic energies of $10^{52.6-53.0}$ ergs. Stellar winds from Wolf-Rayet stars are not sufficient to furnish such kinetic energy, even for a single shell (Oka et al. 2001). Candidates are SN or Hyper Nova (HN) explosions. The high SiO abundance in this complex has been attributed to these explosive events, and/or cloud collisions related to the large scale gas motion in the bar potential (Hüttemeister et al. 1998).

1.3.2 The Peripheral Molecular Zone (PMZ)

Most of the molecular surveys of the GC missed the molecular clouds outside the CMZ. To understand the physical properties of the molecular clouds in the GC, it is needed to study also these outstanding molecular clouds.

1.3.2.1 M+3.2 − 0.3 cloud (Clump 2)

The molecular feature placed at $l \sim 3.2^\circ$, $b \sim +0.4^\circ$ and $v_{\rm LSR} = 0-200$ km s^{-1} discovered by McGee (1970), was called Clump 2 by Bania (1977). This molecular cloud has been observed in many molecular lines by several authors (e.g., CO, ^{13}CO, CS, HNCO, H_2CO, HCN, Stark & Bania 1986; Bally et al. 1988; Boyce & Cohen 1989; Zylka et al. 1992; Lee & Lee 2003, among others). The CO linewidth reaches ~ 100 km s^{-1}, probably one of the largest linewidths of an interstellar cloud in the Galaxy. From ^{13}CO and

CS observations, Stark & Bania (1986) concluded that the large linewidth is due to the superposition of 16 CS emitting cores (having densities $> 2 \times 10^4$ cm^{-3}, and mass of $\gtrsim 5 \times 10^5$ M$_\odot$) gravitationally bound and approximately virialized, but the complete molecular cloud would be not bound. The complex contains mostly positive velocity components permitted by the Galactic rotation and few forbidden negative velocities components. From HCN observations, Lee & Lee (2003) estimated a total mass of $\sim 3.3 \times 10^6$ M$_\odot$.

1.3.2.2 M$-5.3 + 0.4$ cloud (Clump 1)

The molecular cloud at $l \sim -5.5°$ with a velocity $v_{\rm LSR}$ of 100 km s^{-1} was called by Bania (1977) "Clump 1". This molecular cloud was seen in even the earleast 21 cm H I surveys of the GC region (Rougoor & Oort 1960; Rougoor 1964). From CO and ^{13}CO observations, the Clump 1 was decomposed in three large molecular clouds at velocities of $v_{\rm LSR} \sim 68$, 85 and $100\, km\, s^{-1}$ (Bania et al. 1986), where each cloud in the complex are gravitationally bound. The cloud at $v_{\rm LSR} = 100$ km s^{-1} is heated by the HII region G355.67+0.25. Bania et al. (1986) estimate for the Clump 1 a size of 42×72 pc and a molecular H_2 mass of $2.4 \pm 1.5 \times 10^5$ M$_\odot$ from the ^{13}CO data. This molecular cloud (at a negative longitude, where positive velocities inside the solar circle are forbidden) presents the largest noncircular velocity of any Milky Way cloud in many molecular lines (CO, Bania et al. 1986; ^{13}CO, Bania et al. 1986; Bally et al. 1987, 1988; H_2CO, Caswell & Haynes 1982;OH, Cohen & Dent 1983), which could be originated by the gravitational scattering of the barred potential in the GC (Lee et al. 1999). This cloud was identified as part of the 135 km s^{-1} arm (Bania 1980).

1.3.2.3 M$-4.4 + 0.6$ cloud

This molecular cloud is in a region that, from older low angular resolution surveys, was considered as almost "devoid of CO emission". Later, with the better resolution and sensitivity of the CO survey Bitran et al. (1997), it was shown that in this region there are important molecular complexes. According to Bitran et al. (1997), this cloud is placed at $(l, b, v) = (-4.4°\ , 0.6°\ , 72$ km s$^{-1})$

1.3.2.4 M$-3.8 + 0.9$ cloud

From the CO survey of Bitran (1987), this molecular cloud is at $(l, b, v) = (-3.8°\ , 0.9°$,-83 km s$^{-1})$.

1.3.2.5 M$+5.3 - 0.3$ cloud

Placed at $l \sim 5.5°$, this molecular cloud was observed in CO by Bitran et al. (1997), and later in HCN$(1 - 0)$ by Lee (1996). The velocity structure is simple, with most of the emission concentrated at the allowed Galactic rotation velocity of $v_{\rm LSR} \approx 30 - 150$ km s^{-1}), without forbidden velocity components. The molecular mass is $\sim 1.7 \times 10^6$M$_\odot$ (Lee 1996).

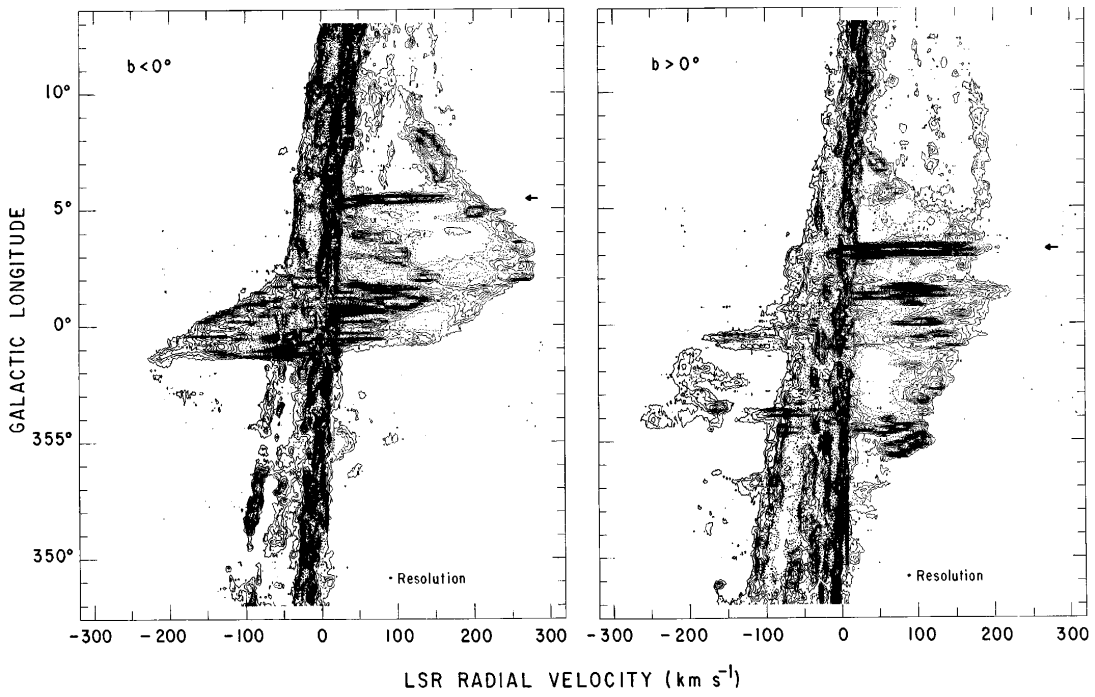

Figure 1.11: Longitude-velocity diagram of CO. The Galactic center region ranges from $l \sim -5°$ to $l \sim 5°$. Figure from Bitran et al. (1997)

1.4 Kinematics and Dynamics of the Molecular Gas

The shape of the longitude-velocity ($l - v$) diagrams shown by the HI and CO (Fig. 1.11) emissions has been matter of many studies for the last 40 years. The noncircular motions shown in those plots have been successfully explained by a stellar bar in our Galaxy (Binney et al. 1991), which is now well established by different methods, like photometry, kinematic studies of gas and stars, star counts (see review of Morris & Serabyn 1996, and references therein).

The broad velocity features observed in the $l - v$ plots have been also explained by the Giant Molecular Loops (GMLs) found by Fukui et al. (2006) in their large scale CO observations of the GC region. In the following, I will describe the response of the interstellar gas to a bar potential, and to the GMLs, and their role in the accretion of the gas towards the Galactic nucleus.

1.4.1 The Galactic bar potential

Any model trying to explain the observed distribution of the molecular emission should be able to account for the observed features, specially for the parallelogram

shape of the $l - v$ diagram (Fig 1.13.B), the forbidden radial velocity observed in the GC, and the large velocity widths of the molecular clouds. Models for the response of orbiting gas to a bar potential have been successful in explaining these features, in particular, the large deviations from circular motions and strong shocks (traced, e.g., by SiO, see §1.2.1.3). However, a quantitatively faithful model is still being sought.

As we mention before (see §1.3.1), the CMZ gas can be divided in two kinematic components: a high velocity component, which defines the parallelogram shape and was called *Expanding Molecular Ring* (EMR) or the *180-pc Molecular Ring* (see Fig. 1.12), and the lower velocity components which are the known molecular clouds (Sgr A... E). The EMR feature was seen in the early data and was interpreted as a radially expanding molecular ring surrounding the GC (Scoville 1972; Kaifu et al. 1972), produced by an explosive event in the center with an energy of 10^{55} erg, which could give a radial momentum impulse to $\sim 10^7$ $M_\odot$ of nearby gas (Bania 1977). There is little observational evidence (apart of the single plane defined by the EMR) that supports this scenario. Uchida et al. (1994a) related two molecular features to the interaction of the EMR with the ambient medium. One is a molecular structure associated with the FIR source AFGL 5376 at $(l, b) = (359.5, +0.43)$, which is a site of large scale (100 pc) shocks perpendicular to the plane, and the other is a vertical complex at $l = 1.2^\circ$. Uchida et al. (1994a,b) also note that when we exclude from the average the CO emission within 0.15° of the Galactic plane, the resultant $l - v$ plot reveals an elliptical envelope. Sofue (1995) argues that the EMR is indeed an expanding molecular shell with an oblate spheroidal shape which is pinched around its equatorial waist, because its expansion is hampered by the high density in the midplane of the CMZ (see Fig 1.12.C). This feature also has an explanation in the bar potential model, which offers a natural explanation for other gas kinematic characteristics too.

Binney et al. (1991) the kinematics of the GC can be accounted for by a barred potential, which allows to reproduce the H I, CO and CS emission in the region $|l| \leq 10^\circ$, $|b| \leq 0.5^\circ$. In their model, the bar has a corotation at $r = 2.4 \pm 0.5$ kpc, a semi-major axis arbitrarily adopted of $a_0 = 1.2$ kpc, axis ratios of 4:3:3, and is viewed at an angle of $\theta_{\rm inc} = 16 \pm 2^\circ$ from its major axis (see Fig. 1.13). The mass of the bar is $1 - 3 \times 10^{10}$ $M_\odot$ (Morris & Serabyn 1996).

In the presence of a bar, the gas follows closed and elongated orbits. The gas loses angular momentum which leads its fall towards less energetic inward nested closed orbits, producing gas accretion to the CG. Gas orbiting between the corotation radius and the Inner Linbland Resonance (ILR) of the bar pattern moves on the X1 orbits (Contopoulos & Mertzanides 1977), which are elongated oval orbits with the major axis aligned with the bar. When the ILR is approached, there is an innermost stable X1 orbit (Binney et al. (1991) propose that these orbits correspond to the 180-pc Molecular Ring), inside which these orbits become self-intersected or cusped. Any angular momentum loss by gas in the innermost stable X1 orbits leads to orbits crossing and shocks, and these shocks will produce an abrupt loss of angular momentum which causes the gas to fall inwards until it settle onto a new family of elongated orbits lying deeper in the potential, called X2 orbits, which are perpendicular to the bar (see Fig. 1.14).

The apocenter of the outermost X2 orbits graze the pericencer of the innermost X1 orbits, thus the angular momentum loss by the gas in the innermost X1 orbits (by viscous transport of angular momentum outwards or by orbits crossing near

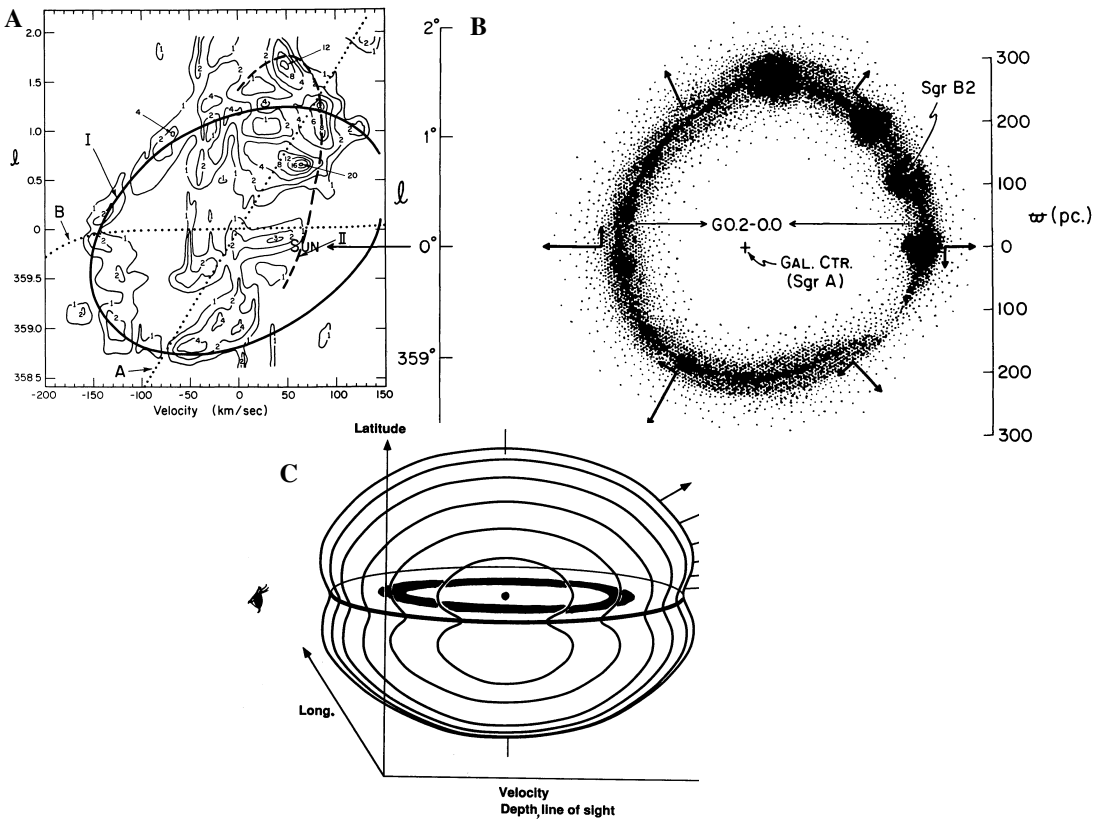

Figure 1.12: A and B: EMR model by Scoville (1972). C: EMR model by Sofue (1995)

the cusp) leads to shocks between gas in the X2 orbits, probably creating a spray producing shocks at the far side of the innermost X1 orbits and giving rise to the characteristic dust lanes that are observed near the leading edges of the bars in external galaxies (Binney et al. 1991; Athanassoula 1992; Jenkins & Binney 1994; Gerhard 1996; Rodriguez-Fernandez et al. 2006) (see Fig. 1.14).

The rate of the mass flow through the ILR (considering the mass on the EMR and that the gas cannot stay in the cusped orbits for more than one orbital period of 2×10^7 yrs) is $\dot{M}_{\rm ILR} \approx 0.1 - 1$ M$_\odot$. The mass budget of the GC gas reservoir is fed by gas that comes from bulge stars placed within 2 kpc with a rate of 0.07 M$_\odot$ yr^{-1} (Jenkins & Binney 1994) and from further out in the disk. The matter shed by the bulge stars does indeed have to migrate down to the Galactic plane without been lifted off by bulge winds.

The X2 orbits gather $\sim 85 - 90\%$ of the molecular mass available in the CMZ, therefore the residence time on these orbits is much longer than in the X1 orbits. However, gas in the X2 orbits is also subject to inward motions due to lose of angular momentum triggered by several mechanisms[8] which accrete mass to the center on

[8]bar-induced torques, dynamical friction, magnetic viscosity, shocks associated with the X1-X2 transition, viscous drag in the differentially rotating Galactic disk, including that resulting from cloud-cloud collisions, and dilution of the gaseous disk's specific angular momentum by stellar mass loss material

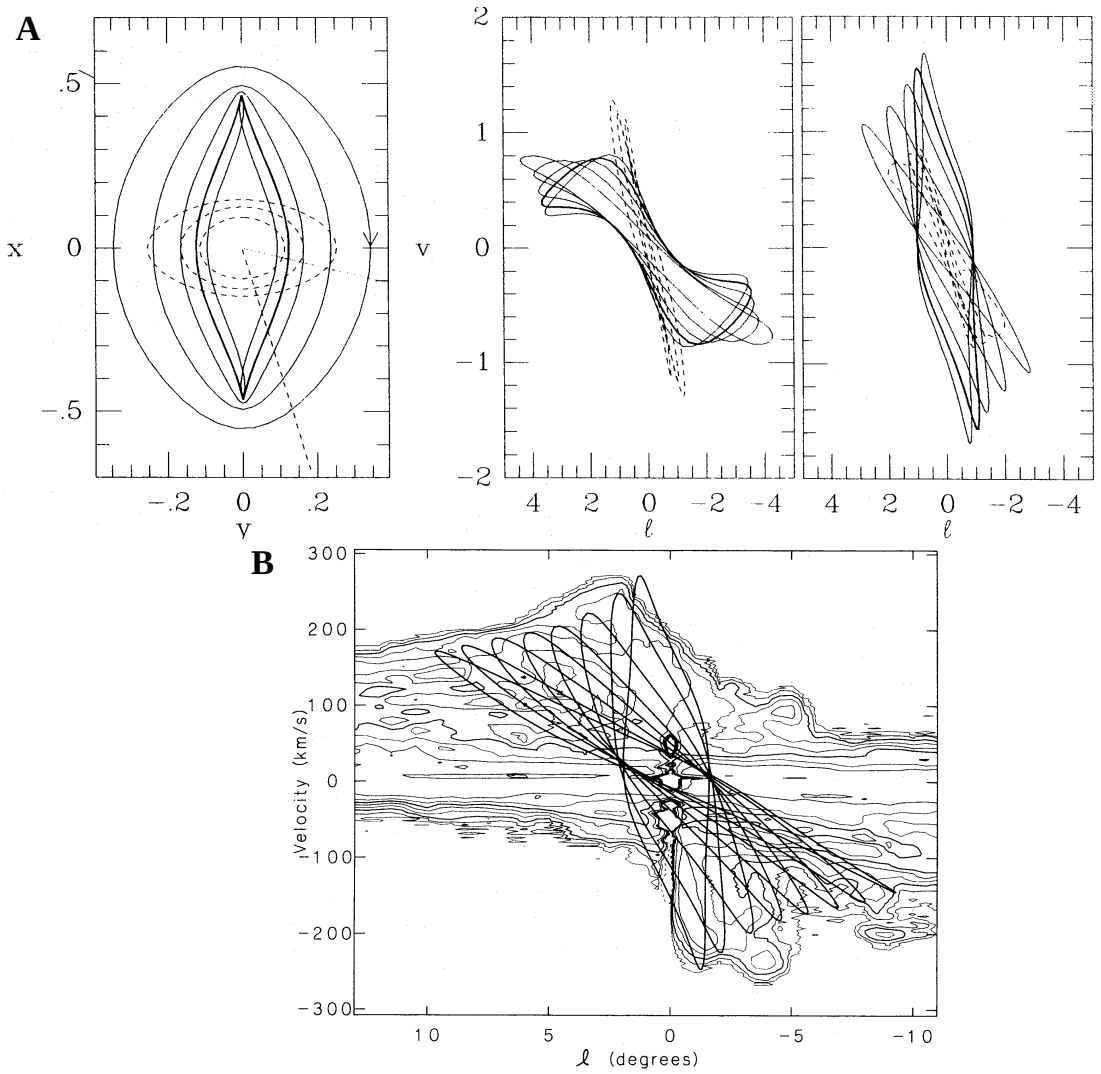

Figure 1.13: A) Closed orbits in the potential $\phi = \frac{1}{2}v_0^2 \ln(x^2 + y^2/q^2)$. Continuum lines represent the X1 orbits and dashed lines correspond to X2 orbits. B) The contours show intensity of 21-cm emission at $|b| < 0.5°$ from Burton & Liszt (1978). X1-orbits are shown from the potential of the density distribution $\rho(a) = (a/a_0)^{-1.75}$ if $a \leq a_0$ and $\rho(a) = (a/a_0)^{-3.5}$ if $a \geq a_0$ and $a_0 = 1.2$ kpc. (Binney et al. 1991)

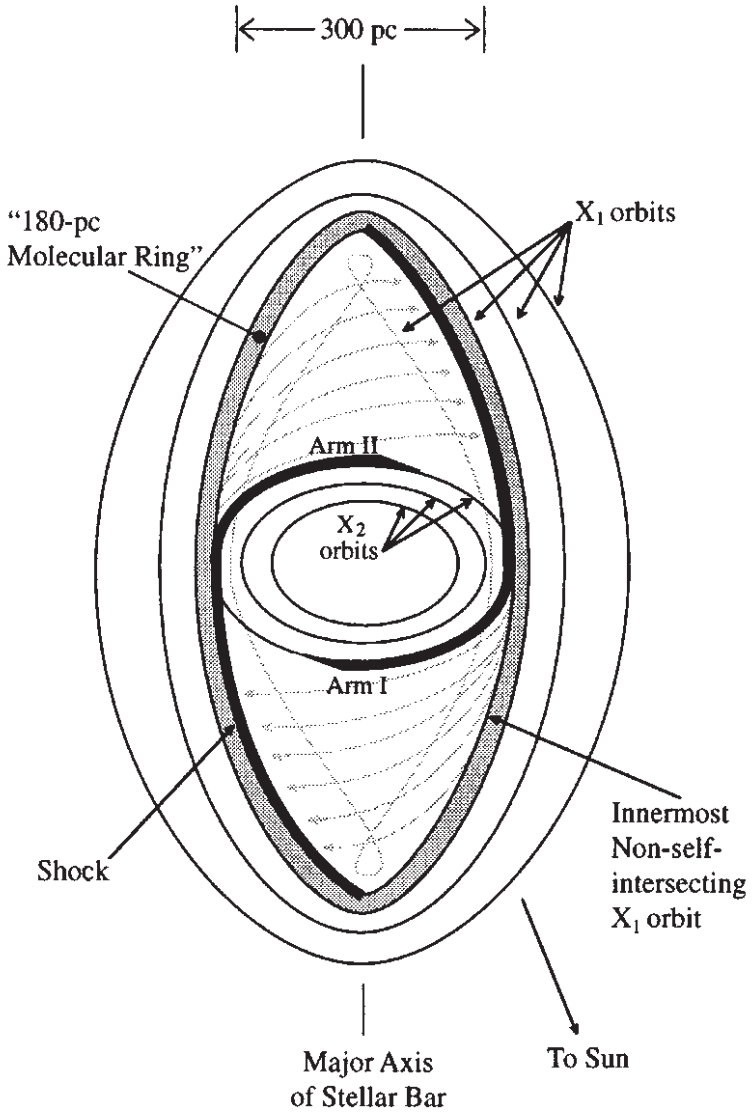

Figure 1.14: Sketch of the shapes and orientations of the X1 and X2 orbits and the features described in the text (from Morris & Serabyn 1996)

time scales much smaller than a Hubble time. The mean residence time for gas in the X2 orbits is $0.4 - 1 \times 10^9$ yrs assuming steady inflow, which is similar to that for dynamical friction to extract angular momentum from massive clouds. The gas moves inward from $\sim$ 150 pc at a mean rate of $0.2 - 2$ km s^{-1}, and will experiment mostly star formation, but also galactic winds or fountains and accretion into the circunnuclear disk (at a rate of $0.03 - 0.05$ M$_\odot$ year^{-1}.

The work of Binney et al. (1991) inspired many subsequent investigations. Jenkins & Binney (1994) simulated interstellar gas flows in the bar model of Binney, confirming the dynamical scenario described before, but failing to reproduce the pronounced

raining down out of the slowly rotating Galactic bulge (see Morris & Serabyn 1996, and references therein)

lopsidedness observed in CO data and to simultaneously explain the $l-v$ diagrams of CO and H I. Englmaier & Gerhard (1999) performed two-dimensional hydrodynamical simulations of gas flows in barred gravitational potentials to model the near-infrared luminosity distribution deduced from COBE/DIRBE data, and found an inclination angle for the bar of $\theta_{\rm inc} = 15 - 35 \pm 2^\circ$, with a preferred value of 20° . Taking into account this value, the semi-major axis of the bar is $a_0 \sim 2$ kpc, the axis ratios 5:3:2, and the corotation radius, $r_{\rm CR} = 3$ kpc. Bissantz et al. (2003) derive $\theta_{\rm inc} = 20^\circ$, $a_0 \sim 1.75$ kpc, axis ratios of 5:2:1.5 and $r_{\rm CR} = 3.4$ kpc, and they computed closed X1 and X2 orbits finding that the outermost X2 orbit does not reach out the cusped X1 orbits. Fux (1999) performed three-dimensional self-consistent simulations of the inner Galaxy, evolving at the same time the stellar bar (with a N-body code) and interstellar gas (with smoothed-particle hydrodynamics codes), and taking into account all the gravitational interactions. From the comparison between their synthetic and the previously observed CO and H I (l, b) diagrams, the author derives $\theta_{\rm inc} = 25\pm4^\circ$, $a_0 \sim 3.2$ kpc, $a : b = 5 : 3$ for its face-on axis ratio, $r_{\rm CR} = 4.0 \pm 0.5$ kpc, and obtain a size for the cusped X1 orbit of $\simeq 3.2 \times 1.3$ kpc, which is larger than the derived from previous works, and would imply that the cusped X1 orbits cannot correspond to the paralellogram in the (l, b) CO diagram. Fux (1999) propose that the paralellogram could corresponds to interstellar gas streams originating from the cusped orbit or from dust lanes connecting the cusped orbits to the X2 disk, and grazing the X2 disk. Their work solves the problem of the observed longitudinal asymmetry in the CO intensity maps, but opens new questions because the large extension of the cusped X1 orbits and the large corotation radius are difficult to reconcile with the deficit of gas observed between $r \sim 1.5 - 3$ kpc and with the Galactic disk starting at $r \sim 3.5$ kpc. Other effors to explain the asymmetry of the molecular distribution in the GC involve a second smaller bar as proposed by Combes (1996). Rodriguez-Fernandez et al. (2006) study the physical conditions of the clouds moving in noncircular orbits placed in different kinematic structures throughout the GC region (see Fig. 1.15), and support the presence of shocks influenced by the dynamics of the GC. Recently, Rodriguez-Fernandez & Combes (2008) proposed that the observed asymmetry of the CMZ can be due to infalling of gas in the 1.3° complex, which is supported by the clear signal of shocks found in this region (see e.g., Rodriguez-Fernandez et al. (2006); Hüttemeister et al. (1998), and Chapters §3, §4, and §5 of this thesis).

Molinari et al. (2011) imaged the central $2^\circ \times 2^\circ$ region of the GC at five photometric bands centered at 70, 160, 250, 350, and 500 μm using PACS (Photodetector Array Camera and Spectrometer) and SPIRE (Spectral and Photometric Imaging REceiver) instruments of *Herschel*, which trace the cold dust. They find a continuous chain of cold and dense clumps ($T_{\rm dust} > 20$ K, $N(H) > 2 \times 10^{23}$ cm^{-2}) organized along an $\infty-$shaped feature that dominates the image between the Sgr C complex and Sgr B2. The top view of this $\infty-$shaped feature form a 100×60 pc elliptical ring of gas orbiting around the X2 orbits predicted by the barred Galactic potential (see Fig. 1.16).

1.4.2 Giant Molecular Loops scenario

In their wide-field imaging of the $J = 1 - 0$ ^{12}CO observations, Fukui et al. (2006) find huge loop structures (known as "Gigant Molecular Loops"; GMLs) of dense molecular gas with strong velocity dispersions in the GC (see Fig. 1.17). They explained the

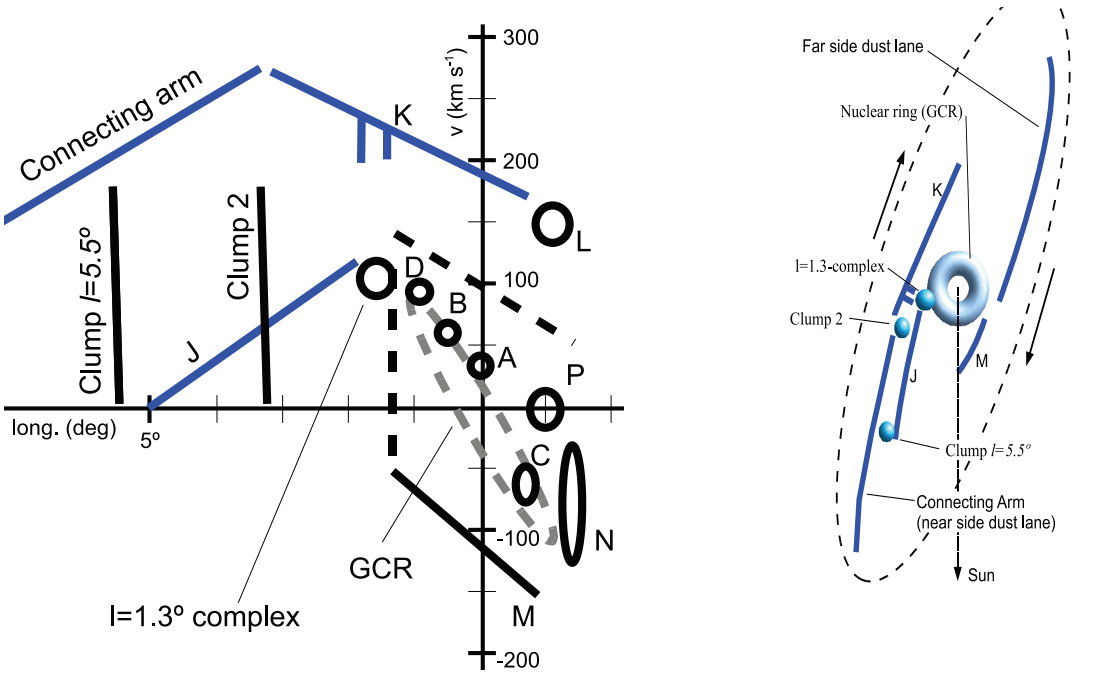

Figure 1.15: Different kinematical structures studied by Rodriguez-Fernandez et al. (2006). Left: main kinematical structures in the $l - v$ diagrams. Right: Schema of a plausible face-on view of the GC region. Fig. from Rodriguez-Fernandez et al. (2006).

formation of the loops by a magnetic flotation model caused by Parker instabilities. First, they identified two molecular loops (Loop 1 and 2) and they proposed the existence of another loop at positive longitudes (from l = 3° −5°). The Loops 1 and 2 range in latitude from $b \sim 0°$ to 2° , and in longitude from $l \sim 356°$ to 358° , and from $l \sim 355°$ to 356° respectively, at negative radial velocities. The typical widths of the loops are $\sim 0.2°$. Both loops have strong velocity gradients: ~ 80 km s^{-1} per 250 pc along the loop 1 and ~ 60 km s^{-1} per 150 pc along the loop 2. Subsequently, they found another loop structure at positive velocity, called by them "Loop 3" (Fujishita et al. 2009), which is placed at l = 355° −359° and b = 0° −2° . At each end of the loops, there are remarkable features, which they called "foot points" of the loops. Those features show very broad linewidths of $\sim$ 40 to 80 km s^{-1}. The projected lengths of the loops are $\sim$ 500 pc (Loop 1) and 300 pc (Loop 2), with a typical width of 30 pc. They are located at $\sim$ 220 to 300 pc from the Galactic plane, well above than the scale height of the nuclear disk ($\sim$ 100 pc). Fukui et al. (2006) classified this feature as being located in the GC due the large linewitdhs which is a characteristic of the molecular gas at the GC. They estimate the kinetic energy of the loops of about $0.9{\times}10^{51}$ erg, and argue that the loops cannot be formed neither by supernova nor by supershells. On one hand, in the supernova scenario only a part of the explosion energy can be converted into the gas kinetic energy. On the other hand, in the supershell case, the maximum velocity width of CO is $\sim$ 20 km s^{-1}, which is much smaller than the $\sim$ 80 km s^{-1}found in the loops. Also they discard this option because in the position-velocity diagram a supershell looks like a circle instead of the observed linear feature.

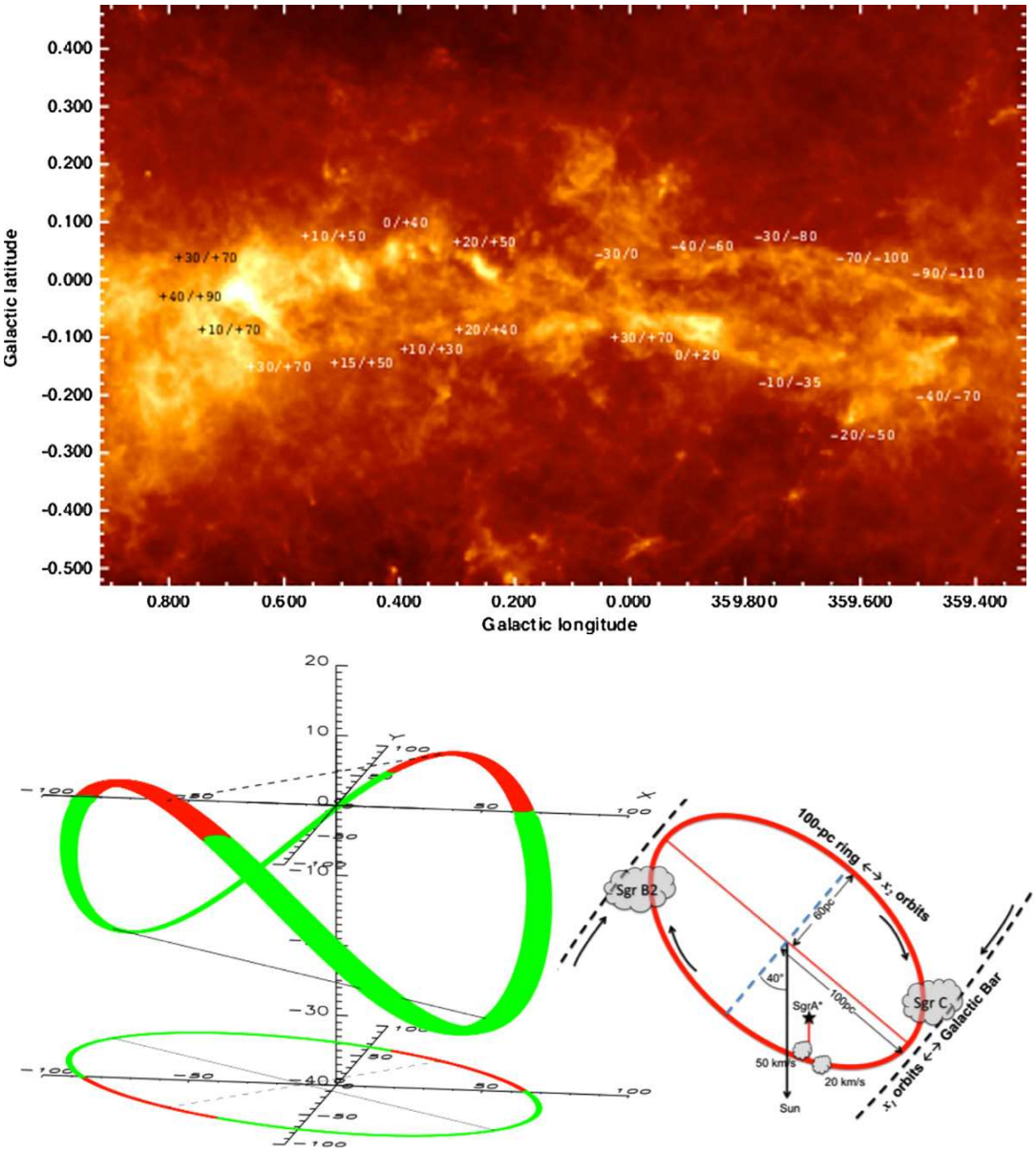

Figure 1.16: Top: Atomic hydrogen column density map with the velocity information for the contour of the ∞−shape, extracted from the CS survey of Tsuboi et al. (1999). Bottom: Left. Sketch of the three-dimensional structure and placement of the 100 pc ring proposed by Molinari et al. (2011). Right. Top view of the 100 pc ring (which follows the X2 orbits) with the location of major clouds, and showing the innermost X1 orbits (Fig. from Molinari et al. 2011).

1.4.2.1 Formation of the molecular loops

Fukui et al. (2006) propose a model to explain the formation of the GMLs based on the Parker instabilities.

The Parker instability is a magnetohydrodynamic instability that occurs when a gas layer is supported in part by horizontal magnetic field against the vertical gravitational field. Parker (1966) pointed out that this configuration is not stable; any vertical indentation in the magnetic field on a large scale will provide a pool into which interstellar gas will sink as it slides down the field lines in response to gravity. The pooled section gathers mass deforming the field and accelerating the flow of gas toward the plane. The gas concentration become denser, the gas cools relatively quickly, forming dense molecular clouds via Jeans instabilities (Morris 2006; Elmegreen 1982). Fukui et al. (2006) assume that the initial state is a nuclear gas disk of 1.3 kpc radius of atomic and molecular gas (which has an ionization degree of 10^{-7}, allowing the dynamical coupling of the molecular gas to the magnetic field), and they only consider the azimuthal toroidal field component. The instabilities occur in a disk of floating gas which has a near parallel or helical magnetic field. The flotation may be rapid, and the gas inside the loop become gravitationally attracted to the plane during the flotation, which accelerates the molecular gas along the field lines downward, reaching high velocities at the foot point of the loops (near Alfvén velocity) and forming shock fronts. Molecular gas moves toward both ends of the magnetic loop.

Machida et al. (2009) carried out global three-dimensional magneto hydrodynamical simulations of the gas disk in the GC. They found that buoyantly rising magnetic loops are formed above the differentially rotating, magnetically turbulent disk, with typical length of 1 kpc and height of 200 pc. The line of sight velocity changes linearly along the loops and shows large dispersions around the foot-points. Numerical results indicate that the loops emerge preferentially from the region where magnetic pressure is large.

1.5 Galaxy evolution

The Milky Way is part of the Local group, which gathers a large number of galaxies (including dwarf galaxies), with its gravitational center located somewhere between the Milky Way and the M31 (Andromeda) Galaxy (Fig. 1.18). The galaxies of the Local Group cover a 10 million light-year diameter. The group is part of the Virgo Supercluster. For a review of the Local Group see van den Bergh (2000). Our Galaxy interacts with their neighborhood, which triggers gas accretion into the Galaxy. To sustain the star formation rate, a galaxy like ours should accrete fresh gas at a rate of $\sim 1\ M_\odot\ yr^{-1}$.

There are several phenomena occuring in the disk-halo transition zone in spiral galaxies which will influence the evolution of galaxies. Star formation can produce energetic events that can lift gas several kpc into the halo. Some spirals have an associated population of extra-planar HI clouds that are probably being accreted from elsewhere. Gas accreted due to tidal streams suffered by dwarf galaxies also fed spiral galaxies. In the following, I discuss two scenarios which allow that fresh gas plunges into the Milky Way.

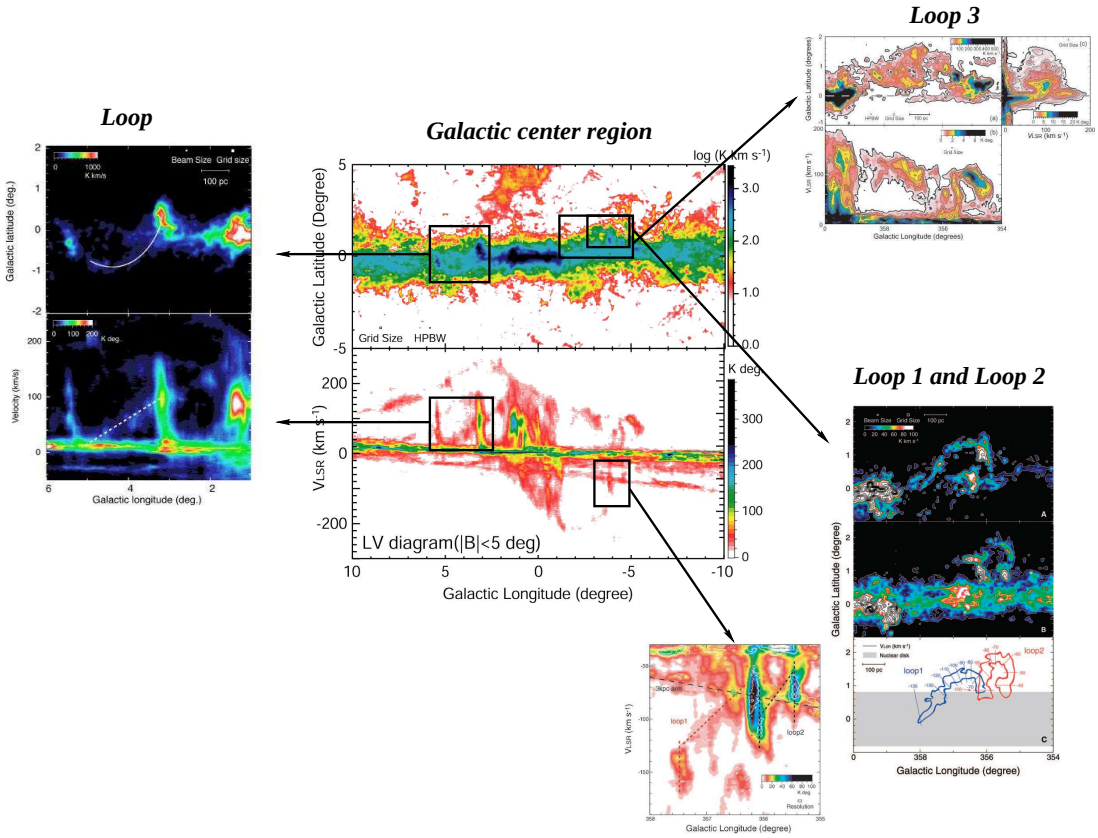

Figure 1.17: Giant Molecular loops (Fukui et al. 2006)

1.5.1 Sagittarius streams: Milky Way satellites

The interplay between the Milky Way and their neighborhood influences the evolution, morphology and structure of the Galaxy. For example, Sagittarius dwarf spheroidal galaxy (Ibata et al. 1994) is the closest satellite galaxy of the Milky Way. It is a prolate body with axis ratios of 3:1:1 oriented perpendicular to the Galactic plane from $b = -4°$ to $b = -26°$ and the longest dimension extend for ≥ 9 kpc at $l \sim 5°$ (Ibata et al. 1997). The Sgr dwarf galaxy has survived for many orbits around the Milky Way, and it is estimated that should loss half of their mass every 2-4 orbits and be completely disrupted long before now. Fig 1.19 shows one model of Ibata & Lewis (1998) of the remnant of the galaxy. In the figure, Sgr dwarf galaxy has evolved 12 Gyr in the Milky Way potential and has become disrupted by the Galactic tides. Currently it is only 25 kpc from the Sun and 16 kpc from the GC, it is near the point of its closest approach to the Galaxy. Such proximity produces huge tidal stress on the dwarf, modifying their morphology and eventually disrupting it. Since their discovery, several model calculations has been done to trace their structural evolution (Ibata & Lewis 1998). At the same time, Sgr dwarf galaxy provides significant perturbations to the outer disk and influences the evolution and formation of the central bar of the Milky Way. Fig 1.20 shows the effect that the passage of Sgr dwarf galaxy has on the Milky Way.

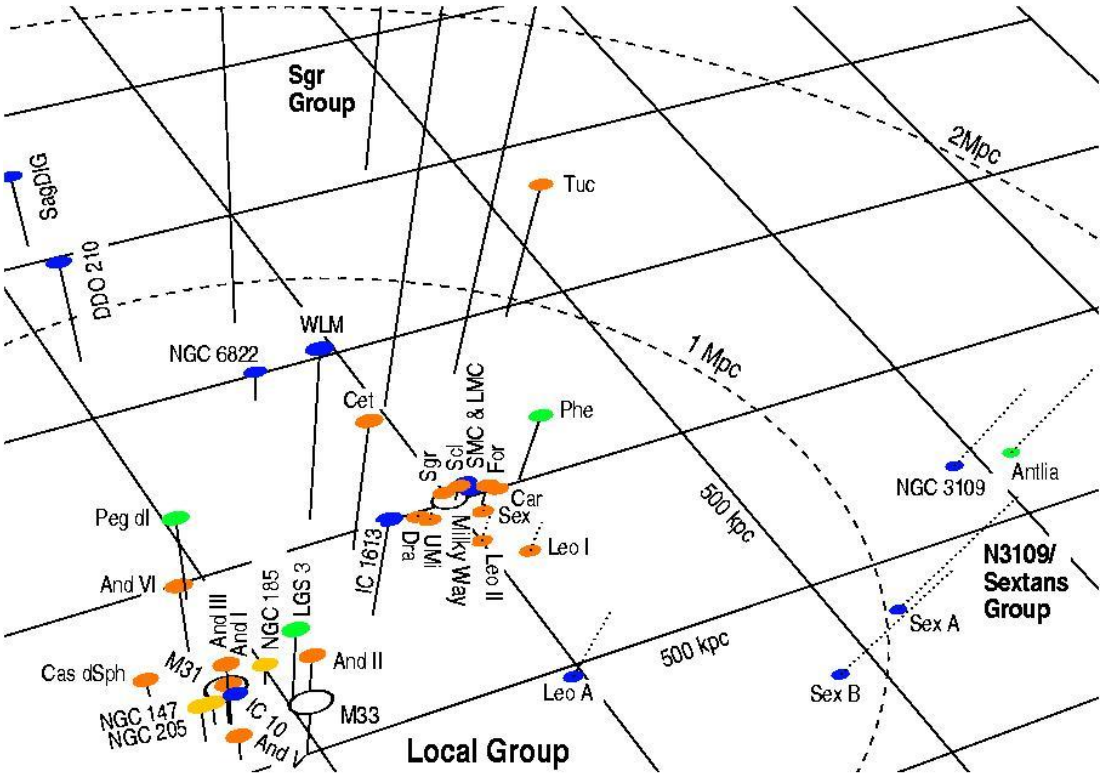

Figure 1.18: Local Group scaled 3-D representation. The dashed ellipsoid marks a radius of 1 Mpc around the Local Group barycenter (assumed to be at 462 kpc toward $l = 121.7$ and $b = -21.3$). Distances of galaxies from the the arbitrarily chosen plane through the Milky Way are indicated by solid lines (above the plane) and dotted lines (below). Figure from Grebel (2001).

1.5.2 Fountain clouds, accretion of coronal gas

In the galactic fountain model, hot gas heated by supernovae rises buoyantly then cools, condenses and returns to the disk (see Fig. 1.21). There are some populations of clouds that can be explained by this scenario, but still it is not conclusive. The H I disk-halo clouds is an example of this population. It is not clear whether these clouds are recent condensations from a hot Galactic halo, or a component of the disk ISM ejected from the plane (see Lockman 2011, and references therein). They are rotating with the Galactic disk, their number decrease exponentially with the distance to the plane, and their velocity dispersions are at least one order of magnitude lower to account for the scale height. Ford et al. (2010) conclude that the cloud numbers and scale-height are related to star formation. Therefore, the disk-halo clouds could be formed by the breakup of supperbubbles, but how they evolved in discrete H I clouds is not known. Pidopryhora et al. (2007) argue that they have been lofted away from the disk in structures that existed for 10 Myr before breaking up.

The high velocity clouds (HVC) are clouds of neutral hydrogen above $b = 10°$ with a velocity greater than 80 km s^{-1}(see Bregman 1980, and references therein).

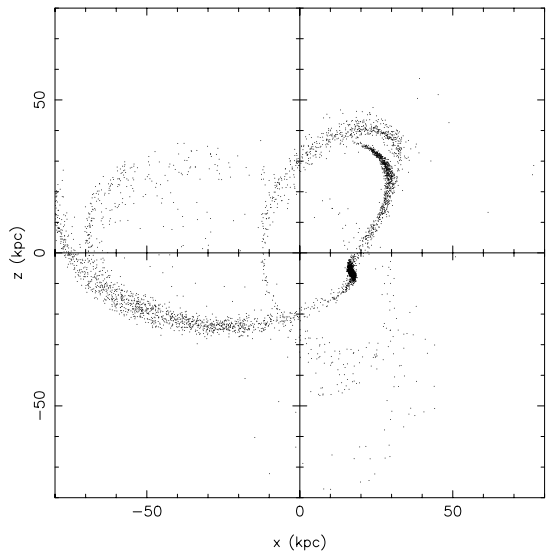

Figure 1.19: Remnant of one model of Sagittarius dwarf galaxy from Ibata & Lewis (1998)

They are common objects in the Galaxy, detected at any longitude and latitude in the Galaxy, most of them having negative velocities, a few kpc above the plane. It has been suggested that HVC are accreting from a hot halo that is either a relic of the formation of the Galaxy, or is powered by a galactic fountain. The origin of these HVC is not well known, but the low metallicity of this clouds in principle discard the galactic fountain approach. They are a successful candidate for the gas accretion in the Galaxy.

Recently, Marinacci et al. (2011) presented hydrodynamic simulation showing that the interaction between the cold galactic fountain clouds and the hot corona leads to the cooling and the accretion of the latter on to the star-forming disc at a rate comparable to that at which gas is transformed into stars.

1.6 Aims of this thesis

To understand the formation and evolution of galaxies, it is of crucial importance to explore their central few hundred parsecs. In spite of being embedded in the Milky Way, observations of selected regions of the center of our Galaxy offers the best opportunity to study in detail, with a very high spatial spatial resolution, the physical processes responsible for gas accretion and ejection, the role of the magnetic fields and galactic winds, in the interaction regions. In this thesis, we aim at studying two kinds of phenomena which would be responsible for gas accretion in the center of our Galaxy; the barred potential model, and the Giant Molecular Loops (GMLs).

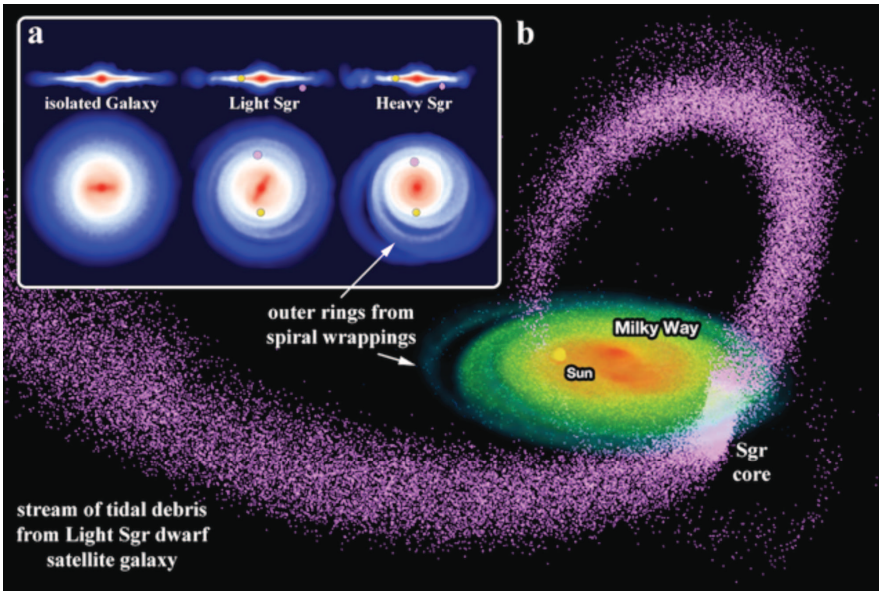

Figure 1.20: Effect that Sagittarius dwarf galaxy has on the structure and morphology of the Milky Way. a)Edge-on and face-on surface density view of the different Milky Way scenarios (isolated Galaxy subject to secular evolution, Milky Way in presence of a light and heavy Sgr dwarf galaxy). The position of the sun and Sgr dwarf galaxy are marked in yellow and pink respectively b) Final state of the Sgr dwarf galaxy "light model". Figure from Purcell et al. (2011).

- We study the molecular clouds of the Galactic center region, emphasizing the zones where they are interacting with molecular gas from the halo ("disk-halo interaction") or from the disk of the Galaxy. This zones are named after us "interaction regions". Our first aim was to identify the regions to be studied in detail.

- We aim at discovering the processes (accretion or ejection of gas) are occurring in the "interaction regions". To achieve this goal , we used the $^{12}C/^{13}C$ isotopic ratio. This ratio has a well established value of $20 - 25$ in the GC region, which indicate a high degree of proccesing by stars. If the gas in the interaction regions shows a similar value, it would indicate that this gas has been ejected from the GC plane to high latitude. In contrast, if the gas presents a higher ratio, it would indicate that this gas has a different origin, and it would be likely accreted from somewhere else.

- It is well known that the molecular clouds in the GC region have high kinetic temperatures of $T_{\rm kin} \sim 100$ k . However the $T_{\rm kin}$ of the molecular complexes found at high latitudes is so far unknown. We derive the $T_{\rm kin}$ towards the disk-halo interaction regions and find the heating mechanisms responsible of the high temperatures in the GC region.

- We aim at studying in detail the kinematics and the physical conditions of the

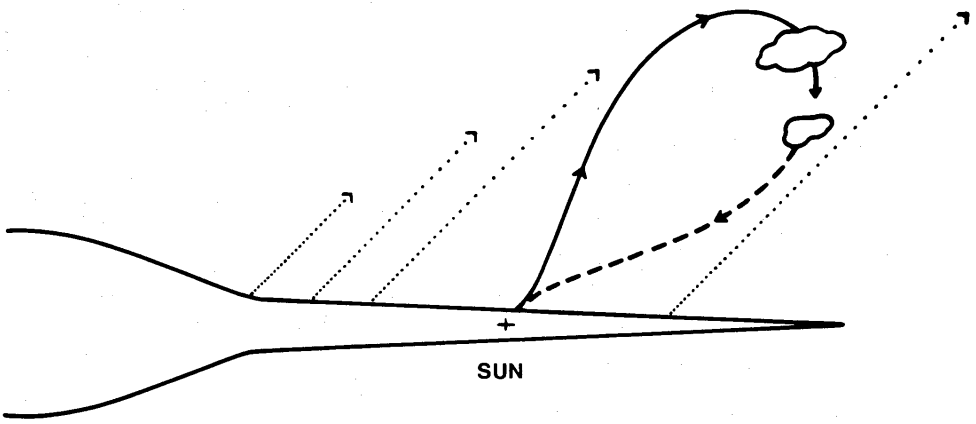

Figure 1.21: Fountain model. Dotted lines with arrows represent hot gas rising from the disk. The solid and dashed lines shows the cycle in which gas moves outward before suffering a thermal instability and forming into a cloud which falls towards its point of origin. (Fig. from Bregman 1980).

molecular clouds which are placed in the foot points of the giant molecular loops found by Fukui et al. (2006). The kinematics is assumed to be dominated by shocks, produced when the gas in the loops flows down their sides, along the magnetic field lines, and joins with the gas layer of the Galactic plane. We mapped the clouds with high spatial resolution in a number of molecular lines tracers, like SiO, HCN, HNCO, HNC, HCO^+, N_2H^+ among others.

Chapter 2

Physical Basics

2.1 Measuring the radiation using a radiotelescope

Consider a receiving antenna with a normalized power pattern $P_n(\Theta, \Phi)$ and an aperture efficiency of A_e. The total power per unit bandwith received by the antenna from a source having a specific intensity $I_\nu(\Theta, \Phi)$[erg s^{-1} cm^{-2} Hz^{-1}sr^{-1}] is (Wilson et al. 2009b)

$$W = \eta_R \frac{1}{2} A_e \int P_n(\Theta, \Phi) I_\nu(\Theta, \Phi) d\Omega \, , \tag{2.1}$$

where η_R is the radiation efficiency (the ratio of the available power of the antenna terminals to the total power absorbed by the antenna, which is ~ 1), and the factor $\frac{1}{2}$ originates from the fact that we detect a single polarization.
We can introduce an equivalent antenna temperature T_A by

$$W = kT_\mathrm{A} \, , \tag{2.2}$$

where k is the Boltmann constant ($1.3806503 \times 10^{-23}$[m^{2}kg s^{-2}K^{-1}]). Thus,

$$T_\mathrm{A} = \frac{A_e}{2k} \int P_n(\Theta, \Phi) I_\nu(\Theta, \Phi) d\Omega \, . \tag{2.3}$$

From the antenna theorem (Kraus 1986), $A_e \Omega_a = \lambda^2$, where $\Omega_a = \int_{4\pi} P_n(\Theta, \Phi) d\Omega$ is the beam solid angle of the antenna we can rewrite Eq. 2.3 as

$$\begin{aligned} T_A &= \frac{\lambda^2}{2k\Omega_a} \int P_n(\Theta, \Phi) I_\nu(\Theta, \Phi) d\Omega \\ &= \frac{1}{\Omega_a} \int P_n(\Theta, \Phi) T_R d\Omega \, , \end{aligned} \tag{2.4}$$

and using that $T_A = \eta_M T_\mathrm{MB}$, where $\eta_M = \frac{\Omega_M}{\Omega_A}$ is the main beam efficiency (Ω_M is the solid angle of the main beam of the antenna),

$$T_\mathrm{MB} = \frac{1}{\Omega_\mathrm{MB}} \int P_n(\Theta, \Phi) T_R d\Omega \, . \tag{2.5}$$

2.2 Planck law and the brightness temperature T_b

In thermodynamical equilibrium, the radiation and matter are in equilibrium, and its intensity (I_ν) correspond to the *Planck law* (B_ν) for a black body at temperature T,

$$B_\nu = \frac{2h\nu^3/c^2}{e^{(h\nu/kT)} - 1} \, . \tag{2.6}$$

In general, the radiation and matter are not in equilibrium, therefore I_ν is not well described by the Planck law. We can still define a brightness temperature T_b for each frequency (ν), where the intensity of the radiation at this ν is given by the Planck law at the temperature T_b,

$$I_\nu = B_\nu(T_b) \, . \tag{2.7}$$

In the Rayleigh-Jeans (R-J) regime ($h\nu << kT$),

$$I_\nu \simeq \frac{2k\nu^2}{c^2} T_b \, . \tag{2.8}$$

If the R-J does not hold, still it is useful to define the radiation temperature T_R (which coincide with the T_b in the R-J regime) by

$$T_R \equiv \frac{c^2}{2k\nu^2} I_\nu \, . \tag{2.9}$$

Therefore, using Eq. 2.7

$$T_R = J_\nu(T_b) \, , \tag{2.10}$$

where J_ν is the intensity in temperature units, given by

$$J_\nu = \frac{h\nu/k}{e^{(h\nu/kT)} - 1} \, . \tag{2.11}$$

2.3 Radiative transport

The specific intensity I_ν from a source is constant along the line of sight in free space. The radiation will change only if it interacts with the matter, which absorbs part of the radiation and emits radiation at the same time. This change of I_ν is described by the Eq. of transfer:

$$\frac{dI_\nu}{ds} = -\alpha_\nu I_\nu + j_\nu \, , \tag{2.12}$$

where α_ν is the absorption coefficient (in cm^{-1}) and j_ν is the emission coefficient (in $\mathrm{erg\,s^{-1}\,cm^{-3}\,sr^{-1}\,Hz^{-1}}$). It is useful to rewrite this Eq. by defining the optical depth

$$\begin{aligned} d\tau_\nu &= \alpha(\vec{r})ds \\ \tau_\nu(s) &= \int_{s_0}^{s} \alpha(s')ds' \, . \end{aligned} \tag{2.13}$$

Defining the source function S_ν by the ratio of the emission to absorption coefficient, Eq. 2.12 becomes

$$\frac{dI_\nu}{d\tau} = -I_\nu + S_\nu(\vec{r}) \, , \tag{2.14}$$

where the formal solution is

$$I_\nu(\tau_\nu) = I_\nu(0)e^{-\tau_\nu} + \int_0^{\tau_\nu} S_\nu(\tau'_\nu)e^{-(\tau_\nu-\tau'_\nu)}d\tau'_\nu \, . \tag{2.15}$$

If we assume that the source function is constant, it is possible to evaluate the integral in Eq. 2.15, obtaining

$$I_\nu(\tau_\nu) = I_\nu(0)e^{-\tau_\nu} + S_\nu(1 - e^{-\tau_\nu}) \, . \tag{2.16}$$

Using the radiation temperature (eq. 2.9), and defining the excitation temperature $T_{\rm ex}$ by

$$S_\nu = B_\nu(T_{\rm ex}) = \frac{2h\nu^3/c^2}{e^{(h\nu/k_BT_{\rm ex})} - 1} \, , \tag{2.17}$$

and $T_{\rm bg}$ as the brightness temperature for the cosmic baground intensity, $I_\nu(0)$, we can rewrite the Eq. 2.16 as

$$T_R = J_\nu(T_b) = J_\nu(T_{\rm ex})(1 - e^{-\tau_\nu}) + J_\nu(T_{\rm bg})e^{-\tau_\nu} \, , \tag{2.18}$$

and in the R-J approximation:

$$T_R = T_b = T_{\rm ex}(1 - e^{-\tau_\nu}) + T_{\rm bg}e^{-\tau_\nu} \, . \tag{2.19}$$

The specific intensity I_ν observed by the telescope, considering that each observation corresponds to the difference of the "on" and "off" position, is

$$\begin{aligned} I_\nu^{\rm obs} &= I_\nu^{\rm on} - I_\nu^{\rm off} \\ &= I_\nu(0)e^{-\tau_\nu} + S_\nu(1 - e^{-\tau_\nu}) - I_\nu(0) \\ &= -I_\nu({\rm bg})(1 - e^{-\tau_\nu}) + S_\nu(1 - e^{-\tau_\nu}) \\ &= [S_\nu - I_\nu({\rm bg})]\,(1 - e^{-\tau}) \, , \end{aligned} \tag{2.20}$$

where $I_\nu({\rm bg}) = I_{CMB} + I_c$ (I_{CMB} is the intensity of the cosmic microwave background at $T = 2.73$ K, and I_c corresponds to any possible continuum source).

Rewriting Eq. 2.20 in terms of T_R (Eq. 2.9), we get

$$T_R^{\rm obs} = [J_\nu(T_{\rm ex}) - J_\nu(T_{\rm bg})](1 - e^{-\tau}) \, , \tag{2.21}$$

which in the R-J approximation, becomes

$$T_R^{\rm obs} = (T_{\rm ex} - T_{\rm bg})(1 - e^{-\tau}) \, . \tag{2.22}$$

2.4 Line emission. The Einstein coefficients

The Einstein coefficients are a convenient way to describe the interaction between the radiation and matter by the emission or absorption of photons.

Lets us consider the transition between two states of an atom, ion or molecule: the upper (2) and lower (1) level. The energy levels E_1 and E_2 have a finite energy spread so that $E_2 - E_1$ will have a certain energy distribution, therefore the frequency

of the transition is $\nu_{21} = (E_2 - E_1)/h$. The transitions between both states, are described microscopically by three processes: the *spontaneous emission*, the *stimulated emission* and the *absorption*.

The coefficient of **spontaneous emission** A_{21}, represents the probability of the spontaneous deexcitation of the particle from the level 2 to level 1 per time (in units of s^{-1}), and the lifetime of the particle in the upper level is defined by $t = A_{21}^{-1}$. To obtain the emission coefficient, we multiply the coefficient of spontaneous emission A_{21} by the density of the upper level n_2 and by the energy of the emitted photon $h\nu$, divide by the total solid angle (4π), and multiply by the line profile $\phi(\nu)$:

$$j_\nu = \frac{n_2 A_{21}}{4\pi} h\nu\phi(\nu) \, . \tag{2.23}$$

The line profile is sharply peaked and normalized

$$\int_0^\infty \phi(\nu) d\nu = 1 \, . \tag{2.24}$$

The contribution of the spontaneous emission to the variation of the both levels population is given by $\dot{n}_1 = -\dot{n}_2 = n_2 A_{21}$.

The **absorption** of a photon of frequency ν_{21} from the radiation field, produces an excitation of the particle from the level 1 to the level 2. This process is described by the absorption coefficient B_{12} and by the intensity of the radiation field. The units of B_{12} are [erg^{-1} cm^2 sr Hz]. Therefore, the contribution of the absorption to the variation of the levels population is given by $\dot{n}_2 = -\dot{n}_1 = n_1 B_{12} \bar{J}$, where the intensity $\bar{J}$[1] corresponds to

$$\bar{J} = \int\int I_\nu \phi(\nu) d\Omega d\nu \, . \tag{2.25}$$

The **stimulated emission** process is the deexcitation of a molecule/atom from the level 2 to the 1 triggered by an incident photon producing the emission of other photon. The coefficient of stimulated emission is B_{21}, and the probability of this to occur is $B_{21}\bar{J}_\nu$. Therefore, the contribution of the stimuled emission to the level populations is given by $\dot{n}_1 = -\dot{n}_2 = n_2 B_{21} \bar{J}$.

The absorption coefficient α_ν is obtained from the last two processes:

$$\alpha_\nu = \frac{n_1 B_{12} - n_2 B_{21}}{4\pi} h\nu\phi(\nu) \, . \tag{2.26}$$

The Einstein coefficients A_{21}, B_{21} and B_{12} are not independent as can be seen if we consider a system in thermodynamic equilibrium (TE), where the number of excitations and deexcitations is the same, i.e.,

$$n_2 A_{21} = (n_1 B_{12} - n_2 B_{21}) \bar{J} \, . \tag{2.27}$$

The population of the level can be described by the Boltzmann law at a temperature T,

$$\frac{n_2}{n_1} = \frac{g_2}{g_1} e^{-h\nu/kT} \, , \tag{2.28}$$

[1] do not confuse $\bar{J}$ with J_ν defined by eq. 2.11

where g_1 and g_2 are the statistical weights. Solving eq. 2.27 for $\bar{J}$,

$$\bar{J} = \frac{A_{21}}{\frac{n_1}{n2}B_{12} - B_{21}} , \tag{2.29}$$

and replacing eq. 2.28 in eq. 2.29

$$\bar{J} = \frac{A_{21}}{\frac{g_1}{g_2}e^{-h\nu/kT}B_{12} - B_{21}} . \tag{2.30}$$

In termodinamical equilibrium, the intensity is given by the Planck law, so

$$\bar{J} = \frac{A_{21}}{\frac{g_1}{g_2}e^{-h\nu/kT}B_{12} - B_{21}} = \frac{2h\nu^3/c^2}{e^{(h\nu/k_BT)} - 1} . \tag{2.31}$$

To hold this Eq. we should have

$$g_1B_{12} = g_2B_{21} , \tag{2.32}$$

$$A_{21} = \frac{2h\nu^3}{c^2}B_{21} . \tag{2.33}$$

These equations hold also in non-LTE, because they are not dependent on the temperature.

2.5 Excitation temperature and Boltzmann equation

In the case of arbitrary excitation, a different temperature may characterize the population of each level relative to other. The excitation temperature $T_{\rm ex}$ is defined by the relative populations or column densities of two levels (e.g., level 1 and 2) of statistical weights g_1 and g_2,

$$\frac{n_2}{n_1} = \frac{g_2}{g_1}e^{-h\nu/kT_{\rm ex}} . \tag{2.34}$$

This definition is equivalent at the one given in Eq. 2.17. Using the Einstein coefficients, we have

$$\begin{aligned} S_\nu &= \frac{j_\nu}{\alpha_\nu} \\ &= \frac{A_{21}/B_{21}}{n_1B_{12}/n_2B_{21} - 1} \\ &= \frac{2h\nu^3/c^3}{n_1g_2/n_2g_1 - 1} , \end{aligned} \tag{2.35}$$

and due to $S_\nu = B_\nu(T_{\rm ex}) = \frac{2h\nu^3/c^3}{e^{h\nu/kT_{\rm ex}}-1}$, it is deduced that the relationship between the level populations is given by Eq. 2.34.

2.6 Optical depth

In Eq. 2.13, we define the optical depth. Replacing eq. 2.26 in eq. 2.13,

$$\tau_\nu = \int_{s_0}^{s} \frac{n_1 B_{12} - n_2 B_{21}}{4\pi} h\nu\phi(\nu) ds \, . \tag{2.36}$$

Using the relationship between the Einstein coefficient (eq. 2.32 and 2.33),

$$\begin{aligned}
\tau_\nu &= \int_{s_0}^{s} (n_1 B_{12} - n_2 B_{21}) \frac{h\nu_{21}}{4\pi} \phi(\nu) ds \\
\tau_\nu &= \int_{s_0}^{s} \left(n_1 \frac{g_2}{g_1} B_{21} - n_2 B_{21} \right) \frac{h\nu_{21}}{4\pi} \phi(\nu) ds \\
\tau_\nu &= \int_{s_0}^{s} \left(\frac{n_1 g_2}{n_2 g_1} - 1 \right) \frac{B_{21} h\nu_{21}}{4\pi} \phi(\nu) ds \\
\tau_\nu &= \int_{s_0}^{s} \left(\frac{n_1 g_2}{n_2 g_1} - 1 \right) \frac{c^2 A_{21}}{8\pi\nu_{21}^2} \phi(\nu) ds \, .
\end{aligned} \tag{2.37}$$

Using eq. 2.34 in eq. 2.37, converting from density to column density ($\int nds = N$), and integrating in frequency,

$$\int \tau_\nu d\nu = \left(e^{\frac{h\nu}{kT_{\rm ex}}} - 1 \right) \frac{c^2 A_{21}}{8\pi\nu^2} N_2 \int \phi(\nu) d\nu \, . \tag{2.38}$$

In the ISM the Doppler broadening dominates other processes. The observed line widths are much larger than expected from the kinetic temperatures (except in very cold and dark cloud cores) which is attributed mainly to large gas motions, or turbulence. The line profile usually takes a Gaussian form:

$$\phi_\nu = \frac{1}{\nu_D \sqrt{\pi}} \exp\left[- \frac{(\nu - \nu_{21} - \overrightarrow{v} \cdot \overrightarrow{n} \frac{\nu_{21}}{c})^2}{\nu_D^2} \right] , \tag{2.39}$$

where ν_D is the Doppler width, $\overrightarrow{v}$ is the velocity vector of the moving gas at the position of the line emission, $\overrightarrow{n}$ is a unit vector in the direction of the of the propagating beam of radiation, and c is the speed of light. The Doppler width is $(\Delta V)/(2\sqrt{\ln(2)})$, where ΔV is the full width at half maximum.

2.7 Collisional excitation

Besides the radiative transitions in a two level system described above, other mechanisms that could produce excitation and de-excitations are **collisions**. In the collisions between a particle and the atoms/molecules, part of the kinetic energy can be used to produce the excitation from level 1 to 2, or in the other way around, transfer energy to the particle, producing a de-excitation from the level 2 to 1.

The collisional rate is given by

$$C_{21} = n_{\rm coll} \gamma_{21} \, , \tag{2.40}$$

where $n_{\rm coll}$ is the number density of the collision partner (in cm^{-3}), and γ_{21} is the downward collision rate coefficient (in cm^3 s^{-1}). The collision rate coefficient is the Maxwellian average of the collision cross section $\sigma(v)$:

$$\begin{aligned}\gamma_{21} &= \int \sigma_{21}(v) v f(v) dv \\ \gamma_{21} &= 4\pi \left(\frac{\mu}{2\pi k T_{\rm kin}}\right)^{\frac{3}{2}} \int \sigma_{21}(v) v^3 e^{-\frac{\mu v^2}{2kT_{\rm kin}}} dv \,,\end{aligned} \tag{2.41}$$

where v and $f(v)$ are the velocity and velocity distribution of the collisional particles, $T_{\rm kin}$ is the kinetic temperature, and μ the reduced mass of the system. The collisional excitation and de-excitation are not independent, and their relationship can be deduced by a given temperature from the detailled balance equations:

$$g_1 \gamma_{12} = g_2 \gamma_{21} e^{-\frac{h\nu}{kT}} \,. \tag{2.42}$$

2.8 Relationship between the brightness temperature and the column density

In Eq. 2.21, we obtained the radiation temperature observed in a source:

$$T_R^{\rm obs} = [J_\nu(T_{\rm ex}) - J_\nu({\rm bg})](1 - e^{-\tau_\nu}) \,. \tag{2.43}$$

Rearranging to solve for τ_ν (following Ginsburg et al. (2011)),

$$\tau_\nu = -\ln\left(1 - \frac{T_R^{\rm obs}}{J_\nu(T_{\rm ex}) - J_\nu(T_{\rm bg})}\right) . \tag{2.44}$$

Integrating in velocity (we convert from frequency to velocity units using $dv = \nu/cdv$), and replacing eq. 2.44 in eq. 2.38, we get

$$N_2 = \frac{8\pi\nu_{21}^3}{c^3 A_{21}} \left[e^{\frac{h\nu_{21}}{kT_{\rm ex}}} - 1\right]^{-1} \int -\ln\left(1 - \frac{T_R^{\rm obs}}{J_{\nu_{21}}(T_{\rm ex}) - J_{\nu_{21}}(T_{\rm bg})}\right) dv \,, \tag{2.45}$$

which is the LTE upper level column density. If we assume optically thin emission, $\tau << 1$, we take the first term of the Taylor expansion $\ln(1+x) \approx x - \frac{x^2}{2} + \frac{x^3}{3}$...,

$$\begin{aligned} N_2 &= \frac{8\pi\nu_{21}^3}{c^3 A_{21}} \left[e^{\frac{h\nu_{21}}{kT_{\rm ex}}} - 1\right]^{-1} \int \frac{kT_R^{\rm obs}}{h\nu_{21}} \left[\left(\frac{1}{e^{h\nu_{21}/kT_{\rm ex}} - 1}\right) - \left(\frac{1}{e^{h\nu_{21}/kT_{\rm bg}} - 1}\right)\right]^{-1} dv \\ &= \frac{8\pi k \nu_{21}^2}{c^3 h A_{21}} \left(\frac{e^{h\nu_{21}/kT_{\rm bg}} - 1}{e^{h\nu_{21}/kT_{\rm bg}} - e^{h\nu_{21}/kT_{\rm ex}}}\right) \int T_R^{\rm obs} dv \,. \end{aligned} \tag{2.46}$$

If we assume that $T_{\rm bg} \ll T_{\rm ex}$, we get

$$N_2 = \frac{8\pi k \nu_{21}^2}{A_{21} h c^3} \int T_R^{\rm obs} dv \,. \tag{2.47}$$

For the GC, we assume that the source is extended filling up to the main beam and uniform in the beam, therefore eq. 2.5 becomes

$$T_{\rm MB} = T_R^{\rm obs} \frac{1}{\Omega_{\rm MB}} \int_{\Omega_{\rm MB}} P_n(\Theta, \Phi) d\Omega = T_R^{\rm obs} \, . \tag{2.48}$$

Then, to derive the column density, we replace eq. 2.48 in eq. 2.47,

$$N_2 = \frac{8\pi k \nu_{21}^2}{A_{21} h c^3} \int T_{\rm MB} dv \, . \tag{2.49}$$

2.9 Comparing observations with model calculations

To infer physical and chemical properties (temperature, density and molecular abundances) of the ISM, it is usual to use different models. To translate the observation into astrophysical parameters, we need to estimate the excitation and optical depth. The method used for this task will depend on the available observations (van der Tak et al. 2007). There are three methods widely used to derive physical properties: *the LTE Rotation Diagram, the local model, and the non-local models*. In this thesis we used the first two methods, therefore, they will be discussed in detail.

2.9.1 Single excitation temperature: Rotation diagram ("LTE" model)

The simplest technique to analyze cloud properties from their molecular line emission is the *LTE rotational diagram*. It is based on the analysis of the column density per statistical weight $\left(\frac{N_i}{g_i}\right)$ of a number of molecular energy levels, as a function of their energy (E_i) above the ground state (Goldsmith & Langer 1999). For a system in Local thermodynamical equilibrium (LTE), all excitation temperatures ($T_{\rm ex}$) are considered to be the same ($T_{\rm ex} = T$). Since the level population will be represented by the Boltmann distribution, a plot of the logarithm of N_i/g_i versus E_i/k will produce a straight line with a slope of $1/T$. This temperature is called *rotational temperature*, which corresponds to the kinetic temperature only if all the levels are thermalized.

To derive this relation, we compute the fraction of the total population in a particular state, e.g, u,

$$\frac{N_u}{N} = \frac{N_u}{\sum_{\text{all the levels}} N_i} \, , \tag{2.50}$$

and, using eq. 2.34 we get

$$\begin{aligned} \frac{N_u}{N} &= \frac{N_u}{\sum_{\text{all the levels}} N_i} \qquad (2.51) \\ &= \frac{1}{\sum_{\text{all the levels}} \frac{g_i}{g_u} e^{-(E_i - E_u)/kT}} \\ &= \frac{g_u}{Z} e^{-E_u/kT} \qquad (2.52) \end{aligned}$$

where Z is the partition function

$$Z = \sum_{\text{all the levels}} g_i e^{-E_i/kT} \tag{2.53}$$

Substituting 2.47 in 2.51, taking u as the upper level (level 2), and calling the lower level generically as l, we obtain

$$\log\left(\frac{8\pi k\nu^2 \int T_{MB}}{hc^3 A_{ul} g_u}\right) = \log\left(\frac{N}{Z}\right) - \log(e)\frac{E}{kT} \tag{2.54}$$

For the NH_3 transitions observed in this work, we have the molecular parameters values shown in Table 2.1, and for the CS transitions, see Table 2.2 (taken from the LAMDA webpage[2]).

Table 2.1: Molecular constants for the observed transitions of NH_3.

transition	frequency [GHz]	g_u	A_{ul} $\times 10^{-7}$ [s^{-1}]	E_u/k [K^{-1}]
(1,1)	23.6944955	6	1.712	23.372
(2,2)	23.7226335	10	2.291	64.885
(3,3)	23.8701296	28	2.625	123.54
(4,4)	24.1394170	18	2.897	202.336
(5,5)	24.5329892	22	3.167	298.272
(6,6)	25.0560250	52	3.470	408.06

Table 2.2: Molecular constants for the observed transitions of CS.

transition	frequency [GHz]	g_u	A_{ul} $\times 10^{-5}$ [s^{-1}]	E_u/k [K^{-1}]
2-1	97.9809533	3	1.6792	7.05
3-2	146.969028	5	6.0710	14.11

2.9.2 Statistical equilibrium (SE) Local modeling

This kind of models, retain the assumption of a local radiative excitation for the optically thick case, but solve for the balance equation of excitation and de-excitation rates from and to a given state. Both collisional and radiative processes contribute to this balance, and these "non-LTE" models require molecular collision data as input, in addition to spectroscopic data. Therefore they require knowledge of molecular collisional data, which are not available for all astrophysical relevant species. Using these methods, we can constrain column density, kinetic temperature and volume density from multiline observations. These models are based on the *escape probability*

[2]LAMDA: http://www.strw.leidenuniv.nl/~moldata/

and the most popular use the *Large Velocity gradient (LVG)* aproximation (Sobolev 1960).The LVG model assumes that the cloud has large velocity gradient of the order of 1 $\mathrm{km\,s^{-1}\,pc^{-1}}$ or more. The resulting Doppler shift of the line profile has the effect of to decouple the excitation at one end of the cloud from radiation from the other, making local the radiative excitation problem. Such models match observed spectra, but the reliability of the derived parameters is unclear since most clouds do not have systematic velocity gradients (Ossenkopf 1997). The escape probability approximation introduces a parameter β (which is the chance for photons to leave the cloud), which depends on an assumed geometry and in the optical depth. Because this is the used method in this thesis, we explain it in the next subsections. Due to the coupling of the molecular excitation and the radiative transfer, the method is iterative.

2.9.2.1 Statistical equilibrium

If the level populations n_i are known, the radiative transfer Eq. can be solved exactly. The population of the level i, n_i is given by

$$\frac{dn_i}{dt} = 0 = \sum_{j\neq i}^{N} n_j P_{ji} - n_i \sum_{j\neq i}^{N} P_{ij} = F_i - nD_i \,, \tag{2.55}$$

where P_{ij} and P_{ji} are the destruction and formation rate coefficients of level i respectively given by

$$P_{ij} = \begin{array}{ll} A_{ij} + B_{ij}\bar{J} + C_{ij} & i > j \\ B_{ij}\bar{J} + C_{ij} & i < j \end{array}. \tag{2.56}$$

2.9.2.2 Escape probability

The radiation field appears in the Eq. of the statistical equilibrium of level populations, throughout the absorption and stimulated emissions rates, which are proportional to the intensity I_ν integrated over the line profile and average over the solid angle ($\bar{J}$, see eq. 2.25). Therefore, to solve the coupled equations, we need iterative solution methods. To simplify the calculations, it is useful to introduce a geometrically averaged escape probability, β, which is the probability that a photon will escape the medium from where it was created. $\bar{J}$ corresponds to the radiation *inside* the source, therefore for a completely opaque source we have $\bar{J} = S_\nu$, and in general

$$\bar{J} = S_\nu(1-\beta) \,. \tag{2.57}$$

The probability depends only on the optical depth τ and on geometry, but not on the radiation field. The first expression was derived by Sobolev (1960) for an expanding spherical shell, which is called the large velocity gradient (LVG) approximation. The RADEX code includes this type of approximation given by the formula of Mihalas (1978) and de Jong et al. (1980):

$$\beta_{\mathrm{LVG}} = \frac{1}{\tau}\int_0^\tau e^{-\tau'} d\tau' = \frac{1-e^{-\tau}}{\tau} \,. \tag{2.58}$$

For a spherically symmetric and homogeneous medium, the escape probability is (Osterbrock & Ferland 2006)

$$\beta_{\rm sphere} = \frac{1.5}{\tau}\left[1 - \frac{2}{\tau^2} + \left(\frac{2}{\tau} + \frac{2}{\tau^2}\right)e^{-\tau}\right] . \tag{2.59}$$

For a plane-parallel slab geometry, which is applicable for instance to shocks, the escape probability is derived by de Jong et al. (1975):

$$\beta_{\rm slab} = \frac{1 - e^{-3\tau}}{3\tau} . \tag{2.60}$$

2.9.2.3 RADEX

The statistical equilibrium radiative transfer code "RADEX" software is one simple method to constrain abundances and physical conditions from observations. The software was written originally by J.H. Black, with improvements made in Leiden, and is publicablyy available and offers for public use[3]. RADEX uses the escape probability formulation assuming an homogeneous medium without large-scale-velocity fields. The input of the programs are the collisional and radiative rates of the specie, the kinetic temperature of the molecular cloud, the column density of the specie, the colission partner and their volume density (usually H_2, but in some cases, separate cross sections exist for collisions with the ortho and para H_2, and electron collision may be important for ionic species), the temperature of the background radiation ($T_{\rm CMB} = 2.725(1+z)$ K, for a galaxy at redshift z), and the FWHM line width [km s^{-1}]. It is possible to obtain the molecular data from the Leiden Atomic and Molecular Database (LAMDA)[4], which include all the species modeled in this thesis. The programs iteratively solves the SE equations starting from optically thin SE for the initial level populations, taking into account only the background radiation field. The solution of the level population is used to derive the optical depth, which is used to re-calculate the molecular excitation by using the escape formalism. The new iteration treats the background radiation as internally produced radiation (see below). The program finds a consistent solution for the level populations and radiation field, and stop when $\tau > 10^{-2}$) is stable at a given tolerance of 10^{-6}.

It is important to clarify what the internal radiation field is. The continuum contribution of the rate equations may be composed by an external component which arise outside the emitting region (e.g., the CMB and the interstellar radiation field) and always fill the entire sky, and an internal continuum that arise in the emitting region (e.g., dust emission from the line emitting region) which only fill a fraction of it:

$$J^{int} = \beta[B_\nu(T_{\rm CMB} + \eta I^{\rm user_\nu}] + (1-\beta)[B_\nu(T_{\rm T_{ex}} + \theta(1-\eta)I^{\rm user_\nu}] , \tag{2.61}$$

where $I^{\rm user_\nu}$ is the continuum spectrum defined by the user, η is the fraction of local continuum which arise outside the line emitting region, and θ is the fraction of local sky filled by the internal continuum.

The output of the program is, apart of the molecular data parameters (quantum number, upper state energy [K], frequency [GHz], and wavelength [νm]), the excitation

[3] http://www.sron.rug.nl/~vdtak/radex/index.shtml
[4] http://www.strw.leidenuniv.nl/~moldata/

temperature, the line optical depth, the line intensity (defined as the Rayleigh-Jeans equivalent temperature T_R [K], see Eq. 2.22), the line flux. To constrain the physical properties of a molecular cloud it is usual to run RADEX in a grid of possible values using a known physical parameter derived from other methods or from theory. For example, in this thesis, to derive the column density of CS and the volume density, we use the kinetic temperature derived from metastable inversion transitions of para-NH_3 and we run RADEX in a grid of N(CS) from 10^{12} to 10^{16} [cm^{-2}] and n(H_2) from 10^2 to 10^7 [cm^{-3}].

2.9.3 Non-local models

The most advanced and sophisticated radiative transfer methods drop the assumption of local excitation and solve for the molecular excitation as a function of position in the cloud. They are two main types of this kind of methods; the Accelerated Lambda Iteration (ALI) and Monte Carlo (MC) (also exist hybrids of them). These programs estimate the local radiation field at all line frequencies due to radiation from everywhere else in the cloud, and can constrain temperature, density, velocity gradients within sources and molecular abundance profile (if enough observations are available). The ALI program discretize the cloud onto a grid of points and split off the local contribution from the full radiation field at each point. MC method divide the cloud into grid cells and send photon packages in random directions from each cell. The performance and convergence of both types of programs has been tested for HCO^+ (van Zadelhoff et al. 2002) and for H_2O (van der Tak et al. 2005). The drawback of these models is that calculations can take several hours due to complicated model geometries, large gradients in excitation conditions, and molecules with many energy levels.

The RATRAN software (Hogerheijde & van der Tak 2000) is a MC program which is publicly available in the 1D version. The 2D version is available upon request[5]. Recently, there is a new program that perform 3D non-local calculations, call *LIME* (Brinch & Hogerheijde 2010), which is not publicly available, but the authors provide a copy upon request[6].

[5]http://www.sron.rug.nl/~vdtak/ratran/
[6]http://www.strw.leidenuniv.nl/~brinch/website/limecode.html

Chapter 3

A large scale survey of the Galactic center region in HCO^+, $H^{13}CO^+$, and SiO

3.1 The large scale survey of the Galactic center

There are many molecular and atomic surveys of the inner few hundred pc of the Galaxy (see Table 3.1). This kind of studies, requires telescopes of small or medium size, which allow to observe large regions in a reasonable amount of time, with a good signal-to-noise ratio. This kind of studies are usually very time consuming. Therefore, due to the declination of the GC, it is better to observe it from southern telescopes.

Recently, Jones et al. (2011) published the most complete survey in terms of number of lines of the CMZ so far in 20 molecular lines from 85.3 GHz to 93.3 GHz using the 22m Mopra telescope. This is a molecular line mapping survey extending approximately 2.5° along the Galactic plane and 0.25° out of the plane – an extent of 450×150 pc. That survey was done using the on-the-fly mapping, and consists of data-cubes with a velocity resolution of 1 km/s over the 8 GHz bandwidth, an angular resolution of 40" and an RMS noise of $T_{\rm MB}$ = 0.05 K per channel. However, the data only cover the CMZ, missing the PMZ and high latitude features. The CMZ has been observed in far-infrared and submillimeter emission, using e.g., JCMT SCUBA at 850 and 450 μm (Pierce-Price et al. 2000), APEX ATLASGAL at 870 μm (Schuller et al. 2009), BOLOCAM at 1100 and 350 μm (Bally et al. 2010) and HiGAL at 70, 170, 250, 350, 500 μm. This emission traces the $T \sim 20$ K dust associated with the molecular gas.

Most of these surveys do not include the PMZ. As disscussed in §1, the PMZ shares characteristics with the CMZ (large velocity dispersions, large CO luminosities). To understand the physical processes that govern the GC as a whole, it is crucial to study the molecular clouds belonging to the PMZ. In the following, we present a paper we have published in Astronomy & Astrophysics in 2010. The paper presents a complete map in the molecular lines $HCO^+(1-0)$, $H^{13}CO^+(1-0)$, and SiO(2-1) observed with the 4m NANTEN telescope placed in "Las Campanas" Observatory in Chile. Our survey is so far largest in extent in molecules other than CO. The data is for public use (data cubes are available at http://www.das.uchile.cl/galcendata). The paper presents the complete survey in the three molecular lines in the form of channel maps integrated in velocity

interval of 10 km s^{-1}, longitude-velocity plots, and latitude-velocity plots. This data are presented in the electronic Appendix B, C, and D of the published paper. The full set of plots can be inspected under http://dx.doi.org/10.1051/0004-6361/200913359, and is attached to this thesis in digital form. In the printed version of this thesis, we only show an example for each of these plots. The main result of this paper was the identification of the shocks regions throughout the GC, as traced by the enhancement of the SiO emission with respect to the HCO^+ emission. These shocks regions were associated to two phenomena: The foot point of the Giant Molecular Loops, and to the large scale dynamic in the GC. These shock regions were identified as the places where gas at the high latitude are interacting with gas of the plane of the GC, and also as the places where gas coming from the disk of the Galaxy is accreted towards the GC, defining the "interaction regions" discussed in the following chapters of this thesis.

The data were observed between 1999-2003 by Drs. Leonardo Bronfman, Jorge May, and Fernando Olmos, and from 2003 onward by myself. I did all the data reduction and analysis. These data in the preliminary form were presented in my Master thesis at the Universidad de Chile. During my PhD at IRAM, I reanalyzed the data, leading the scientific disscussion and the writing of the paper. I would like to dedicate this Chapter of the thesis to Fernando Olmos (†) who taught me how to reduce my first spectra and with whom I shared many hours in his office.

A&A 523, A45 (2010)
DOI: 10.1051/0004-6361/200913359

Astronomy & Astrophysics

A survey of the Galactic center region in HCO^+, $H^{13}CO^+$, and SiO

D. Riquelme[1,2], L. Bronfman[2], R. Mauersberger[1,3], J. May[2], and T. L. Wilson[4]

[1] Instituto de Radioastronomía Milimétrica (IRAM), Av. Divina Pastora 7, Local 20, 18012 Granada, Spain
e-mail: riquelme@iram.es
[2] Departamento de Astronomía, Universidad de Chile, Casilla 36-D, Santiago, Chile
[3] Joint ALMA Observatory, Av. Alonso de Córdova 3107, Vitacura, Santiago de Chile, Chile
[4] Naval Research Laboratory, Code 7210, Washington, DC 20375, USA

Received 26 September 2009 / Accepted 7 June 2010

ABSTRACT

Aims. A large-scale survey of the Galactic center region in the 3 mm rotational transitions of SiO, HCO^+ and $H^{13}CO^+$ (beamsize ~3.′6) was conducted to provide an estimate of cloud conditions, heating mechanisms, chemistry, and other properties.
Methods. Using the NANTEN 4 m telescope from Nagoya University, a region between $-5.^\circ75 < l < 5.^\circ6$ and $-0.^\circ68 < b < 1.^\circ3$ was mapped in the $J = 1 \rightarrow 0$ lines of HCO^+ and $H^{13}CO^+$ and in the $J = 2 \rightarrow 1$ line of SiO with a spacing of 3.′75 (HCO^+) and 1.′875 (SiO and $H^{13}CO^+$).
Results. Velocity channel maps, longitude-velocity maps, and latitude-velocity maps are presented. We identify 51 molecular clouds; 33 of them belong to the Galactic center and 18 to disk gas. We derive an average of the luminosity ratio of SiO($J = 2 \rightarrow 1$)/CO($J = 1 \rightarrow 0$) in clouds belonging to the Galactic center of 4.9×10^{-3} and for disk clouds of 3.4×10^{-3}. The luminosity ratio of HCO^+($J = 1 \rightarrow 0$)/CO($J = 1 \rightarrow 0$) in the Galactic center is 3.5×10^{-2}, and for disk clouds it is 1.5×10^{-2}. We can distinguish clearly between regions where the SiO or HCO^+ dominate.

Key words. ISM: clouds – ISM: molecules – Galaxy: center – surveys

1. Introduction

To understand the evolution, dynamics, and constitution of our Galaxy, it is crucial to explore its central kiloparsec. This region is obscured by intervening dust in the optical, but not in the millimeter to far infrared wavelength range. It contains a large amount (~3×10^7 $M_\odot$, see Dahmen et al. 1998) of molecular gas, the Central Molecular Zone[1] (CMZ, Morris & Serabyn 1996), which is traced by the mm-emission of CO and its isotopomers (e.g. Bitran et al. 1997; Dahmen et al. 1998; Bally et al. 1987). The distribution and mass of the components of the interstellar medium (ISM) in the central part of the Galaxy is discussed by Ferrière et al. (2007).

Clouds in the Galactic center region are influenced by large potential gradients, and the proximity to the center of our Galaxy, which may lead to frequent cloud-cloud collisions and exposes the clouds to enhanced magnetic fields, cosmic ray fluxes, X-rays, and explosive events. As a consequence, in the CMZ, the lines are first, typically wider than 10 km s^{-1} (e.g. Morris & Serabyn 1996). Second, the thermal emission of SiO is extended, finding it over parsec-size regions (e.g. Martín-Pintado et al. 1997; Hüttemeister et al. 1998), which is also seen in the central regions of external galaxies (Mauersberger & Henkel 1991). In contrast, in the Galactic disk, SiO is observed mainly at the leading edges of outflows, which has been interpreted as a signature of shocked gas (e.g. Ziurys et al. 1990). In general, Galactic disk sources are compact with sizes of <0.1 pc or at most 1 pc (Jiménez-Serra et al. 2010). Third, a substantial amount of the gas has a kinetic temperature of ~200 K (e.g. Hüttemeister et al. 1993), while the bulk of the dust has a much lower temperature of $T_{\rm dust} < 40$ K (Rodríguez-Fernández et al. 2002; Odenwald & Fazio 1984; Cox & Laureijs 1989). Our survey results provide additional information about the heating and chemistry of Galactic center clouds that cannot be easily obtained from an analysis of CO data alone.

HCO^+ is a molecule known to vary considerably in abundance relative to neutral molecules with similar dipole moments and rotational constants, such as HCN, within a galaxy and from galaxy to galaxy (Nguyen et al. 1992; Seaquist & Frayer 2000; Krips et al. 2008). Seaquist & Frayer (2000) argue that, in the environment of circumnuclear galactic or extragalactic gas, the abundance of HCO^+ decreases with increasing CR ionization rates. However, Krips et al. (2008) observe that the HCO^+ abundance tends to be higher in galaxies with nuclear starbursts than in galaxies with active galactic nuclei (AGN), which would be unexpected if HCO^+ is destroyed by the CRs produced by SNRs. Using chemical model computations for photon-dominated regions (PDRs), Bayet et al. (2009) found that the molecular fractional abundance of HCO^+ is insensitive to changes in both the CR ionization rate and the far-UV radiation. Loenen et al. (2008) also point out that in PDRs the ratios of HCO^+ to HCN or HNC decrease with increasing density and that a change in the UV flux of two orders of magnitude only produces modest changes in the line ratio because the UV field is attenuated at the high column densities. To provide information about the chemistry of HCO^+ in circumnuclear regions and to relate this to CR ionization rates and to heating mechanisms, we mapped this molecule and its rare $H^{13}CO^+$ isotopomer in its $J = 1-0$ transition throughout the Galactic center. These results can be combined with CO data to provide insight into conditions

[1] Following the notation of Morris & Serabyn (1996), we refer to the "CMZ" as the region about $-0.^\circ5 < l < 1.^\circ5$, and to the "Galactic center region" as the region between $-5^\circ < l < 5^\circ$, which is the region observed in this work.

Table 1. Atomic and molecular surveys of the Galactic bulge.

Species	Frequ. [GHz]	Observed Area l [°]	b [°]	Sampling interval	*FWHM*	Ref.
H I	1.4	$-11 \le l \le 13$	$-10 \le b \le 10$	30′	21′	1
C I	492	$-0.5 \le l \le 1.5$	0	3′	2′	2
C II	1900	$-100 \le l \le 60$	$-3 \le b \le 3$		15′	3
^{12}CO (1–0)	115	$-10 \le l \le 25$	0[b]	30′[c]	65′	4
^{12}CO (1–0)	115	$-12 \le l \le 13$	$-2 \le b \le 2$	7.′5[a]	8.′8	5
^{12}CO (1–0)	115	$-12 \le l \le 12$	$-5 \le b \le 5$	4′	2.′7	6
^{12}CO (2–1)	231	$-3 \le l \le 3$	0	7.′5	9′	7
^{12}CO (2–1)	231	$-6 \le l \le 6$	$-2 \le b \le 2$	7.′5	9.′2	8
^{12}CO (3–2)	345	$-1.5 < l < +1.0$	$-0.2 < b < +0.2$	34″	22″	9
^{13}CO (1–0)	110	$-5 \le l \le 5$	$-0.6 \le b \le 0.6$	1.′7	6′	10
^{13}CO (1–0)	110	$-6 \le l \le 8$	$-1 \le b \le 1$	2′	2.′6	6
^{13}CO (2–1)	220	$-1.5 \le l \le 3.25$	0	7.′5	9.′2	8
C^{18}O (1–0)	110	$-1.05 \le l \le 3.6$	$-0.9 \le b \le 0.9$	9′	9′	11
NH_3 (1, 1)–(3, 3)	24	$-2 \le l \le 2$	0	1.′7	5.′3	12
SiO (1–0)	43	$-0.8 \le l \le 0.9$	$-0.25 \le b \le 0.2$	2′	2′	13
OH	1.7	$-6 \le l \le 8$	$-1 \le b \le 1$	12′	10′	14
H_2CO	4.8	$0.5 \le l \le 4$	$-0.5 \le b \le 0.9$	3′	3′	15
CS (2–1)	98	$-1 \le l \le 3.7$	$-0.4 \le b \le 0.4$	1′	2′	10
HNCO($5_{0,5}$–$4_{0,4}$)	110	$-1.05 \le l \le 3.6$	$-0.9 \le b \le 0.9$	9′	9′	11
HCN (1–0)	89	$-0.2 \le l \le 0.7$	$-0.2 \le b$[d] ≤ 0.1	2′	2′	16
HCN (1–0)	89	$-2.15 \le l \le 2.15$	$-0.3 \le b \le 0.2$	0.′8	1′	17
HCN (1–0)	89	$-6 \le l \le 6$	$-0.8 \le b \le 0.87$	4′[e]	1′	18

References. 1) Burton & Liszt (1983); 2) Jaffe et al. (1996); 3) Nakagawa et al. (1995); 4) Bania (1986); 5) Bitran et al. (1997); 6) Fukui et al. (2006); 7) Oka et al. (1996); 8) Sawada et al. (2001); 9) Oka et al. (2007); 10) Bally et al. (1987); 11) Dahmen et al. (1997); 12) Morris et al. (1983); 13) Martín-Pintado et al. 1997, 2000; 14) Boyce & Cohen (1994); 15) Zylka et al. (1992); 16) Fukui et al. (1977); 17) Jackson et al. (1996); 18) Lee (1996).

Notes. [a] for $-1° \le l \le 1°$; [b] also 4 strips in latitude at ±10′ and ±20′; [c] at $b = 0$, $\Delta l = 6'$; [d] few positions towards SgrB; [e] 8′ in regions of weak emission.

in the Galactic center. SiO emission, on the other hand, is a tracer of hot, shocked gas, since it can be formed from silicon that is liberated from dust grains, either by low-velocity shock waves or by evaporation at high temperatures. Such shocks are expected, e.g., at the foot points of the giant molecular loops detected by Fukui et al. (2006), who explain such features by the magnetic buoyancy caused by a Parker instability.

Large-scale surveys have been made in ^{12}C^{16}O and its isotopomers in the $J = 1 \rightarrow 0$, as well as in $J = 2 \rightarrow 1$ spectral lines (e.g. Bitran et al. 1997; Dahmen et al. 1998; Oka et al. 2001). Up to now, there are few complete maps in species that are less abundant than CO (e.g. CS: Bally et al. 1987, 1988; HNCO: Dahmen et al. 1997; NH_3: Handa et al. 2006; OH: Boyce & Cohen 1994). A compilation of existing spectral line surveys updated from Mauersberger & Bronfman (1998) is given in Table 1. There have been two previous surveys of SiO in the Galactic center region. Martín-Pintado et al. (1997) mapped the $J = 1 \rightarrow 0$ spectral line, but did not cover the entire CMZ. Hüttemeister et al. (1998) measured a number of SiO and CO spectral line transitions toward 33 cloud maxima, to investigate the excitation of the SiO and estimate SiO/H_2 ratios for the clouds. There is a map of the $J = 1 \rightarrow 0$ spectral line of main isotopic HCO^+ by Linke et al. (1981), which does not, however, extend far beyond the Sgr A* region. Fukui et al. (1980) also present HCO^+ ($J = 1 \rightarrow 0$) observations, but only toward Sgr A and a few positions in Sgr B2. In the following, we present maps of the $J = 2 \rightarrow 1$ spectral line of SiO and the $J = 1 \rightarrow 0$ spectral lines of HCO^+ and $H^{13}CO^+$. These are the first complete maps of both species in the Galactic center region.

In Sect. 2 the observations and data reduction are described. In Sect. 3, the survey data are presented. These consist of the full set of the spatial maps of the integrated intensity, longitude-velocity diagrams, and latitude-velocity diagrams for each molecule. We present an analysis in Sect. 4. Four appendices are also included, beginning with Appendix A which presents complementary figures for the paper. Also, Appendices B–D present the complete data set in HCO^+, SiO, and $H^{13}CO^+$, respectively, showing velocity channel maps of 10 km s^{-1} velocity width, longitude-velocity, and latitude-velocity diagrams. Appendix E contains the Gaussian fits for each cloud in the survey, identifying the temperature peaks, velocity center, and velocity width. In a subsequent paper, the results will be discussed in the context of other available data.

2. Observations and data reduction

2.1. Observations

This survey was carried out with the NANTEN 4 m telescope operated by Nagoya University at the Las Campanas Observatory, Chile. With its southern location and moderate angular resolution, this instrument is well-suited to large-scale mapping of the Galactic center region. It has a 3.′5 beamwidth at the HCO^+ frequency (89.188518 GHz, Lovas et al. 1979) and a 3.′6 beamwidth at the SiO frequency (86.846998 GHz, Lovas et al. 1979), which corresponds to a spatial resolution of about 9 pc at a distance of 8.5 kpc (Blitz et al. 1993). The front end was a 4 K cryogenically cooled NbN superconductor-insulator-superconductor (SiS) mixer receiver that provided a typical system temperature of ~280 K (single side band). The spectrometer was an acousto-optical spectrometer (AOS) with 2048 channels. The frequency coverage and resolution were 250 MHz and 250 kHz, corresponding to a velocity coverage of 840 km s^{-1}

Table 2. Parameters of the survey.

	HCO^+	**SiO**	**$H^{13}CO^+$**
Velocity resolution	1 km s^{-1}	1 km s^{-1}	1 km s^{-1}
Rms sensitive	28 mK	20 mK	20 mK
Spatial range:			
CMZ	$-1.^\circ5 \le l \le 2.^\circ25$	$-1.^\circ375 \le l \le 2.^\circ0$	$-1.^\circ375 \le l \le 2.^\circ0$
	$-0.^\circ5625 \le b \le 0.^\circ5625$	$-0.^\circ5 \le b \le 0.^\circ5$	$-0.^\circ5 \le b \le 0.^\circ5$
M+3.2+0.3 (Clump 2)	$2.^\circ5625 \le l \le 3.^\circ5$	$2.^\circ5625 \le l \le 3.^\circ4375$	$2.^\circ5625 \le l \le 3.^\circ4375$
	$-0.^\circ3125 \le b \le 0.^\circ8125$	$-0.^\circ25 \le b \le 0.^\circ875$	$-0.^\circ25 \le b \le 0.^\circ875$
M−5.3+0.4	$-5.^\circ75 \le l \le -4.^\circ6875$	$-5.^\circ8125 \le l \le -4.^\circ6875$	$-5.^\circ8125 \le l \le -4.^\circ6875$
	$-0.^\circ125 \le b \le 0.^\circ5625$	$-0.^\circ125 \le b \le 0.^\circ5625$	$-0.^\circ125 \le b \le 0.^\circ5625$
M−4.4+0.6	$-4.^\circ75 \le l \le -4.^\circ25$	$-4.^\circ75 \le l \le -4.^\circ3125$	$-4.^\circ75 \le l \le -4.^\circ3125$
	$0.^\circ25 \le b \le 0.^\circ8125$	$0.^\circ1875 \le b \le 0.^\circ84375$	$0.^\circ1875 \le b \le 0.^\circ84375$
M−3.8+0.9	$-4.^\circ0 \le l \le -3.^\circ625$	$-4.^\circ0625 \le l \le -3.^\circ625$	$-4.^\circ0625 \le l \le -3.^\circ625$
	$0.^\circ5625 \le b \le 1.^\circ1875$	$0.^\circ5625 \le b \le 1.^\circ21875$	$0.^\circ5625 \le b \le 1.^\circ21875$
M+5.3−0.3	$5.^\circ125 \le l \le 5.^\circ625$	$5.^\circ0625 \le l \le 5.^\circ6875$	$5.^\circ0625 \le l \le 5.^\circ6875$
	$-0.^\circ6875 \le b \le 0.^\circ125$	$-0.^\circ8125 \le b \le 0.^\circ125$	$-0.^\circ8125 \le b \le 0.^\circ125$
Sampling interval:	$3.'75$	$3.'75$	$3.'75$
		$1.'875^a$	$1.'875^a$
Velocity range:			
CMZ	-350 km s$^{-1} \le v \le 350$ km s^{-1}	-280 km s$^{-1} \le v \le 300$ km s^{-1}	-300 km s$^{-1} \le v \le 250$ km s^{-1}
M+3.2+0.3	-300 km s$^{-1} \le v \le 300$ km s^{-1}	-150 km s$^{-1} \le v \le 350$ km s^{-1}	-180 km s$^{-1} \le v \le 200$ km s^{-1}
M−5.3+0.4	-350 km s$^{-1} \le v \le 350$ km s^{-1}	-150 km s$^{-1} \le v \le 210$ km s^{-1}	-190 km s$^{-1} \le v \le 260$ km s^{-1}
M−4.4+0.6	-350 km s$^{-1} \le v \le 350$ km s^{-1}	-150 km s$^{-1} \le v \le 210$ km s^{-1}	-190 km s$^{-1} \le v \le 260$ km s^{-1}
M−3.8+0.9	-350 km s$^{-1} \le v \le 350$ km s^{-1}	-320 km s$^{-1} \le v \le 190$ km s^{-1}	-190 km s$^{-1} \le v \le 130$ km s^{-1}
M+5.3−0.3	-300 km s$^{-1} \le v \le 300$ km s^{-1}	-100 km s$^{-1} \le v \le 270$ km s^{-1}	-190 km s$^{-1} \le v \le 280$ km s^{-1}

Notes. [(a)] In the most intense zones, see Fig. 2. M+3.2+0.3, M−5.3+0.4, M−4.4+0.6, M−3.8+0.9, M+5.3−0.3, are the clouds observed by Bitran et al. (1997) and the positions of the cloud are defined by them.

and a velocity resolution of 0.84 km s^{-1} at the HCO^+ frequency, and a velocity coverage of 863 km s^{-1} and a velocity resolution of 0.86 km s^{-1} at the SiO frequency. The data were calibrated using the standard chopper-wheel method (Kutner & Ulich 1981). The measured quantity, $T_{\rm obs}$, was converted to antenna temperature, using $T_{\rm A}^* = T_{\rm obs}/(2 \times 0.89) = T_{\rm obs}/1.78$. The factor of 2 is needed because our raw NANTEN data were calibrated as double sideband, while the receiver used was single sideband. The factor of 0.89 is a measured correction arising from the less-than-perfect image band suppression. Throughout this work, all values are given in $T_{\rm A}^*$. The main beam temperature scale, $T_{\rm MB}$, can be obtained using $T_{\rm MB} = T_{\rm A}^*/\eta_{\rm MB}$, where the main beam efficiency is $\eta_{\rm MB} = 0.87$ at 86 GHz (value provided by the Nanten team).

The data were observed between 1999 and 2003. The area mapped is from about $l = -5.^\circ7$ to $l = 5.^\circ6$ and from $b = -0.^\circ7$ to $b = 1.^\circ3$. The survey contains about 1500 positions in the $J = 1 \rightarrow 0$ spectral line of HCO^+, at a uniform spacing of $3.'75$. Each map point was observed for at least 1 min on source, for an rms noise antenna temperature of 28 mK at a velocity resolution of 1 km s^{-1}. More than 3000 positions were observed in the $J = 2 \rightarrow 1$ spectral line of the vibrational ground state of SiO, fully sampling at $1.'875$ spacing in the most intense regions (see Fig. 2). Each map point was observed for 2.5 min on source, for an rms noise antenna temperature of 20 mK at a 1 km s^{-1} velocity resolution. The survey consisted of the CMZ, and five molecular clouds observed in CO by Bitran et al. (1997) with large velocity widths that we call here "Peripheral Molecular Zone" (PMZ). We also observed the presumably optically thin formyl ion isotopic $H^{13}CO^+$ $J = 1 \rightarrow 0$ line (86.754330 GHz, Lovas et al. 1979), which is in the same spectrometer range as SiO (see Table 2 for parameters of the survey)[2].

[2] The data cubes are available at http://www.das.uchile.cl/galcendata

2.2. Data reduction

The data were reduced using the NDRS (Nanten Data Reduction Software) package. Each data point was reduced individually, fixing the velocity emission interval, and the order of the polynomial to fit the spectrum baseline. Most baselines were polynomials of first order, but a few spectra required second and third order baselines to produce flat spectra where no spectral line emission was expected. To determine the emission interval, we used the velocity intervals where CO($1 \rightarrow 0$) emission appears in the Galactic center (Bitran et al. 1997).

For the reduction of spectra belonging to the CMZ and M+3.2+0.3 cloud, we used the longitude-velocity diagrams of CO (Bitran et al. 1997) as a guide to determine the range of possible molecular emission required for baseline subtraction. The reduction and evaluation of HCO^+ data was straightforward since this spectral line is not blended with other strong molecular emission. The SiO reduction was more difficult since within the SiO band, spectra are offset by +320 km s^{-1} from the $H^{13}CO^+$ ($1 \rightarrow 0$) spectral line. Given the large linewidths present in the CMZ, these spectra are sometimes nearly blended. These two spectral lines were reduced independently. In most of the spectra, the SiO and $H^{13}CO^+$ emission are clearly separated, but toward $l < -0.^\circ5$ in CMZ, the SiO spectrum shows high-velocity emission (~170 km s^{-1}, see Fig. 4 middle), and a priori is not clear whether this emission corresponds to a high velocity clouds in SiO, or to a low velocity cloud in $H^{13}CO^+$ (~ − 150 km s^{-1}). In most cases, a comparison with (unblended) main isotopic HCO^+ could settle this ambiguity. For very few spectra (~10 spectra), we had to study adjacent spectra to distinguish between emission from SiO and $H^{13}CO^+$. This kind of problem was only found in the CMZ in longitudes lower than $-0.^\circ5$. In most cases (~90%), the emission appears to come from high-velocity SiO cloud, rather than $H^{13}CO^+$.

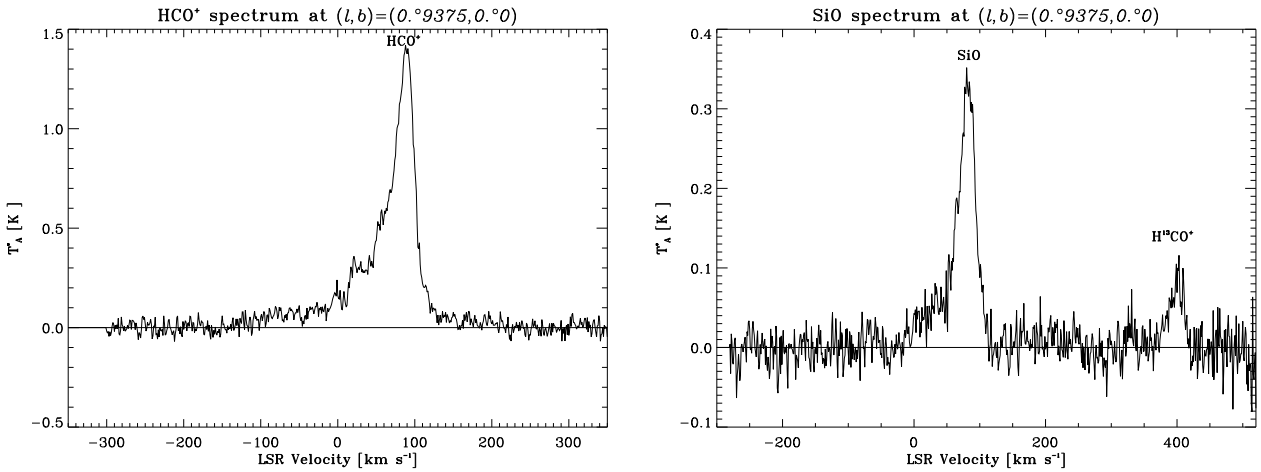

Fig. 1. Typical spectra of HCO^+ (*left*) and SiO and $H^{13}CO^+$ (*right*) at l and b (0.°9375, 0.°0).

In the PMZ, the data reduction was more difficult owing to the low signal-to-noise ratios in the spectra (∼5 and even less in M−3.8+0.9 cloud in $H^{13}CO^+$) and the high linewidths. In these cases, we used the CO data from Bitran (1987) to define the velocity interval range where the emission is possible. We first obtained a summed spectrum over the total cloud and from that defined the velocity range of emission. To establish the baseline, we subsequently reduced each spectrum individually. To reduce the HCO^+ spectra we interpolated the CO data, which have a sampling of 7.′5, to the same grid as the HCO^+ (3.′75), and then compared spectrum by spectrum. For SiO, we interpolated the HCO^+ data to the SiO sampling (1.′875), and finally, for $H^{13}CO^+$, we used HCO^+ and SiO data to define the velocity range where emission might be present. The polynomial order of the subtracted baselines was typically higher than for the CMZ. Most spectra required a polynomial order below 3, but in a few cases, we had to use fourth grade. The basic result of the survey are data cubes, i.e. only, spectra obtained point by point in longitude and latitude, forming a three-dimensional array of T_A^*. We obtained three data sets with coordinates galactic longitude-galactic latitude-radial velocity for each observed molecule.

3. Results

In this section we present the results of the HCO^+ (1 → 0), SiO (2 → 1), and $H^{13}CO^+$ (1 → 0) Galactic center survey. Figure 1 shows typical spectra of HCO^+, $H^{13}CO^+$, and SiO. The HCO^+ spectrum shows emission over a very broad velocity range between −150 km s^{-1} and 100 km s^{-1}.

3.1. The integrated intensity maps

In Fig. 2, we show the integrated intensity maps, $\int T_A^* \mathrm{d}v$, of the entire observed region in the HCO^+, SiO, and $H^{13}CO^+$ spectral lines. For a better display of the observations, we chose the velocity integration range in each spectral line to cover only the emission visible in the respective longitude-velocity diagram, which is indicated in the figure captions. The lowest contour level is at 3σ. The value of σ was calculated as

$$\sigma_{lb} = \sqrt{N_v} \times \Delta v \times T_A^*(\mathrm{rms}), \quad (1)$$

where N_v is the number of velocity channels covered by the emission (for example, in HCO^+, the emission is within −230 to 270 km s^{-1}, therefore N_v = 501), Δv is the velocity resolution (1 km s^{-1}), and T_A^*(rms) is 28 mK for HCO^+ and 20 mK for SiO and $H^{13}CO^+$. In Fig. 2, we can distinguish both the CMZ and the PMZ. In the SiO and $H^{13}CO^+$ maps, the spacing of the observations was variable (1.′875 in the most intense regions and 3.′75 for the remaining of the maps, see top of Fig. 2). We therefore interpolated the map to the positions with no observations.

For an easy comparison with previous work, most of which include only the CMZ and the cloud at l ∼ 3.°2, in Appendix A, we plot the integrated intensity emission only in this region in all spectral lines observed (Fig. A.1). In this figure we can see the well-known asymmetry of molecular distribution with respect to the Galactic center, with the emission concentrated on the positive longitude side (e.g. Sawada et al. 2001; Oka et al. 1996), and the broad features of the CMZ such as Sgr A (l ∼ 0°), Sgr B (l ∼ 0.°6), Sgr C (l ∼ −0.°5), Sgr D (l ∼ 1.°1), Sgr E (l ∼ −1.°1, v − 200 km s^{-1}, see e.g. Liszt 2006), and the 1.°3 complex. In the HCO^+ spectral line, both in the velocity-integrated map and in the channel maps (Appendix B), the most intense source corresponds to l = 0.°0625 and b = −0.°0625 (in Sgr A region). In SiO emission, the intensity peak of the whole map is at l = 0.°75 and b = −0.°0625, i.e. the Sgr B2 region. In $H^{13}CO^+$, the highest intensity is toward Sgr B and Sgr A; the other CMZ features are less intense. In the Appendices B.1, C.1, and D.1, we present integrated intensity maps in these spectral lines in 10 km s^{-1} wide velocity intervals.

3.2. Longitude-velocity plots

In Fig. 3, we plot the intensity integrated in latitude for the survey ($\int T_A^* \mathrm{d}b$), covering all the observed range as a function of l. In HCO^+ and SiO maps, we can clearly see the CMZ and the PMZ, which appear as broad features. In $H^{13}CO^+$, the CMZ is weak as seen, and the only cloud clearly seen is the M−3.8+0.9. The lowest level of the contours is 3σ, which was calculated using

$$\sigma_{lv} = \sqrt{N_b} \times \Delta b \times T_A^*(\mathrm{rms}), \quad (2)$$

where N_b is the number of latitude points with latitude emission (e.g., 17 pixels for HCO^+ in the CMZ), and Δb the spacing in latitude (0.°0625 for HCO^+ data and 0.°03125 for SiO and $H^{13}CO^+$ data).

In Appendix A, we plot the integrated intensity in latitude for the CMZ and M+3.2+0.3 cloud (Fig. A.2). We see the well known asymmetry in longitude and velocity as a parallelogram

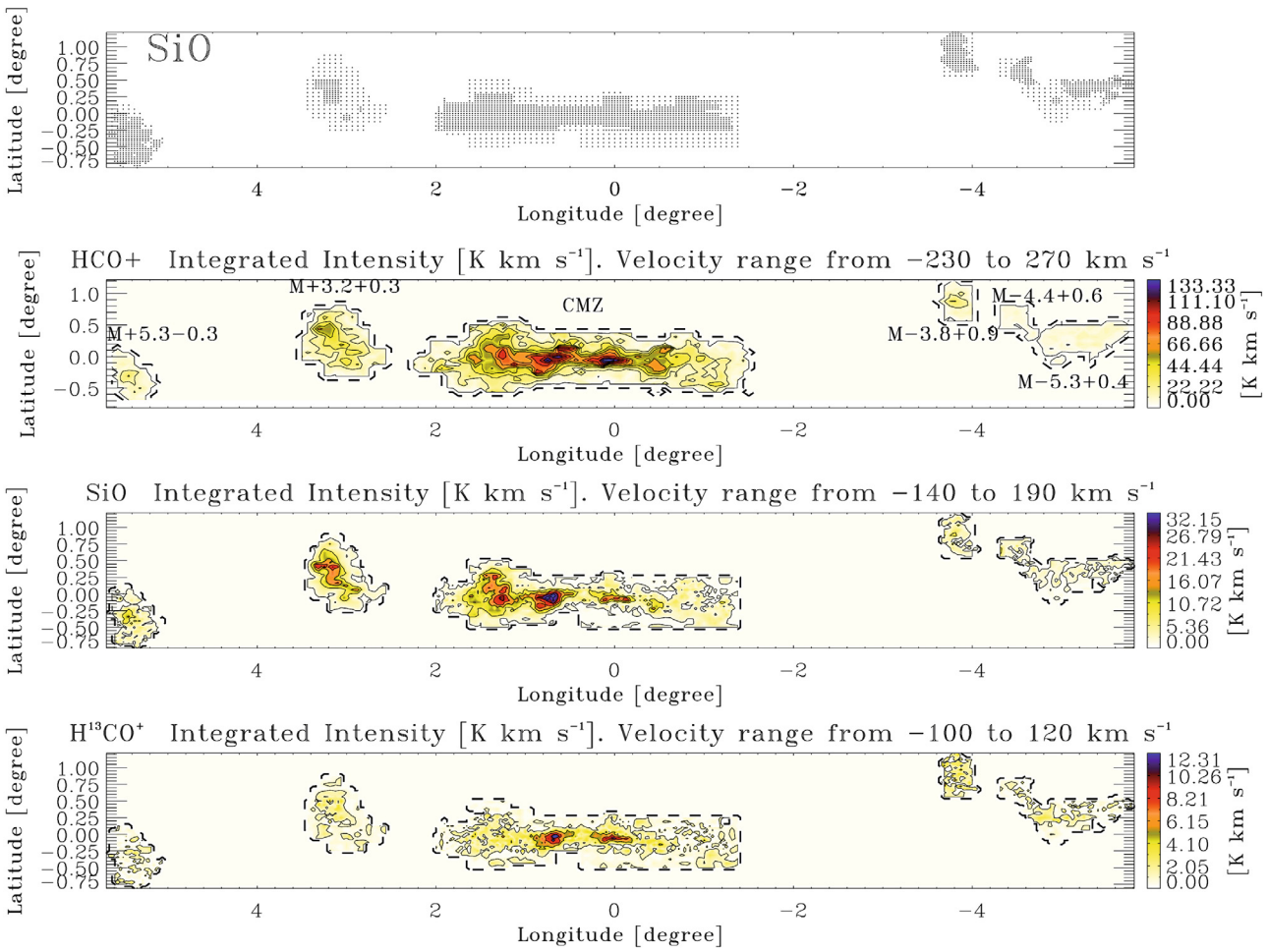

Fig. 2. *From top to bottom*: spatial coverage of the observations in SiO and $H^{13}CO^+$ (HCO^+ has uniform sampling of 3.′5). Emission integrated over velocity from −230 to 270 km s^{-1} for the region measured in HCO^+. The solid contour levels start at 1.9 K km s^{-1} (3σ) and increase in steps of 12.53 K km s^{-1} (20σ). Emission integrated over velocity from −140 to 190 km s^{-1} for the region measured in SiO. The solid contours start at 1.09 K km s^{-1} (3σ) and increase in steps of 5.46 K km s^{-1} (15σ). Emission integrated over velocity from −100 to 120 km s^{-1} for the region measured in $H^{13}CO^+$. The solid contours start at 0.89 K km s^{-1} (3σ) and increase in steps of 2.97 K km s^{-1} (10σ). In all plots, the dashed line shows the coverage of the survey in each molecule. For a better display of the observations, we choose the velocity integration range in each spectral line to cover only the emission visible in the respective longitude-velocity diagram.

shape, with the emission placed primarily at positive velocities for $l > 0°$ and at negative velocities for $l < 0°$. We see the large molecular complex features, such as Sgr C ($l \sim -0.°7$ to $-0.°1$; $v < 0$ km s^{-1}), Sgr A ($l \sim 0°$, $v \sim 50$ km s^{-1}; Fukui et al. 1977), Sgr B ($l \sim 0.°6$, $v \sim 50$ km s^{-1}), and Sgr D ($l \sim 0.°9$, $v \sim 80$ km s^{-1}) and the 1.°3 complex, with a strong peak at $l \sim 1.°25$ and $v \sim 90$ km s^{-1}. The molecular gas complex associated to Sgr E is barely seen toward $l \sim -1.1°$, $v \sim -200$ km s^{-1} (e.g., Liszt 2006). As already noted in previous surveys of CO and HI (e.g. Bitran et al. 1997; Burton & Liszt 1983), the molecular gas at the Galactic center shows non-circular movements with velocities forbidden for galactic rotation, negative for $l > 0°$, and positive for $l < 0°$.

In the HCO^+ map, the foreground spiral arms appear as narrow absorption features at $l = 0°$ with $v_{LSR} \sim -50$ km s^{-1} (3 kpc arm), $v_{LSR} \sim -30$ km s^{-1} (Norma arm), and $v_{LSR} \sim 0$ km s^{-1} (Crux am). These absorption features were previously observed in HCO^+ and HCN (Fukui et al. 1977, 1980; Linke et al. 1981). In SiO we do not detect any absorption. The SiO emission appears to be more fragmented than HCO^+. Sgr E is weaker than other features. At $l \sim 0°$, we detect the well-known clouds associated with Sgr A. Compared with the others features, Sgr B is very intense. The 1.°3 complex is the most intense feature in this map. In SiO, there is less emission with forbidden velocities than in HCO^+. One example of a region where it is not immediately clear whether the emission arises from high-velocity (forbidden) SiO or from $H^{13}CO^+$ can be seen in the mid panel of Fig. 3 (or with more detail in Fig. A.2) at $l \sim -0.°8$ and $v \sim 150$ km s^{-1}. A comparison with the unblended HCO^+ emission (top panel) clearly suggests that this feature arises from a forbidden velocity component of SiO. In $H^{13}CO^+$, we can see the features of the CMZ, but these are much weaker than in the other molecular lines. Sgr C shows a very weak emission, and we can barely detect the cloud at $l = -0.°5$ and $v = -50$ km s^{-1}. Sgr A is more intense, and one can see three clouds at $(l, v) \sim (0°, -15$ km s$^{-1})$, $(l, v) \sim (-0.°125, 15$ km s$^{-1})$, and at $(l, v) \sim (0.125°, 50$ km s$^{-1})$. The last two could correspond to the molecular complex M−0.13−0.08 y M−0.02−0.07, with velocities of +20 km s^{-1} and +50 km s^{-1}, respectively (Martín-Pintado et al. 1997). Sgr B2 is the most intense feature, with an intensity peak at $l = 0.°65625$ and $v = 50$ km s^{-1}. Sgr D is less intense than in the other molecular lines, and the 1.°3 complex is very weak. In this spectral line, M+3.2+0.3 is barely visible. In Appendices B.2, C.2, and D.2, we present a set

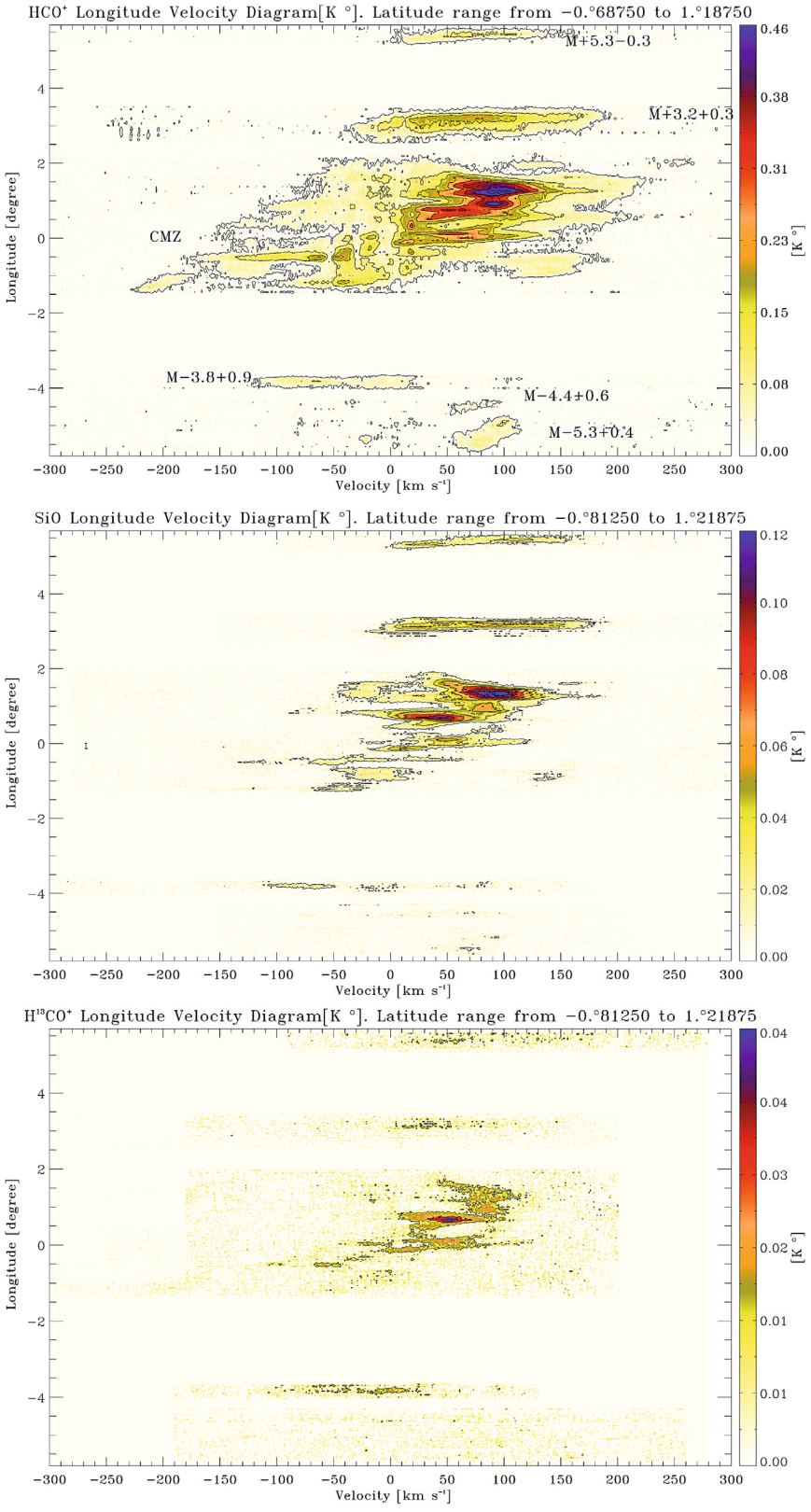

Fig. 3. *Top*: longitude-velocity diagram of HCO^+ emission from the CMZ and PMZ covering the whole survey in the latitude range between $b = -0.^\circ6875$ to $b = 1.^\circ1875$. The contour levels start at 0.021 K (3σ), and increase in steps of 0.058 K (8σ). *Middle*: longitude-velocity diagram of SiO emission from the CMZ and PMZ covering the whole survey in the latitude range between $b = -0.^\circ8125$ to $b = 1.^\circ21875$. The contour levels start at 0.01 K (3σ), and increase in steps of 0.018 K (5σ). *Bottom*: longitude-velocity diagram of $H^{13}CO^+$ emission from the CMZ and PMZ covering the whole survey in the latitude range between $b = -0.^\circ8125$ to $b = 1.^\circ21875$. The contour levels start at 0.009 K (3σ), and increase in steps of 0.016 K (5σ).

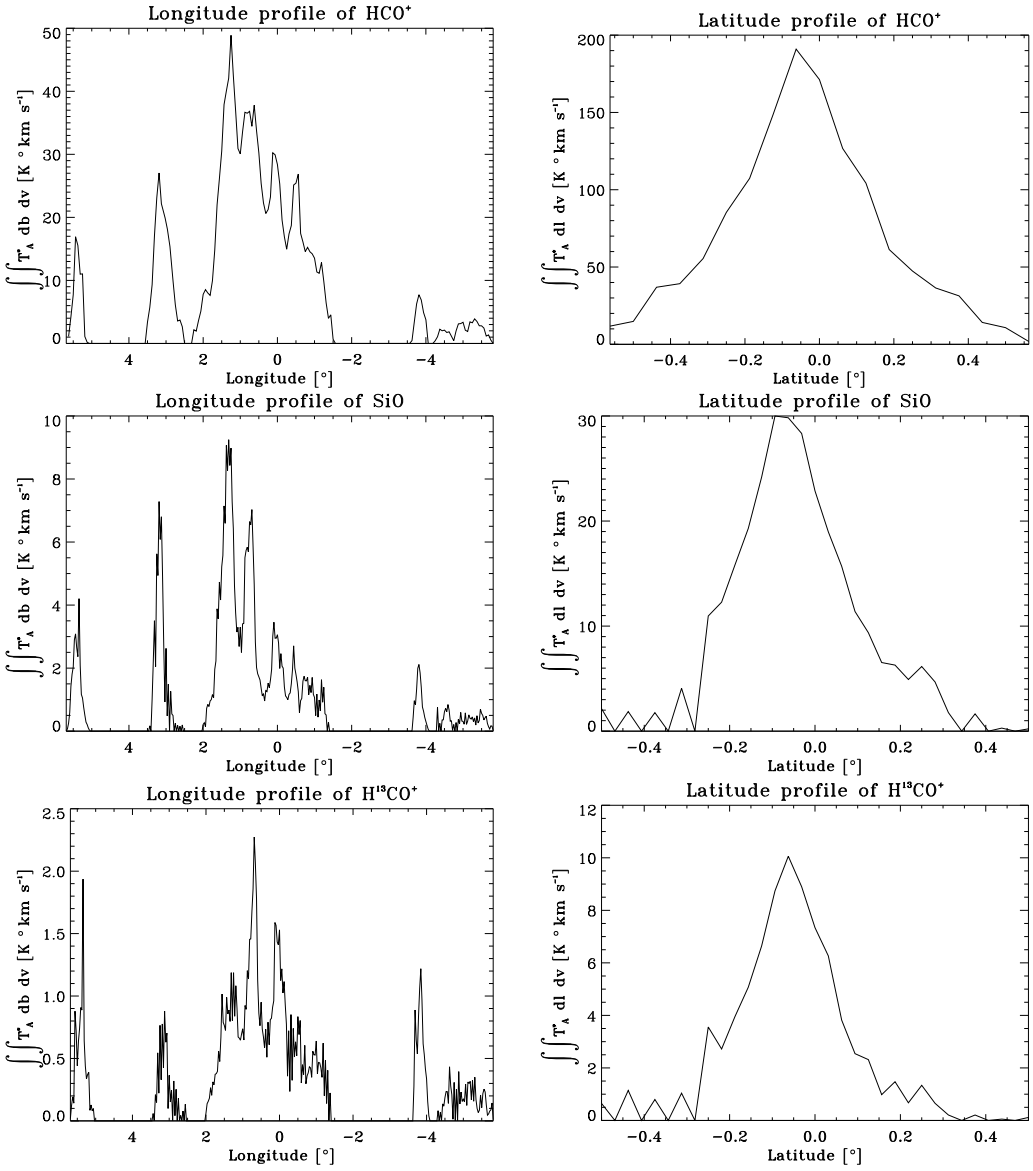

Fig. 4. *Left*: longitude profile for the entire latitude range observed in HCO$^+$ (*top*), SiO (*middle*) and H^{13}CO$^+$ (*bottom*) emission. *Right*: latitude profile for entire longitude range observed of the CMZ ($-1\overset{\circ}{.}5 < l < 2\overset{\circ}{.}25$) in HCO$^+$ (*top*), SiO (*middle*) and H^{13}CO$^+$ (*bottom*) emission.

of longitude-velocity diagrams, one for each observed latitude in HCO$^+$, SiO, and H^{13}CO$^+$.

We show the longitudinal distribution of the molecular emission in Fig. 4, $I(l) = \int\int T_{\rm A}^{*} {\rm d}b{\rm d}v$, integrated over the whole observed latitude. We can see that, in the longitude corresponding to the CMZ, the emission appears asymmetrically distributed toward $l > 0°$, and the 5 clouds in the PMZ clearly appear as intensity peaks at $l \sim 3°$, $5\overset{\circ}{.}5$, $-3\overset{\circ}{.}8$, $-4\overset{\circ}{.}4$, and $-5\overset{\circ}{.}3$. In the CMZ, most of the emission is found toward $l > 0°$, obtaining an average longitude weighted by intensity of $0\overset{\circ}{.}5$ for HCO$^+$, $0\overset{\circ}{.}7$ for SiO, and $0\overset{\circ}{.}4$ for H^{13}CO$^+$.

3.3. Latitude-velocity plots

We present the intensity integrated in longitude ($\int T_{\rm A}^{*} {\rm d}l$), covering all observed range for the CMZ and M+3.2+0.3 cloud. Figure 5 shows the CMZ, integrated in all observed longitude corresponding to this region. In Fig. 6, we show the integrated intensity in longitude from HCO$^+$, SiO, and H^{13}CO$^+$ for the M+3.2+0.3 cloud. In the HCO$^+$ map, the absorption produced by the spiral arms in ~ -50 km s^{-1}, ~ -30 km s^{-1}, and ~ 0 km s^{-1} is apparent.

We present the latitude profile of the CMZ, $I(b) = \int\int T_{\rm A}^{*} {\rm d}l{\rm d}v$ (Fig. 4), integrated over the entire observed longitude. The average latitude weighted by intensity in HCO$^+$ emission is $-0\overset{\circ}{.}04$ (which agrees with the value of $-0\overset{\circ}{.}05$ obtained by Bitran 1987 for CO emission), in SiO, $-0\overset{\circ}{.}04$, and in H^{13}CO$^+$ is $-0\overset{\circ}{.}06$.

In the Appendices B.3, C.3, and D.3 we show the latitude-velocity diagrams, one for each observed longitude.

4. Discussion

As mentioned in the previous section, all molecules observed by us are widely distributed throughout the Galactic center region. To distinguish between the dominant heating mechanism for the molecular gas in well-determined space and velocity regions, we compare the maps of SiO and HCO$^+$ and the maps of SiO and H^{13}CO$^+$.

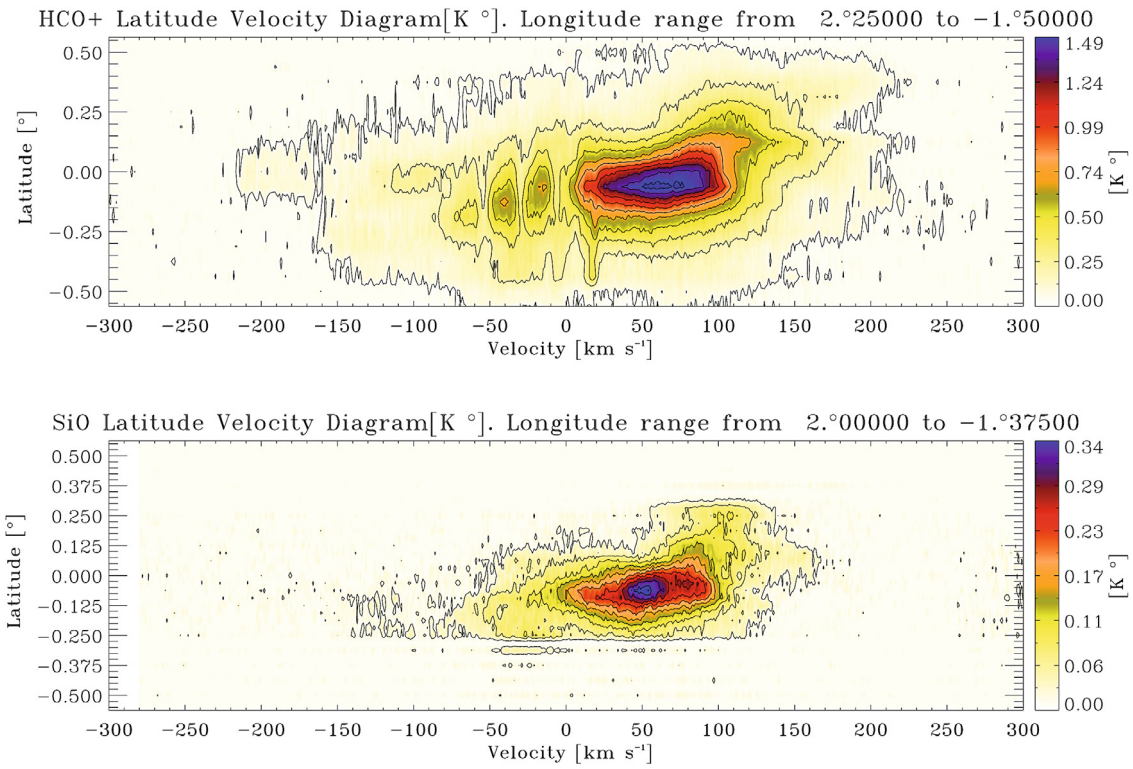

Fig. 5. Latitude-velocity diagram of the CMZ. *Top*: HCO^+. The contours start at 0.041 K (3σ value) and increase in steps of 0.136 K (10σ). *Bottom*: SiO. The contours start at 0.02 K (3σ value) and increase in steps of 0.03 K (5σ).

4.1. The spatial and velocity distributions of the spectral line emission ratios

To compare SiO and HCO^+ emission, we plot the logarithm of the integrated intensity ratio for all positions where the emission of both spectral lines is above 3σ and in different velocity channels. In regions where the emission is below this value we use the 3σ threshold. We also compare the SiO emission with the $H^{13}CO^+$ emission, and use the 3σ threshold in both transitions.

The $H^{13}CO^+$ is useful since it is optically thin and therefore traces the deeper regions of the clouds. Because it has a high critical density of $\sim 10^5$ cm^{-3} (Wilson et al. 2009), it picks out the densest regions in our maps. In Fig. 7 we plot the logarithm of the integrated intensity ratio for SiO and HCO^+ in the velocity range from 30 to 130 km s^{-1}, and for SiO and $H^{13}CO^+$ in the velocity range from −110 to −50 km s^{-1}. In Appendix A, we plot the logarithm of the integrated intensity ratio for velocity intervals of 50 km s^{-1} (Figs. A.3 and A.4). We can clearly identify regions where the HCO^+ (blue regions), or where SiO dominates (yellow and red regions). The SiO-dominated regions are, M−3.8+0.9 cloud (Fig. 7, and in the velocity range from v_{LSR} = −100 to −50 km s^{-1} in Fig. A.4), M+3.2+0.3 cloud, and M+5.3−0.3 cloud (Fig. 7, and in the velocity range from v_{LSR} = 50 to 150 km s^{-1} in Fig. A.3), the 1.°3 complex ($v > 0$ km s^{-1}) and toward Sgr E region, both in negative velocity and in forbidden velocity between $100 < v < 150$ km s^{-1} (Fig. A.4). The HCO^+ is dominant toward Sgr A ($-50 < v < 100$) and Sgr C ($-150 < v < 0$) in the CMZ. In the velocity range of $v_{LSR} = 0$ to 50 km s^{-1}, we observe a very intense SiO zone toward Sgr B, but this velocity range could be contaminated by local gas seen by absorption in HCO^+, toward $v \sim 0$ km s^{-1} (see e.g. top of Fig. A.2), which could increase the SiO to HCO^+ ratio emission (as can be seen in the Fig. 8 at $v \sim 0$ km s^{-1}.

In Fig. 8, we plot the logarithm of the ratio of the intensities integrated in latitude between SiO and HCO^+ emission, using the 3σ threshold. In the region toward Sgr C, Sgr A and Sgr D are dominated by HCO^+, and the region toward the 1.3° complex, Sgr B, M+3.2+0.3, and M+5.3−0.3 are dominated by SiO.

To relate the observed line intensities and intensity ratios to molecular column densities and abundance ratios, assumptions on the excitation conditions of the gas are required. First of all, it is necessary to estimate whether the observed transitions are optically thick or optically thin. In the case of HCO^+, we have measurements of its rarer isotopomere $H^{13}CO^+$. The $^{12}C/^{13}C$ isotopic ratio in the Galactic center region is about 20 (Wilson & Matteucci 1992). If both, HCO^+ and $H^{13}CO^+$ are optically thin in its $J = 1 \rightarrow 0$ transitions one would expect that their line intensity ratio is close to 20. On average, the measured line intensity ratio in the observed region is typically between 10 and 30, with an average of 19.8 (see Fig. A.5). This indicates that the HCO^+ (1−0) emission is indeed optically thin or just moderately optically thick in most of the positions measured by us. This cannot be taken for granted for other galactic centers; for example, in the nearby starbust galaxy NGC 253, the HCO^+ emission is on average optically thick (Henkel et al. 1993).

This allows column densities of the levels involved in the transition to be determined (see e.g. Mauersberger & Henkel 1991, for the corresponding equations). More difficult is the task of determining the total column densities of the corresponding molecules since, depending on the excitation conditions (T_{kin}, $n(H_2)$), the observed levels may represent only a small fraction of the total column density. However, SiO and HCO^+ have very similar dipole moments, namely 3.1 (Raymonda et al. 1970) and 3.9 Debye (Botschwina et al. 1993), and therefore

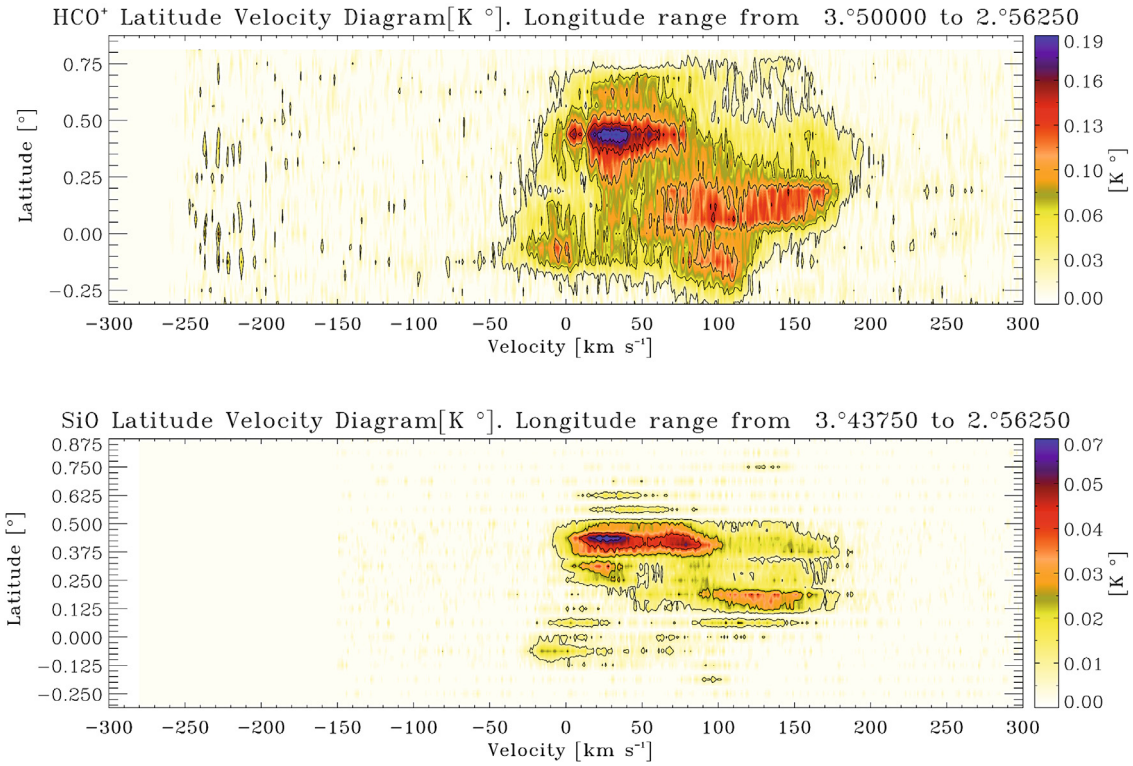

Fig. 6. Latitude-velocity diagram of M+3.2+0.3. *Top*: HCO^+. The contours start at 0.021 K (3σ value) and increase in steps of 0.035 K (5σ). *Bottom*: SiO. The contours start at 0.009 K (3σ value) and increase in steps of 0.015 K (5σ).

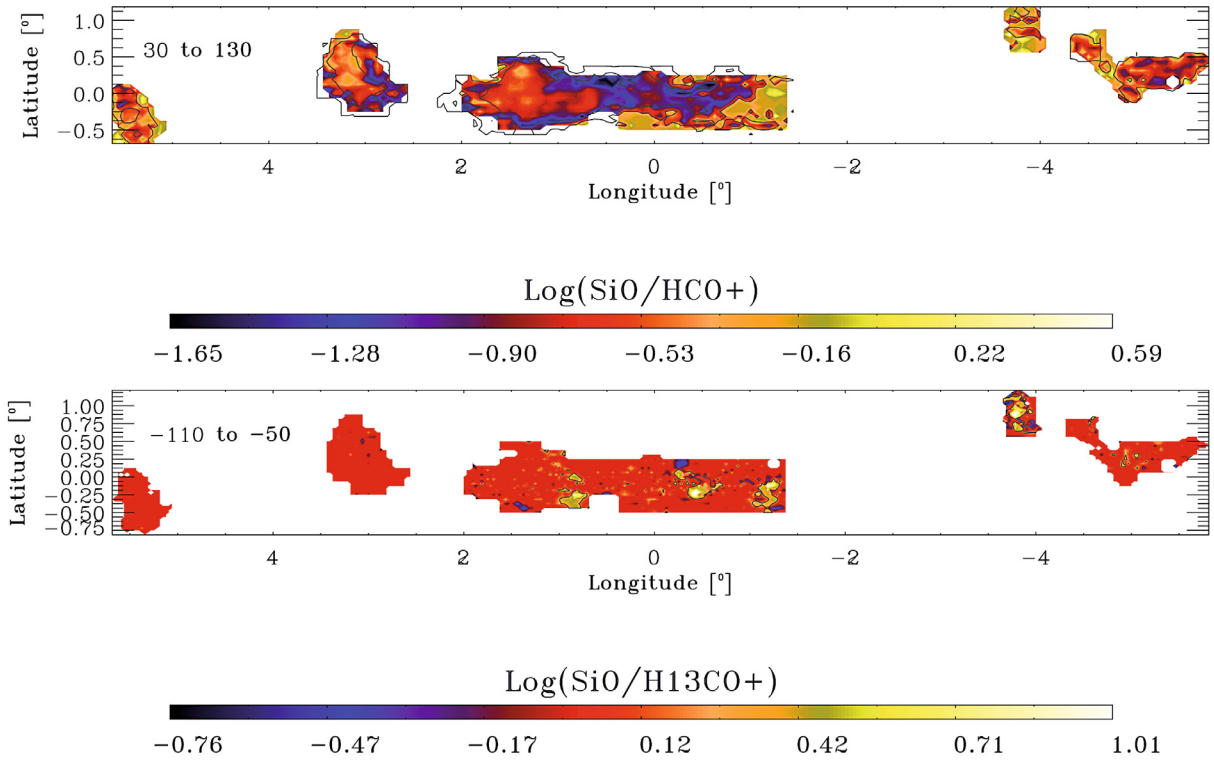

Fig. 7. Logarithm of the integrated intensity ratio. *Top*: $\log(\int T(\mathrm{SiO})\mathrm{d}v / \int T(\mathrm{HCO^+})\mathrm{d}v)$ in the velocity range from 30 to 130 km s^{-1}. The contours correspond to the HCO^+ emission at 3σ and 30σ. We can identify clearly regions where either the SiO (e.g. in the 1.3 Complex and in the M+3.2+0.3 cloud) or HCO^+ (e.g. towards Sgr A region) dominate. *Bottom*: $\log(\int T(\mathrm{SiO})\mathrm{d}v / \int T(\mathrm{H^{13}CO+})\mathrm{d}v)$ in the velocity range from −110 to −50 km s^{-1}. The contours correspond to the SiO emission at 3σ and 30σ. In this velocity range, we can see the enhacement of the SiO toward the M−3.8+0.9 cloud.

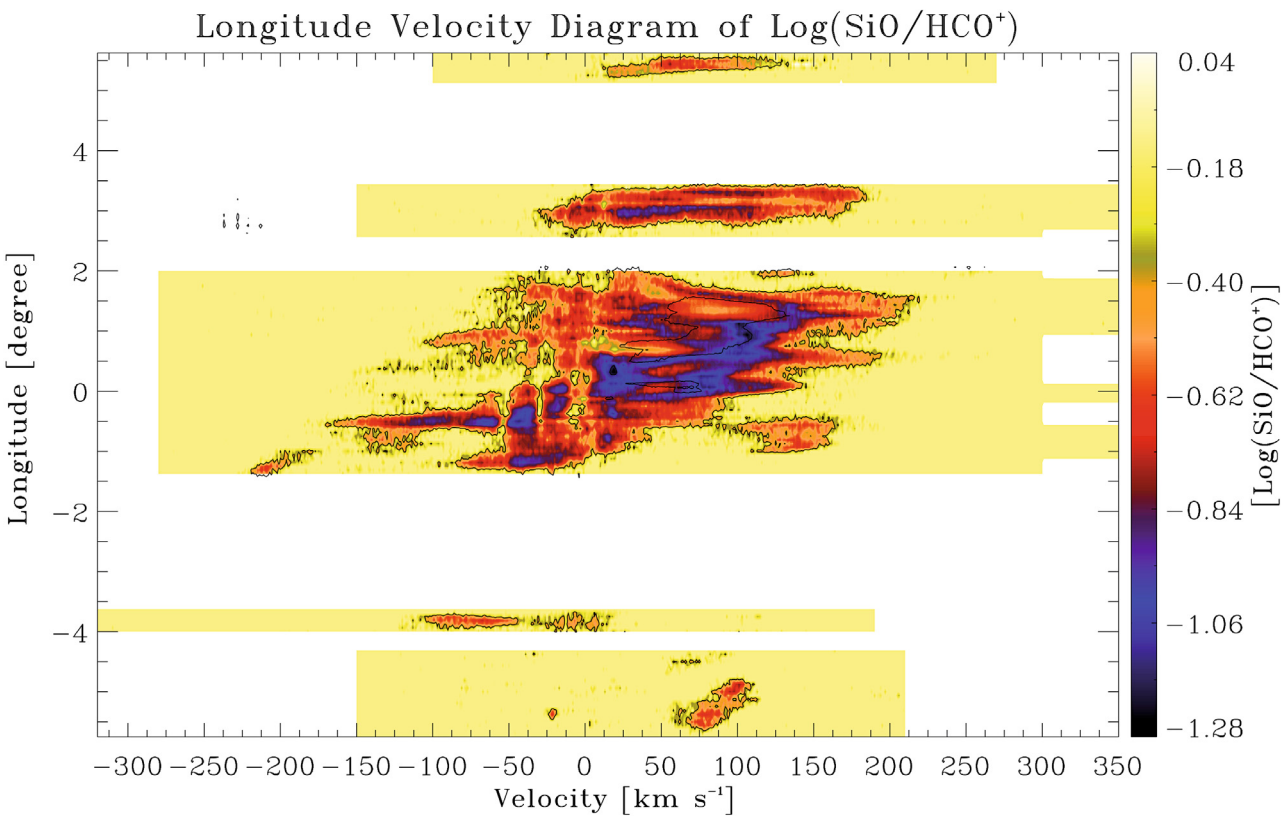

Fig. 8. Longitude-velocity emission comparison between the SiO and HCO+ emission. We plot $\log(\int T(\mathrm{SiO}(J = 2 \rightarrow 1))\mathrm{d}b / \int T(\mathrm{HCO^+}(J = 1 \rightarrow 0))\mathrm{d}b)$. In the region toward Sgr C, Sgr A, and Sgr D are dominated by HCO+, and the region toward the 1.3 deg complex, Sgr B, M+3.2+0.3, and M+5.3−0.3 are dominated by SiO.

their excitation conditions expressed in terms of critical density should be similar.

4.2. Intensity ratio of molecular emission

We also determined the ratio of the apparent luminosity S between the molecular emissions of HCO^+ to CO, SiO to CO, and HCO^+ to SiO, integrated over the observed regions to characterize the physical properties of different clouds. The apparent luminosity S is defined as the total emission integrated over velocity and solid angle, in units of K km s^{-1} deg^2 (Dame et al. 1986). The $HCO^+(J = 1 \rightarrow 0)/CO(J = 1 \rightarrow 0)$ ratio can be related to the ionization fraction of the gas, and the intensity ratio $SiO(J = 2 \rightarrow 1)/CO(J = 1 \rightarrow 0)$ is a measure of the amount of material subject to shocks compared to "quiescent" gas. We also plot the apparent luminosity ratio $SiO(J = 2 \rightarrow 1)/HCO^+(J = 1 \rightarrow 0)$. To define the molecular clouds, we use the average spectrum of each region in HCO^+, SiO, $H^{13}CO^+$, and CO from Bitran et al. (1997). In the average spectrum, we perform Gaussian fits to identify each molecular cloud. Different molecular clouds can be distinguished by one dimensional Gaussian fits (Online Appendix E), which yield temperature peaks (T_o), velocity centers, and velocity widths (*FWHM*) of the average spectra of the different regions (Table 3). Also, we list central positions for the clouds. All the values and errors in the Table 3 come from the Gaussian fits. Also, we assign locations to the clouds in this table. In cases where the Gaussian fits did not give unique results or did not converge, the values were obtained by visual inspection. Such cases are marked with an asterisk.

Clump-finding algorithms, such as "Clumpfind" (Williams et al. 1994), have shown to be themselves useful for identifying clumps in Galactic molecular cloud. In the present work, we aim to identify the different velocity molecular clouds (with 10^5–10^6 M_o) along the line of sight toward the Galactic center region. It is not intended to derive the internal substructure within every molecular cloud identified. That is why we only fit Gaussians in the velocity dimension. We identified 51 molecular clouds, 33 of them belonging to the Galactic center region and 18 to the Galactic disk, local gas, or clouds along the line of sight. The molecular clouds classified as outside the Galactic center are characterized by narrow linewidths (<10 km s^{-1}). However, there are still some clouds classified as outside the Galactic center, which present large linewidths. A possible reason is that the clouds could be under the strong influence of the Galactic center tidal forces (e.g. cloud numbers 44 and 48, see Table 3). For example, cloud number 51 has a large linewidth in HCO^+. This cloud belongs to the 135 km s^{-1} arm (Bania 1980), which is supposedly located outside from the Galactic center, but it is strongly influenced by it.

The apparent luminosity for each molecular component was obtained using

$$S = \int_{\Omega_s} \int_v T_{\mathrm{A}}^* \mathrm{d}v \mathrm{d}\Omega, \tag{3}$$

where T_{A}^* is the antenna temperature. Figure 9 shows an example of the average spectra and the Gaussian fit. In this cloud the different intensities of the emission in the main velocity component ($v \sim -79$ km s^{-1}) belonging to the Galactic center are evident. The HCO^+ and SiO emission in the main velocity component have a noticeable increase of the intensity when compared with, e.g., the gas at velocities $v \sim 0$ km s^{-1}, which, presumably

Table 3. Gaussian fits of the each component of the molecular clouds.

Region	Cloud number	Line	Central velocity [km s^{-1}]	Velocity width[a] [km s^{-1}]	T_0 [K]	Luminosity [K km s^{-1} $degree^2$]	Associated Object
Sgr A	1	CO	–126 ± 8	60 ± 18	1.3 ± 0.2	56.5 ± 19.6	EMR
Sgr A	1	HCO^+	–76 ± 2	127 ± 3	0.032	2.57 ± 0.10	EMR
Sgr A	1	SiO	–110 ± 3	108 ± 8	0.0045 ± 0.0003	0.17 ± 0.02	EMR
Sgr A	2	CO	–34 ± 18	68 ± 42	1.9 ± 0.3	95.7 ± 61.0	
Sgr A	2	HCO^+	–39 ± 1	12 ± 1	0.066	0.5	
Sgr A	2	HCO^+	–18 ± 1	13 ± 1	0.10	0.85	
Sgr A	2	$H^{13}CO^+$	–26 ± 10	74± 11	0.004 ± 0.002	0.12 ± 0.05	
Sgr A	3	CO	11 ± 5	36 ± 14	2.5 ± 1.6	65.7 ± 50.9	MM
Sgr A	3	HCO^+	17 ± 1	24 ± 1	0.12	1.9	MM
Sgr A	4	CO	66 ± 8	71 ± 38	2.3 ± 0.2	124 ± 67	Sgr A cloud
Sgr A	4	HCO^+	61 ± 1	72 ± 1	0.19	8.4	Sgr A cloud
Sgr A	4	SiO	44 ± 1	94 ± 1	0.035	1.16	Sgr A cloud
Sgr A	4	$H^{13}CO^+$	40 ± 5	96 ± 6	0.016 ± 0.001	0.55 ± 0.05	Sgr A cloud
Sgr A	5	CO	147 ± 31	72 ± 49	0.8 ± 0.3	44 ± 35	EMR
Sgr A	5	HCO^+	135 ± 4	79 ± 5	0.027 ± 0.001	1.3 ± 0.1	EMR
Sgr B	6	CO	–61 ± 7	100 ± 15	1.8 ± 0.1	110 ± 17	EMR
Sgr B	6	HCO^+	–56 ± 1	115 ± 3	0.046	2.47	EMR
Sgr B	6	SiO	–49 ± 3	83 ± 7	0.0053	0.092	EMR
Sgr B	7*	CO	30 ± 5	60 ± 5	4.1 ± 0.1	147 ± 12	Sgr B cloud
Sgr B	7	HCO^+	42 ± 1	63 ± 1	0.26	7.56	Sgr B cloud
Sgr B	7	SiO	38 ± 1	59 ± 1	0.12	1.43	Sgr B cloud
Sgr B	7	$H^{13}CO^+$	43 ± 1	55 ± 1	0.044	0.505	Sgr B cloud
Sgr B	8*	CO	90 ± 5	35 ± 5	2.75 ± 0.05	58 ± 8	
Sgr B	8	HCO^+	95 ± 1	47 ± 1	0.16	3.4	
Sgr B	8	SiO	93 ± 1	37 ± 1	0.028	0.214	
Sgr B	8	$H^{13}CO^+$	94 ± 1	26 ± 1	0.013	0.070	
Sgr B	9	CO	170 ± 12	56 ± 19	1.0 ± 0.3	33 ± 15	
Sgr B	9	HCO^+	144 ± 3	97 ± 4	0.056	2.6	
Sgr C	10	CO	–123 ± 5	80 ± 14	1.8 ± 0.2	88 ± 18	EMR
Sgr C	10	HCO^+	–103 ± 1	91 ± 1	0.095	2.8	EMR
Sgr C	10	SiO	–116 ± 1	50 ± 2	0.012	0.109	EMR
Sgr C	10	$H^{13}CO^+$	–99 ± 1	29 ± 1	0.006	0.031	EMR
Sgr C	11	CO	–64 ± 4	16 ± 11	1.1 ± 0.5	11 ± 9	Sgr C cloud
Sgr C	11	CO	–41 ± 3	15 ± 8	1.6 ± 0.7	14 ± 10	Sgr C cloud
Sgr C	11	CO	–24 ± 3	6 ± 7	0.9 ± 0.8	3 ± 4	Sgr C cloud
Sgr C	11	HCO^+	–65 ± 1	15 ± 1	0.079	0.38	Sgr C cloud
Sgr C	11	HCO^+	–41 ± 1	15 ± 1	0.16	0.79	Sgr C cloud
Sgr C	11	HCO^+	–21 ± 1	11 ± 1	0.067	0.235	Sgr C cloud
Sgr C	11	SiO	–50 ± 1	43 ± 2	0.019 ± 0.002	0.15 ± 0.02	Sgr C cloud
Sgr C	11	$H^{13}CO^+$	–54 ± 1	33 ± 2	0.011 ± 0.001	0.064 ± 0.007	Sgr C cloud
Sgr C	12*	CO	10 ± 5	40 ± 5	4.1	99 ± 12	
Sgr C	12	HCO^+	22 ± 1	73 ± 1	0.099	2.37	
Sgr C	12	SiO	3 ± 2	73 ± 10	0.016	0.21 ± 0.03	
Sgr C	12	$H^{13}CO^+$	–14 ± 4	75 ± 10	0.0063	0.09 ± 0.01	
Sgr C	13*	CO	60 ± 5	30 ± 5	1.3 ± 0.1	24 ± 4	3 kpc far
Sgr C	13	SiO	57 ± 1	29 ± 4	0.007 ± 0.001	0.034 ± 0.007	3 kpc far
Sgr C	13	$H^{13}CO^+$	57 ± 1	33 ± 3	0.0026 ± 0.0002	0.015 ± 0.002	3 kpc far
Sgr C	14	CO	126 ± 6	76 ± 14	1.5 ± 0.2	68 ± 16	EMR
Sgr C	14	HCO^+	132 ± 1	85 ± 1	0.057	1.57	EMR
Sgr C	14	SiO	153 ± 1	26 ± 2	0.0064	0.030	EMR
Sgr D	15	CO	–53 ± 48	62 ± 73	2.2 ± 1.6	59 ± 83	
Sgr D	15	HCO^+	–56 ± 2	73 ± 4	0.043	1.35	
Sgr D	15	SiO	–48 ± 3	65 ± 4	0.009	0.118	
Sgr D	16	CO	8 ± 26	56 ± 70	3.0 ± 1.8	74 ± 104	
Sgr D	16	HCO^+	–10 ± 1	32 ± 2	0.054	0.75 ± 0.07	
Sgr D	16	SiO	18 ± 1	58 ± 3	0.019	0.23	
Sgr D	16	$H^{13}CO^+$	4 ± 2	79 ± 5	0.0048	0.077	
Sgr D	17	CO	86 ± 8	65 ± 28	5.4 ± 0.8	157 ± 71	Sgr D cloud
Sgr D	17	HCO^+	27 ± 1	31 ± 2	0.062	0.83	Sgr D cloud
Sgr D	17	HCO^+	88 ± 1	71 ± 1	0.31	9.6	Sgr D cloud
Sgr D	17	SiO	81 ± 1	55 ± 1	0.085	0.941	Sgr D cloud
Sgr D	17	$H^{13}CO^+$	83 ± 1	40 ± 1	0.026	0.216	Sgr D cloud
Sgr D	18	CO	176 ± 26	60 ± 62	1.3 ± 0.8	35 ± 42	EMR
Sgr D	18*	HCO^+	180 ± 5	50 ± 5	0.045 ± 0.005	1.0 ± 0.1	EMR

Table 3. continued.

Region	Cloud number	Line	Central velocity [km s^{-1}]	Velocity width[a] [km s^{-1}]	T_0 [K]	Luminosity [K km s^{-1} degree^2]	Associated Object
Sgr E	19	CO	–201± 14	33 ± 34	0.7± 0.6	20.7 ± 27.9	Sgr E cloud
Sgr E	19	HCO^+	–203± 1	29± 1	0.024	0.477	Sgr E cloud
Sgr E	19	SiO	–180 ± 3	40 ± 7	0.0030 ± 0.0003	0.040 ±0.008	Sgr E cloud
Sgr E	19	$H^{13}CO^+$	–185 ± 1	40 ± 2	0.0032	0.042	Sgr E cloud
Sgr E	20	CO	–128 ± 23	83 ± 96	0.76± 0.37	57 ± 71	EMR
Sgr E	20	HCO^+	–124 ±1	103 ± 4	0.03	2	EMR
Sgr E	20	SiO	–124 ±2	40 ± 4	0.005	0.063 ±0.008	EMR
Sgr E	20	$H^{13}CO^+$	–123 ± 1	22 ± 2	0.0016± 0.0001	0.012 ±0.002	EMR
Sgr E	21	CO	–59 ± 25	28± 43	1.2 ± 1.6	31± 62	
Sgr E	21	CO	–26 ± 9	33 ± 44	2.7 ±0.6	79± 108	
Sgr E	21	CO	–3 ±4	11± 11	2.1± 2.2	22± 32	
Sgr E	21	HCO^+	–31 ± 1	49 ± 1	0.096	3.2	
Sgr E	21	SiO	–23 ± 1	67 ± 1	0.021	0.47	
Sgr E	21	$H^{13}CO^+$	–23 ± 1	81± 1	0.007	0.19	
Sgr E	22	CO	13 ± 5	16 ± 11	2.1 ±0.9	30± 25	MM
Sgr E	22*	HCO^+	12 ± 5	25 ± 5	1.1 0.2		MM
Sgr E	23*	CO	140 ± 5	55 ± 5	0.50 ± 0.05	24.7±3.3	EMR
Sgr E	23	HCO^+	131 ± 1	68 ± 1	0.028	1.28	EMR
Sgr E	23	SiO	134 ± 1	36 ± 1	0.009	0.114	EMR
Sgr E	23	$H^{13}CO^+$	105 ± 1	60 ± 2	0.002	0.048	EMR
1.3 complex	24	CO	–1 ± 8	88 ± 17	2.9 ± 0.2	265 ± 55	
1.3 complex	24	HCO^+	–22 ± 1	75 ± 1	0.048	2.99	
1.3 complex	24	SiO	–16 ± 1	54 ± 1	0.018	0.462	
1.3 complex	24	$H^{13}CO^+$	–24 ± 1	47 ± 2	0.0046	0.102	
1.3 complex	25	CO	85 ± 6	64 ± 18	3.1 ± 1.0	206 ± 89	1.3 complex cloud
1.3 complex	25	HCO^+	83 ± 0	90 ± 1	0.18	13.6	1.3 complex cloud
1.3 complex	25	SiO	81 ± 1	76 ± 1	0.076	2.735	1.3 complex cloud
1.3 complex	25	$H^{13}CO^+$	75 ± 1	82 ± 1	0.01	0.388	1.3 complex cloud
1.3 complex	26	CO	167 ± 43	121 ± 73	1.1 ± 0.3	143 ± 93	EMR
1.3 complex	26	HCO^+	178 ± 2	86 ± 3	0.031	2.19	EMR
M+3.2+0.3	27	CO	–42 ± 18	35 ± 42	0.5 ± 0.4	29 ± 41	3 kpc
M+3.2+0.3	27	$H^{13}CO^+$	–45 ± 3	48 ± 7	0.0025 ± 0.0002	0.033 ± 0.006	3 kpc
M+3.2+0.3	28	CO	11 ± 4	40 ± 14	2.3 ± 0.5	150 ± 62	
M+3.2+0.3	28	HCO^+	32 ± 1	84 ± 2	0.09	6.4	
M+3.2+0.3	28	SiO	23 ± 1	51 ± 1	0.045	0.64	
M+3.2+0.3	28	$H^{13}CO^+$	24 ± 2	55 ± 5	0.0094	0.14	
M+3.2+0.3	29	CO	93 ± 10	97 ± 49	1.7 ± 0.3	276 ± 146	Clump 2
M+3.2+0.3	29	HCO^+	103 ± 1	68 ± 3	0.074	4.4	Clump 2
M+3.2+0.3	29	SiO	80 ± 1	54 ± 2	0.039	0.59	Clump 2
M+3.2+0.3	29	$H^{13}CO^+$	85 ± 6	63 ± 9	0.0042	0.07 ± 0.01	Clump 2
M+3.2+0.3	30	CO	159 ± 11	27 ± 37	0.6 ± 0.6	24 ± 45	
M+3.2+0.3	30	HCO^+	159 ± 1	38 ± 1	0.037	1.21	
M+3.2+0.3	30	SiO	139 ± 1	61 ± 2	0.031	0.52 ± 0.02	
M+3.2+0.3	31	CO	237 ± 32	55 ± 76	0.3 ± 0.3	25 ± 45	EMR
M+3.2+0.3	31	HCO^+	219 ± 13	137 ± 24	0.0055	0.6 ± 0.1	EMR
M−5.3+0.4	32	CO	–81 ± 3	14 ± 7	1.0 ± 0.4	12 ± 8	3 kpc
M−5.3+0.4	32	HCO^+	–78 ± 4	29 ± 7	0.012 ± 0.002	0.19 ± 0.06	3 kpc
M−5.3+0.4	32	SiO	–91 ± 1	8 ± 3	0.0027 ± 0.0008	0.006 ± 0.003	3 kpc
M−5.3+0.4	32	$H^{13}CO^+$	–80 ± 1	8 ± 3	0.0025 ± 0.0008	0.005 ± 0.003	3 kpc
M−5.3+0.4	33	CO	–44 ± 8	25 ± 21	0.7 ± 0.3	16 ± 15	Norma
M−5.3+0.4	33	HCO^+	–43 ± 5	33 ± 23	0.008 ± 0.001	0.15 ± 0.1	Norma
M−5.3+0.4	33*	SiO	–50 ± 5	20 ± 5	0.008	0.04 ± 0.01	Norma
M−5.3+0.4	33	$H^{13}CO^+$	–55 ± 4	33 ± 16	0.0019 ± 0.0004	0.018 ± 0.009	Norma
M−5.3+0.4	34	CO	–18 ± 3	17 ± 7	1.6 ± 0.4	24 ± 12	Crux
M−5.3+0.4	34	HCO^+	–21 ± 1	9 ± 2	0.021 ± 0.003	0.11 ± 0.03	Crux
M−5.3+0.4	34*	SiO	–20 ± 5	10 ± 5	0.0078	0.02 ± 0.01	Crux
M−5.3+0.4	34	$H^{13}CO^+$	–23 ± 2	17 ± 4	0.0037 ± 0.0006	0.017 ± 0.005	Crux
M−5.3+0.4	35	CO	3 ± 1	10 ± 2	3.0 ± 0.5	27 ± 7	MM
M−5.3+0.4	35*	HCO^+	5 ± 5	10 ± 5	0.030 ± 0.003	0.18 ± 0.09	MM
M−5.3+0.4	35	SiO	12 ± 3	37 ± 9	0.004 ± 0.0004	0.04 ± 0.01	MM
M−5.3+0.4	35	$H^{13}CO^+$	11 ± 2	26 ± 7	0.0024 ± 0.0004	0.017 ± 0.005	MM
M−5.3+0.4	36	CO	87 ± 3	42 ± 7	1.7 ± 0.2	65 ± 13	Clump 1
M−5.3+0.4	36	HCO^+	86 ± 1	41 ± 1	0.069	1.65	Clump 1
M−5.3+0.4	36	SiO	72 ± 1	51 ± 2	0.015	0.206	Clump 1
M−5.3+0.4	36	$H^{13}CO^+$	83 ± 2	92 ± 5	0.0061	0.15 ± 0.01	Clump 1

Table 3. continued.

Region	Cloud number	Line	Central velocity [km s^{-1}]	Velocity width[a] [km s^{-1}]	T_0 [K]	Luminosity [K km s^{-1} degree^2]	Associated Object
M−4.4+0.6	37	CO	–75 ± 1	28 ± 3	1.2 ± 0.1	8 ± 1	3 kpc
M−4.4+0.6	37*	HCO^+	–70 ± 5	10 ± 5	0.014 ± 0.003	0.025 ± 0.01	3 kpc
M−4.4+0.6	37	SiO	–75 ± 1	14 ± 2	0.0062 ± 0.0009	0.009 ± 0.002	3 kpc
M−4.4+0.6	37	$H^{13}CO^+$	–70 ± 2	22 ± 4	0.0047 ± 0.0006	0.011 ± 0.002	3 kpc
M−4.4+0.6	38	CO	–34 ± 1	16 ± 2	1.3 ± 0.1	5 ± 0.9	Norma
M−4.4+0.6	38*	HCO^+	–45 ± 5	20 ± 5	0.018 ± 0.003	0.06 ± 0.02	Norma
M−4.4+0.6	38	SiO	–40 ± 5	15 ± 5	0.008	0.012 ± 0.004	Norma
M−4.4+0.6	38	$H^{13}CO^+$	–37 ± 1	10 ± 2	0.006 ± 0.001	0.006 ± 0.002	Norma
M−4.4+0.6	39*	CO	–20 ± 5	10 ± 5	0.72 ± 0.05	1.8 ± 0.9	Crux
M−4.4+0.6	39*	HCO^+	–30 ± 5	10 ± 5	0.036 ± 0.003	0.06 ± 0.03	Crux
M−4.4+0.6	39	SiO	–20 ± 5	20 ± 5	0.0092	0.018 ± 0.005	Crux
M−4.4+0.6	39	$H^{13}CO^+$	–23 ± 1	6 ± 2	0.005 ± 0.001	0.003 ± 0.001	Crux
M−4.4+0.6	40*	CO	0 ± 5	10 ± 5	2.75	7 ± 3	MM
M−4.4+0.6	40	$H^{13}CO^+$	–1 ± 2	27 ± 6	0.0041 ± 0.0006	0.012 ± 0.003	MM
M−4.4+0.6	41*	CO	18 ± 5	20 ± 5	1.25 ± 0.05	6 ± 2	
M−4.4+0.6	41	SiO	25 ± 2	30 ± 4	0.011 ± 0.001	0.033 ± 0.005	
M−4.4+0.6	42	CO	70 ± 2	55 ± 6	1.55 ± 0.08	21 ± 2	M−4.4+0.6 cloud
M−4.4+0.6	42	HCO^+	71 ± 1	49 ± 1	0.048	0.42	M−4.4+0.6 cloud
M−4.4+0.6	42	SiO	72 ± 1	51 ± 3	0.014	0.073	M−4.4+0.6 cloud
M−4.4+0.6	42	$H^{13}CO^+$	65 ± 1	39 ± 3	0.0073	0.031 ± 0.003	M−4.4+0.6 cloud
M−3.8+0.9	43	CO	–67 ± 6	81 ± 14	1.0 ± 0.1	28 ± 5	M−3.8+0.9 cloud
M−3.8+0.9	43	HCO^+	–79 ± 1	61 ± 1	0.067	1.05	M−3.8+0.9 cloud
M−3.8+0.9	43	SiO	–80 ± 2	79 ± 4	0.014	0.2	M−3.8+0.9 cloud
M−3.8+0.9	43	$H^{13}CO^+$	–60 ± 4	73 ± 7	0.0097	0.13 ± 0.01	M−3.8+0.9 cloud
M−3.8+0.9	44	CO	0 ± 2	37 ± 5	2.1 ± 0.2	26 ± 4	MM
M−3.8+0.9	44	HCO^+	–4 ± 1	55 ± 2	0.058	0.83	MM
M−3.8+0.9	44	SiO	–5 ± 1	43 ± 3	0.014	0.109	MM
M−3.8+0.9	44	$H^{13}CO^+$	5 ± 2	54 ± 4	0.012	0.12 ± 0.01	MM
M−3.8+0.9	45	CO	60 ± 13	53 ± 51	0.3 ± 0.1	5 ± 5	3 kpc far
M−3.8+0.9	45*	HCO^+	60 ± 5	15 ± 5	0.013 ± 0.002	0.05 ± 0.02	3 kpc far
M−3.8+0.9	45	SiO	40 ± 2	16 ± 5	0.004 ± 0.001	0.013 ± 0.005	3 kpc far
M−3.8+0.9	45	$H^{13}CO^+$	60 ± 1	8 ± 2	0.004 ± 0.001	0.005 ± 0.002	3 kpc far
M−3.8+0.9	46	CO	106 ± 3	19 ± 7	0.74 ± 0.20	5 ± 2	135 km s^{-1}
M−3.8+0.9	46	HCO^+	108 ± 1	17 ± 2	0.019 ± 0.003	0.08 ± 0.02	135 km s^{-1}
M−3.8+0.9	46*	SiO	80 ± 5	20 ± 5	0.012	0.04 ± 0.01	135 km s^{-1}
M−3.8+0.9	46	$H^{13}CO^+$	95 ± 1	7 ± 1	0.006 ± 0.001	0.008 ± 0.002	135 km s^{-1}
M+5.3−0.3	47	CO	–27 ± 1	9 ± 2	1.4 ± 0.2	9 ± 2	3 kpc
M+5.3−0.3	47	HCO^+	–28 ± 1	15 ± 2	0.013 ± 0.001	0.06 ± 0.01	3 kpc
M+5.3−0.3	48	CO	9 ± 1	12 ± 2	2.9 ± 0.2	25 ± 4	MM
M+5.3−0.3	48	CO	23 ± 3	11 ± 6	0.7 ± 0.2	6 ± 4	MM
M+5.3−0.3	48	HCO^+	23 ± 2	39 ± 3	0.05	0.61	MM
M+5.3−0.3	48*	SiO	26 ± 1	48 ± 1	0.014	0.207	MM
M+5.3−0.3	48	$H^{13}CO^+$	8 ± 13	49 ± 14	0.003 ± 0.001	0.043 ± 0.02	MM
M+5.3−0.3	49	CO	40 ± 12	62 ± 15	1.3 ± 0.5	55 ± 26	
M+5.3−0.3	49	HCO^+	59 ± 1	32 ± 3	0.062 ± 0.007	0.6 ± 0.1	
M+5.3−0.3	49*	SiO	65 ± 5	35 ± 5	0.017	0.18 ± 0.03	
M+5.3−0.3	49	$H^{13}CO^+$	54 ± 5	51 ± 11	0.0068 ± 0.0009	0.11 ± 0.03	
M+5.3−0.3	50	CO	104 ± 28	83 ± 52	0.8 ± 0.2	45 ± 31	M+5.3−0.3 cloud
M+5.3−0.3	50	HCO^+	98 ± 2	47 ± 8	0.061 ± 0.007	0.81 ± 0.13	M+5.3−0.3 cloud
M+5.3−0.3	50*	SiO	105 ± 5	60 ± 5	0.021	0.38 ± 0.03	M+5.3−0.3 cloud
M+5.3−0.3	50	$H^{13}CO^+$	120 ± 4	61 ± 9	0.0045	0.08 ± 0.01	M+5.3−0.3 cloud
M+5.3−0.3	51	CO	190 ± 6	38 ± 15	0.4 ± 0.1	10 ± 5	135 km s^{-1}
M+5.3−0.3	51	HCO^+	150 ± 6	50 ± 8	0.020 ± 0.002	0.31 ± 0.06	135 km s^{-1}
M+5.3−0.3	51	$H^{13}CO^+$	173 ± 1	12 ± 2	0.0041 ±0.0004	0.015 ± 0.003	135 km s^{-1}

Notes. In most, the nominal Gaussian fits do the data give uncertainties smaller that 10%, the estimated relative calibration uncertainty of our data, only in cases where the errors from the Gaussian fit exceed 10%, these uncertainties are indicated. The size of each region is given in Table 2. [(a)] Gaussian *FWHM*. Central velocity, Velocity width and temperature peaks (T_0) derived by the average spectrum shown in Appendix D. EMR: "Expanding Molecular Ring" (Bitran 1987); MM: "Main Maximum" (Bitran 1987); 3 kpc: "3 kpc Arm" (Bitran 1987; Sawada et al. 2001); Norma: "Norma Arm" (Bitran 1987; Sawada et al. 2001); Crux: "Crux Arm" (Bitran 1987; Sawada et al. 2001); 135 km s^{-1}: "135 km s^{-1} Arm" (Bitran 1987; Bania 1980); Clump 1 (Bania 1977; Bania et al. 1986; Bitran 1987); Clump 2 (Bania 1977; Bitran 1987). The cloud number 15 is formed by the 3 kpc, Crux and Norma arms. M−4.4+0.6 cloud, identifyed by Bitran (1987). M−3.8+0.9 cloud, identifyed by Bitran (1987). M+5.3−0.3 cloud, identifyed by Bitran (1987).

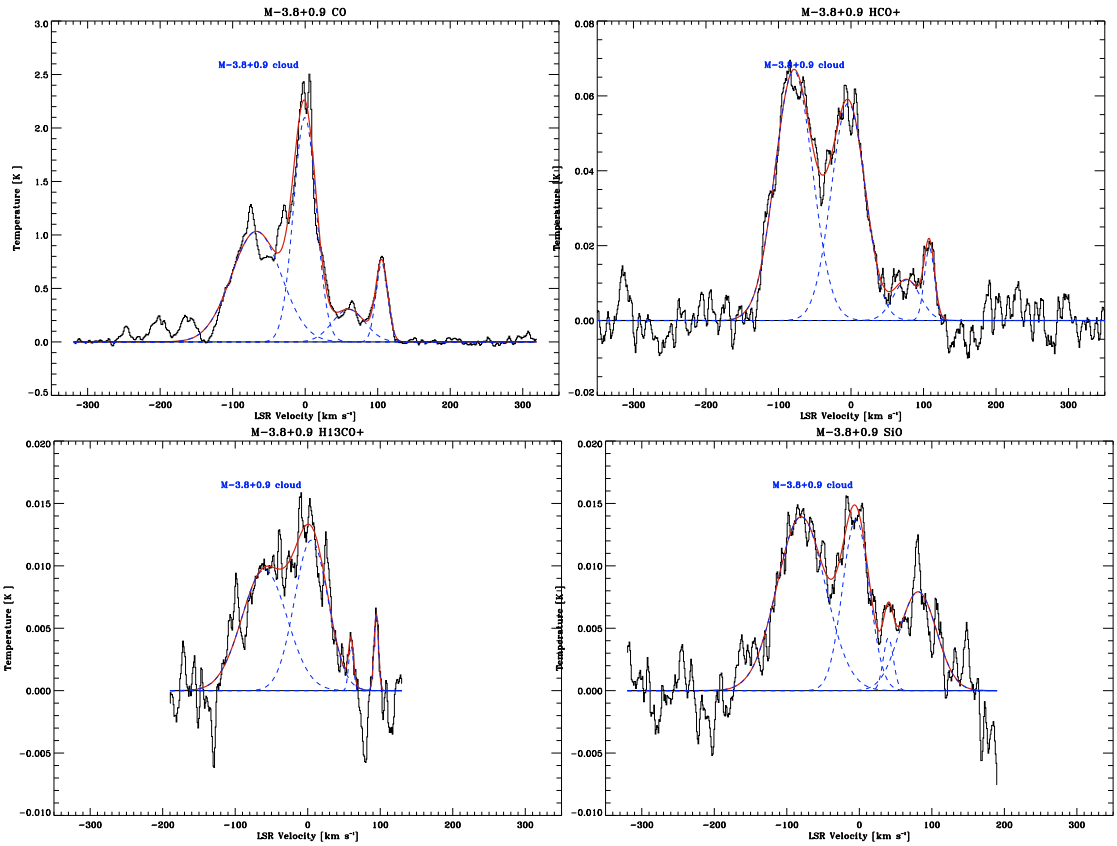

Fig. 9. CO, HCO^+, SiO, and $H^{13}CO^+$ average spectra over the angular size of M−3.8+0.9 cloud (from $l = -4.^\circ0$ to $-3.^\circ625$, and from $b = 0.^\circ5625$ to $1.^\circ1875$). The angular size considered for each region is listed in Table 2. The red lines indicate the Gaussian fit for the complete region and blue dashed lines show the Gaussian fits of each velocity components.

correspond to gas in the line of sight[3]. In the CO emission, the main component ($v \sim -79$ km s^{-1}) show less emission when compared with the gas in the line of sight at $v \sim 0$ km s^{-1}. This plot clearly shows the differences in the molecular gas in the Galactic center and in the disk. In the Appendix D, we show the Gaussian fits for all the molecular complexes.

Figures A.6 and A.7 show the ratio of HCO^+ and SiO to CO luminosities, respectively, while Fig. A.8 shows the ratio of SiO to HCO^+ luminosities for each molecular cloud. The "main component" is the most prominent Galactic center cloud in the region (see Table 4), and it was identified by Bitran (1987). It is noticeable that we could identify some SiO clouds as belonging to the local gas and/or spiral arms, while it is supposed that SiO only traces the gas belonging to the Galactic center. From their velocities and line shape these clouds appear to be in the Galactic disk rather than in the Galactic center. That they are emitting SiO radiation would, however, indicate a location within the Galactic center region. A more detailed study of these clouds would be interesting, since they are either Galactic center clouds with an unusual velocity footprint or they are disk clouds with unusual chemistry and/or excitation conditions. The average of the ratio of HCO^+ to CO luminosity in clouds belonging to the Galactic center is 0.035 ± 0.003 and for disk clouds is 0.015 ± 0.004. The higher intensity ratios are found toward cloud 9 in Sgr B, cloud 4 in Sgr A, cloud 17 in Sgr D, cloud 23 in Sgr E, and cloud 25 in the $1.^\circ3$ complex. In the same way, we display the ratio between SiO and CO. The average of the ratio of SiO to CO luminosity in clouds belonging to the Galactic center is 0.0049 ± 0.0005 and for disk cloud is 0.0034 ± 0.0009. A higher abundances of SiO($J = 2 \rightarrow 1$)/CO($J = 1 \rightarrow 0$) is observed in the M+3.2+0.3 cloud, $1.^\circ3$ complex, and in the M+5.3−0.3 cloud. The luminosity ratio of SiO($J = 2 \rightarrow 1$)/HCO^+($J = 1 \rightarrow 0$) in Fig. A.8, gives an average of 0.15 ± 0.002 for the Galactic center and 0.26 ± 0.05 for the disk clouds. The higher ratios in the Galactic center are found in the M+3.2+0.3 cloud, M+5.3−0.3 cloud, and Sgr D region, and the lower in Sgr A, Sgr C, and Sgr B. For the clouds belonging to the Galactic disk, the average was obtained without considering the clouds with large linewidths discussed before (clouds number 44, 48, and 51), and for the cloud belonging to the Galactic center we did not consider the clouds that present self absorption in HCO^+ and CO, which would decrease the integrated intensity of the cloud (clouds number 2, 11, and 21).

We also investigated the relationship between the HCO^+($J = 1 \rightarrow 0$)/CO($J = 1 \rightarrow 0$) and SiO($J = 2 \rightarrow 1$)/CO($J = 1 \rightarrow 0$) luminosity ratio and the velocity width of the respective clouds in Fig. 10. Here we show disk clouds, clouds in the Galactic center, and cloud that presumably belong to the Galactic disk but they present large linewidth, probably because of the strong Galactic center tidal forces in this region. It is evident, in general, that Galactic center clouds show higher HCO^+($J = 1 \rightarrow 0$)/CO($J = 1 \rightarrow 0$) and SiO($J = 2 \rightarrow 1$)/CO($J = 1 \rightarrow 0$) luminosity ratios and larger linewidths than disk clouds.

[3] The line of sight components are shown in the Appendix A, Fig. A2.2 as a narrow emission (∼5−10 km s^{-1}), whereas the Galactic center emission is characterized by broad velocity width lines (≳50 km s^{-1}). Thus, the emission coming from the region at $l \sim -0.^\circ4$ to $l \sim 0.^\circ6$ and $b \sim -0.^\circ4375$ to $b \sim -0.^\circ375$ at ∼0 km s^{-1} corresponds to local gas.

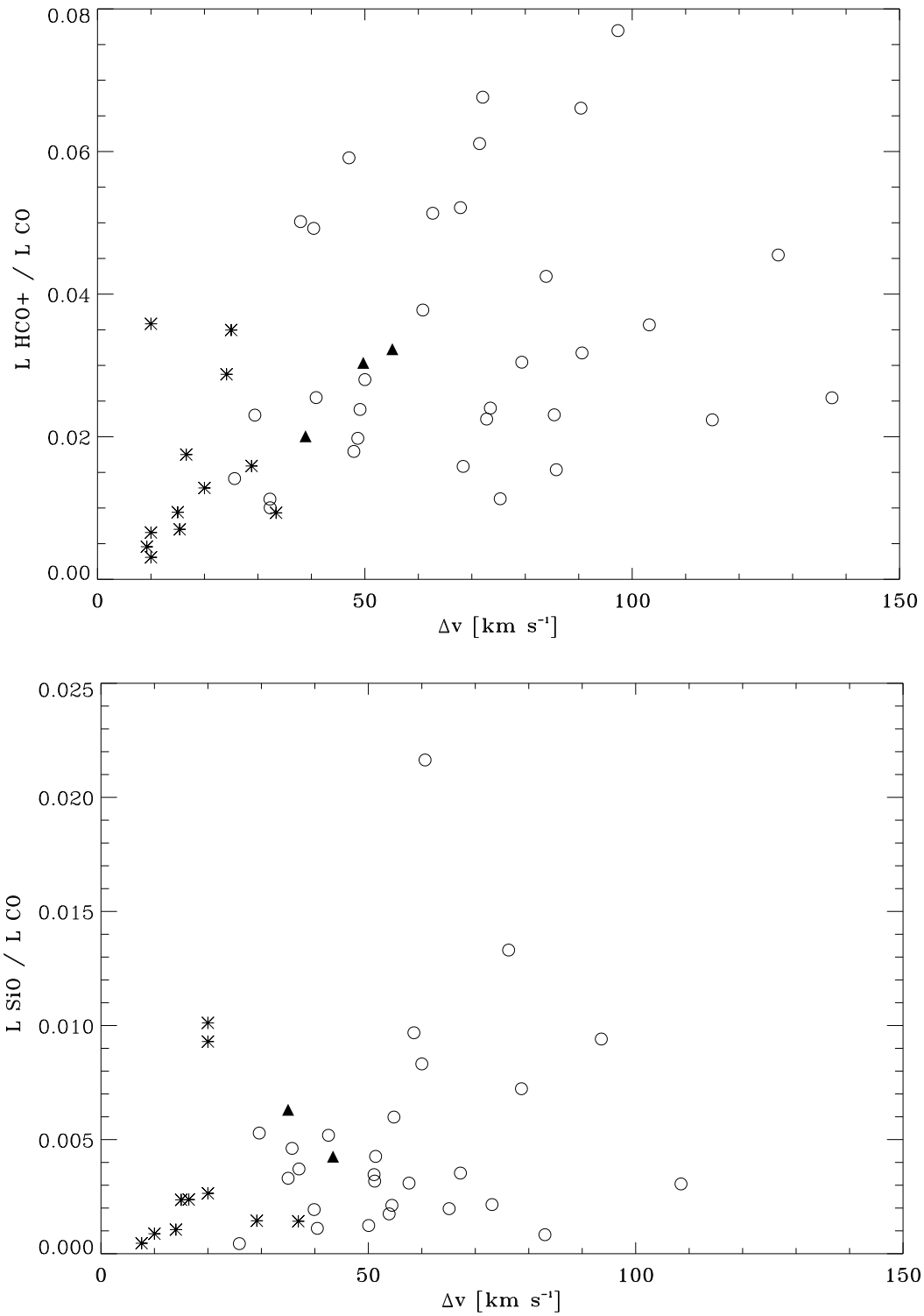

Fig. 10. Relationship between the luminosity ratio HCO^+ to CO (*top*) and the HCO^+ velocity width, and the luminosity ratio SiO to CO (*bottom*) and the SiO velocity width for each molecular cloud of the survey. Open circles denote Galactic center clouds, an asterisk the disk clouds, and filled triangles are clouds that probably are in an intermediate region, influenced by a bar, and that present large linewidth, probably due the strong Galactic center tidal forces in this region. There is a cloud (number 35 in SiO) with a large linewidth (~35 km s^{-1}) in the bottom plot. This cloud is also not considered in our analysis owing the poor fit (see Fig. E.8).

4.3. Comparison with previous work

As shown before, we can distinguish regions where either SiO or HCO^+ dominates. Roughly, in the CMZ at longitudes lower than $l \sim 0.^\circ6$, HCO^+ dominates, and at longitudes $l > 0.^\circ6$, SiO prevails, indicating shock. Nevertheless, we find clouds with an enhancement of SiO toward lower longitudes in the CMZ. For cloud 4 in Sgr A and cloud 7 in Sgr B, the SiO is also intense. In the PMZ, the clouds M+3.2+0.3, M+5.3−0.3, and M−3.8+0.9 show an enhancement of SiO, which is a clear signal of shocks.

The SiO abundance can be increased, e.g., as a consequence of cloud-cloud collisions, interactions with supernova remnants,

Table 4. Velocity components of each region with the longitude and latitude ranges used to defined different regions.

Zone	Region	Longitude [deg]	Latitude [deg]	Velocity center [km s^{-1}]				
				v_{LSR}	v_{LSR}	v_{LSR}	v_{LSR}	v_{LSR}
CMZ	Sgr A	$-0.3125 < l < 0.3125$	$-0.5 < b < 0.5$	−76	−28[a]	17	**61**	135
CMZ	Sgr B	$0.375 < l < 0.8125$	$-0.5 < b < 0.5$	−56	**42**	95	144	
CMZ	Sgr C	$-0.6875 < l < -0.375$	$-0.5 < b < 0.5$	−103	**−43**[b]	22	132	
CMZ	Sgr D	$0.875 < l < 1.1875$	$-0.5625 < b < 0.5625$	−56	−10	27	**88**	180
CMZ	Sgr E	$-0.75 < l < -1.5$	$-0.5 < b < 0.5$	**−203**	−124	−31	17	131
CMZ	1.3 complex	$1.25 < l < 2.0$	$-0.5625 < b < 0.5625$	−22	**83**	178		
PMZ	M+3.2+0.3	$2.5625 < l < 3.5$	$-0.25 < b < 0.875$	32	**103**	159	219	
PMZ	M−5.3+0.4	$-5.75 < l < -4.75$	$-0.125 < b < 0.5625$	−78	−43	−21	5	**86**
PMZ	M−4.4+0.6	$-4.6875 < l < -4.3125$	$0.4375 < b < 0.8125$	−70	−45	−30	**71**	
PMZ	M−3.8+0.9	$-4.0 < l < -3.6875$	$0.5625 < b < 1.1875$	**−79**	−4	77	108	
PMZ	M+5.3−0.3	$5.125 < l < 5.5625$	$-0.6875 < b < 0.125$	−28	23	59	**98**	150

Notes. The velocity component are defined by HCO^+ Gaussian fits, see Appendix E. The main cloud is indicated in bold face. [(a)] Has 2 velocity components; [(b)] has 3 velocity components.

expanding bubbles, and large-scale dynamics in the Galactic center. The SiO predominance that we find in clouds 4 and 7 has been noted by other authors. Martín-Pintado et al. (1997) show that SiO emission is detected throughout the whole Galactic center region. They related the intense SiO emission that they found toward the Sgr A molecular complex (M−0.13−0.08 which is the 20 km s^{-1} cloud, M−0.02−0.07 which correspond to the 50 km s^{-1} cloud, and a condensation close to Sgr A*) to the interaction of the molecular clouds with nearby supernova remnants. Their SiO emission spots could correspond to our cloud number 4 in Sgr A region, but in our data they are blended because of our lower resolution (see Table 4). Minh et al. (1992) also found high abundances of SiO and HCO^+ toward Sgr A region, which indicate that shock chemistry and ion-molecule reactions are important in this region.

The enhancement of SiO that we found toward greater longitudes ($l > 0.^\circ6$ and in the PMZ) has been also reported by Hüttemeister et al. (1998). They performed multiline observations of the $C^{18}O$ and also SiO isotopes in the Galactic center region toward 33 selected positions from the CS survey of Bally et al. (1987). All the sources were easily detected in SiO, where the higher abundances are found at $l > 0.^\circ8$. They found two regimens of densities and temperatures, one dense and cool, and other thin and hot, which are in pressure equilibrium, where the SiO emission arise in a cool, moderately dense component (Hüttemeister et al. 1998). The enhancement of the SiO emission was related to the large-scale gas dynamics in the Galactic center region where the movement of the gas can be understood as the response of a rapidly rotating bar potential (Binney et al. 1991), and the higher abundances of SiO can be identified with the collision region. This molecular cloud has also been studied by Tanaka et al. (2007). They identified 9 expanding shells with broad-velocity-width features in their HCN and HCO^+ maps and isolated SiO clouds that should be related to the expanding shells. They propose that the expanding shells may be in the early stage of supperbubble formation caused by massive cluster formation or continuous star formation $10^{6.8-7.6}$ years ago. Both Hüttemeister et al. (1998) and Martín-Pintado et al. (1997) observed a decrease of X(SiO) in the CMZ (between Sgr B2 and Sgr C, $-0.^\circ35 < l < 0.^\circ6$) with respect to higher longitudes ($l > 0.9$), which is also seen in our data. Figures A.6 and A.7 show that the SiO emission mainly comes from $l > 0.^\circ6$ and that HCO^+ emission is dominant in this region, which shows the densest zones where star formation is ongoing.

In this work we relate the SiO enhancement throughout the Galactic center region to the Giant molecular loops scenario proposed by Fukui et al. (2006). Fukui et al. (2006) observed an area of 240 square degrees toward $-12^\circ < l < 12^\circ$ and $-5^\circ < b < 5^\circ$ in ^{12}CO(1−0) using the NANTEN 4 m telescope from Nagoya University (the NANTEN Galactic plane survey, GPS). They find huge structures in loop shapes, and propose that there are "giant molecular loops" (huge loops of dense molecular gas with strong velocity dispersions) at the Galactic center, formed by a magnetic buoyancy caused by the Parker instability. The loops have two "foot points", one at each end, which are produced when the gas inside the loops flows down to the disk by stellar gravity and forms shock fronts above the disk. This scenario is supported by numerical simulations (Matsumoto et al. 1988; Machida et al. 2009; Takahashi et al. 2009) and by the broad velocity features of ∼40 to 80 km s^{-1} observed by Fukui et al. (2006). The shocked regions detected in SiO in the present work are correlated with the foot points they found. The enhancement of SiO emission, in comparison with the HCO^+ emission that we found in the M−3.8+0.9 cloud (Figs. A.3, A.4), is correlated with the foot point of the loop 1 (toward $l \sim -4^\circ$ to -2°, in the velocity range from −180 to −90 km s^{-1}) and loop 2 (toward $l \sim -5^\circ$ to -4°, in the velocity range of −90 to −40 km s^{-1}). Those features are studied in detail by Torii et al. (2010b,a). The enhancement of SiO in M+3.2+0.3 and M+5.3−0.3 clouds are correlated with the foot point of the loop at positive longitudes, shown in the Fig. S6 on the "Supporting Online Material" in Fukui et al. (2006). This feature is placed at positive longitudes between $l \sim 3^\circ$ to 5°. The enhancement of SiO found toward $l \sim -1^\circ$ corresponds to the location of loop 3, which has recently been discovered by Fujishita et al. (2009). This loop is located toward $l \sim -5^\circ$ to -1° in the velocity range of 20 to 200 km s^{-1} (Fujishita et al. 2009). The coincidence of the enhancement of SiO to the HCO^+ in the "foot point", together with the high-velocity width of the clouds belonging to the Galactic center (see Table 3), support Fukui's scenario. This association will be addressed in more detail in a subsequent paper.

5. Conclusions

1. All of the species measured in this work, HCO^+, SiO, and $H^{13}CO^+$, have been detected throughout the Galactic center region. We find the characteristic asymmetry in longitude found for many other species, with most of the emission

toward $l > 0$ and $v > 0$. We identify 51 molecular clouds, where 33 belong to the Galactic center region and 18 to the Galactic disk or local gas.

2. The luminosity ratios $SiO(J = 2 \rightarrow 1)/CO(J = 1 \rightarrow 0)$ and $HCO^+(J = 1 \rightarrow 0)/CO(J = 1 \rightarrow 0)$, as well as the velocity widths, are higher for Galactic center clouds than for typical disk clouds. The highest $SiO(J = 2 \rightarrow 1)/CO(J = 1 \rightarrow 0)$ luminosity ratios for the Galactic center region correspond, in general, to the highest velocity widths. The average of the luminosity ratio of $SiO(J = 2 \rightarrow 1)/CO(J = 1 \rightarrow 0)$ in clouds belonging to the Galactic center region is 0.0049 ± 0.0005 and for disk clouds is 0.0034 ± 0.0009. The luminosity ratio of $HCO^+(J = 1 \rightarrow 0)/CO(J = 1 \rightarrow 0)$ in the Galactic center is 0.035 ± 0.003, and for disk clouds is 0.015 ± 0.004.
3. The clouds M+3.2+0.3, M−3.8+0.9, M+5.3−0.3, and 1.3° complex show high SiO to HCO^+ ratios, which may indicate the importance of shocks as heating sources. Toward the densest regions, the $SiO(J = 2 \rightarrow 1)/HCO^+(J = 1 \rightarrow 0)$ ratio is low (Sgr A and Sgr B regions).
4. The SiO emission can be correlated with several phenomena. The SiO predominance over the HCO^+ emission could be related to the molecular loops, formed by a Parker instability, where the shocks are ongoing.

Acknowledgements. We acknowledge support by the Chilean Center for Astrophysics FONDAP N 15010003 and by Center of Excellence in Astrophysics and Associated Technologies PFB 06. D.R. and R.M. were supported by DGI grant AYA 2008-06181-C02-02. We thank Fernando Olmos for help with the observations. We are grateful to the personnel and students from Nagoya University who supported observations at the telescope and keep the data reduction pack at Cerro Calán. We also want to thanks Jesús Martín-Pintado for helpful discussions. We thank the referee, Y. Fukui, and the editor of A&A, M. Walmsley, for valuable comments.

References

Bally, J., Stark, A. A., Wilson, R. W., & Henkel, C. 1987, ApJS, 65, 13
Bally, J., Stark, A. A., Wilson, R. W., & Henkel, C. 1988, ApJ, 324, 223
Bania, T. M. 1977, ApJ, 216, 381
Bania, T. M. 1980, ApJ, 242, 95
Bania, T. M. 1986, ApJ, 308, 868
Bania, T. M., Stark, A. A., & Heiligman, G. M. 1986, ApJ, 307, 350
Bayet, E., Viti, S., Williams, D. A., Rawlings, J. M. C., & Bell, T. 2009, ApJ, 696, 1466
Binney, J., Gerhard, O. E., Stark, A. A., Bally, J., & Uchida, K. I. 1991, MNRAS, 252, 210
Bitran, M. E. 1987, Ph.D. Thesis, University of Florida
Bitran, M., Alvarez, H., Bronfman, L., May, J., & Thaddeus, P. 1997, A&AS, 125, 99
Blitz, L., Binney, J., Lo, K. Y., Bally, J., & Ho, P. T. P. 1993, Nature, 361, 417
Botschwina, P., Horn, M., Flugge, J., & Seeger, S. 1993, J. Chem. Soc., Faraday Trans., 623, 2219
Boyce, P. J., & Cohen, R. J. 1994, A&AS, 107, 563
Burton, W. B., & Liszt, H. S. 1983, A&AS, 52, 63
Cox, P., & Laureijs, R. 1989, in The Center of the Galaxy, ed. M. Morris, IAU Symp, 136, 121
Dahmen, G., Hüttemeister, S., Wilson, T. L., et al. 1997, A&AS, 125, 1
Dahmen, G., Hüttemeister, S., Wilson, T. L., & Mauersberger, R. 1998, A&A, 331, 959
Dame, T. M., Elmegreen, B. G., Cohen, R. S., & Thaddeus, P. 1986, ApJ, 305, 892
Ferrière, K., Gillard, W., & Jean, P. 2007, A&A, 467, 611
Fujishita, M., Torii, K., Kudo, N., et al. 2009, PASJ, 61, 1039
Fukui, Y., Iguchi, T., Kaifu, N., et al. 1977, PASJ, 29, 643
Fukui, Y., Kaifu, N., Morimoto, M., & Miyaji, T. 1980, ApJ, 241, 147
Fukui, Y., Yamamoto, H., Fujishita, M., et al. 2006, Science, 314, 106
Handa, T., Omodaka, T., Nagayama, T., Bebe lahak, H., & Matsuyama, N. 2006, J. of Phys. Conf. Ser., 54, 42
Henkel, C., Mauersberger, R., Wiklind, T., et al. 1993, A&A, 268, L17
Hüttemeister, S., Wilson, T. L., Bania, T. M., & Martín-Pintado, J. 1993, A&A, 280, 255
Hüttemeister, S., Dahmen, G., Mauersberger, R., et al. 1998, A&A, 334, 646
Jackson, J. M., Heyer, M. H., Paglione, T. A. D., & Bolatto, A. D. 1996, ApJ, 456, L91
Jaffe, D. T., Plume, R., Evans, II, N. J., & Bally, J. 1996, in The Galactic Center, ed. R. Gredel, ASP Conf. Ser., 102, 16
Jiménez-Serra, I., Caselli, P., Tan, J. C., et al. 2010, MNRAS, 661
Krips, M., Neri, R., García-Burillo, S., et al. 2008, ApJ, 677, 262
Kutner, M. L., & Ulich, B. L. 1981, ApJ, 250, 341
Lee, C. W. 1996, ApJS, 105, 129
Linke, R. A., Stark, A. A., & Frerking, M. A. 1981, ApJ, 243, 147
Liszt, H. S. 2006, A&A, 447, 533
Loenen, A. F., Spaans, M., Baan, W. A., & Meijerink, R. 2008, A&A, 488, L5
Lovas, F. J., Johnson, D. R., & Snyder, L. E. 1979, ApJS, 41, 451
Machida, M., Matsumoto, R., Nozawa, S., et al. 2009, PASJ, 61, 411
Martín-Pintado, J., de Vicente, P., Fuente, A., & Planesas, P. 1997, ApJ, 482, L45
Martín-Pintado, J., de Vicente, P., Rodríguez-Fernández, N. J., Fuente, A., & Planesas, P. 2000, A&A, 356, L5
Matsumoto, R., Horiuchi, T., Shibata, K., & Hanawa, T. 1988, PASJ, 40, 171
Mauersberger, R., & Henkel, C. 1991, A&A, 245, 457
Mauersberger, R., & Bronfman, L. 1998, in Rev. Mod. Astron. 11, ed. R. E. Schielicke, 209
Minh, Y. C., Irvine, W. M., & Friberg, P. 1992, A&A, 258, 489
Morris, M., & Serabyn, E. 1996, ARA&A, 34, 645
Morris, M., Polish, N., Zuckerman, B., & Kaifu, N. 1983, AJ, 88, 1228
Nakagawa, T., Doi, Y., Yui, Y. Y., et al. 1995, ApJ, 455, L35
Nguyen, Q.-R., Jackson, J. M., Henkel, C., Truong, B., & Mauersberger, R. 1992, ApJ, 399, 521
Odenwald, S. F., & Fazio, G. G. 1984, ApJ, 283, 601
Oka, T., Hasegawa, T., Handa, T., Hayashi, M., & Sakamoto, S. 1996, ApJ, 460, 334
Oka, T., Hasegawa, T., Sato, F., et al. 2001, ApJ, 562, 348
Oka, T., Nagai, M., Kamegai, K., Tanaka, K., & Kuboi, N. 2007, PASJ, 59, 15
Raymonda, J. W., Muenter, J. S., & Klemperer, W. A. 1970, J. Chem. Phys., 52, 3458
Rodríguez-Fernández, N. J., Martín-Pintado, J., de Vicente, P., & Fuente, A. 2002, Ap&SS, 281, 331
Sawada, T., Hasegawa, T., Handa, T., et al. 2001, ApJS, 136, 189
Seaquist, E. R., & Frayer, D. T. 2000, ApJ, 540, 765
Takahashi, K., Nozawa, S., Matsumoto, R., et al. 2009, PASJ, 61, 957
Tanaka, K., Kamegai, K., Nagai, M., & Oka, T. 2007, PASJ, 59, 323
Torii, K., Kudo, N., Fujishita, M., et al. 2010a, PASP, 62, 675
Torii, K., Kudo, N., Fujishita, M., et al. 2010b, PASJ, 62, 1307
Williams, J. P., de Geus, E. J., & Blitz, L. 1994, ApJ, 428, 693
Wilson, T. L., & Matteucci, F. 1992, A&A Rev., 4, 1
Wilson, T. L., Rohlfs, K., & Hüttemeister, S. 2009, Tools of Radio Astronomy, ed. T. L. Wilson, K. Rohlfs, S. Hüttemeister (Springer-Verlag)
Ziurys, L. M., Wilson, T. L., & Mauersberger, R. 1990, ApJ, 356, L25
Zylka, R., Güsten, R., Henkel, C., & Batrla, W. 1992, A&AS, 96, 525

Appendix A: Complementary figures

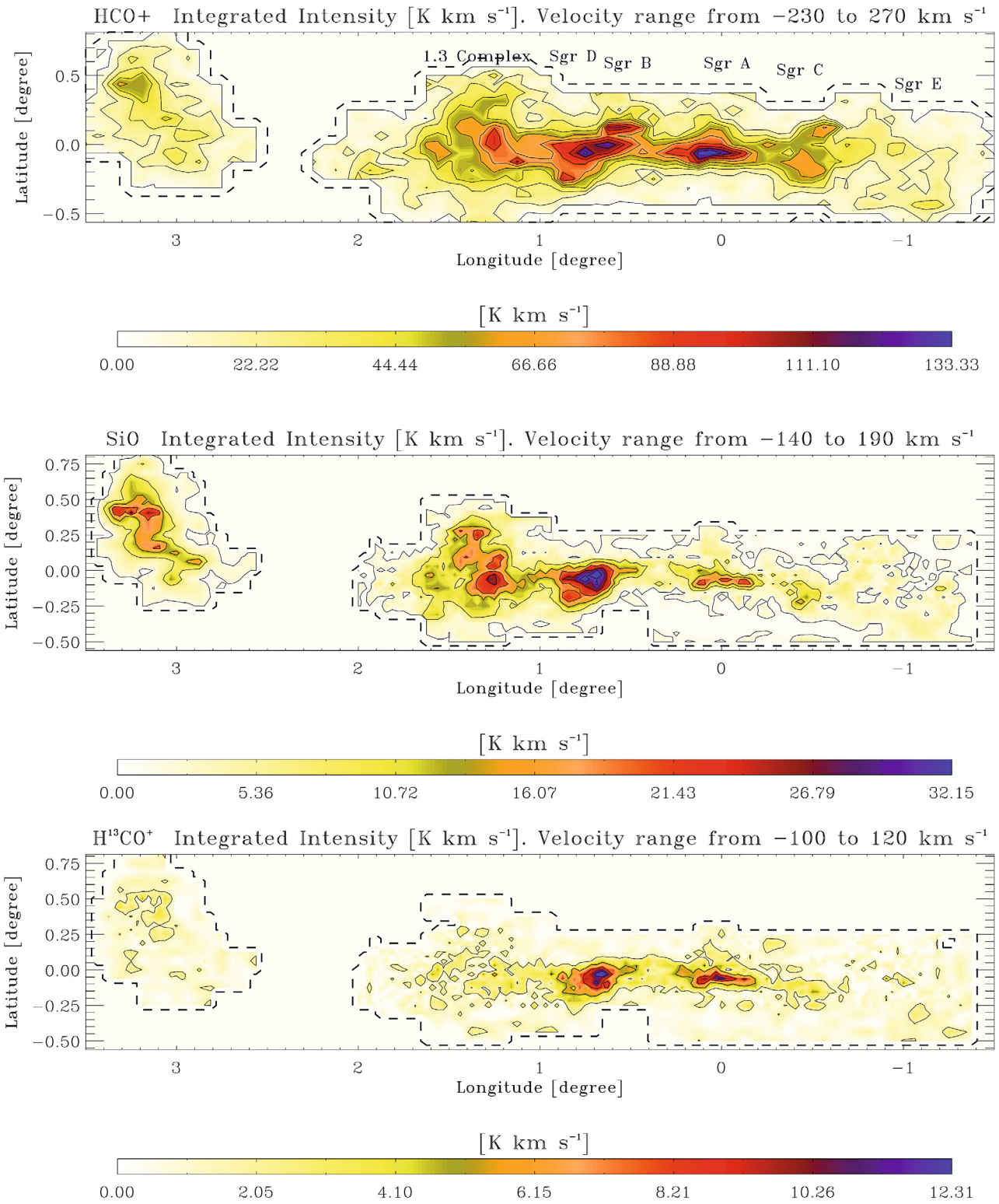

Fig. A.1. *Top*: emission from the CMZ and M+3.2+0.3 integrated over velocity from −230 to 270 km s^{-1}. This plot shows the more northerly part of the CMZ in more detail and includes source names. The solid contour levels start at 1.9 K km s^{-1} (3σ) and increase in steps of 12.53 K km s^{-1} (20σ). *Middle*: emission integrated over the velocity range listed above this plot in SiO. The solid contours start at 1.09 K km s^{-1} (3σ) and increase in steps of 5.46 K km s^{-1} (10σ). *Bottom*: emission from the CMZ and M+3.2+0.3 integrated over the velocity range listed above this plot in $H^{13}CO^+$. The solid contours start at 0.89 K km s^{-1} (3σ) and increase in steps of 2.97 K km s^{-1} (10σ). In all plot, the dashed line show the coverage of the survey in each molecule.

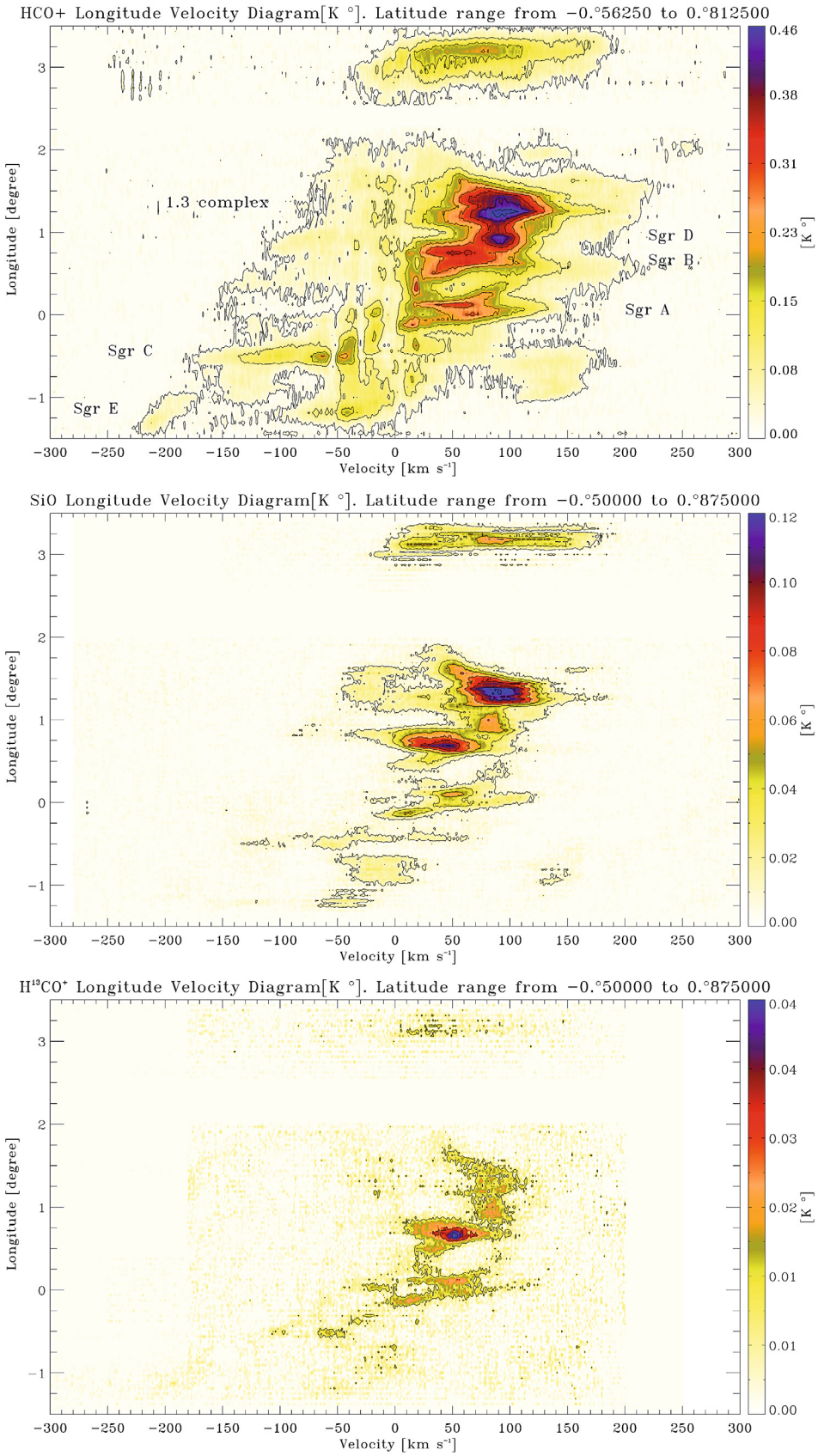

Fig. A.2. *Top*: longitude-velocity diagram of HCO^+ emission in the CMZ and M+3.2+0.3 in the latitude range between $b = -0.^\circ5625$ to $b = 0.^\circ8125$. The contour levels start at 0.021 K (3σ) and increase in steps of 0.058 K (8σ). *Middle*: longitude-velocity diagram of SiO emission in the CMZ and M+3.2+0.3 in the latitude range between $b = -0.^\circ5$ to $b = 0.^\circ875$. The contour levels start at 0.01 K (3σ) and increase in steps of 0.018 K (5σ). *Bottom*: longitude-velocity diagram of $H^{13}CO^+$ emission in the CMZ and M+3.2+0.3 in the latitude range between $b = -0.^\circ5$ to $b = 0.^\circ875$. The contour levels start at 0.009 K (3σ) and increase in steps of 0.016 K (5σ).

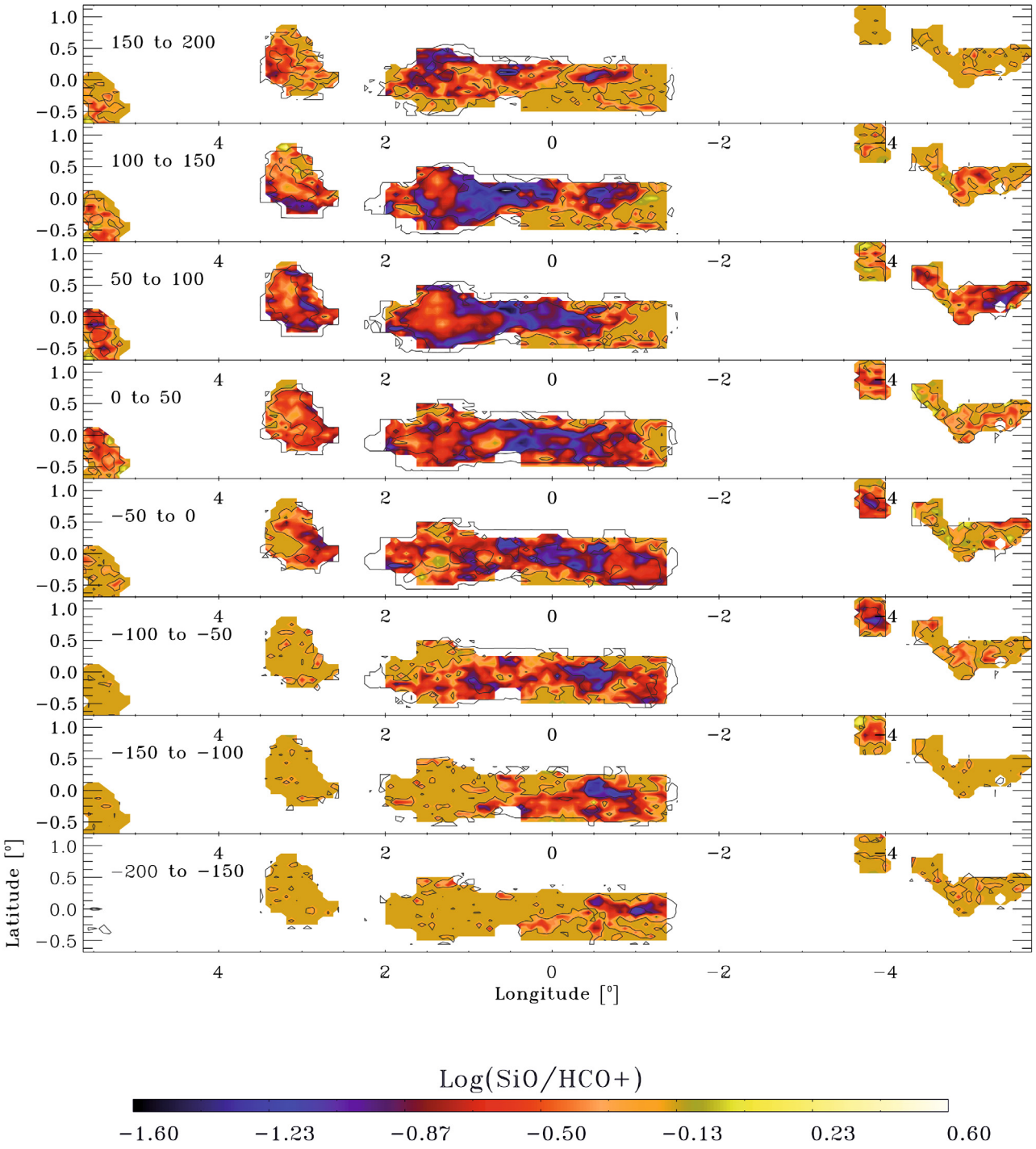

Fig. A.3. Spatial comparison in channel maps of $\log(\int T(\mathrm{SiO})\mathrm{d}v / \int T(\mathrm{HCO^+})\mathrm{d}v)$. The velocity intervals are indicated in each frame. The contours correspond to the HCO^+ emission at 3σ and 30σ. We can identify clearly regions where either the SiO (e.g. in the 1.3 complex and in the M+3.2+0.3 cloud) or HCO^+ (e.g. towards Sgr A region) dominate.

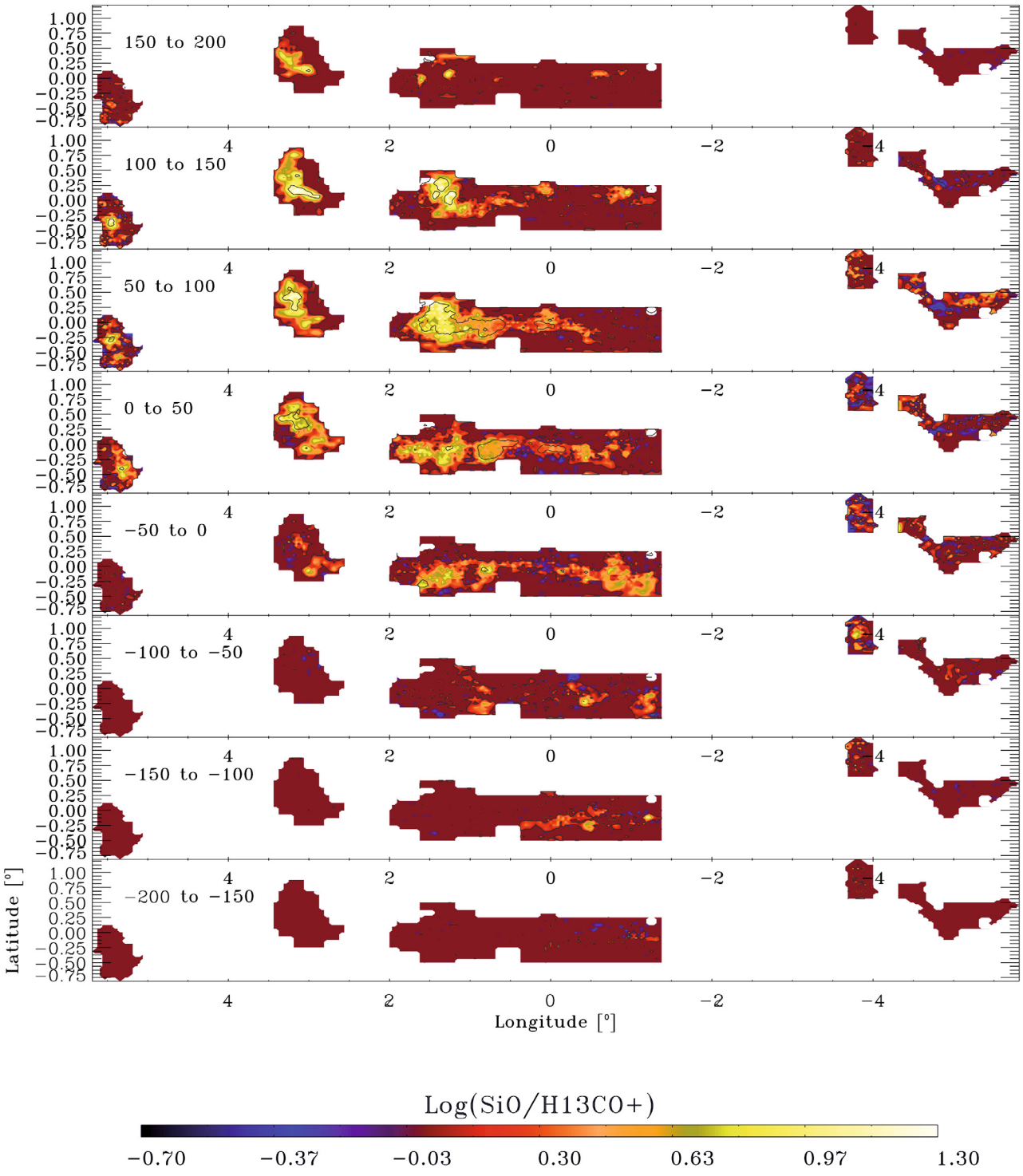

Fig. A.4. Spatial comparison in channel maps of $\log(\int T(\mathrm{SiO})\mathrm{d}v / \int T(\mathrm{H^{13}CO^+})\mathrm{d}v)$. The velocity intervals are indicated in each frame. The contours correspond to the SiO emission at 3σ and 30σ.

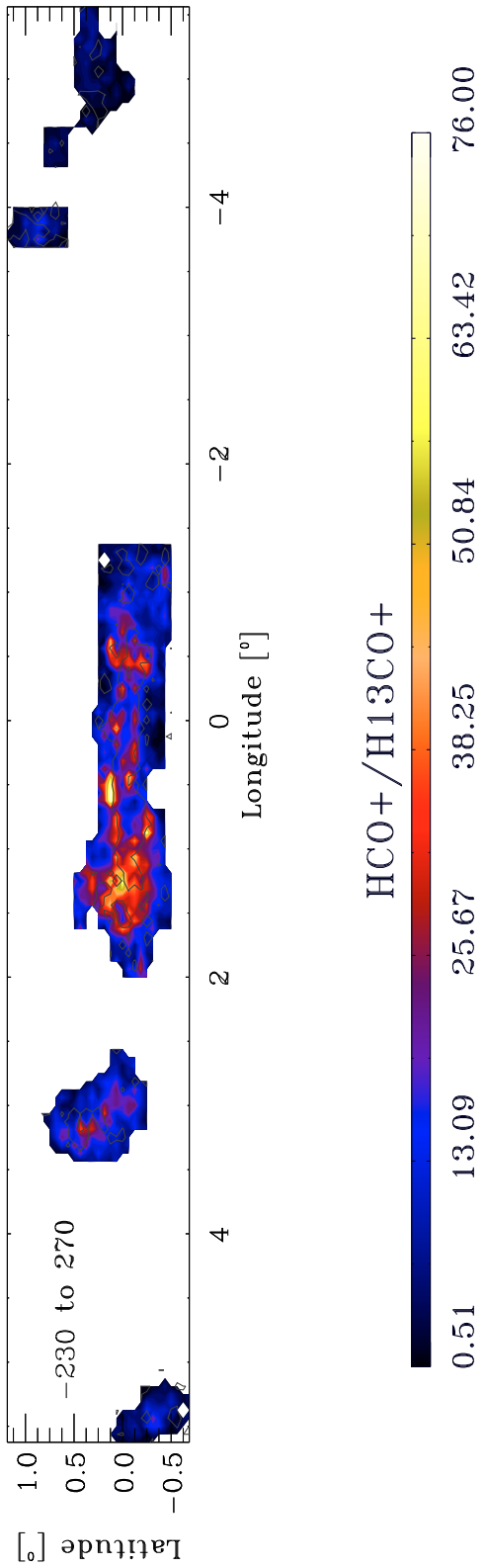

Fig. A.5. Spatial comparison of $\int T(\mathrm{HCO^+})\mathrm{d}v / \int T(\mathrm{H^{13}CO^+})\mathrm{d}v)$ in the velocity range from −230 to 270 km s^{-1}. The line intensity ratio typically range from 10 to 30 whith an average of 19.8.

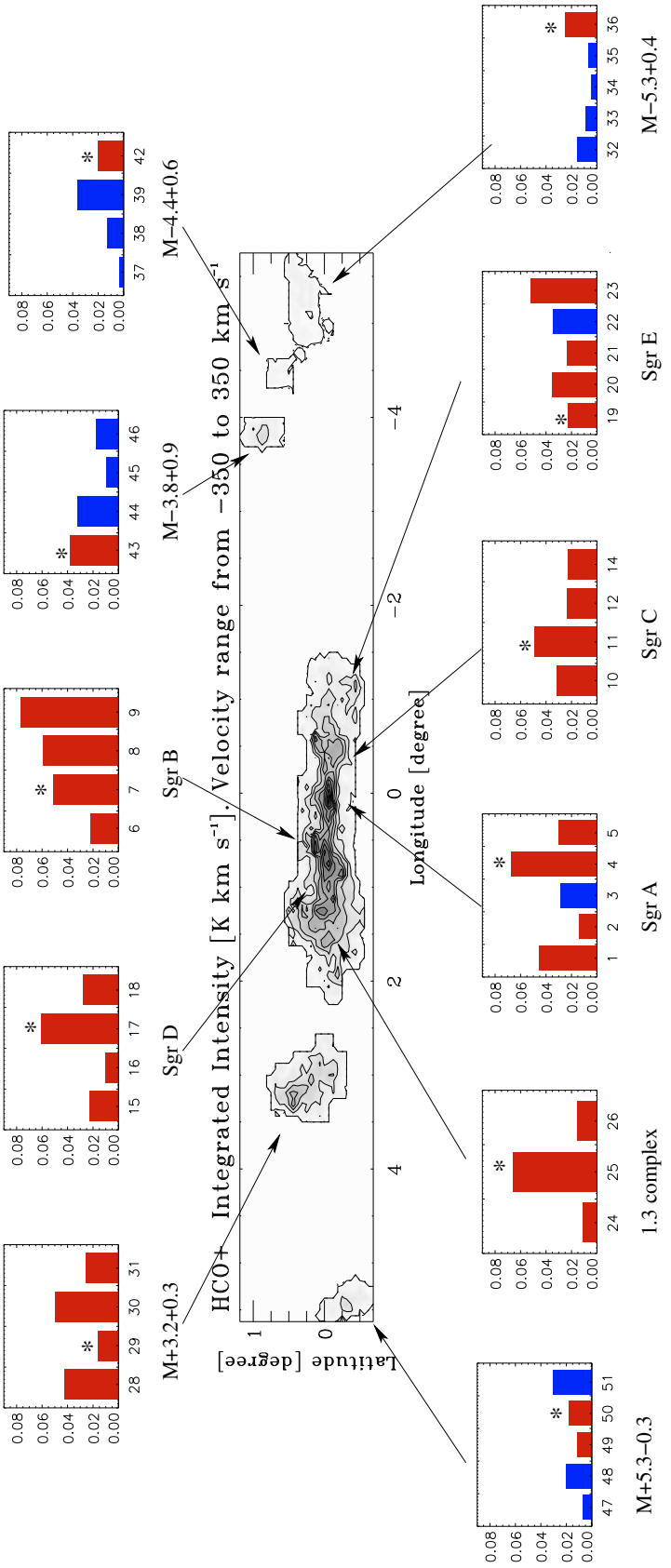

Fig. A.6. Luminosity ratio of HCO^+ to CO for each molecular complex. We show one plot for each region. The *x*-labels indicate the number of each velocity componet as defined by Gaussian fit (see Table 3). The main component is indicated by an asterisk. In blue we show the luminosity ratio for disk clouds and in red we show the luminosity ratio for Galactic center clouds. Each region is located in the HCO^+ integrated intensity map with an arrow. The highest intensities ratio belong to the Galactic center cloud (for example in Sgr B region).

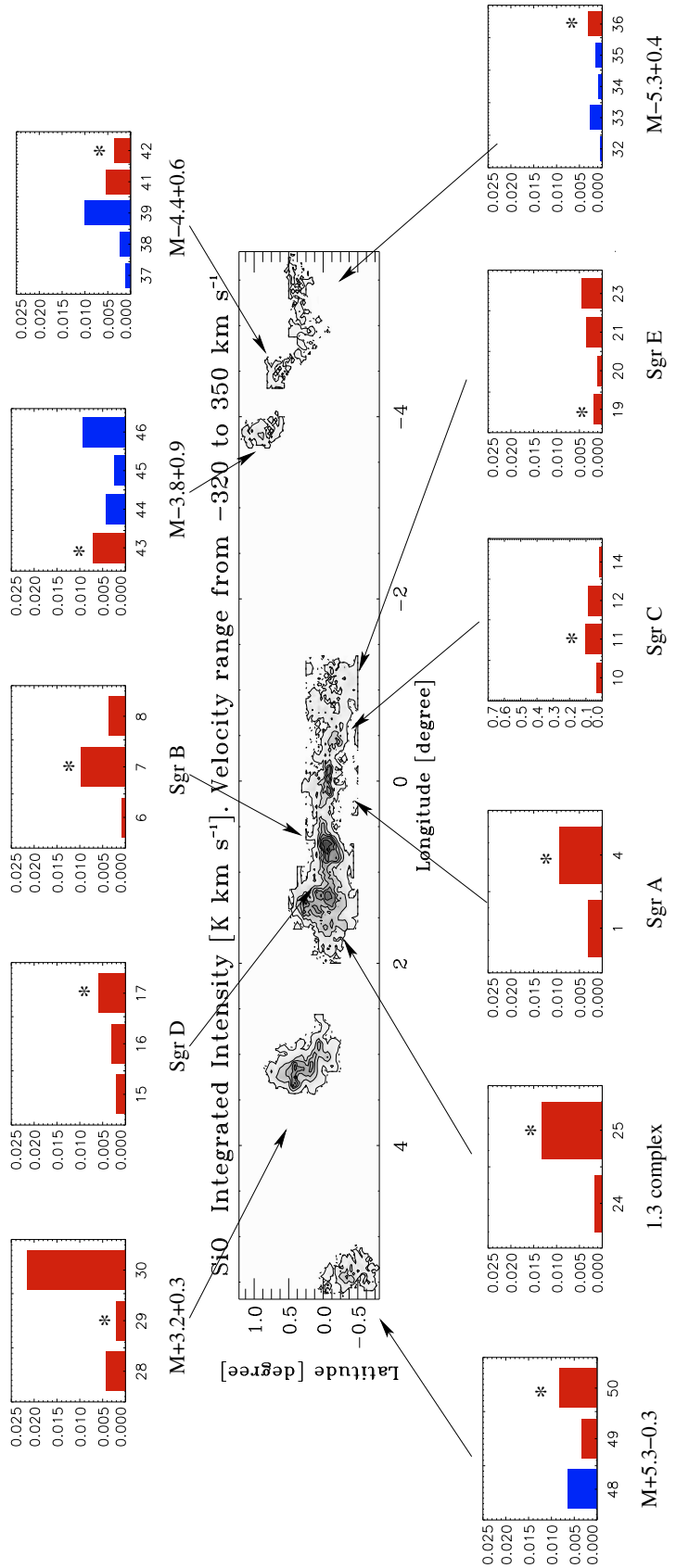

Fig. A.7. Same as Fig. A.6, but for the luminosity ratio of SiO to CO for each molecular complex. We show one plot for each region. The *x*-labels indicate the number of each velocity componet as defined by Gaussian fit (see Table 3). The main component is indicated by an asterisk. In blue we show the luminosity ratio for disk clouds and in red we show the luminosity ratio for Galactic center clouds. The ubication of each region is shown in the SiO integrated intensity map with an arrow. The highest intensities ratio are placed at $l > 1°$.

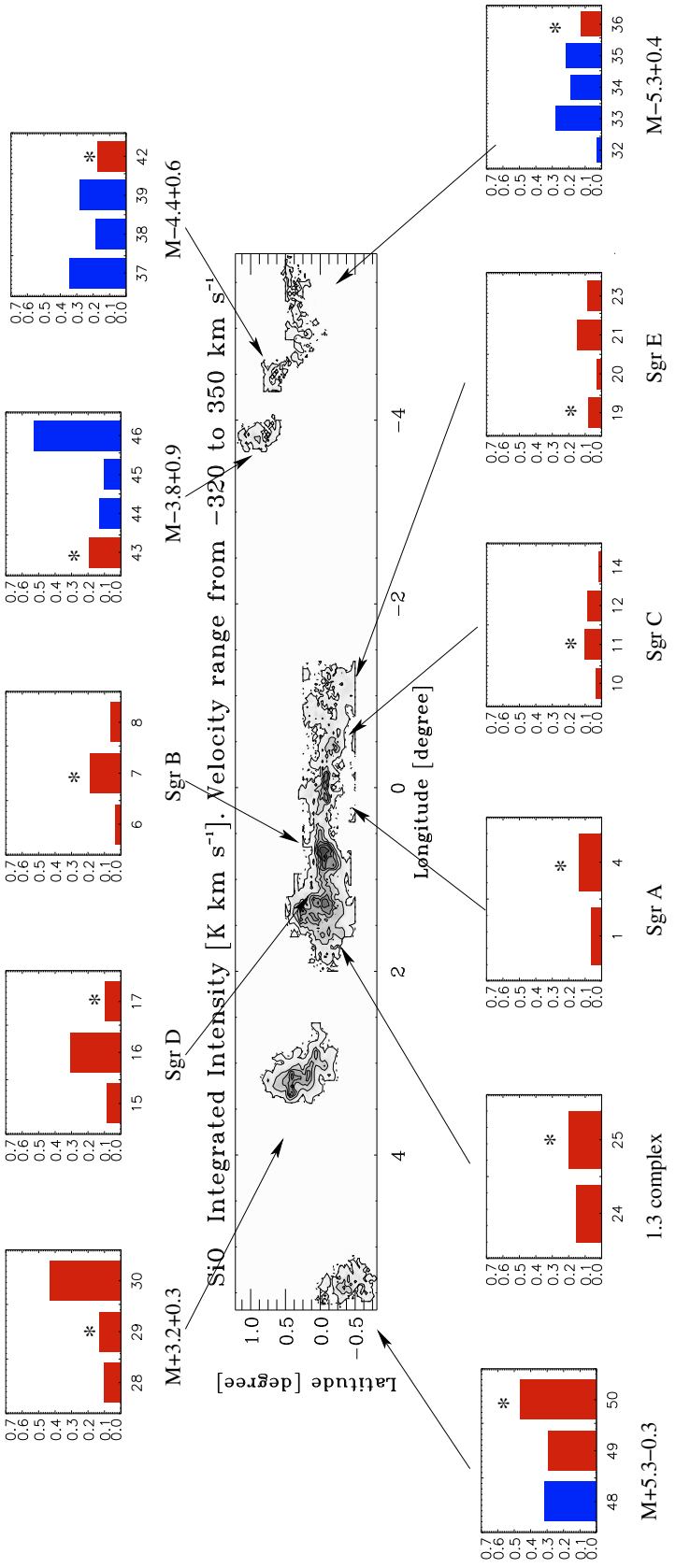

Fig. A.8. Same as Fig. A.6, but for SiO to HCO^+ luminosity ratio for each molecular complex. We show one plot for each region. The *x*-labels indicate the number of each velocity componet as defined by Gaussian fit (see Appendix E). The main component is indicated by an asterisk. In blue we show the luminosity ratio for disk clouds and in red we show the luminosity ratio for Galactic center clouds. Each region is located in the SiO integrated intensity map with an arrow.

Appendix B: HCO^+ Galactic center survey

This Appendix presents the HCO^+ data. In Fig. B.1, we show the channel maps of the HCO^+ emission in the Galactic center region integrated over velocity channels of 10 km s^{-1}. The maps at negative velocities range, show emission coming from Sgr C complex at $l < 0$. M−3.8+0.9 is the only molecular complex observed at negative longitude. Other clouds at negative longitudes are barely detectable with 5σ. In the −60 to 60 km s^{-1} range, the emission is contaminated by spiral arms in absorption. The molecular complexes Sgr A, Sgr B, Sgr D, and the 1.°3 complex, the M+5.3−0.3 cloud and M+3.2+0.3 cloud are visible. At greater velocities, Sgr A, Sgr B. M+3.2+0.3, M−5.3+0.4, M−4.4+0.6 and M+5.3−0.3 show a very intense emission.

In Fig. B.2, we present $l - v$ diagrams for each observed latitude. We show 31 maps covering $b = -0.°6875$ to $b = 1.°1875$ with an spacing of $0.°0625$. We can clearly see in 0 km s^{-1} the emission from the local gas emission superimpose to the Galactic center emission. The local gas components are shown in Fig. B2.2 as a narrow emission (∼5−10 km s^{-1}) while the Galactic center emission is characterized by broad velocity widh lines (≳50 km s^{-1}).

Figure B.3 shows a set of latitude-velocity diagram for each observed longitude. The contours levels start at 0.0021 K (3σ) and increase them in step of 0.0042 K (6σ).

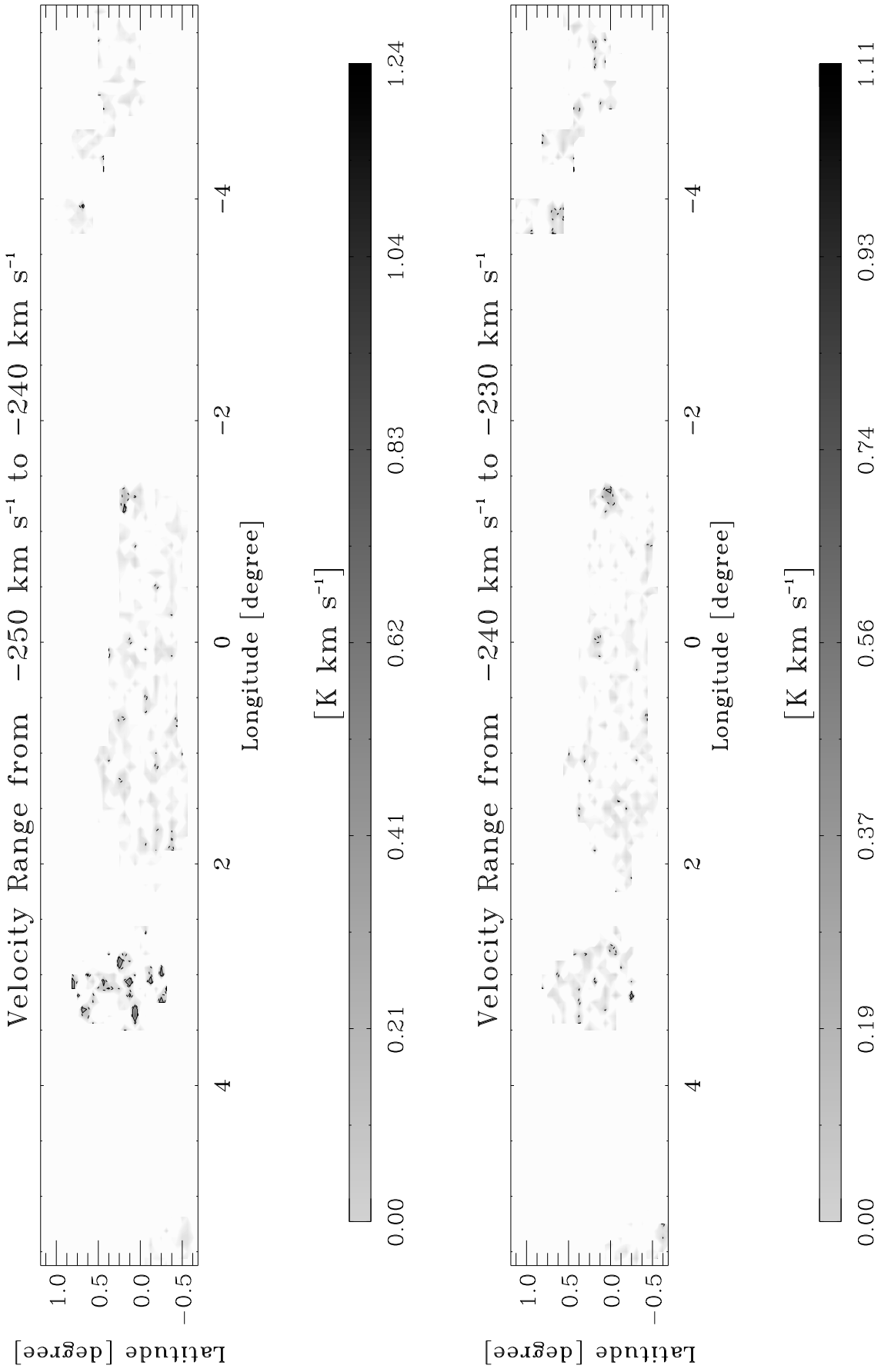

Fig. B1.1. The integrated intensity of the Galactic center region in HCO^+ (1–0) in velocity intervals of 10 km s^{-1} width. The solid contour levels start at 0.46 K km s^{-1}, which is the 5σ-level, and increase in steps of 1.4 K km s^{-1} (15σ). The dotted contours is at 0.28 K km s^{-1} (3σ).

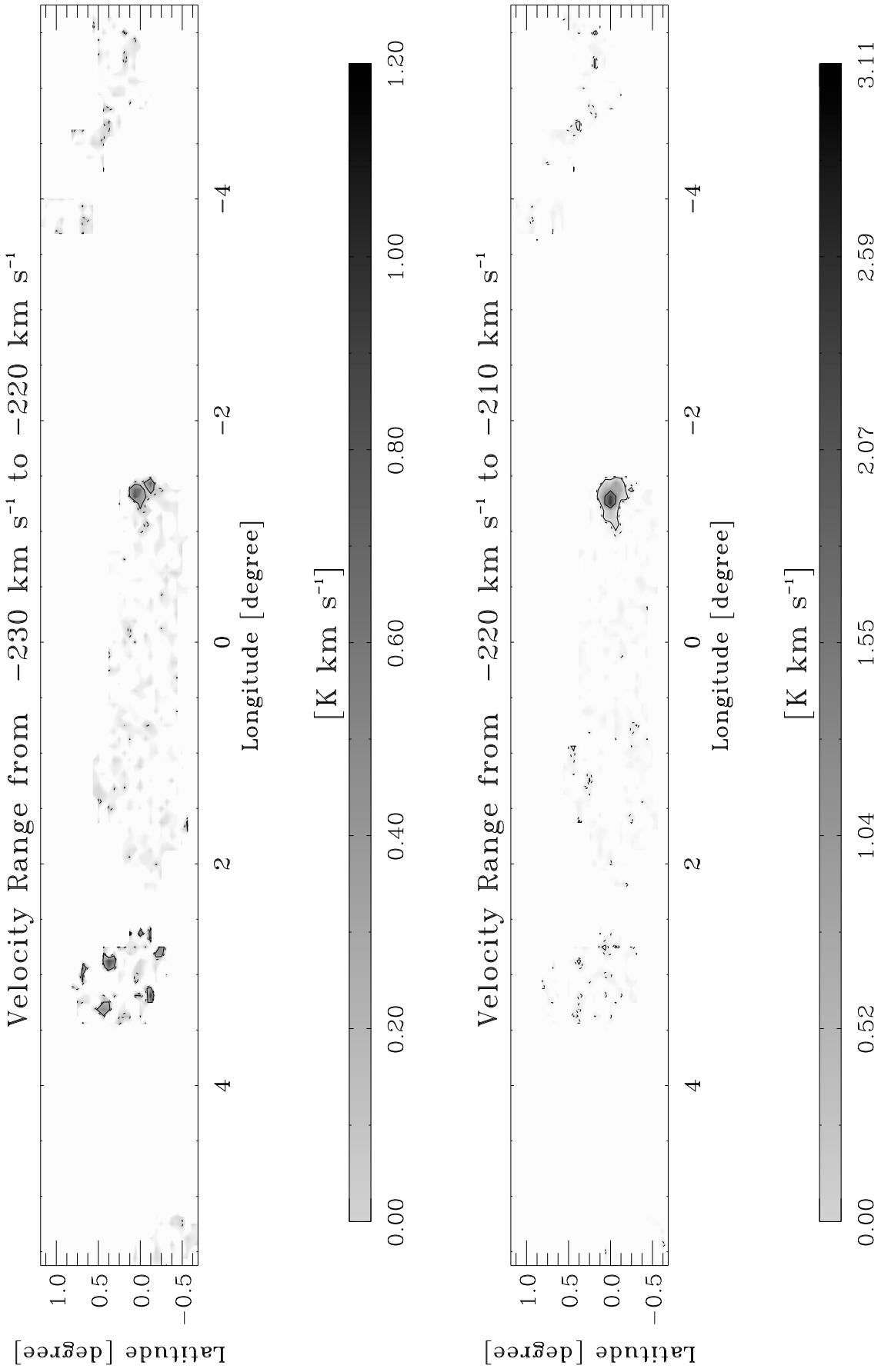

Fig. B1.2. continued.

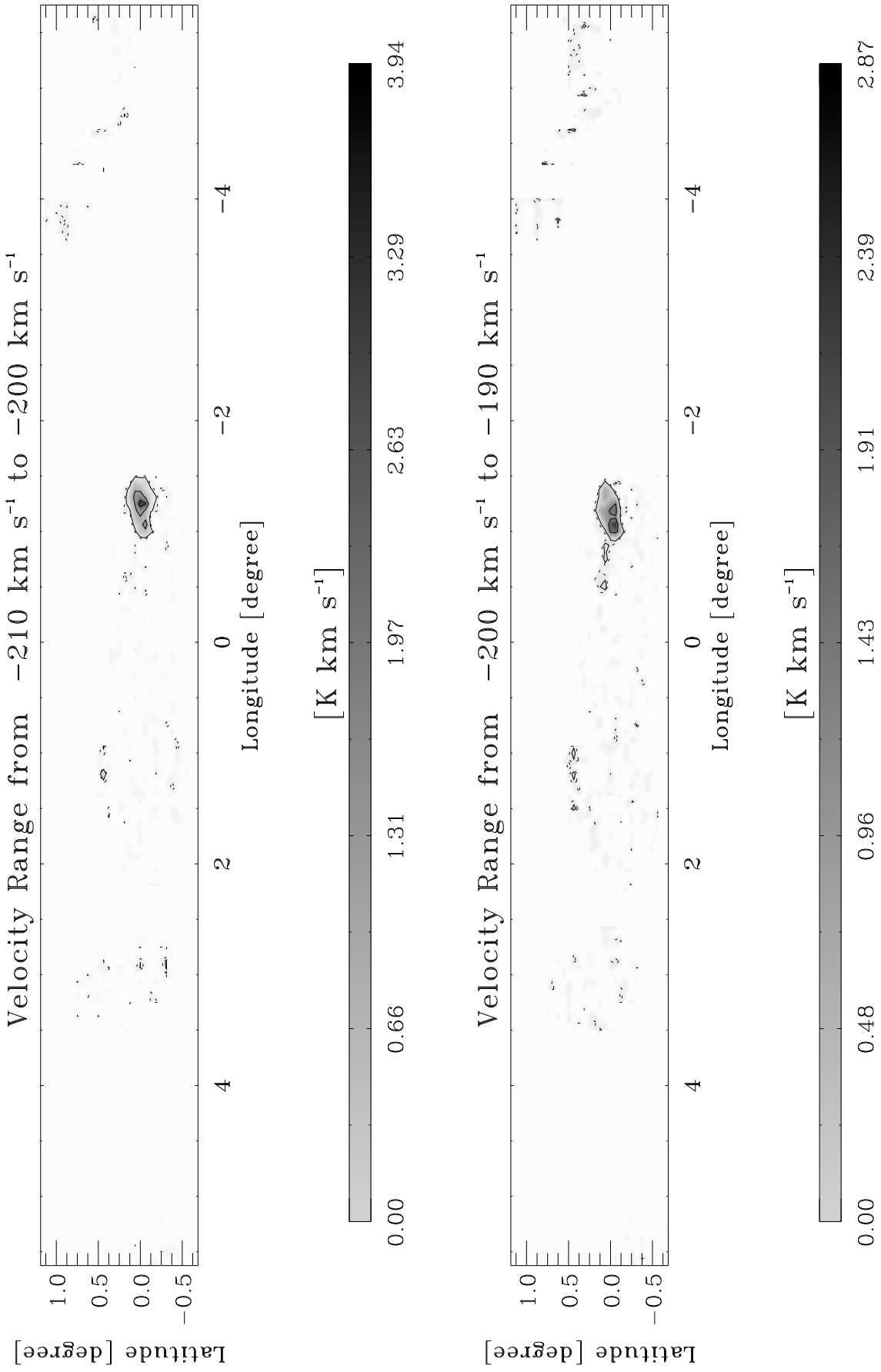

Fig. B1.3. continued.

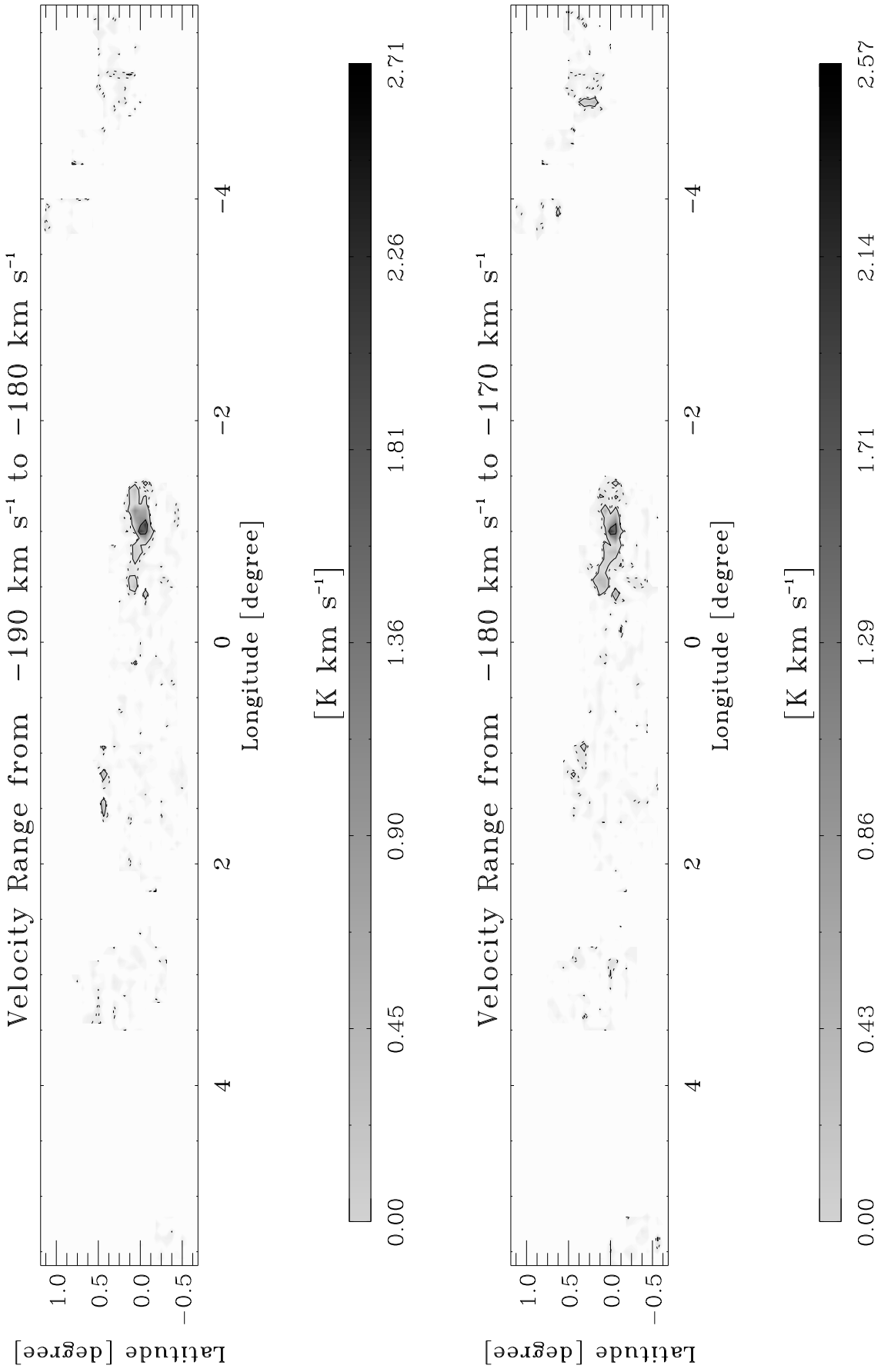

Fig. B1.4. continued.

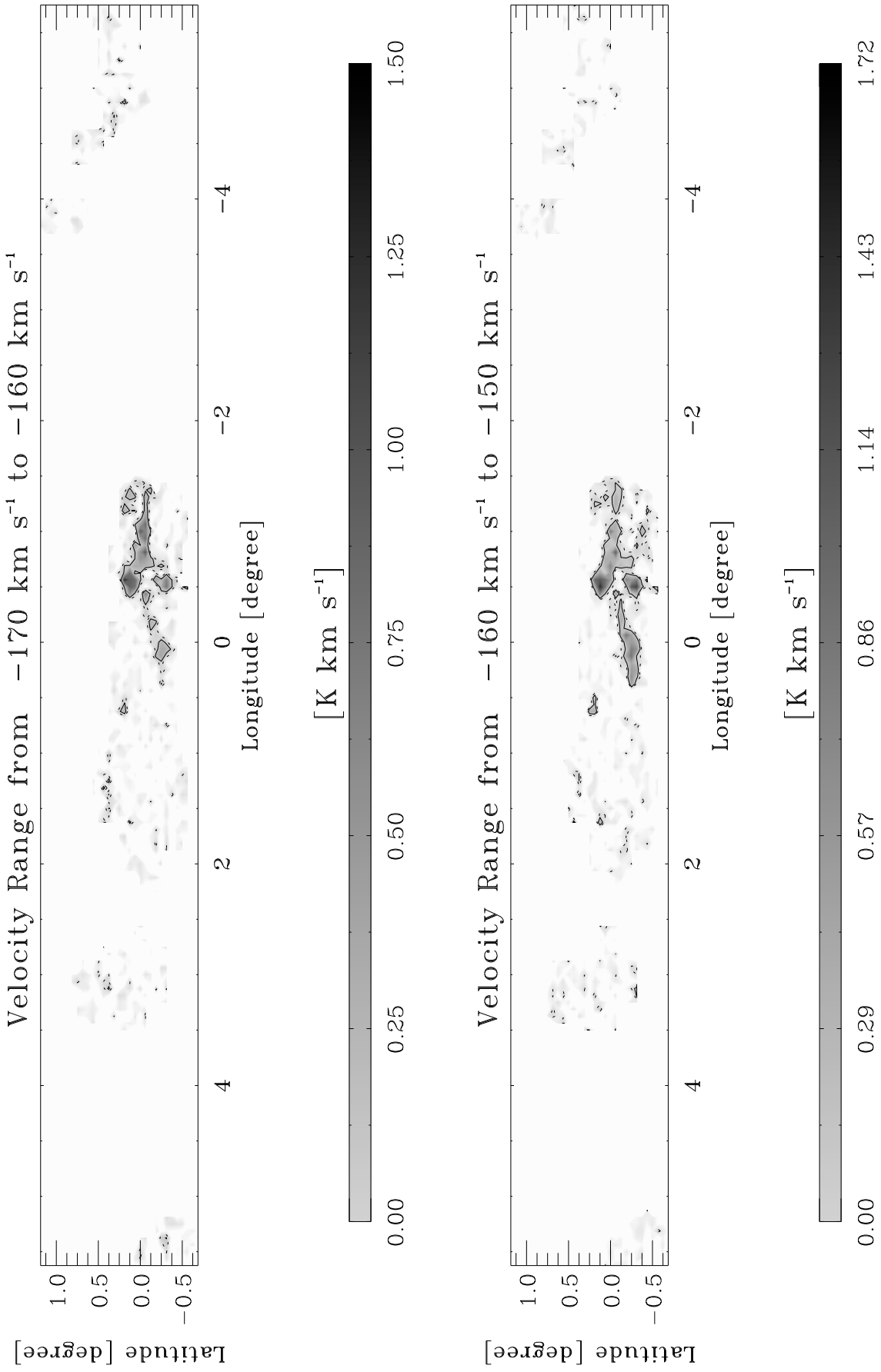

Fig. B1.5. continued.

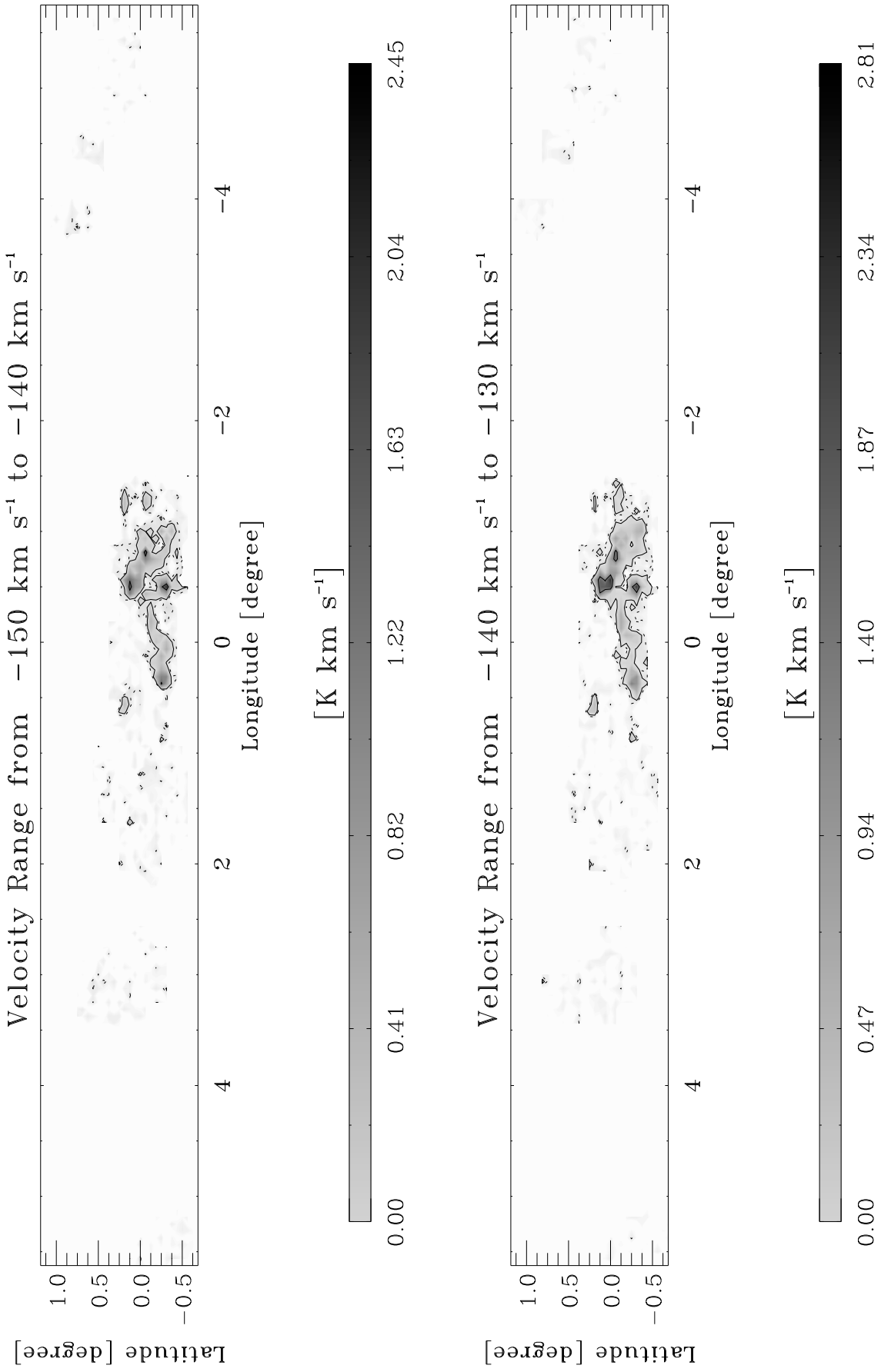

Fig. B1.6. continued.

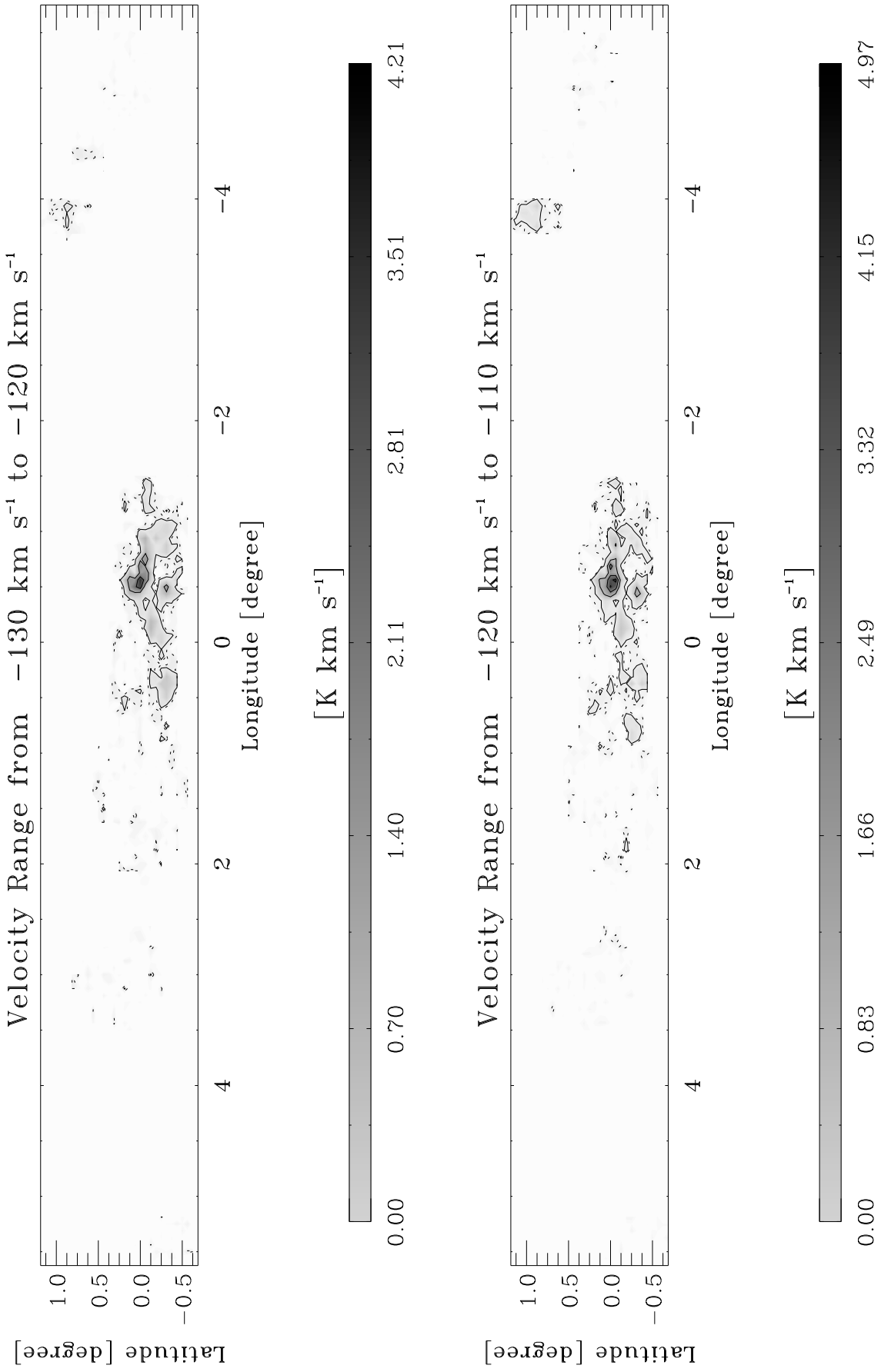

Fig. B1.7. continued.

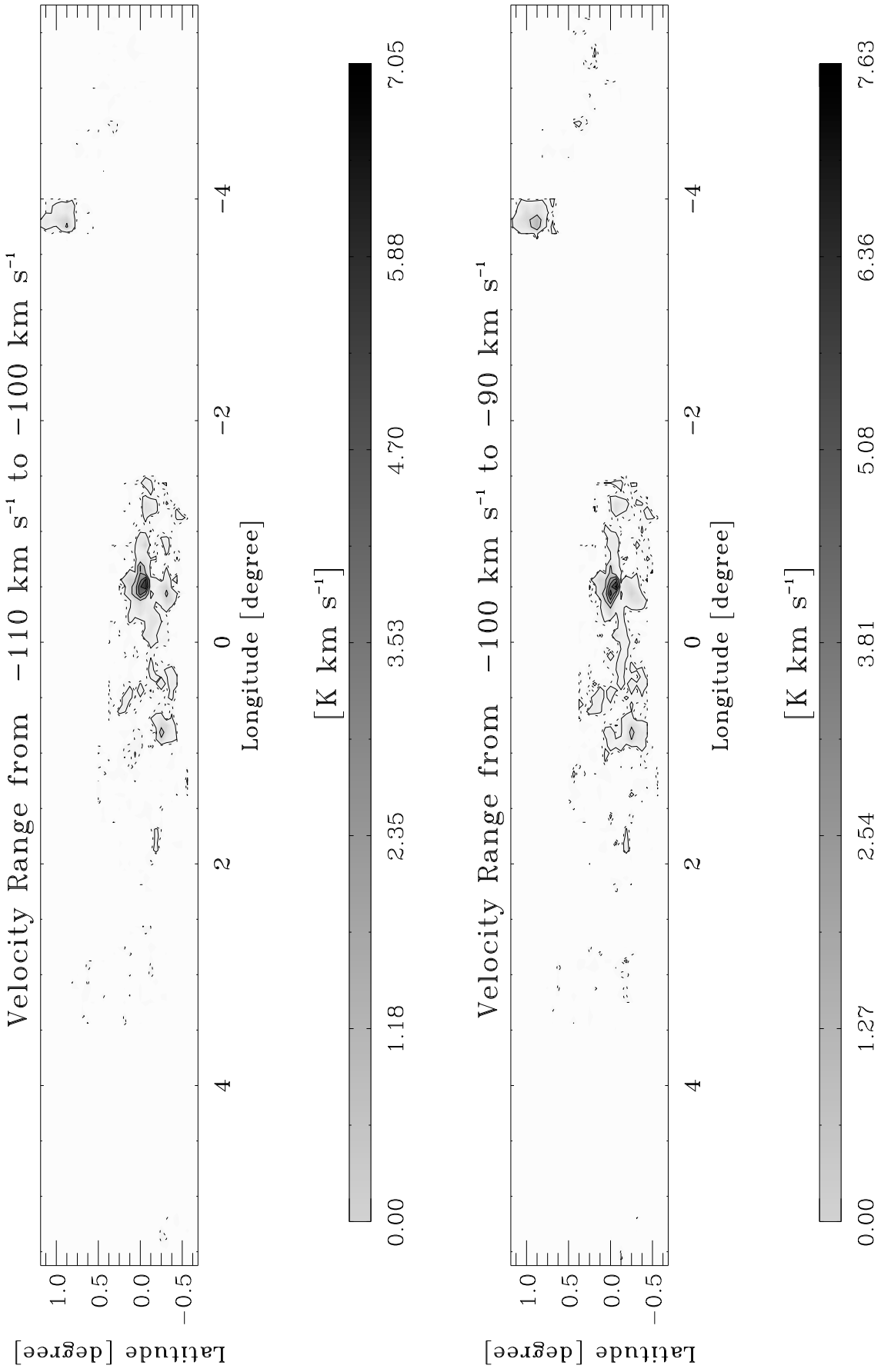

Fig. B1.8. continued.

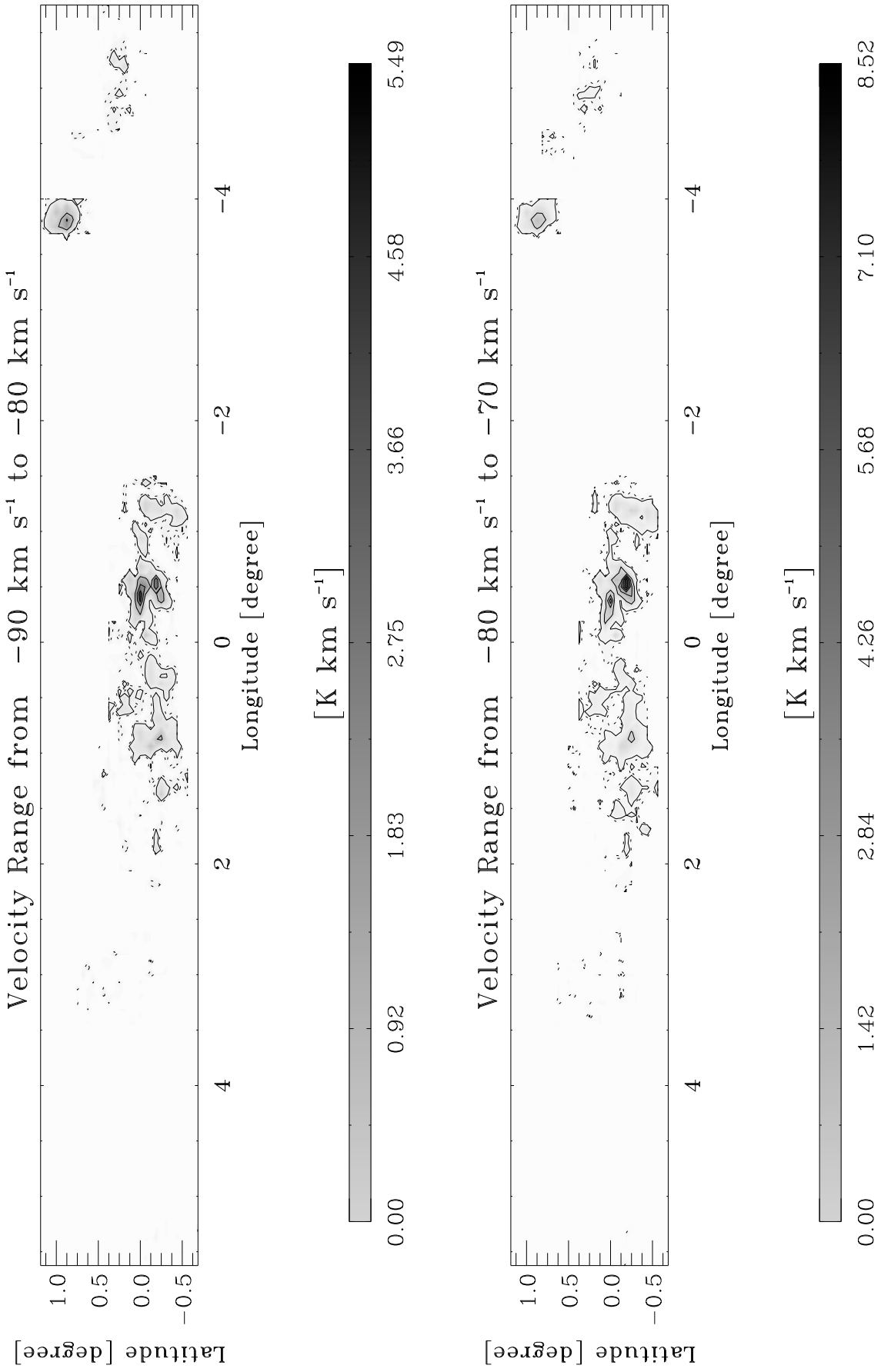

Fig. B1.9. continued.

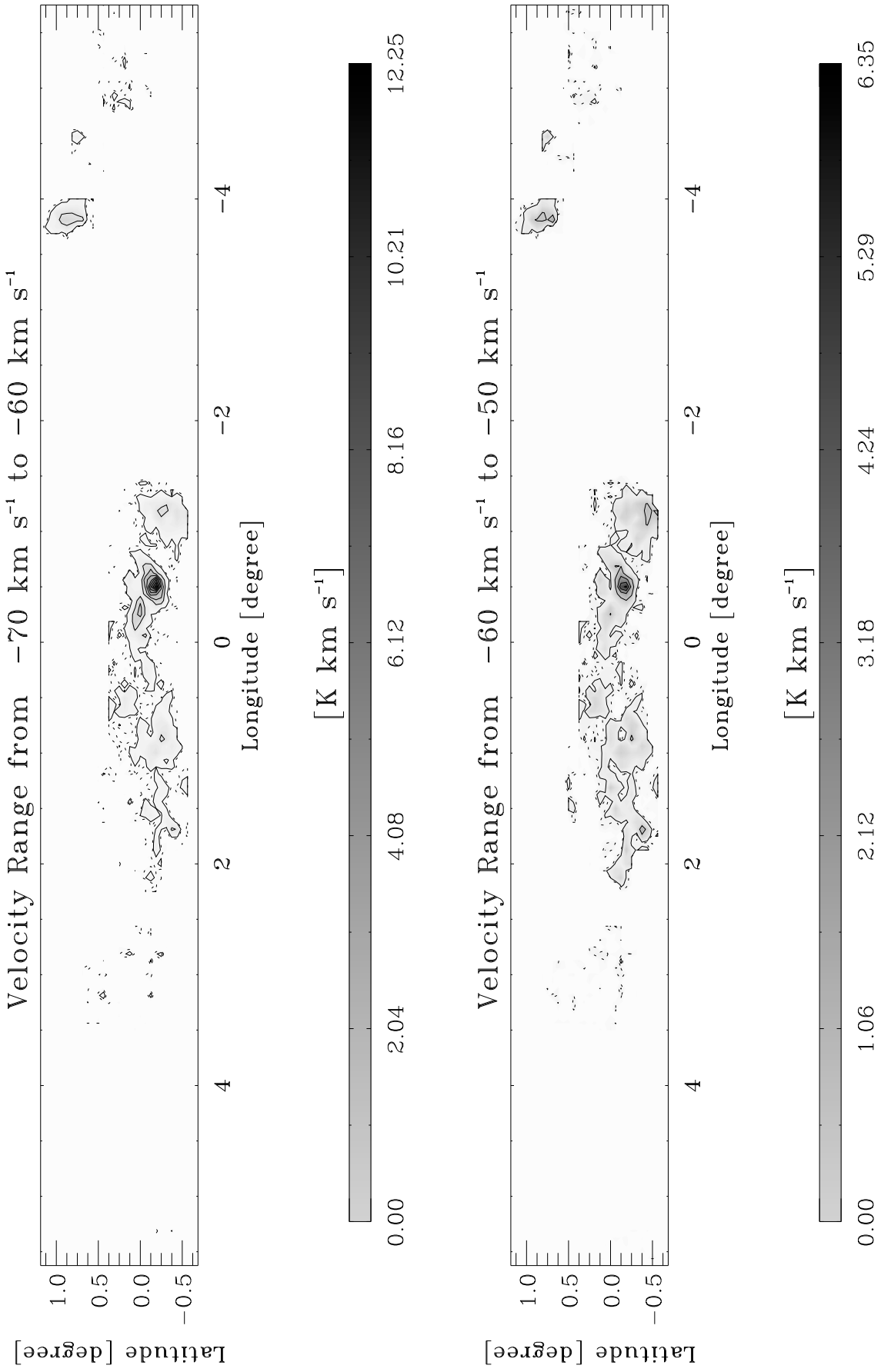

Fig. B1.10. continued.

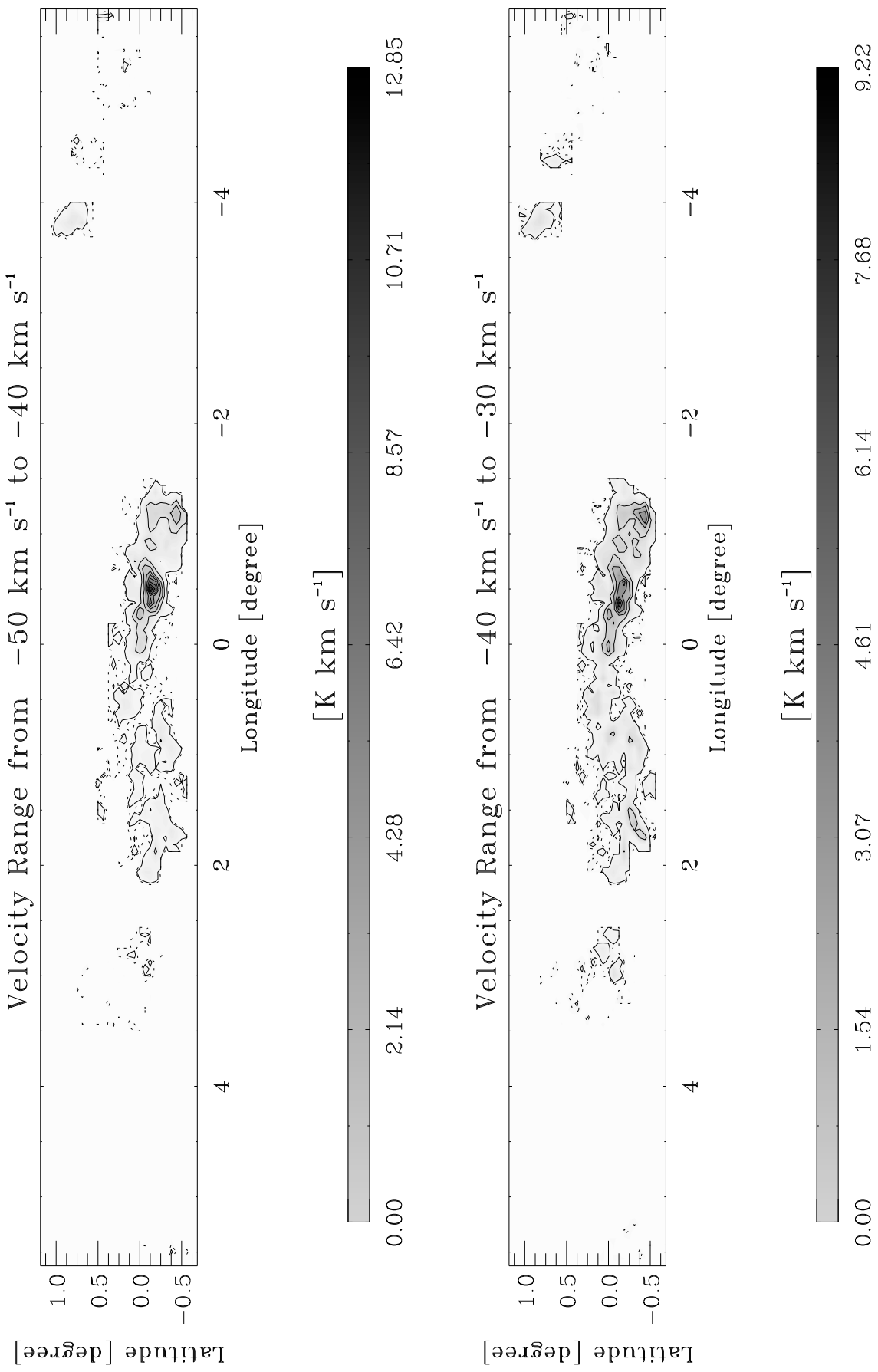

Fig. B1.11. continued.

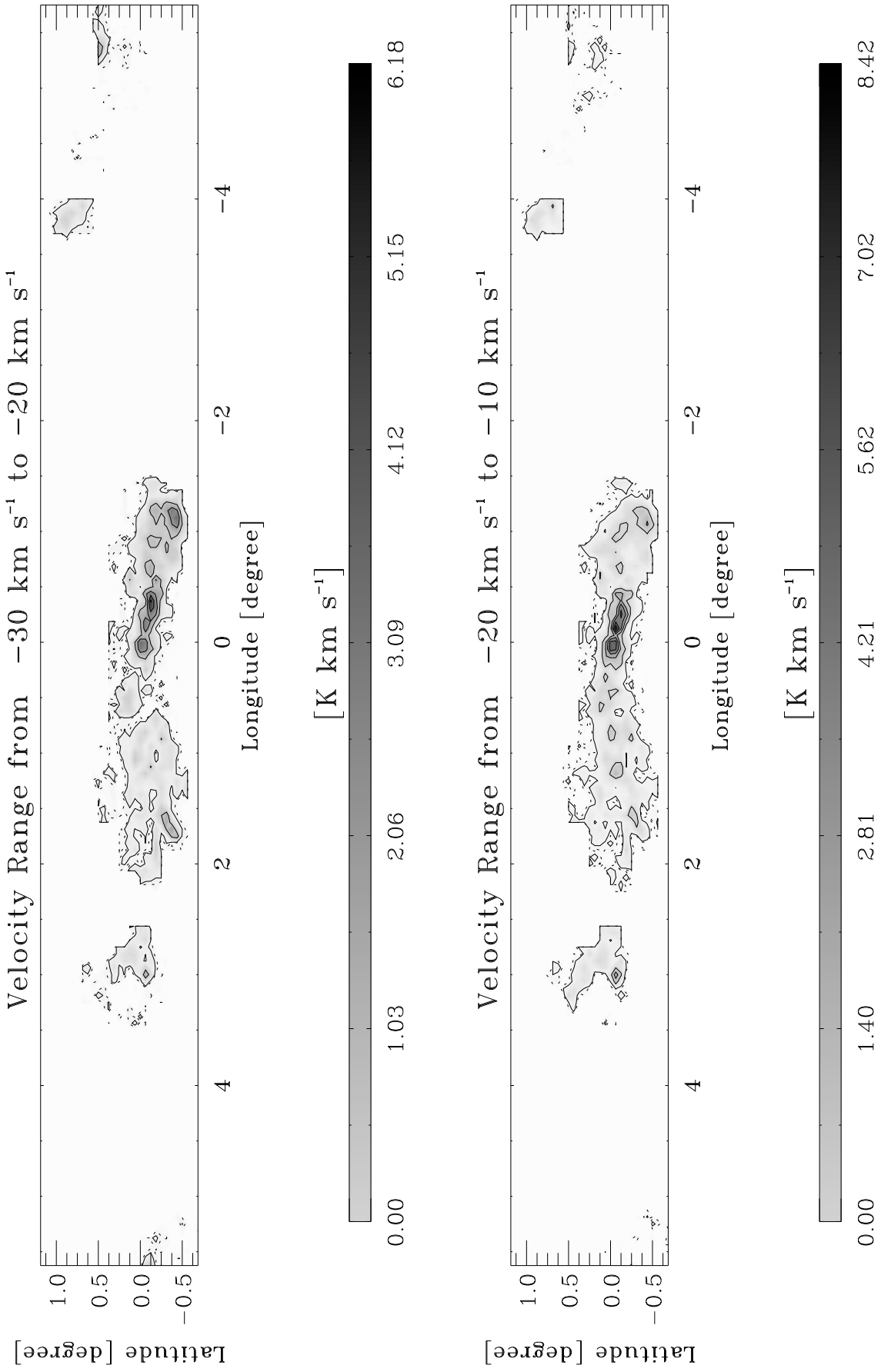

Fig. B1.12. continued.

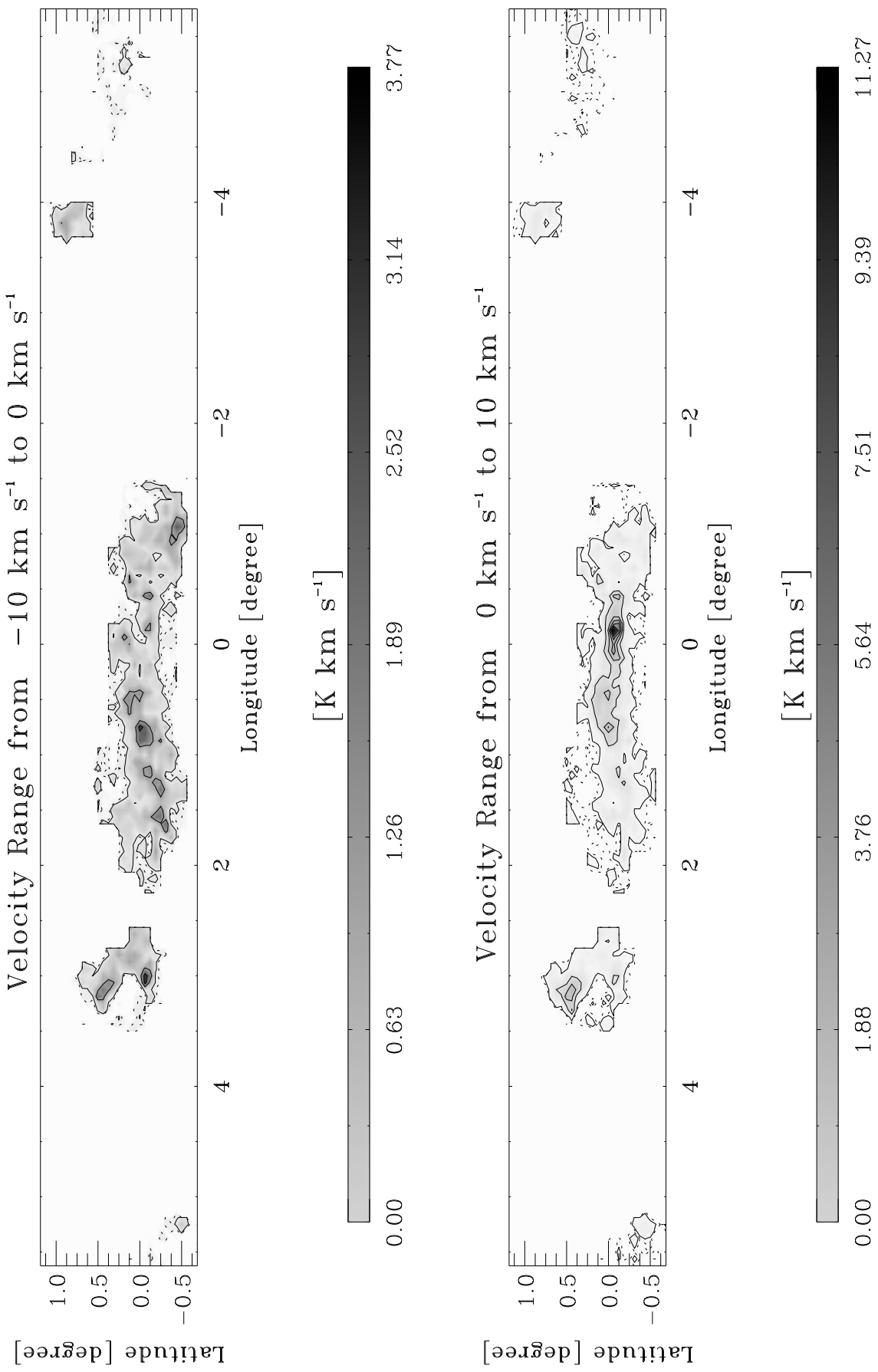

Fig. B1.13. continued.

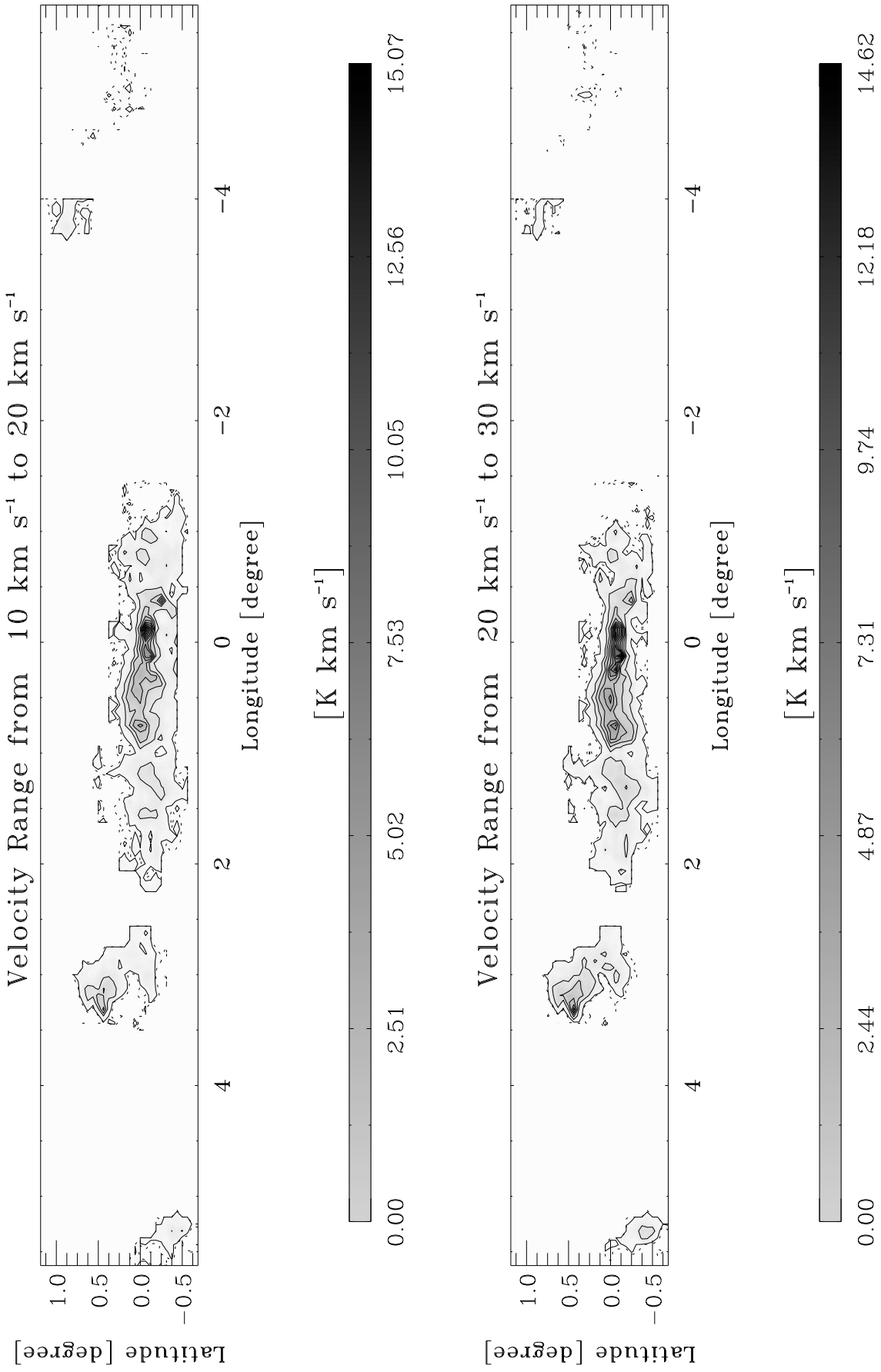

Fig. B1.14. continued.

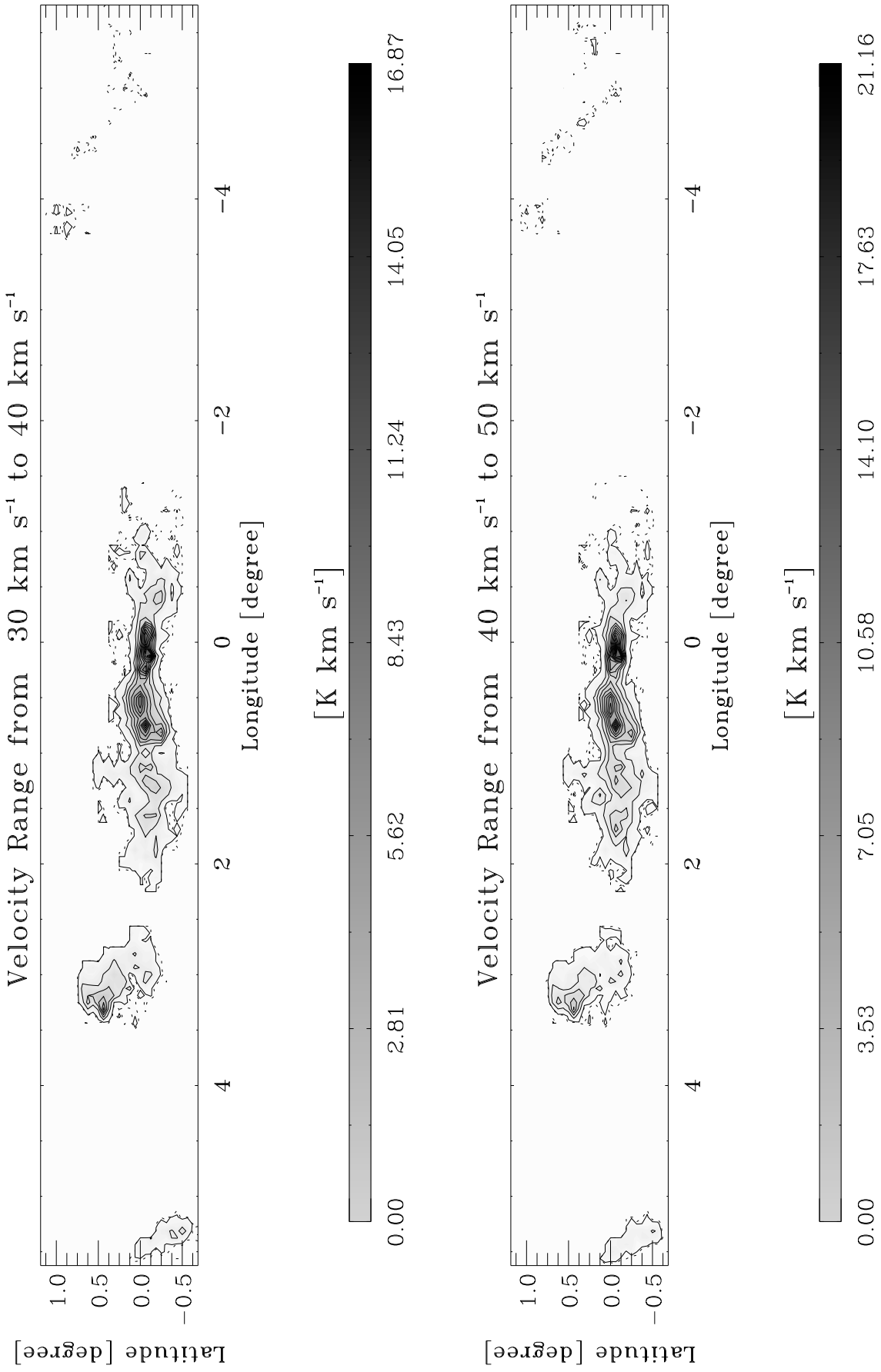

Fig. B1.15. continued.

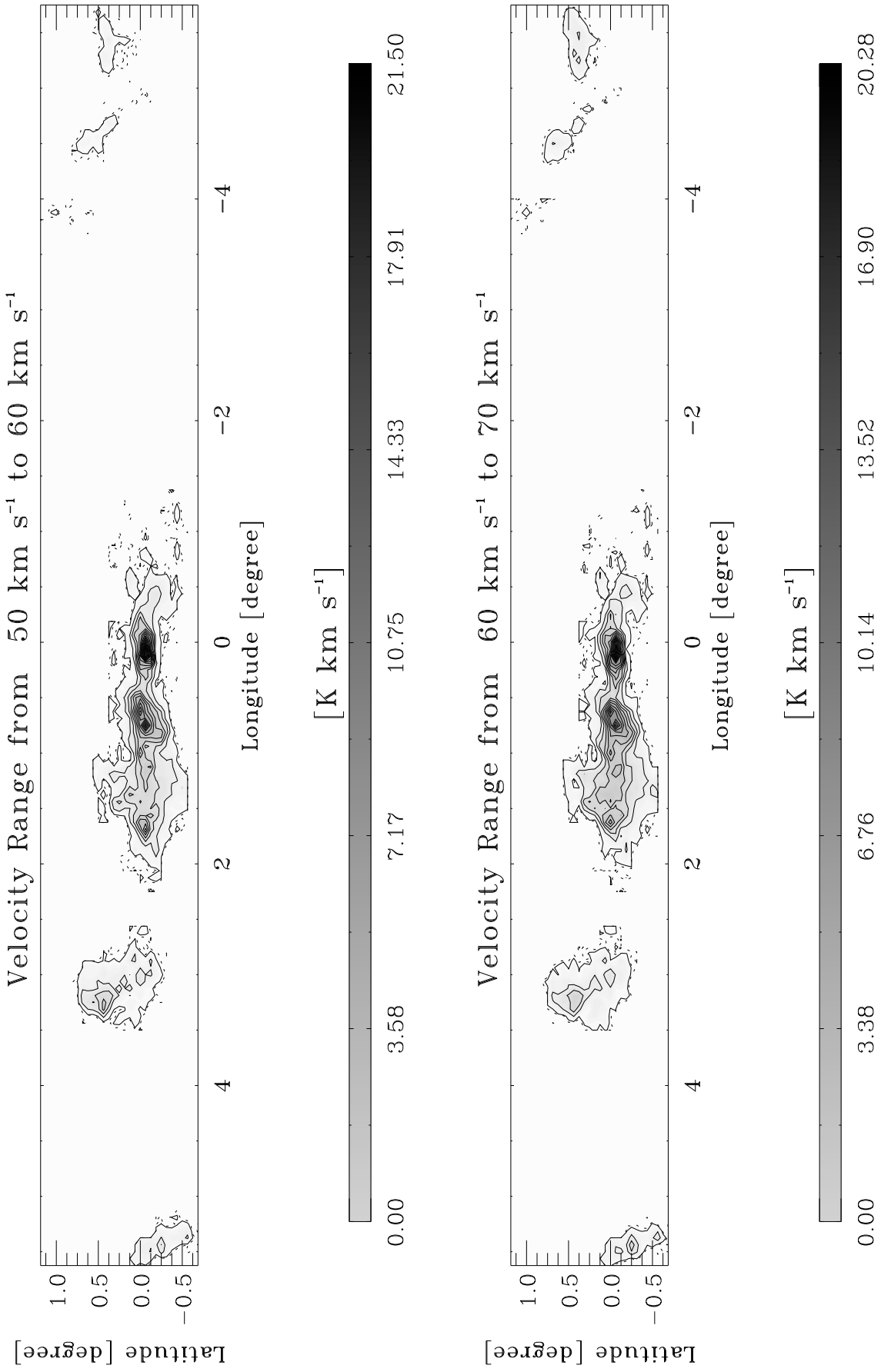

Fig. B1.16. continued.

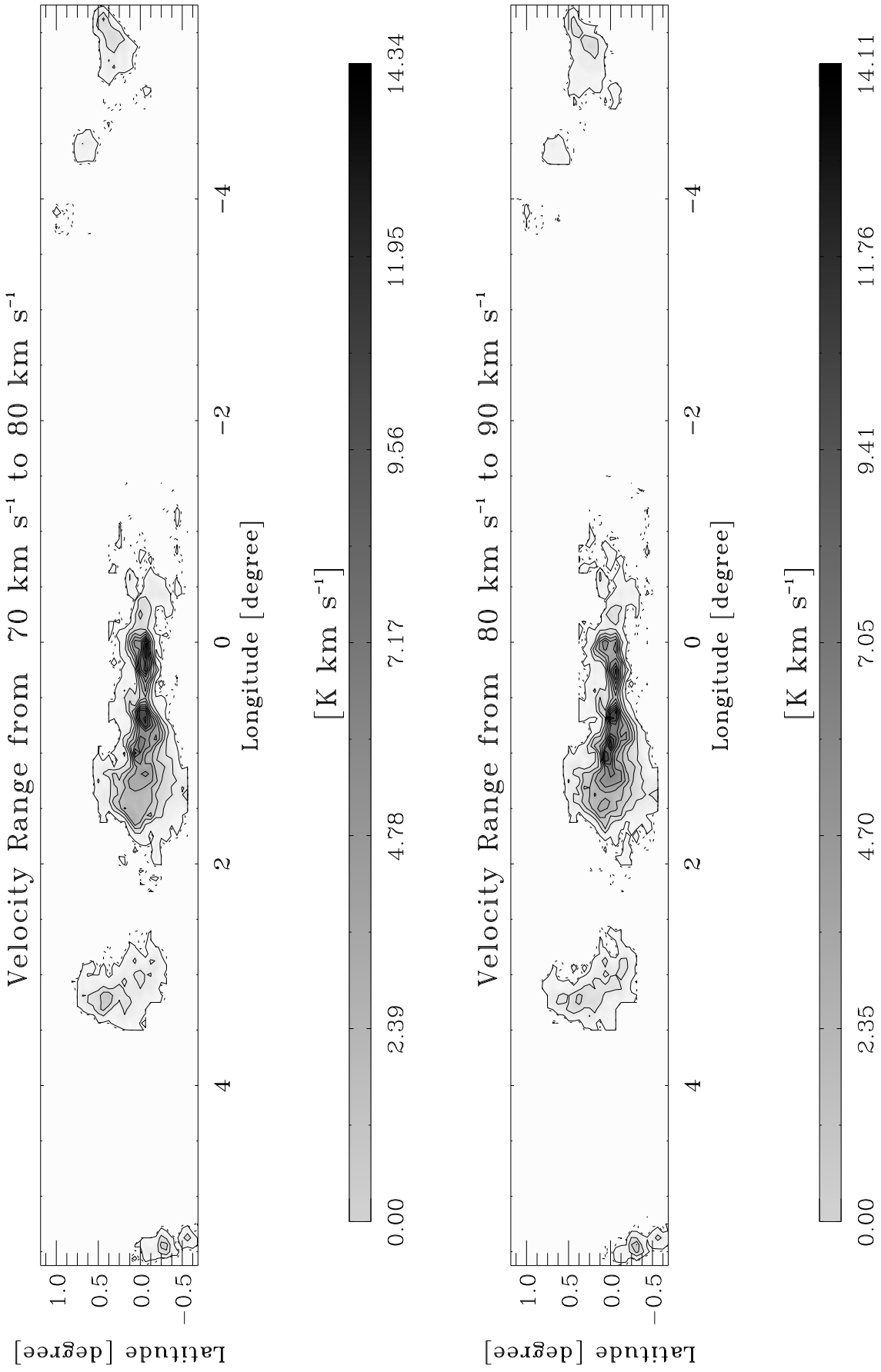

Fig. B1.17. continued.

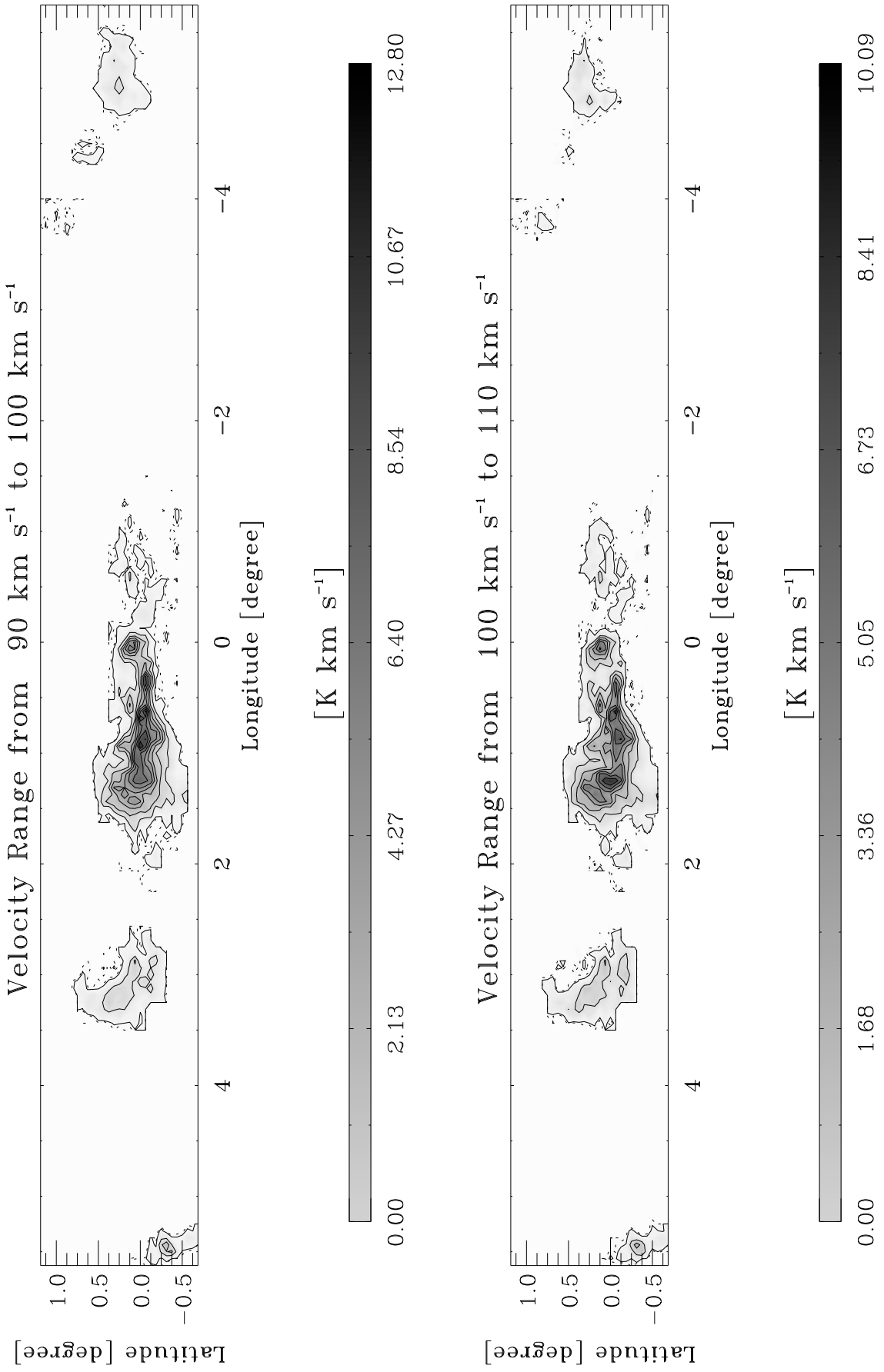

Fig. B1.18. continued.

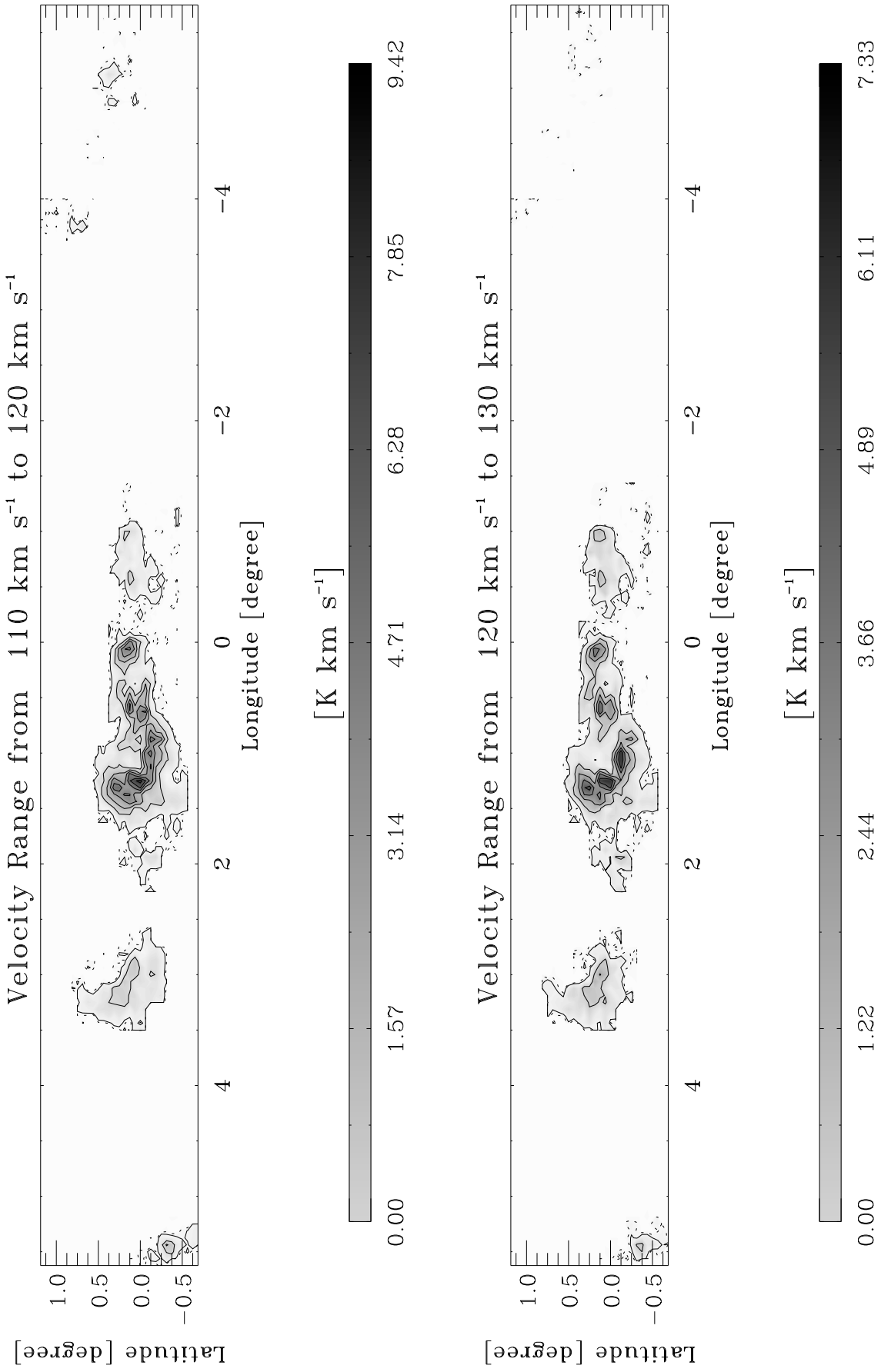

Fig. B1.19. continued.

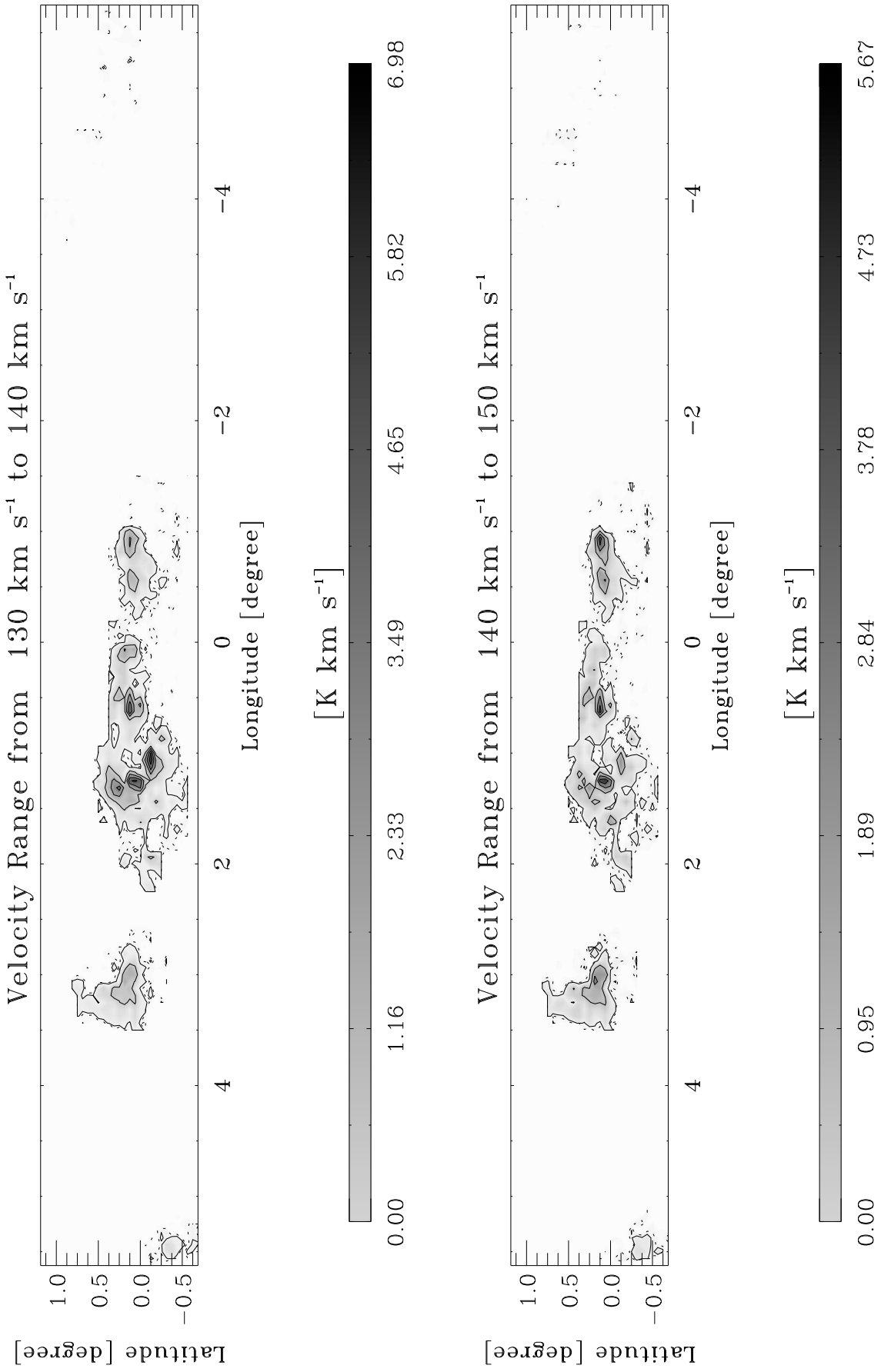

Fig. B1.20. continued.

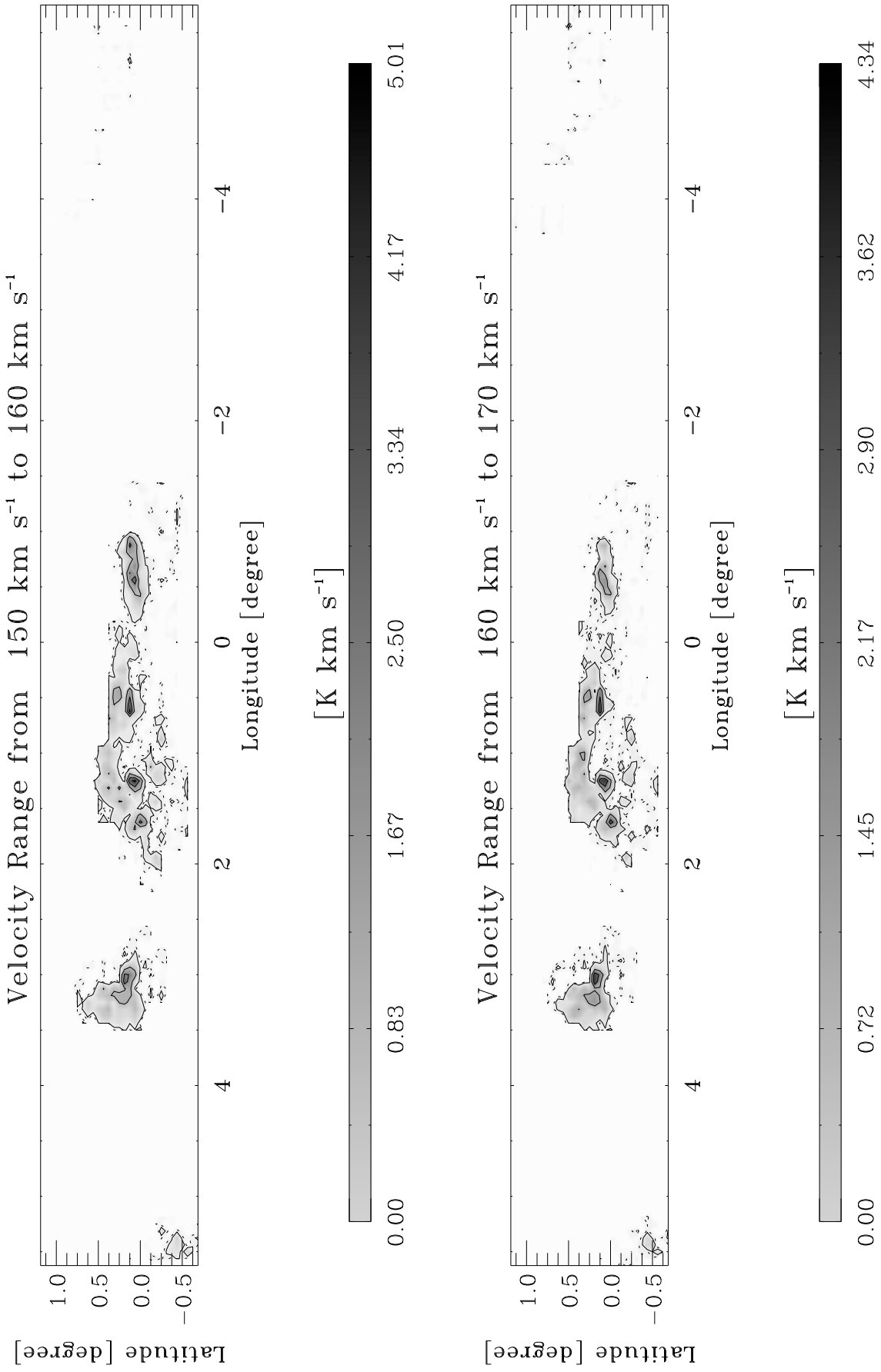

Fig. B1.21. continued.

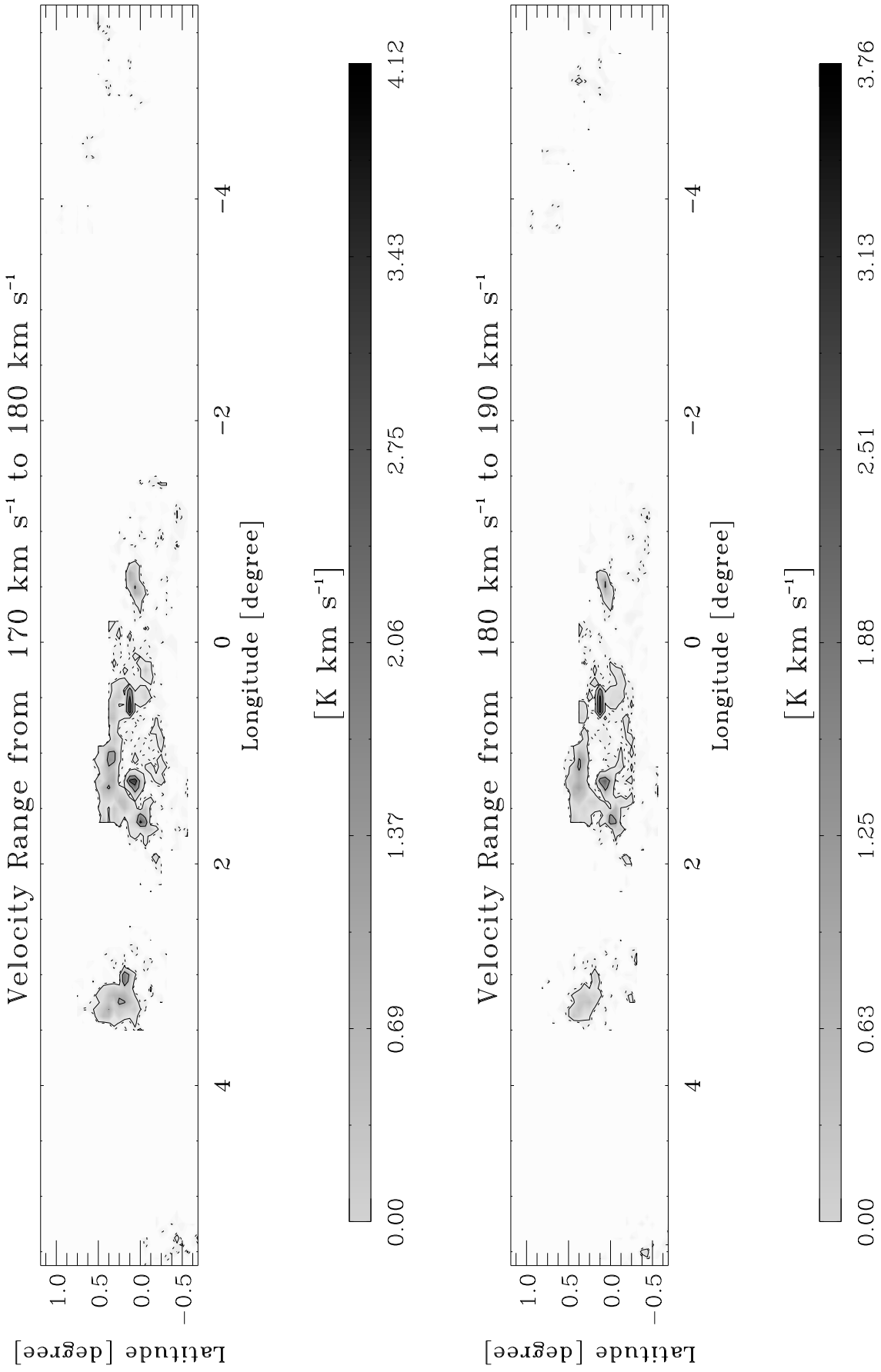

Fig. B1.22. continued.

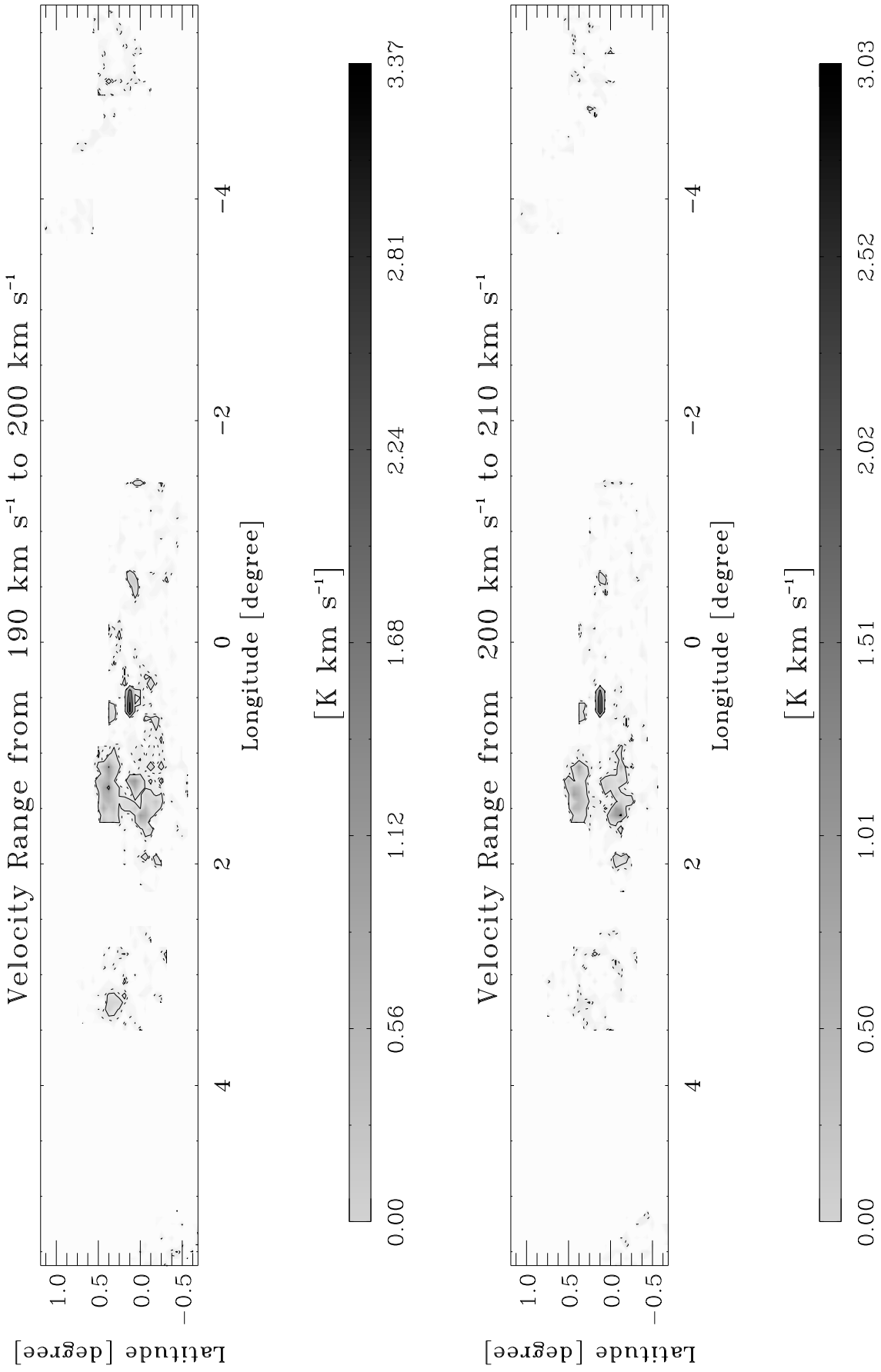

Fig. B1.23. continued.

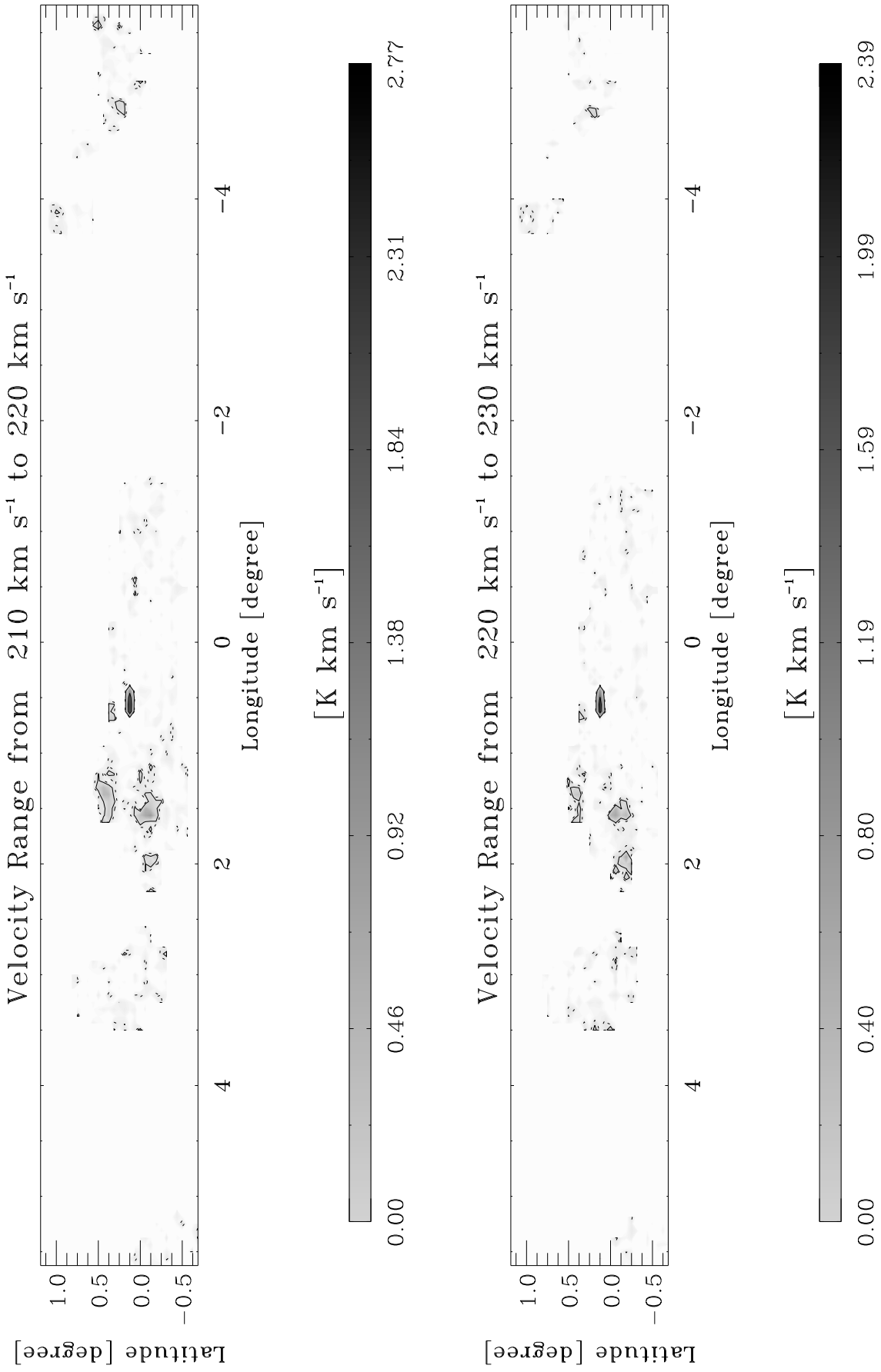

Fig. B1.24. continued.

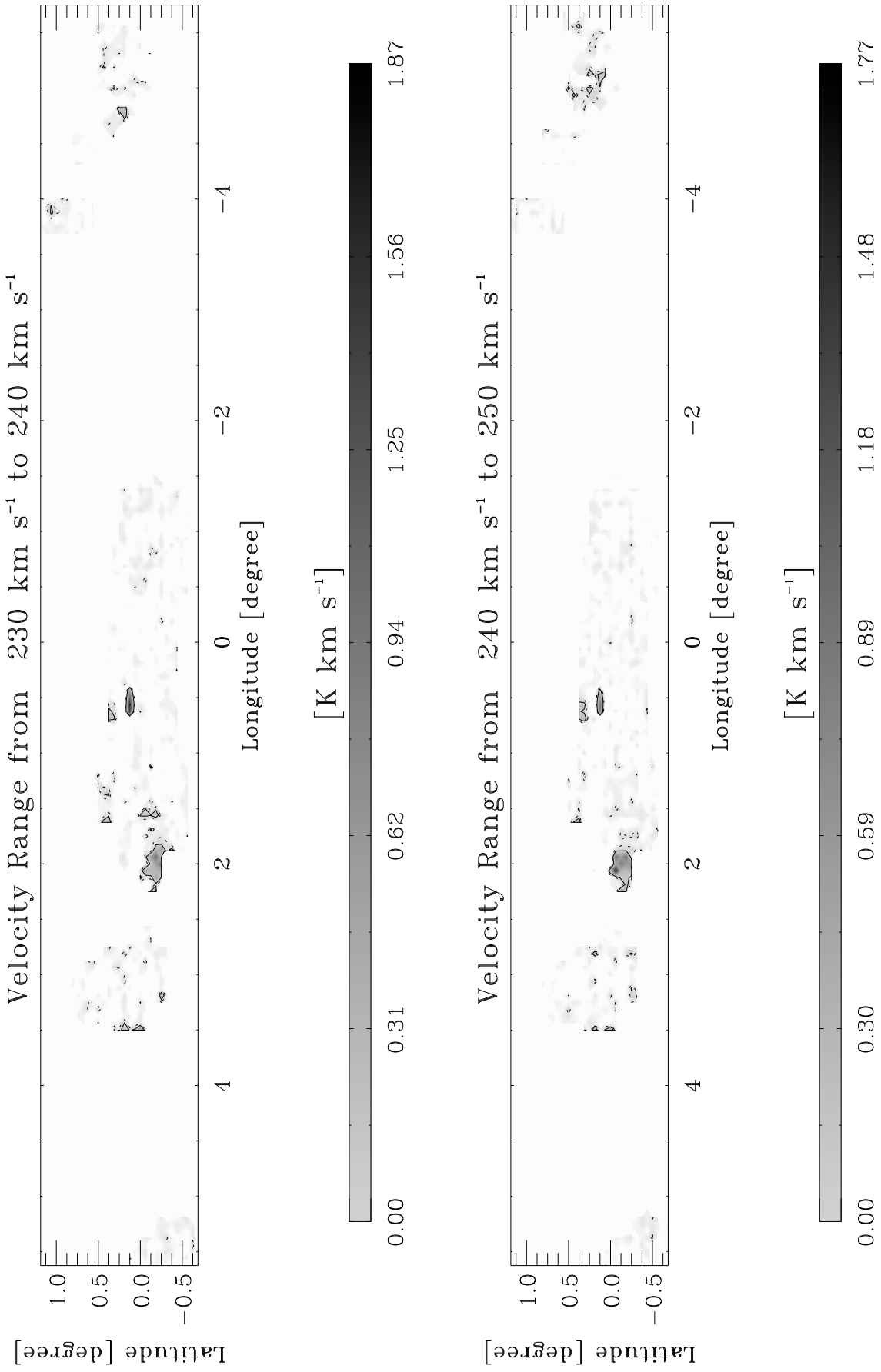

Fig. B1.25. continued.

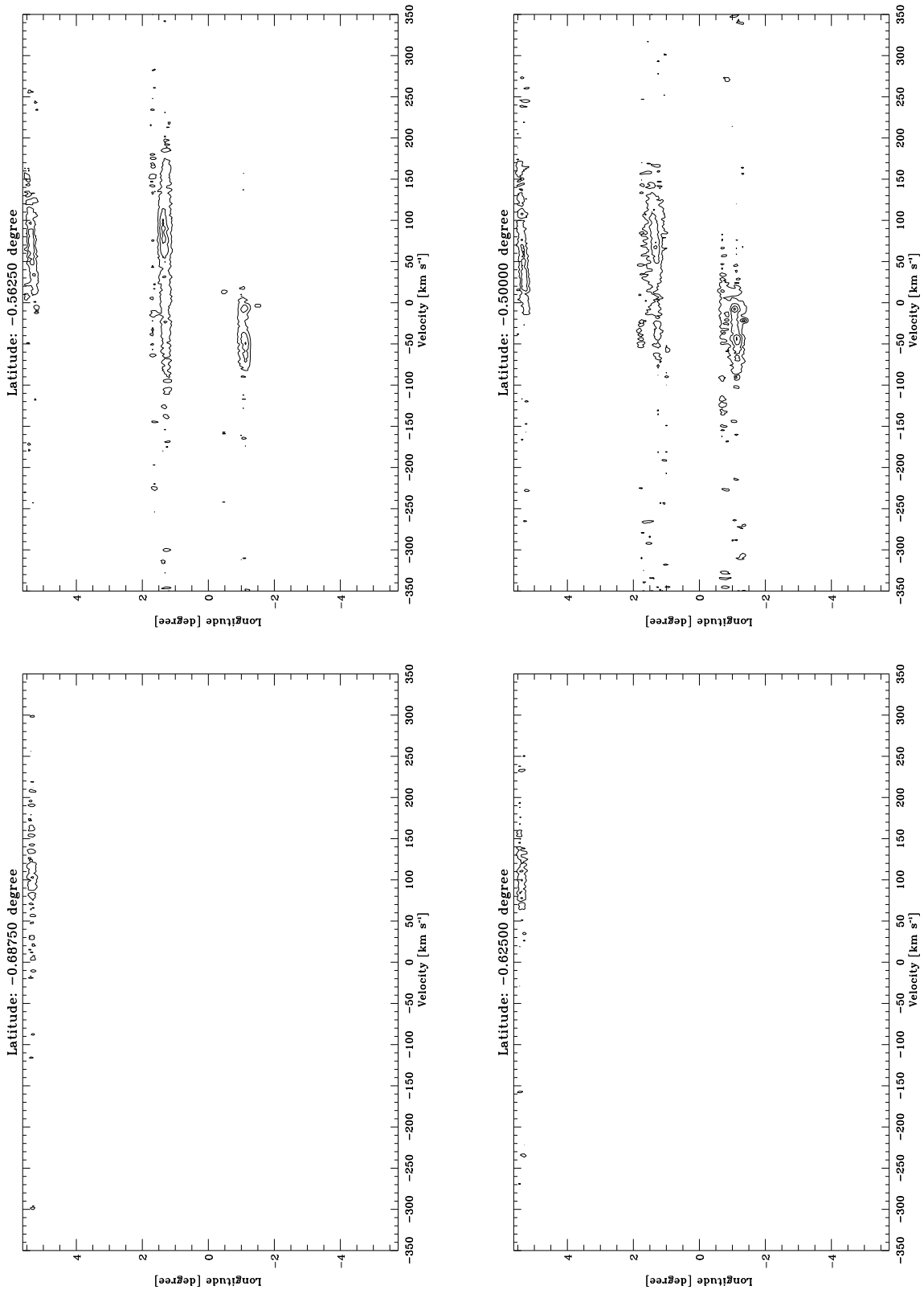

Fig. B2.1. Longitude-velocidad contour diagrams for each observed latitude in HCO^+. The lowest contour is at 0.0021 K (3σ). The following contours increase them in step of 0.0042 K, which correspond to 6σ.

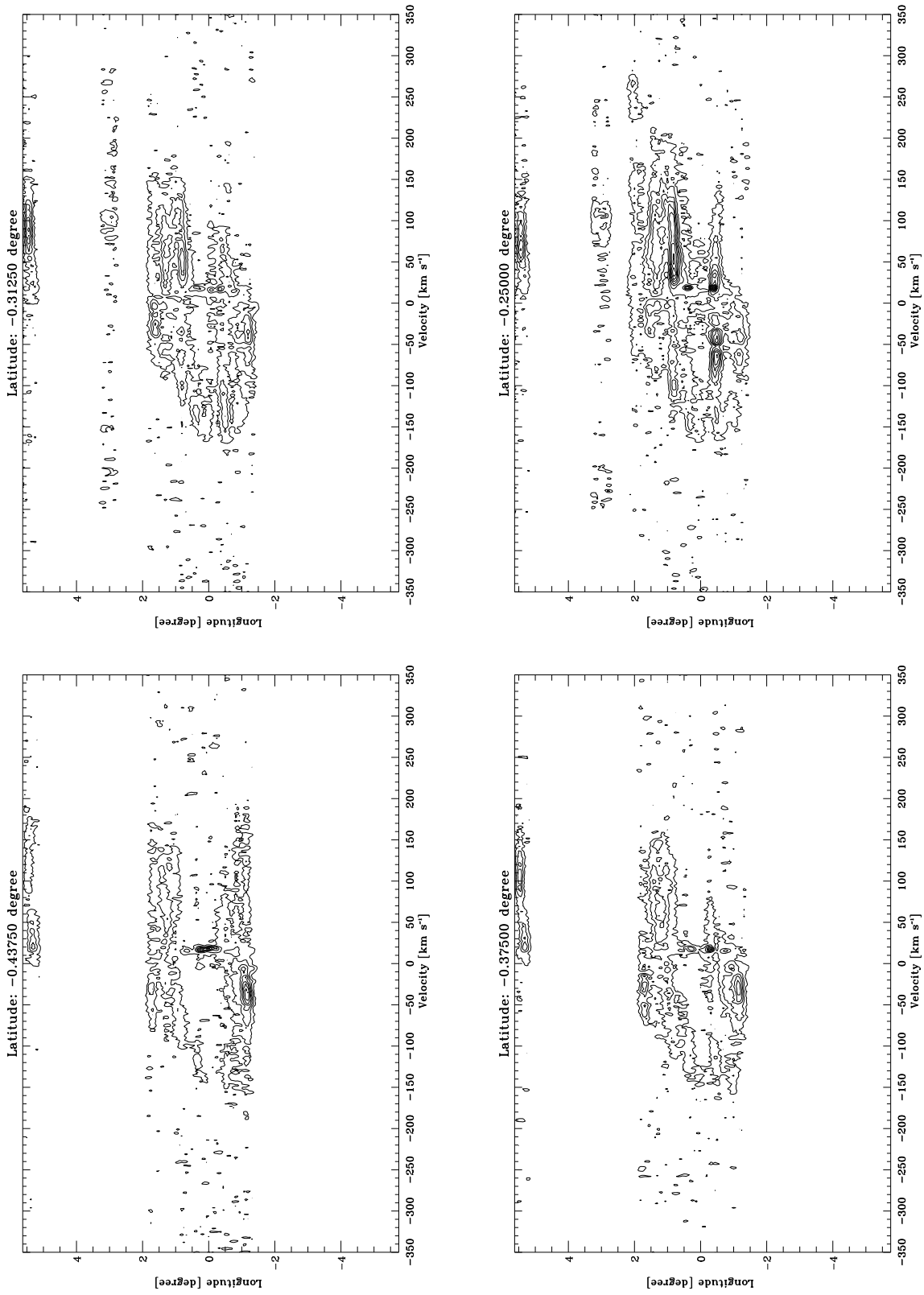

Fig. B2.2. continued.

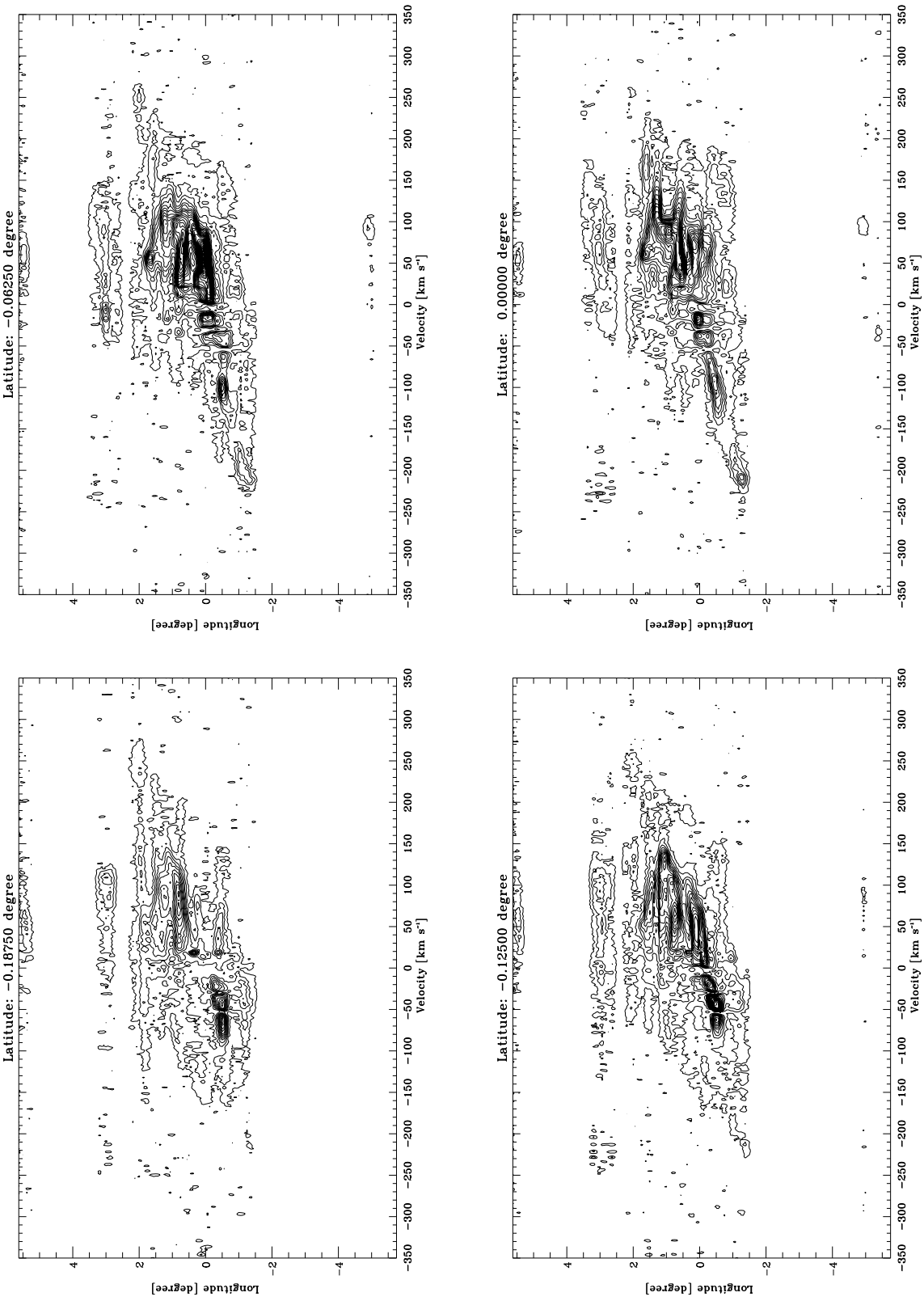

Fig. B2.3. continued.

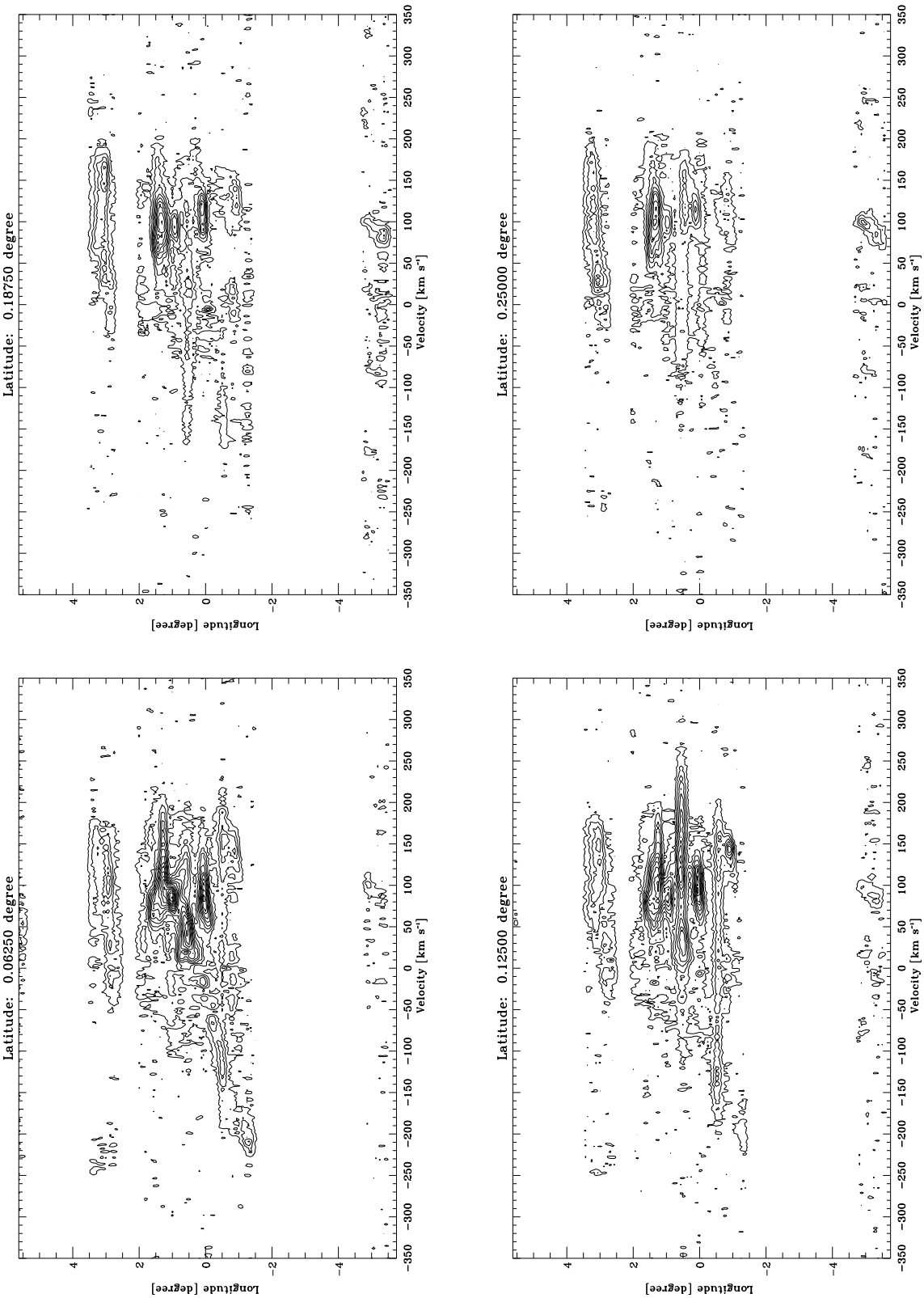

Fig. B2.4. continued.

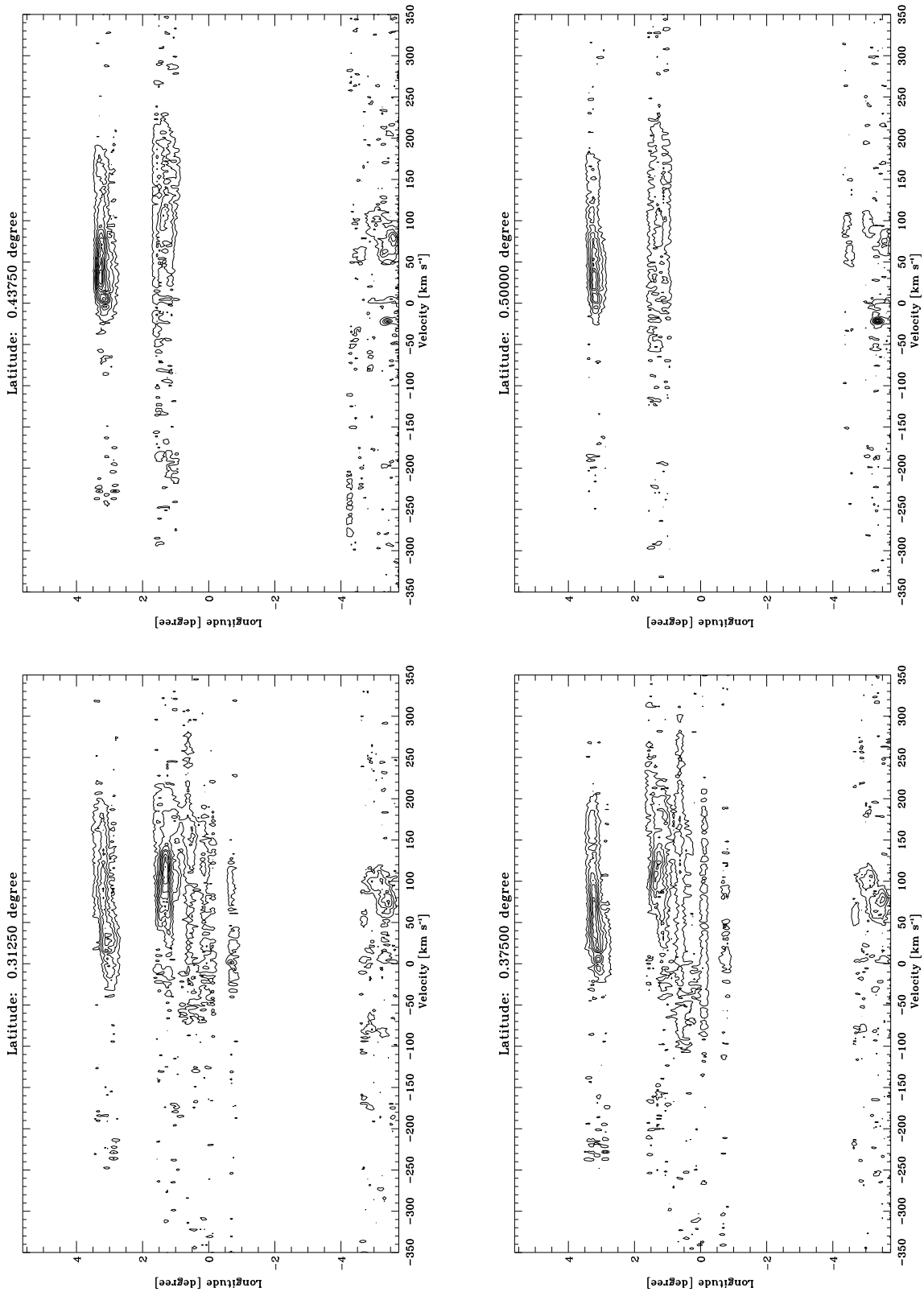

Fig. B2.5. continued.

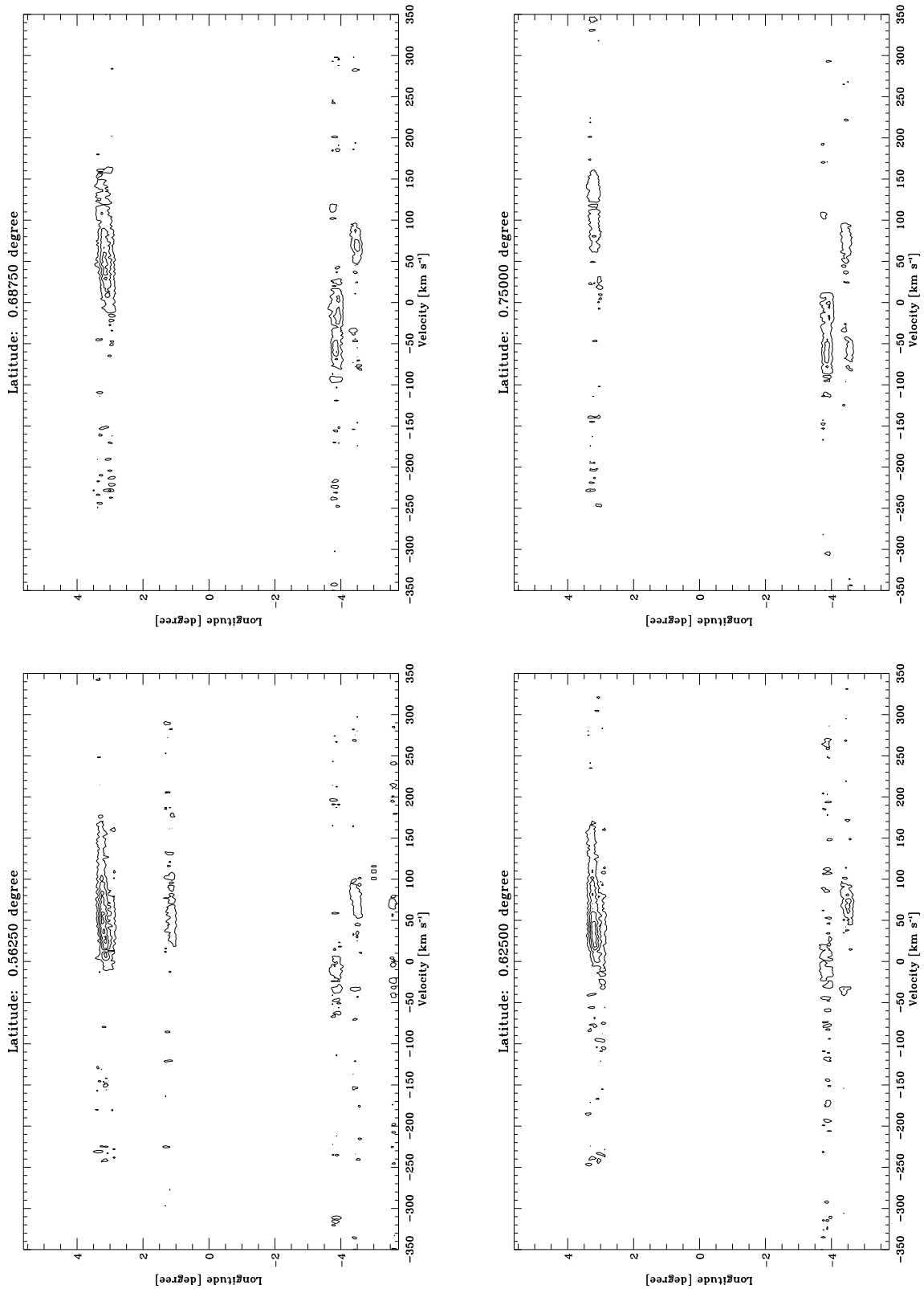

Fig. B2.6. continued.

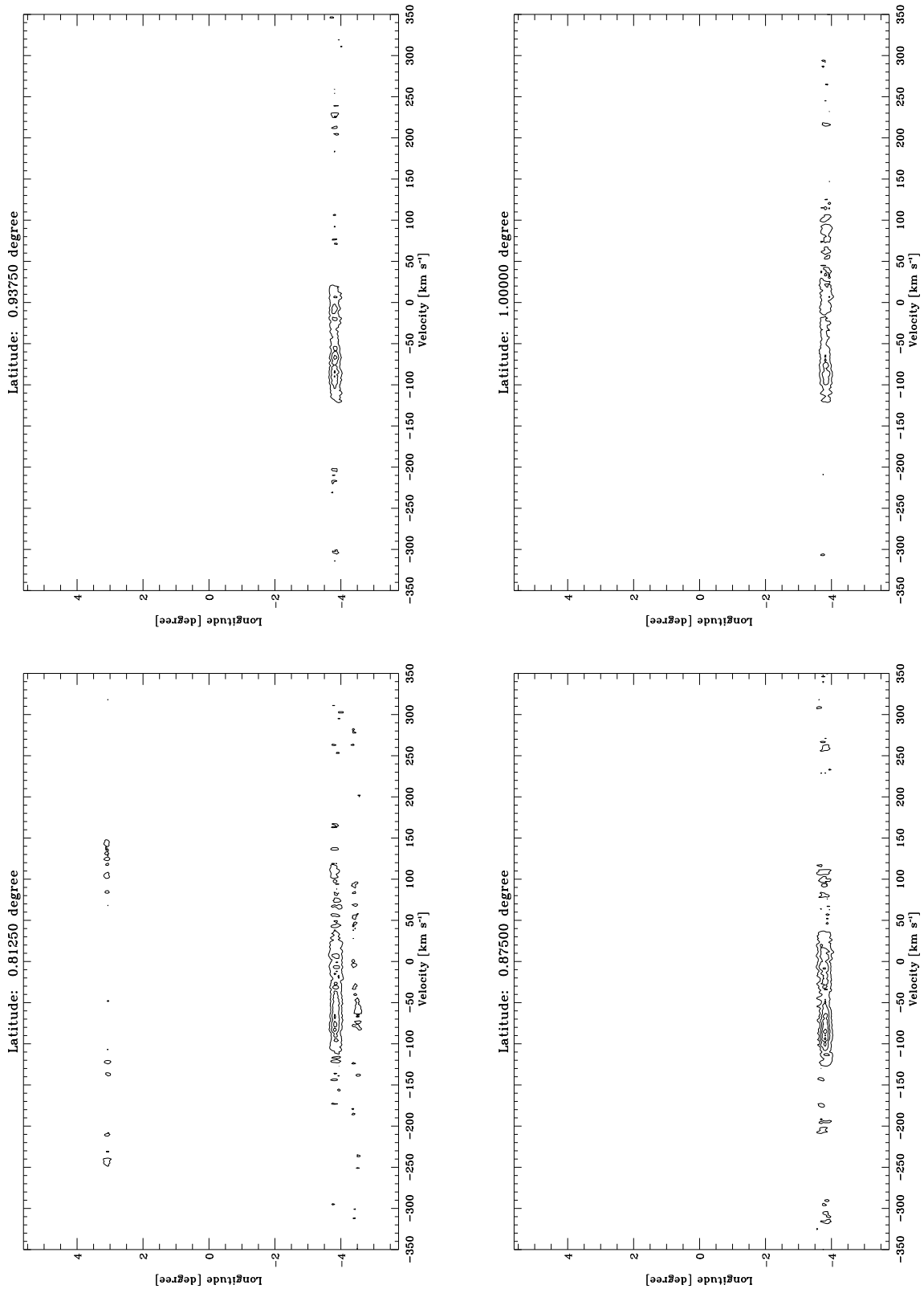

Fig. B2.7. continued.

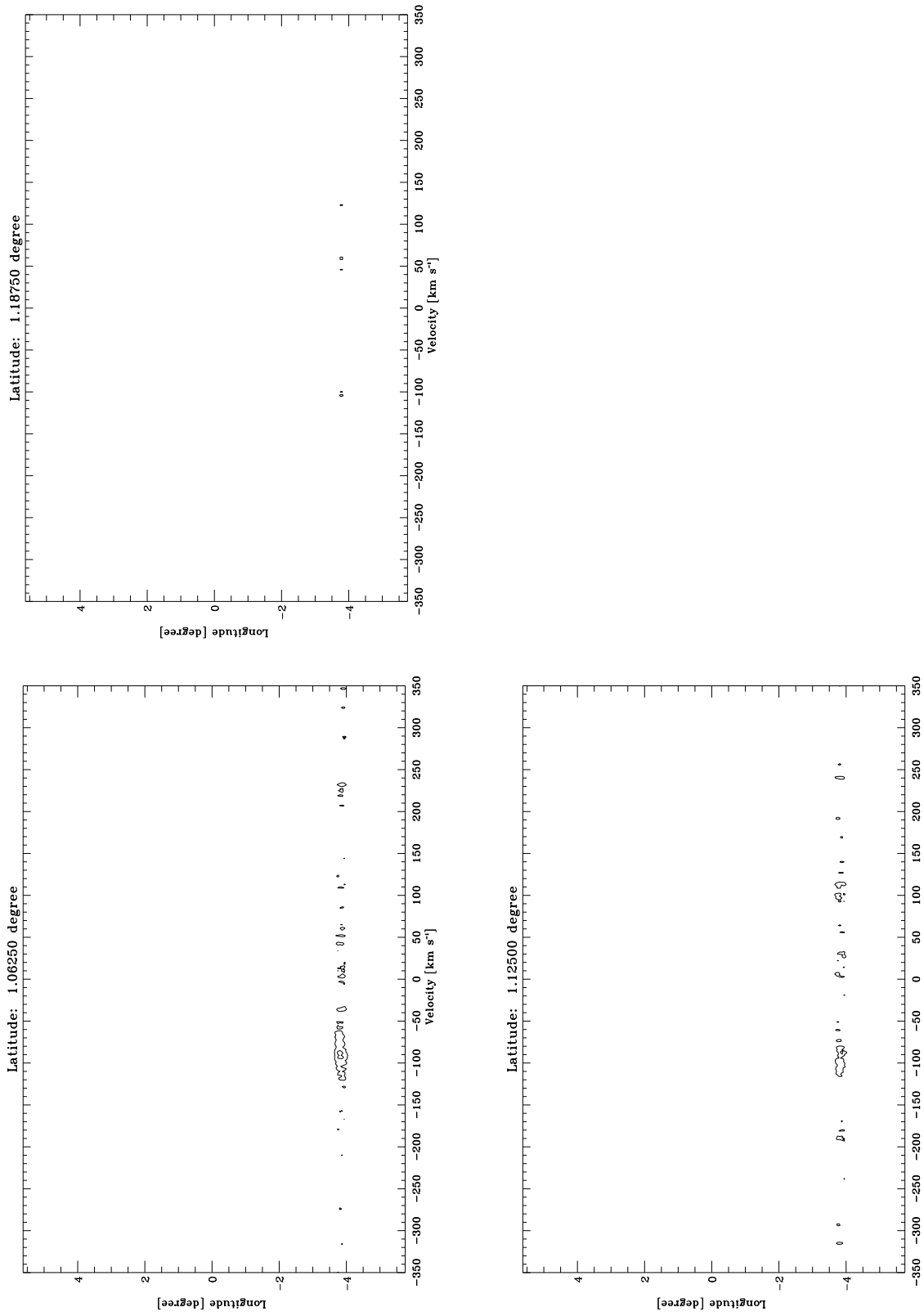

Fig. B2.8. continued.

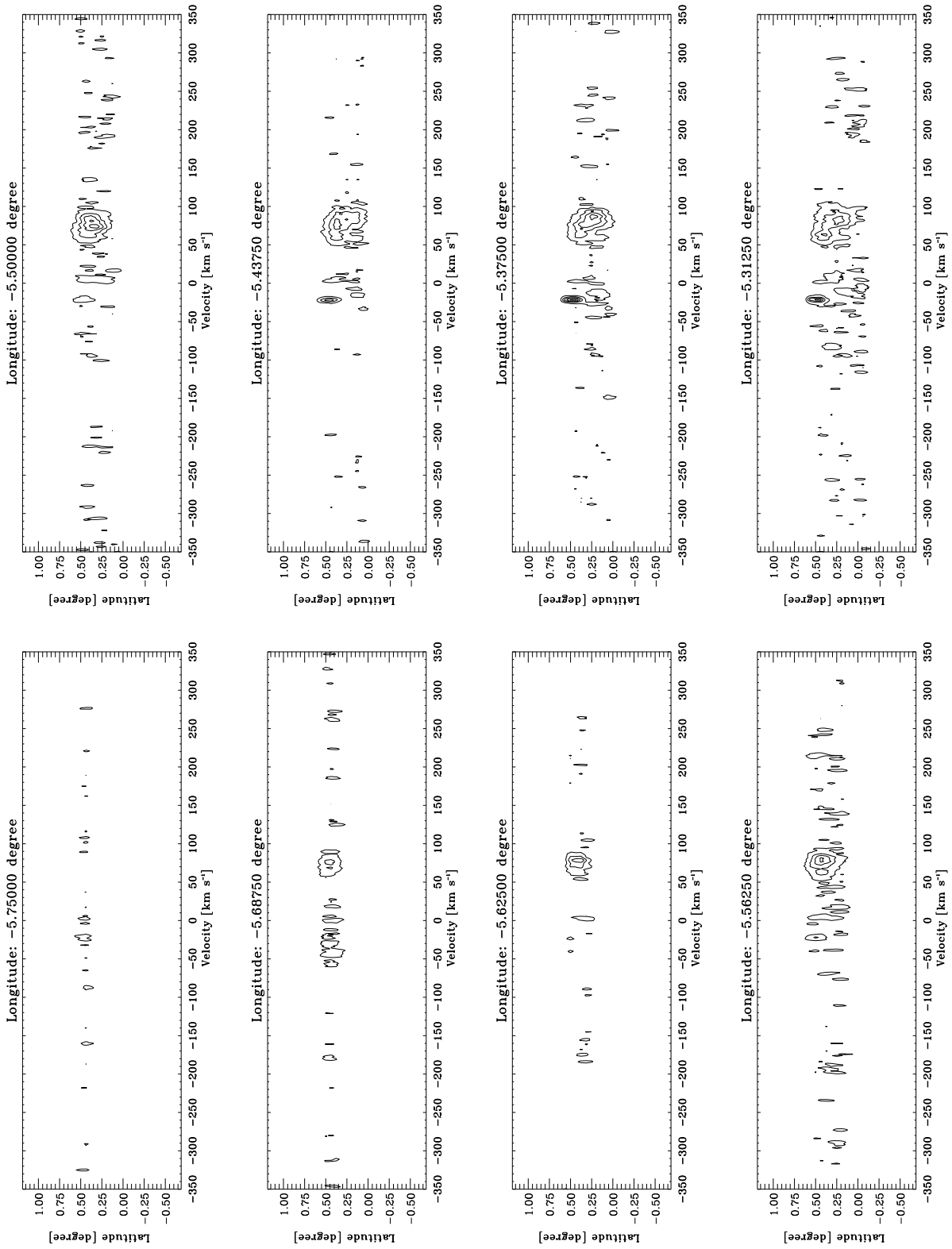

Fig. B3.1. Latitude-velocity diagrams for each observed longitude in HCO^+. The lowest contour is at 0.0021 K (3σ). The following contours increase them in step of 0.0042 K, which correspond to 6σ.

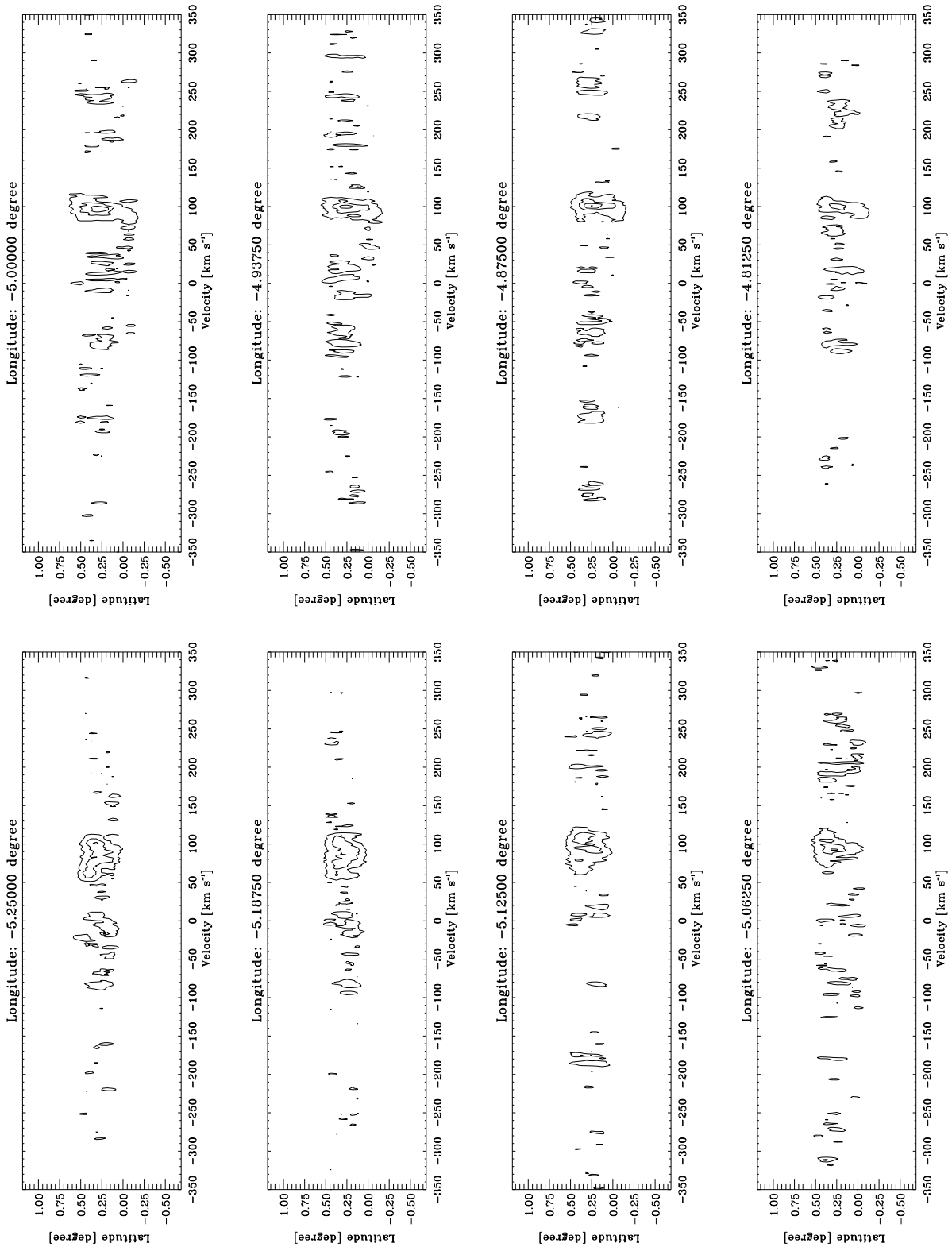

Fig. B3.2. continued.

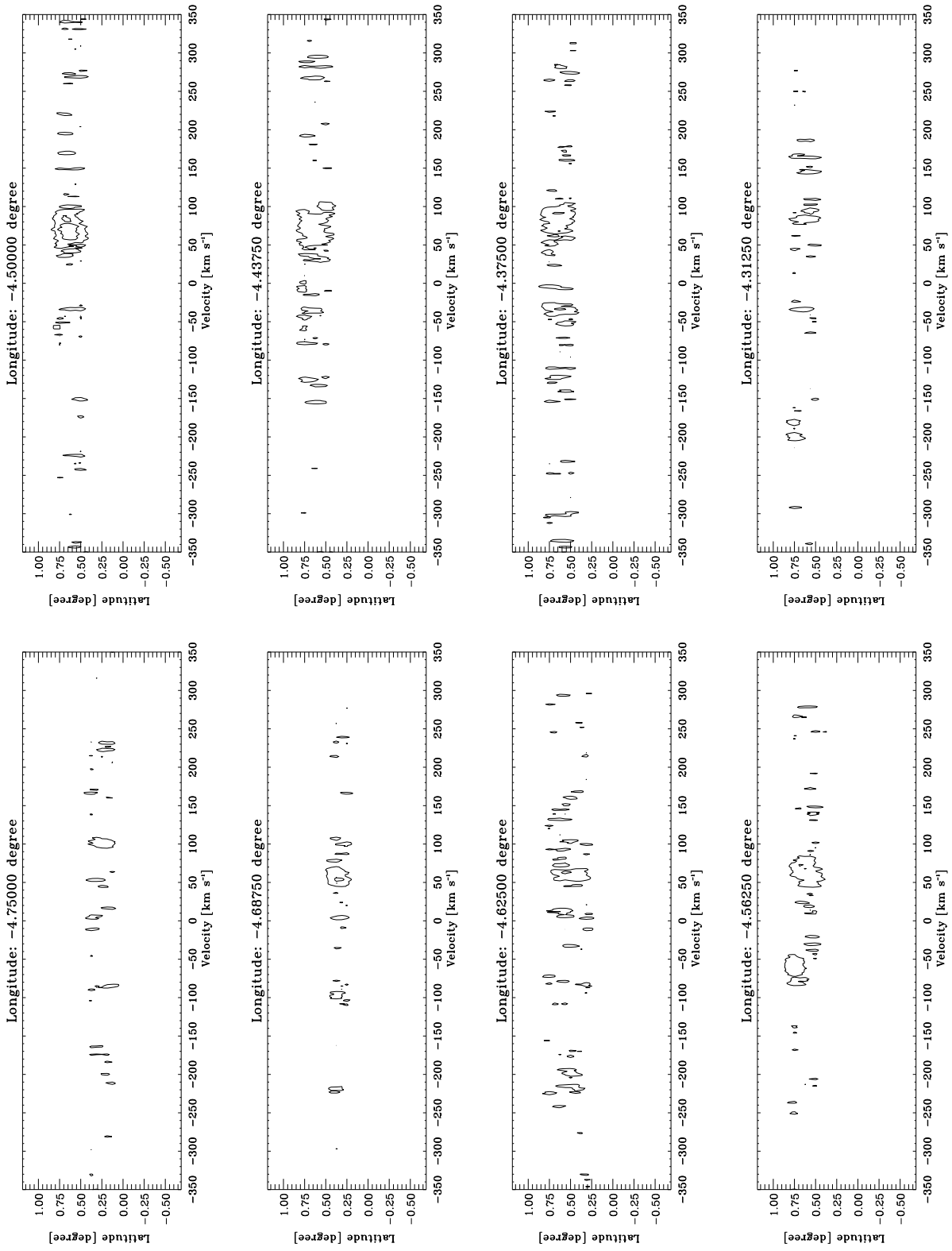

Fig. B3.3. continued.

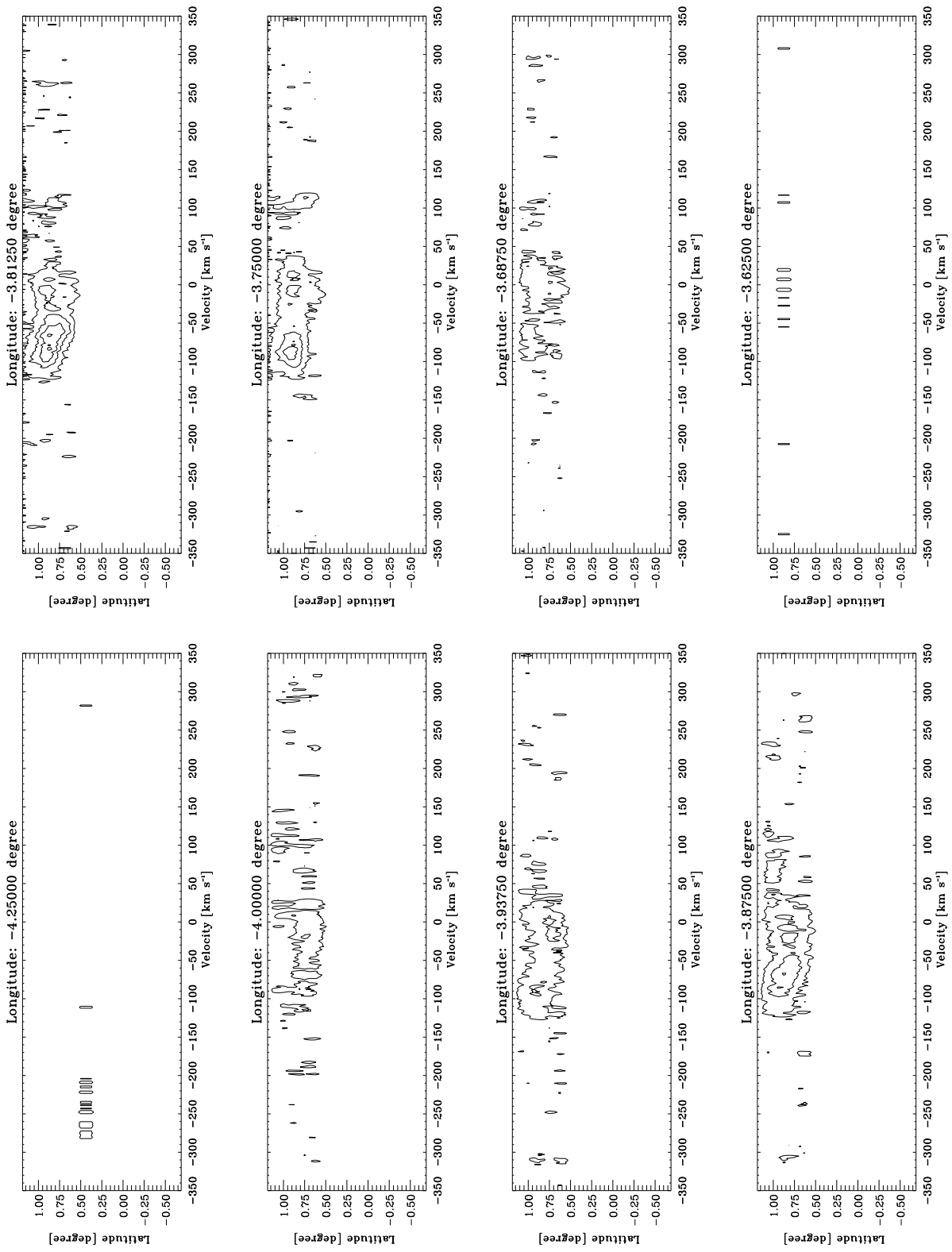

Fig. B3.4. continued.

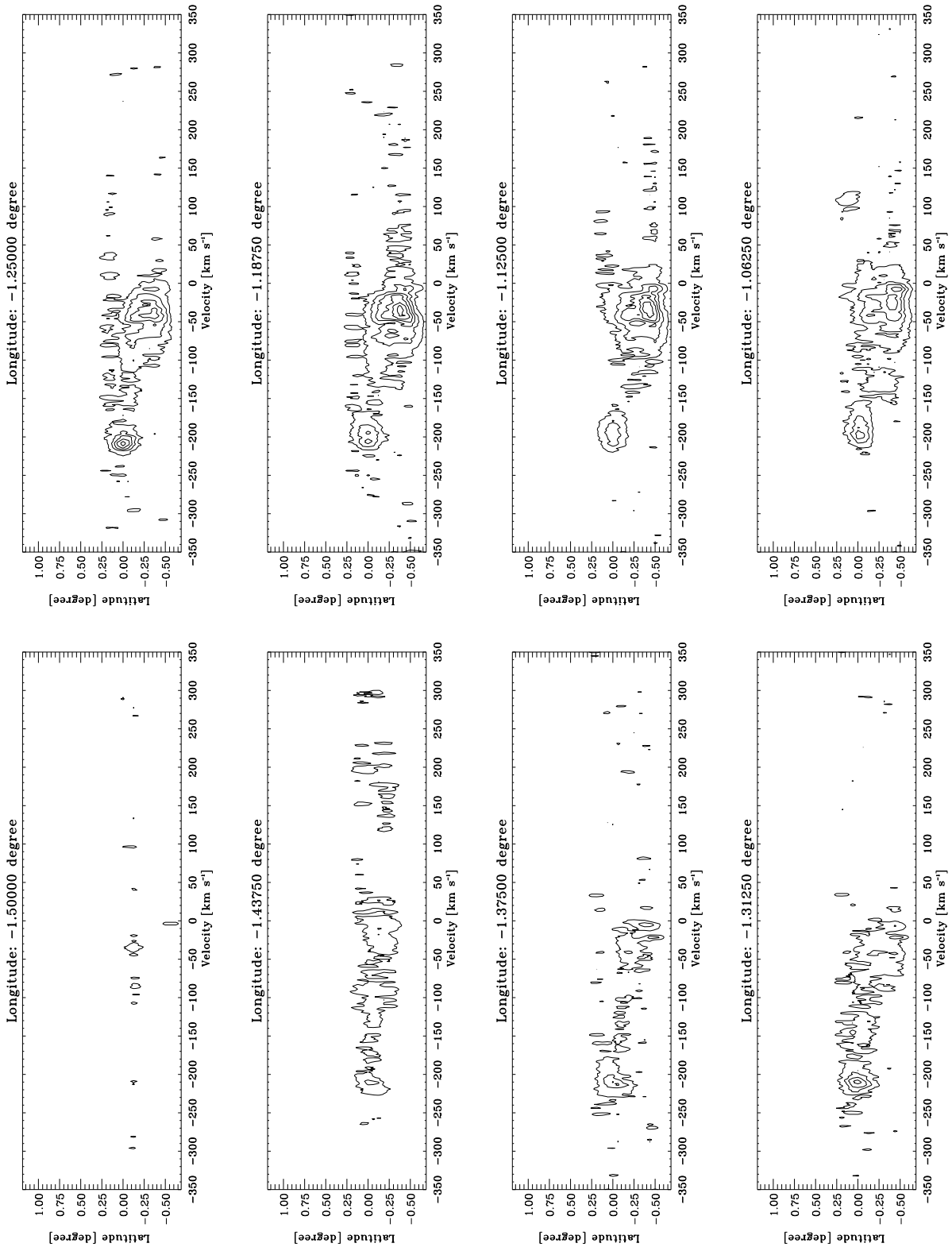

Fig. B3.5. continued.

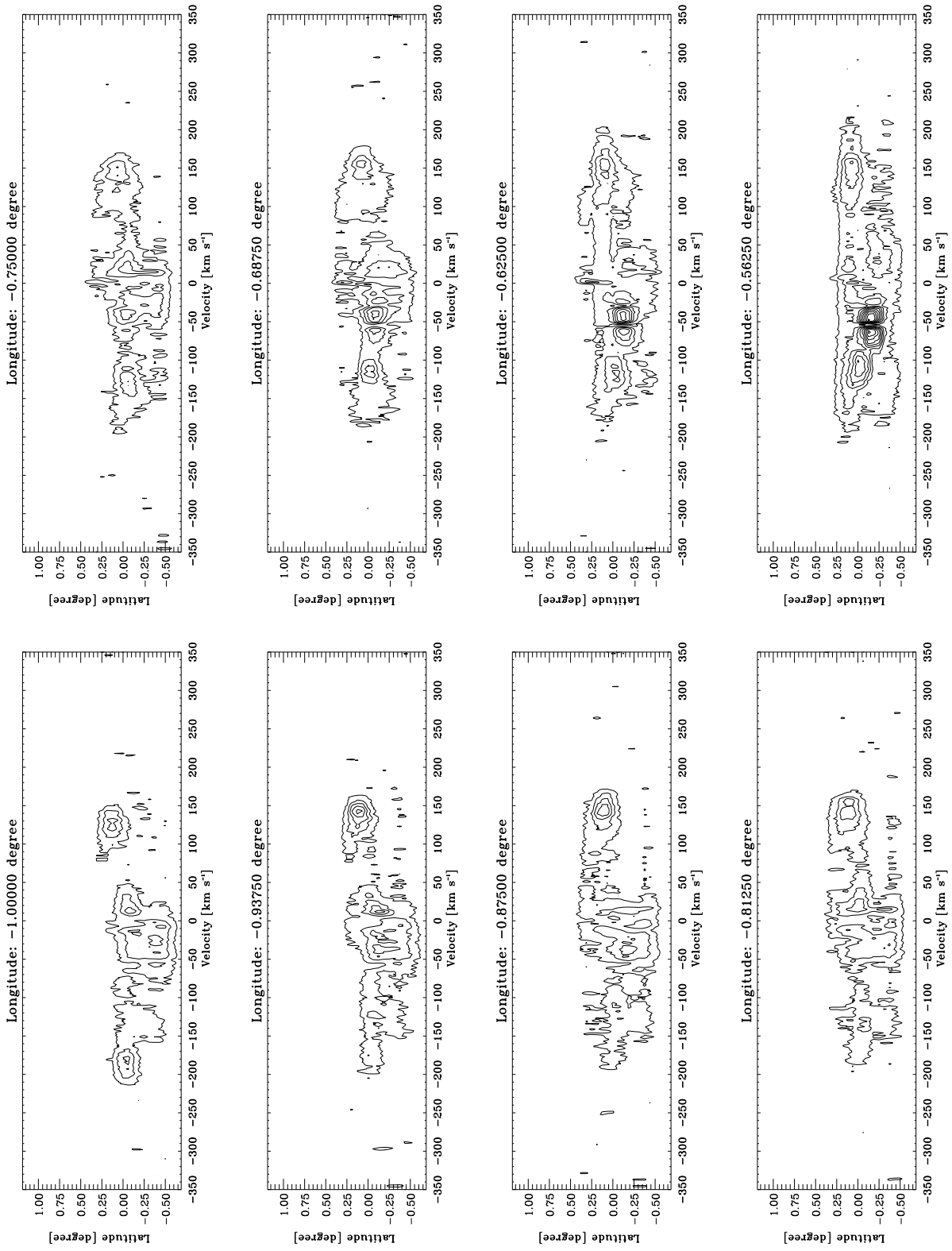

Fig. B3.6. continued.

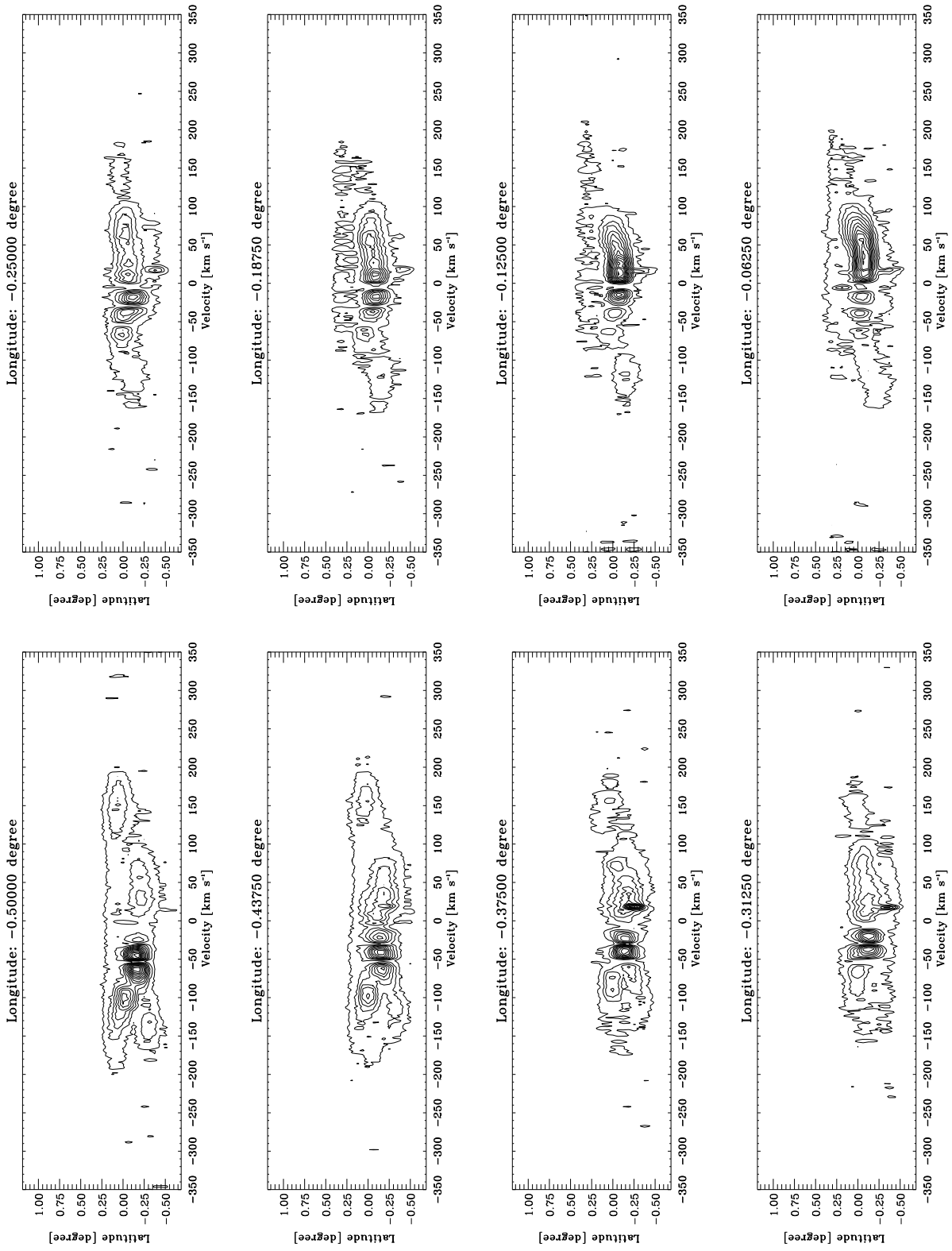

Fig. B3.7. continued.

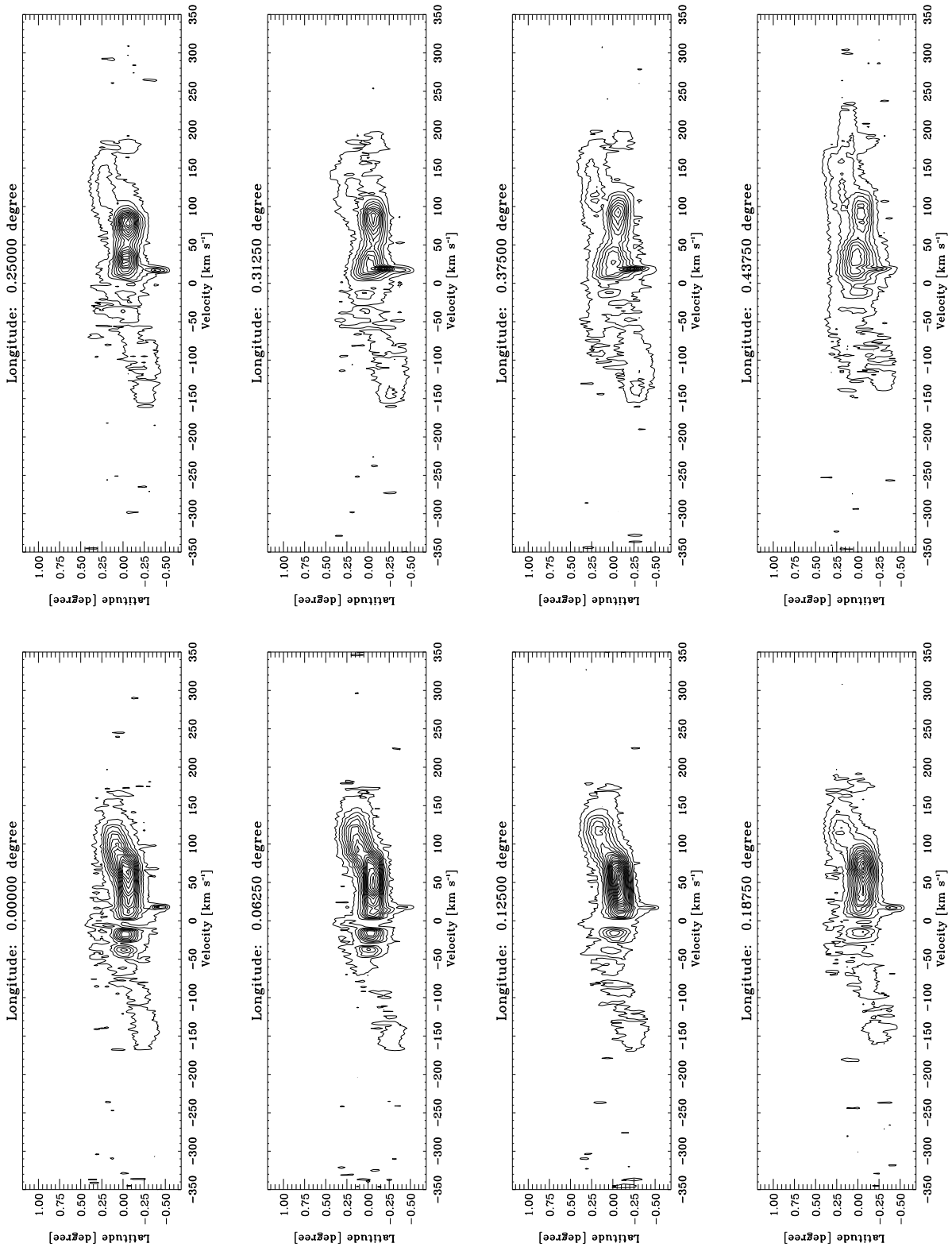

Fig. B3.8. continued.

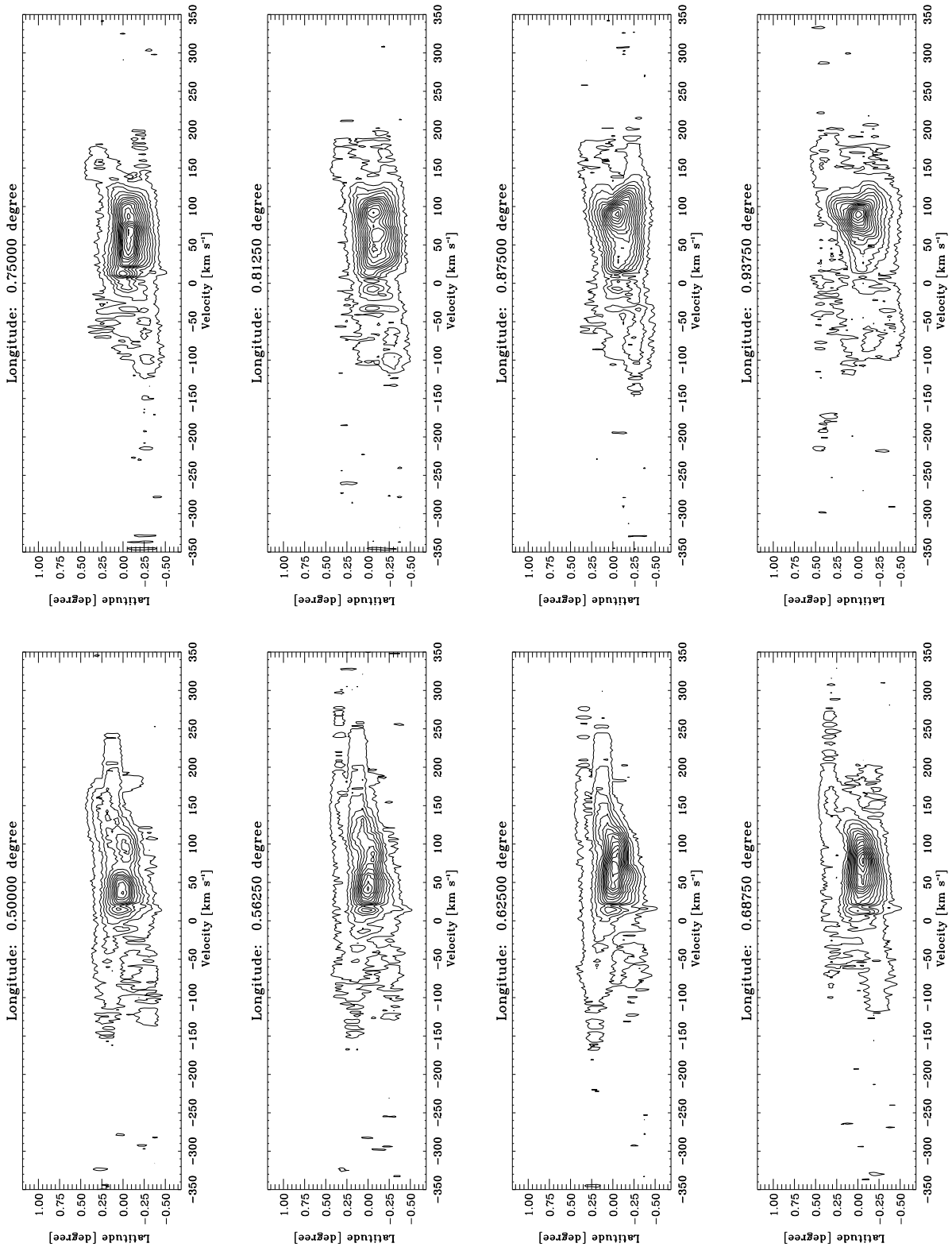

Fig. B3.9. continued.

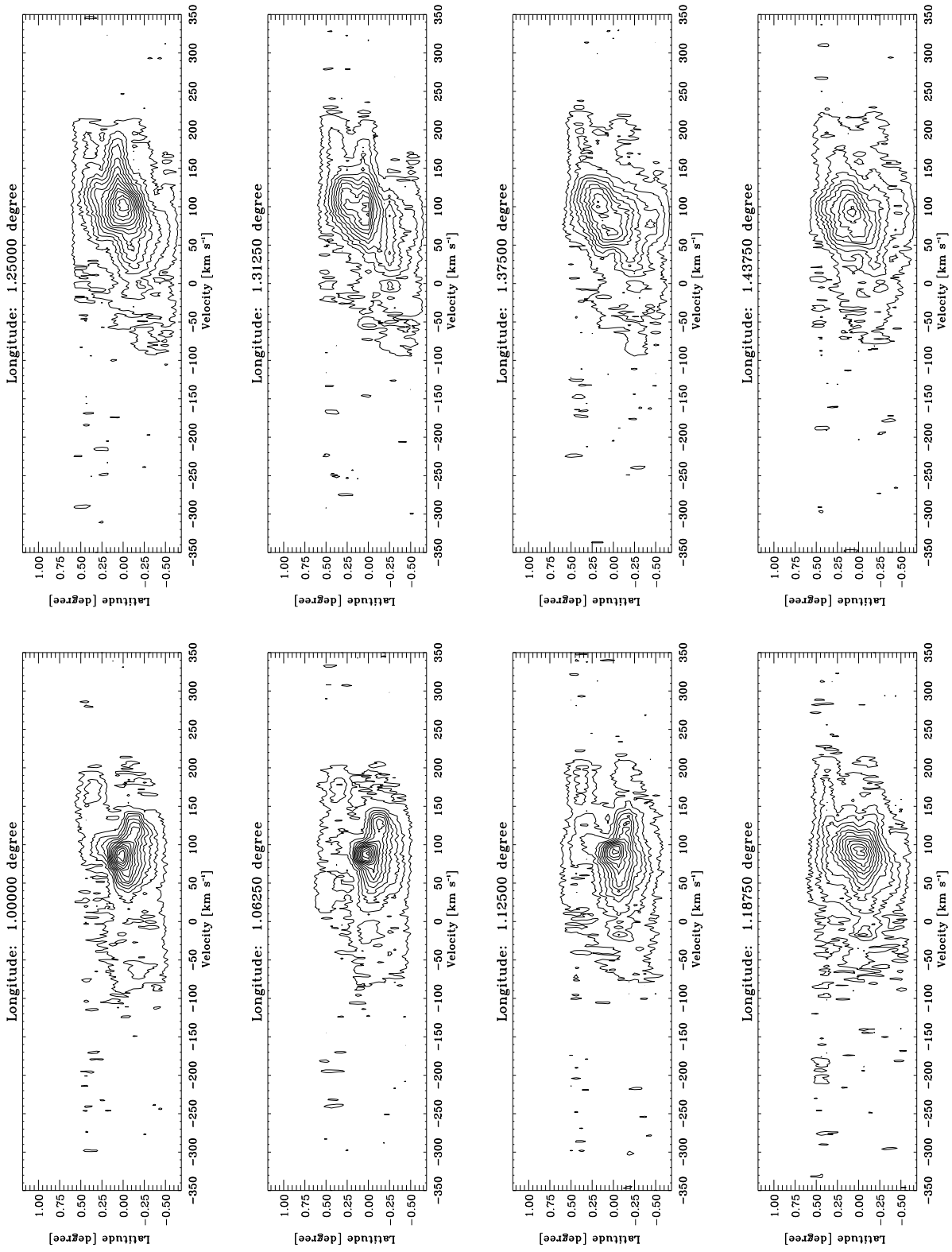

Fig. B3.10. continued.

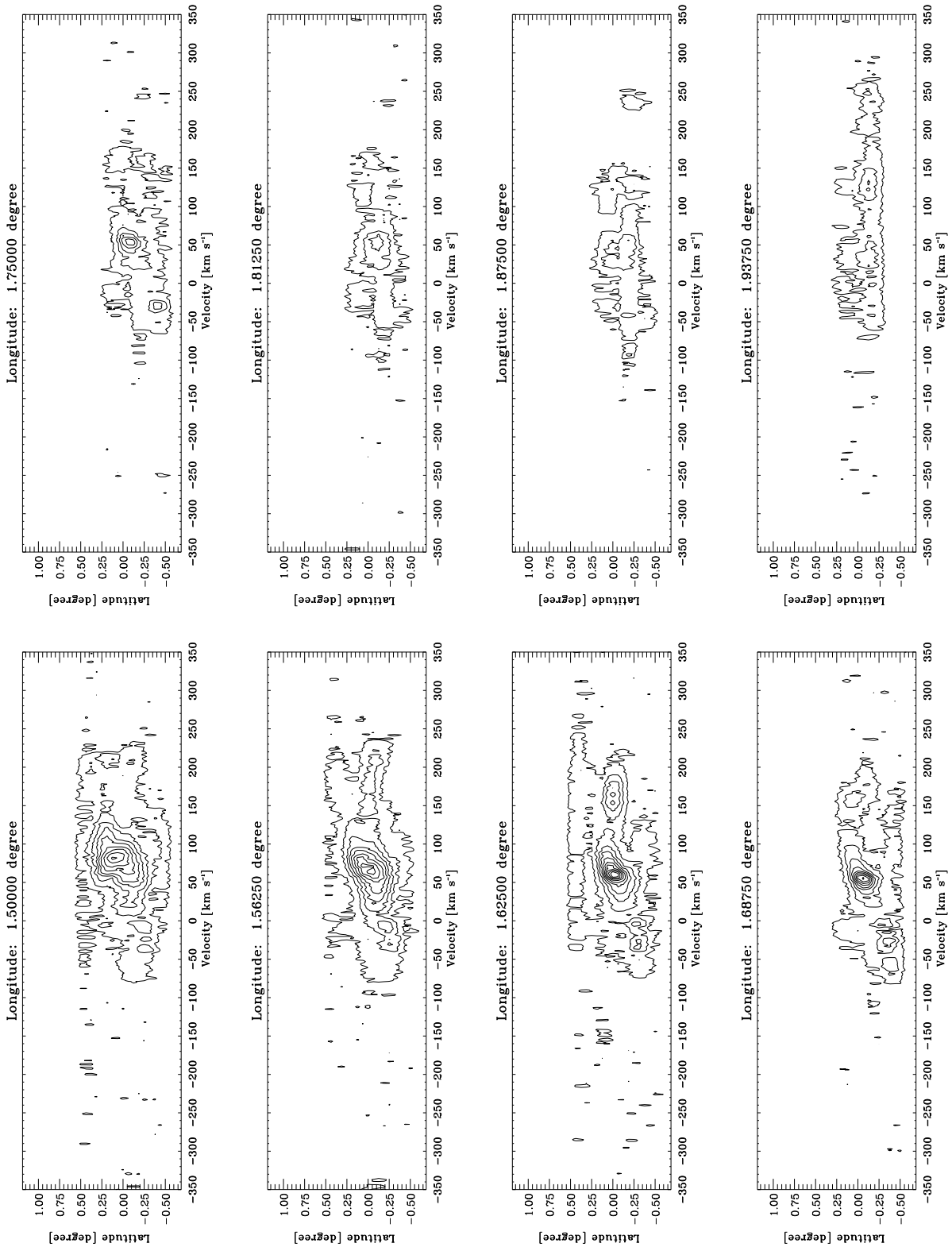

Fig. B3.11. continued.

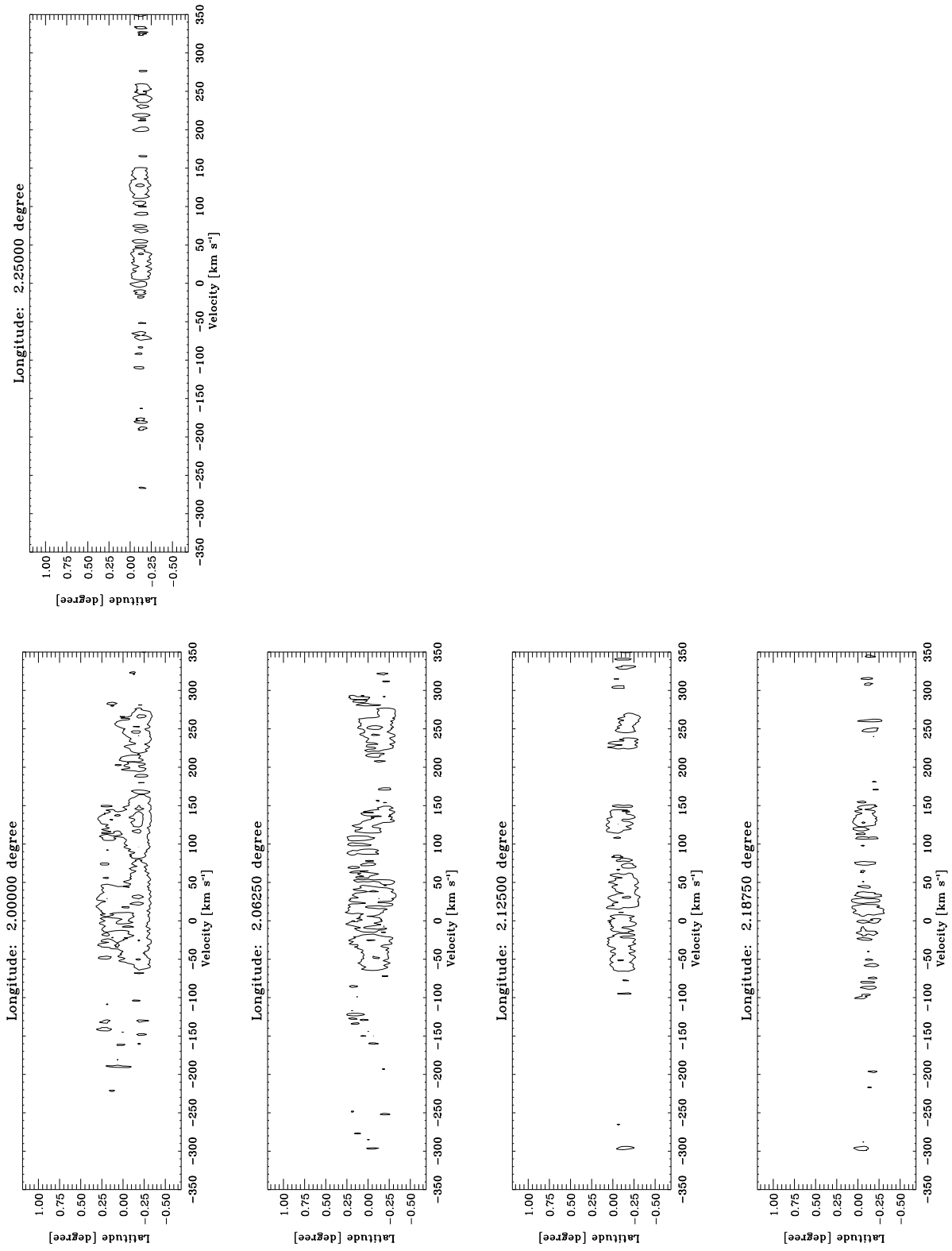

Fig. B3.12. continued.

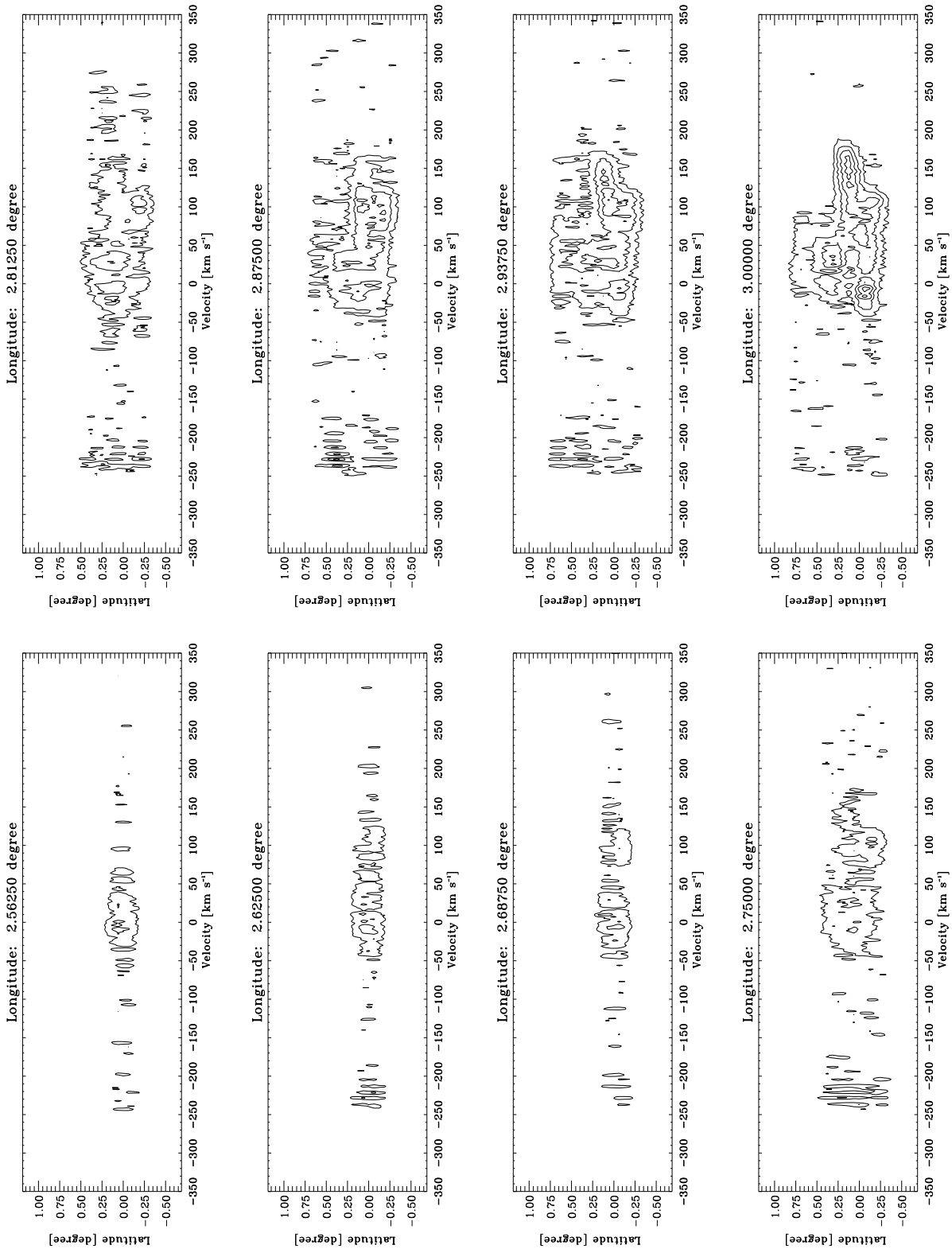

Fig. B3.13. continued.

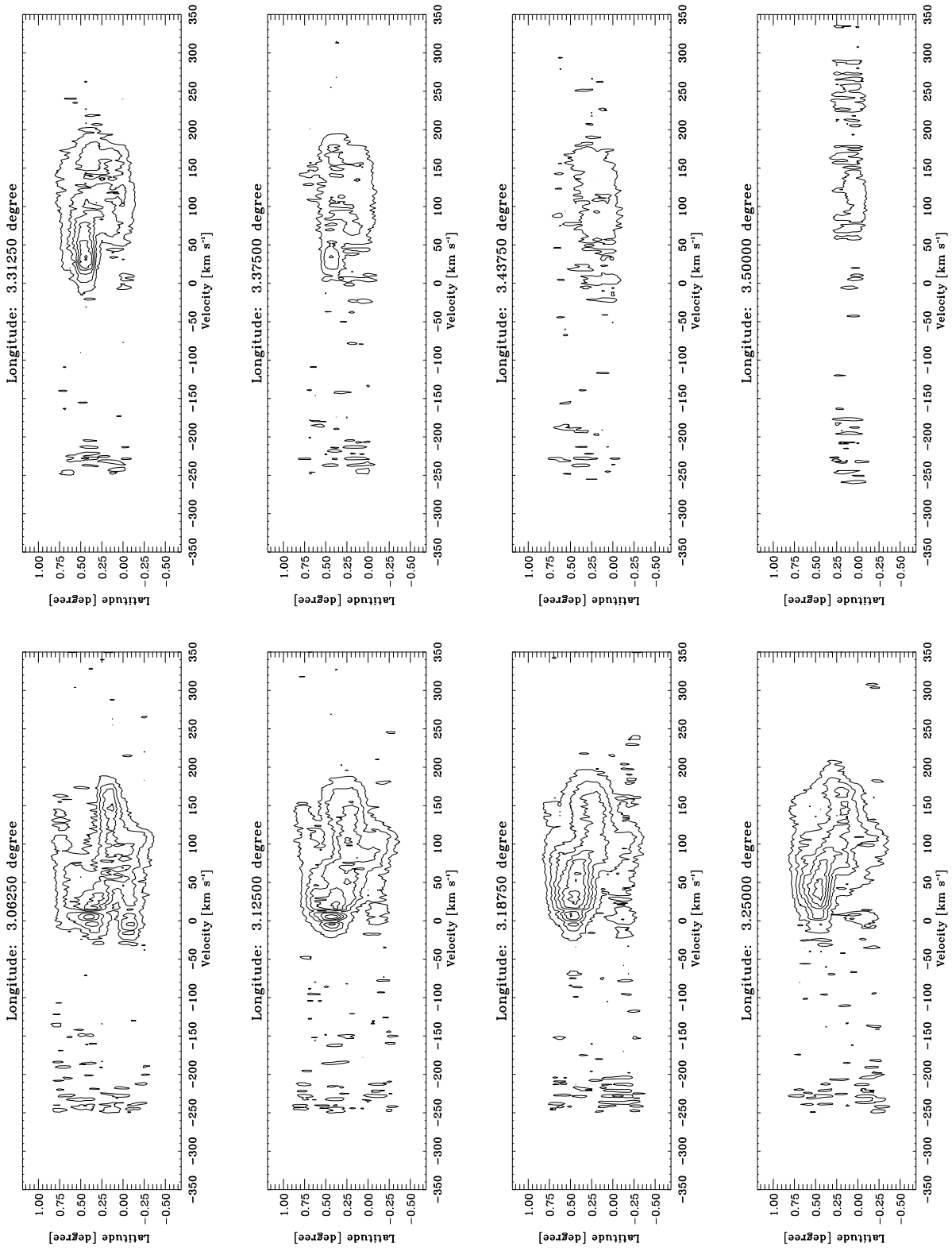

Fig. B3.14. continued.

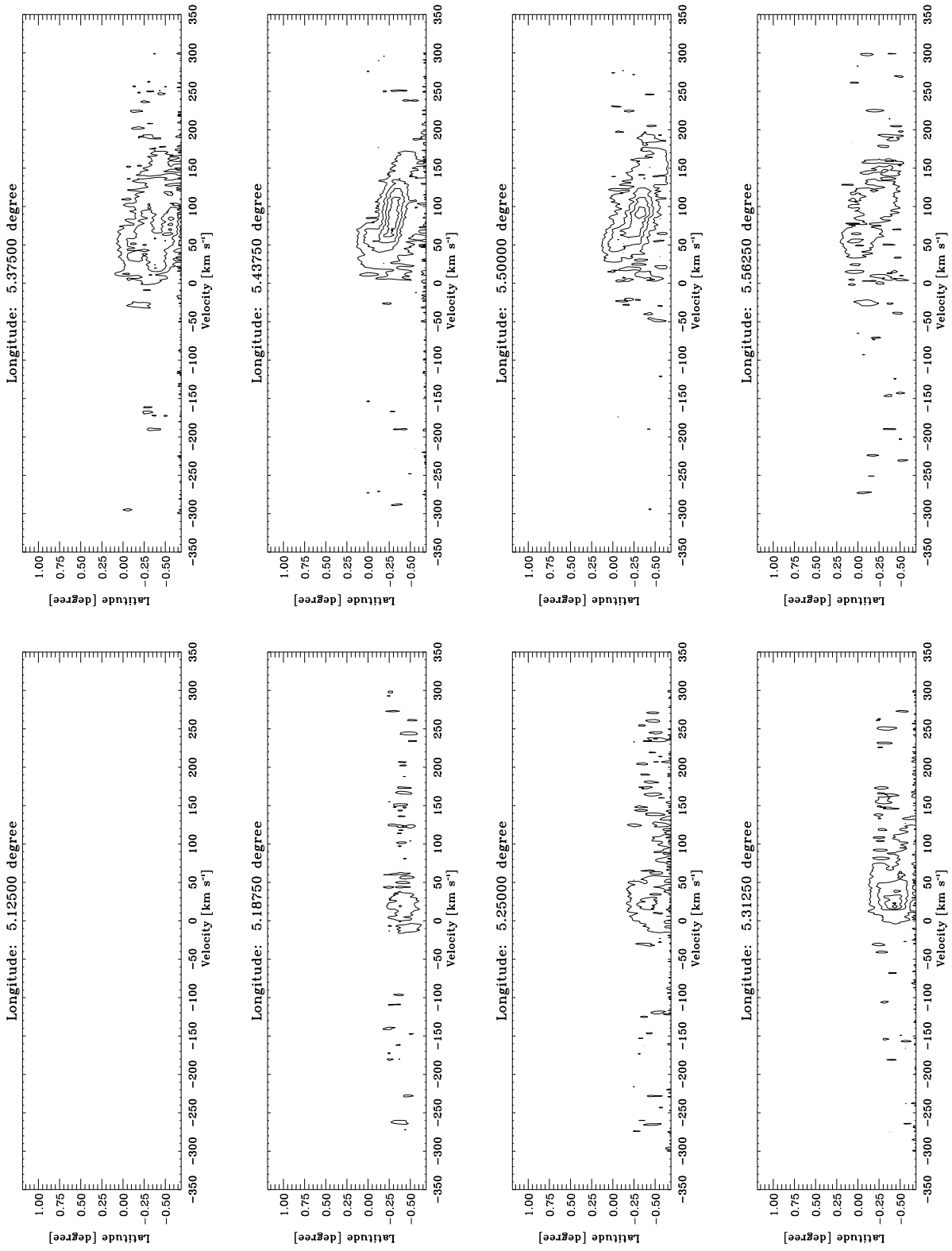

Fig. B3.15. continued.

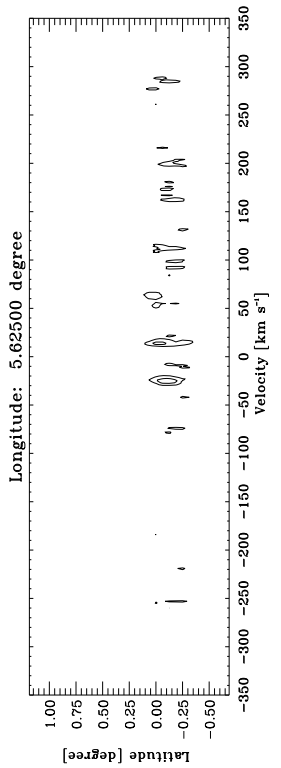

Fig. B3.16. continued.

Appendix C: SiO Galactic center survey

In this section we present the channel maps of the SiO emission in the Galactic center region integrated in velocity over 10 km s^{-1} wide channels. The contour levels start at 0.2 K km s^{-1} (3σ) and increase in steps of 0.66 K km s^{-1} (10σ). The dotted contour is at 0.13 K km s^{-1} (2σ).

Figure C.2 shows $l-v$ diagrams integrated in latitude in steps of $0\overset{\circ}{.}0625$ in SiO. The contours levels start at 0.0013 K (3σ) and increase them in steps of 0.0018 K (4σ).

Figure C.3 is a set of latitude-velocity diagrams integrated in steps of $0\overset{\circ}{.}0625$. The contours levels start at 0.0013 K (3σ) and increase them in step of 0.0026 K (6σ).

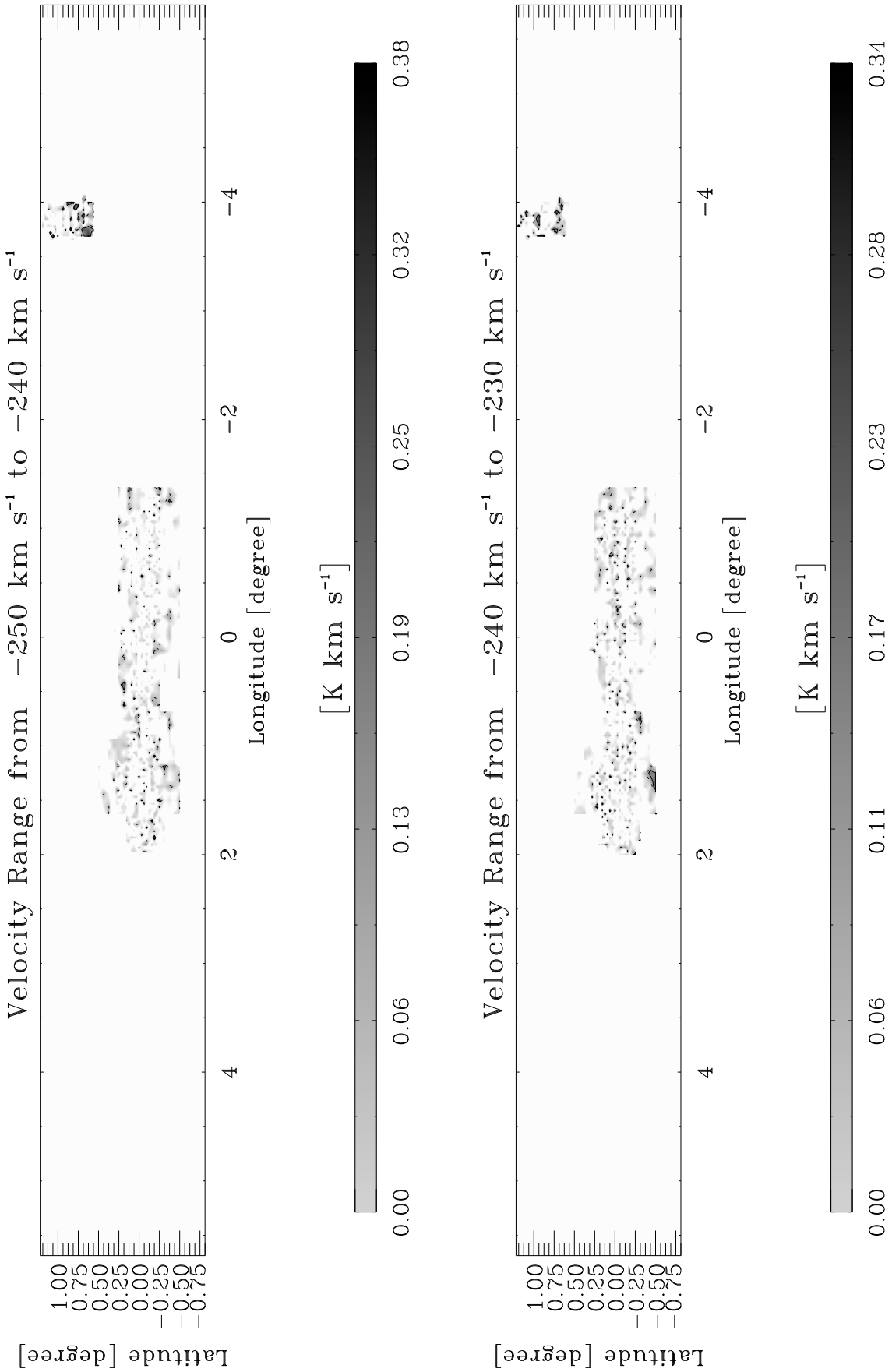

Fig. C1.1. The integrated intensity of the Galactic center region in SiO (1−0) in velocity intervals of 10 km s^{-1} width. The solid contour levels start at 0.2 K, which is the 3σ-level, and increase in steps of 0.66 K km s^{-1} (10σ). The dotted contour is at 0.13 K km s^{-1} (2σ).

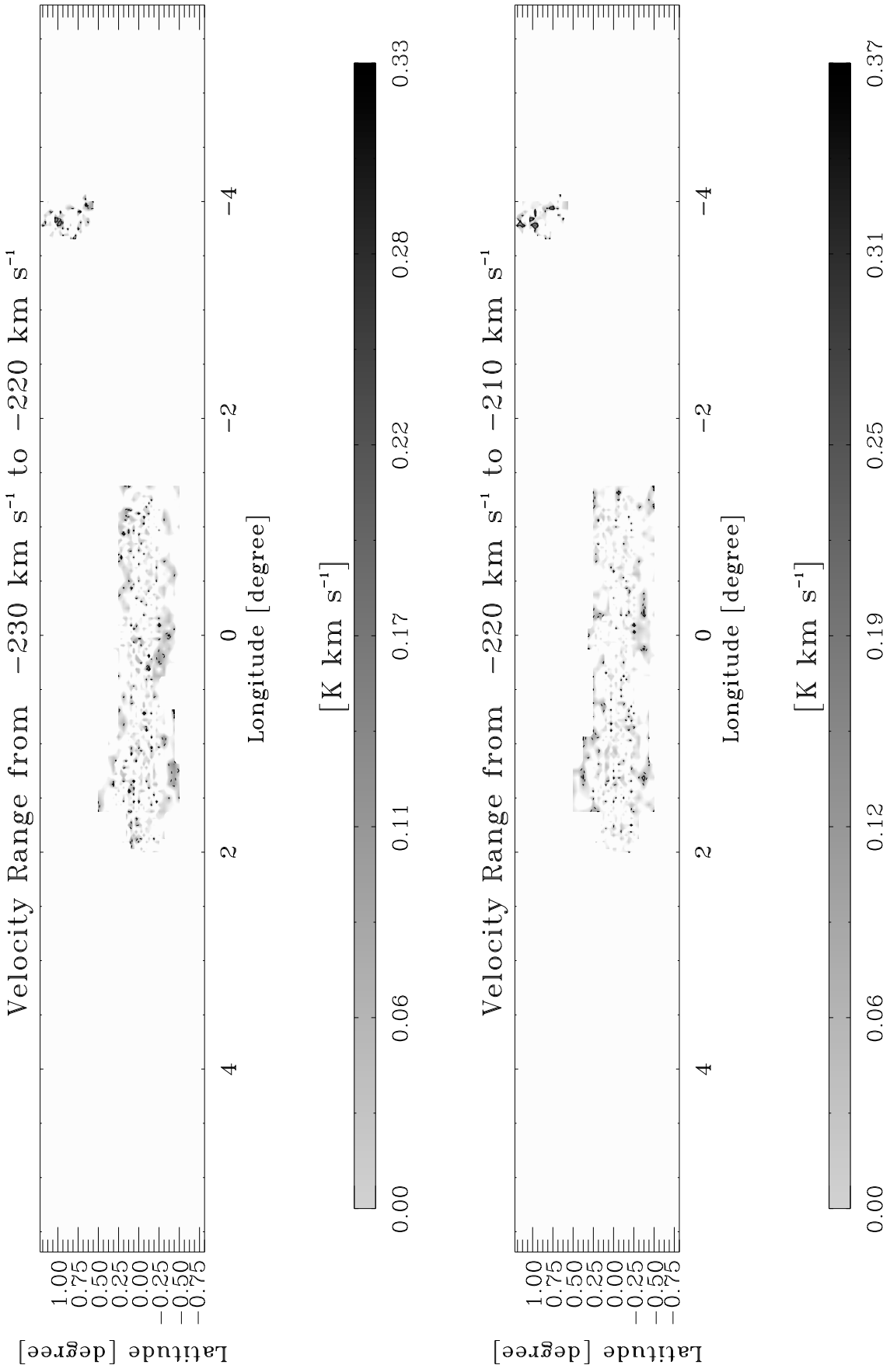

Fig. C1.2. continued.

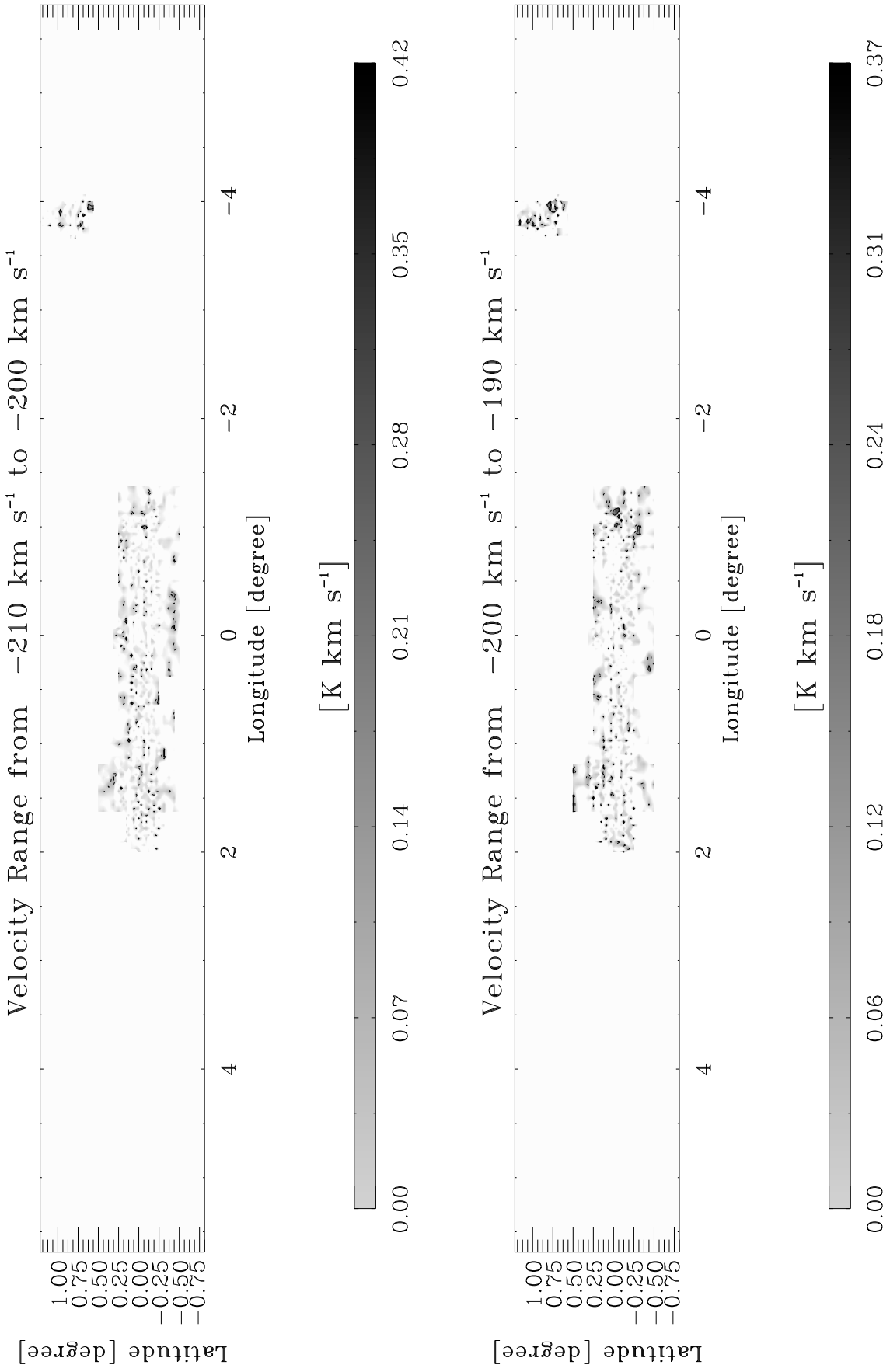

Fig. C1.3. continued.

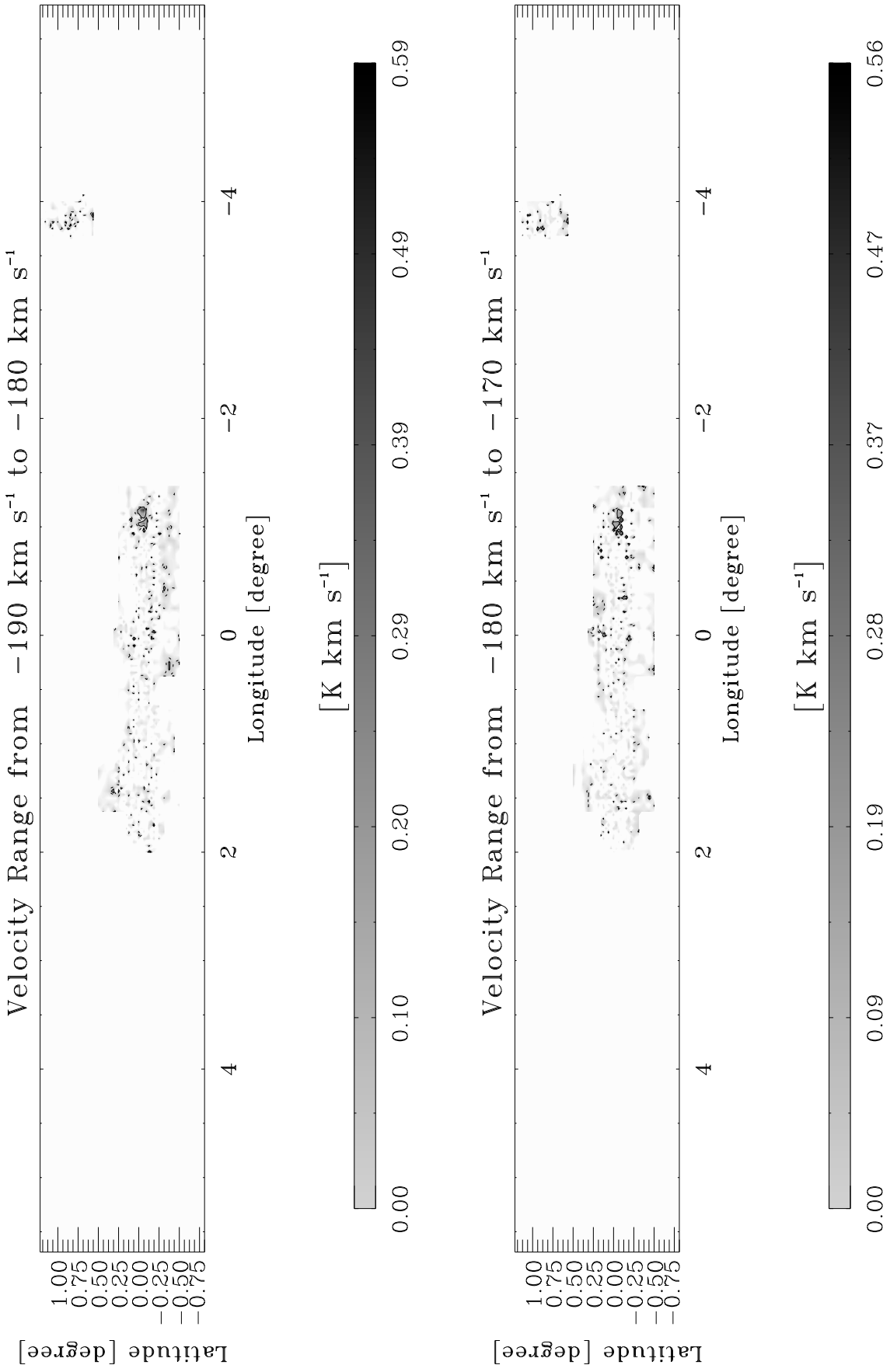

Fig. C1.4. continued.

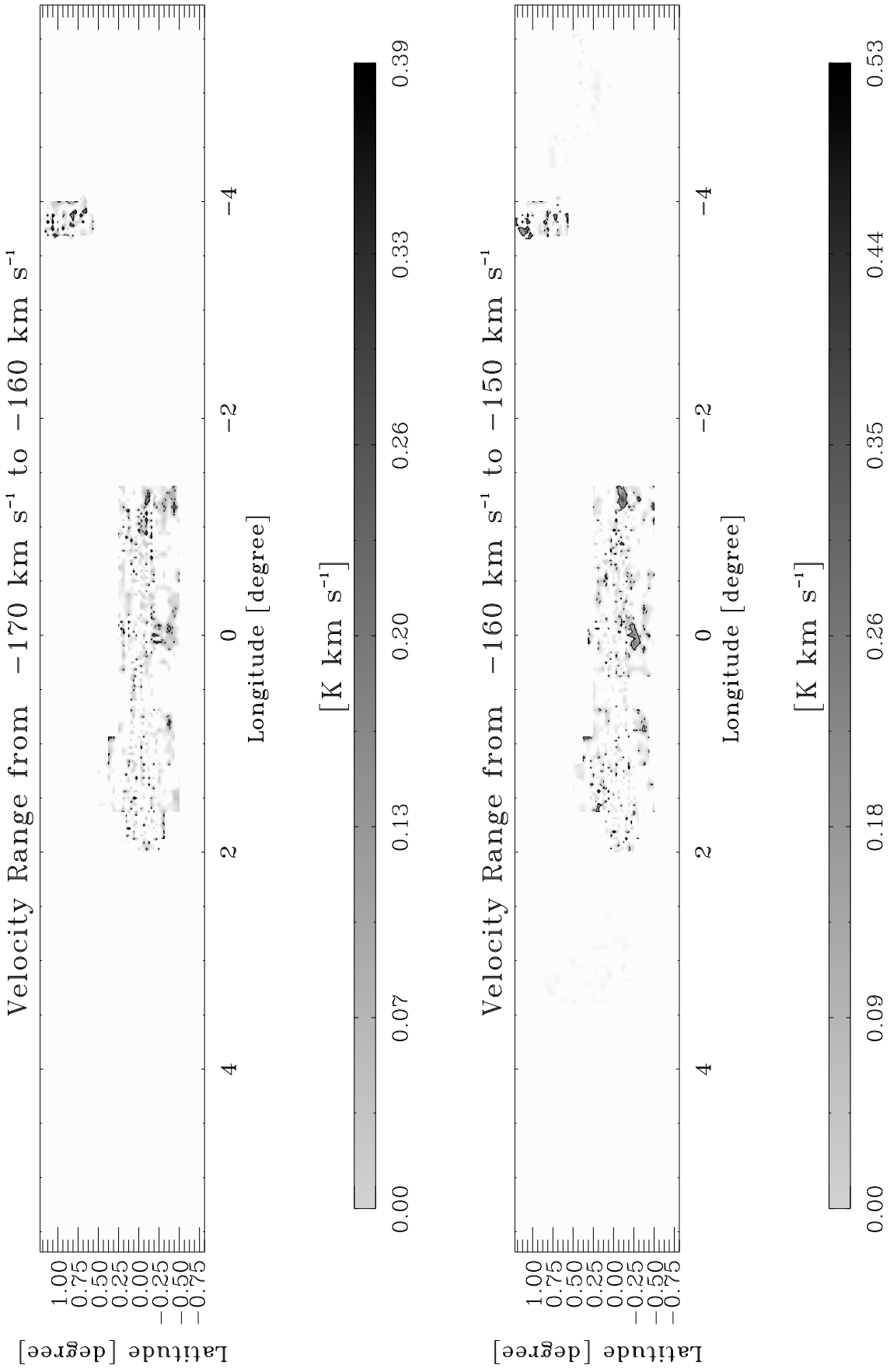

Fig. C1.5. continued.

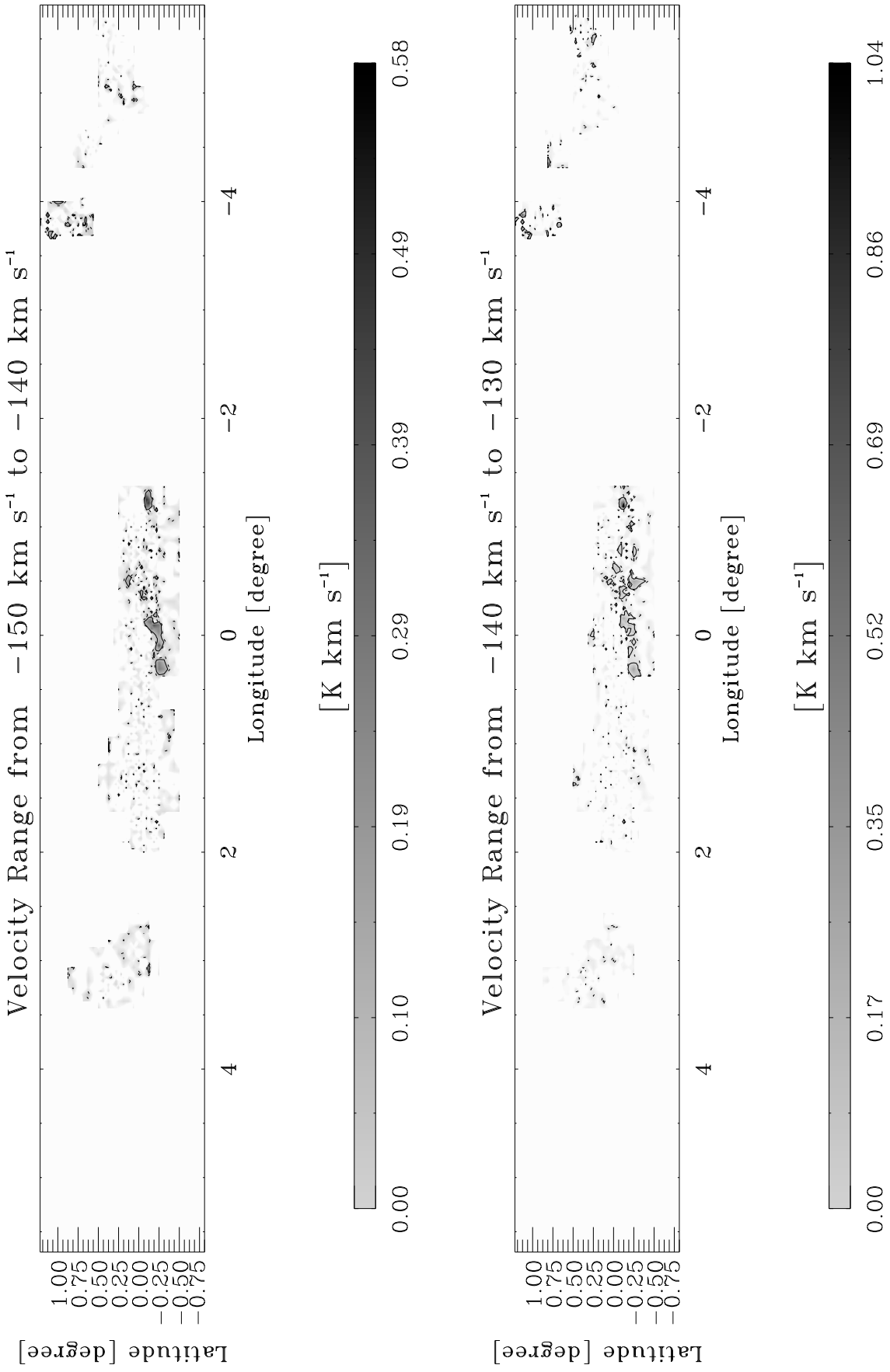

Fig. C1.6. continued.

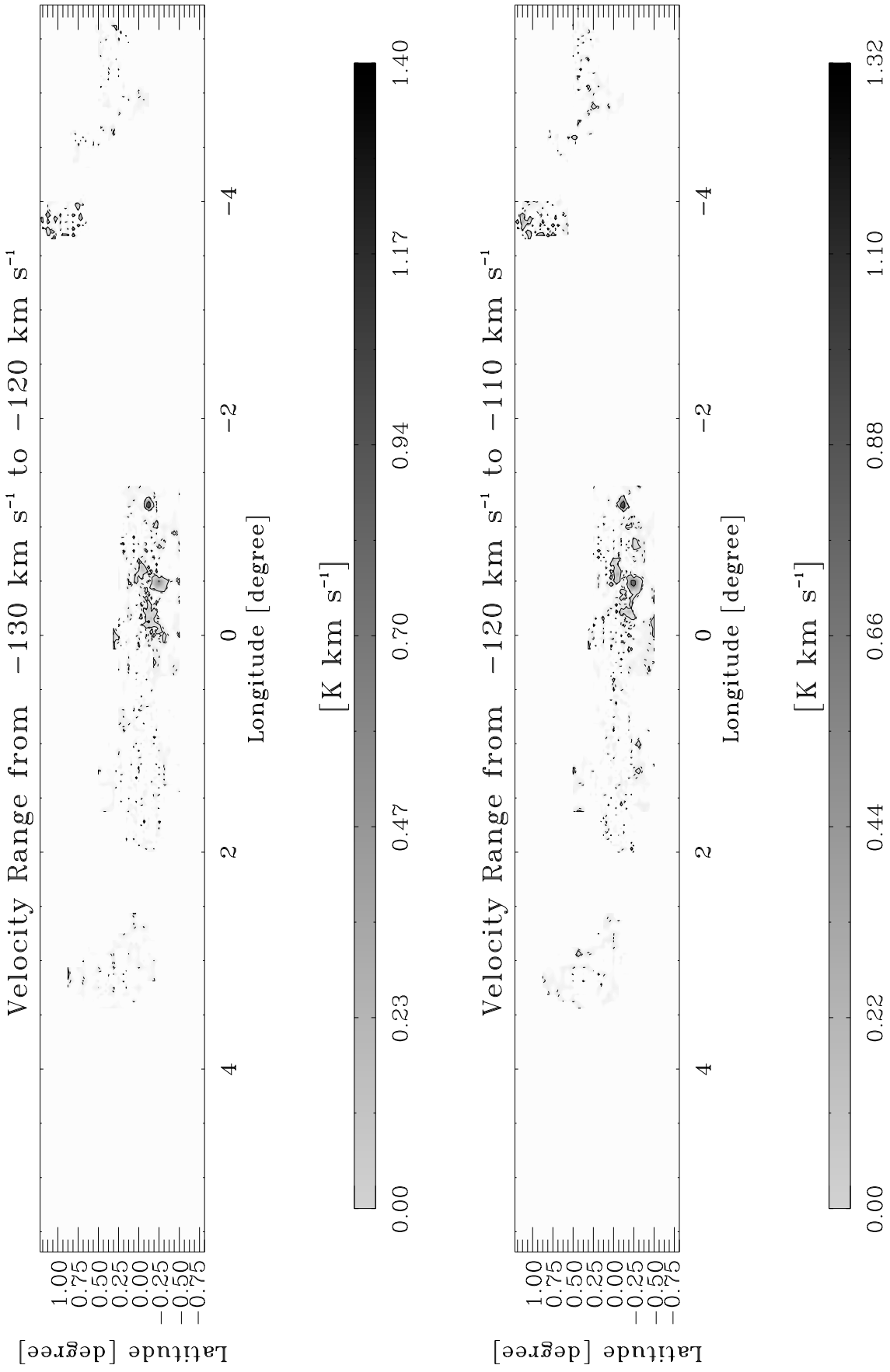

Fig. C1.7. continued.

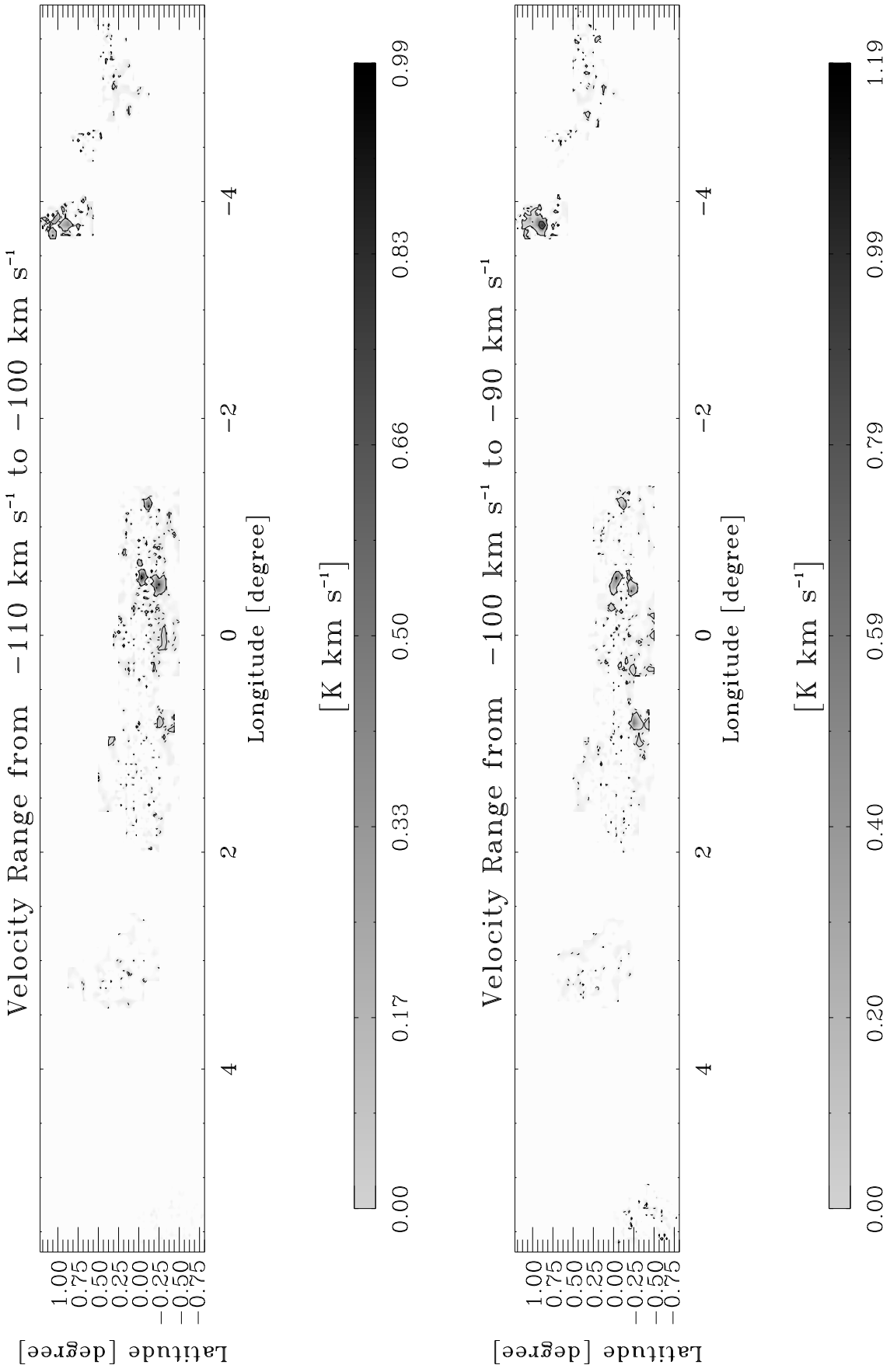

Fig. C1.8. continued.

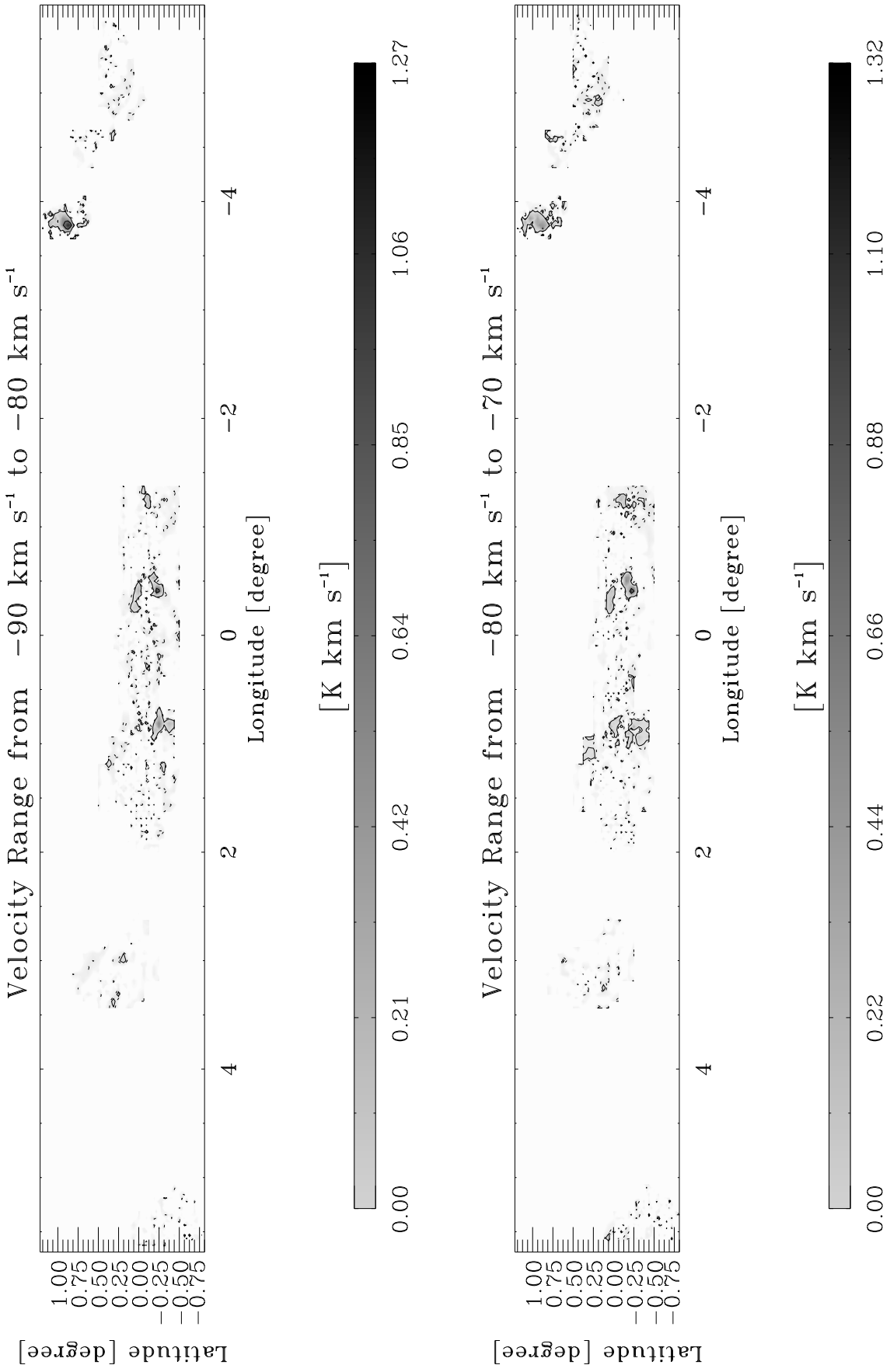

Fig. C1.9. continued.

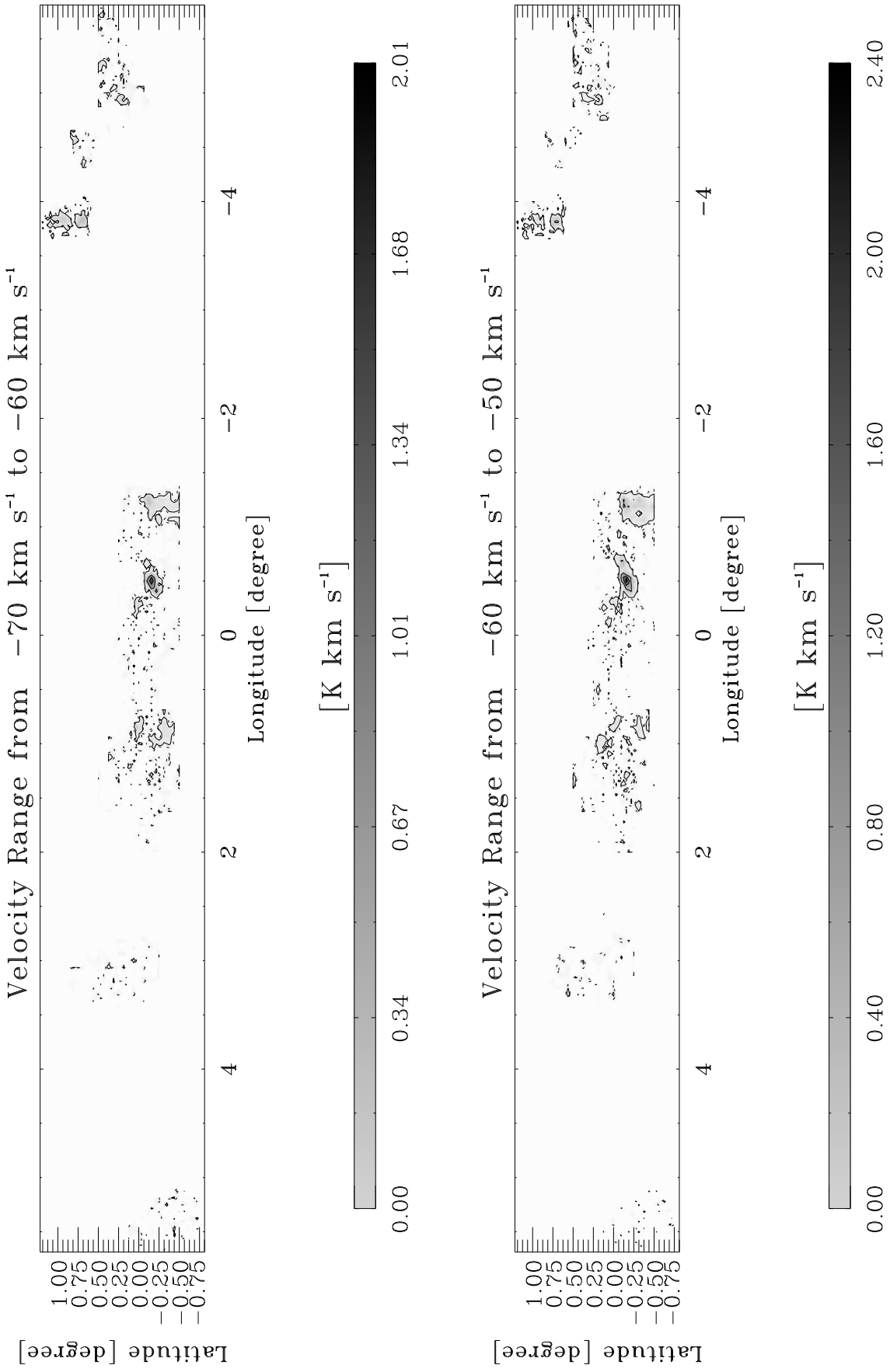

Fig. C1.10. continued.

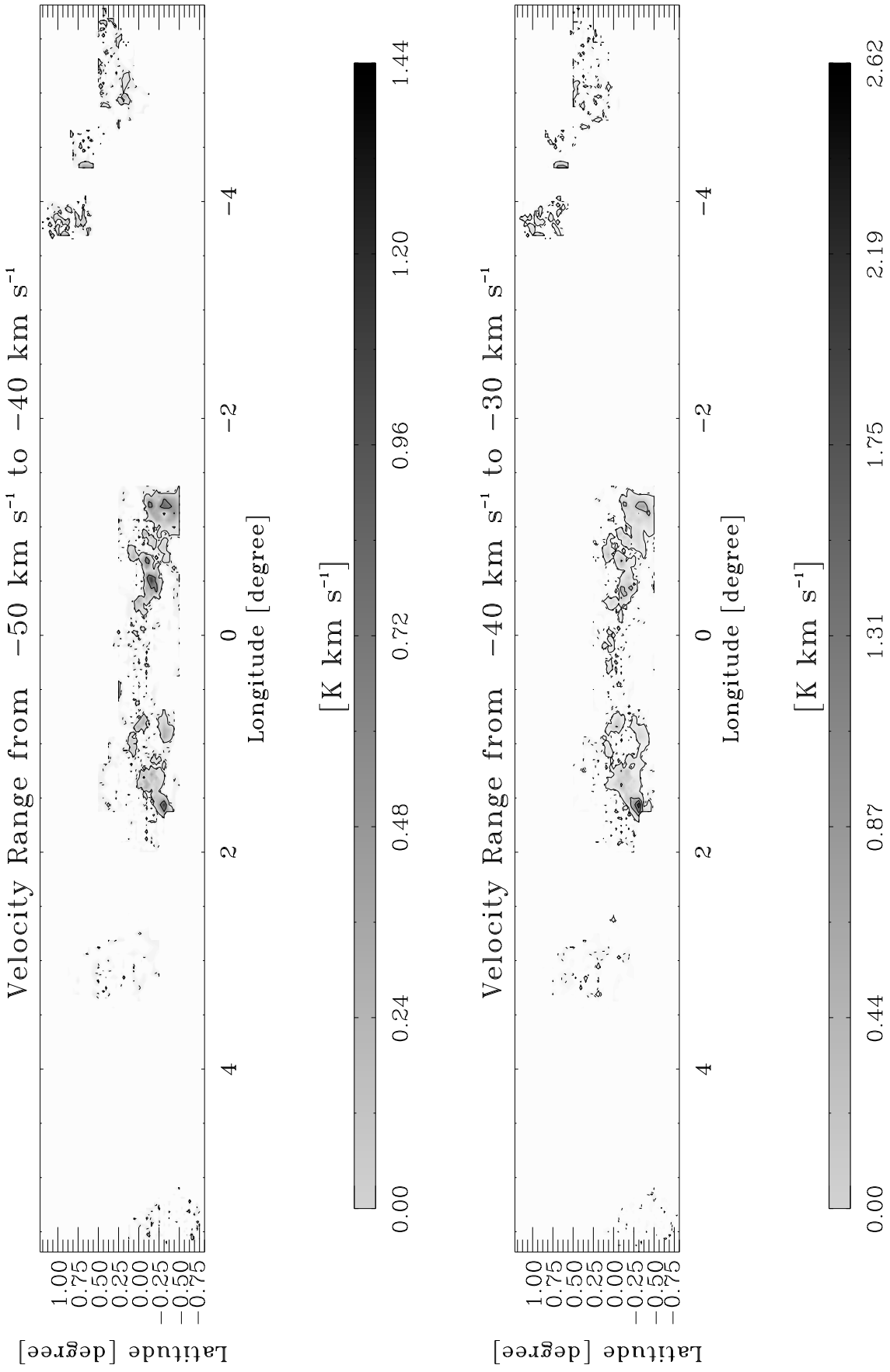

Fig. C1.11. continued.

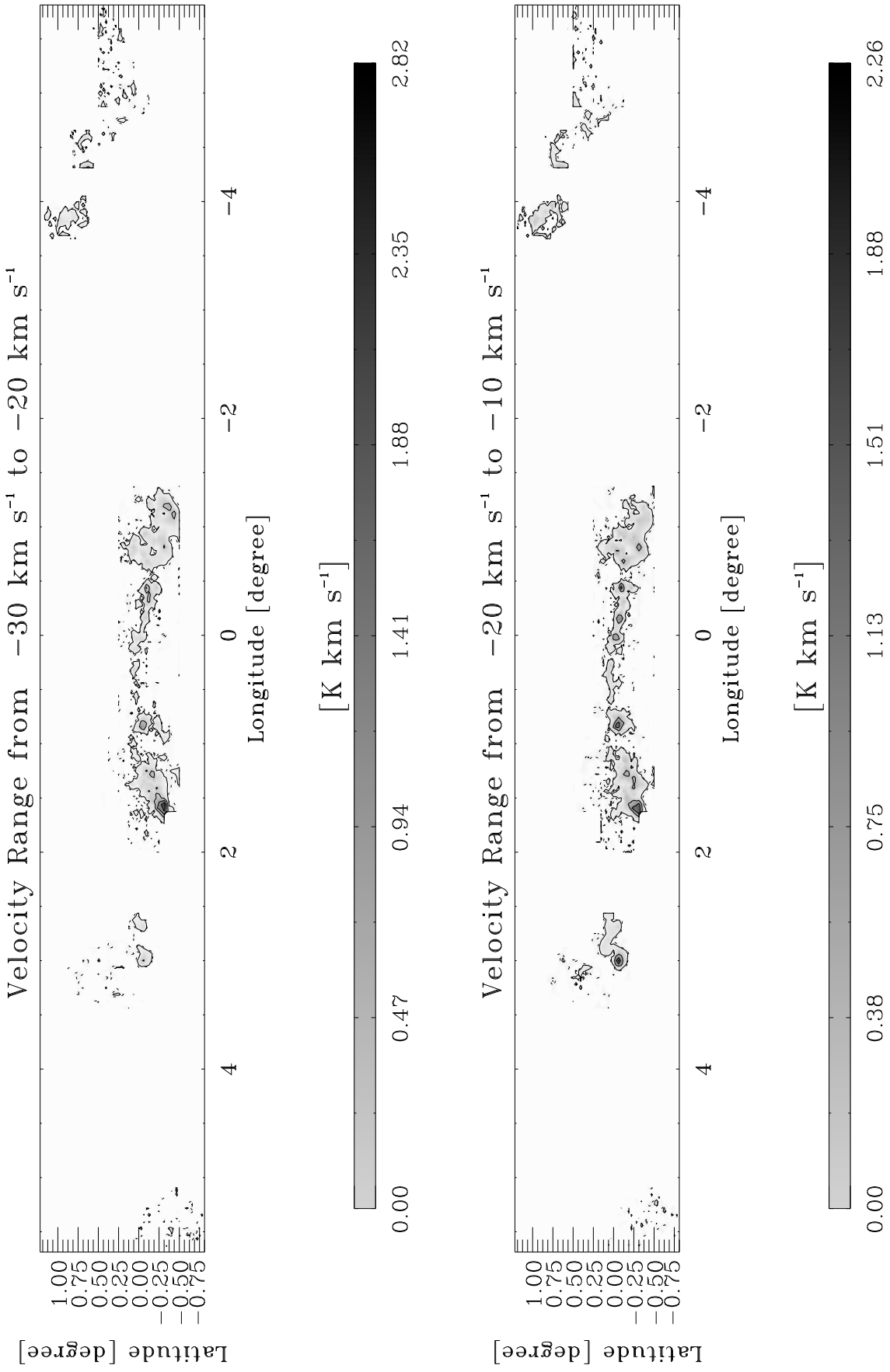

Fig. C1.12. continued.

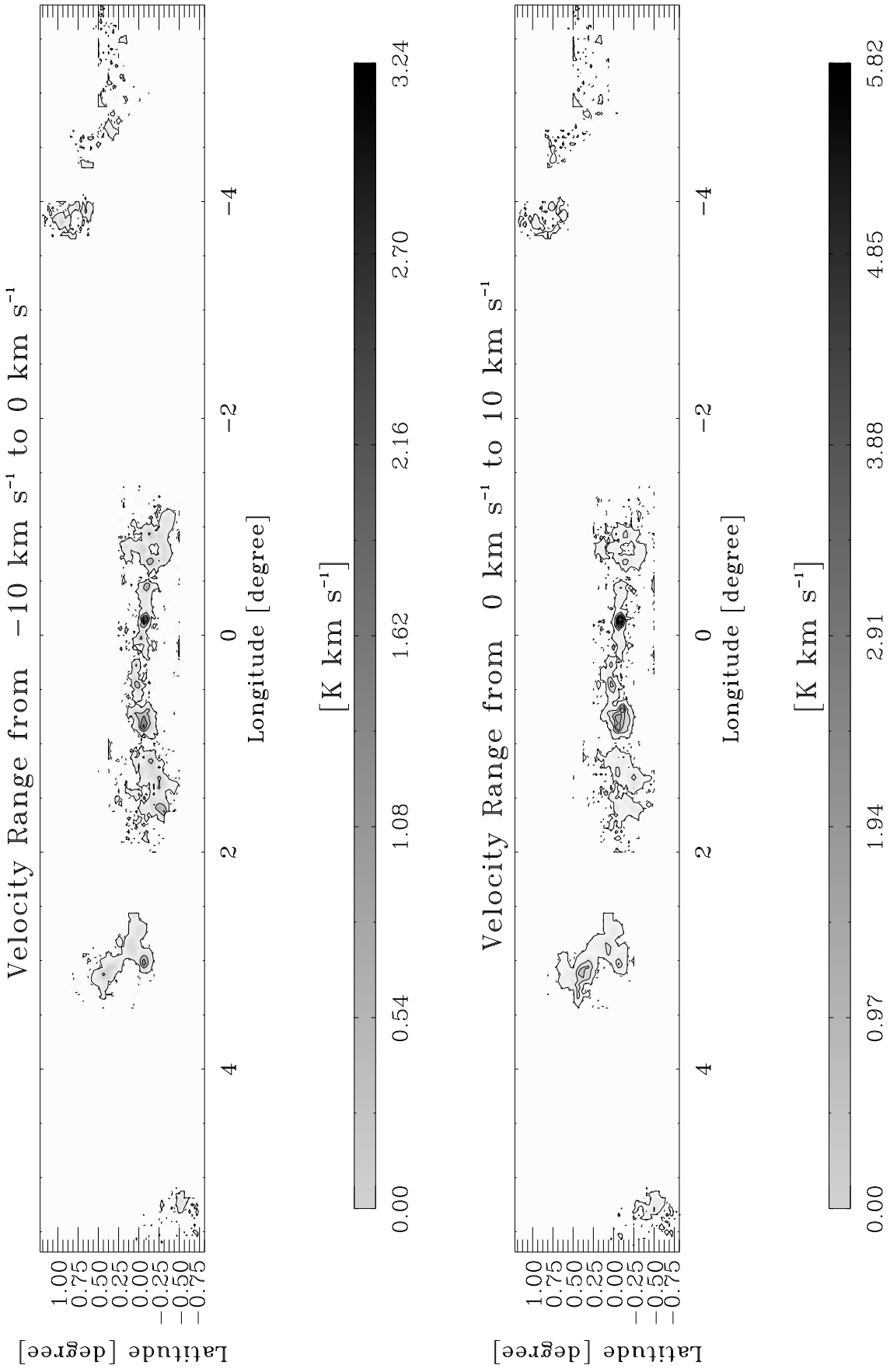

Fig. C1.13. continued.

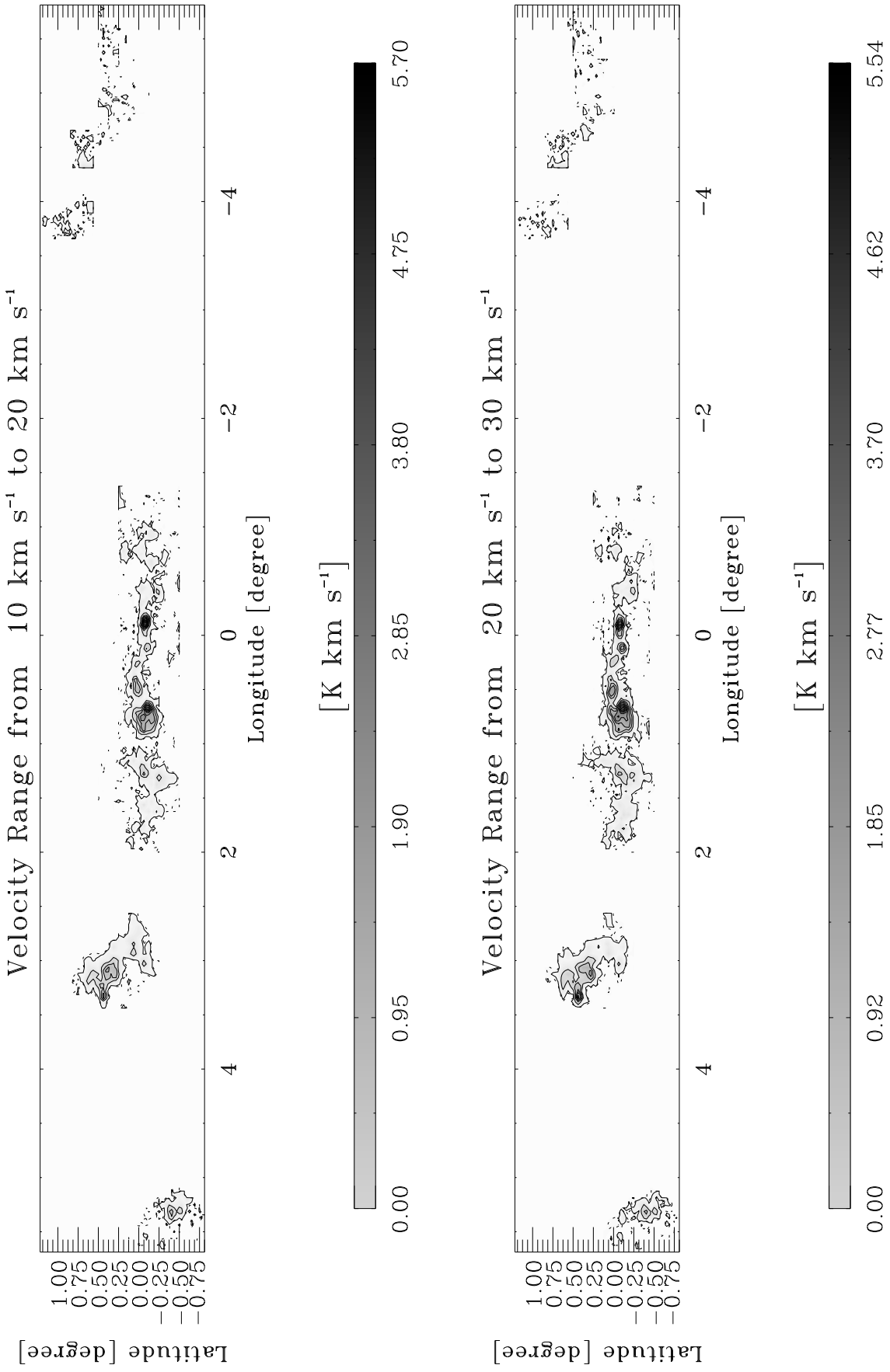

Fig. C1.14. continued.

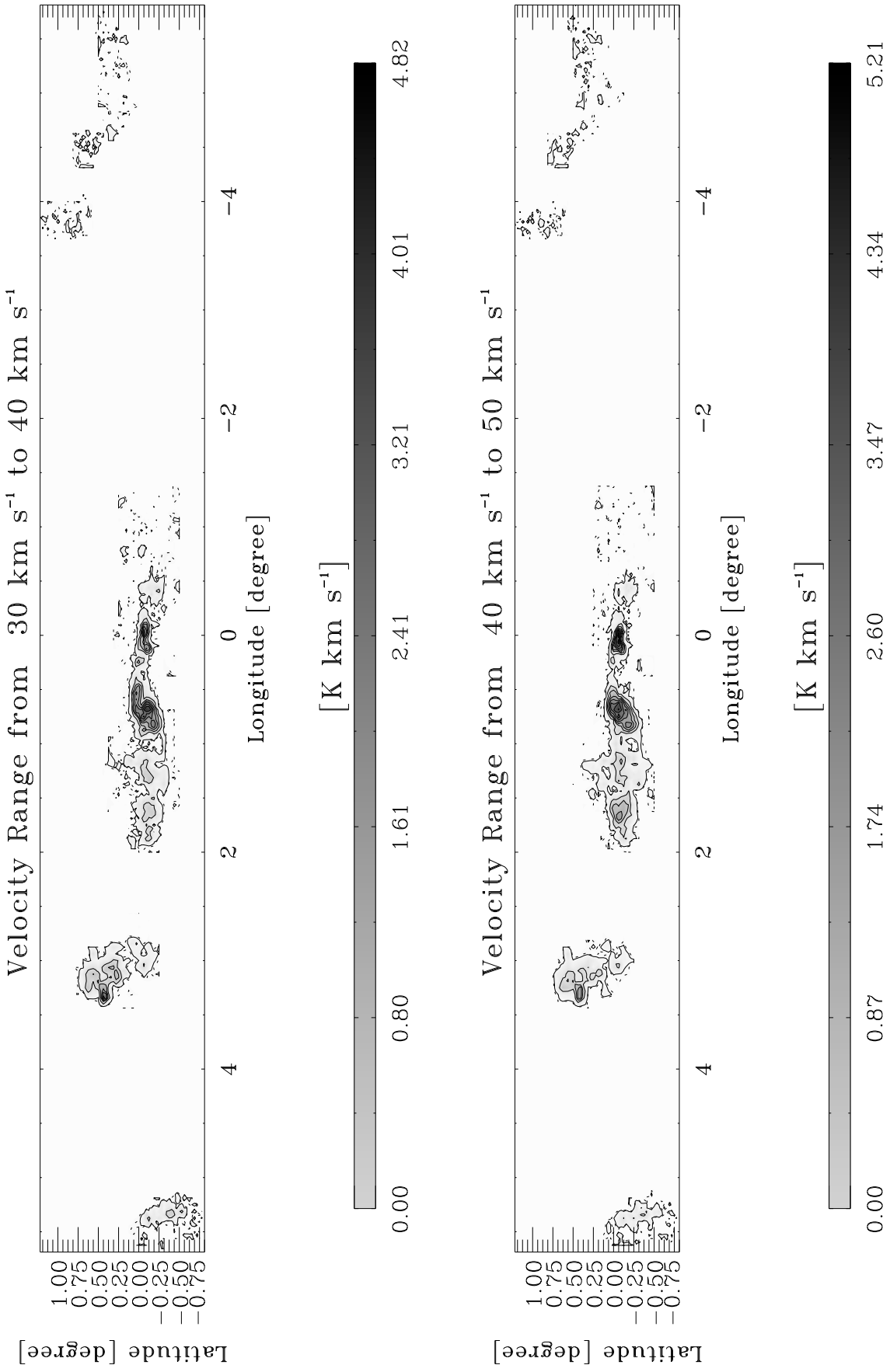

Fig. C1.15. continued.

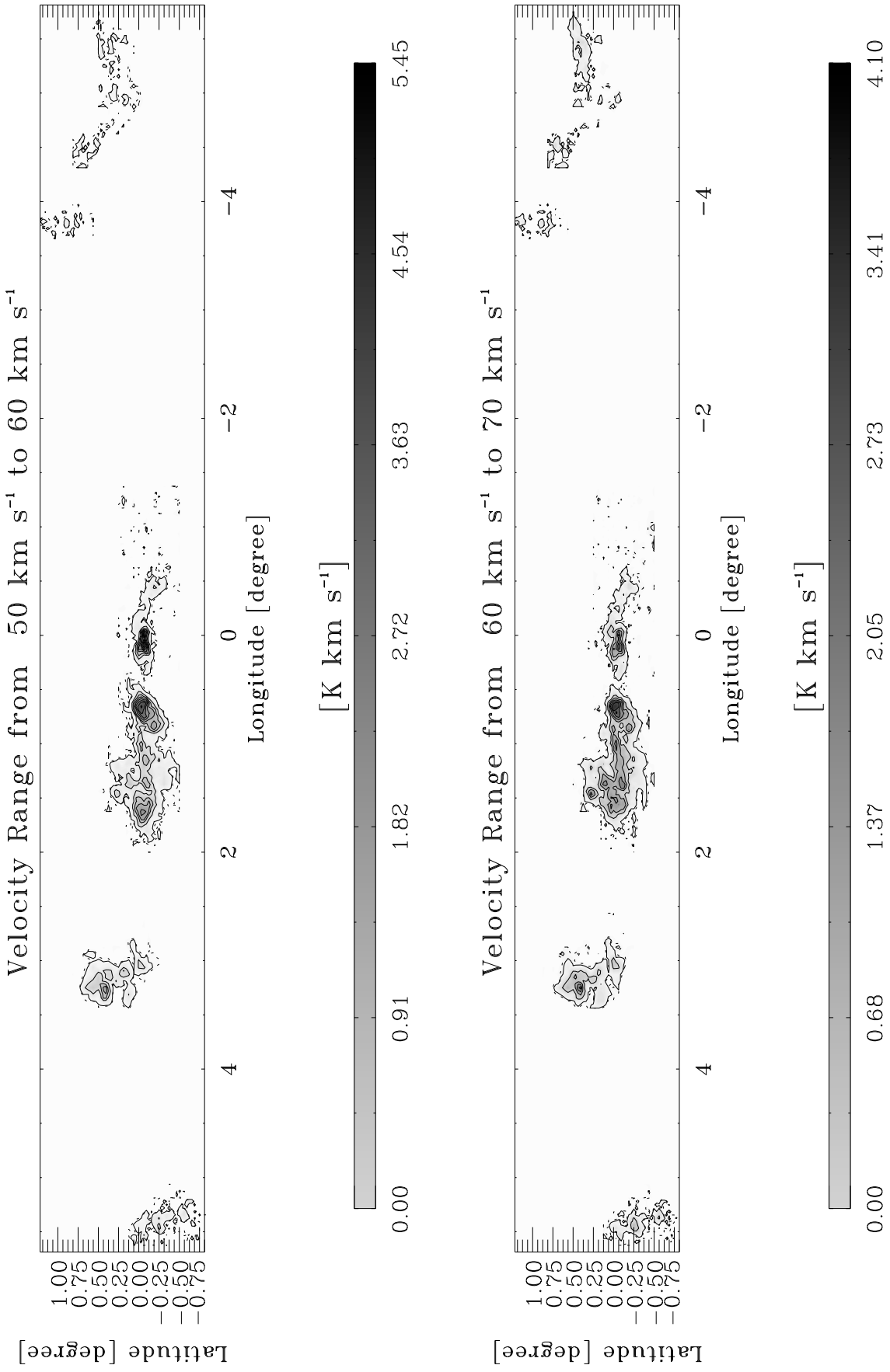

Fig. C1.16. continued.

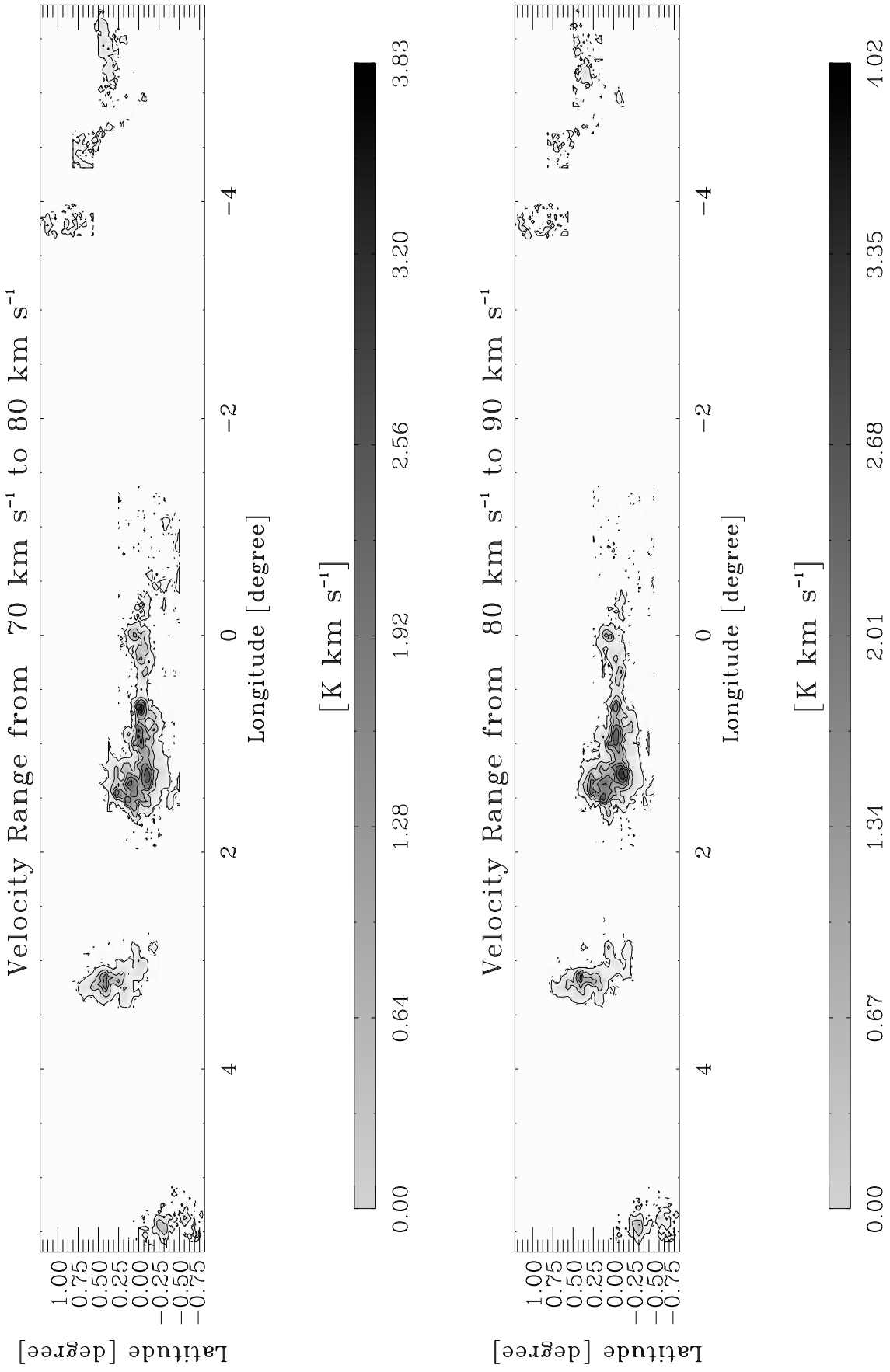

Fig. C1.17. continued.

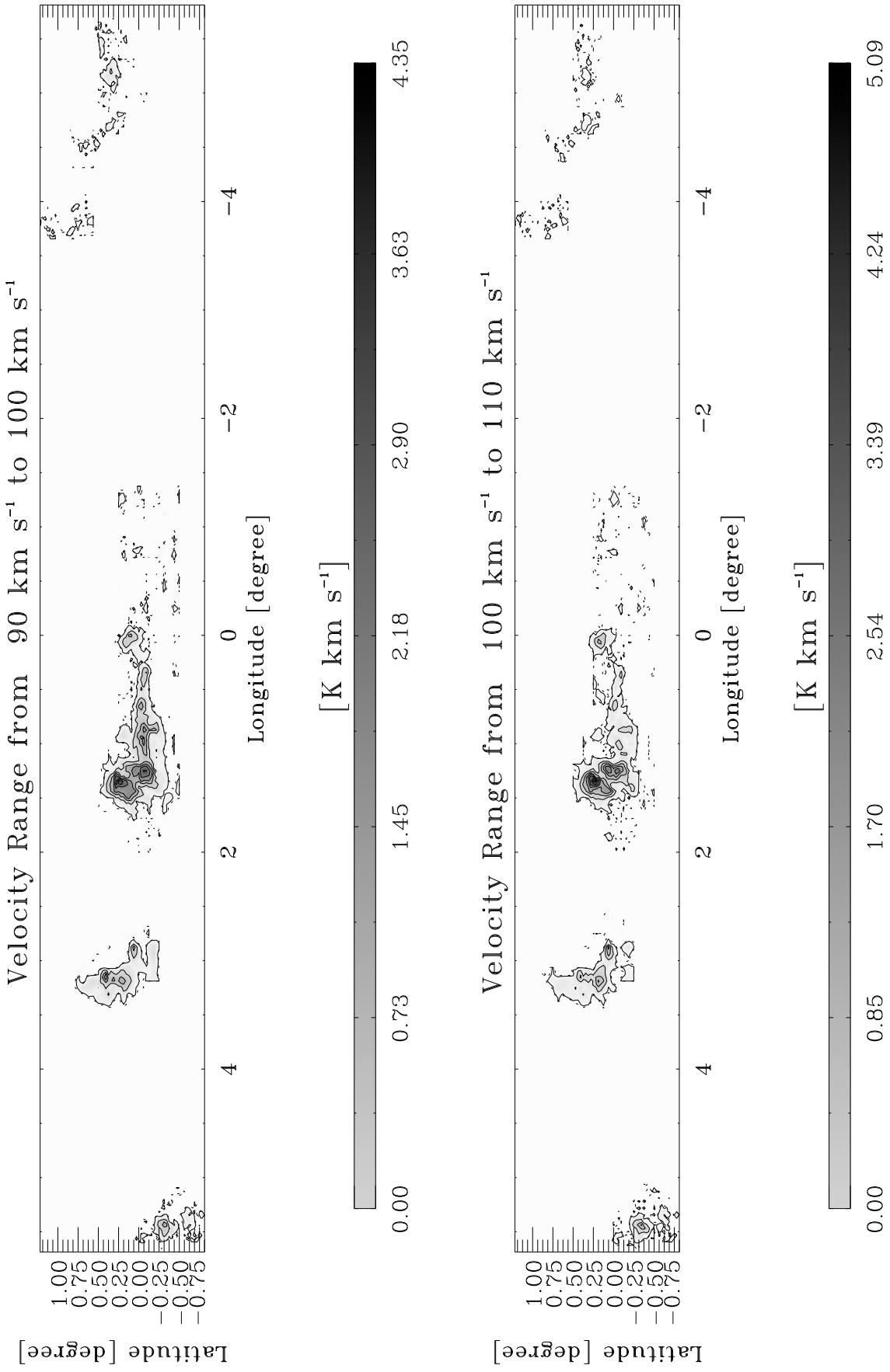

Fig. C1.18. continued.

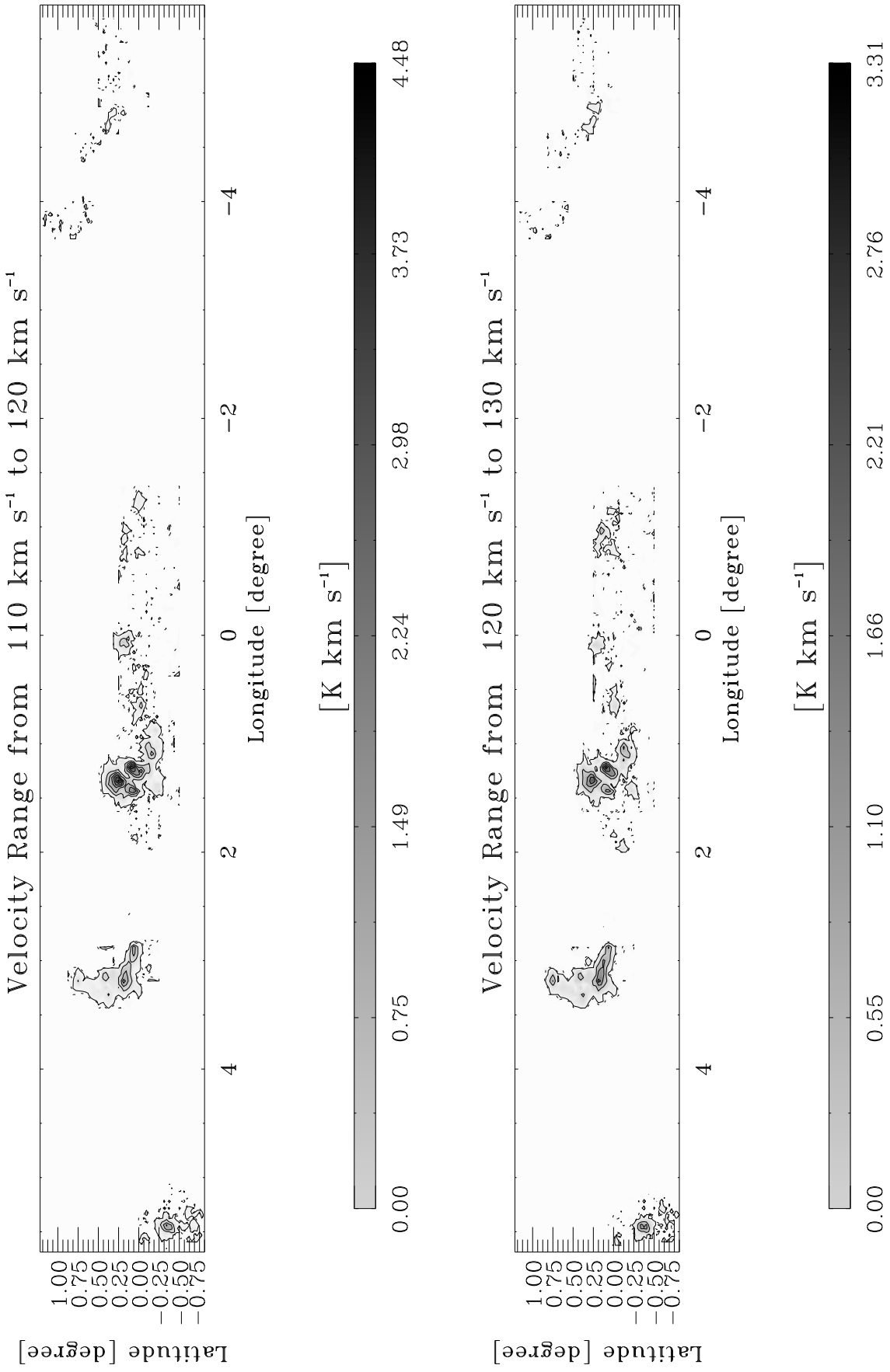

Fig. C1.19. continued.

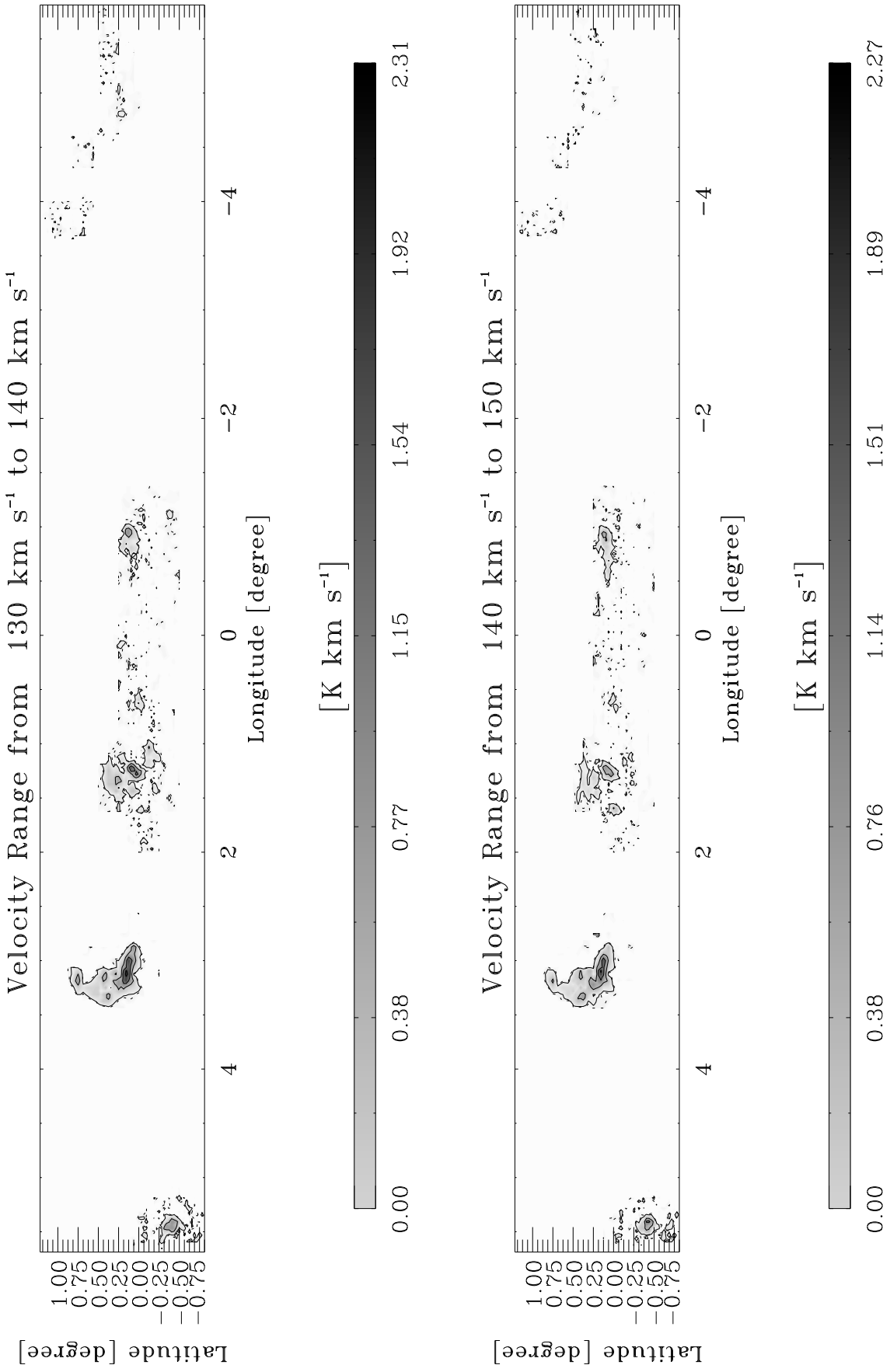

Fig. C1.20. continued.

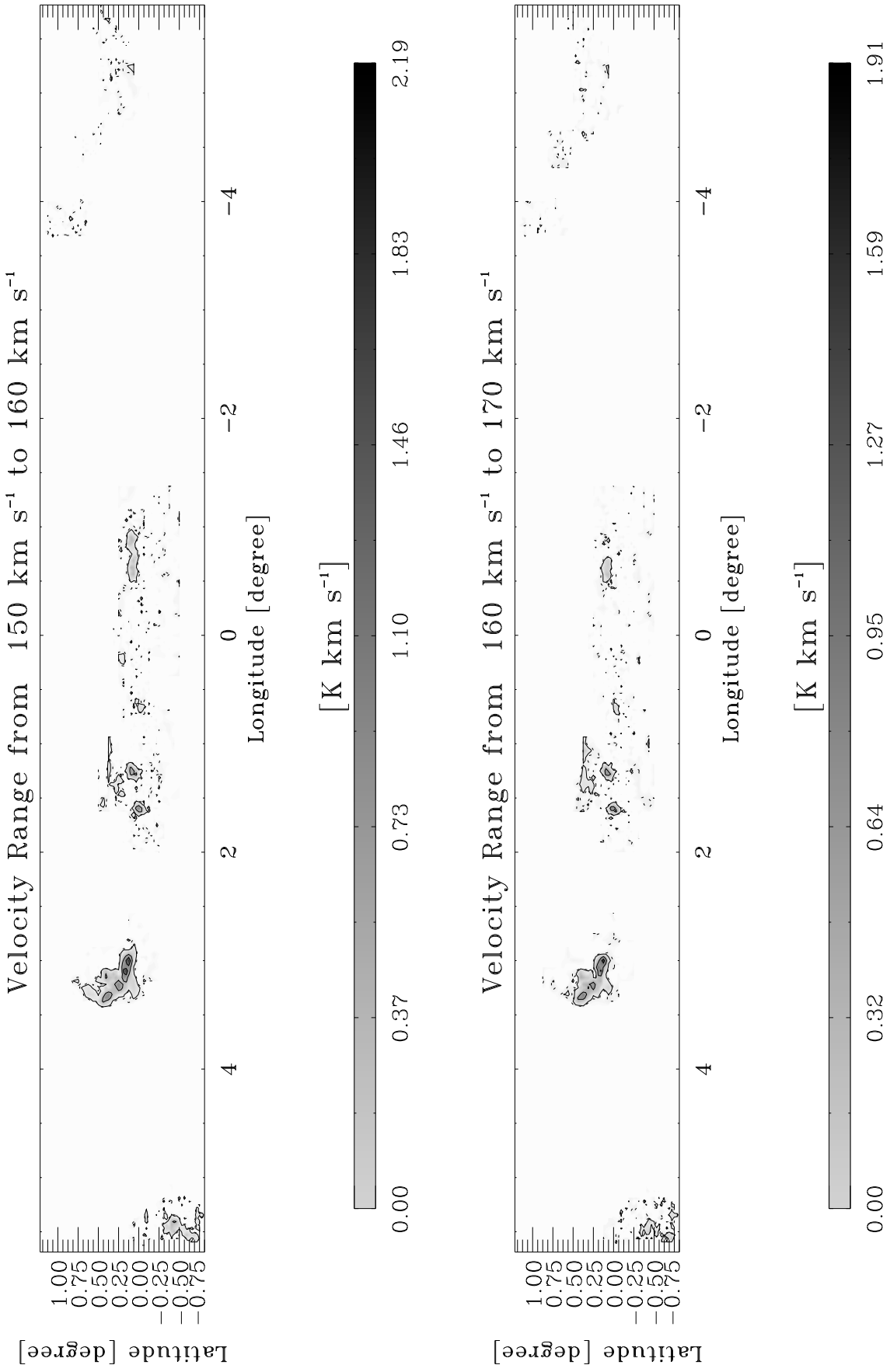

Fig. C1.21. continued.

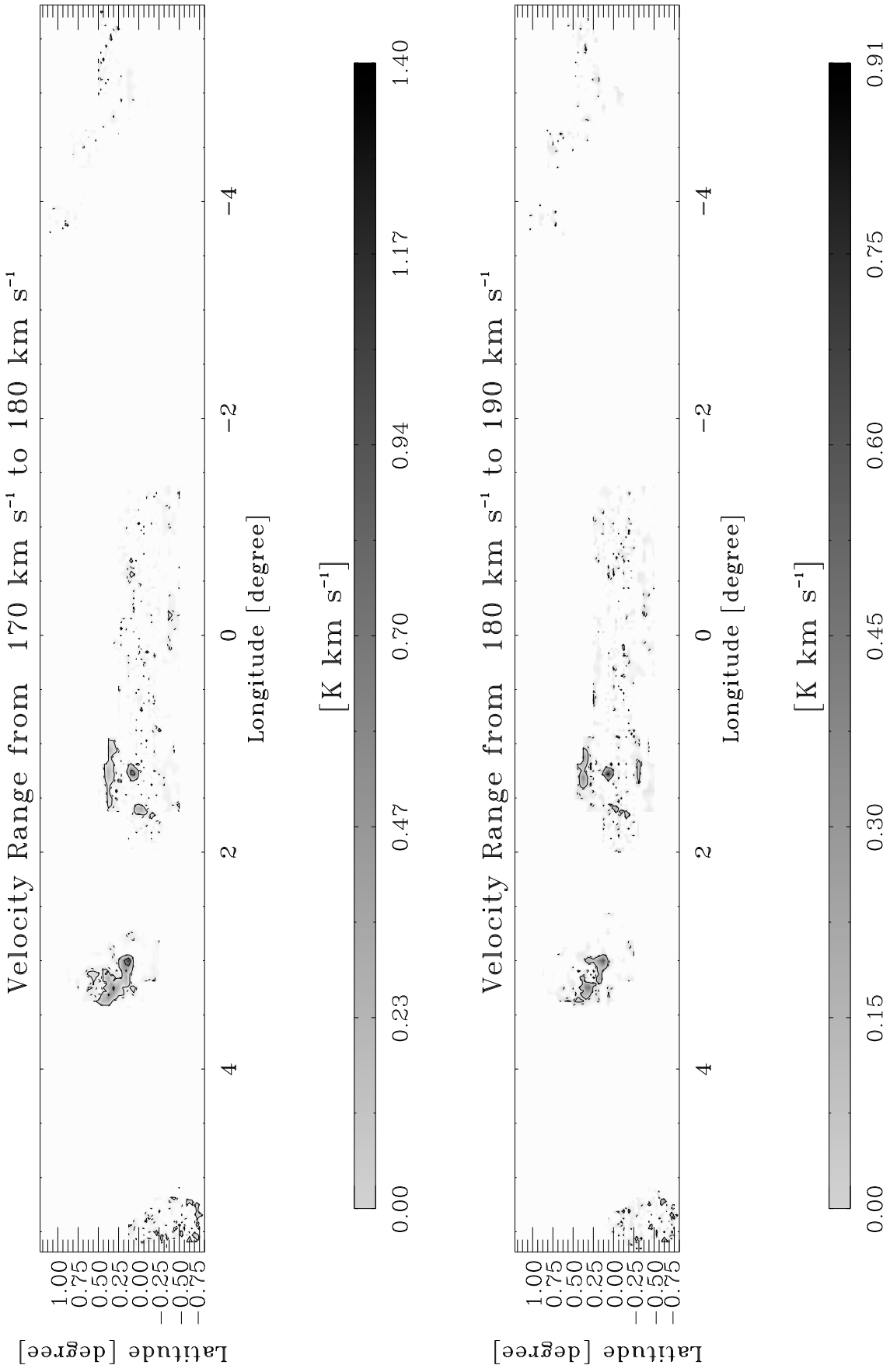

Fig. C1.22. continued.

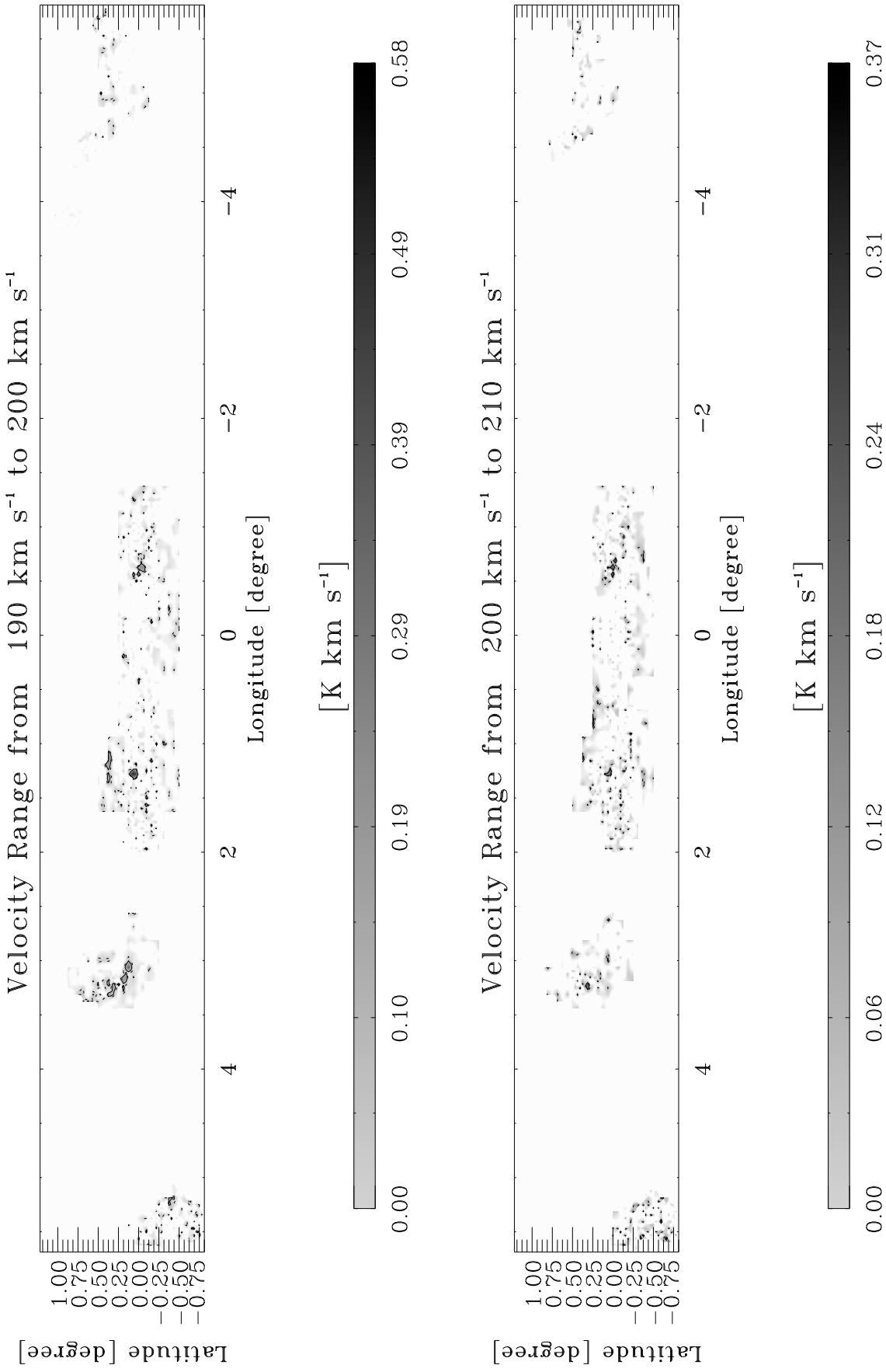

Fig. C1.23. continued.

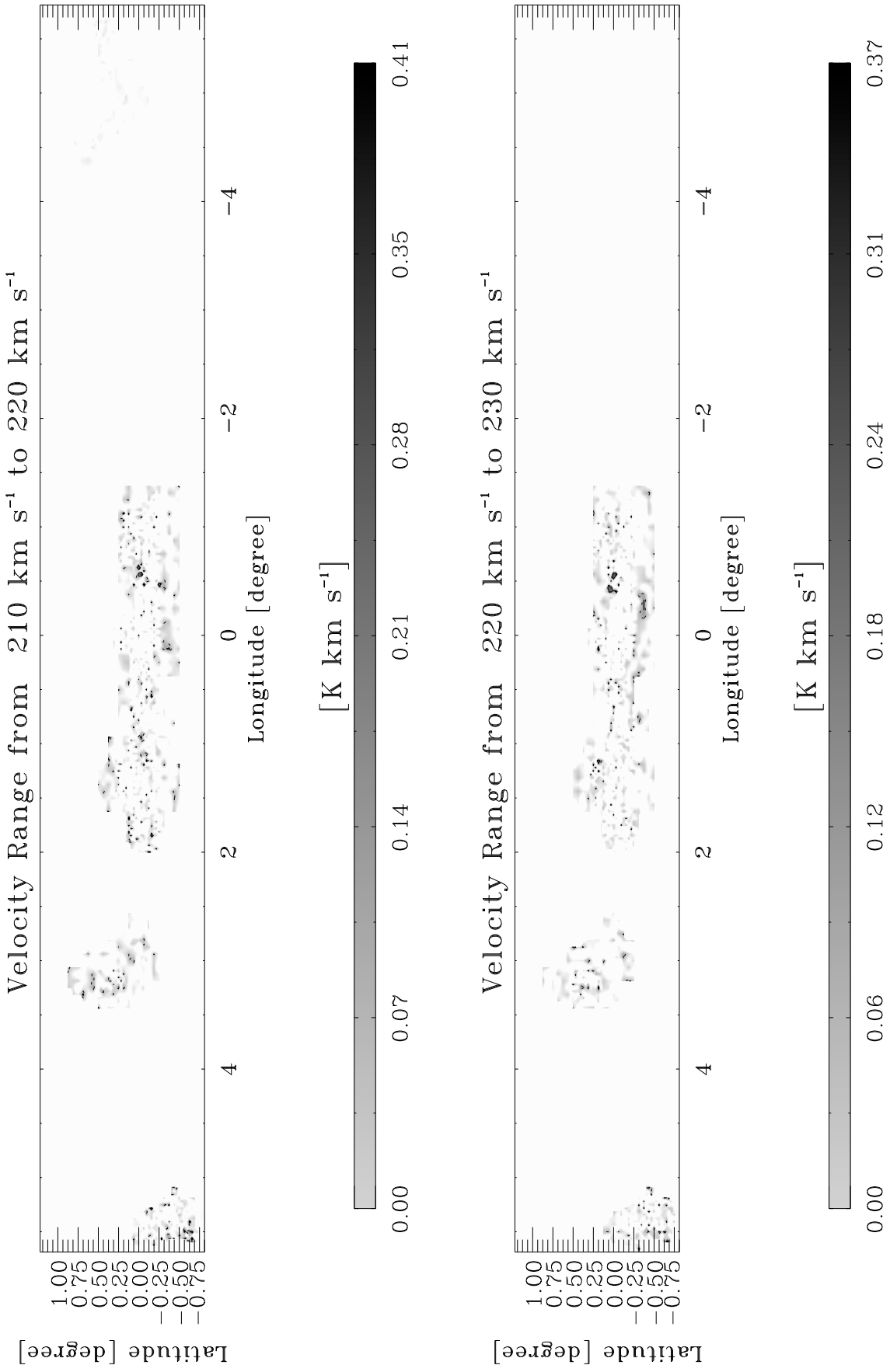

Fig. C1.24. continued.

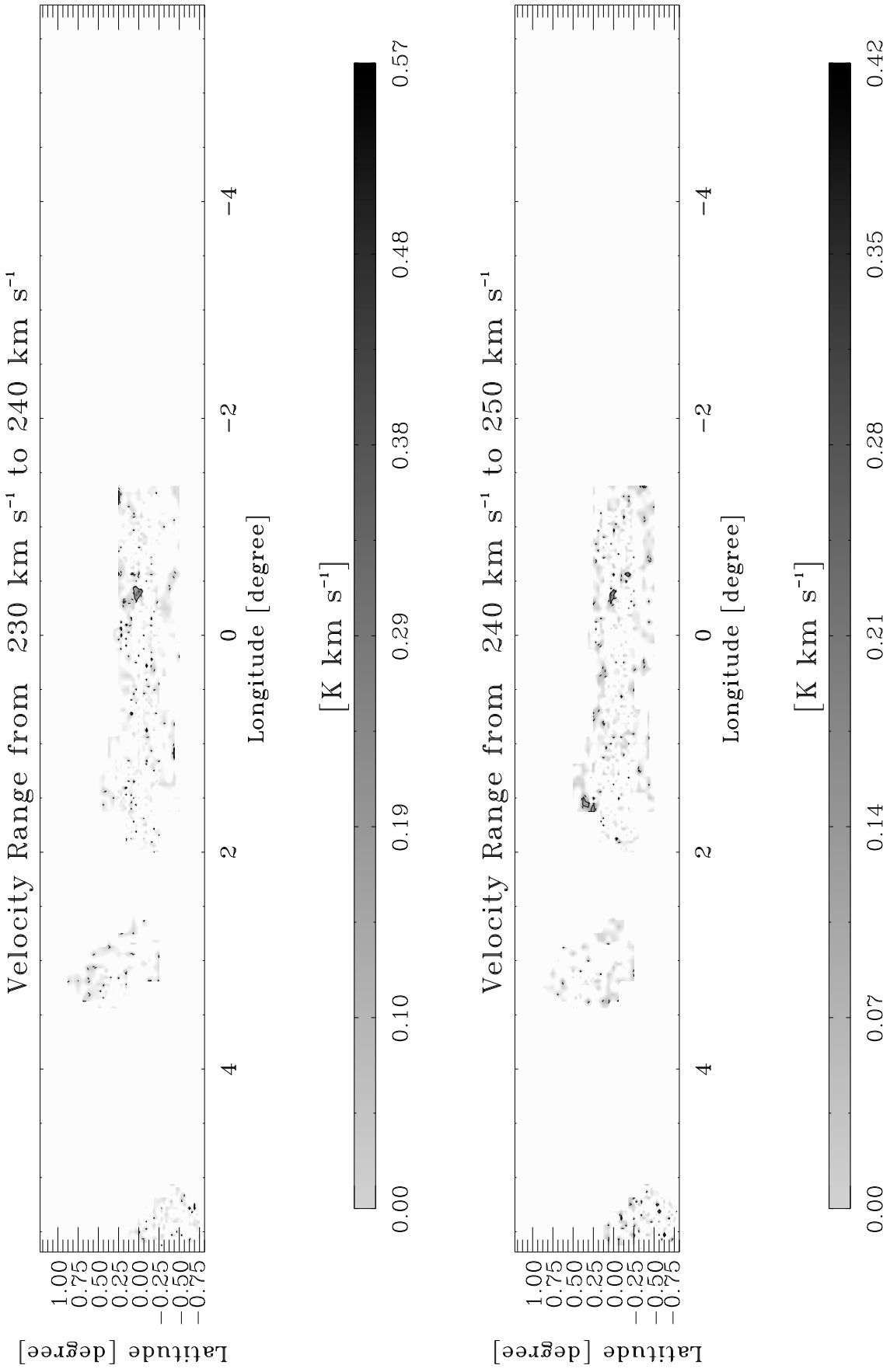

Fig. C1.25. continued.

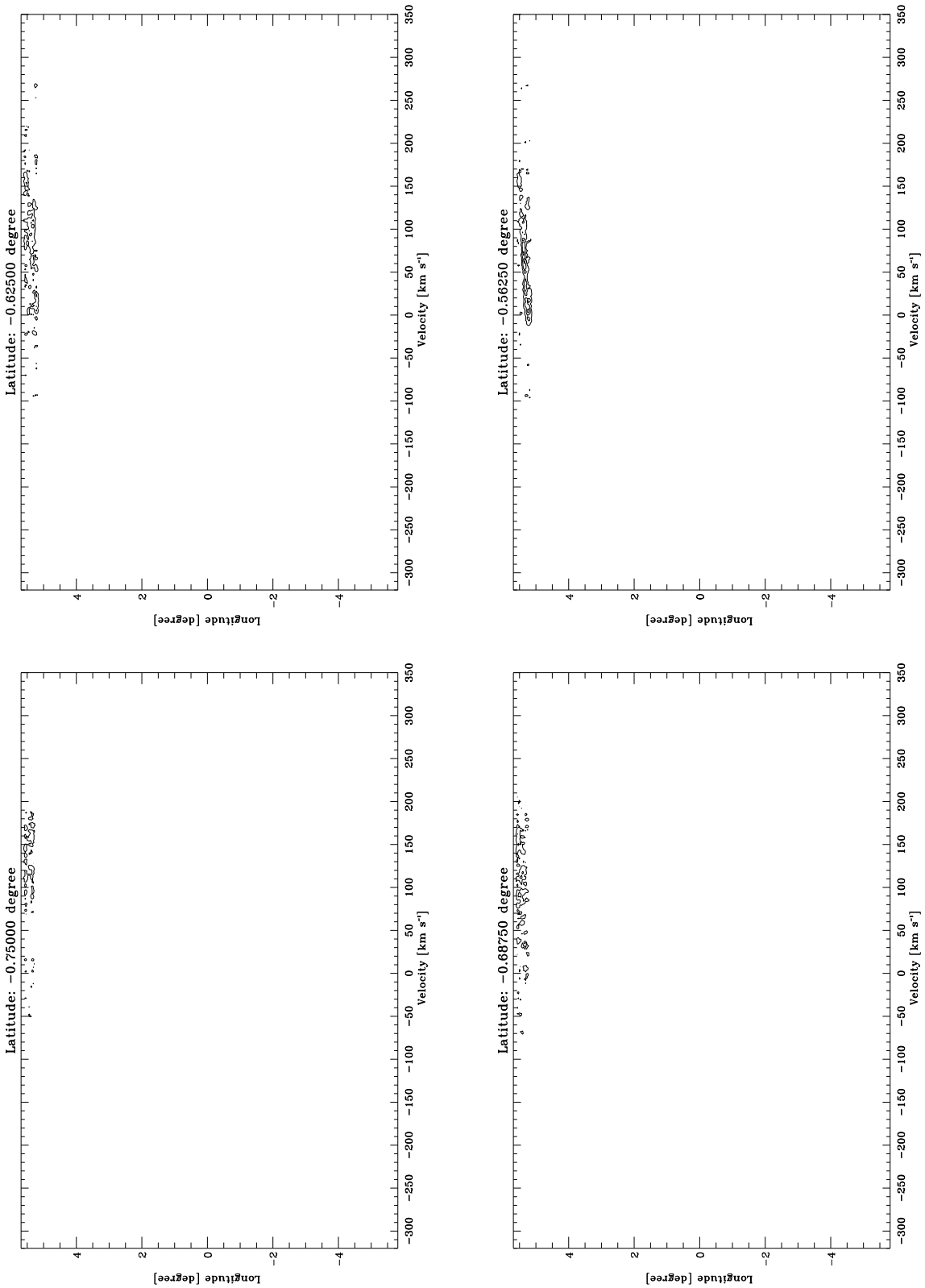

Fig. C2.1. Longitude-velocidad contour diagrams integrated in latitude in step of 0.0625 in SiO. The lowest contour is at 0.0013 K (3σ). The following contours increase them in step of 0.0018 K, which correspond to 4σ.

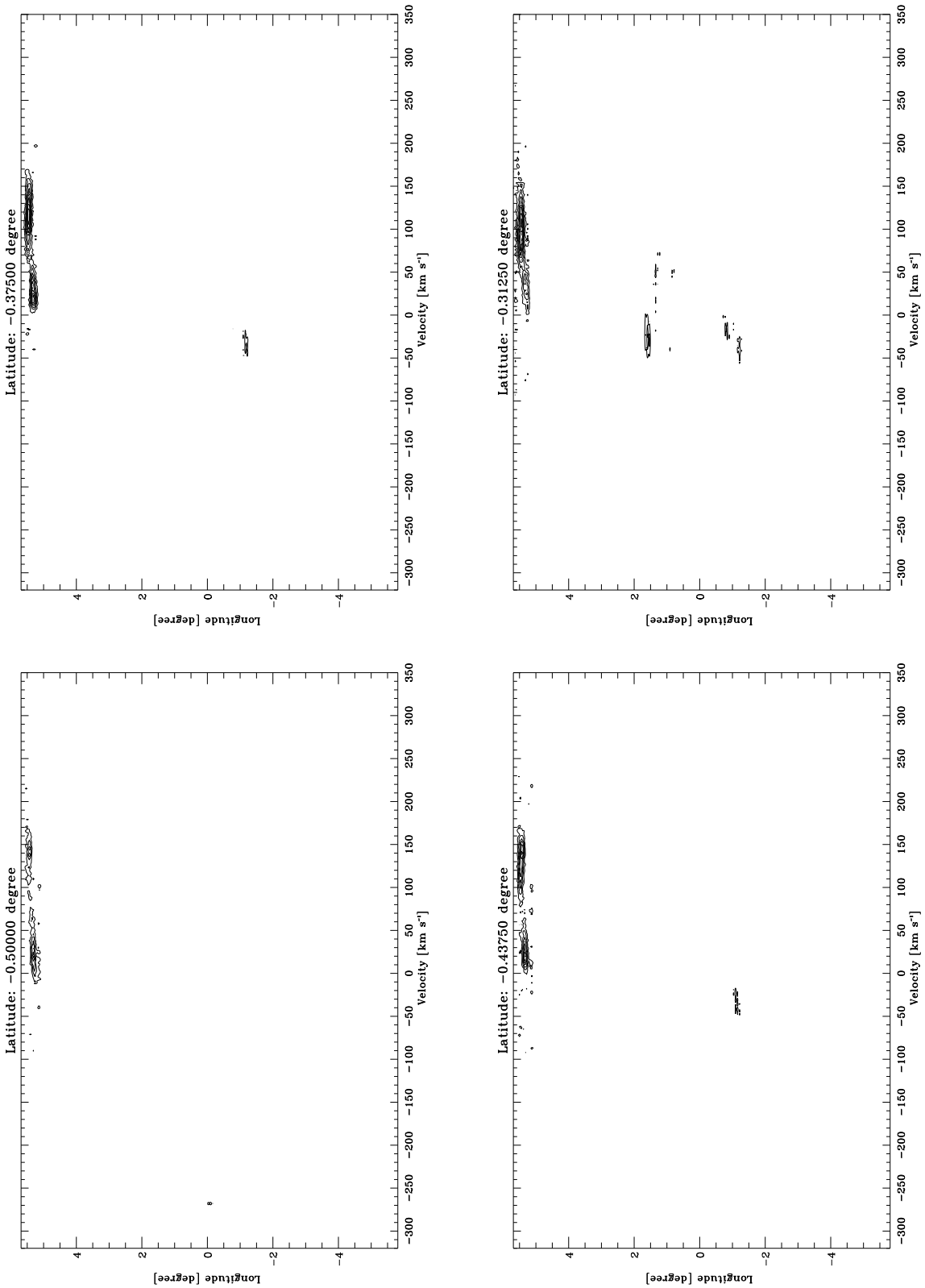

Fig. C2.2. continued.

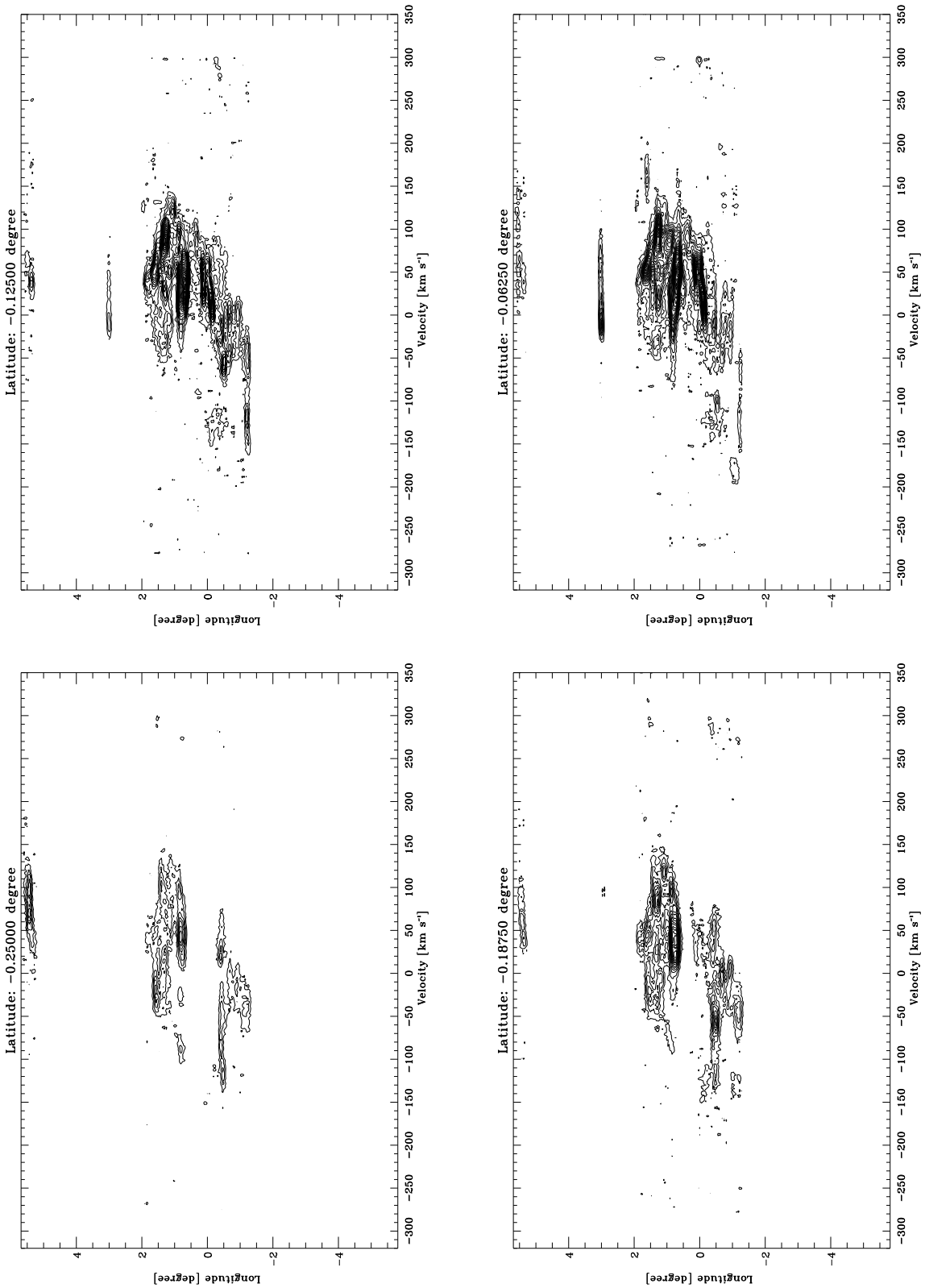

Fig. C2.3. continued.

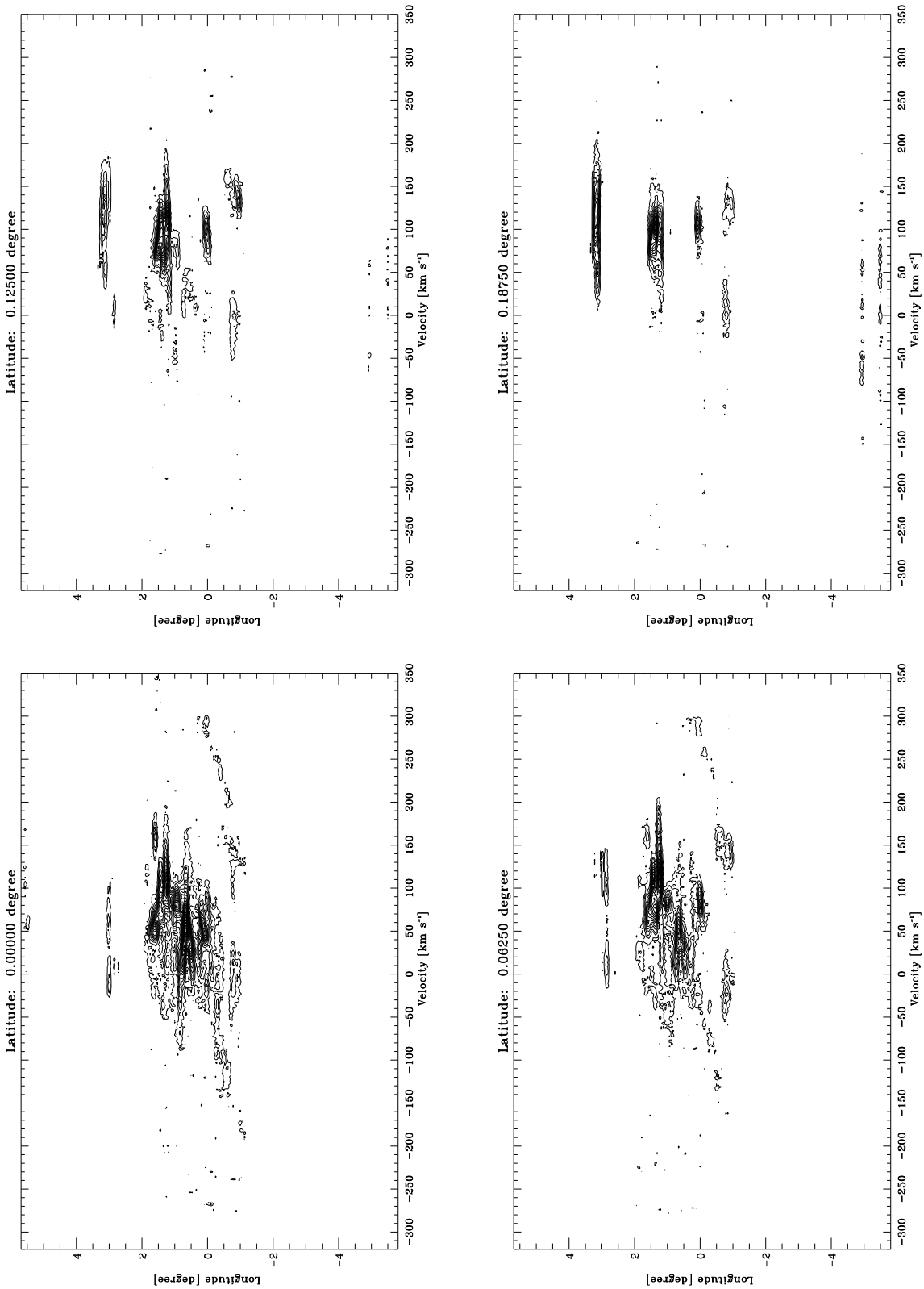

Fig. C2.4. continued.

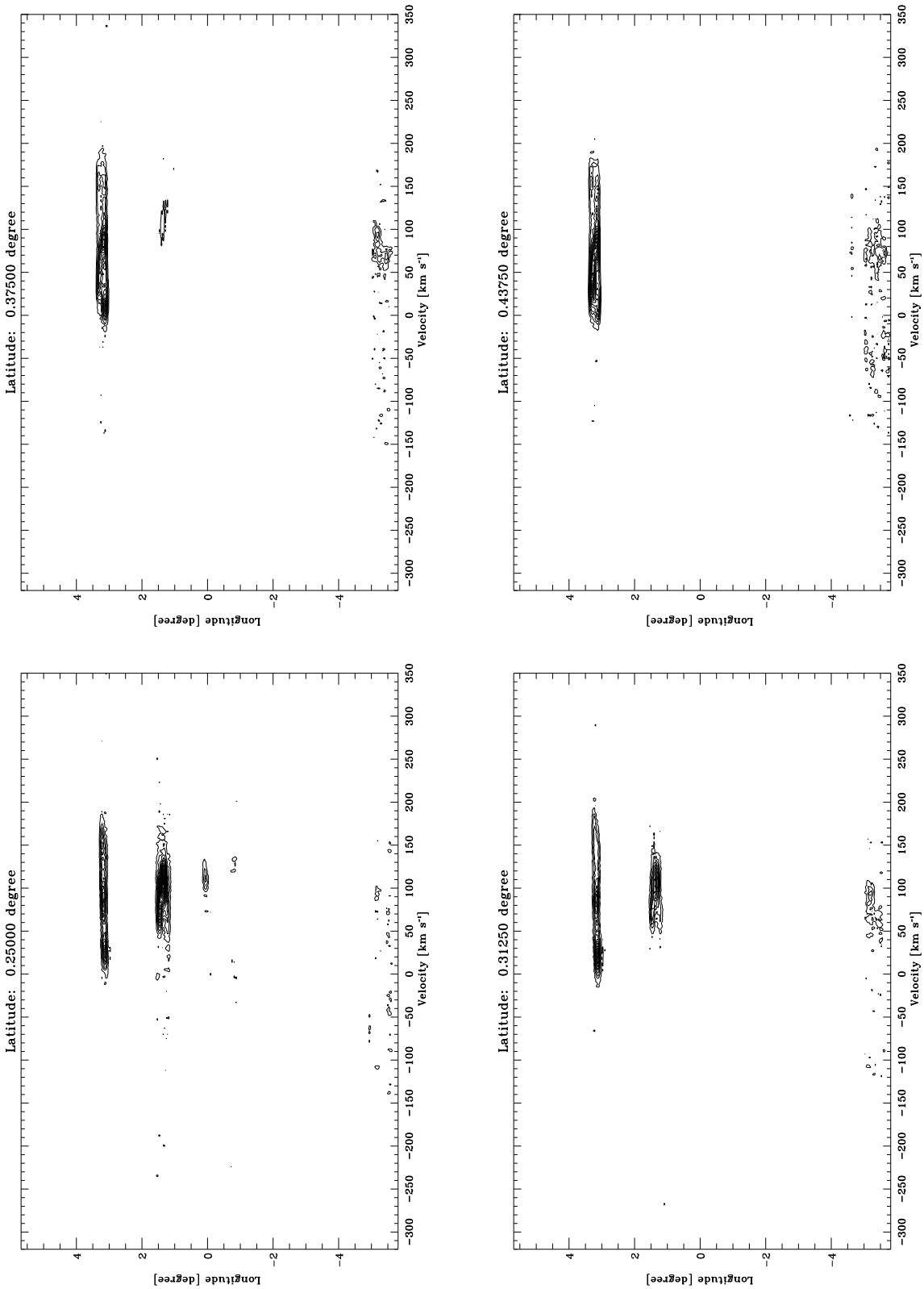

Fig. C2.5. continued.

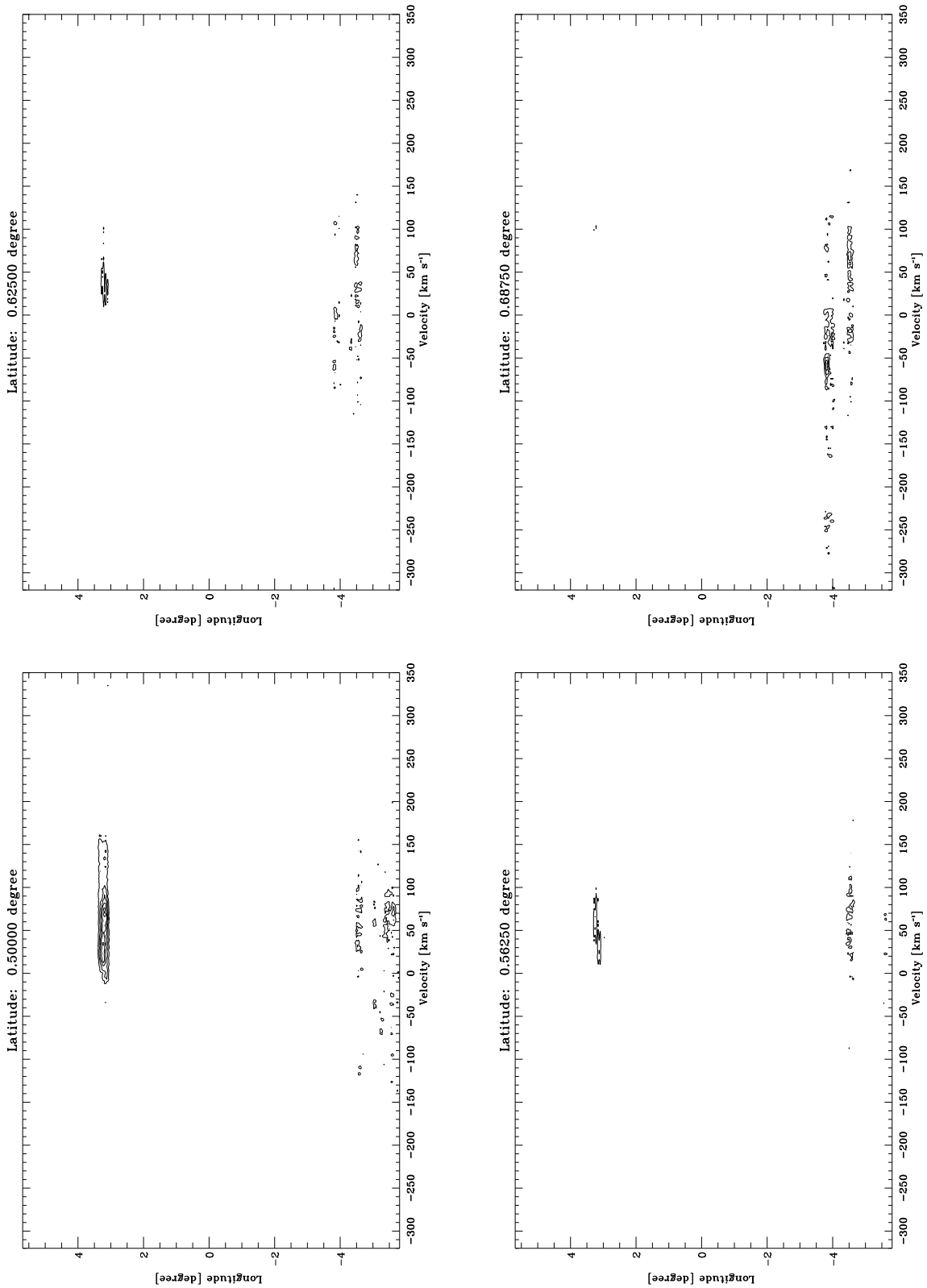

Fig. C2.6. continued.

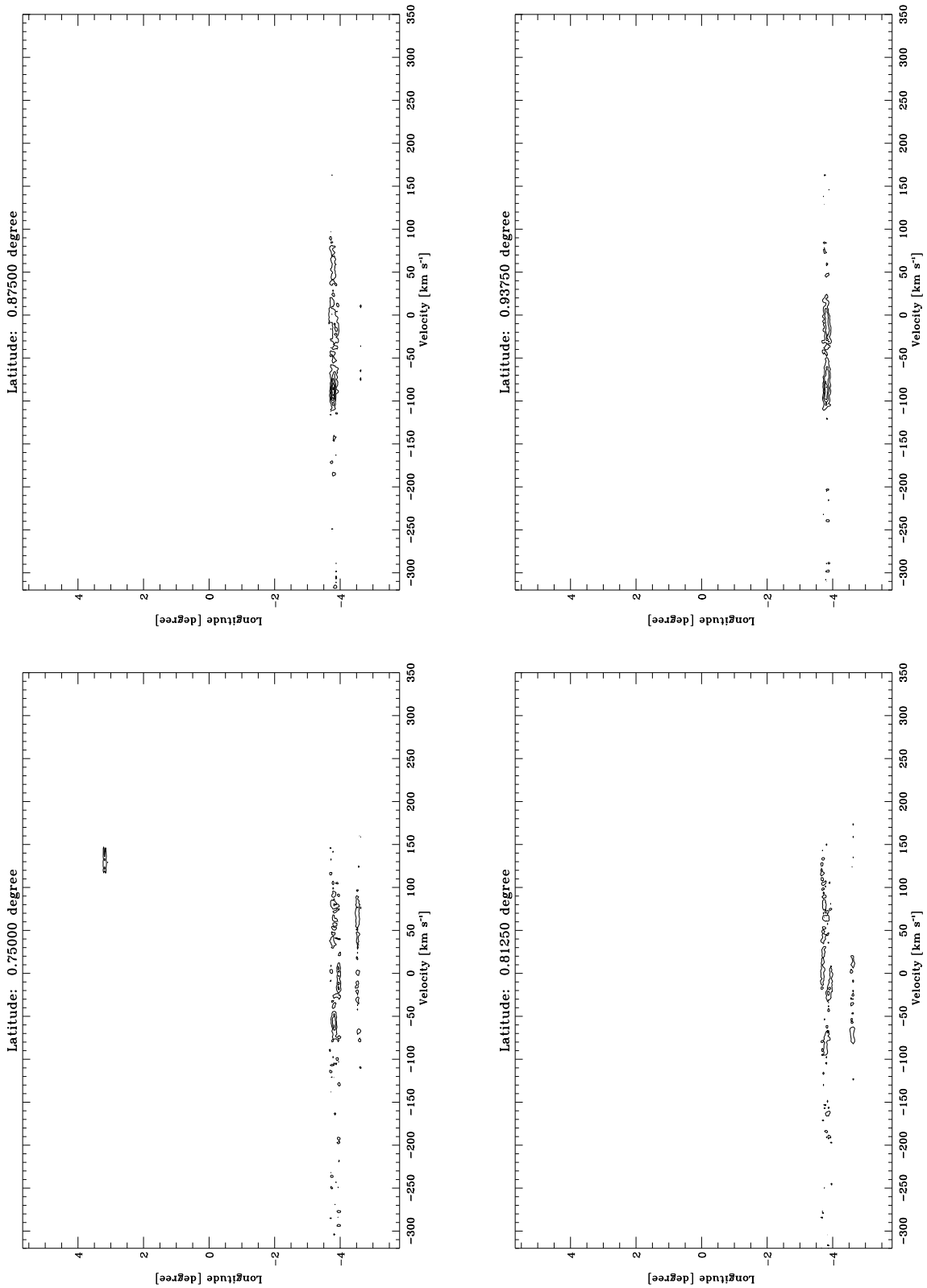

Fig. C2.7. continued.

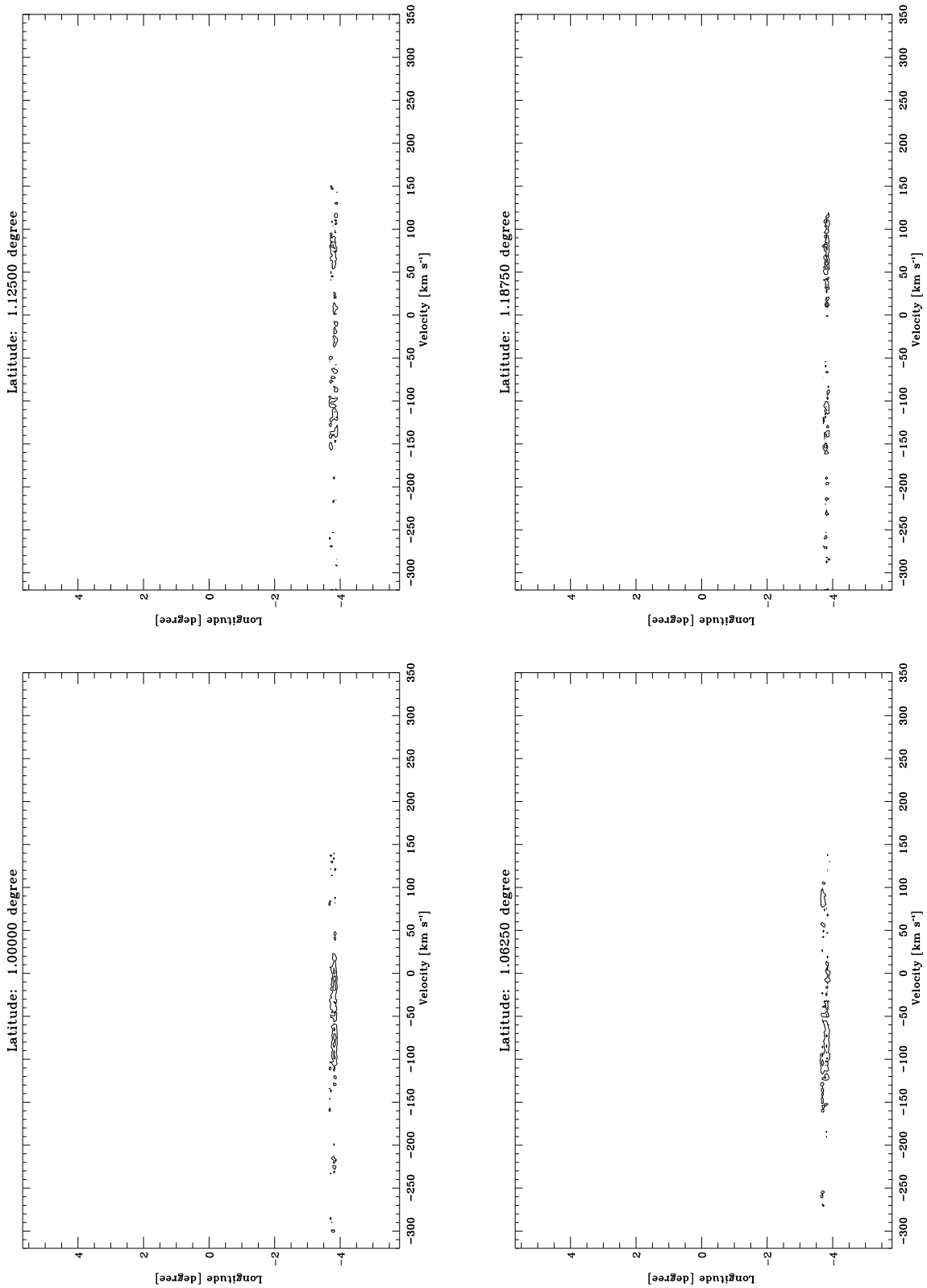

Fig. C2.8. continued.

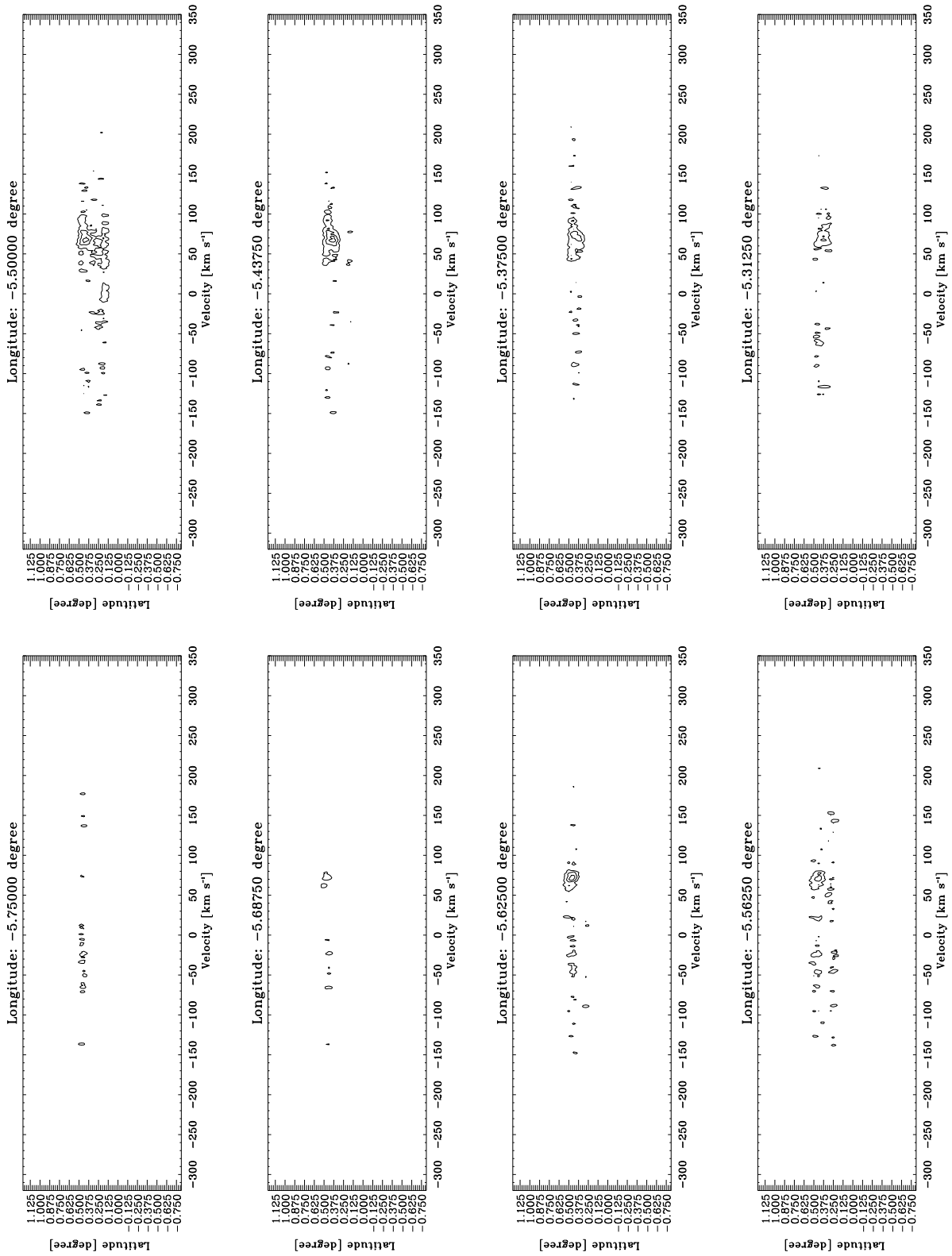

Fig. C3.1. Latitude-Velocity diagrams integrated in longitude in step of 0.°0625 for SiO. The lowest contour is at 0.0013 K (3σ). The following contours increase them in step of 0.0026 K, which correspond to 6σ.

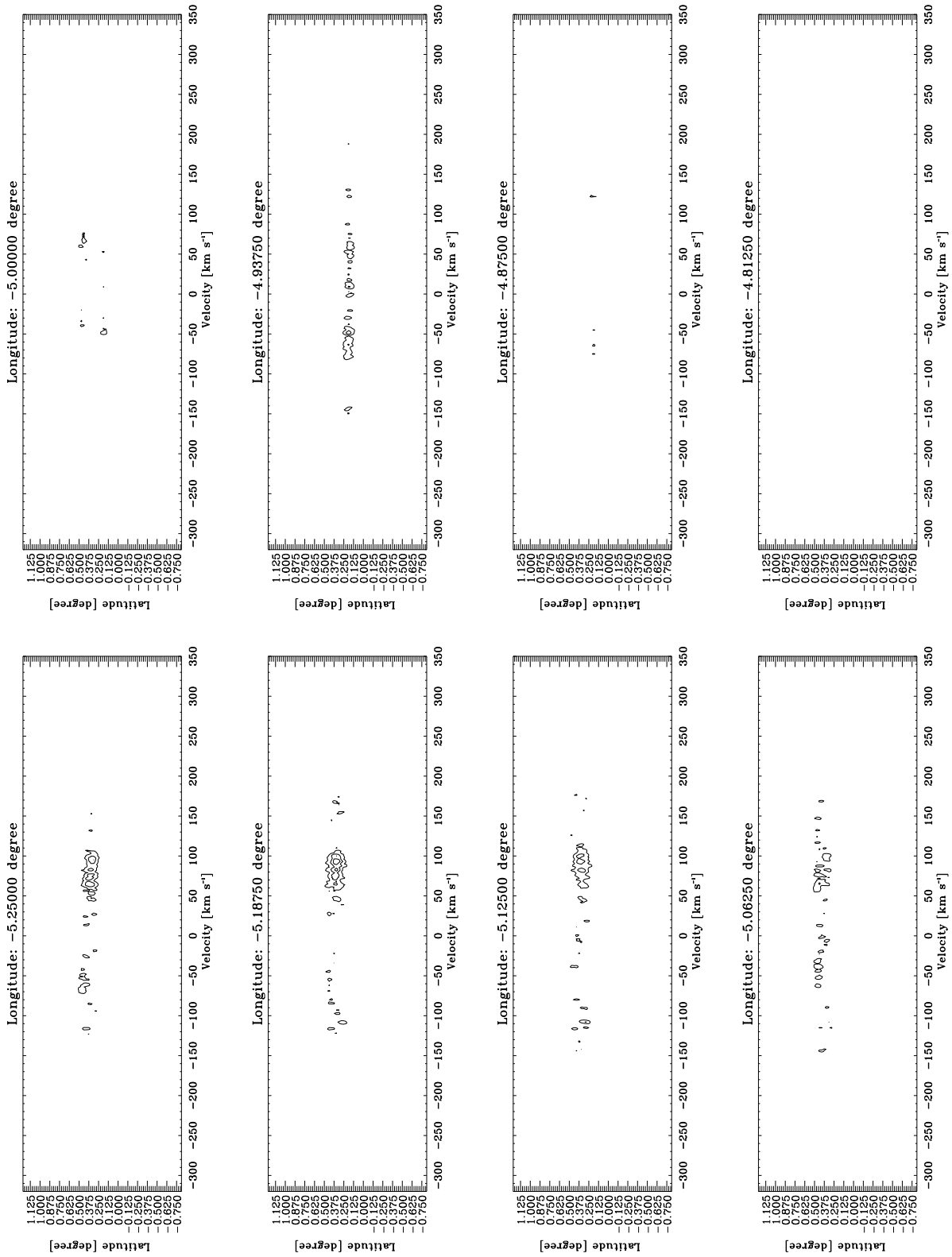

Fig. C3.2. continued.

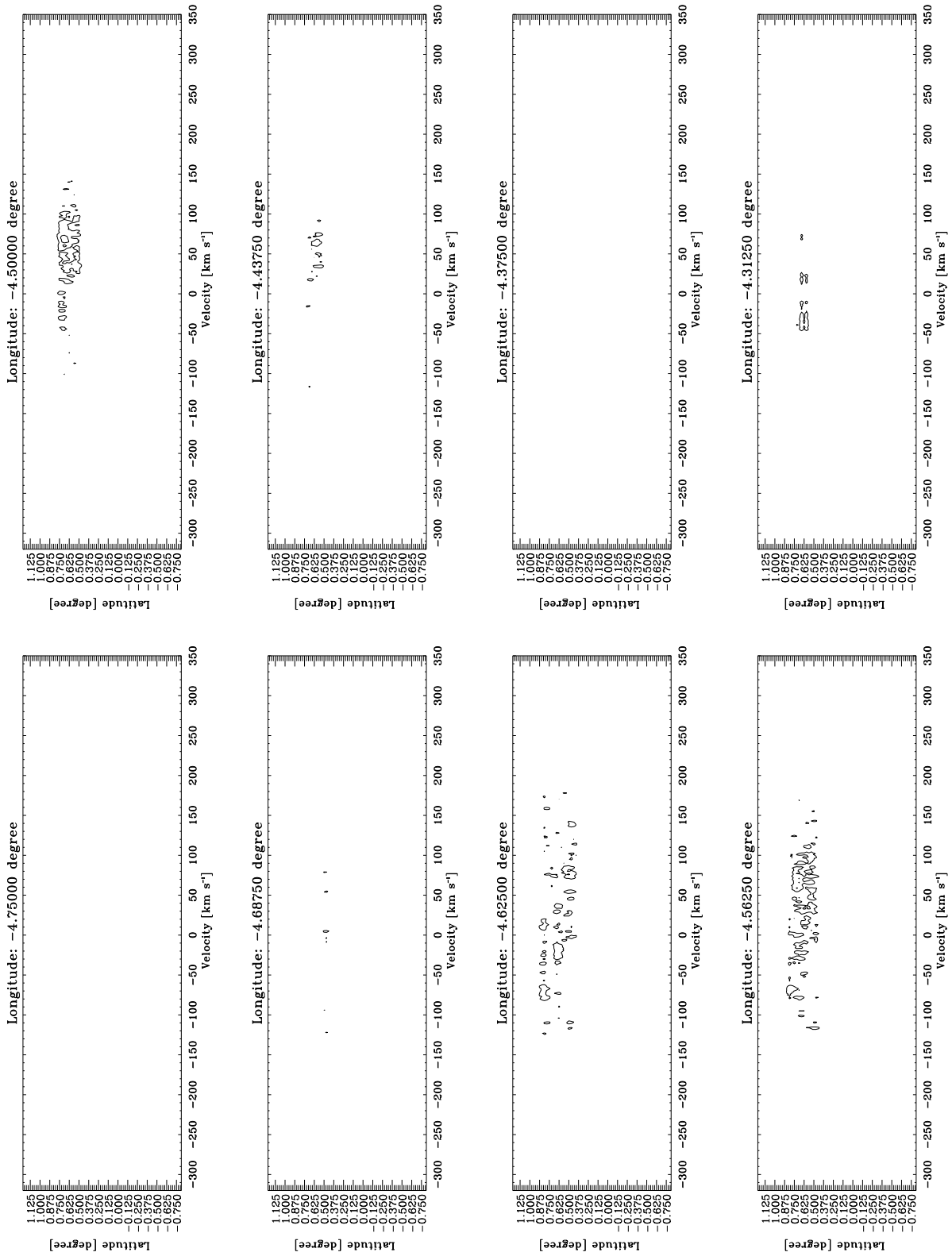

Fig. C3.3. continued.

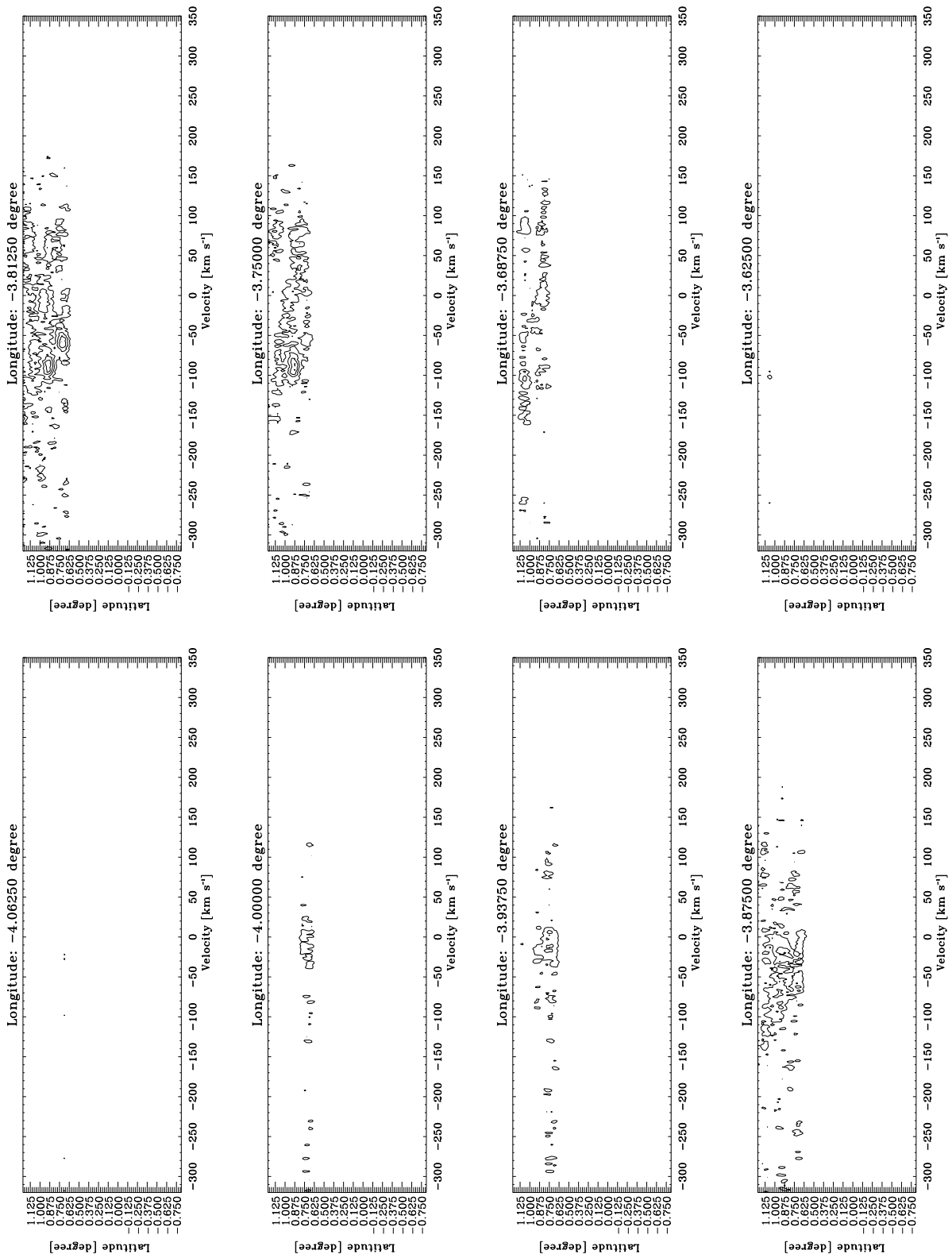

Fig. C3.4. continued.

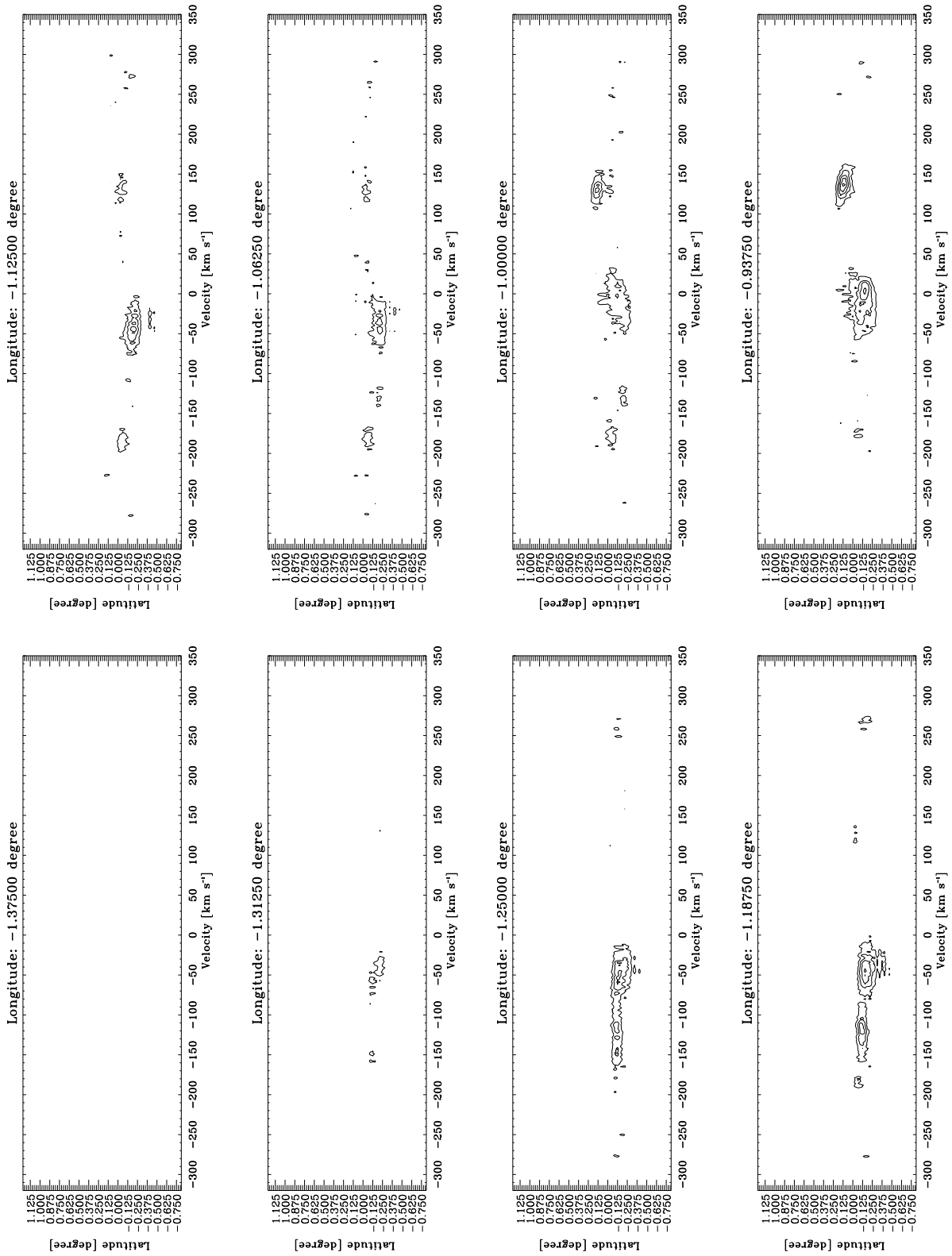

Fig. C3.5. continued.

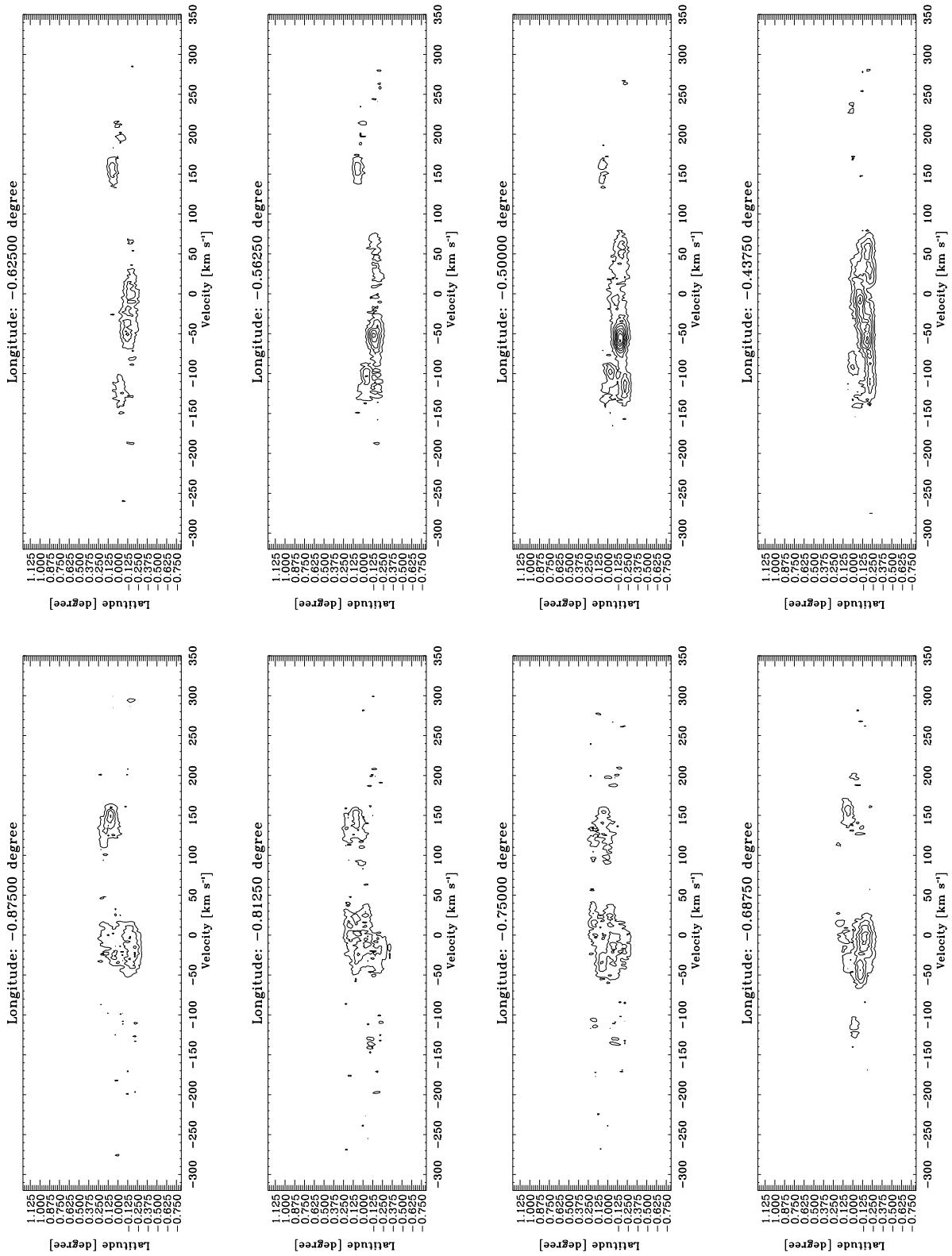

Fig. C3.6. continued.

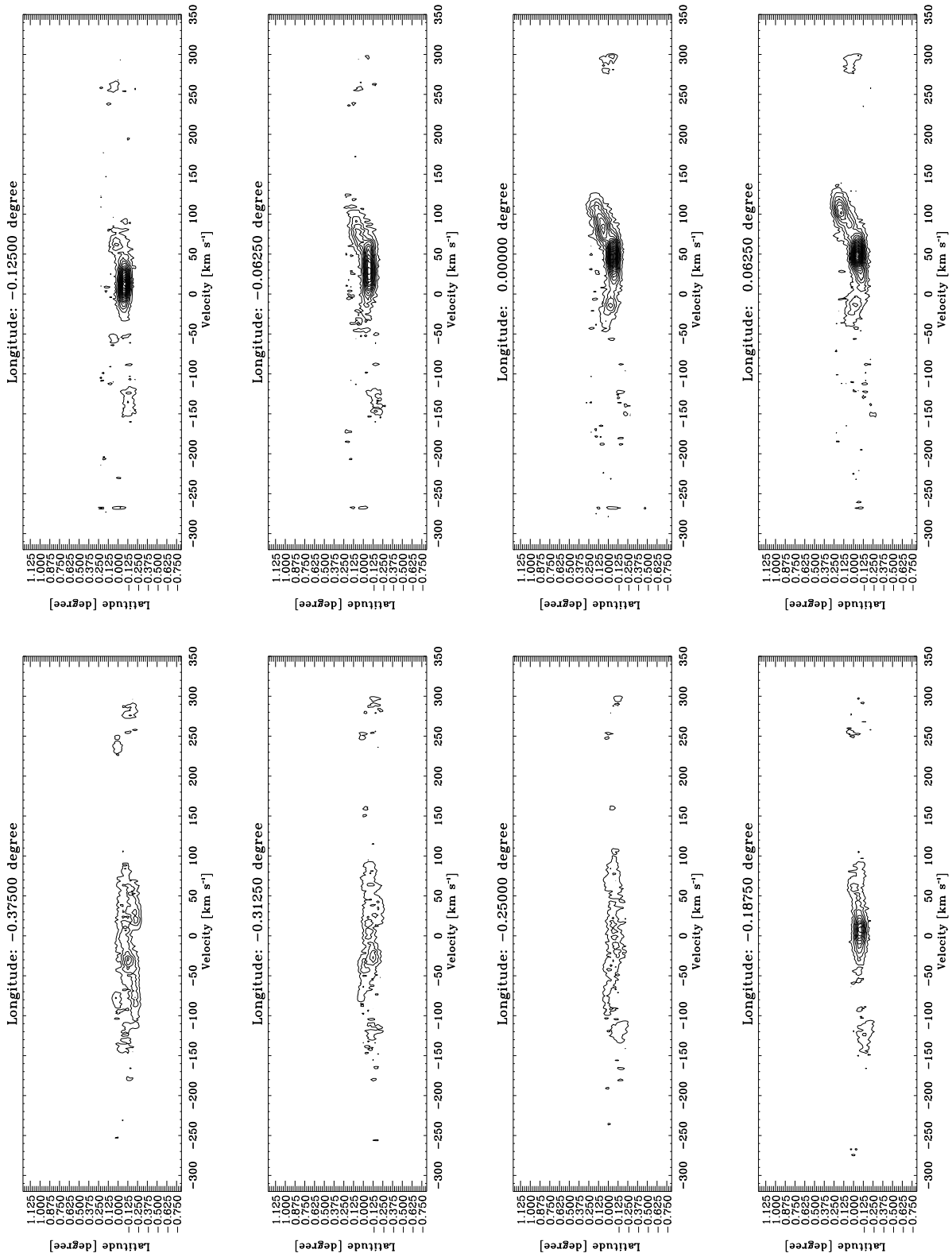

Fig. C3.7. continued.

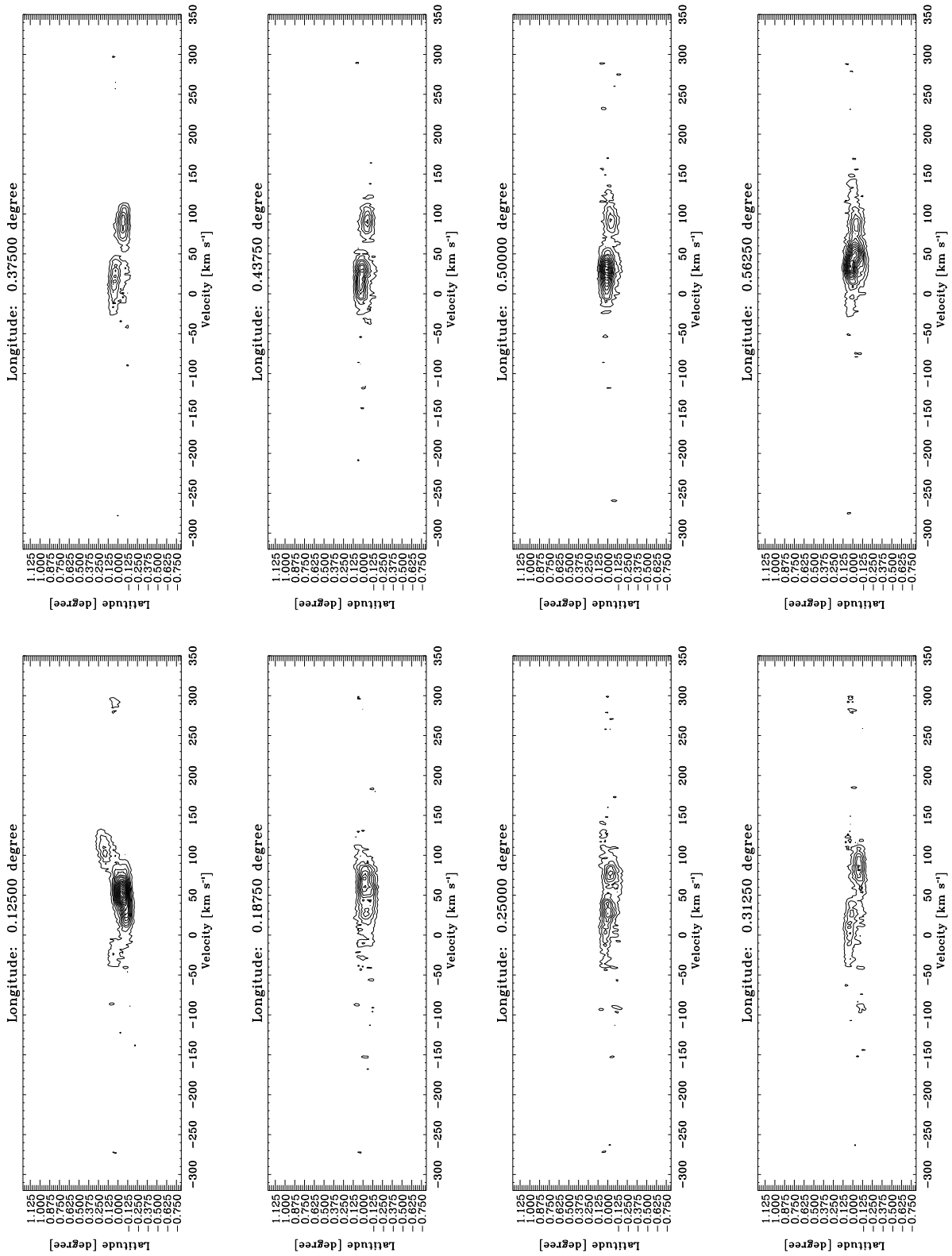

Fig. C3.8. continued.

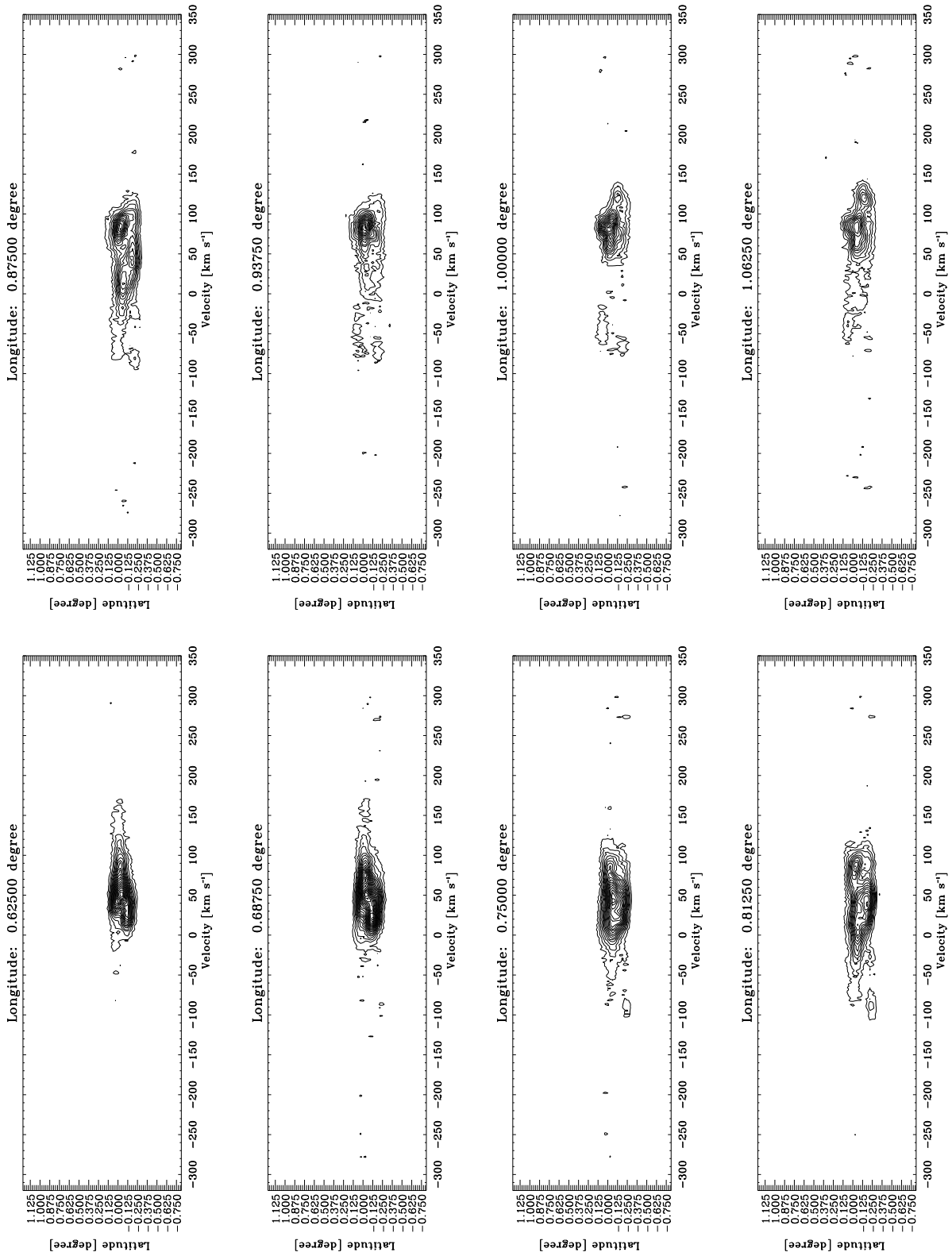

Fig. C3.9. continued.

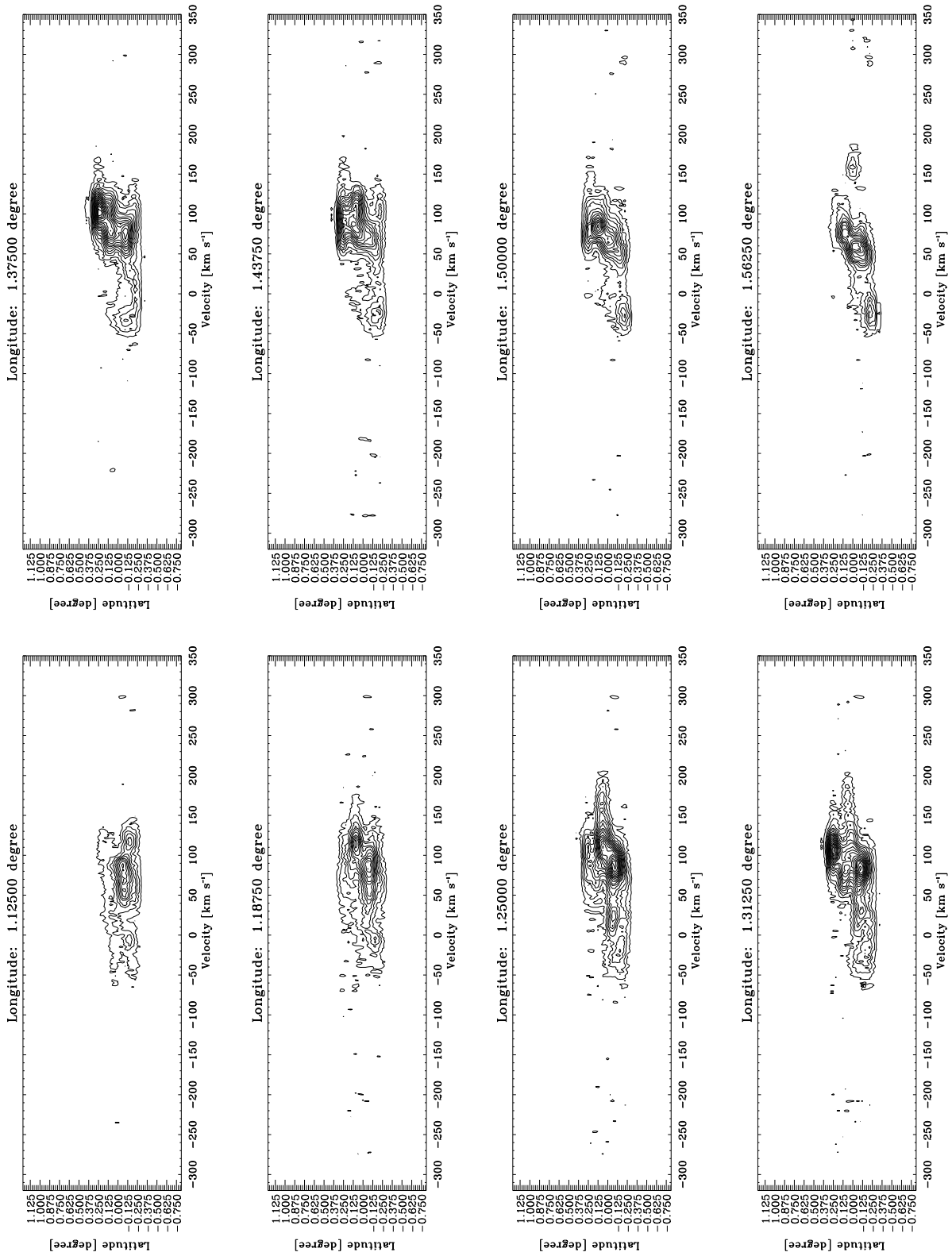

Fig. C3.10. continued.

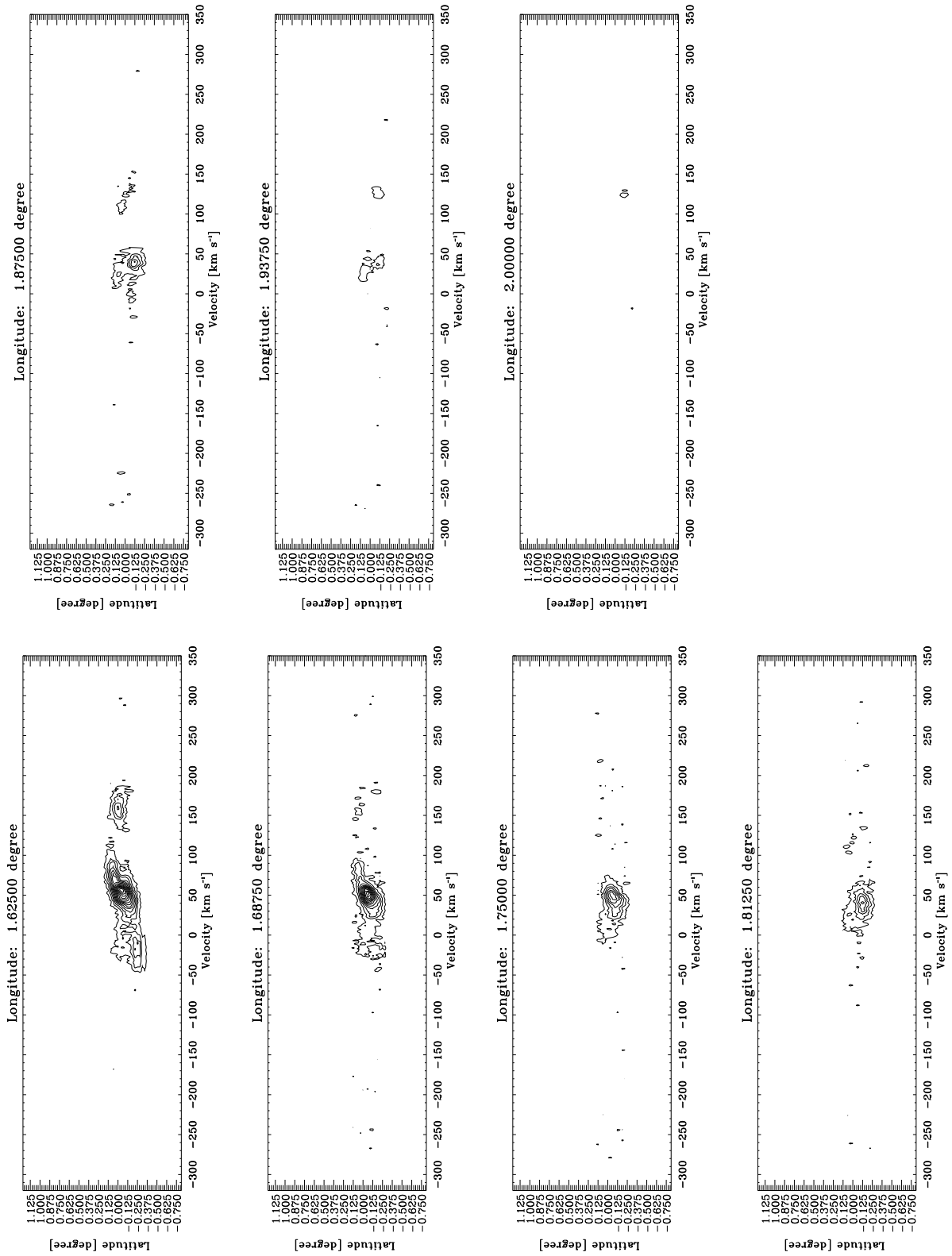

Fig. C3.11. continued.

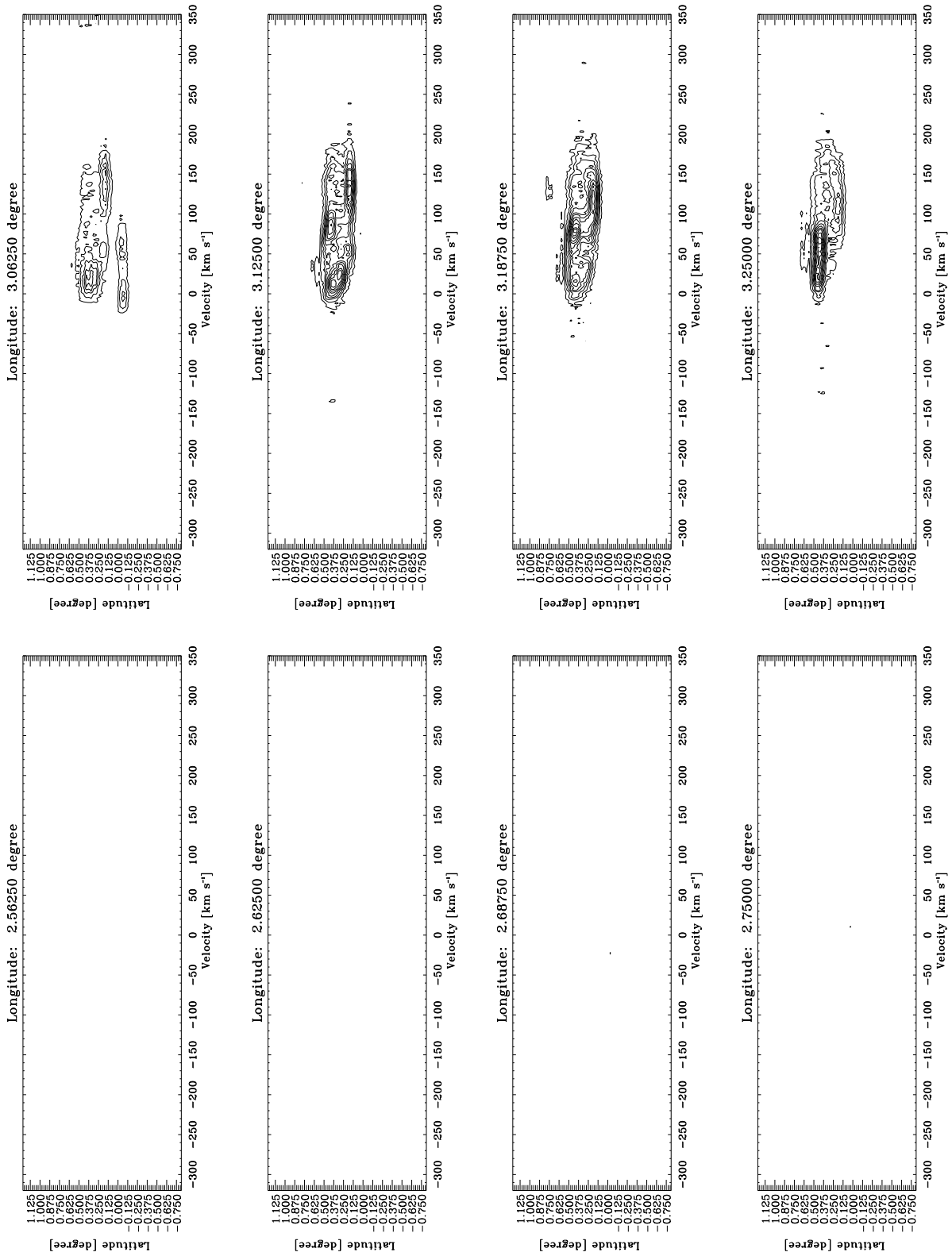

Fig. C3.12. continued.

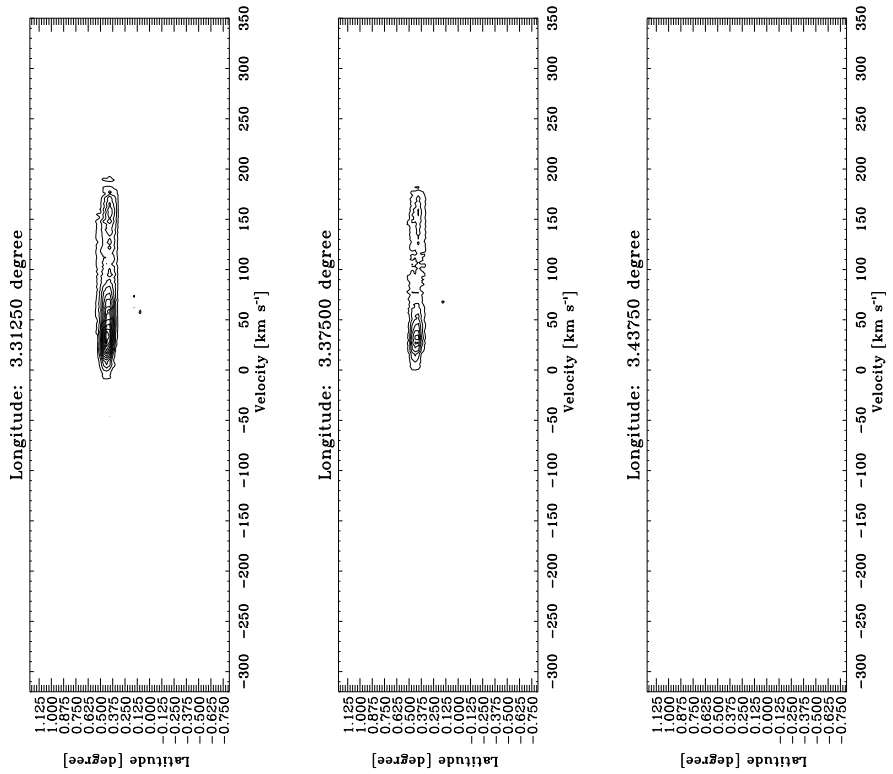

Fig. C3.13. continued.

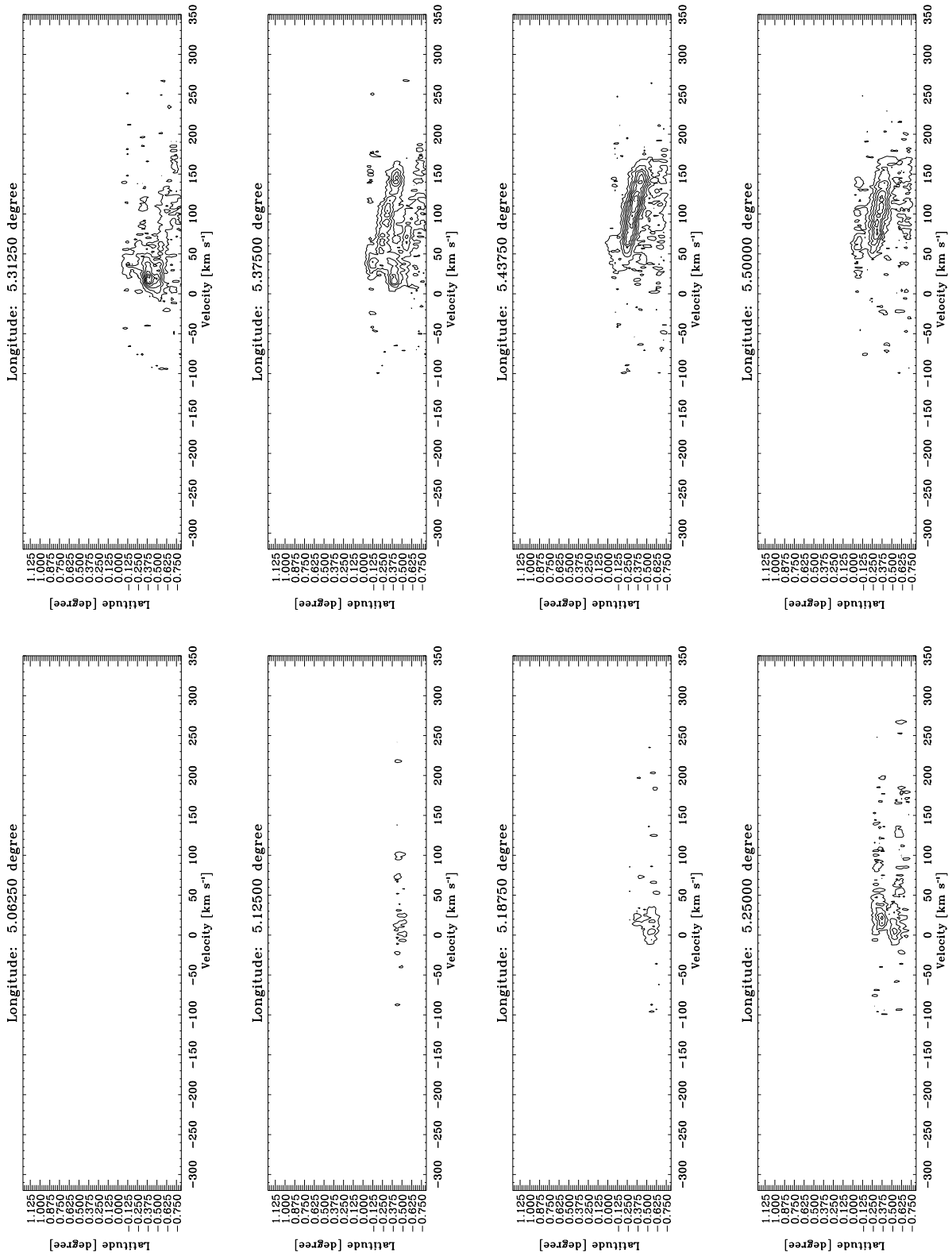

Fig. C3.14. continued.

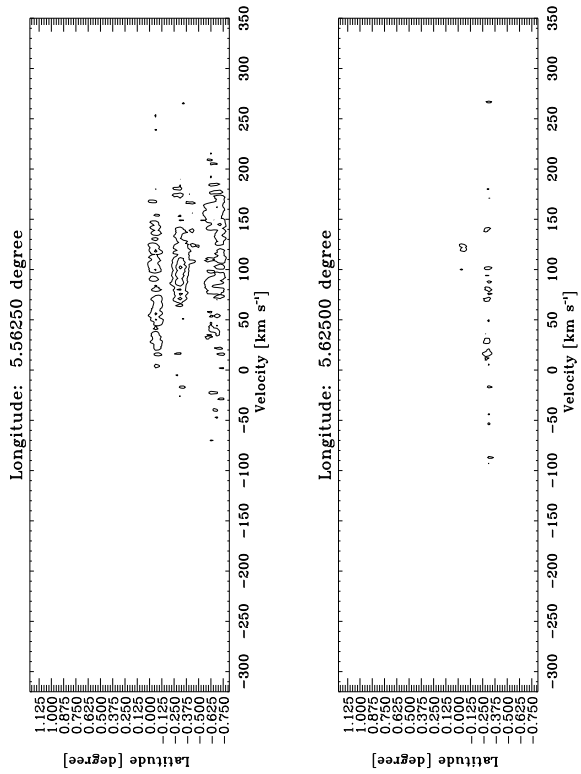

Fig. C3.15. continued.

Appendix D: $H^{13}CO^+$ Galactic center survey

In Fig. D.1, we present the channel map of the $H^{13}CO^+$ emission in the Galactic center region integrated in velocity widh of 10 km s^{-1}.

Figure D.2 presents the $l - v$ diagram integrated in latitude in steps of 0.°0625 in $H^{13}CO^+$. The contours levels start at 0.0013 K (3σ) and increase them in steps of 0.0018 K (4σ).

Figure D.3 is a set of latitude-velocity diagrams integrated in steps of 0.°0625. The contours levels start at 0.0013 K (3σ) and increase them in step of 0.0026 K (6σ).

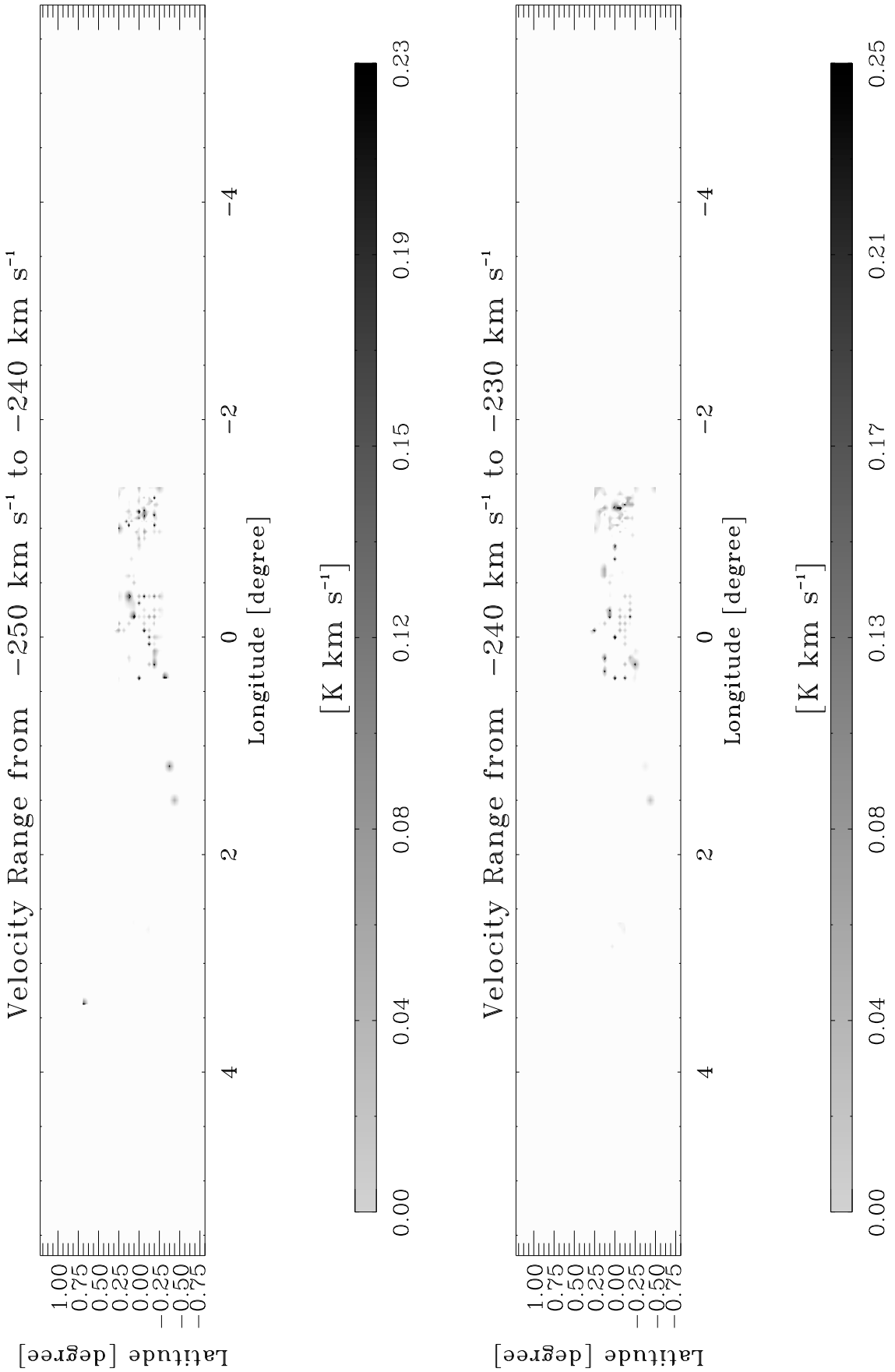

Fig. D1.1. The integrated intensity of the Galactic center region in $H^{13}CO^+$ (1−0) in velocity intervals of 10 km s^{-1} width. The solid contour levels start at 0.2 K km s^{-1}, which is the 3σ level, and increase in steps of 0.33 K km s^{-1} (5σ). The dotted contours is at 0.13 K km s^{-1} (2σ).

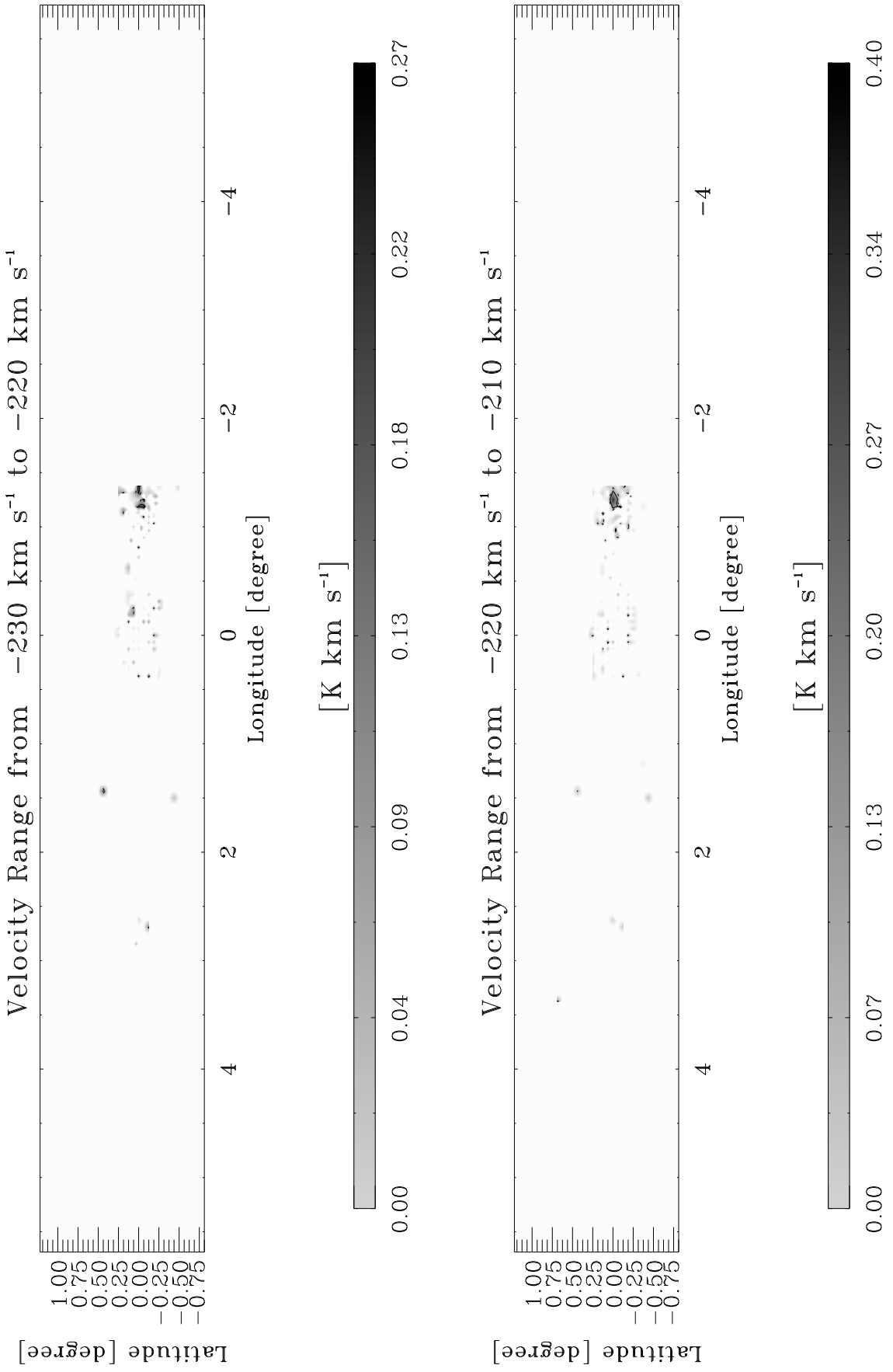

Fig. D1.2. continued.

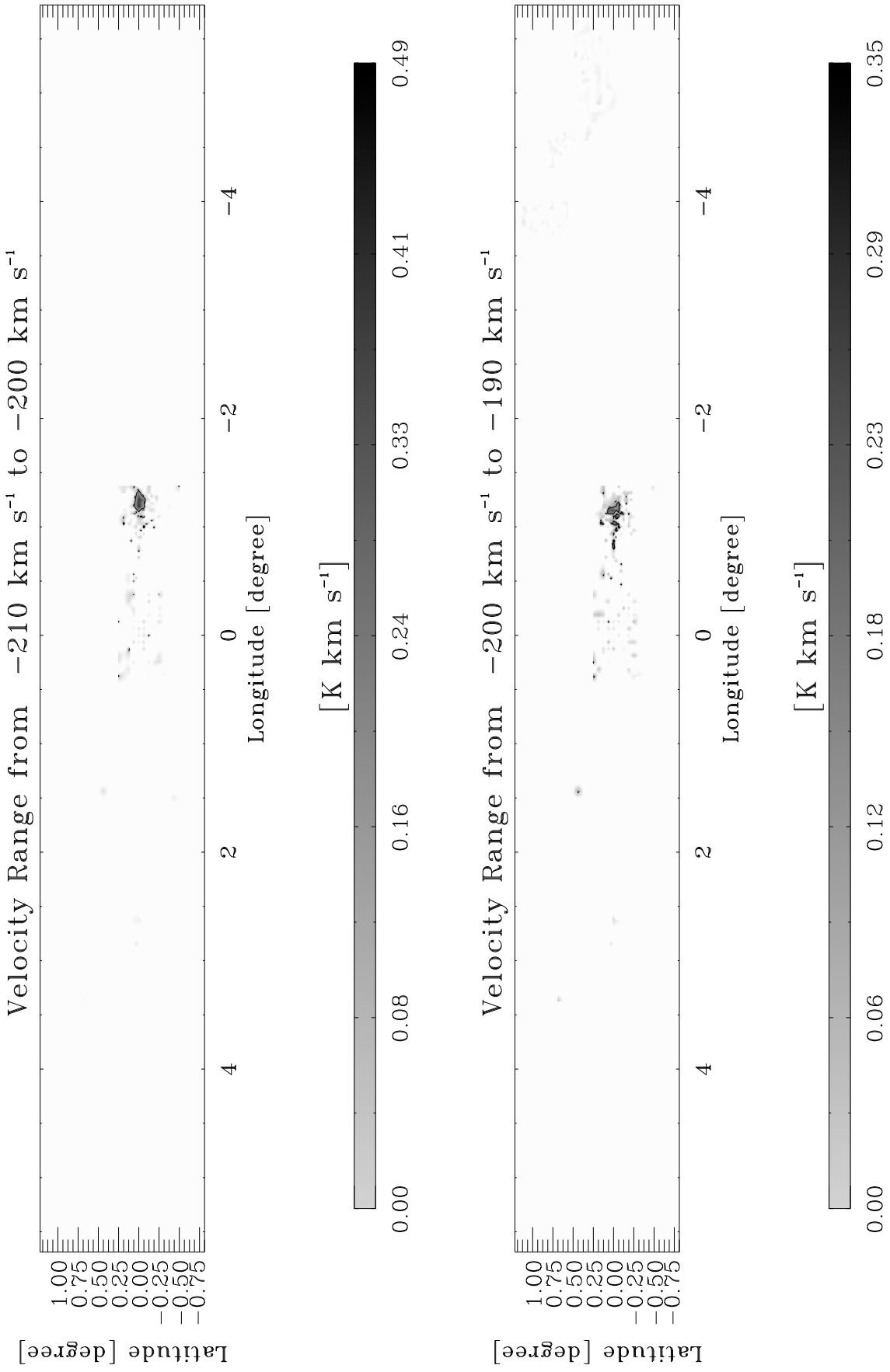

Fig. D1.3. continued.

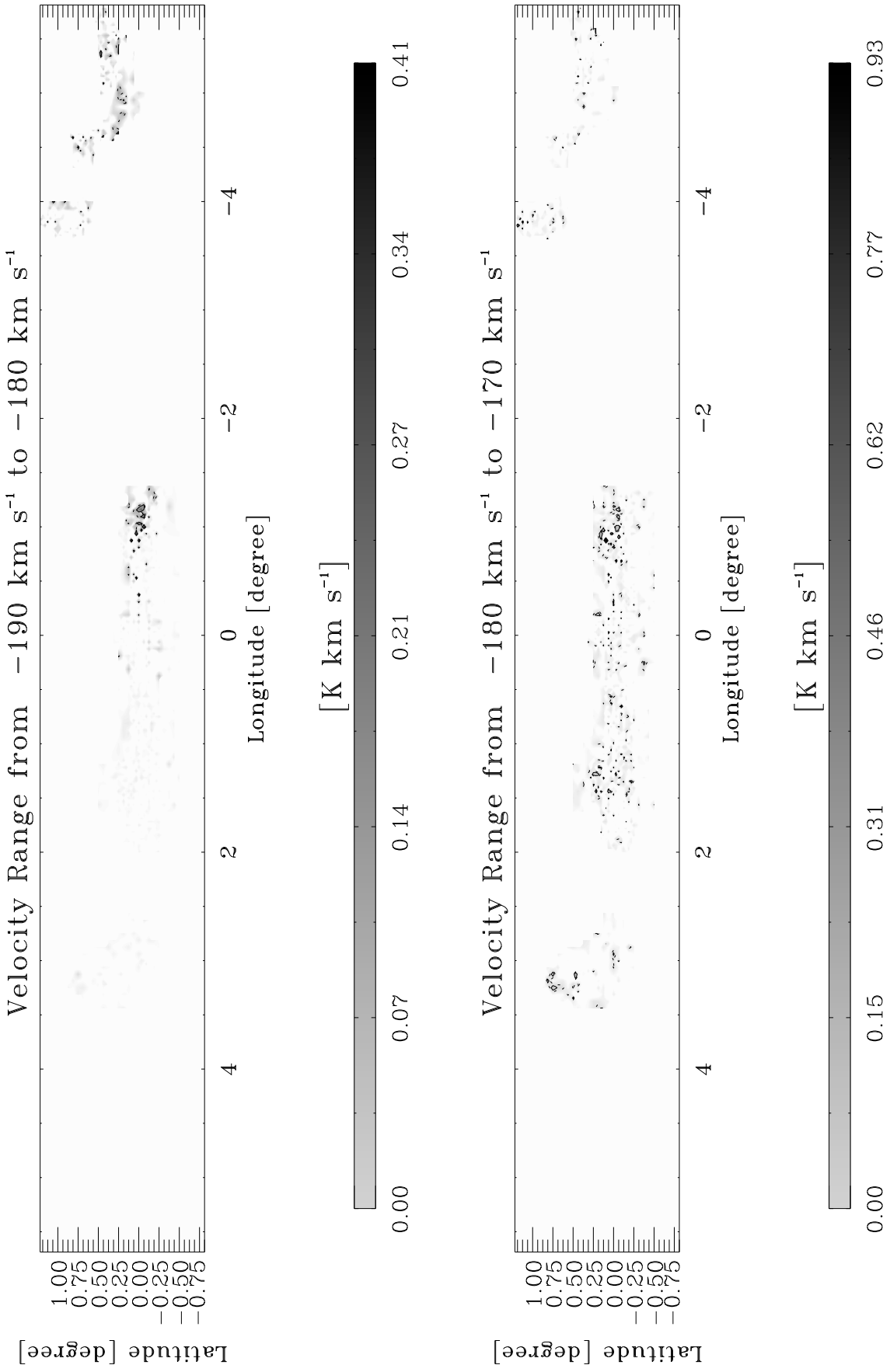

Fig. D1.4. continued.

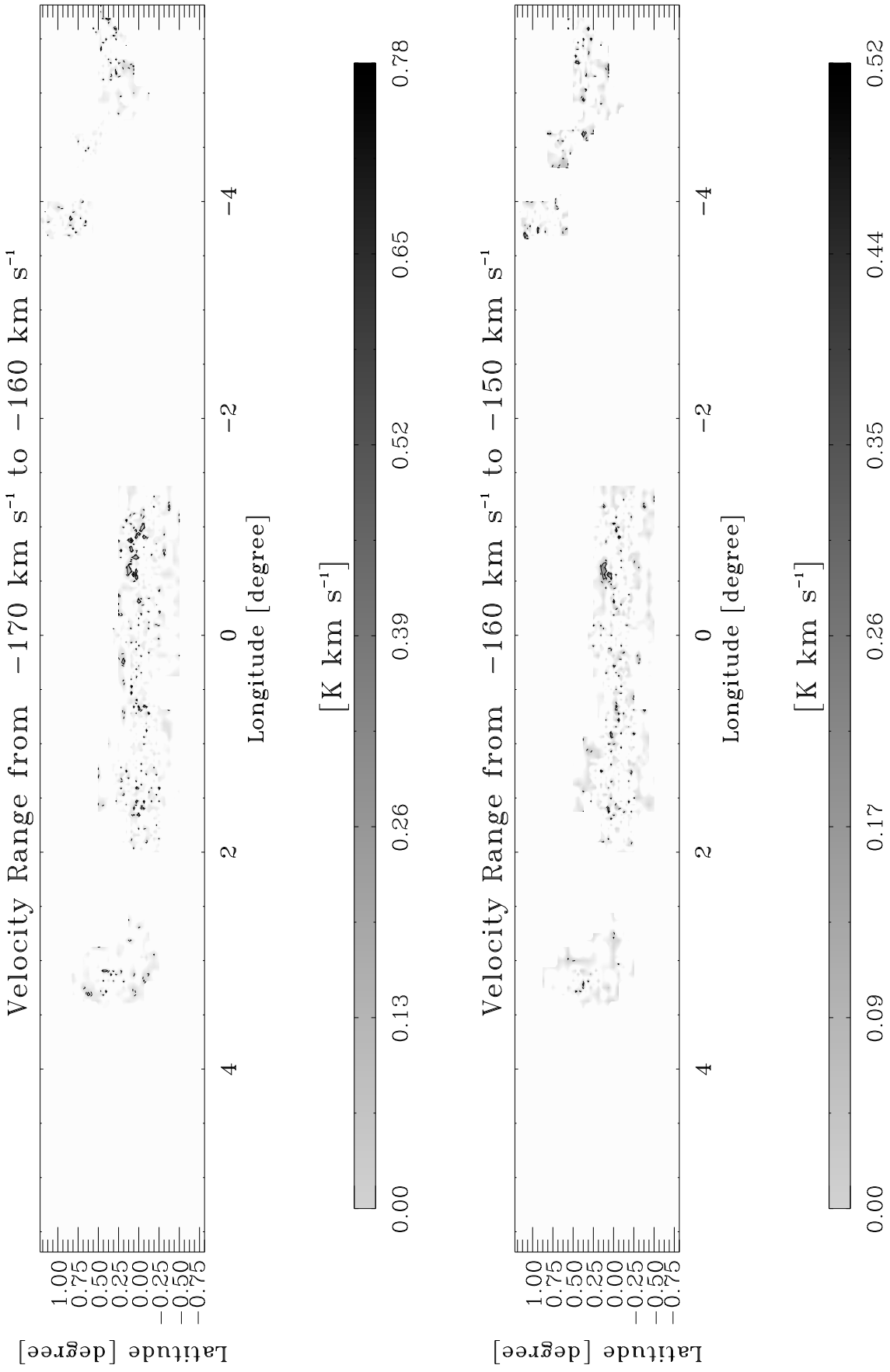

Fig. D1.5. continued.

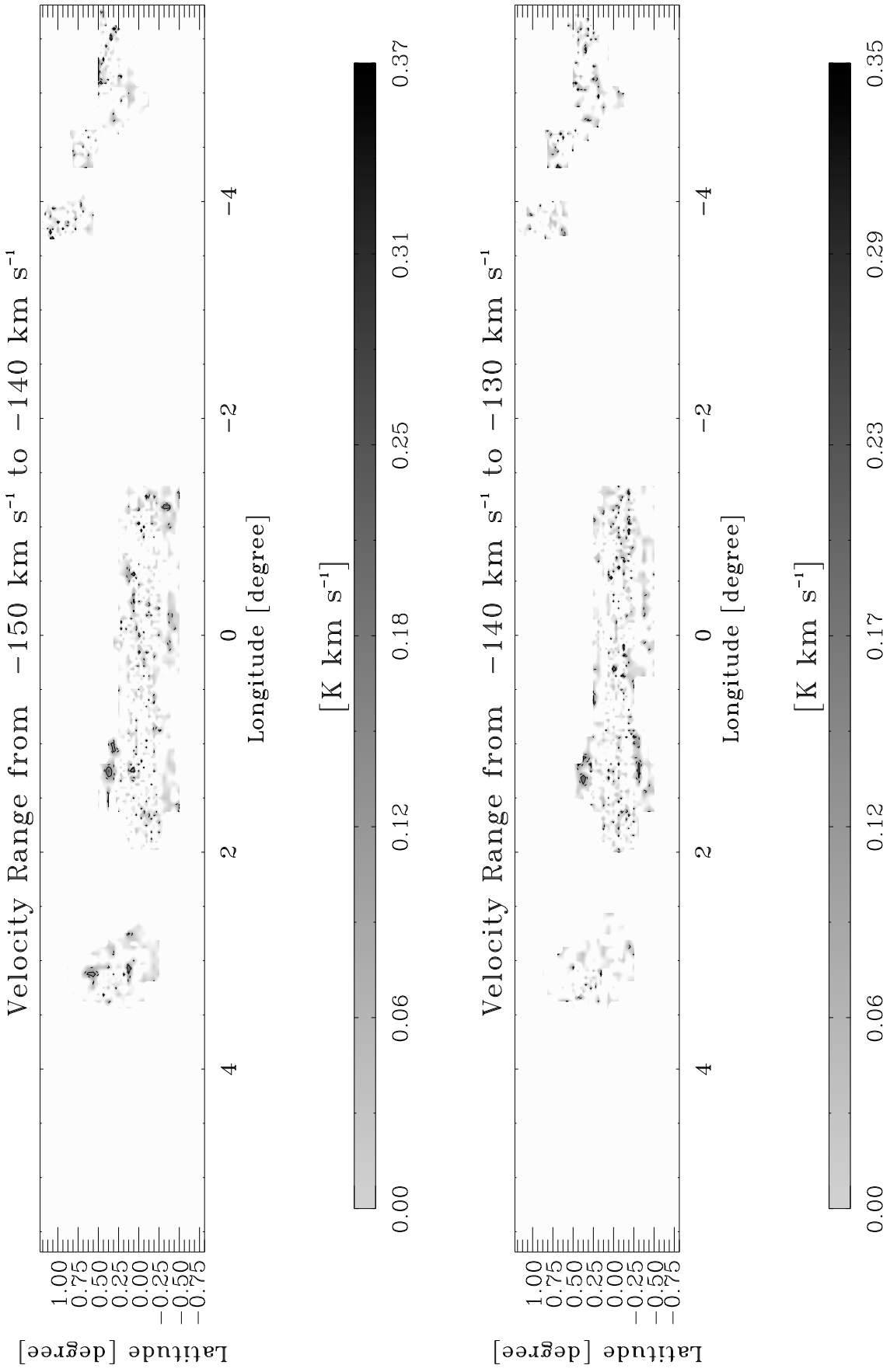

Fig. D1.6. continued.

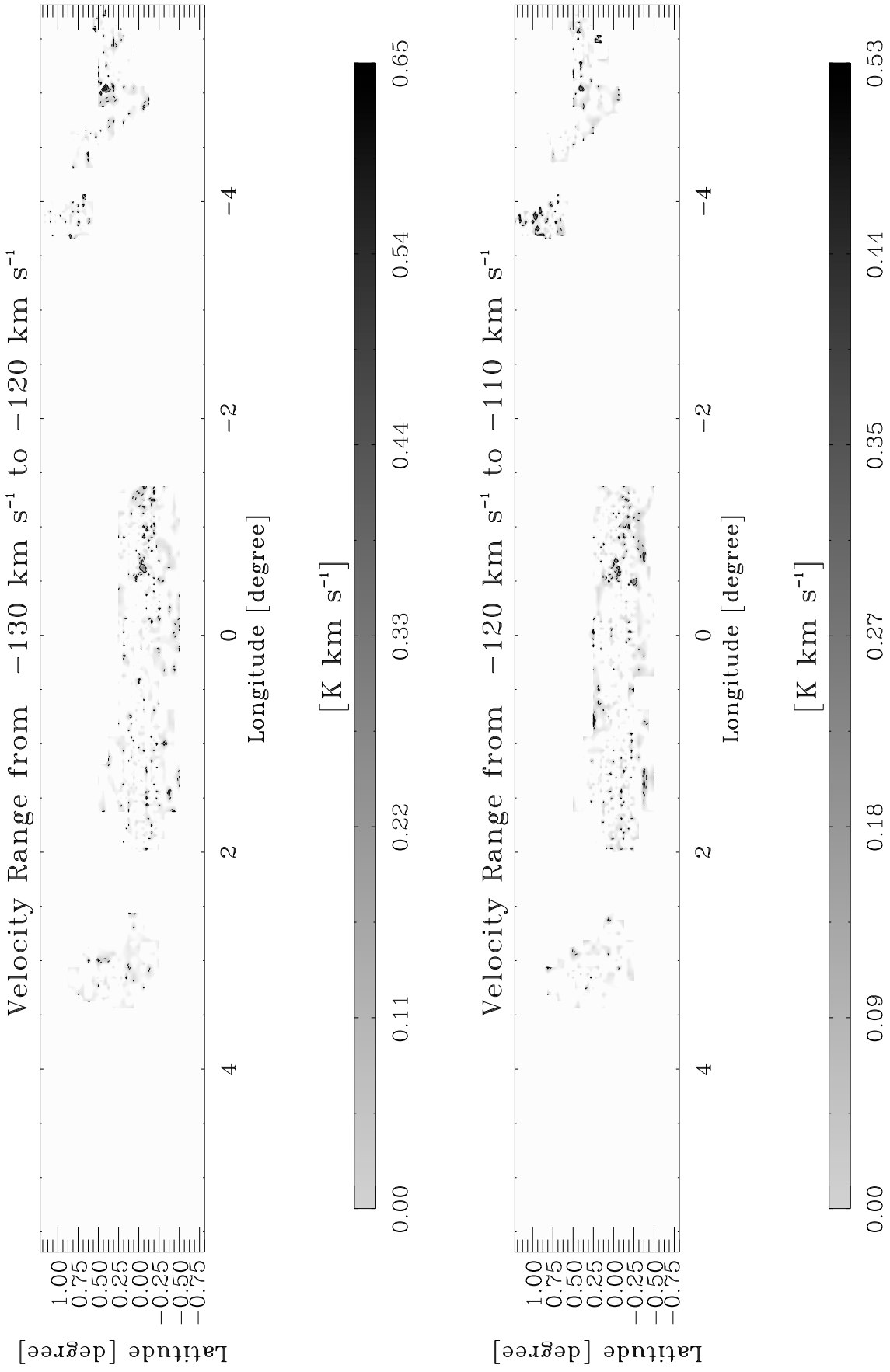

Fig. D1.7. continued.

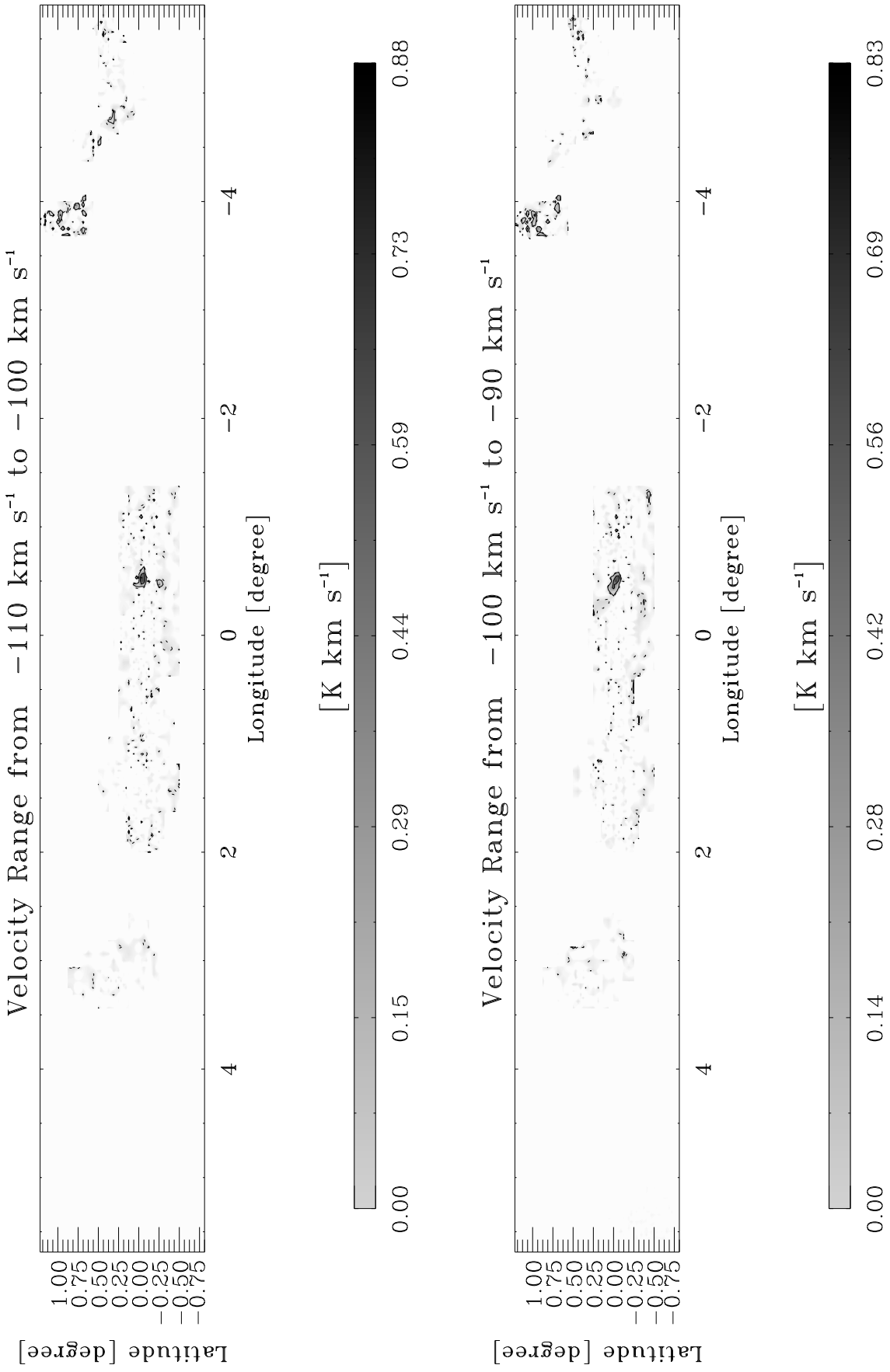

Fig. D1.8. continued.

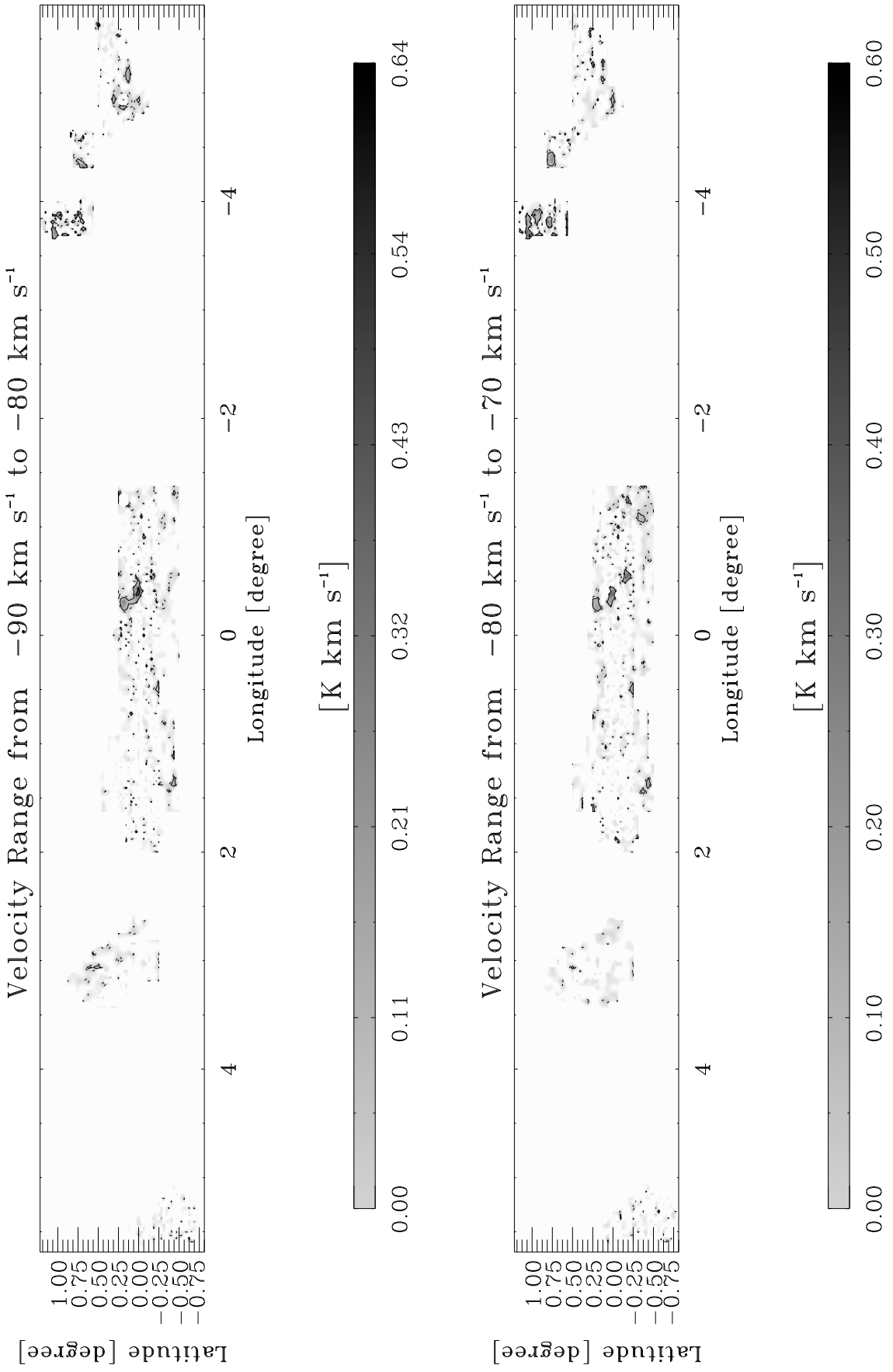

Fig. D1.9. continued.

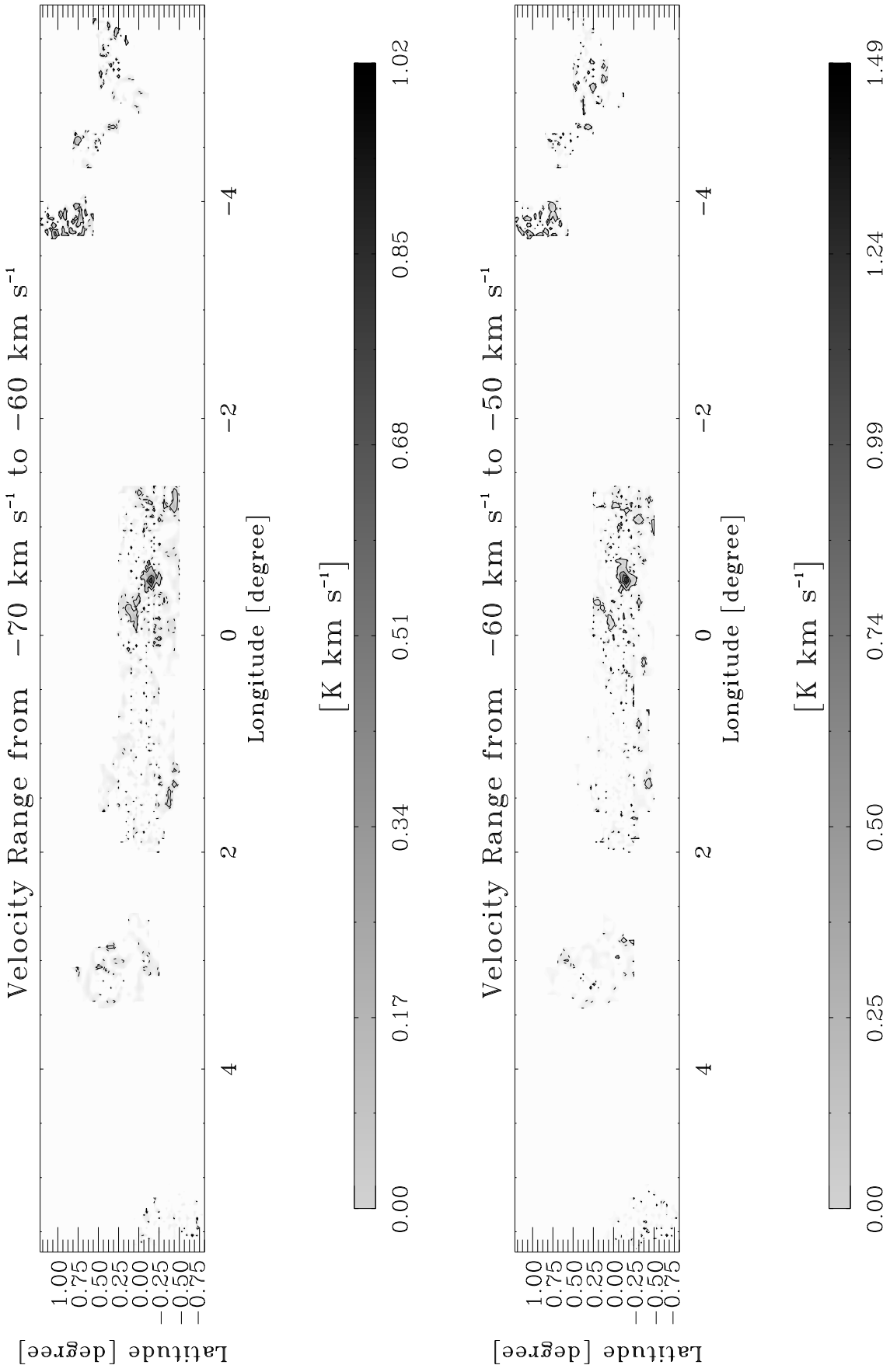

Fig. D1.10. continued.

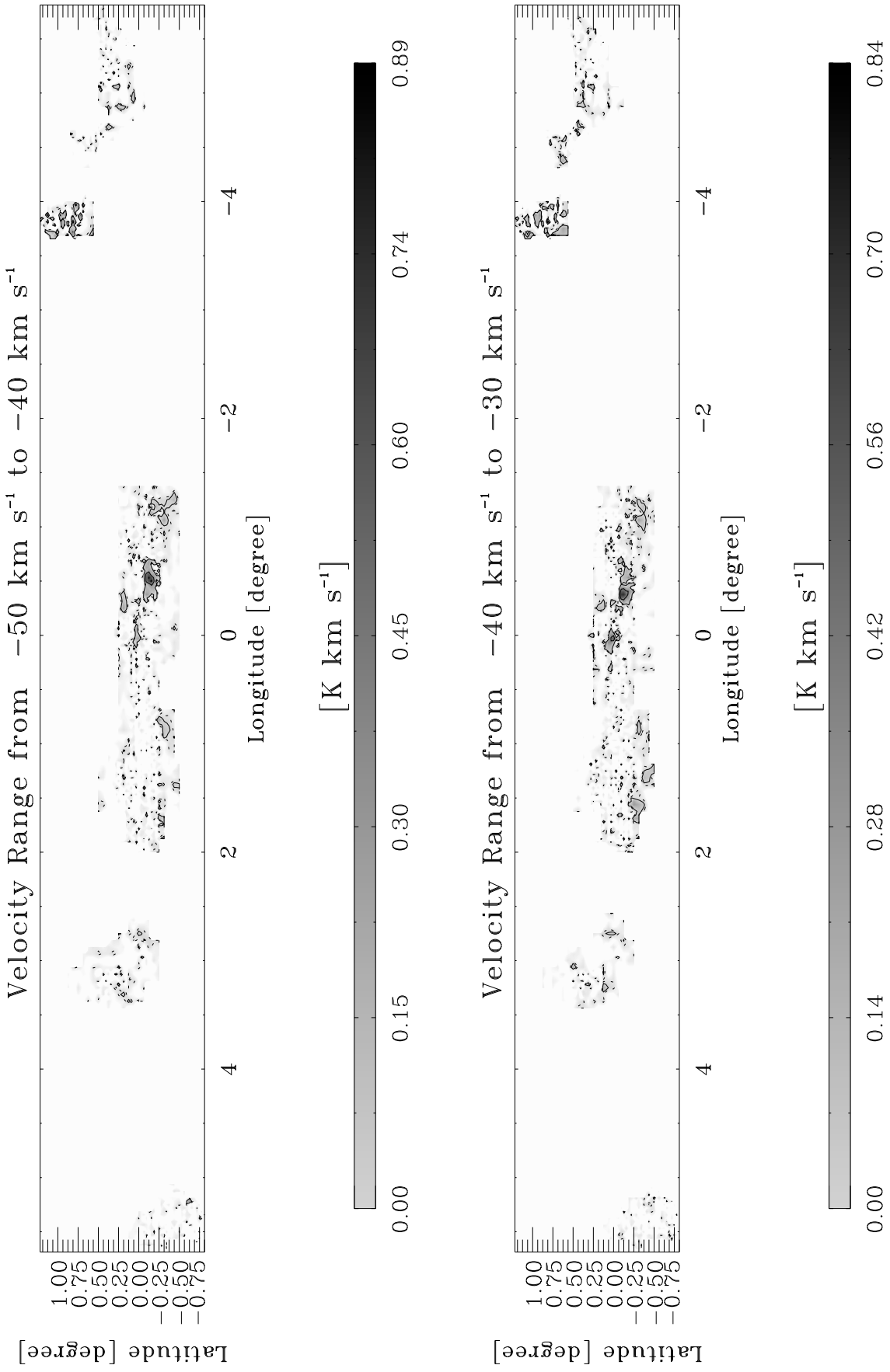

Fig. D1.11. continued.

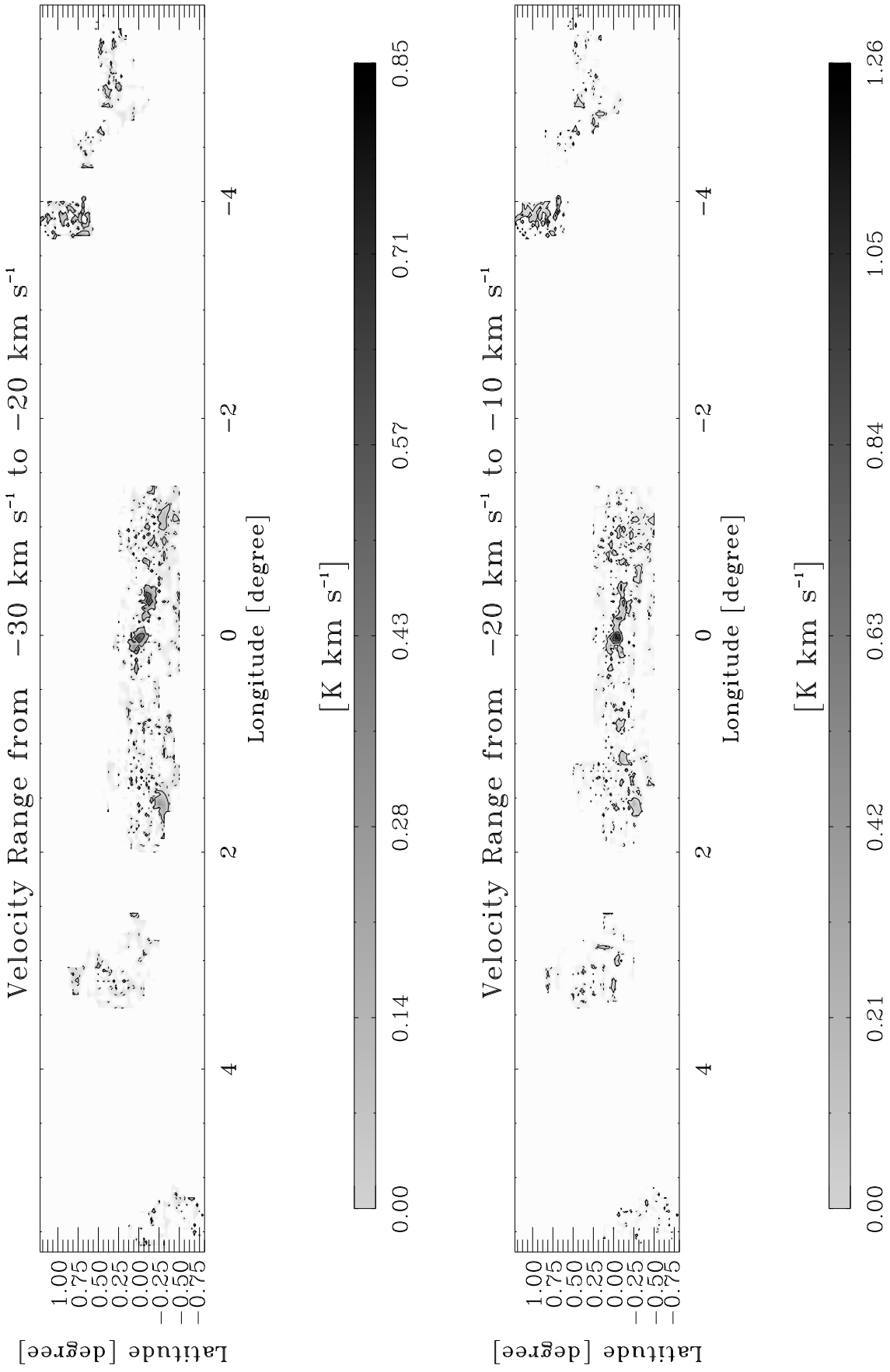

Fig. D1.12. continued.

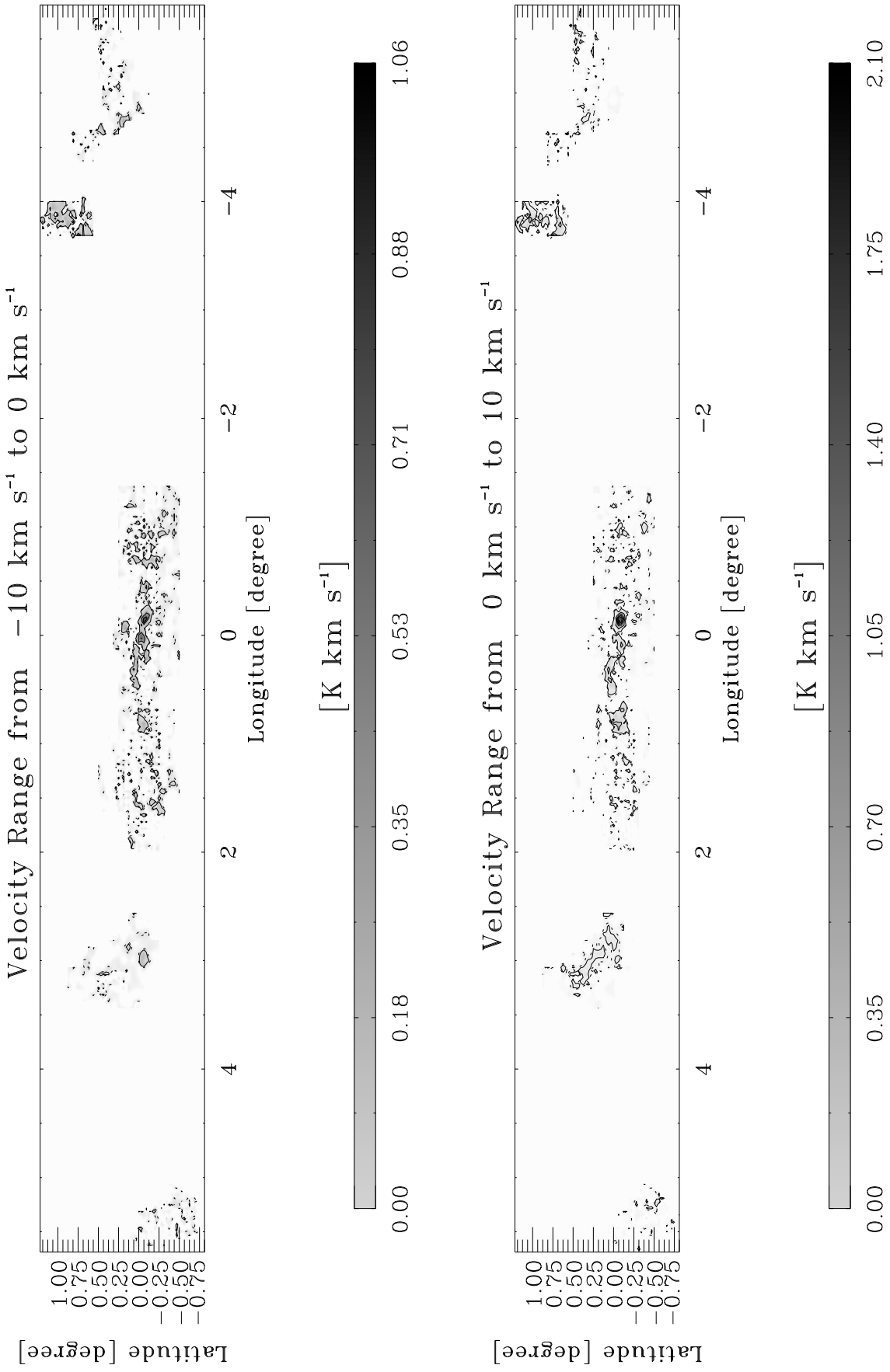

Fig. D1.13. continued.

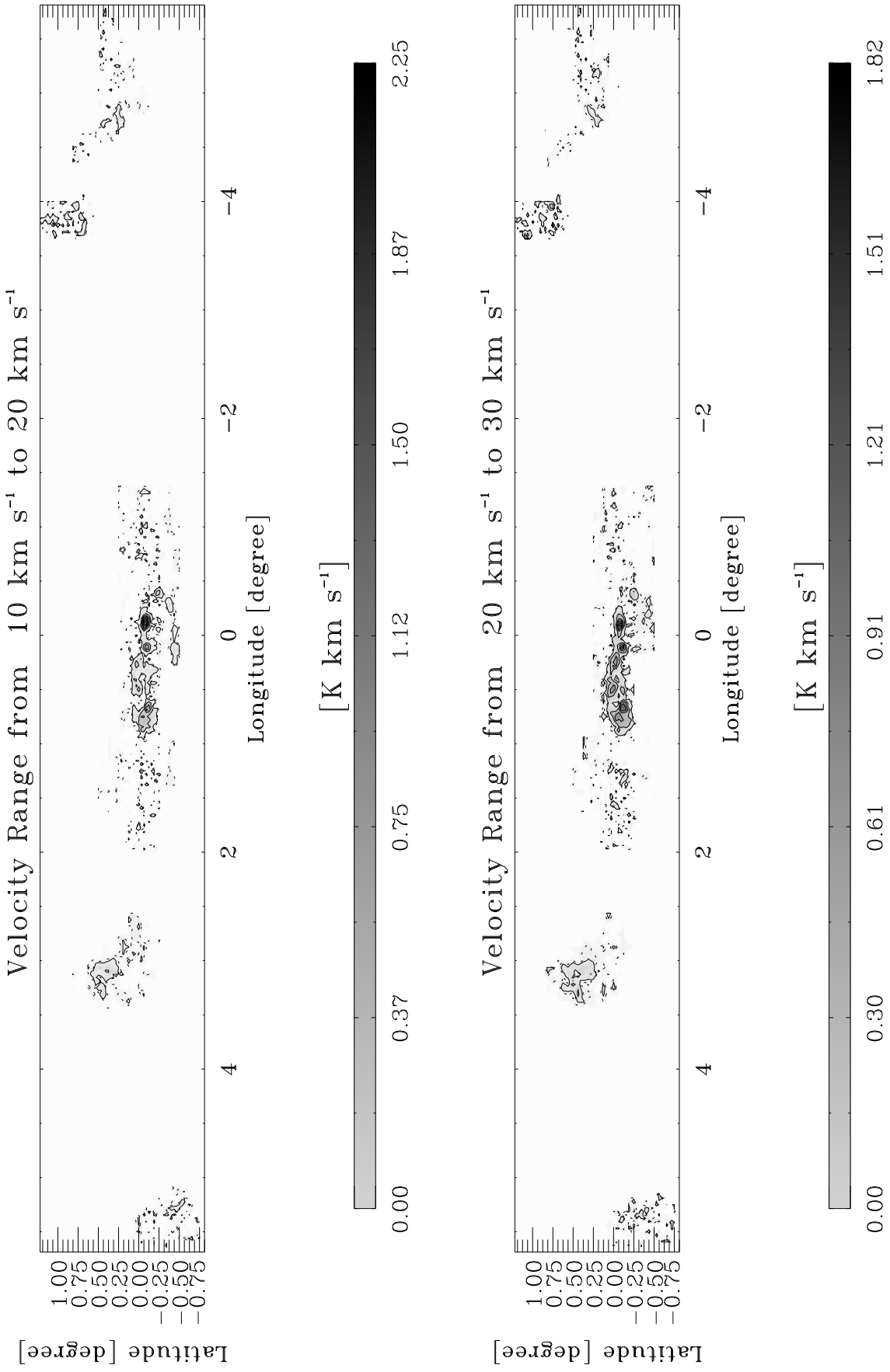

Fig. D1.14. continued.

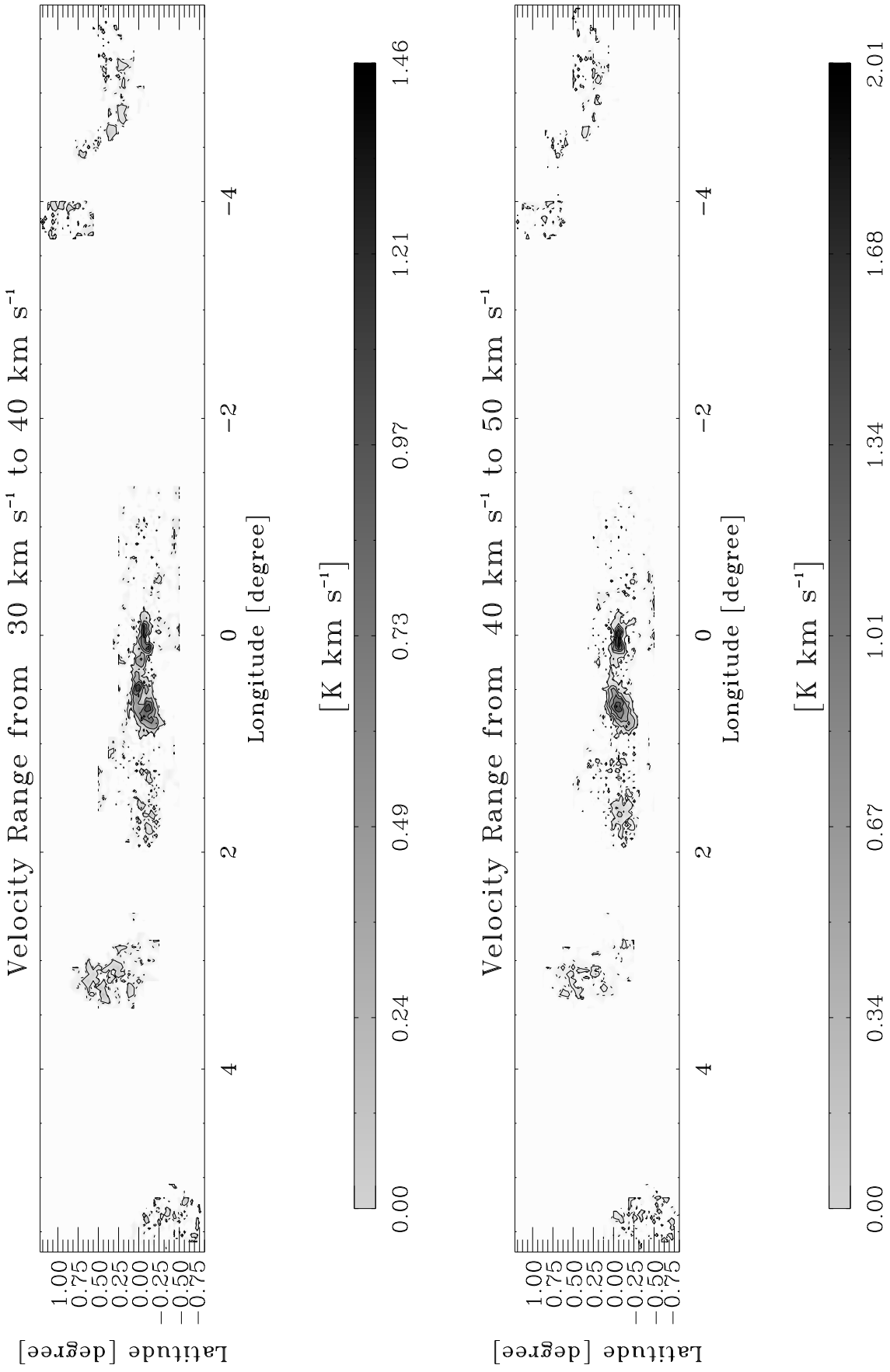

Fig. D1.15. continued.

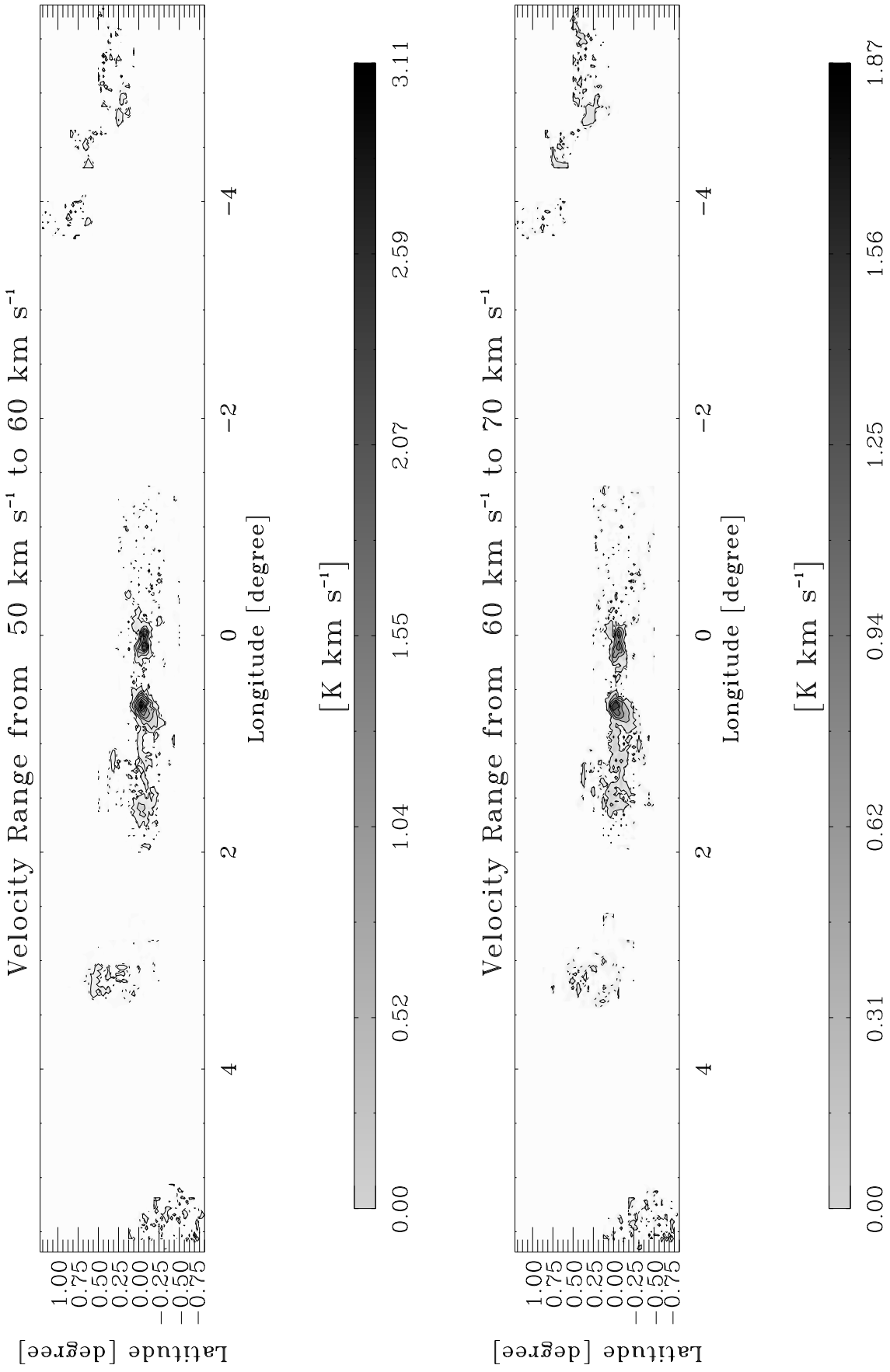

Fig. D1.16. continued.

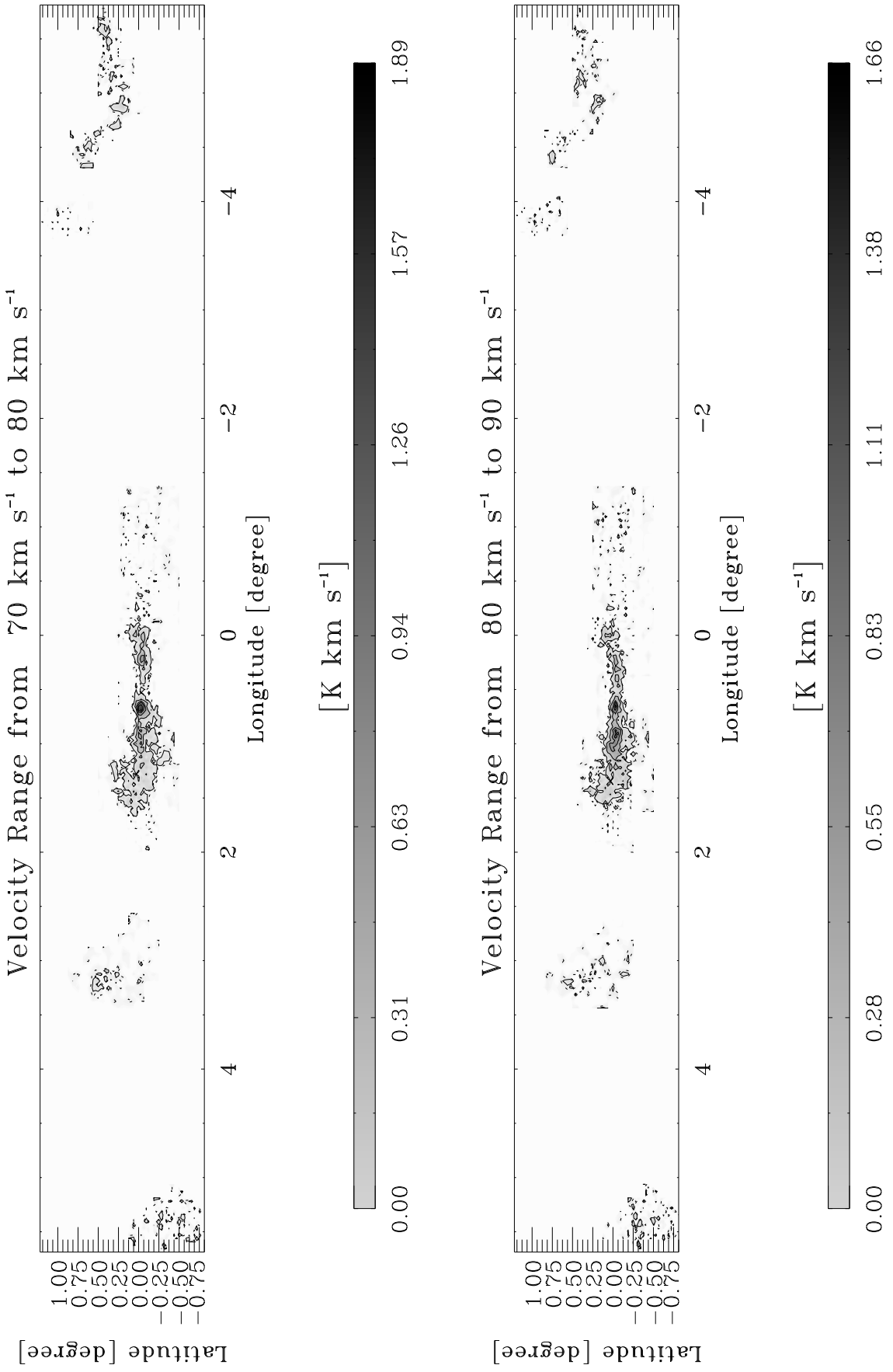

Fig. D1.17. continued.

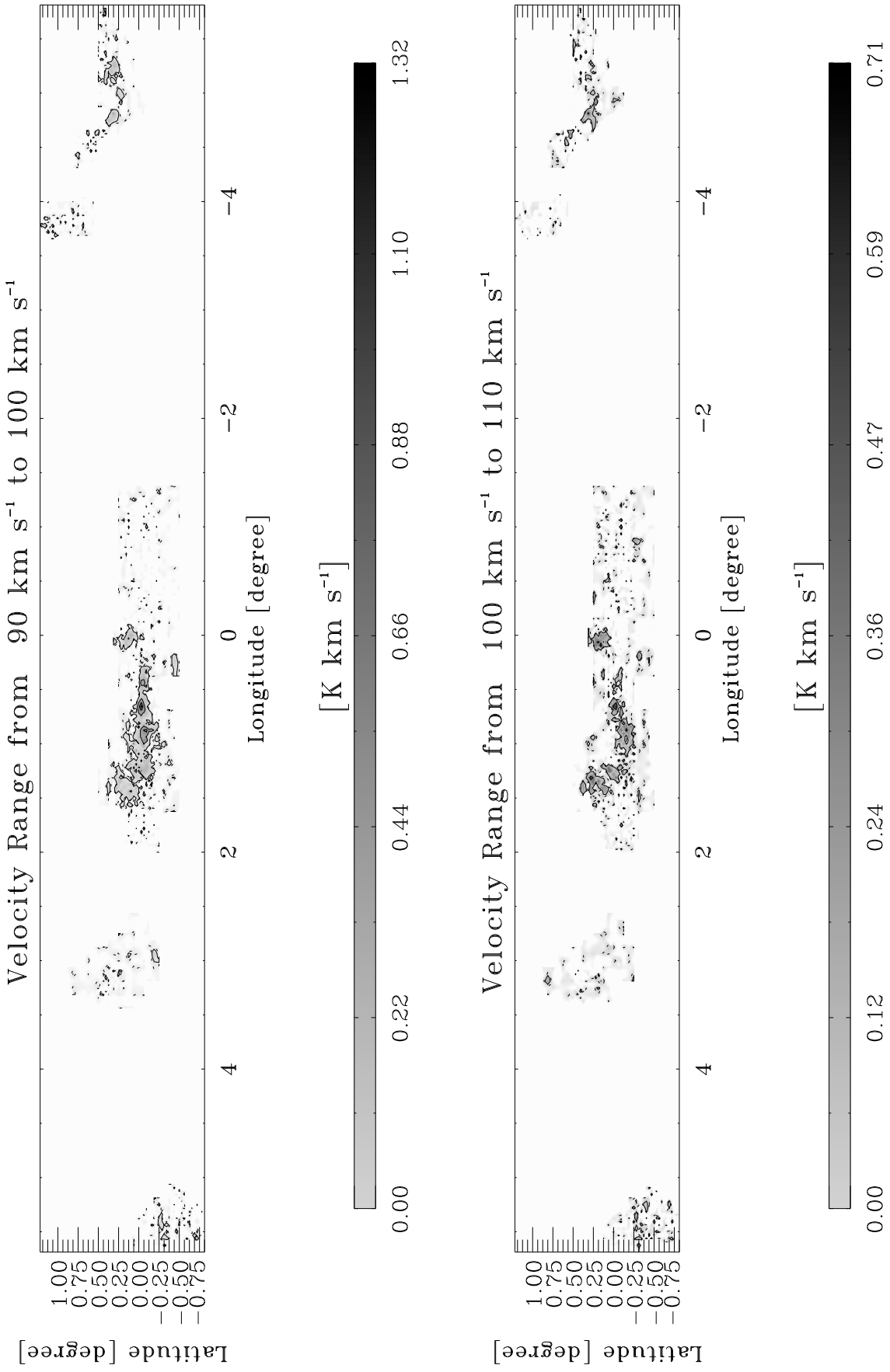

Fig. D1.18. continued.

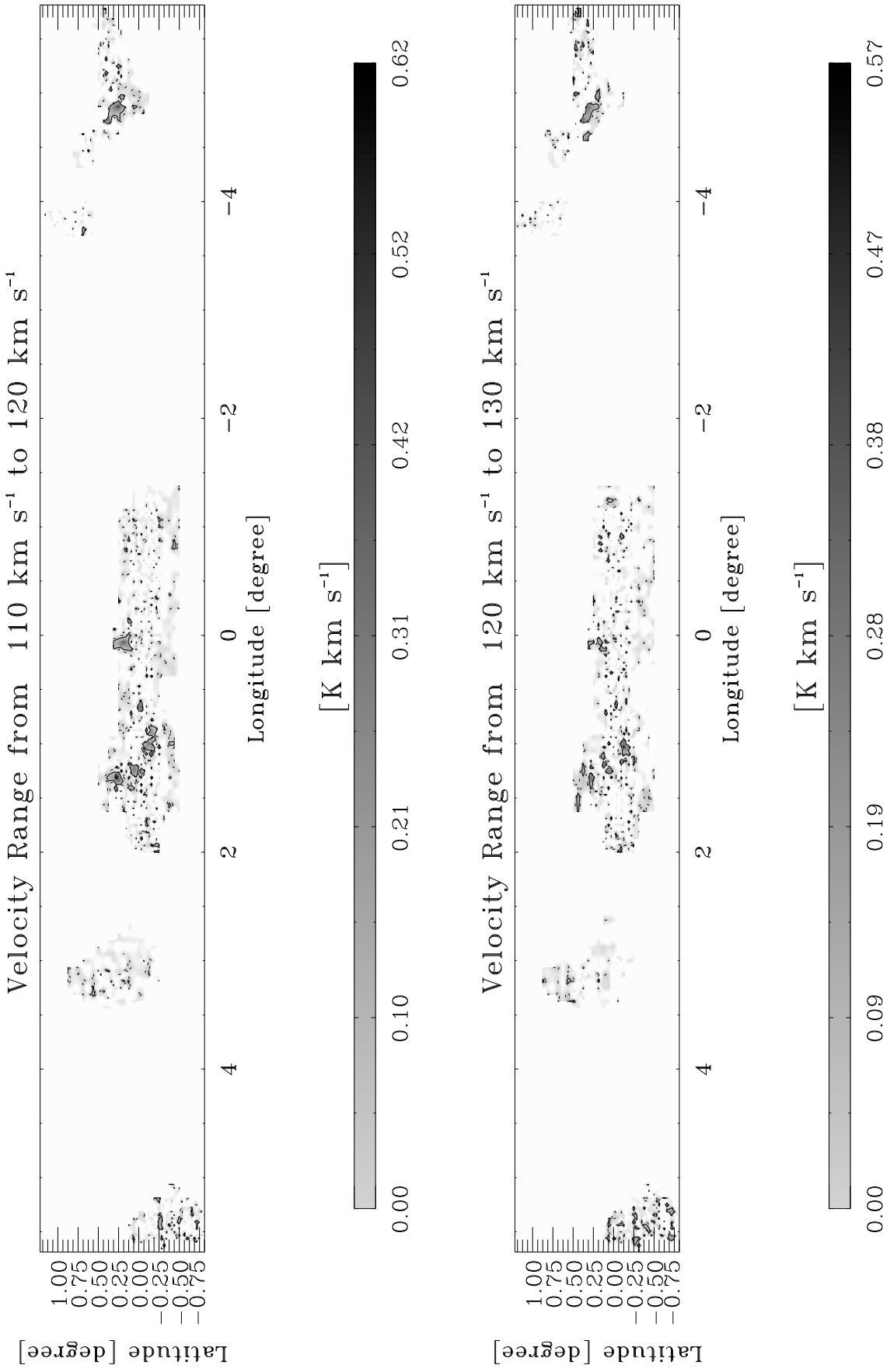

Fig. D1.19. continued.

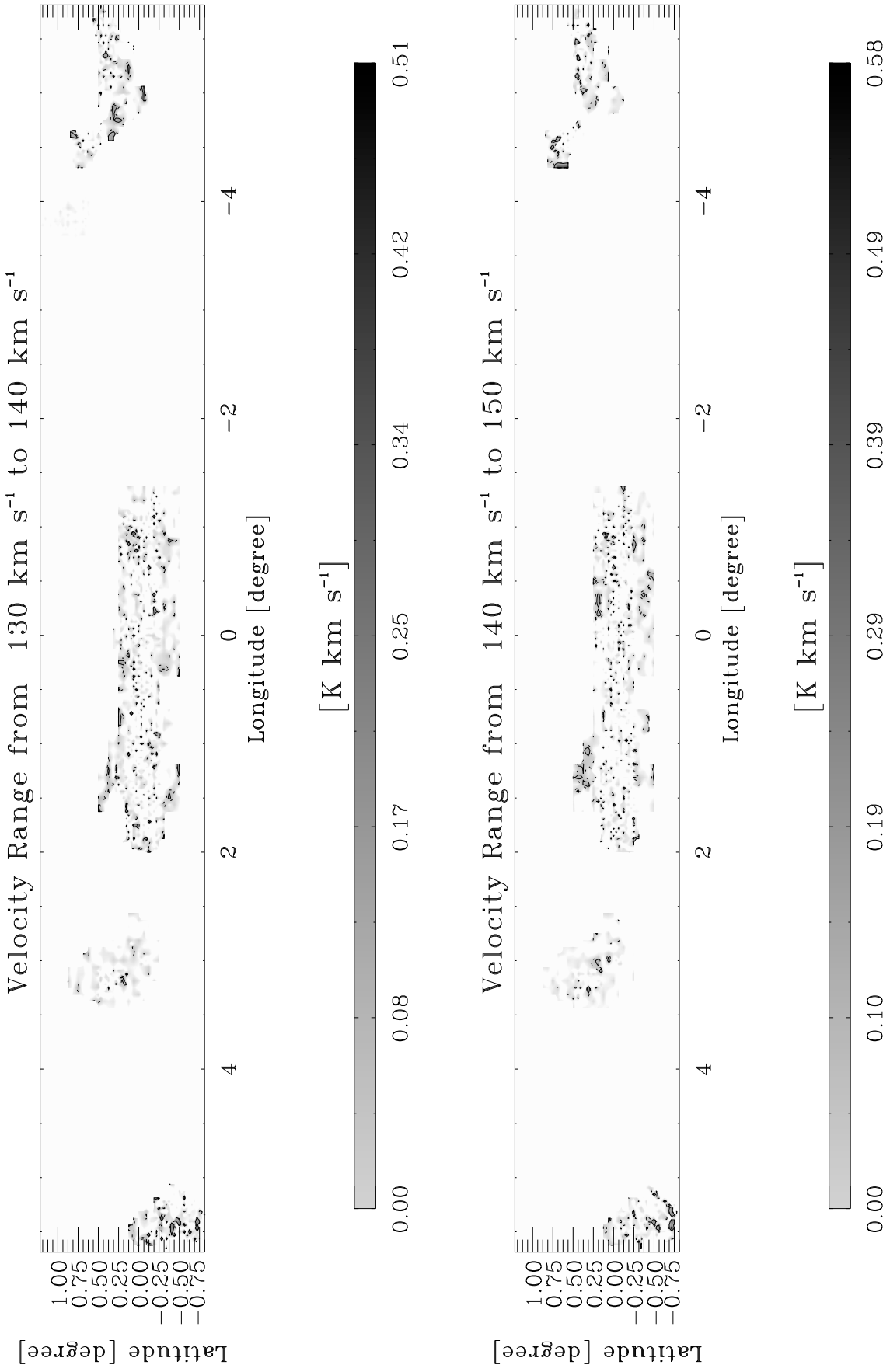

Fig. D1.20. continued.

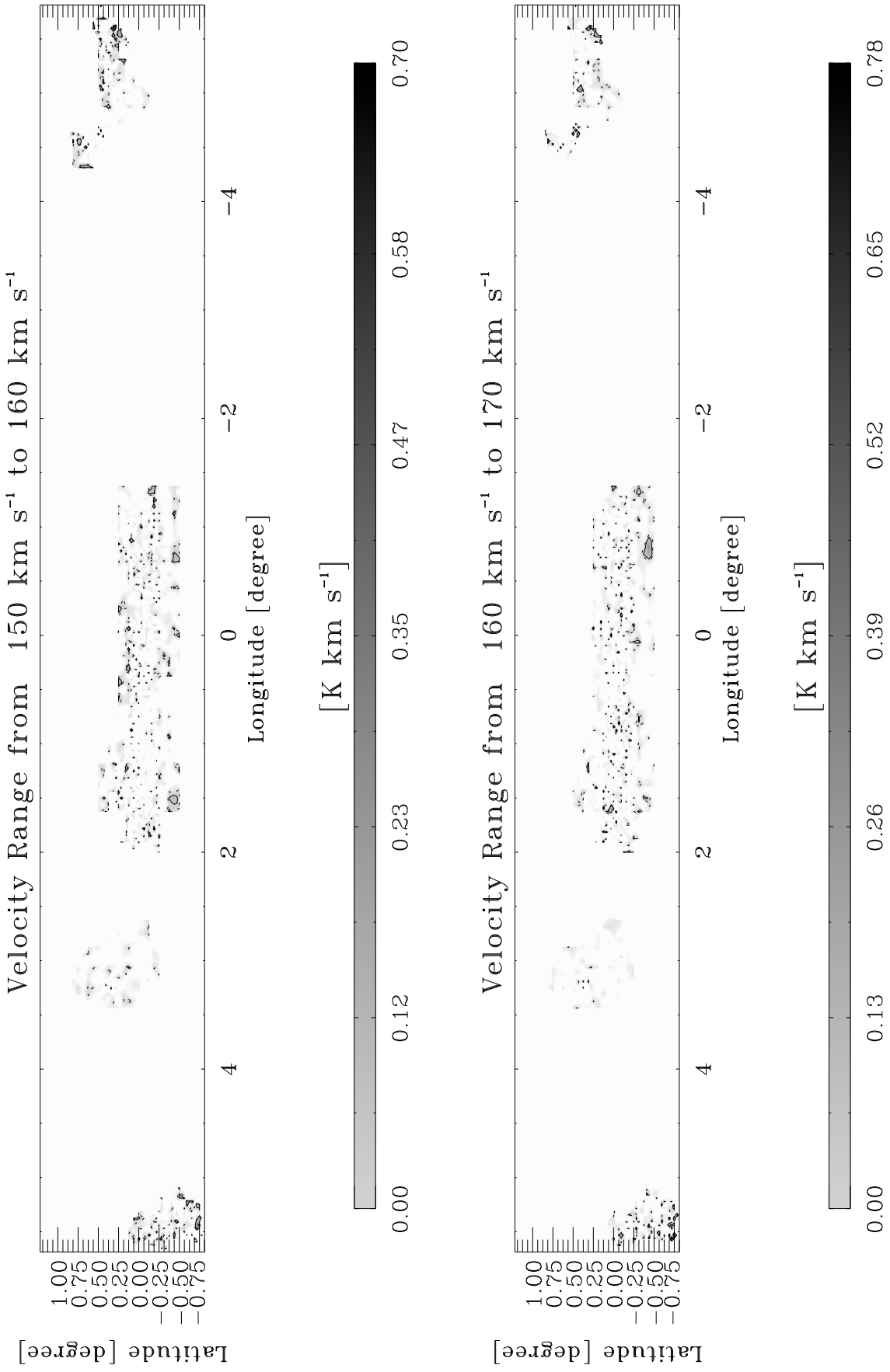

Fig. D1.21. continued.

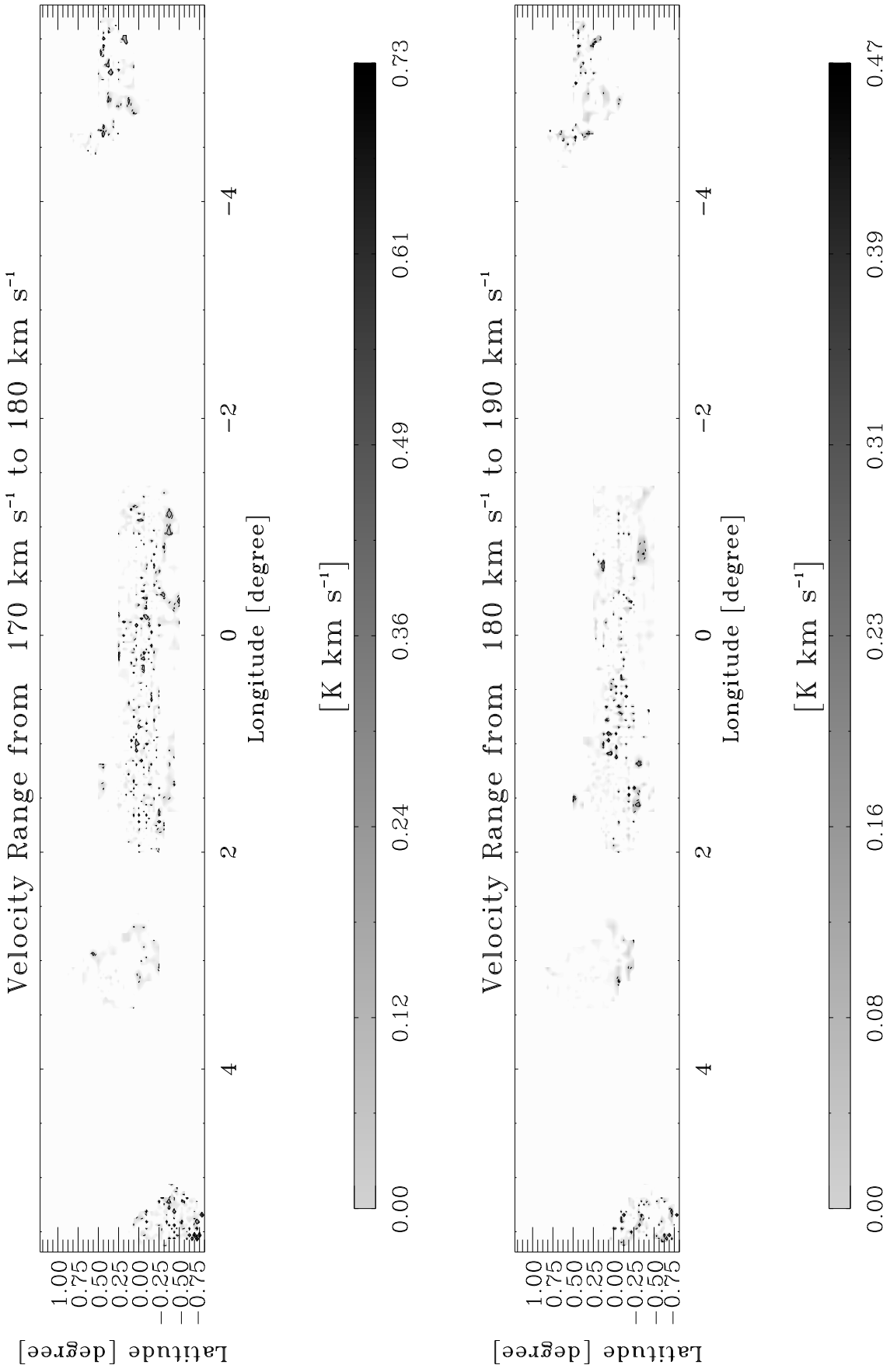

Fig. D1.22. continued.

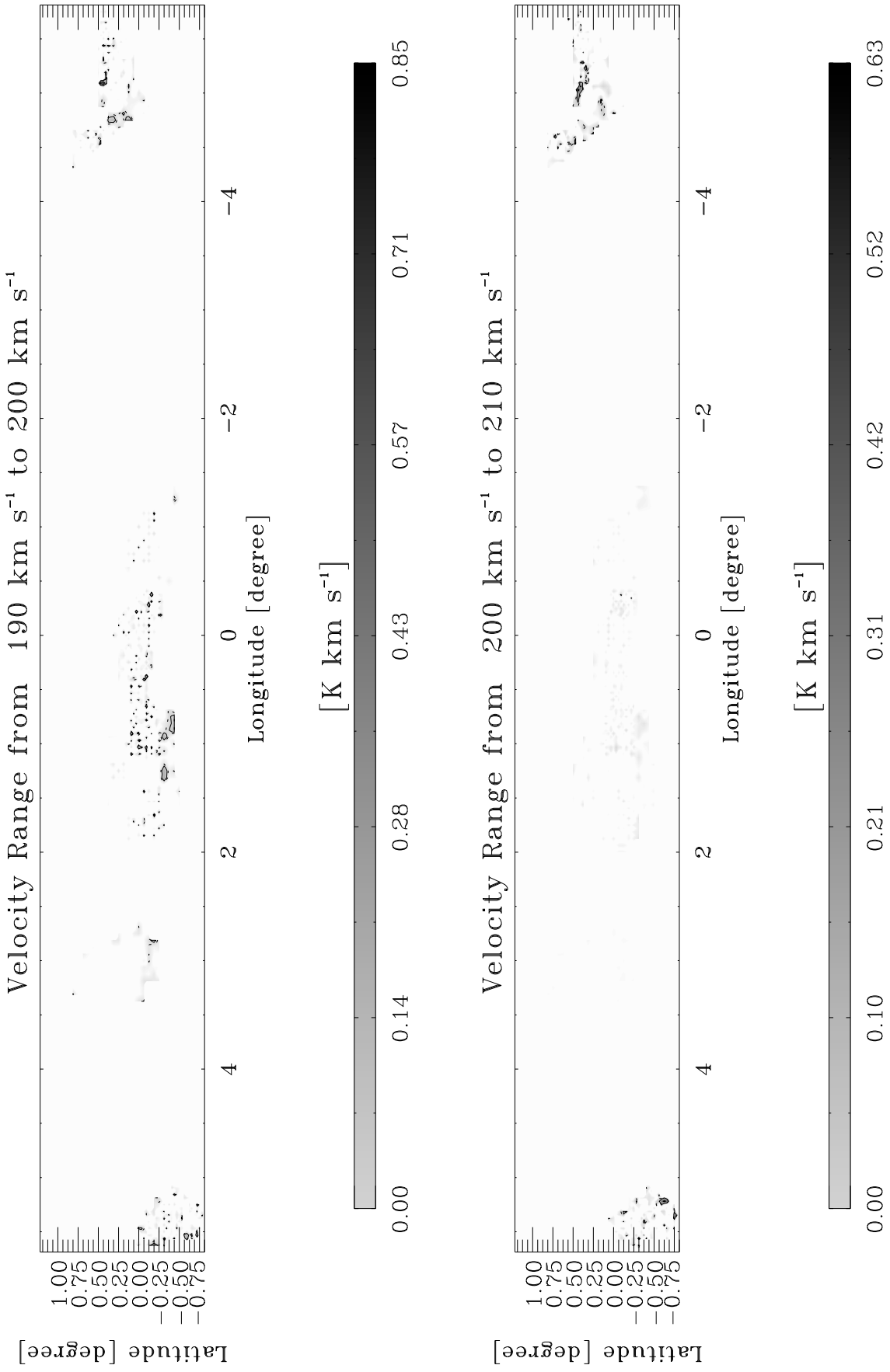

Fig. D1.23. continued.

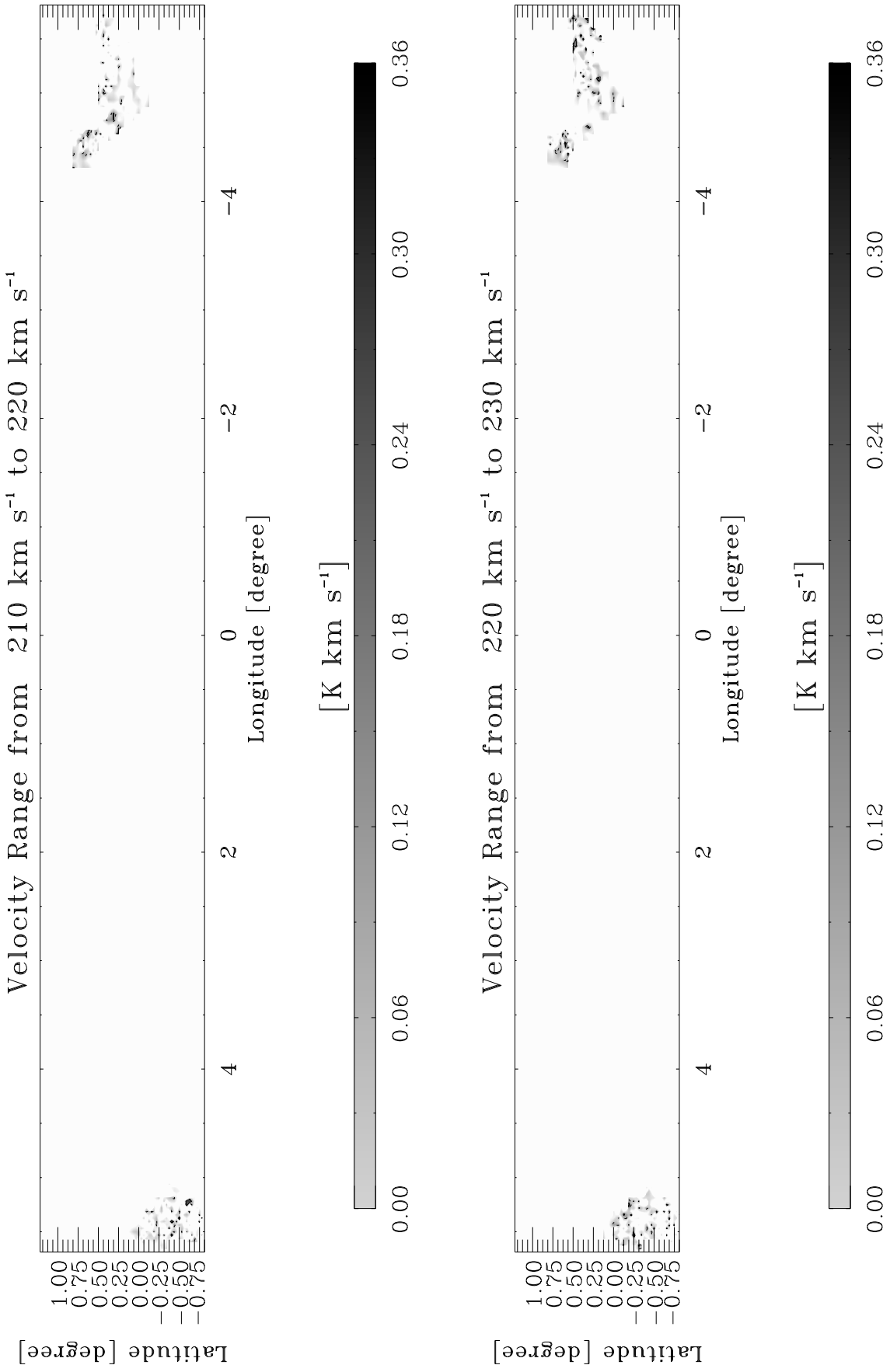

Fig. D1.24. continued.

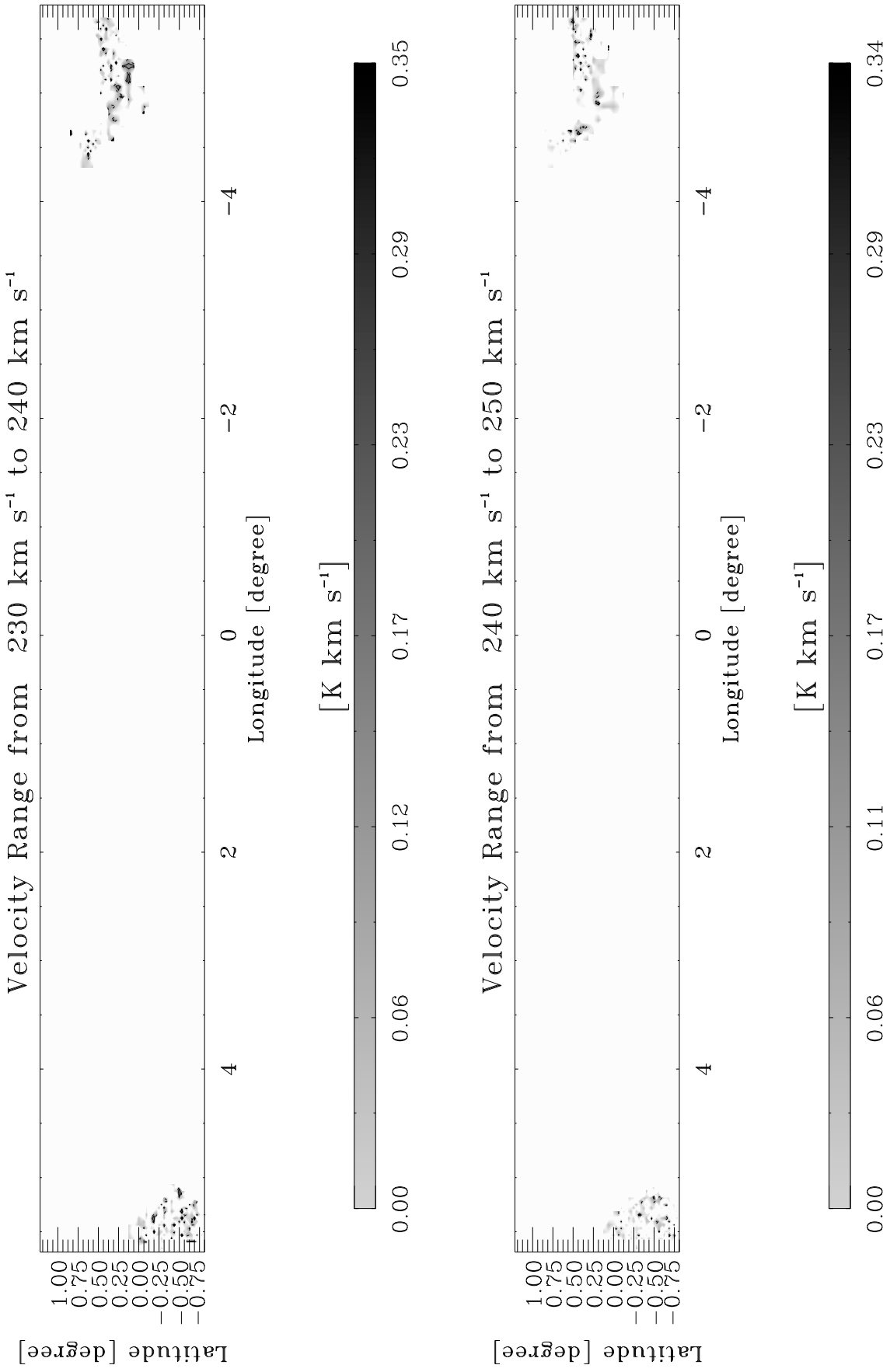

Fig. D1.25. continued.

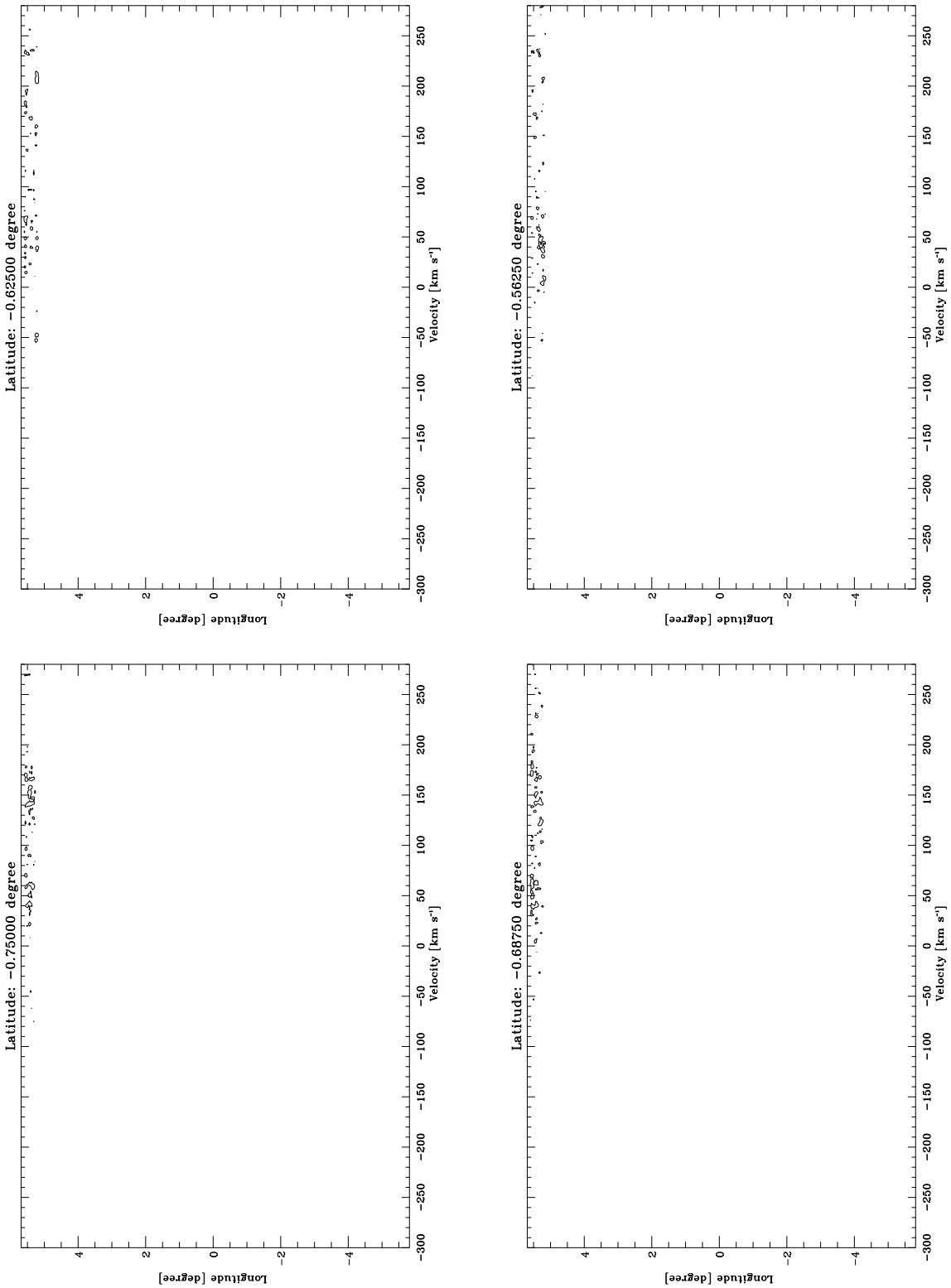

Fig. D2.1. Longitude-velocidad contour diagrams integrated in latitude in step of 0.0625 in H13CO+. The lowest contour is at 0.0013 K (3σ). The following contours increase them in step of 0.0018 K, which correspond to 4σ.

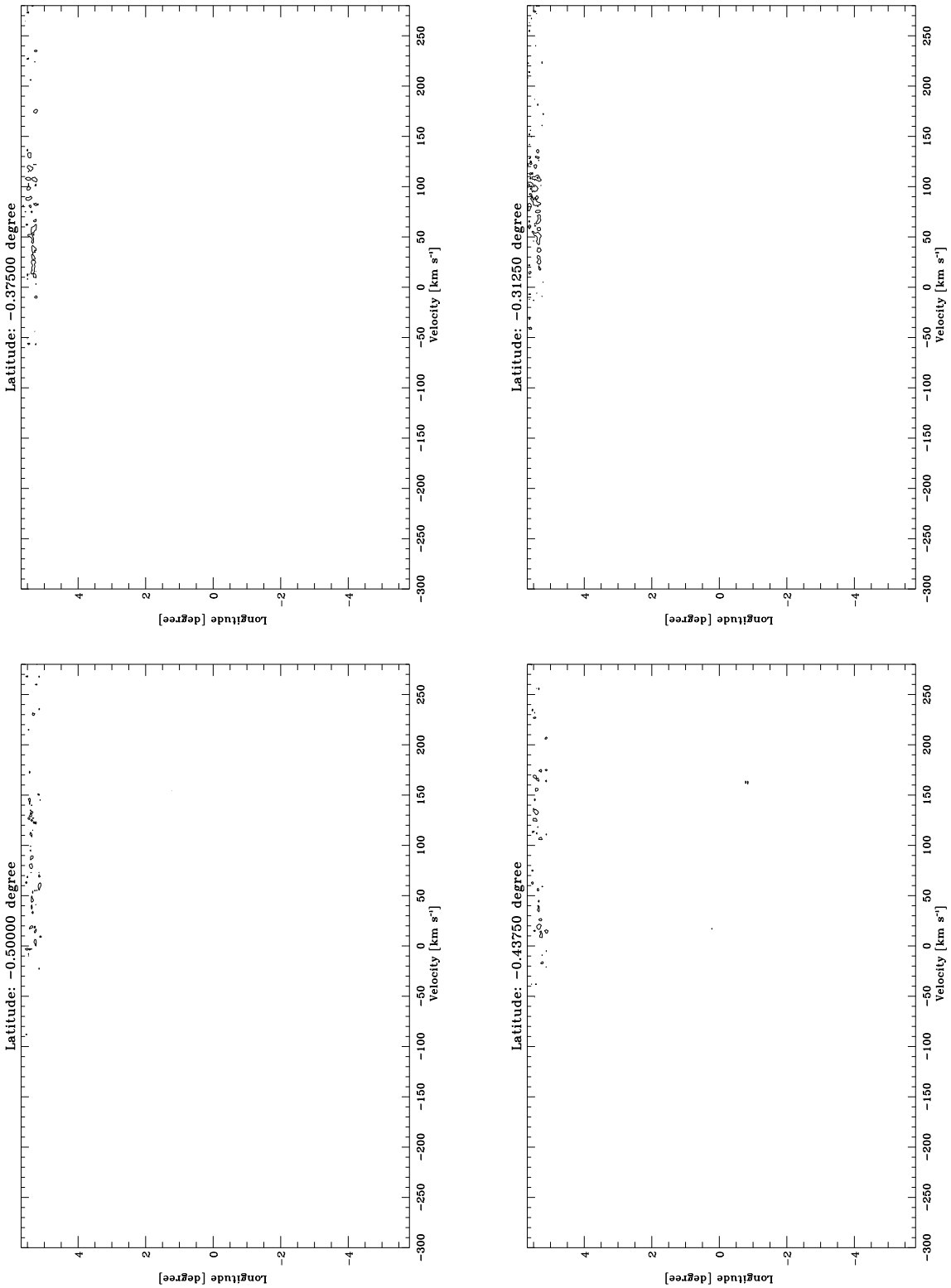

Fig. D2.2. continued.

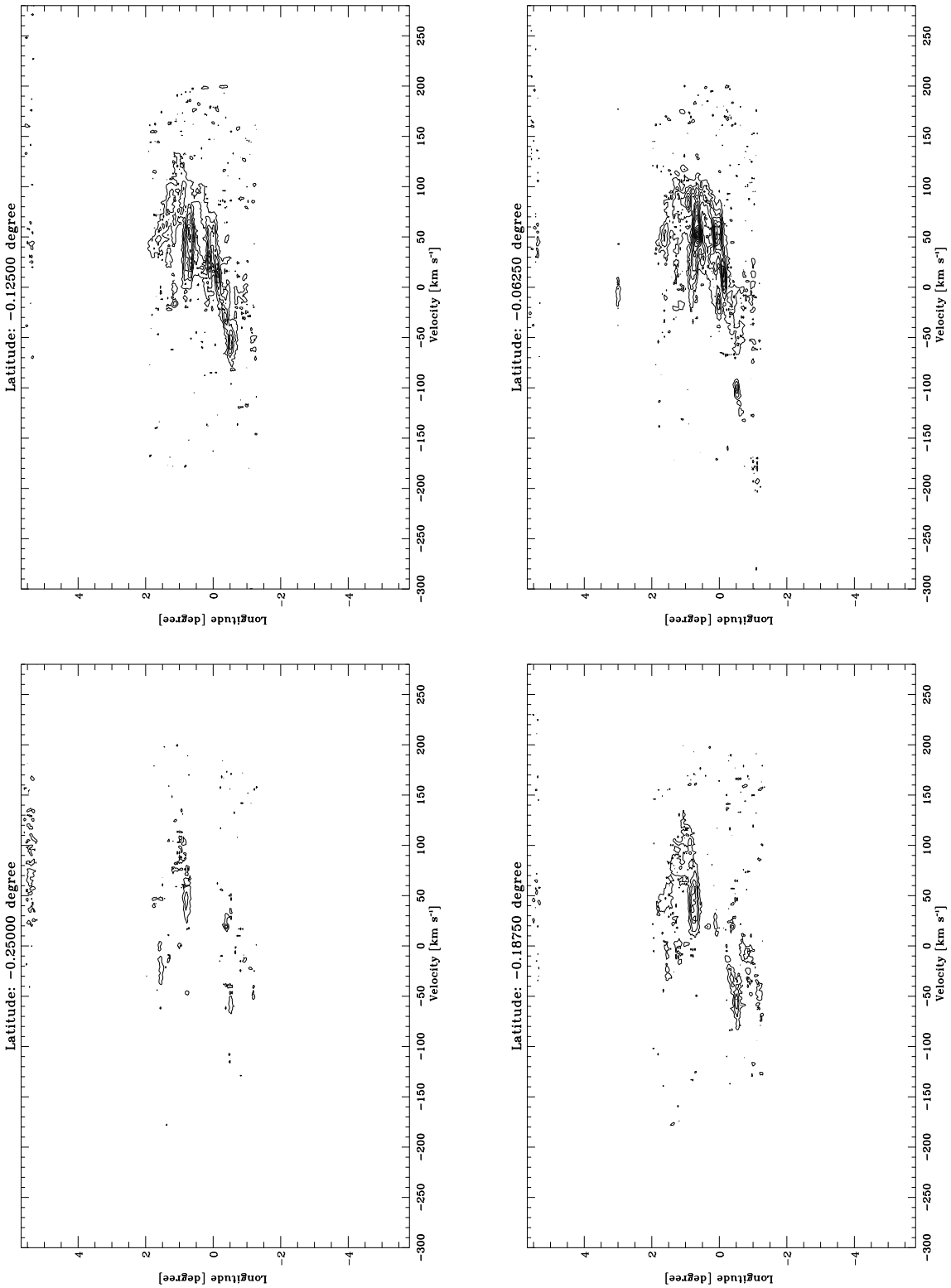

Fig. D2.3. continued.

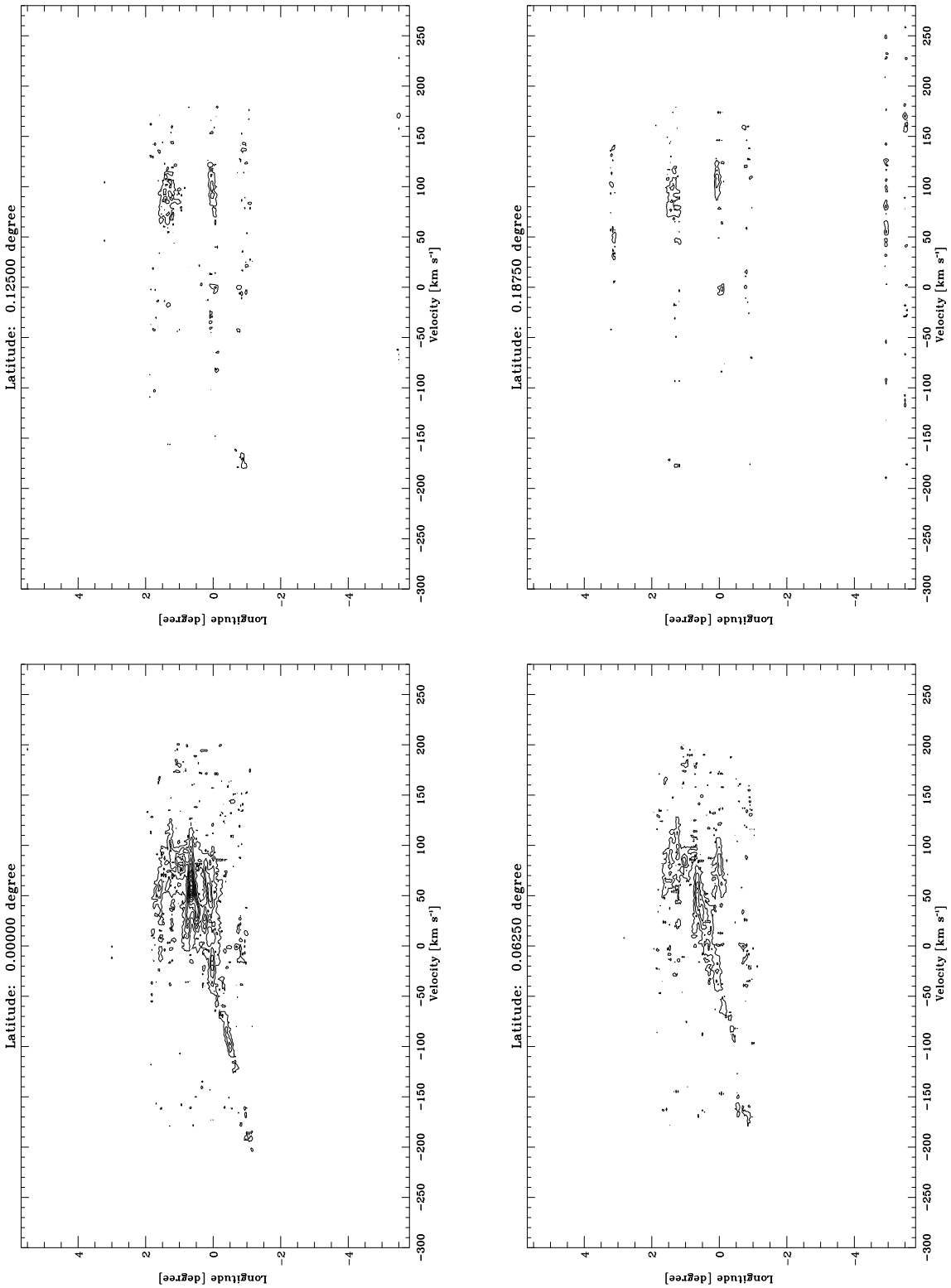

Fig. D2.4. continued.

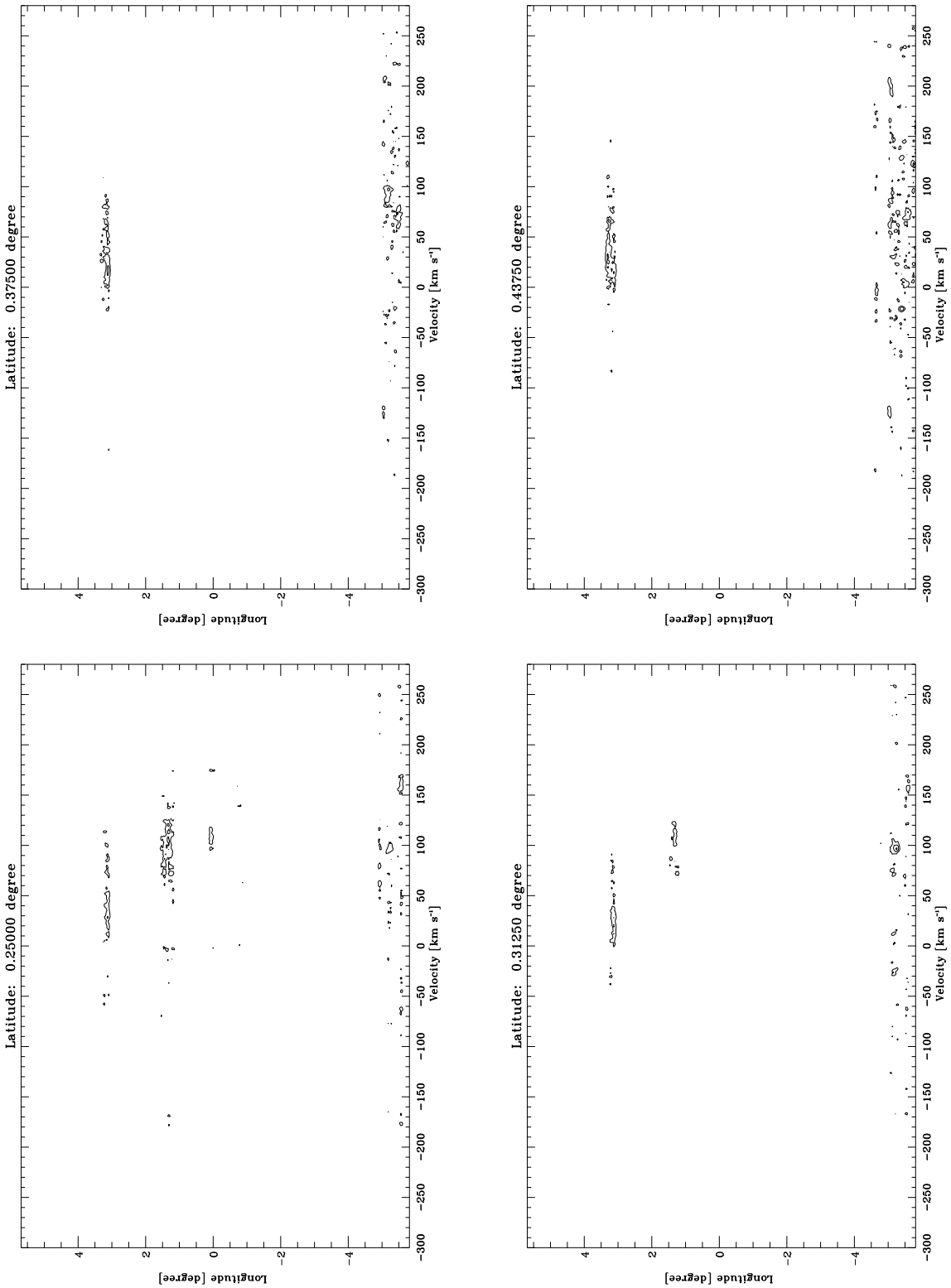

Fig. D2.5. continued.

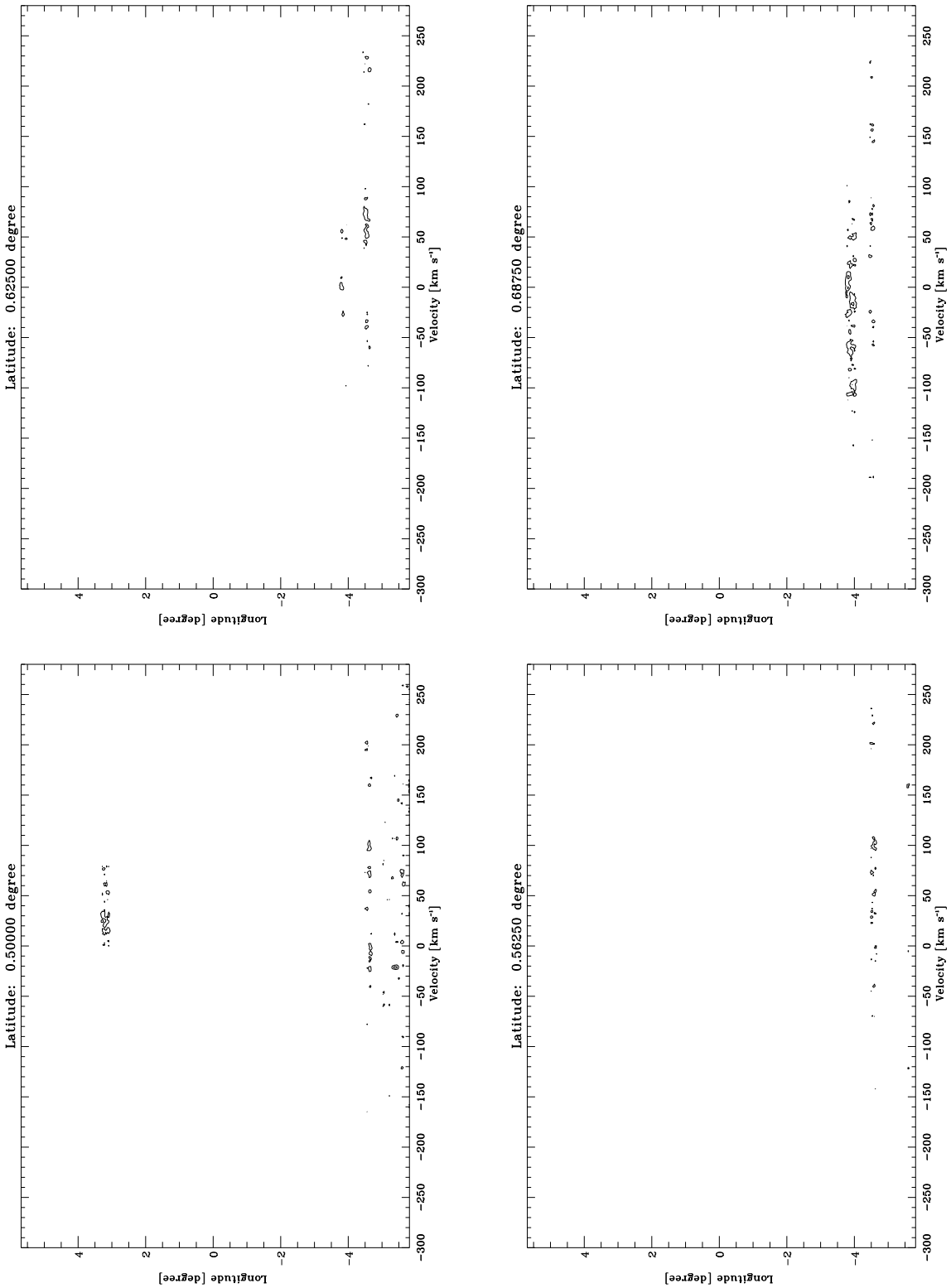

Fig. D2.6. continued.

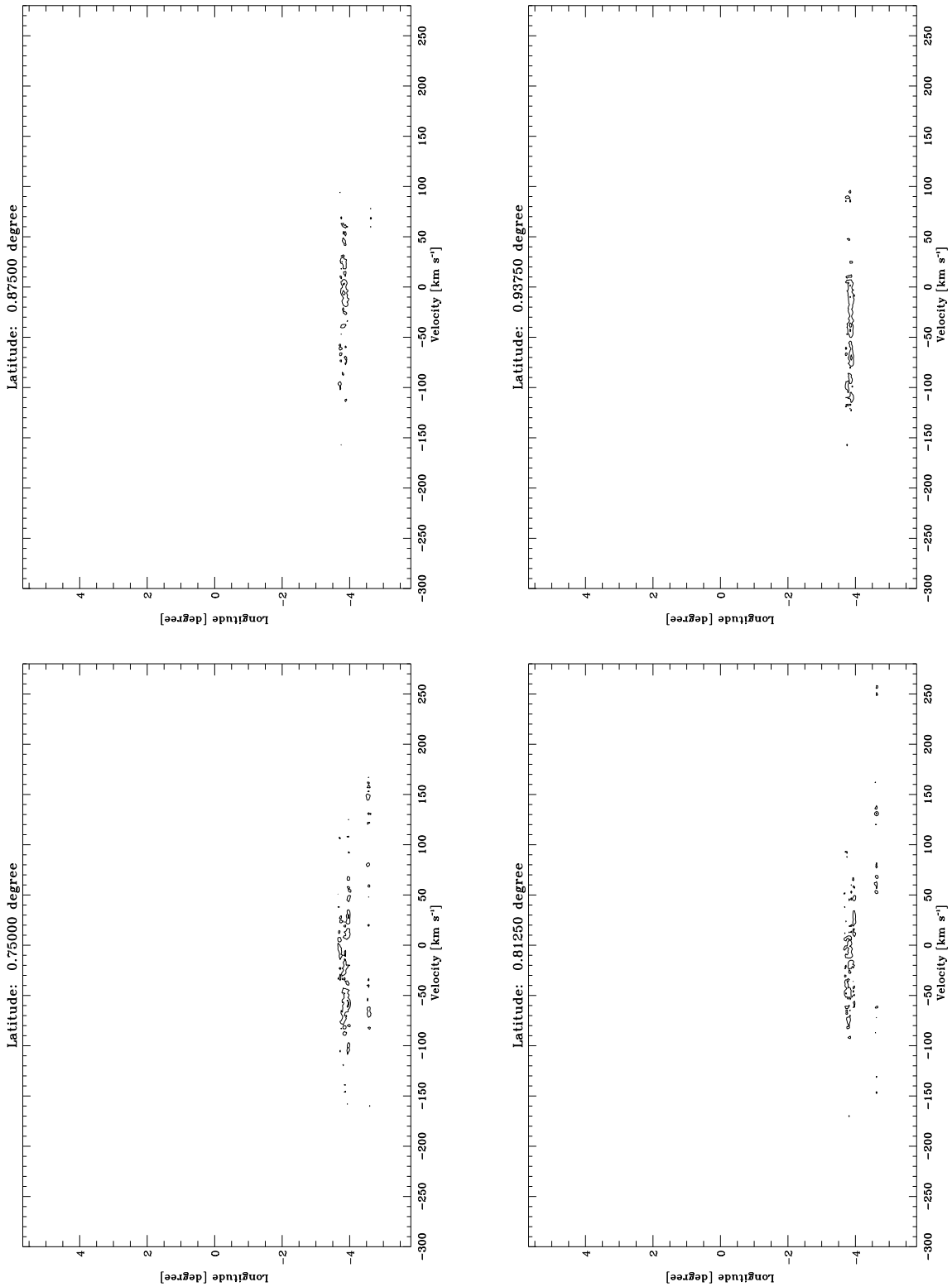

Fig. D2.7. continued.

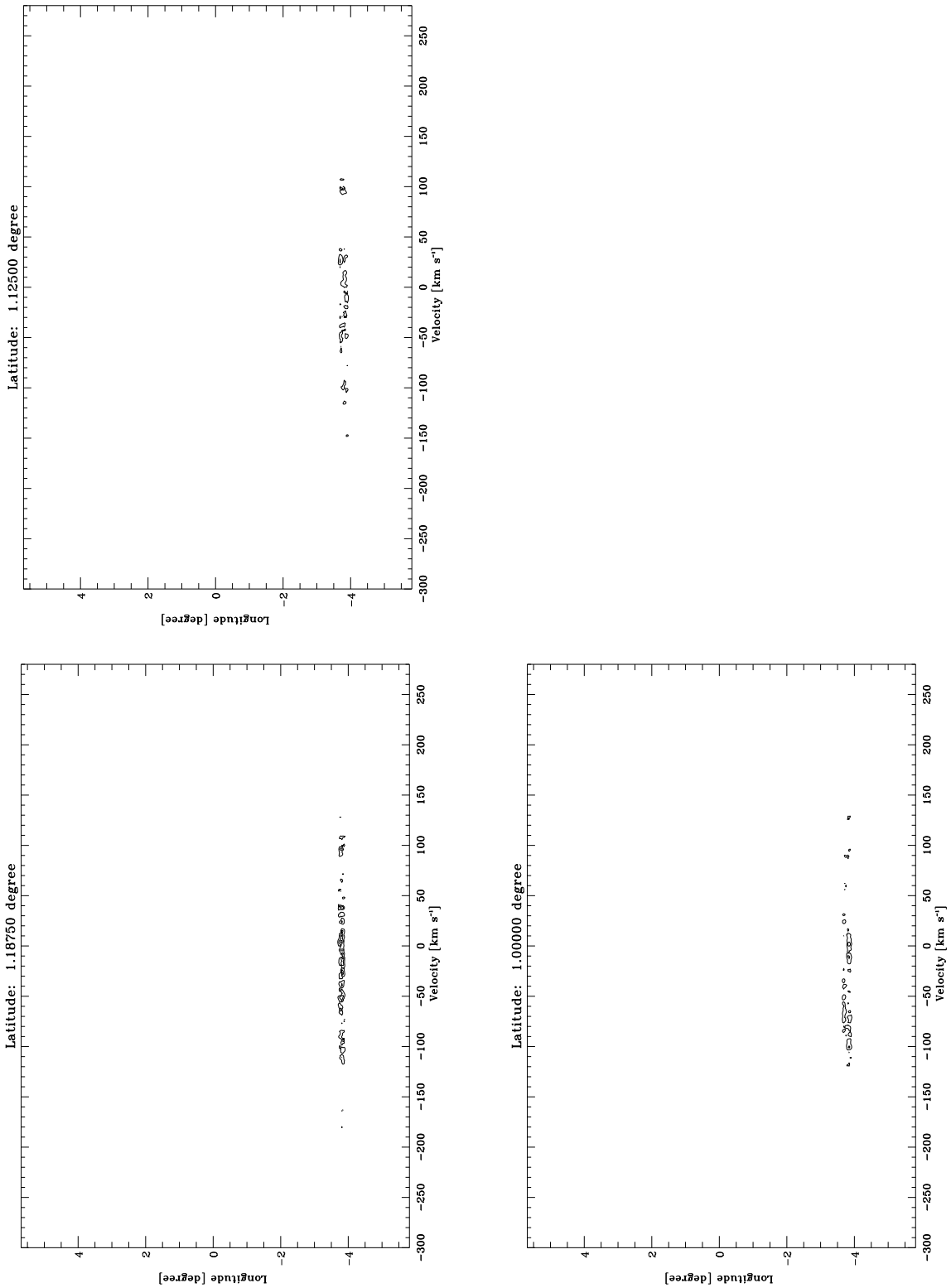

Fig. D2.8. continued.

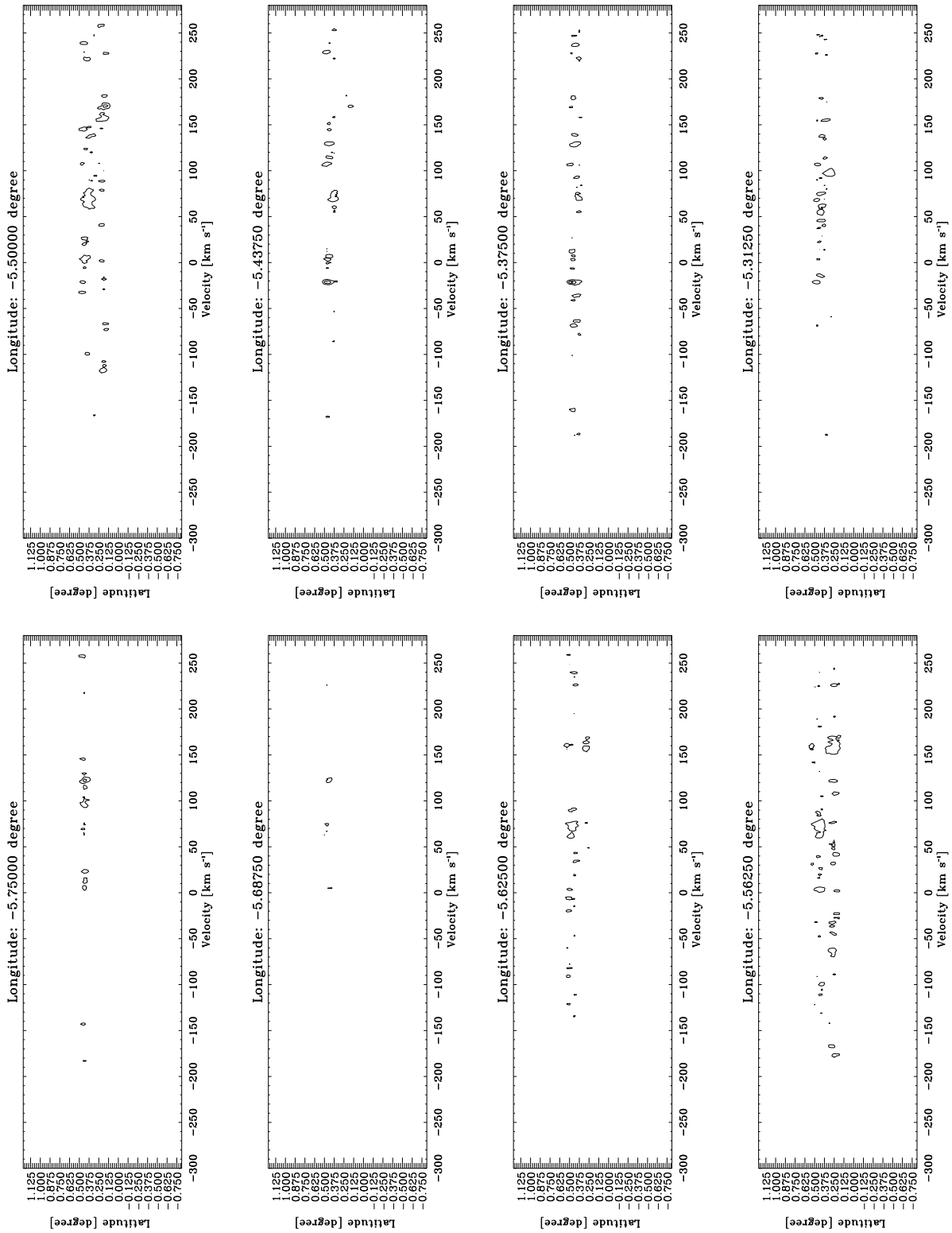

Fig. D3.1. Latitude-Velocity diagrams integrated in longitude in step of 0.0625 for H13CO+. The lowest contour is at 0.0013 K (3σ). The following contours increase them in step of 0.0026 K, which correspond to 6σ.

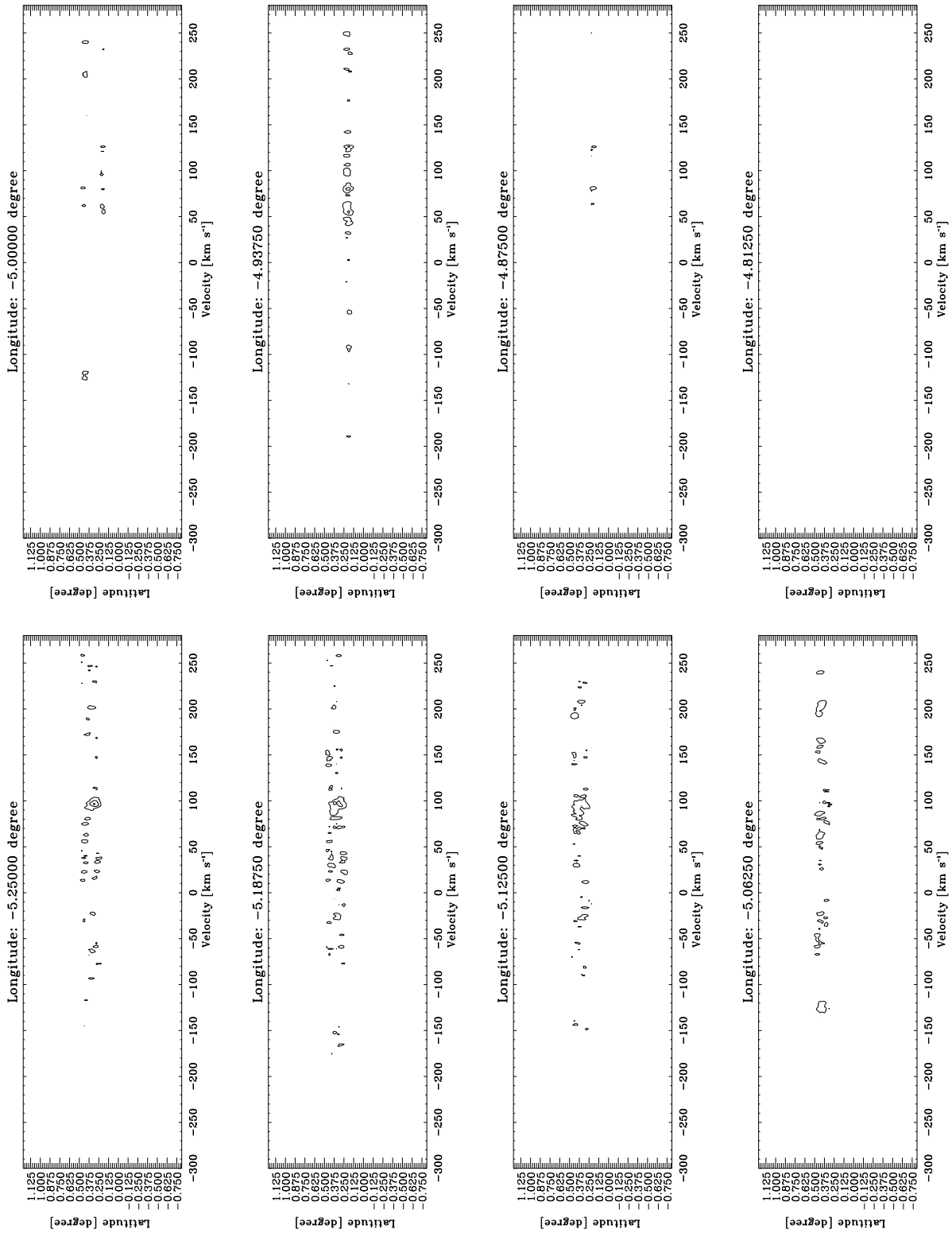

Fig. D3.2. continued.

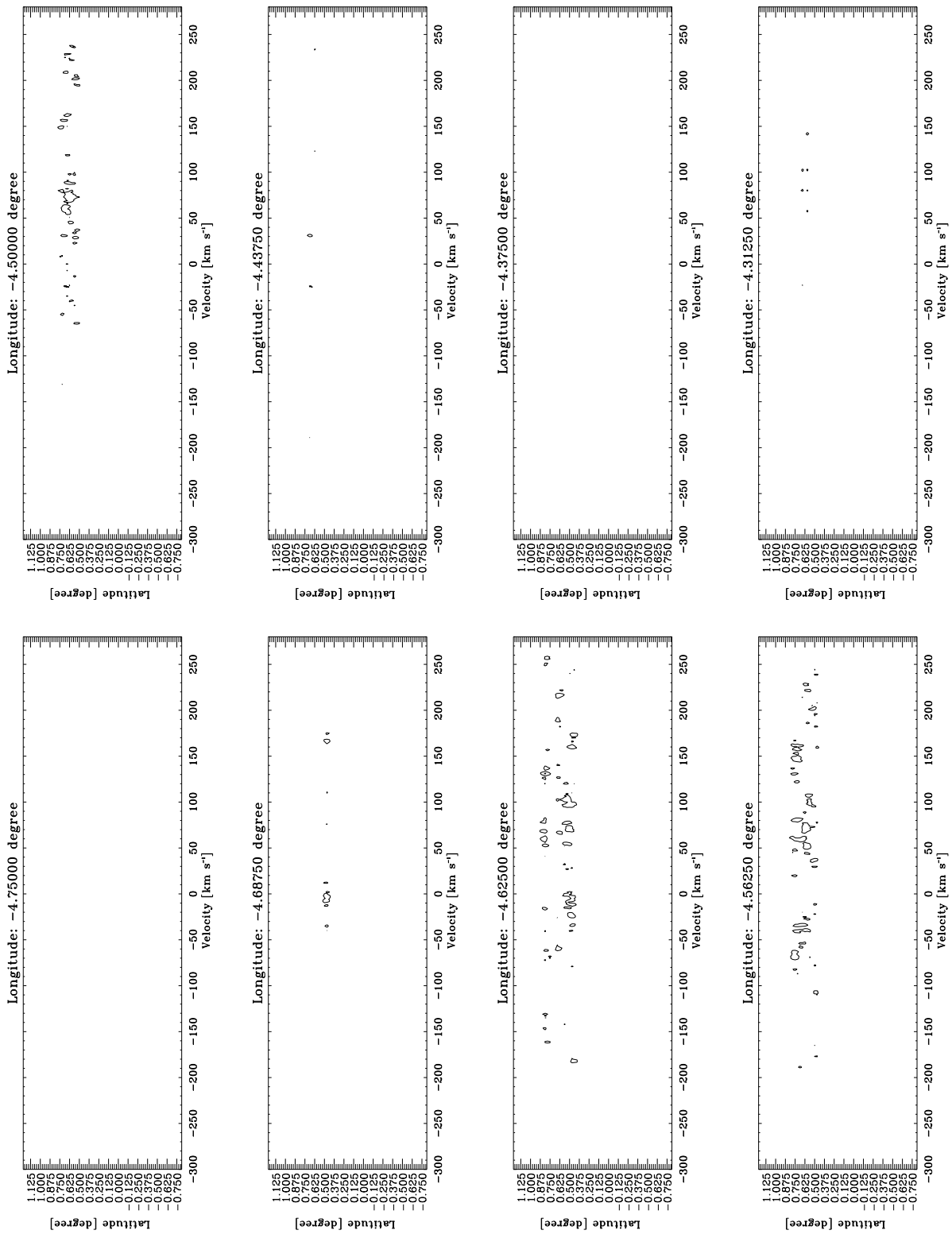

Fig. D3.3. continued.

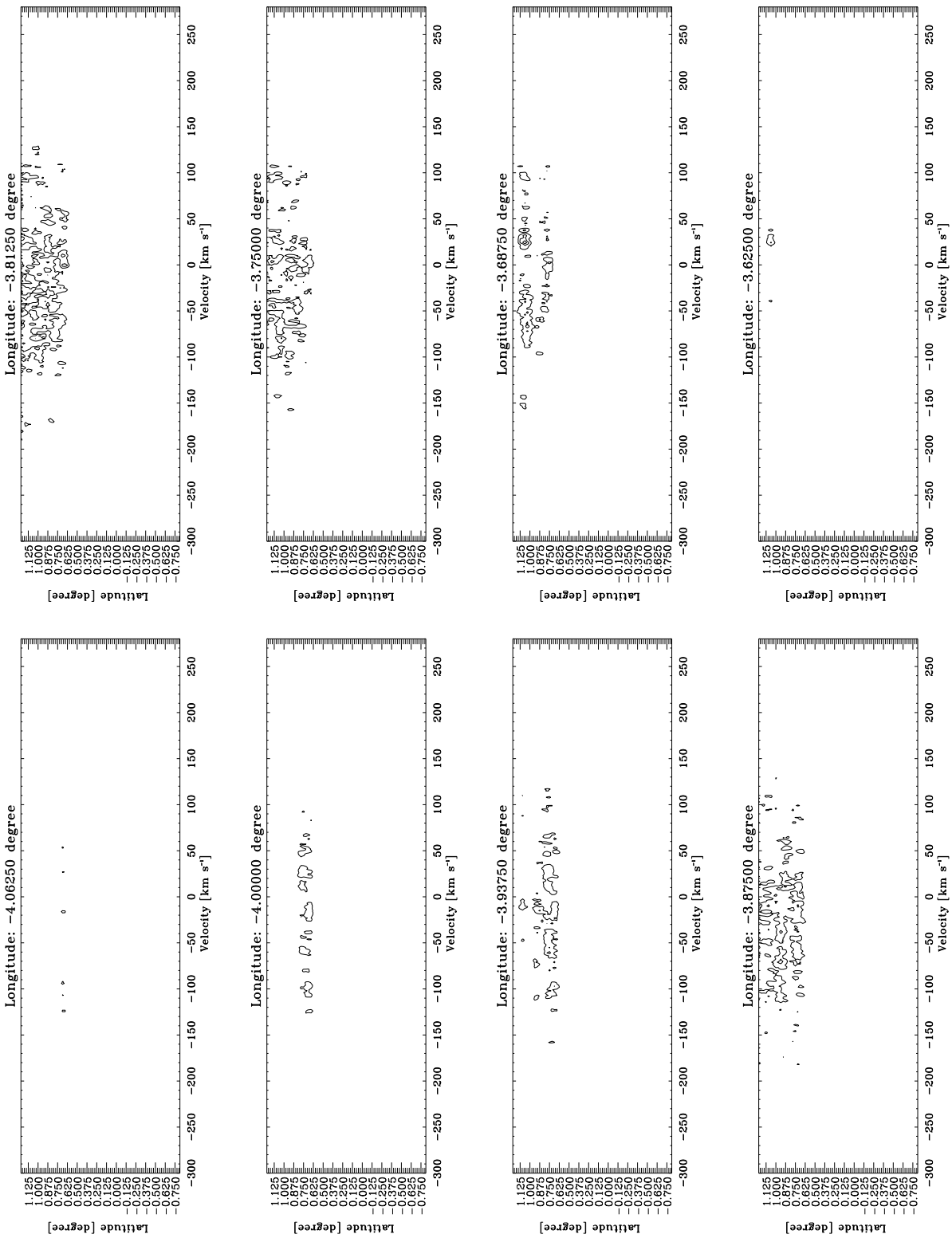

Fig. D3.4. continued.

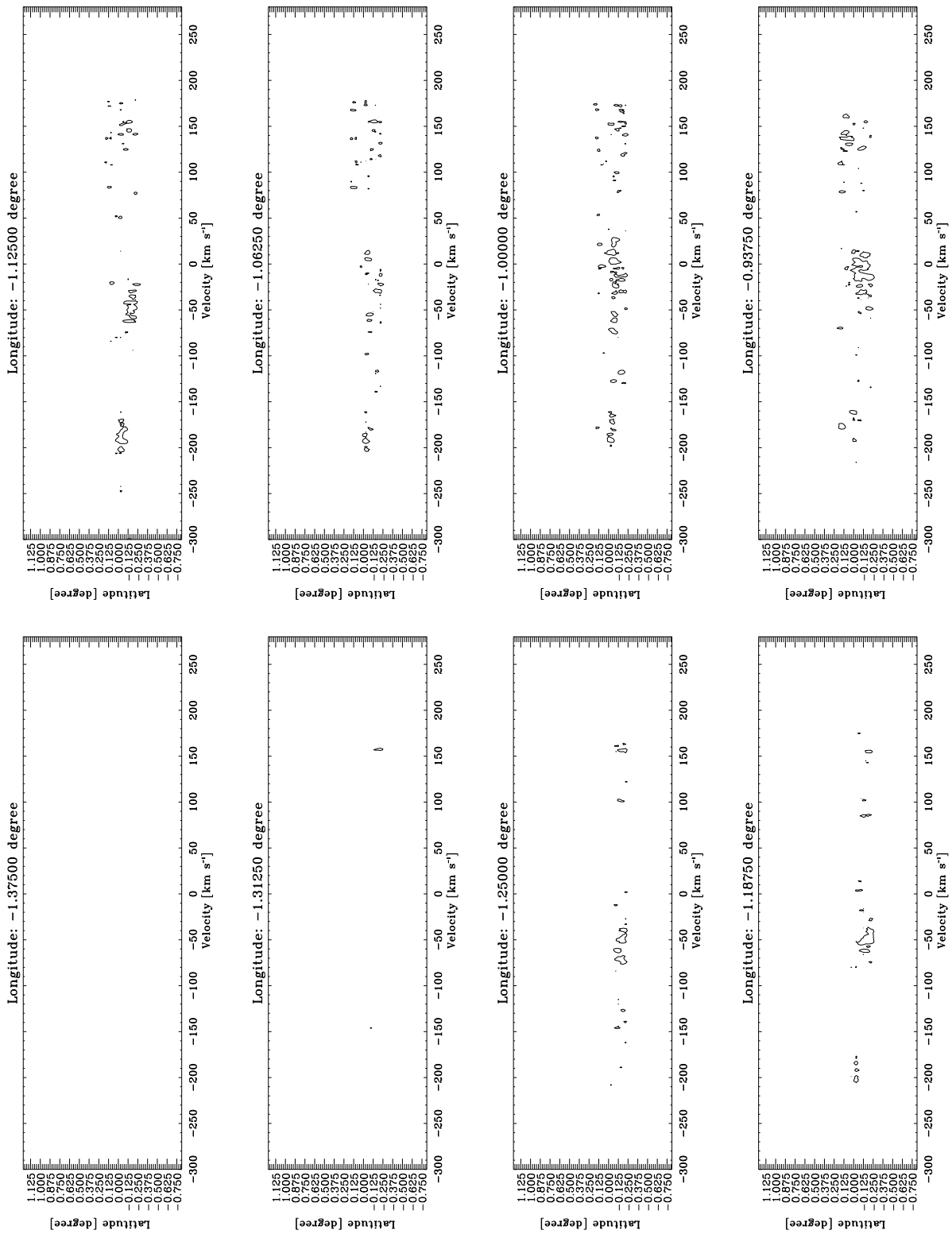

Fig. D3.5. continued.

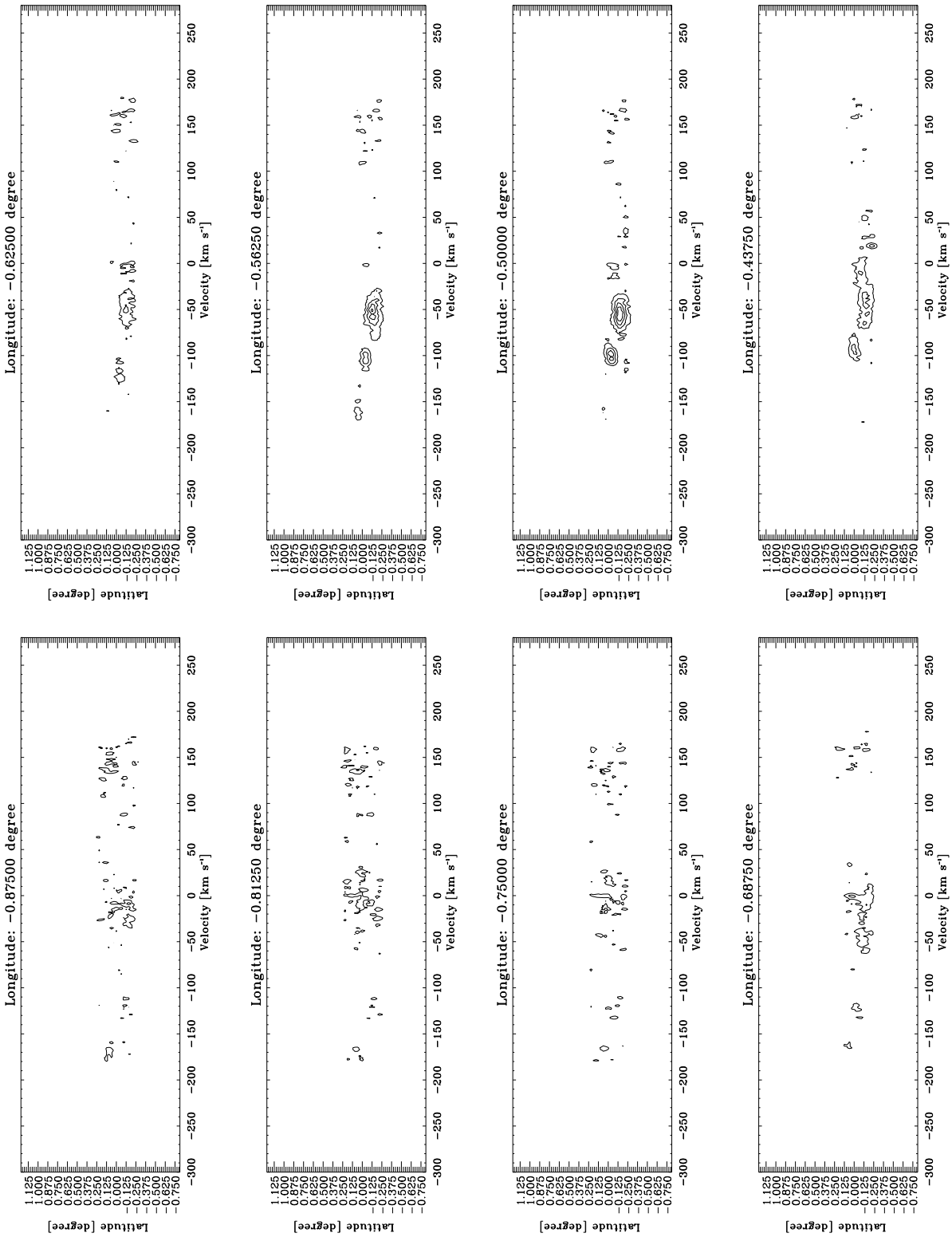

Fig. D3.6. continued.

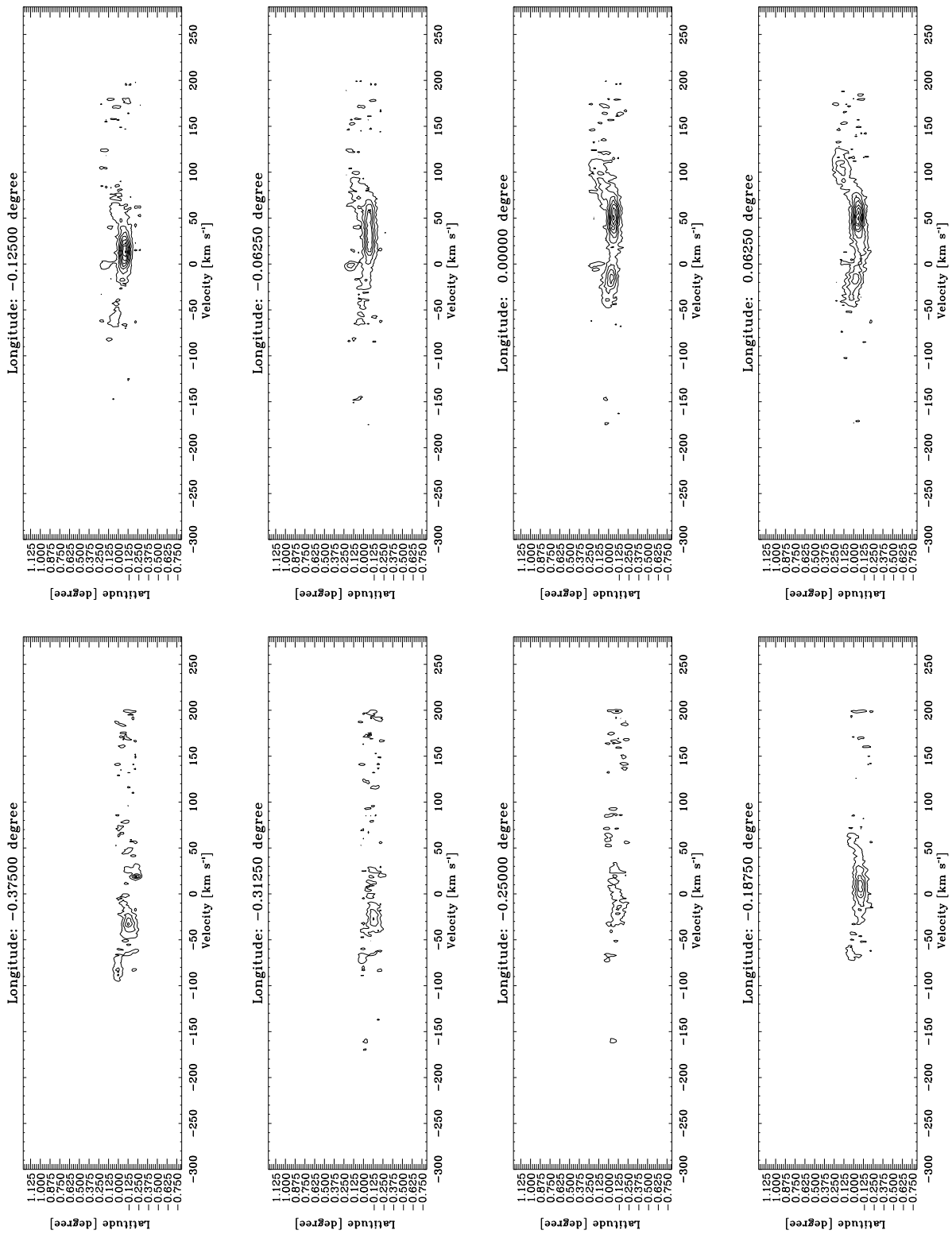

Fig. D3.7. continued.

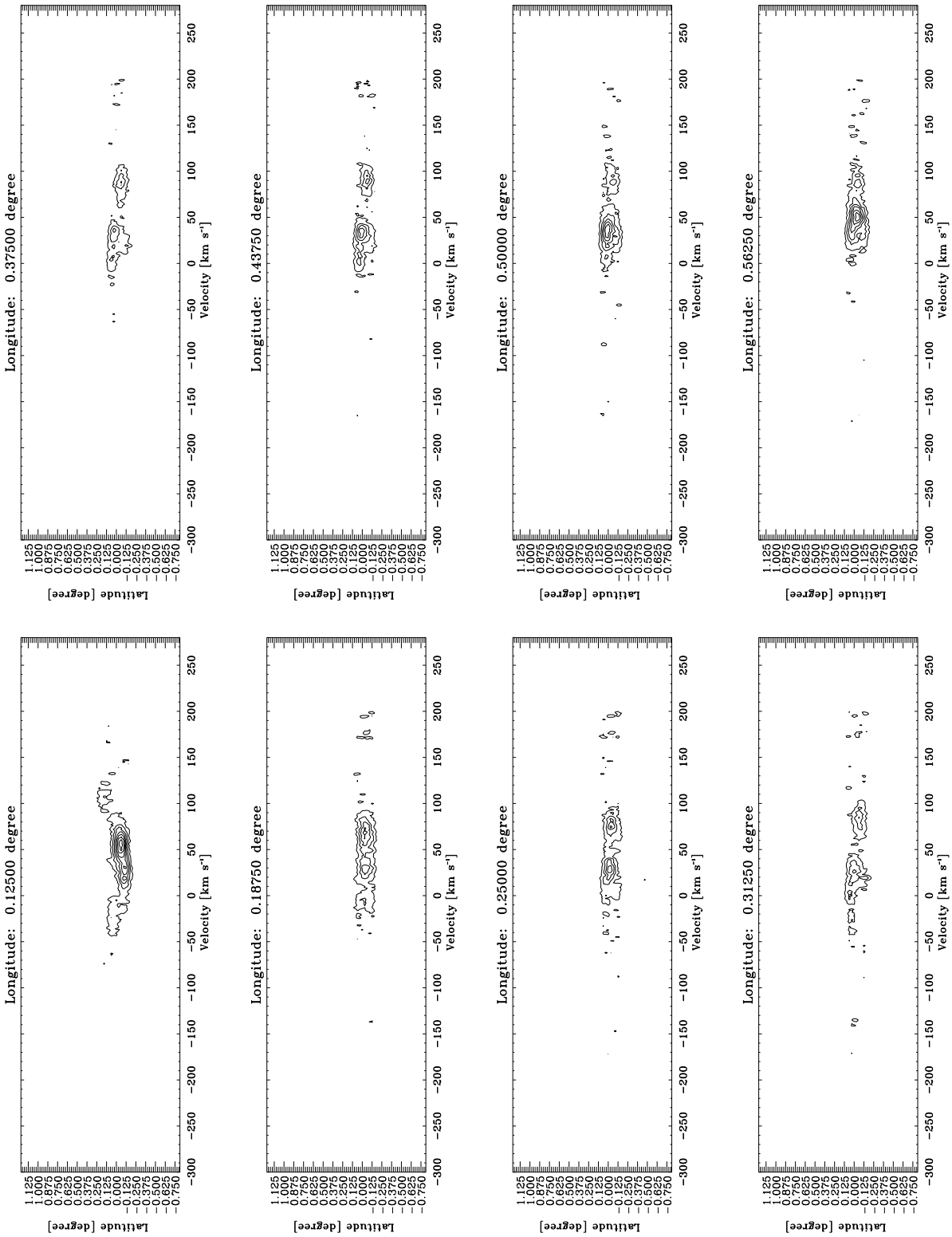

Fig. D3.8. continued.

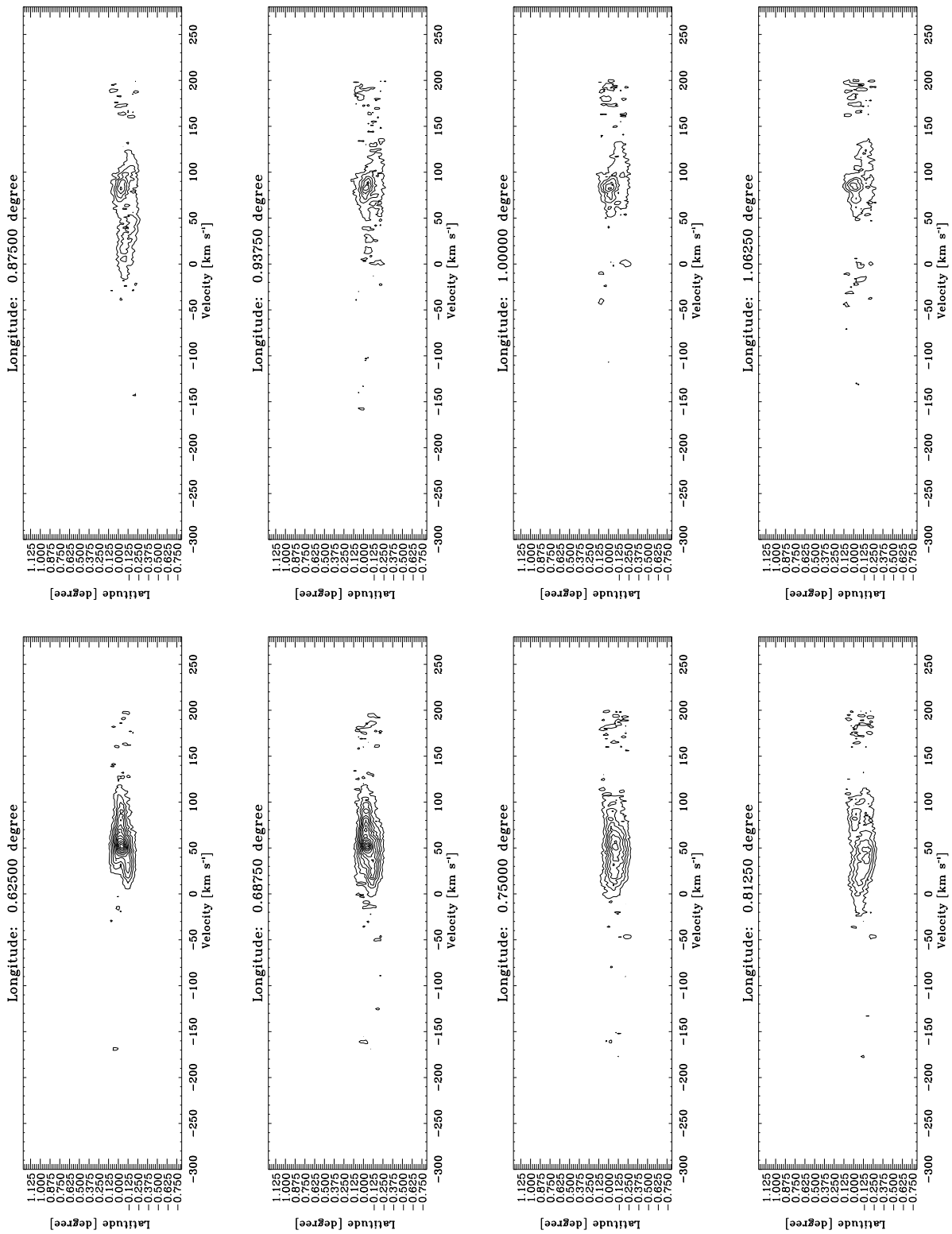

Fig. D3.9. continued.

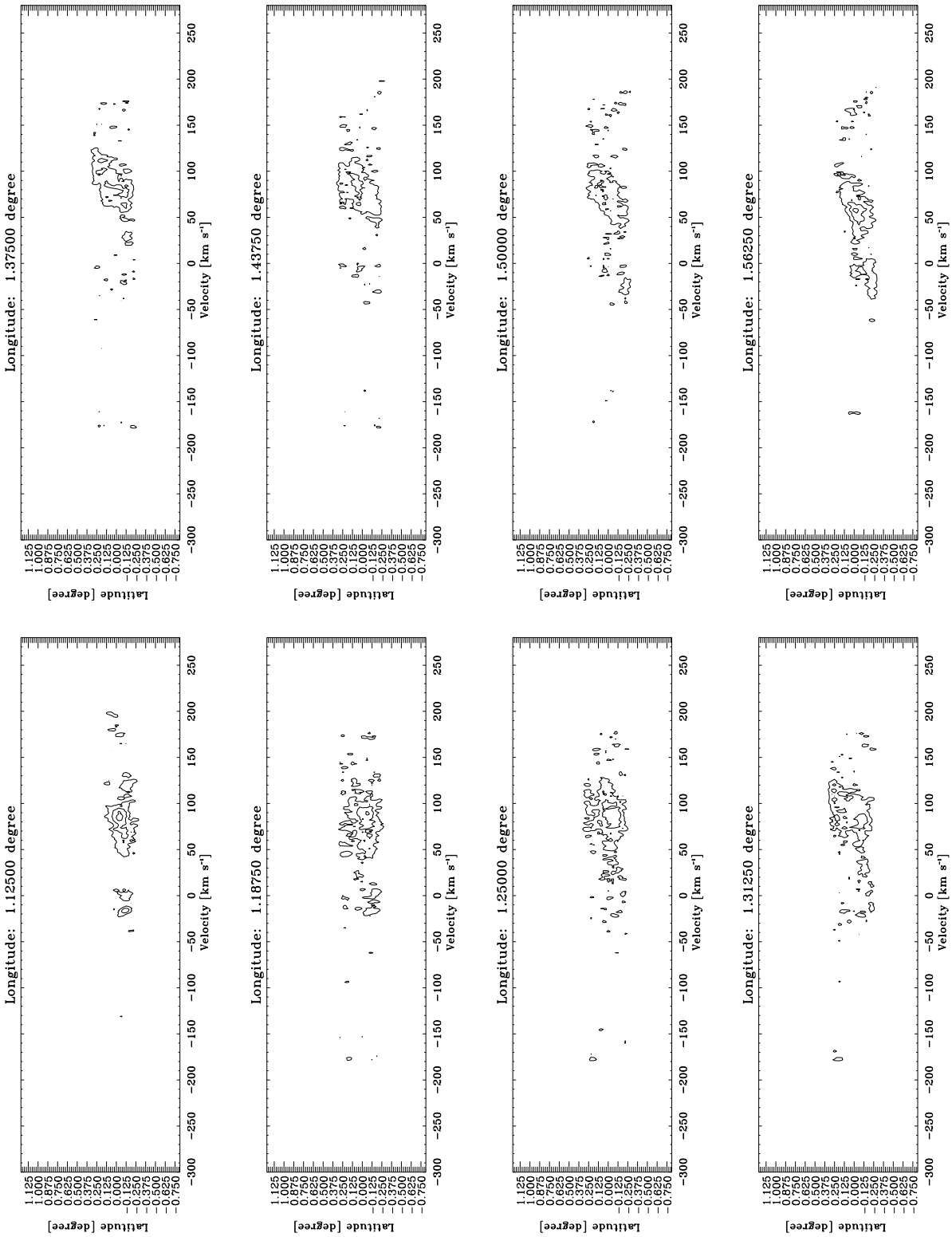

Fig. D3.10. continued.

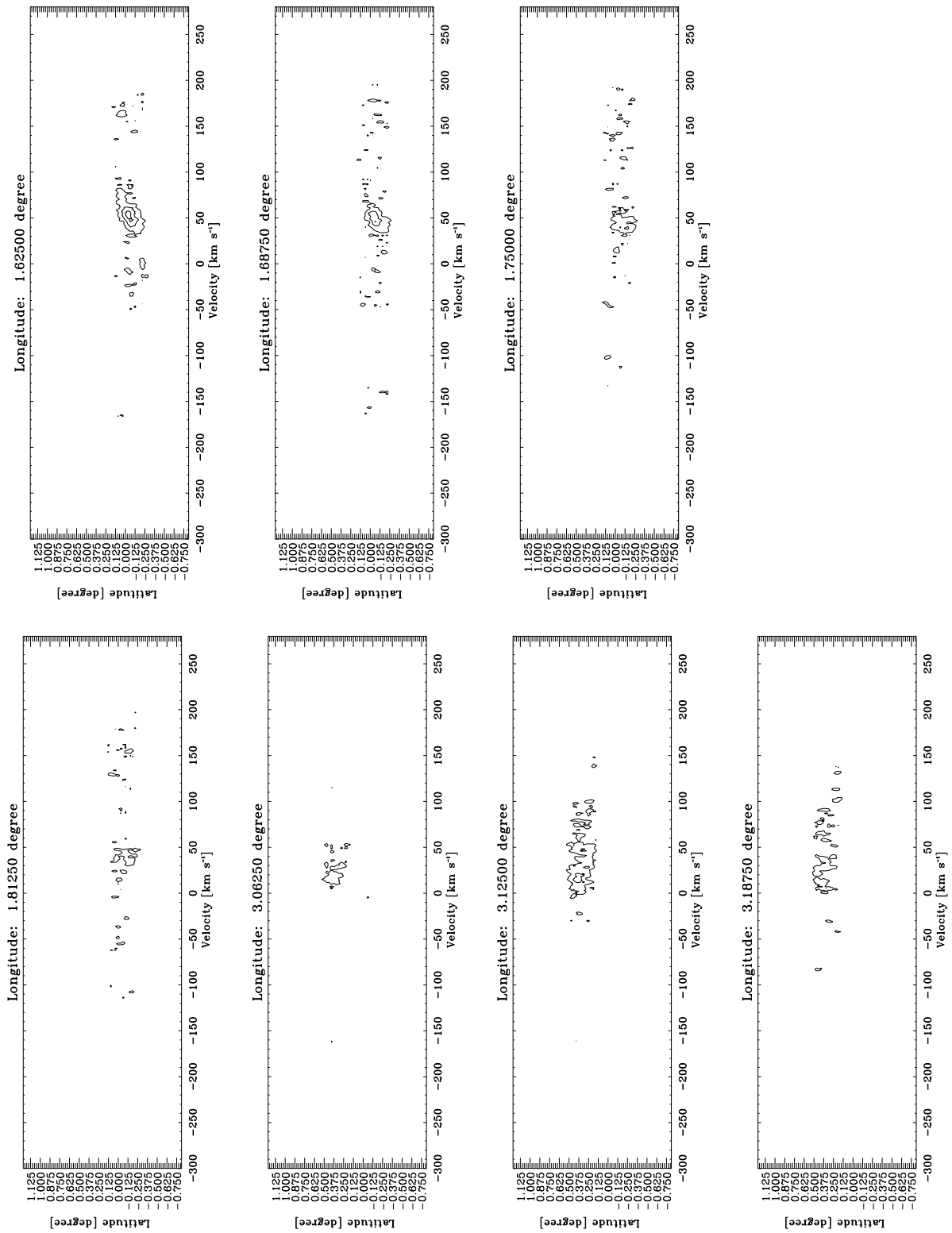

Fig. D3.11. continued.

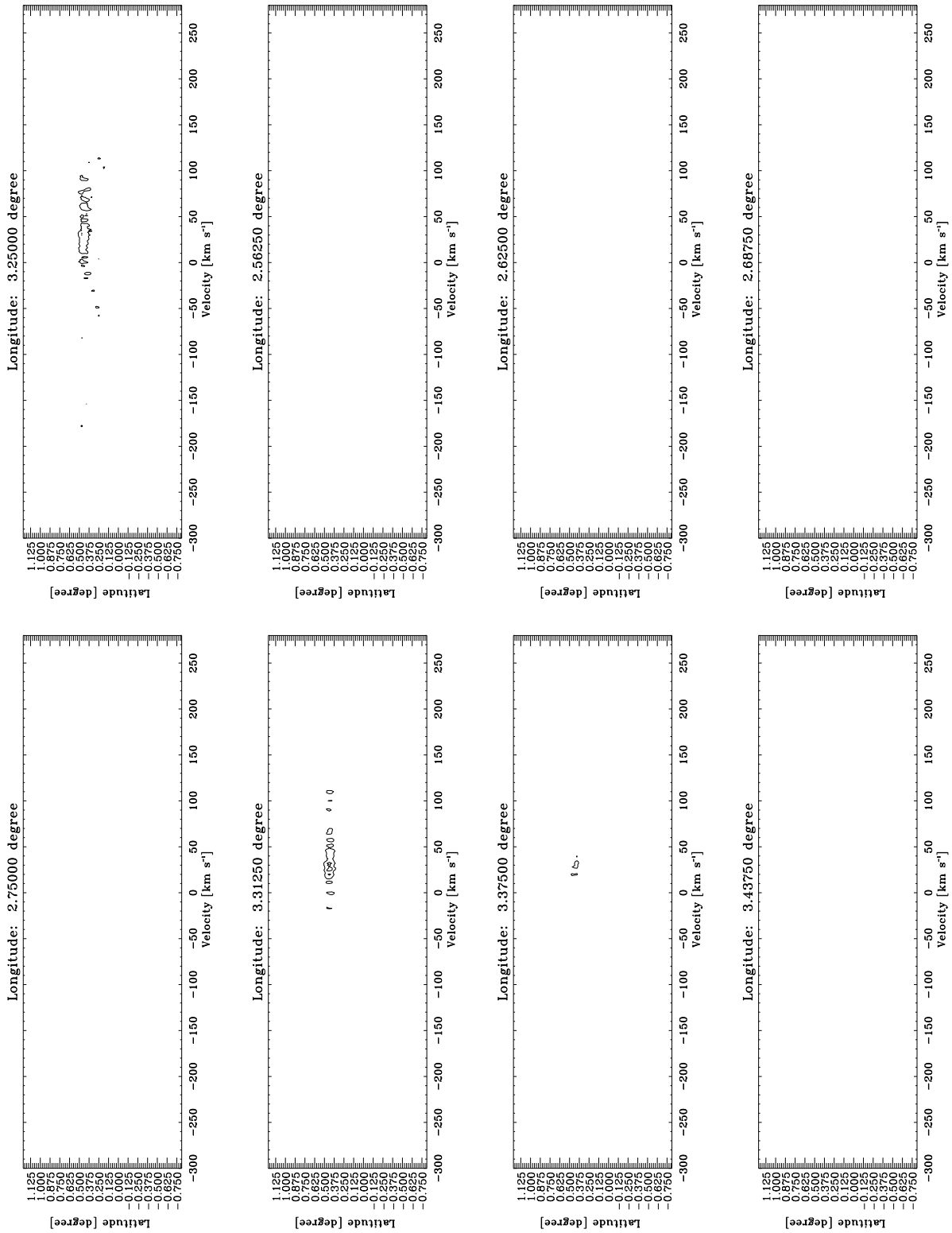

Fig. D3.12. continued.

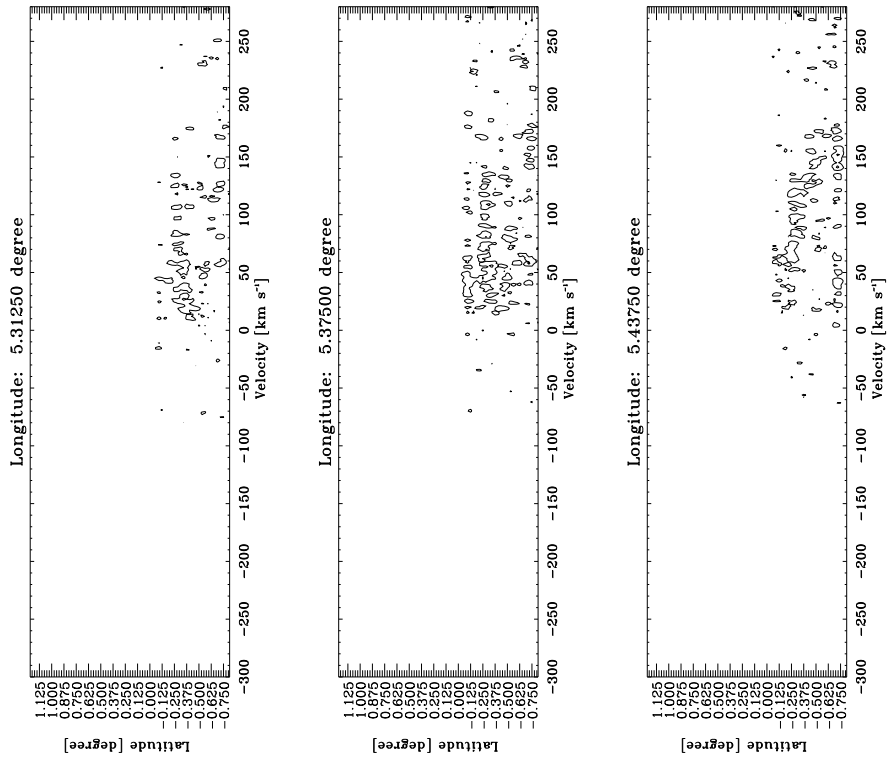

Fig. D3.13. continued.

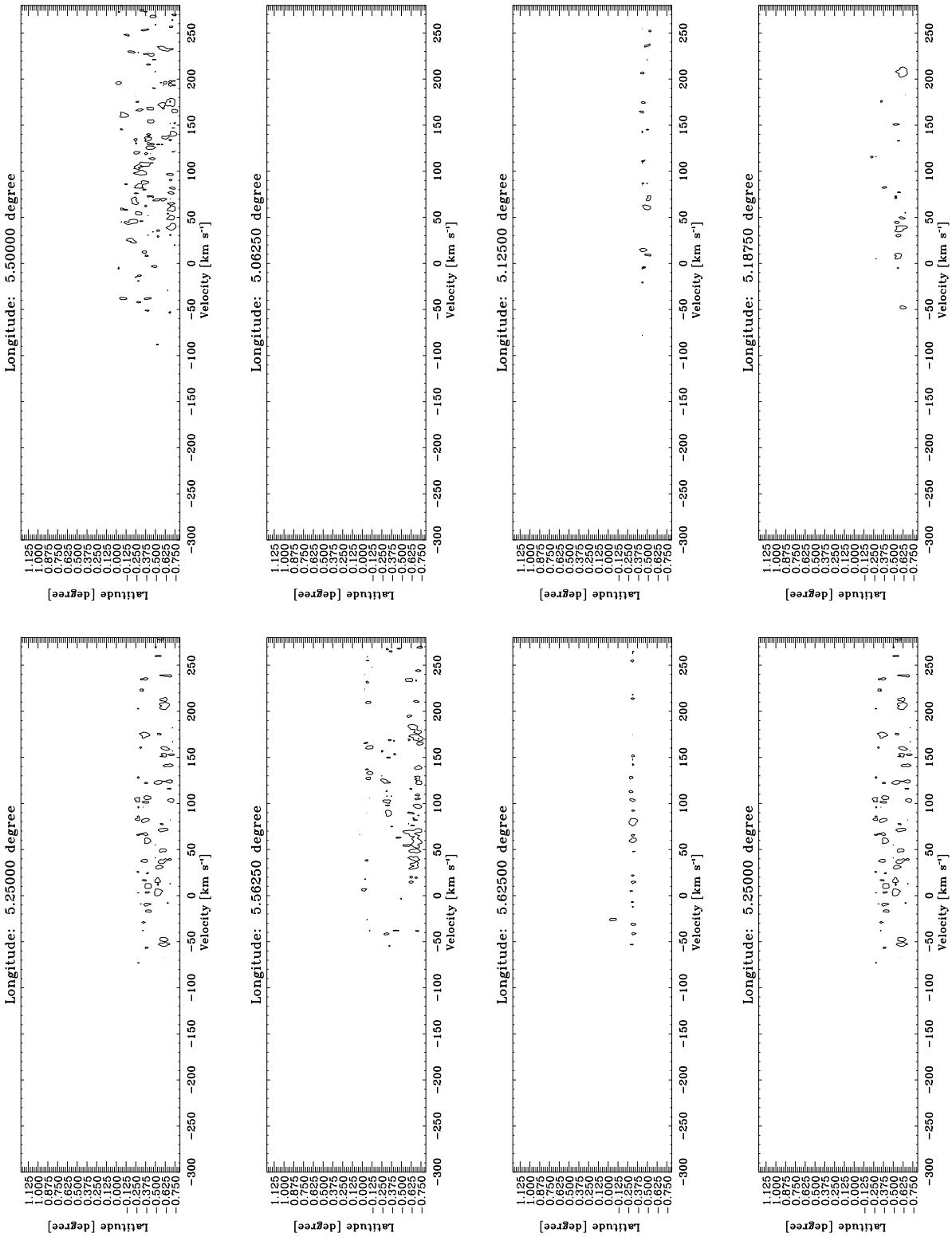

Fig. D3.14. continued.

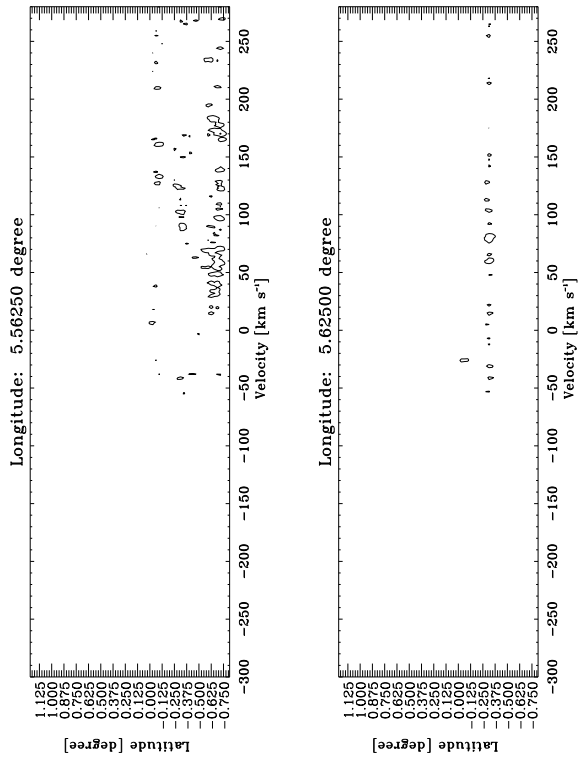

Fig. D3.15. continued.

Appendix E: Gaussian fits

We present the Gaussian fits of the average spectrum over the angular size of each region, as defined in Table 4.

Figure E.1 shows the average spectra toward the Sgr A complex. At negative velocities, we can see the EMR, in the HCO^+ and SiO and CO spectra. At v 0 km s^{-1}, we can see material strongly contaminated by the absorption produced by spiral arms, which can be clearly seen in the HCO^+ spectra. The ∼50 km s^{-1} component correspond to the "Sgr A cloud", which is well identifying in all molecules. Finally, toward positive velocities, in HCO^+ and CO the positive part of the EMR is visible.

Figure E.2 we show the average spectra toward Sgr B complex. Both, in HCO^+ and CO we can see the EMR toward high positive and negative velocities. The "Sgr B cloud" correspond to the component in $v \sim 50$ km s^{-1}.

In Fig. E.3 the EMR appears very strong both in its positive and negative velocity component in all the molecular lines, less in $H^{13}CO^+$. The component corresponding to Sgr C cloud is found toward negative velocities, and both CO and HCO^+ appears very contaminated by the spiral arms, but it is clearly seeing in SiO and $H^{13}CO^+$.

The Fig. E.4 shows the average spectra toward Sgr D. The main component is at $v \sim 90$ km s^{-1}.

The Fig. E.5 shows the average spectra toward Sgr D. The main component is at $v \sim 210$ km s^{-1}.

Figure E.6, show the average spectra for the region toward the 1.3° complex. The main cloud is at $v \sim 80$ km s^{-1}, and in this longitude we can see the positive velocity of the EMR at $v \sim 200$ km s^{-1}.

In Fig. E.7 we show the average spectra for the region toward M+3.2+0,3. The main cloud identify by Bitran (1987) is found in $v \sim 100$ km s^{-1} ("Clump 2"), but the 3 wide velocity component belong to the Galactic center region. In the CO spectrum, we can see the spiral arms in emission at negative velocities and at high positive velocities we see the end of the EMR.

Figure E.8 shows the average spectra toward the M−5.3+0.4 region, where the main cloud is at $v \sim 80$ km s^{-1}. In the four plots, we can clearly identify the spiral arm in emission. We can see that the Galactic center component have a wide width velocity in comparison to the material from the disk.

Figure E.9 presents the average spectra toward the M−4.4+0.6 region. The main component is at ∼70 km s^{-1}, and the we can see the spiral arm as narrow velocity features.

In Fig. E.10 we can see the average spectra toward the M−3.8+0.9 region. The main cloud is found at negative velocities ($v \sim -80$ km s^{-1}). The SiO and HCO^+ emission show an increase in the intensity in the main cloud in comparison with the CO emission, with respect to other components within the Galactic disk.

Finally, Fig. E.11 shows the average spectra toward the M+5.3−0.3 region. Like in the previous case, the SiO emission in the Galactic center clouds is high in comparison with the other complex, suggesting that in both complex (main clouds of M−3.8+0.9 and M+5.3−0.3) could be subjected to shocks.

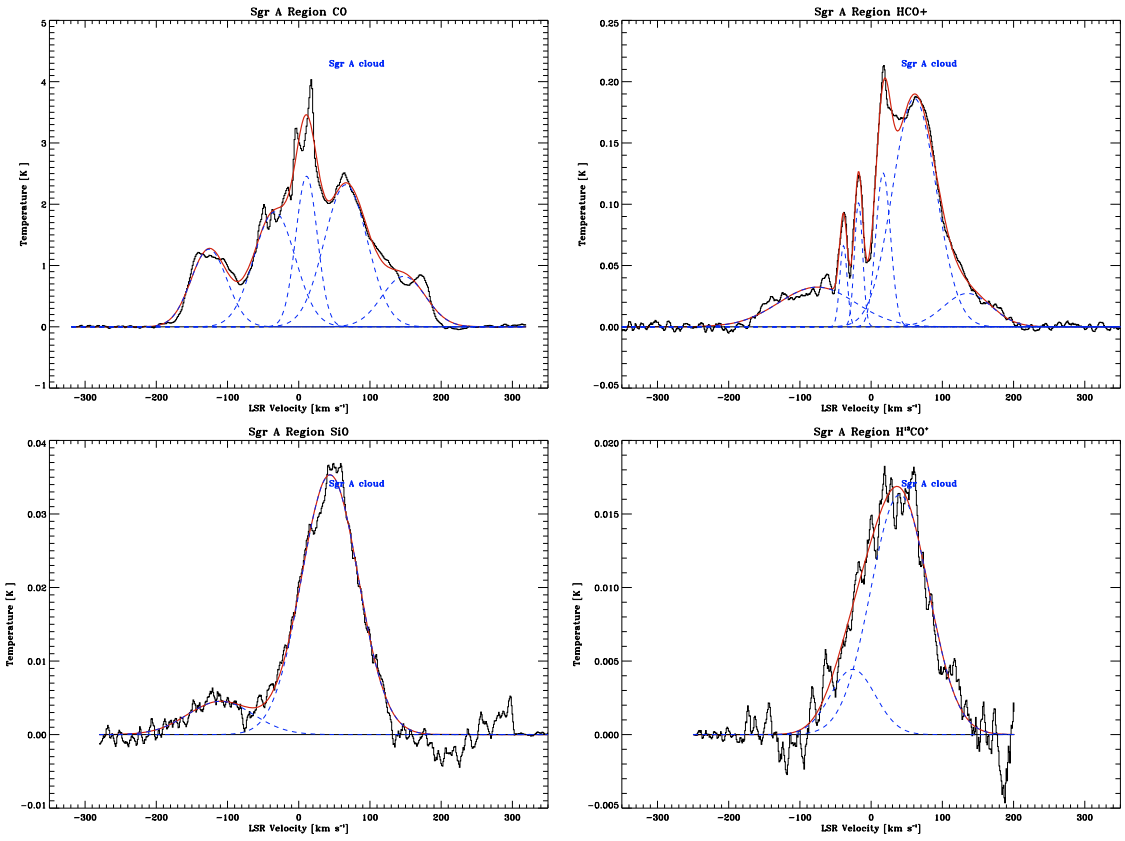

Fig. E.1. CO, HCO^+, SiO y $H^{13}CO^+$ average spectrum over the angular size of Sgr A region (from $l = -0.3125$ to -0.3125, and from $b = -0.5$ to 0.5). In all the figures, the red lines indicate the Gaussian fit for the complete region and blue dashed lines show the Gaussian fits of each velocity components.

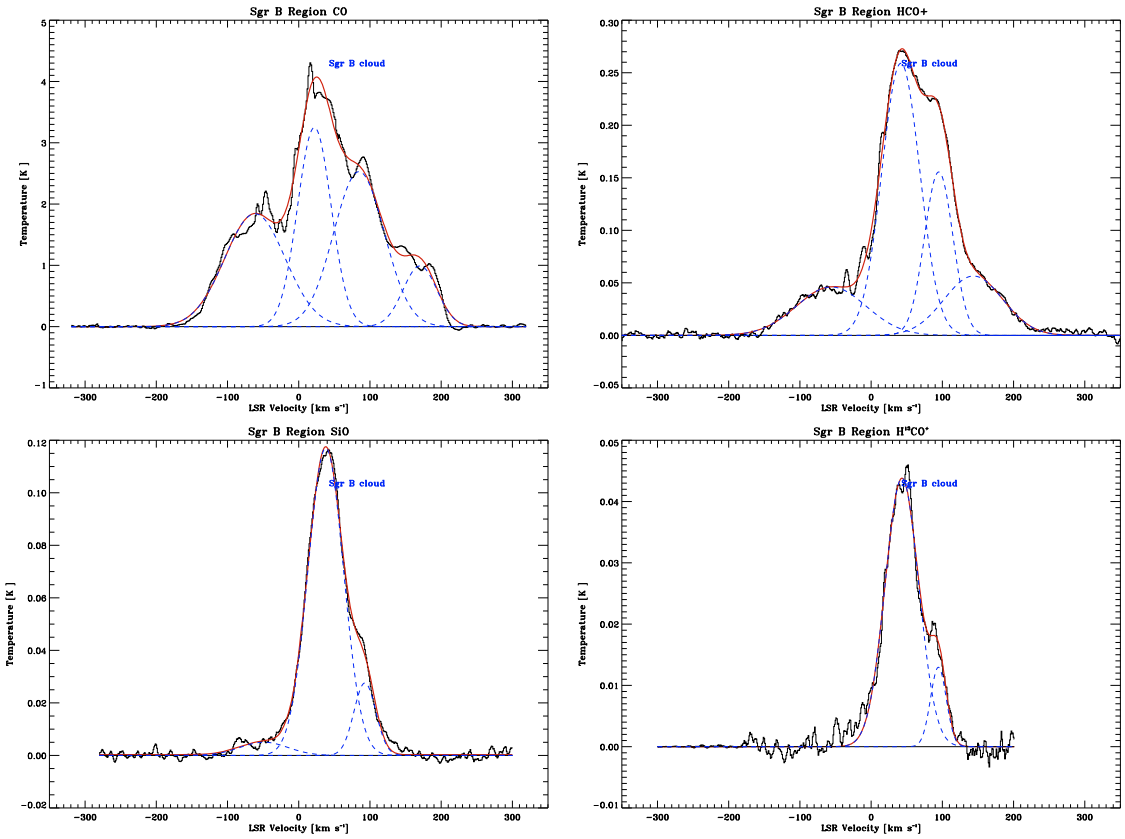

Fig. E.2. CO, HCO^+, SiO y $H^{13}CO^+$ average spectrum over the angular size of Sgr B region (from $l = 0.375$ to 0.8125, and from $b = -0.5$ to 0.5).

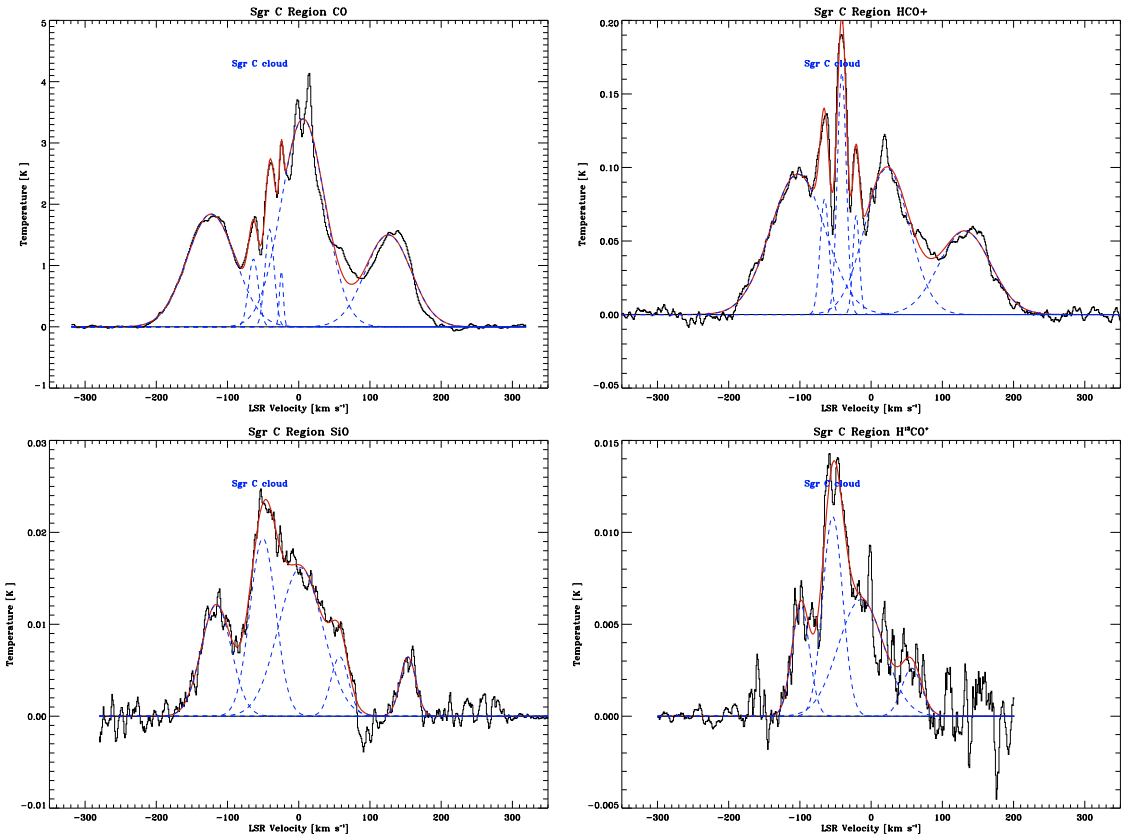

Fig. E.3. CO, HCO^+, SiO y $H^{13}CO^+$ average spectrum over the angular size of Sgr C region (from $l = -0.6875$ to -0.375, and from $b = -0.5$ to 0.5).

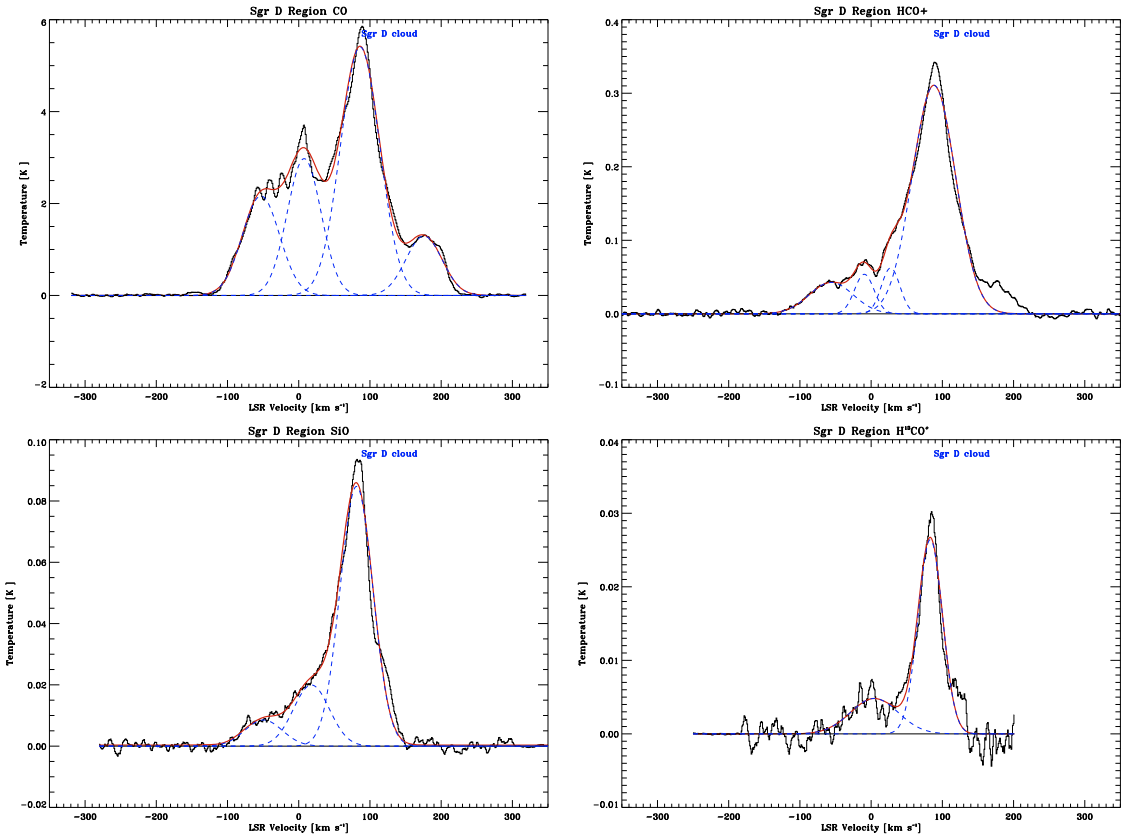

Fig. E.4. CO, HCO^+, SiO y $H^{13}CO^+$ average spectrum over the angular size of Sgr D region (from $l = 0.875$ to 1.1875, and from $b = -0.5625$ to 0.5625).

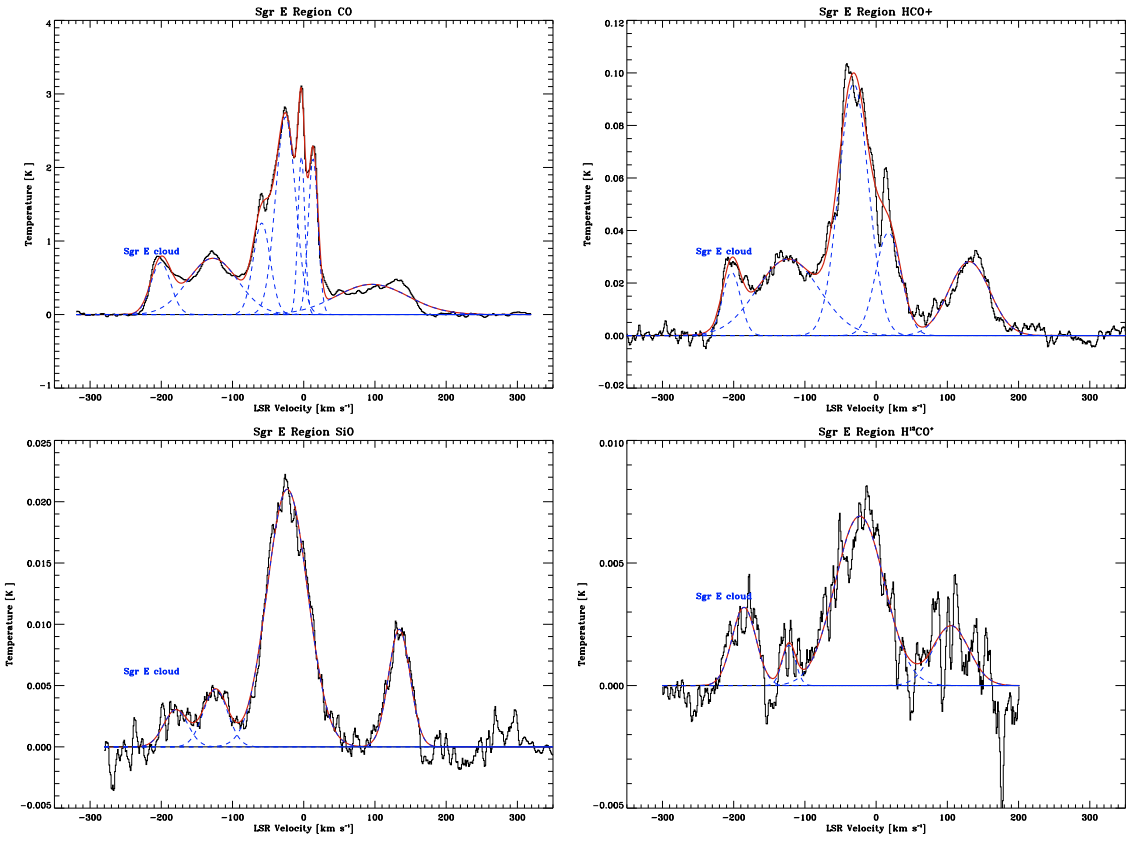

Fig. E.5. CO, HCO^+, SiO y $H^{13}CO^+$ average spectrum over the angular size of Sgr E region (from $l = -1.5$ to -0.75, and from $b = -0.5$ to 0.5).

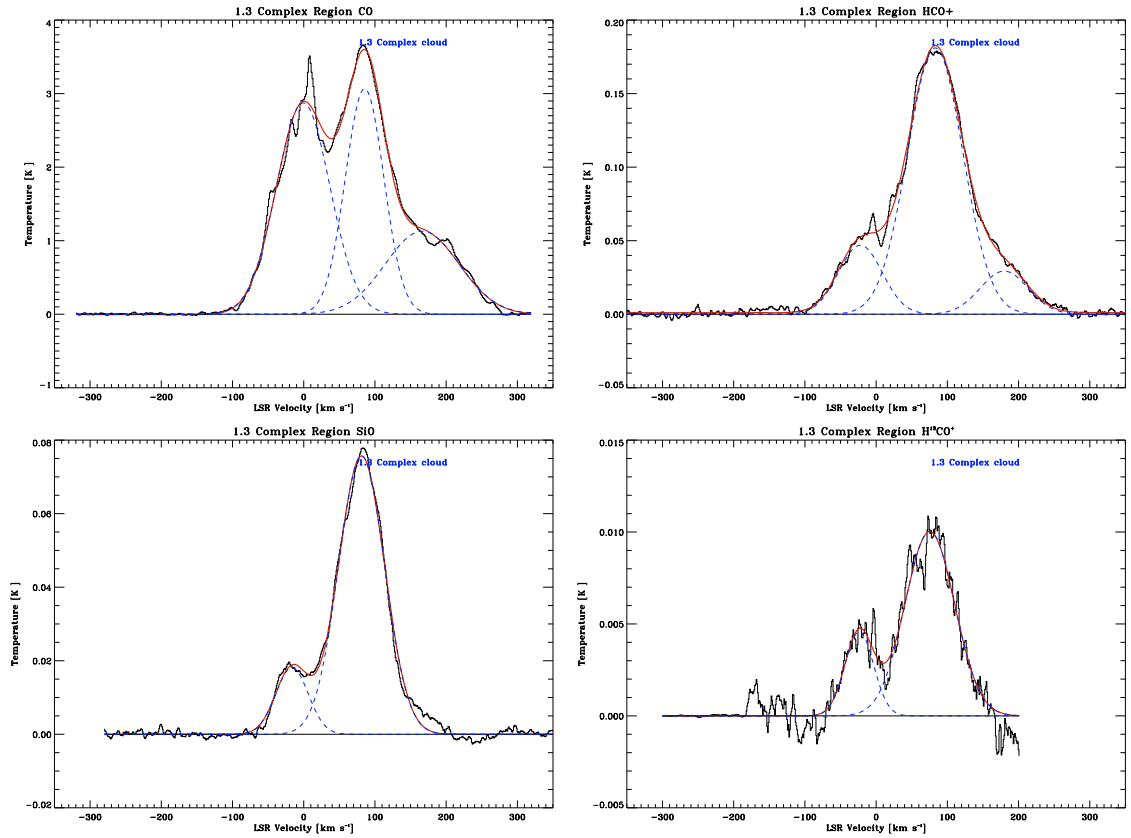

Fig. E.6. CO, HCO^+, SiO y $H^{13}CO^+$ average spectrum over the angular size of 1.3 complex region (from $l = 1.25$ to 2.0, and from $b = -0.5625$ to 0.5625).

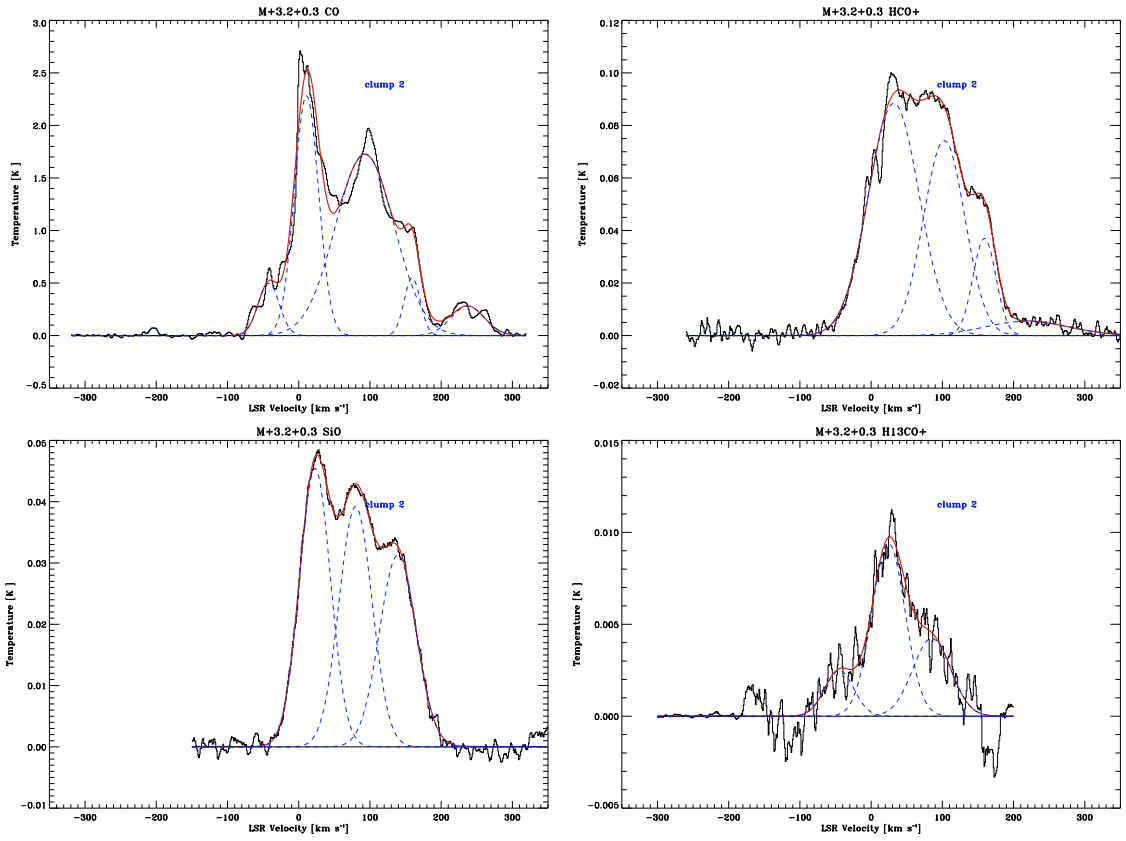

Fig. E.7. CO, HCO^+, SiO y $H^{13}CO^+$ average spectrum over the angular size of M+3.2+0.3 region $(l, b, v) = (3.2, 0.3, 104)$ (from $l = 2.5625$ to 3.5, and from $b = -0.25$ to 0.875).

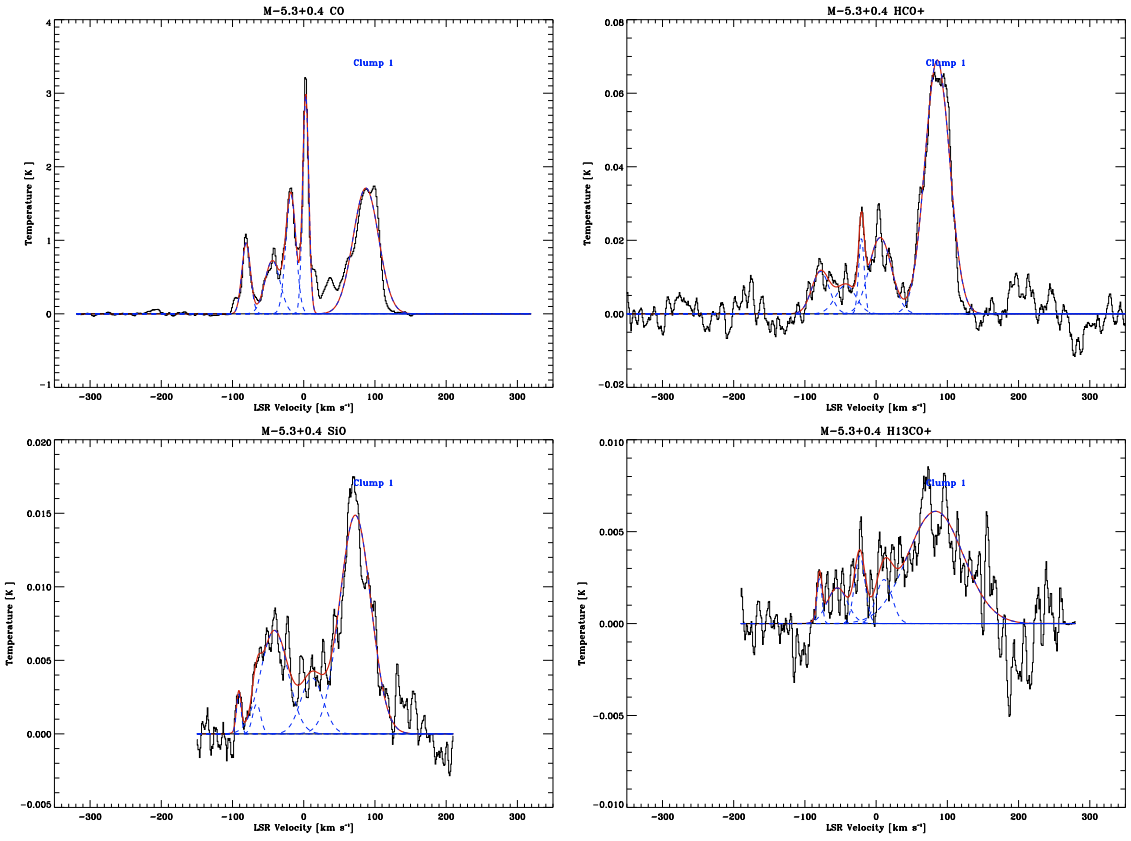

Fig. E.8. CO, HCO^+, SiO y $H^{13}CO^+$ average spectrum over the angular size of M−5.3+0.4 region $(l, b, v) = (-5.3, 0.4, 84)$ (from $l = -5.75$ to −4.75, and from $b = -0.125$ to 0.5625).

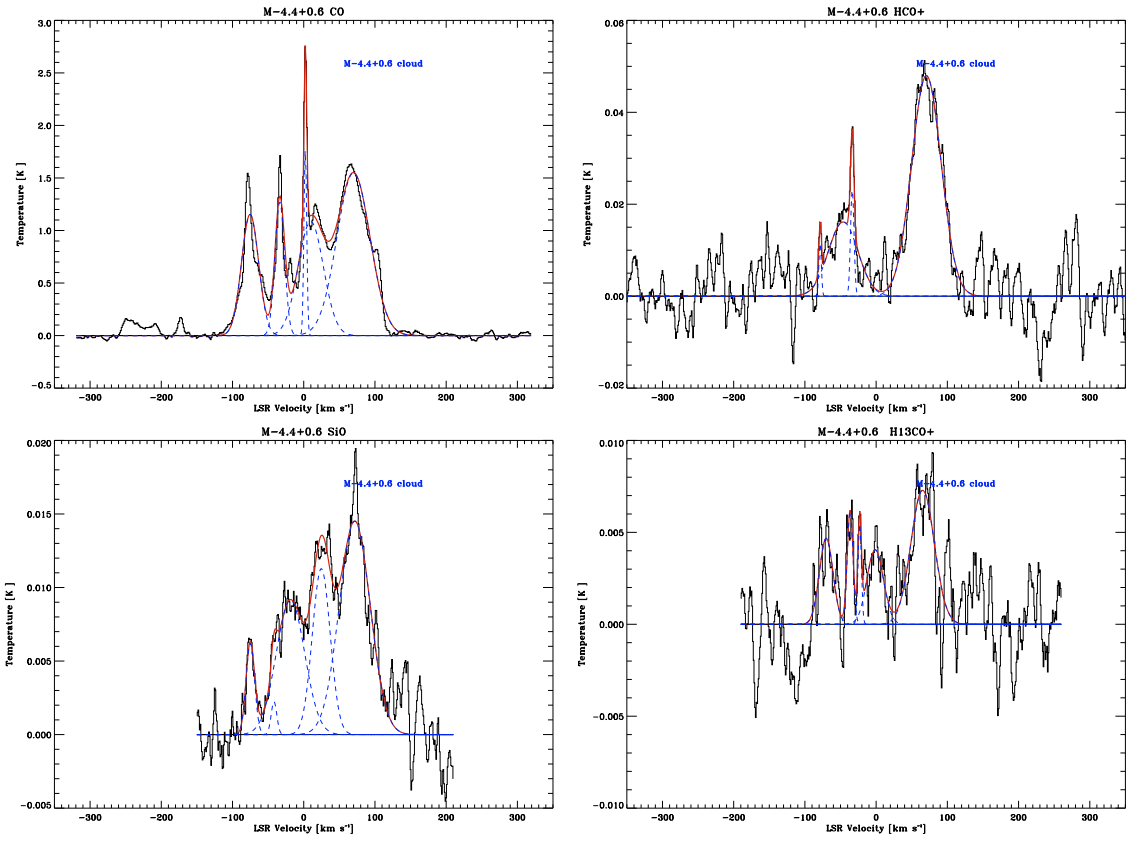

Fig. E.9. CO, HCO^+, SiO y $H^{13}CO^+$ average spectrum over the angular size of M−4.4+0.6 region $(l, b, v) = (-4.4, 0.6, 72)$ (from $l = -4.6875$ to -4.3125, and from $b = 0.4375$ to 0.8125).

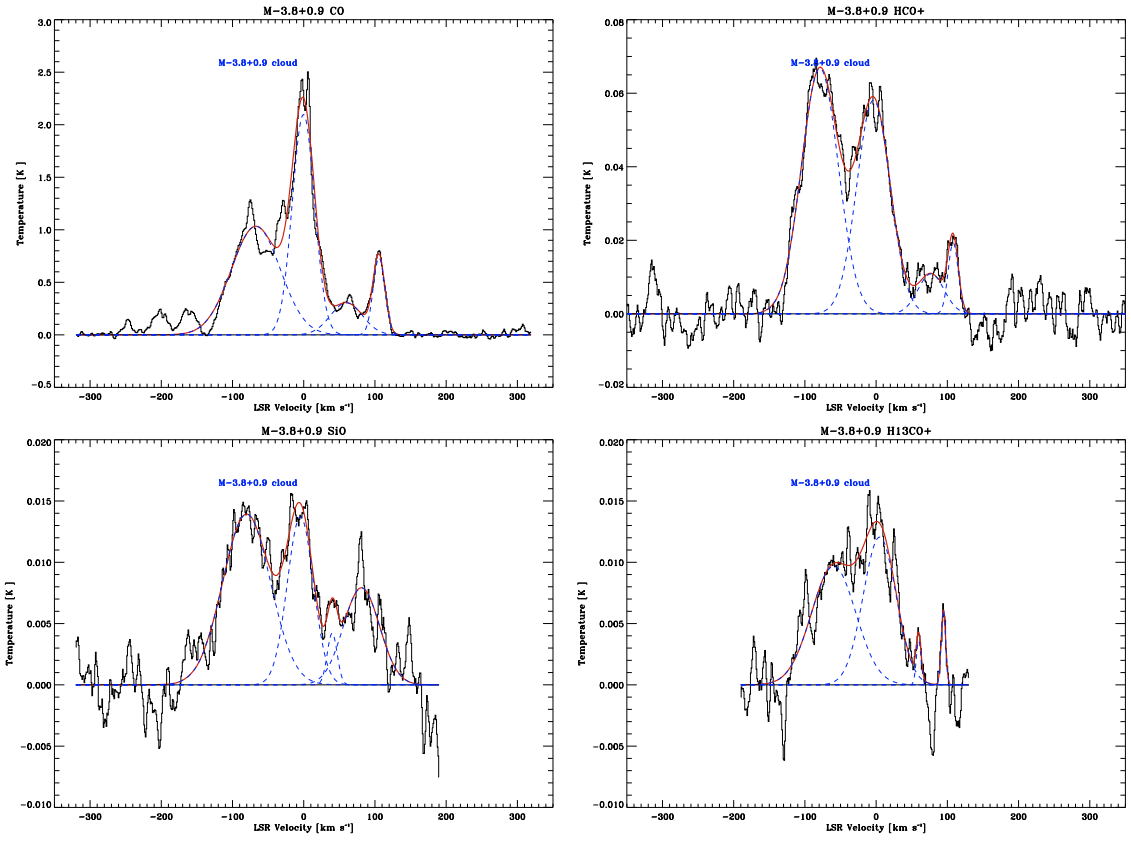

Fig. E.10. CO, HCO^+, SiO y $H^{13}CO^+$ average spectrum over the angular size of M−3.8+0.9 $(l, b, v) = (-3.8, 0.9, -83)$ (from $l = -4.0$ to -3.6875, and from $b = 0.5625$ to 1.1875).

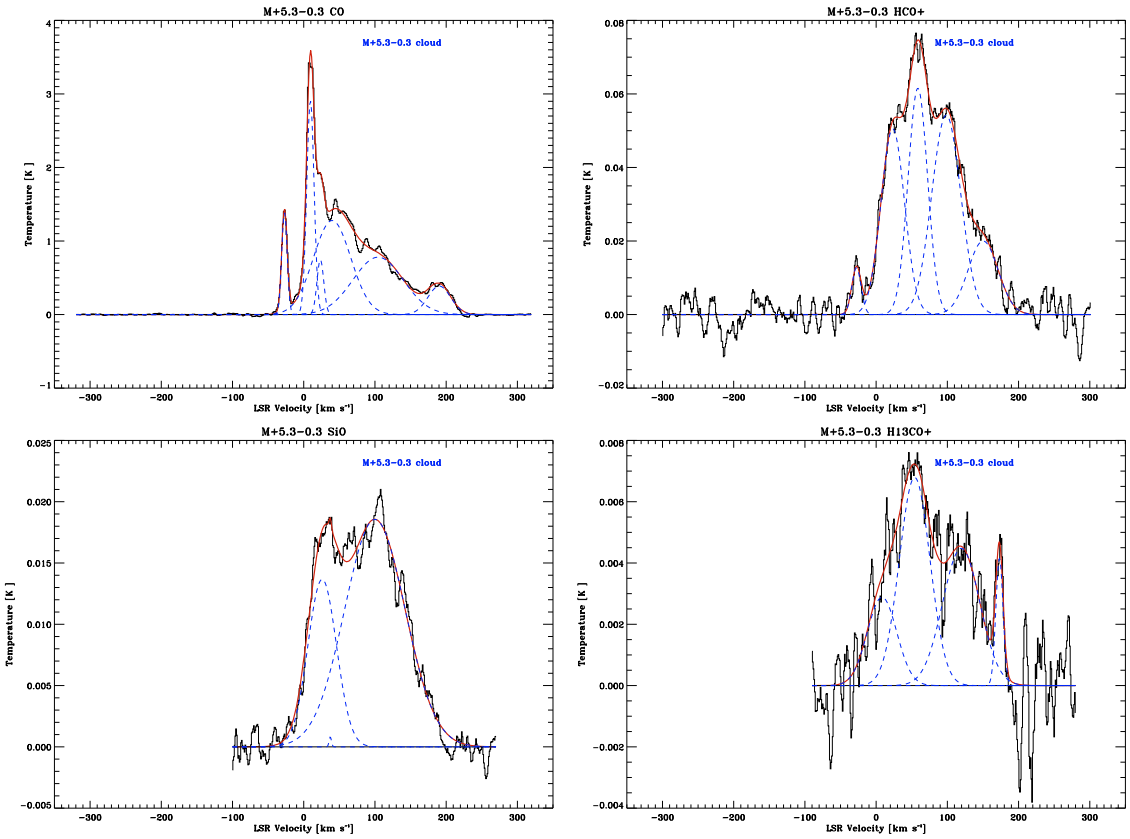

Fig. E.11. CO, HCO^+, SiO y $H^{13}CO^+$ average spectrum over the angular size of M+5.3-0.3 $(l, b, v) = (5.3, -0.3, 95)$ (from $l = 5.125$ to 5.5625, and from $b = -0.6875$ to 0.125).

Chapter 4

Tracing gas accretion in the Galactic center using isotopic ratios

4.1 Chemical evolution of the Galaxy

The standard "Big Bang Nucleosynthesis" can explain the bulk of the elemental abundances up to ^{7}Li (Boesgaard & Steigman 1985), while heavier nuclei must be synthetized in stars, through the "Stellar Nucleosynthesis" (see e.g. Wilson & Matteucci 1992; Wilson & Rood 1994, and references therein). Intermediate and high-mass stars ($> 8\ M_{\odot}$) are responsible for the enrichment of the interstellar medium (ISM) with nucleosynthesis products such as the main isotopes of carbon, nitrogen, and oxygen (CNO)(see, e.g., Wilson 1999, and references therein). They are called primary products, i.e. produced from H and He in a short period of time compared with the age of the Galaxy. Secondary elements are produced from primaries and its abundance grows with time relative to the abundance of primaries (Wilson 1999). Therefore, more processed gas should show lower primary to secondary isotopic ratios than the gas that has recently suffered a massive star-formation event (Table 4.1 summarizes the different types of isotopes).

As an example, the ^{12}C/^{13}C isotopic ratio reflects the relative degree of primary to secondary processing in stars (Wilson & Rood 1994). Since the first study of this isotopic ratio with good signal to noise and accurate calibration by Wannier et al. (1976), the ^{12}C/^{13}C has been the most frequently measured isotopic ratio in the ISM. While ^{12}C is predicted to be formed on rapid time scales in massive stars, primarily via He burning (Meyer 1994), ^{13}C is though to be produced primarily via CNO processing of ^{12}C seeds from previous stellar generations, on a shorter timescale primarily during the red giant phase in low and intermediate-mass stars or novae (Wilson & Matteucci 1992) (Table 4.1). This isotopic ratio has been established in the GC, with values derived from different molecules, e.g., Wannier (CO 1980), Henkel et al. (H_2CO 1980, 1985), Wannier (HCO^+ 1980), Wannier & Linke (HC_3N 1978), among others.

Observations have shown that abundances of elements vary in time and with location in the Galaxy and in other galaxies. Table 4.2 show the isotopic ratios in different regions of the Galaxy and in other galaxies. The comparison of abundances in the local ISM with Solar System abundances allow to trace the chemical evolution with time,

Table 4.1: Dominant source and kind of behavior of CNO+S isotopes (Table compiled by us from the literature).

Isotope	Source	Type of product	References
^{12}C	Intermediate and high-mass stars[a]	Primary	Meyer (1994)
^{13}C	From ^{12}C in low- and intermediate-mass stars, and novae.	Secondary	Wilson & Matteucci (1992) Prantzos et al. (1996)
^{14}N[b]	In stars of all masses from previous ^{12}C	Secondary	Romano & Matteucci (2003)
	Massive low-metallicity stars and intermediate-mass stars	Primary	Romano & Matteucci (2003)
^{15}N[b]	Type II SNe	Primary	Chin et al. (1996)
^{18}O	Massive stars (>8 $M_\odot$). Depends on the initial amount of ^{12}C and ^{16}O	Secondary	Prantzos et al. (1996) Wouterloot et al. (2008)
^{16}O	Massive stars (>10 $M_\odot$)	Primary	Romano & Matteucci (2003)
^{17}O	Intermediate and high-mass stars. Depends on the initial amount of ^{16}O.	Secondary	Prantzos et al. (1996)
^{32}S	Massive stars and type Ia SNe	Primary[c]	Chin et al. (1996)
^{34}S	Overproduced by massive stars		and references therein
^{33}S	Underproduced by massive stars		

[a] However, some authors suggest that the bulk of this isotope originates from low and intermediate-mass stars (see, Romano & Matteucci 2003, and references therein).

[b] Isotope with a controversial origin.

[c] All the S isotopes present a primary origin, but its production is different in massive stars (Type II and Ib/c SN).

where the abundances of the Solar System reflect the conditions of 4.5 Gyr ago[1], when it was formed (Wilson & Rood 1994). The comparison between the Local interstellar medium, the 4 kpc molecular ring, and the GC, shows a gradient with galactocentric distances. The ^{12}C/^{13}C isotopic ratio presents a clear gradient with the distance from the GC (e.g., Wilson 1999), decreasing from 80 − 90 in the solar neighborhood to 20 in the GC (see Table 4.2). This fact is the best example of how the different degree of gas processing translates into different isotopic ratio values.

4.2 The ^{12}C/^{13}C isotopic ratios as useful tool to trace gas accretion

In the following, we present a paper published in the Astronomy & Astrophysics in 2010. We observed 9 positions selected from §3.2 were the SiO emission shown enhancement when compared with HCO^+. As we mentioned before, the ^{12}C/^{13}C

[1] However, there is evidence that contradicts this assumption. For example, Orion A is representative of the Local ISM, and should have larger abundances of O and N than solar, but this is not the case (Wilson & Rood 1994)

Table 4.2: Isotopic ratios in the 4 kpc molecular ring and local ISM (Galactic Disk), and the Galactic Center. Table adapted from Wilson (1999).

Isotope Ratio	Galactic Center	4 kpc molecular ring	Local ISM	Solar System	Nuclei of galaxies	References
$^{12}C/^{13}C$	~ 20−25	53 ± 4	69 ± 6	89	> 81[c]	Wilson (1999)
$^{14}N/^{15}N$	> 600	320 ± 30	388 ± 32	270		Wilson (1999)
$^{16}O/^{18}O$	250	327 ± 32	557 ± 30	490	> 300[c]	Wilson (1999)
$^{18}O/^{17}O$	3.5 ± 0.2	3.6 ± 0.2	3.6 ± 0.2	5.5		Penzias (1981)
	3.1 ± 0.6					Guelin et al. (1982)
	2.88 ± 0.11					Wouterloot et al. (2008)
$^{32}S/^{34}S$	22	22	22	22	> 16	Frerking et al. (1980)
	16−20[a]					Martín et al. (2008)
		24.4 ± 5.0[b]				Chin et al. (1996)
$^{34}S/^{33}S$		6.27 ± 1.01[b]				Chin et al. (1996)

[a] Derived from abundances of $^{13}C^{32}S$ and $^{12}C^{34}S$ in 15 different molecular clouds of the GC.

[b] Average values for the Galactic Disk.

[c] From Martín et al. (2010)

isotopic ratio is well known in the GC region, showing a high degree of chemical processing by stars, but this isotopic ratio was only obtained in low latitude and low velocity molecular clouds in the CMZ. We derived for the first time the $^{12}C/^{13}C$ isotopic ratios towards high latitude and high velocity (also in forbidden velocities by Galactic rotation) molecular clouds. We obtained a systematically higher $^{12}C/^{13}C$ isotopic ratio (>40) toward the halo and the X1 orbits than for the Galactic center molecular clouds (20-25). Because this fresh non-processed gas has a different isotopic ratio than the normal GC gas, we propose that this matter was accreted toward the GC.The first observations of the project were done by Arancha Amo-Baladón using the old receiver at the 30m (receiver A, B, C, and D), and her preliminary analysis allows the following acepted proposals. With the change of the receiver at the 30m by EMIR, the project was rapidilly and successfully completed. I am the first author of the paper, and I was responsible for the observations at the 30m telescope using EMIR receiver, data reduction, analysis, and writing the paper.

A&A 523, A51 (2010)
DOI: 10.1051/0004-6361/201015008

Astronomy & Astrophysics

Tracing gas accretion in the Galactic center using isotopic ratios⋆

D. Riquelme[1], M. A. Amo-Baladrón[2], J. Martín-Pintado[2], R. Mauersberger[3], S. Martín[4], and L. Bronfman[5]

[1] Instituto de Radioastronomía Milimétrica (IRAM), Av. Divina Pastora 7, Local 20, 18012 Granada, Spain
e-mail: riquelme@iram.es
[2] Centro de Astrobiología (CSIC/INTA), Ctra. de Torrejón a Ajalvir km 4, 28850, Torrejón de Ardoz, Madrid, Spain
[3] Joint ALMA Observatory, Av. Alonso de Córdova 3107, Vitacura, Santiago de Chile, Chile
[4] European Southern Observarory, Av. Alonso de Córdova 3107, Vitacura, Casilla 19001, Santiago, Chile
[5] Departamento de Astronomía, Universidad de Chile, Casilla 36-D, Santiago, Chile

Received 17 May 2010 / Accepted 3 August 2010

ABSTRACT

Aims. We study the $^{12}C/^{13}C$ isotopic ratio in the disk of the central molecular zone and in the halo to trace gas accretion toward the Galactic center region in the Milky Way.
Methods. Using the IRAM 30m telescope, we observed the $J = 1-0$ rotational transition of HCO^+, HCN, HNC, and their ^{13}C isotopic substitutions in order to measure the $^{12}C/^{13}C$ isotopic ratio. We observed 9 positions selected throughout the Galactic center region, including clouds at high latitude, locations where the X1 and X2 orbits associated with the barred potential are expected to intersect, and typical Galactic center molecular clouds.
Results. We find a systematically higher $^{12}C/^{13}C$ isotopic ratio (>40) toward the halo and the X1 orbits than for the Galactic center molecular clouds (20–25). Our results point to molecular gas that has undergone a different degree of nuclear processing than observed in the gas towards the inner Galactic center region.
Conclusions. The high isotopic ratios are consistent with the accretion of the gas from the halo and from the outskirts of the Galactic disk.

Key words. Galaxy: center – ISM: clouds – ISM: molecules

1. Introduction

Many galaxies including our Milky Way contain huge amounts of gas in their central few 100 pc (Mauersberger & Henkel 1993; Morris & Serabyn 1996). This gas can be the fuel reservoir that feeds star formation events, and in many cases, the activity of the central object (Usero et al. 2004; García-Burillo et al. 2005). Both processes can occur in bursts. For example, the central region of our Galaxy, which harbors the nearest massive black hole ($\sim 4.0 \times 10^6\ M_\odot$; Ghez et al. 2005), may have been much more active in the past than it is now (Morris et al. 1999). It is obvious that such a high activity level, even if intermittent, can only be maintained if there is a supply of gas from other regions of the Galaxy, e.g. a disk or halo or from intergalactic space.

Modeling the kinematics of the inner regions of galaxies has been successful in explaining inward motion, matching the observations: Binney et al. (1991) have shown that the large-scale gas kinematics in the Galactic center (GC) can be accounted for by a barred galactic potential. In the dynamical model with a barred potential, there are two major families of stable prograde periodic orbits inside the bar: the X1 orbits parallel to the bar, and the X2 orbits orthogonal to it (Contopoulos & Papayannopoulos 1980). In the outer parts of the bar, gas tends to follow the X1 orbits. Farther inwards, these orbits develop cusps and loops (Maciejewski & Sparke 2000), where matter on self-intersecting orbits gets shocked and falls toward the center, and plunges to orbits of the X2 family (Binney et al. 1991).

Another mechanism for gas accretion toward the central region of galaxies is the disk-halo interaction. A clear example of these interactions has been shown recently by Fukui et al. (2006), who found huge loop structures (known as "giant molecular loops"; GMLs) that connect gas at the Galactic plane with gas at higher latitudes.

However, so far there is no clear observational evidence that gas in the outer disk (in X1 orbits) and/or at high latitudes (in the GMLs) flows toward the central regions. Gas in the GMLs could also be ejected to higher latitudes by winds, originated in past massive star formation events (the GC harbors giant molecular clouds with ongoing massive star formation, e.g. in Sgr B and the 1.3 complex). Observations of gas kinematics tell us what is happening now, but do not allow looking into the past. However, studies of the isotope trace the flow since different regions in a galaxy may have their very characteristic isotopic fingerprints. This approach has the potential to reconstruct the migration history to the central part of the galaxy.

Carbon, nitrogen, and oxygen (CNO) isotopic ratios are diagnostic tools for probing models of Galactic chemical evolution (see e.g. Audouze 1985). In particular, the $^{12}C/^{13}C$ isotopic ratio reflects the history of gas proccesing by stars, because this ratio shows the relative degree of primary to secondary processing in stars. While ^{12}C is predicted to be formed in first-generation, metal-poor massive stars, on rapid timescales, ^{13}C is thought to be produced primarily via CNO processing of ^{12}C seeds from earlier stellar generations, on a slower timescale in low and intermediate-mass stars or novae (Meyer 1994; Wilson & Matteucci 1992; Prantzos et al. 1996). The $^{12}C/^{13}C$ isotopic ratio is one of the best-established in the GC. It presents a clear

⋆ Based on observations carried out with the IRAM 30m telescope. IRAM is supported by INSU/CNRS (France), MPG (Germany), and IGN (Spain).

Table 1. Galactic and equatorial coordinates of the emission-free reference positions.

Galactic coordinates		Equatorial coordinates	
l [°]	b [°]	α_{J2000}	δ_{J2000}
5.75	1.0	17:54:56.6	−23:29:13
4.5	−1.29	18:00:57.3	−25:43:12
356.375	1.5	17:30:48.0	−31:11:48
359.75	−0.25	17:46:00.1	−29:16:47
1.0	−1.0	17:51:52.9	−28:35:41
0.65	0.2	17:46:23.0	−28:16:37

gradient with galactocentric distance (e.g., Wilson 1999), decreasing from 80−90 in the solar neighborhood to 20–25 in the inner Galaxy (toward Sgr A and Sgr B, see e.g., Wannier 1980). However, this ratio is, so far, unknown in the galactic halo and in the X1 orbits.

In this paper we present observations of the $J = 1-0$ rotational transition of HCO^+, $H^{13}CO^+$, HCN, $H^{13}CN$, HNC, and $HN^{13}C$ to derive the $^{12}C/^{13}C$ isotopic ratio toward the gas in the halo, the disk, and for the kinematic components associated with the X1 and X2 orbits in the nucleus of our Galaxy. We found very different $^{12}C/^{13}C$ isotopic ratios in the X1 orbits and in the halo from those in the disk and in the X2 orbits. Our findings are consistent with the scenario of less processed gas in the halo and in the X1 orbits, supporting the idea of gas flowing toward the nucleus of the Milky Way.

2. Observations

Observations were carried out with the IRAM-30m telescope at Pico Veleta (Spain) in June and December 2009. We used the E090 band of the new EMIR receiver, which provide a bandwidth of ~8 GHz (from 83.7 to 91.1 GHz) simultaneously in both polarizations. For the backend, we used the WILMA autocorrelator, providing a resolution of 2 MHz or 6.8 km s^{-1}. Observations were performed in position-switching mode where the reference off-positions were checked to be free of emission. Table 1 lists the emission-free positions. The pointing was checked every 2 h against the source 1757-240 providing an accuracy better than 5″. Data were calibrated using the standard dual load system. In this work, we use the antenna temperature scale T_A^*. Main beam temperatures, T_{MB}, can be obtained using $T_{MB} = F_{eff}/B_{eff} \times T_A^*$, where the forward efficiency is $F_{eff} = 95\%$ and the main-beam efficiency is $B_{eff} = 81\%$ at 86 GHz. All positions were observed for no less than 30 min providing an rms noise antenna temperature of about 6 mK in the weakest lines (e.g. $H^{13}CO^+$).

We observed the nine positions shown in Table 2 displayed on the large-scale map of the HCO^+ emission shown in Fig. 1. Five of the observed positions are located in the GMLs (halo in Tables 2, 3, and Fig. 1). Three of them are located at the foot points and two at the top of the loops. Two positions are in the disk toward the locations of the expected interactions between the X1 and X2 orbits (Disks X1 and X2 in Tables 2, 3, and Fig. 1). A pair of positions toward the Galactic plane (Disk in Tables 2, 3, and Fig. 1) were used as reference measurements. The positions at the foot points of the GMLs were selected from the intensity peaks of the SiO maps of Riquelme et al. (2010) and from previous results from higher angular resolution mapping with the Mopra-22 m telescope (Riquelme et al., in prep.). The Fukui et al. (2006) maps of the GMLs were used to select the position at the top of the loop. The positions in the 1.°3 and in Sgr C complexes correspond to the locations where interactions between the X1 and X2 orbits are expected (see, Binney et al. 1991; Stark et al. 2004). The CO and SiO(2−1) maps of these regions (Tanaka et al. 2007; Amo-Baladrón et al., in prep.) were used for final selection of the positions. The control points in the disk are located in Sgr B2 and in the $l = 5.°7$ complex selected from Martín et al. (2008) and Fukui et al. (2006), respectively.

3. Results

Figure 1 shows the spectra taken in all the observed positions in the $J = 1 \rightarrow 0$ transition of the main isotope of HCO^+, HCN and HNC and their ^{13}C isotopologues. All the species have been clearly detected in all our sources, except $HN^{13}C$, with tentative detections in "Halo 1" and "Halo 3", and a nondetection in "Halo 2".

Table 3 shows the integrated line-intensity ratios between the different isotopologues derived for all positions and velocity components. To distinguish between the different kinematical components, the line intensity ratios were obtained by integrating the line profiles in the velocity ranges given in Table 3. We derived line-intensity ratios from three different species, obtained the highest values from HCO^+.

4. The $^{12}C/^{13}C$ isotopic ratios

The isotopologues that we observed in this work have very similar rotational constants and Einstein coefficients, therefore the beam size is very similar. For optically thin emission, one would expect that line intensity ratios would be directly converted into column density ratios, i.e., $\int T_{H^{12}CO^+} dv / \int T_{H^{13}CO^+} dv = N(H^{12}CO^+)/N(H^{13}CO^+) = [H^{12}CO^+]/[H^{13}CO^+]$.

In general, the molecular isotopologue ratios (see Table 3) do not translate directly into $^{12}C/^{13}C$ isotopic ratios. Opacity, chemical fractionation, and selective photodissociation effects must be considered to derive the isotopic ratios from molecular line-intensity ratios. In the following, we discuss the importance of these effects on the $^{12}C/^{13}C$ isotopic ratios that we derive from our integrated intensity ratio of the isotopologues.

4.1. Opacity effects, isotopic fractionation, and selective photodissociation

In our case, it is impossible to estimate the line optical depth from the emission of just one single transition. Since optical depth effects will saturate the emission from the most abundant isotopologue, our derived molecular isotopic ratios must be considered to be lower limits to the actual $^{12}C/^{13}C$ isotopic ratios. In almost all cases, the $HCO^+/H^{13}CO^+$ intensity ratios or their limits are higher than those derived from the HCN and HNC isotopomers. This may be interpreted as HCO^+ being the least optically thick among the three molecular line emissions used in this work. Therefore, $HCO^+/H^{13}CO^+$ intensity ratios give the most stringent limits to the $^{12}C/^{13}C$ isotopic ratios. We still cannot exclude that HCO^+ is also affected by opacity effects, which means that $^{12}C/^{13}C$ isotopic ratios are even higher than inferred from the $HCO^+/H^{13}CO^+$ intensity ratios. In the following, we therefore only consider the isotopologue ratios derived from HCO^+.

Another important effect may be chemical fractionation (Wilson 1999, and references therein). Langer et al. (1984) studied the fractionation of carbon and oxygen isotopes with a time-dependent chemical model. Their model considers a cloud lifetime of 10^8 years, temperatures from 6 to 80 K, H_2 densities

Table 2. Observed positions.

Associated object	Galactic coordinates l [°]	b [°]	Equatorial coordinates α_{J2000}	δ_{J2000}	This work
M+5.3 − 0.3	5.45	−0.324	$17^h59^m17.8^s$	−24°24′38″	Halo 1
M−3.8 + 0.9	356.206	0.83	$17^h32^m59.8^s$	−31°42′17″	Halo 2
M−3.8 + 0.9	356.179	0.925	$17^h32^m33.2^s$	−31°40′31″	Halo 3
Top Loop	4.75	−0.8	$17^h59^m34.9^s$	−25°15′16″	Halo 4
Top Loop	356.549	1.339	$17^h31^m52.5^s$	−31°08′19″	Halo 5
1.3 complex	1.28	+0.07	$17^h48^m21.9^s$	−27°48′19″	Disk X1-1, Disk X2-1
Sgr C	359.446	−0.124	$17^h44^m46.9^s$	−29°28′25″	Disk X1-2, Disk X2-2
Galactic plane at $l \sim 5.'7$	5.75	0.25	$17^h57^m46.5^s$	−23°51′51″	Disk 1
Sgr B2	0.6932	−0.026	$17^h47^m21.9^s$	−28°21′27″	Disk 2

Table 3. Intensity ratios from the observed ^{12}C and ^{13}C isotopomers.

Source	Velocity component LSR [km s^{-1}]	Velocity range [km s^{-1}]	$HCO^+/H^{13}CO^+$ ratio of $\int T_A^* dv$	$HCN/H^{13}CN$ ratio of $\int T_A^* dv$	$HNC/HN^{13}C$ ratio of $\int T_A^* dv$
Halo 1	100	[50, 190]	45.5± 5.4	13.5±0.2	≥ 25.6
	87	[50, 97]	≥73.9	25.8±2.0	≥7.5
	117	[97, 135]	32 ± 3.7	11.3±0.1	≥37.5
	144	[135, 190]	39.1±24.7	16.7±1.8	≥2.7
Halo 2	−62	[−115, −20]	73.1±36.5	14.6 ±1.0	≥15.4
	left wing	[−115, −70]	≥34.4	21.2 ±3.3	≥8
	right wing	[−70, −20]	53.2±26.1	11.6 ±0.9	≥13.6
Halo 3	−60	[−120, −30]	38 ±5.0	13 ±0.3	≥40.1
	left wing	[−120, −80]	54.2 ±37.7	19.2 ±1.9	≥10.4
	central peak	[−80, −30]	35.7 ±4.0	12 ±0.2	48.3 ± 21.8
Halo 4	200	[150, 250]	28.3 ±5.4	11.8 ±0.9	14.9 ±3.1
	peak	[150, 210]	29.2 ±7.5	11.7 ±0.8	17.9 ±3.9
	right wing	[210, 250]	≥10.6	12.4 ±4.0	7.1 ±3.4
Halo 5	−50	[−100, −40]	13.8 ±5.0	6.9 ±0.3	22.8 ±12
Disk X1-1	180	[140, 230]	56 ± 6.4	10.8 ±0.1	25.5 ± 7.5
	left wing	[140, 180]	57.2 ± 7.5	11.6 ±0.1	≥8
	right wing	[180, 230]	54.4 ± 11	9.9 ±0.2	15.7 ± 4.4
Disk X2-1	95	[50, 140]	29 ± 1.6	12.1 ± 0.2	22.1 ± 2.7
	left wing	[50, 92]	32.4 ± 3.7	13.9 ± 0.4	22.8 ± 4.0
	right wing	[92, 140]	27.3 ± 1.7	11.3 ± 0.2	21.7 ± 8.6
Disk X1-2	67	[0, 100]	42.1± 8.6	9.4 ± 0.1	9.9 ± 1.3
Disk X2-2	−43	[−80, −20]	21.7 ±1.9	6.6 ±0.1	13.1 ±1.0
Disk 1	66	[35, 105]	14.0 ±2.8	13.1 ± 1.0	15.8 ± 3.6
	central peak	[35, 70]	16.4 ±4.6	23.1 ± 3.8	≥11.4
	right wing	[70, 105]	11.6 ±3.4	7.8 ± 0.7	11.7 ± 2.7
Disk 2	left wing	[0, 43]	≥29.1	9.1 ± 0.2	≥21.9
	55	[43, 97]	4.1 ± 0.1	3.5 ± 0.1	3.7 ± 0.1
	right wing	[97, 135]	16.1 ± 2.3	13.8 ± 1.3	≥2.6

from 5×10^2 to 1×10^5 cm^{-3}, and a wide range of metal abundances. Fractionation in HCO^+ has also been studied by Woods & Willacy (2009) for protoplanetary disks, which can have a greater impact on the $^{12}C/^{13}C$ ratio, but with temperatures and densities different from the GC. Langer et al. (1984) found that the behavior of the carbon isotope ratios can be split into three groups: CO, HCO^+, and "carbon-isotope pool" (which includes the remaining carbon species, such as C^+, H_2CO, CS, etc). They found that the ^{13}C is enhanced in the CO (specially at low temperature, low density, and high metal abundance), that the ^{12}C is enhanced in the "carbon isotope pool" group, and that the HCO^+ could present both fractionation effects, depending on the physical condition. The behavior of HCO^+ is related to the formation of this molecule from both CO and from the "carbon pool isotopes". The formation of HCO^+ has been explained by the ion-molecule chemistry (Wilson et al. 2009), where the reaction

$$H_3^+ + CO \leftrightarrow HCO^+ + H_2 \quad (1)$$

likely leads the production of HCO^+. $H^{13}CO^+$ is more tightly bound than HCO^+ by 0.8 meV (9 K). The reactions that have the potential to produce isotopic fractionation occurs by proton-switching reactions between formyl ions and carbon monoxide by (Langer et al. 1978, 1984)

$$HCO^+ + ^{13}CO \leftrightarrow H^{13}CO^+ + ^{12}CO + 9\ K. \quad (2)$$

As shown in Fig. 1 of Langer et al. (1984), the isotopic ratio derived from HCO^+ presents only moderate fractionation. The $H^{12}CO^+/H^{13}CO^+$ ratio is slightly enhanced at low density and moderate temperature, and decreases at low temperatures and certain densities ($n(H_2) < 10^3$ and $n(H_2) > 10^{4.5}$). In this model, Langer et al. (1984) considered the formation paths of HCO^+ shown in the Table 2 of Graedel et al. (1982). Hüttemeister et al. (1998) and Rodríguez-Fernández et al. (2002) find that the gas in the GC has temperatures ranging from 20 to 200 K. For this temperature range, the predicted fractionation of HCO^+ is negligible so the fractionation of ^{13}CO cannot occur. In the worst case, the isotopic ratio throughout the GC should not increase

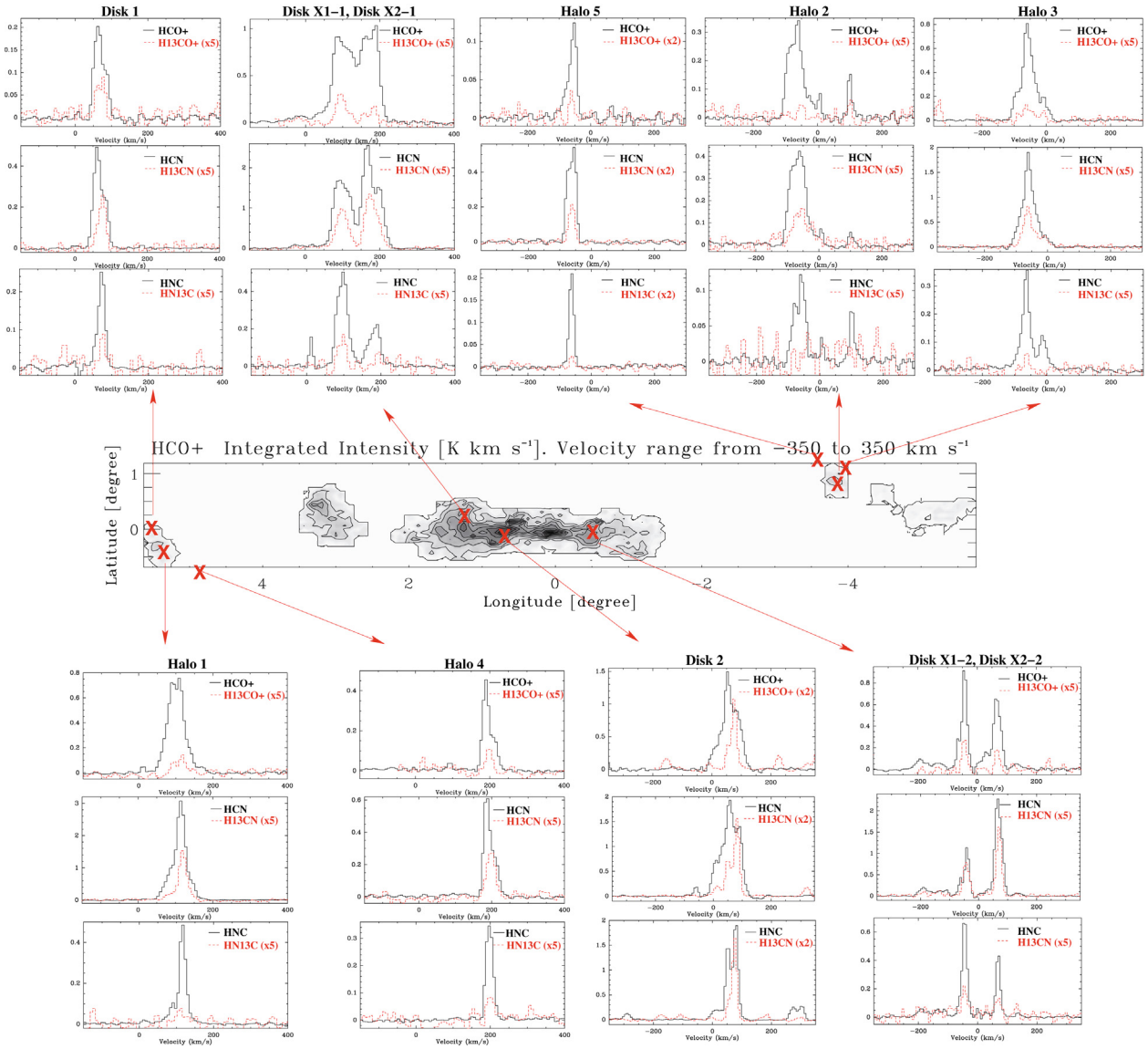

Fig. 1. Spectra toward selected positions in the GC in HCO^+, $H^{13}CO^+$, HCN, $H^{13}CN$, HNC, and $HN^{13}C$. The positions are indicated in the HCO^+ integrated intensity map from Riquelme et al. (2010). The main isotope is plotted in black solid line. The ^{13}C isotope is plotted in red dashed line. The ^{13}C substitution is scaled by a factor of 2 or 5 to allow an easy visualization of the spectra. The factor is indicated in each spectrum.

selectively one of the molecular isotopologue against the other by more than 20%.

For molecular clouds affected by UV radiation, selective photodissociation can take place, which would increase the $^{12}C/^{13}C$ isotopic ratio. The more abundant molecules (the main isotopologues) are less affected by photodissociation through self-shielding against UV radiation than the rarer isotopologues. So far, studies of the HCO^+ and its ^{13}C isotopologue in PDRs have not shown any clear evidence of selective photodissociation (Fuente et al. 2003). Milam et al. (2005) conclude that the $^{12}C/^{13}C$ isotopic ratio derived from high-density tracers like CN are very unlikely to be influenced by isotope-selective photodissociation. However the self-shielding and photodissociation of CO (e.g., Bally & Langer 1982; Chu & Watson 1983; Glassgold et al. 1985) could affect our derived $^{12}C/^{13}C$ ratios through formation of HCO^+ via the reaction in Eq. (1). When modeling this effect, Chu & Watson (1983) concluded that the selective photodissociation will have a negligible impact on the $^{13}CO/^{12}CO$ ratio. Although the local enviroment of the GMLs is so far unknown, there are no signposts of UV radiation. There is only a nearby ultracompact H II region identified at $(l, b) \sim (356.^{\circ}25, 0.^{\circ}7)$, but its radial velocity of ∼120 km s^{-1}suggests that it is not associated with the foot points of the GMLs (Torii et al. 2010), making it very unlikely that there is any effect on our derived isotopic ratios by photodissociation. The low $^{13}CO/^{12}CO$ ratio observed in the GMLs by Torii et al. (2010) does not confirm that the bulk of the gas is neither self-shielded in ^{12}CO nor photodissociated in ^{13}CO. The low ratios likely comes from optically thick emission in ^{12}CO, suggesting rather high CO column densities. Then the bulk of the gas will not be affected by the rather low fluxes of far UV radiation inferred from the lack of H II regions (Torii et al. 2010) in the area. Under these conditions, it is highly unlikely that the fractionation/self-shielding effect in the $^{13}CO/^{12}CO$ could explain the observed high $H^{12}CO^+/H^{13}CO^+$ ratios. We conclude that the line-intensity ratios derived from our data correspond to a lower limit to the actual $^{12}C/^{13}C$ isotopic ratio.

We derived $H^{12}CO^+/H^{13}CO^+$ intensity ratios from 4 to >74. The lowest value of 4 is found toward the source Disk 2 in the position of Sgr B2, where one would expect a value of ∼25. Such a

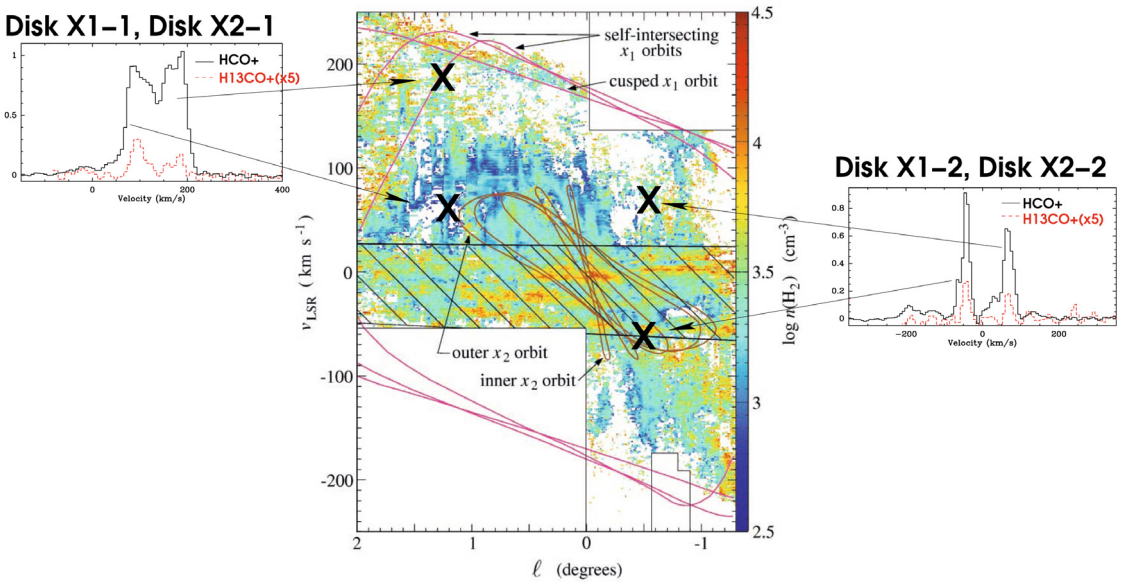

Fig. 2. Spectra toward the X1 and X2 orbits in HCO^+ and $H^{13}CO^+$ (scaled by a factor of 5). *Left*: spectra toward the 1.3 complex. *Center*: l-v diagram showing the X1 and X2 orbits superimposed (Stark et al. 2004). *Right*: spectra toward Sgr C region.

low measured value indicates that HCO^+ is optically thick. From the results in Table 3, we find a systematic trend in the isotopologue ratios with the highest values, >74, found toward Halo 1 and Halo 2. Also Halo 3 and Disk X1-1 and Disk X1-2 show high values of >42.

5. Discussion

It is remarkable that there is a systematic trend by the $^{12}C/^{13}C$ isotopic ratio, found toward the halo and in the disk for the kinematic components associated with the X1 orbits, to be systematically higher by a factor of at least 2 than the standard value in the GC of ~25. This suggests that there is less processed material in the halo and in the X1 orbits than in the X2 orbits and the reference GC positions in the disk.

Surprisingly, the isotopic ratios measured in the Halo 4 and Halo 5 positions at the top of the GMLs show a lower $^{12}C/^{13}C$ isotopic ratio than in the other halo positions, which are closer to the "standard" values of the disk. From our data, it is still not clear if this low isotopic ratio is comes from opacity effects in the main isotope or from a mixture with more processed gas from stellar nucleosynthesis in the GC region, likely ejected to high latitudes from the disk.

5.1. History of the chemical evolution of the molecular gas in the Galactic center

The lower limits to the $^{12}C/^{13}C$ isotopic abundance ratios derived from our HCO^+ data toward the "typical" GC molecular clouds (Disk 1, Disk 2, Disk X2-1, Disk X2-2) range between 4 to 32, with an average value of 20. These results agree with the values found in the literature for the GC (20–25, Wilson 1999) and with the average value derived by Riquelme et al. (2010) of 19.8 (from the $HCO^+/H^{13}CO^+$ integrated intensity ratio throughout the GC region), showing a considerable nuclear processing. In contrast, we have found much higher limits to the isotopic ratios toward the locations where gas in the inner disk[1] is expected to be interacting with gas in the halo and in the disk. Indeed, the gas in the X1 orbits has a different nature than in the X2 orbits, as clearly reflected by their different isotopic ratios of ~55 and ~21−30, respectively. Furthermore, in the halo, the interaction occurs when the gas in the top of the loops flows toward the foot points of the GMLs. In both cases, the isotopic ratio reflects a different nature of the gas than in the GC. The $^{12}C/^{13}C$ isotopic ratio of the gas in the halo and in the X1 orbits are in general higher than 40, reaching values over 70 in "Halo 1".

Previous studies show a clear gradient in the $^{12}C/^{13}C$ ratio with galactocentric distance. The ratio changes from a value of about 50 in the inner Galaxy (4 kpc) to nearly 70 in the local ISM, and ~90 in the solar system, with a value ~20−25 in the GC (Wilson 1999), which reflects higher nuclear processing toward the inner Galaxy. Studies of the isotopic ratios in the GC (Wannier 1980; Stark 1981; Henkel et al. 1985; Langer & Penzias 1990) have shown that the interstellar gas in the GC is in an advanced state of chemical evolution (which corresponds to an enrichment of ~3–4 with respect to the local gas). This gradient indicates that the material is flowing to the inner central kiloparsec of the GC from the Galactic halo (in the case of GMLs) and the outskirts of the Galactic disk (in the case of X1-X2 interacting orbits).

5.2. The origin of molecular gas in the GML

Our lower limits to the $^{12}C/^{13}C$ isotopic ratios in the halo sources for the foot points of the GMLs are close to the values measured in the local ISM (69 ± 6, Wilson 1999). Based on energetic and morphological arguments, Fukui et al. (2006) argue that it is impossible that the loop features are created by supershells or supernova explosions. Our data strongly support their claim. If the loop features were formed by supernova or hypernova explosions, the gas at the foot points should have been ejected from the GC to high latitudes, reflecting the isotopic ratio found throughout the GC. It is likely that the gas in the GMLs has been accreted

[1] Throughout this work, all the positions observed and discussed are in the Galactic center region (in the central kpc of the Galaxy). We denote "disk" as the disk in the CMZ, "inner disk" to the allowed velocities in the X2 orbits, and "outer disk" and "outskirts of the disk" as the noncircular motions (X1 orbits).

from high latitudes. However, if the low isotopologue ratio found at the top of the loops is confirmed to be the actual isotopic ratios, this might indicate that some gas in the halo could also have been ejected from the disk.

Magneto-hydrodynamical simulations have been successful in explaining the formation of the loops (Matsumoto et al. 1988; Horiuchi et al. 1988; Fukui et al. 2006; Machida et al. 2009; Takahashi et al. 2009). They claim that the GMLs have been formed as a natural consequence of a differentially rotating magnetized gas disk under a strong gravitational potential (Machida et al. 2009). It is found that the loop efficiently accumulates gas generating a dense layer at the top of the loops. However, our results are not consistent with the magneto-hydrodynamical loop scenario in which the gas in the GML falling to their foot point should share the same isotopic ratios as the gas in the Galactic disk. Morris (2006) also point out that there is too much gas left at the top of the loops if the gas is flowing down along the magnetic field lines. Morris (2006) and Torii et al. (2009) alternatively propose that ambient HI gas may be converted in the GML into H_2 during flotation. It is likely that the loops are surrounded by H I gas. The rising portion of the magnetic loops suffer shocks that compress the relatively rarefied atomic gas in front of it, leading to rapid cooling and, ultimately, to a phase transition from atomic to molecular gas Morris (2006). Therefore the molecular gas that defines the loops is constantly replenished. This scenario also confirms our results, because the gas in the foot point of the loop has not yet been processed by star formation.

5.3. Gas accretion from the outer disk

We have also found high isotopic ratios toward the noncircular components in the nuclear disk, which have been explained in terms of a stellar-bar driven potential (Binney et al. 1991). The 1.°3 complex has been observed and studied by several authors (Tanaka et al. 2007; Oka et al. 2001; Hüttemeister et al. 1998). This molecular complex shows broad velocity widths and a large latitudinal height scale. The molecular emission shows two velocity components, one centered at ∼110 km s^{-1}and the other at ∼190 km s^{-1}, which correspond to our Disk X2-1 and Disk X1-1 sources, respectively. Tanaka et al. (2007) find an enhancement of the CO $J = 3–2$, HCO^+ $J = 1–0$, HCN $J = 1–0$ with respect to the CO $J = 1–0$, and an enhancement in the abundance of SiO in the high-velocity component (>110 km s^{-1}). They also identify several expanding shells that are very prominent at $v_{LSR} < 110$ km s^{-1}associated with recent star formation. They conclude that the two components correspond to different types of gas with different kinematics and physical conditions. Our Disk X1-1 component presents an enhancement of the SiO/^{13}CO intensity ratio of a factor ∼3 (Tanaka et al. 2007) with respect to the lower velocity component (Disk X2-1). Like Hüttemeister et al. (1998), Tanaka et al. (2007) explains the high SiO abundance as a consequence of recent shock activity.

From our measurements of isotopic ratios, we conclude that the gas associated with the lowest velocity component presents a "typical" GC isotopic ratio consistent with previous ideas of chemistry dominated by shocks generated by supernova explosions. It is very unlikely, however, that the higher velocity component, Disk X1-1, could be associated to the supernova scenario, like the Disk X2-1 component does, as also inferred from the high isotopic ratio found toward this source. The most likely scenario is that the high SiO abundance is the result of the shocks generated by the transfer of gas between the X1 and X2 orbits as suggested by the potential bar scenario.

6. Conclusions

We have determined lower limits to the ^{12}C/^{13}C isotopic ratio toward 9 positions in the GC region, both in the disk and in the halo. In contrast to the values found in the disk sources (∼4–30), we found high isotopic ratios toward the locations where the disk-halo (∼>40–>70) and X1-X2 orbit interactions (>42–>56). Our results are consistent with a scenario where gas from the halo is accreted to the disk and with the transfer of gas from the outskirt of the disk to the GC through X1 and X2 orbits as suggested by the potential bar scenario.

Acknowledgements. D.R. and R.M. were supported by DGI grant AYA 2008-06181-C02-02. J.M-P. and S.M. have been partially supported by the Spanish 74 MICINN under grant number ESP2007-65812-C02-01, and by AYA2010-21697-C05-01. L.B. acknowledges support from FONDAP Center for Astrophysics 15010003 and from Center of Excellence in Astrophysics and Associated Technologies (PFB 06).

References

Audouze, J. 1985, in ESO Astroph. Symp., ed. I. J. Danziger, F. Matteucci, & K. Kjar, 21, 373
Bally, J., & Langer, W. D. 1982, ApJ, 255, 143
Binney, J., Gerhard, O. E., Stark, A. A., Bally, J., & Uchida, K. I. 1991, MNRAS, 252, 210
Chu, Y., & Watson, W. D. 1983, ApJ, 267, 151
Contopoulos, G., & Papayannopoulos, T. 1980, A&A, 92, 33
Fuente, A., Rodríguez-Franco, A., García-Burillo, S., Martín-Pintado, J., & Black, J. H. 2003, A&A, 406, 899
Fukui, Y., Yamamoto, H., Fujishita, M., et al. 2006, Sci., 314, 106
García-Burillo, S., Combes, F., Schinnerer, E., Boone, F., & Hunt, L. K. 2005, A&A, 441, 1011
Ghez, A. M., Salim, S., Hornstein, S. D., et al. 2005, ApJ, 620, 744
Glassgold, A. E., Huggins, P. J., & Langer, W. D. 1985, ApJ, 290, 615
Graedel, T. E., Langer, W. D., & Frerking, M. A. 1982, ApJS, 48, 321
Henkel, C., Güsten, R., & Gardner, F. F. 1985, A&A, 143, 148
Horiuchi, T., Matsumoto, R., Hanawa, T., & Shibata, K. 1988, PASJ, 40, 147
Hüttemeister, S., Dahmen, G., Mauersberger, R., et al. 1998, A&A, 334, 646
Langer, W. D., Graedel, T. E., Frerking, M. A., & Armentrout, P. B. 1984, ApJ, 277, 581
Langer, W. D., & Penzias, A. A. 1990, ApJ, 357, 477
Langer, W. D., Wilson, R. W., Henry, P. S., & Guélin, M. 1978, ApJ, 225, L139
Machida, M., Matsumoto, R., Nozawa, S., et al. 2009, PASJ, 61, 411
Maciejewski, W., & Sparke, L. S. 2000, MNRAS, 313, 745
Martín, S., Requena-Torres, M. A., Martín-Pintado, J., & Mauersberger, R. 2008, ApJ, 678, 245
Matsumoto, R., Horiuchi, T., Shibata, K., & Hanawa, T. 1988, PASJ, 40, 171
Mauersberger, R., & Henkel, C. 1993, Rev. Modern Astron., 6, 69
Meyer, B. S. 1994, ARA&A, 32, 153
Milam, S. N., Savage, C., Brewster, M. A., Ziurys, L. M., & Wyckoff, S. 2005, ApJ, 634, 1126
Morris, M. R. 2006, Sci., 314, 70
Morris, M., & Serabyn, E. 1996, ARA&A, 34, 645
Morris, M., Ghez, A. M., & Becklin, E. E. 1999, Adv. in Space Res., 23, 959
Oka, T., Hasegawa, T., Sato, F., et al. 2001, ApJ, 562, 348
Prantzos, N., Aubert, O., & Audouze, J. 1996, A&A, 309, 760
Riquelme, D., Bronfman, L., Mauersberger, R., May, J., & Wilson, L. T. 2010, 115, A&A, accepted [arXiv:1006.3438]
Rodríguez-Fernández, N. J., Martín-Pintado, J., de Vicente, P., & Fuente, A. 2002, Ap&SS, 281, 331
Stark, A. A. 1981, ApJ, 245, 99
Stark, A. A., Martin, C. L., Walsh, W. M., et al. 2004, ApJ, 614, L41
Takahashi, K., Nozawa, S., Matsumoto, R., et al. 2009, PASJ, 61, 957
Tanaka, K., Kamegai, K., Nagai, M., & Oka, T. 2007, PASJ, 59, 323
Torii, K., Kudo, N., Fujishita, M., et al. 2009, PASJ, 62, 1307
Torii, K., Kudo, N., Fujishita, M., et al. 2010, PASJ, 62, 675
Usero, A., García-Burillo, S., Fuente, A., Martín-Pintado, J., & Rodríguez-Fernández, N. J. 2004, A&A, 419, 897
Wannier, P. G. 1980, ARA&A, 18, 399
Wilson, T. L. 1999, Rep. Progr. Phys., 62, 143
Wilson, T. L., & Matteucci, F. 1992, A&A Rev., 4, 1
Wilson, T. L., Rohlfs, K., & Hüttemeister, S. 2009, Tools of Radio Astronomy (Springer-Verlag)
Woods, P. M., & Willacy, K. 2009, ApJ, 693, 1360

Chapter 5

Kinetic temperatures in the Galactic center disk-halo interaction regions

5.1 The NH_3 molecule

Ammonia, NH_3, is a symetric top molecule with a pyramidal structure. It was the first polyatomic molecule[1] detected in interstellar space (Cheung et al. 1968). Fig.5.1 shows the rotational and inversion transitions diagrams sensitive to a wide range of excitations conditions. This molecule is ubiquitous in the ISM and is observed in a great variety of regions. There are several important properties that make NH_3 an invaluable spectroscopic tool to study the interstellar medium, such as the existence of metastable and nonmetastable states, orto- and para- species, inversion motion of the molecule, and hyperfine structures (Ho & Townes 1983).

The rotational energy of NH_3 are caracterised by two principal quantum numbers (J, K), which correspond to the total angular momentum and its projection along the molecular symetry axis. Unless there is some excitation of vibration transverse to the axis, the molecule has an electric dipole moment only along the molecular axis, with dipole selection rules $\Delta K = 0, \Delta J = 0, \pm 1$. Hence, dipole transitions between K-ladders are normally forbidden. The $K-$ladders are connected by octupole radiative transitions, which require $\Delta K = \pm 3$ (Wilson et al. 2009a), which are very slow. Only collisions produce exchange of population between K ladders. In each $K-$ladder, the states for which $J > K$, decay rapidly $(10 - 10^2 s)$ via far-infrared $\Delta J = 1$ transitions. These are called *non-metastable* and are difficult to populate under low density and low temperature conditions. The *metastable* states are the lower energy state of the $K-$ladders $(J = K)$ (Ho & Townes 1983; Wilson et al. 2009a).

Due to the possible orientations of the hydrogen spins states there are two different species of NH_3: *ortho-NH_3* $(K = 3n, n = 0, 1, 2, ...)$ where all H spins are parallel, and *para-NH_3* $(K \neq 3n)$ where the H spins are not all parallel. Transitions between ortho-NH_3 and para-NH_3 are also forbidden, since radiative and collisional transitions do not change spin orientations. The rotational temperatures between ortho and para-NH_3 may reflect the conditions at the time of the formation of NH_3, while rotational temperatures within the same species may reflect more recent conditions (Ho & Townes 1983; Umemoto et al. 1999).

[1] molecule with three or more atoms

This molecule also has inversion modes. The potential barrier of the H atoms is low enough, to allow rapid quantum mechanical tuneling of the N atom through the plane of the H atoms. This results in two vibrational states with a transition frequency that falls in the microwave range, with wavelengths of $\simeq$ 1.3 cm wavelength. This were the transitions observed in this work. All the (J, K) rotational transitions are split into inversion doublets (except for K=0, where nuclear spin statistics and symmetry considerations eliminate half of the inversion doublets). The $\Delta J = 0, \Delta K = 0$ inversion transitions across the doublets are allowed from symmetry considerations (Townes & Schawlow 1955).

The inversion doublets are split by the interaction between the electric quadrupole moments of the N nucleus and the electric field of the electrons giving rise to hyperfine components (see Fig. 5.2). Since the ^{14}N spin is unity, each level of the doublets is split by the nuclear orientation into 3 hyperfine states, resulting in 5 distinct components of the transition frequency. These are the main line ($\Delta F_1 = 0, F_1 = J + I_N$, where I_N is the nitrogen spin) having at least 50% of the total intensity, and two pairs of satellite lines ($\Delta F_1 = \pm 1$) with rougly equal intensities, separated from the main line by $\sim$ 1 MHz. Weaker magnetic interactions produce splitting of the order of $\sim$ 40 kHz. This splitting occurs due to $I_N \cdot J$ and $I \cdot J$ (I is the sum of the H spins) coupling, as well as H-N and H-H spin-spin interactions (Ho & Townes 1983). For the $(J, K) = (1, 1)$ transition, a total of 18 distinct hyperfine components are obtained (see Fig. 5.2. For typical molecular clouds in the Galaxy, the electric quadrupole hyperfine structure of the lower metastable states $(1, 1)$ and $(2, 2)$ can be detected easily (e.g., Barrett et al. 1977). For nearby dark clouds, the magnetic hyperfine structures have been resolved (e.g., Ho et al. 1977). Due to the large linewidth typical for the molecular cloud in the GC (see §1.2.1.3), only the electric hyperfine splitting is barely resolved. The hyperfine structure allows us to estimate the optical depth of the transition (see §5.9).

5.2 Formation and dissociation mechanisms

Several observational studies actually indicate that a large amount of NH_3 exists in the gas phase in star-forming regions and in shocked regions in our Galaxy (e.g., Suzuki et al. 1992; Umemoto et al. 1992, 1999; Hüttemeister et al. 1993b,a; Bachiller et al. 1993; Tafalla & Bachiller 1995).

There are two ways to produce NH_3 in interstellar space: gas-phase reactions and grain surface reactions (Takano et al. 2002).

5.2.1 Gas phase reactions

The most probable formation mechanism in the gas phase is successive hydrogenations of N^+ by H_2 as follows (Herbst & Klemperer 1973):

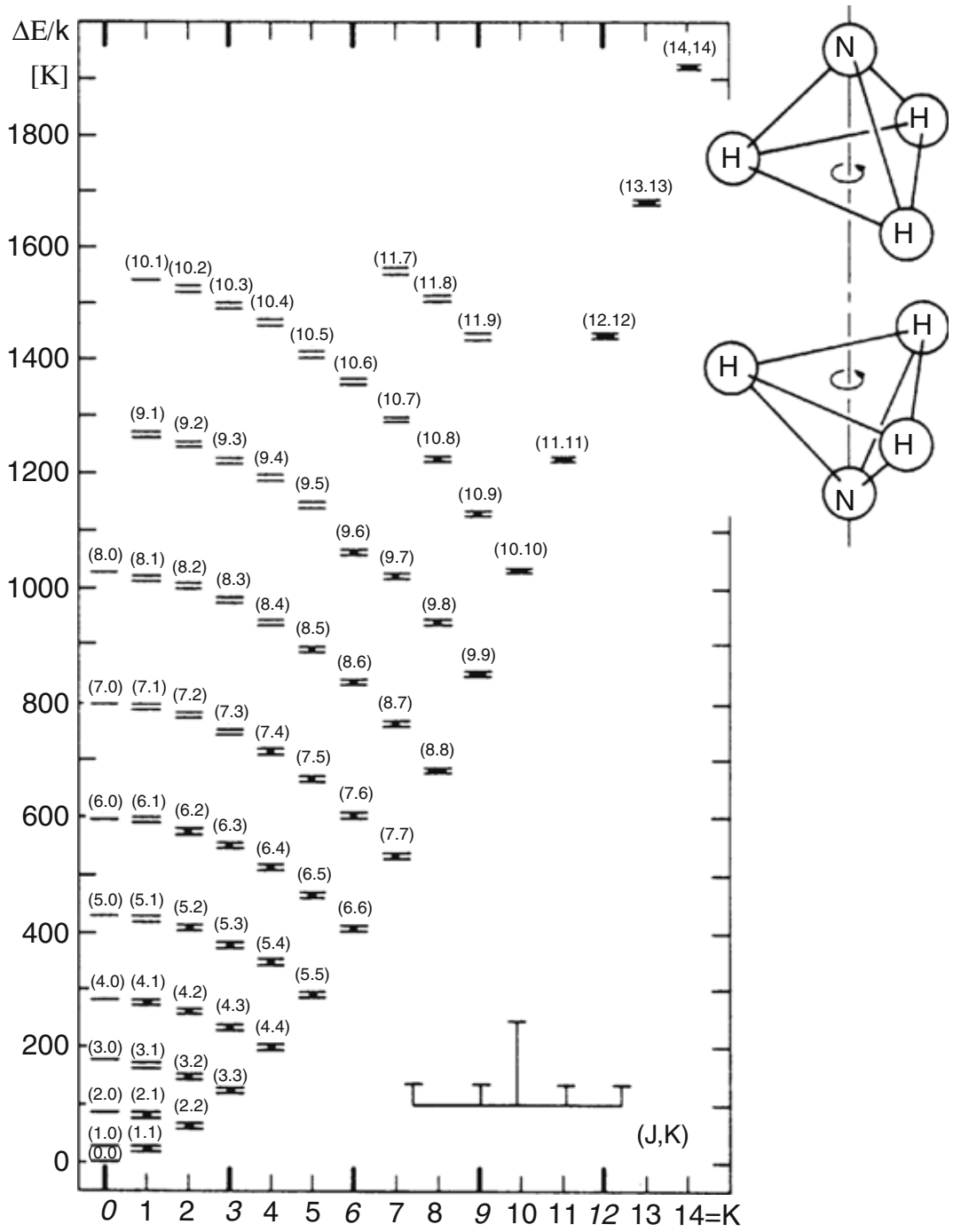

Figure 5.1: Energy level diagram of the vibrational ground state of the prolate symmetric top molecule NH_3. Ortho-NH_3 has $K = 0, 3, 6..$, and para-NH_3, $K = 1, 2, 4, 5, 7...$ Rotational transitions with $\Delta J = 1$, $\Delta K = 0$ produce lines in the far-IR. The inversion transitions $\Delta J = 0$, $\Delta K = 0$ produce lines in the microwave regime (the upper right figure is a sketch of the molecule before and after the inversion transition). The interaction of the nuclear spin of ^{14}N with the electrons produces hyperfine structure, then the line is splitted in 5 groups of components (the lower right part of the plot show a sketch of the hyperfine components of the (1, 1) inversion transition) (Fig. from Wilson et al. 2009a)

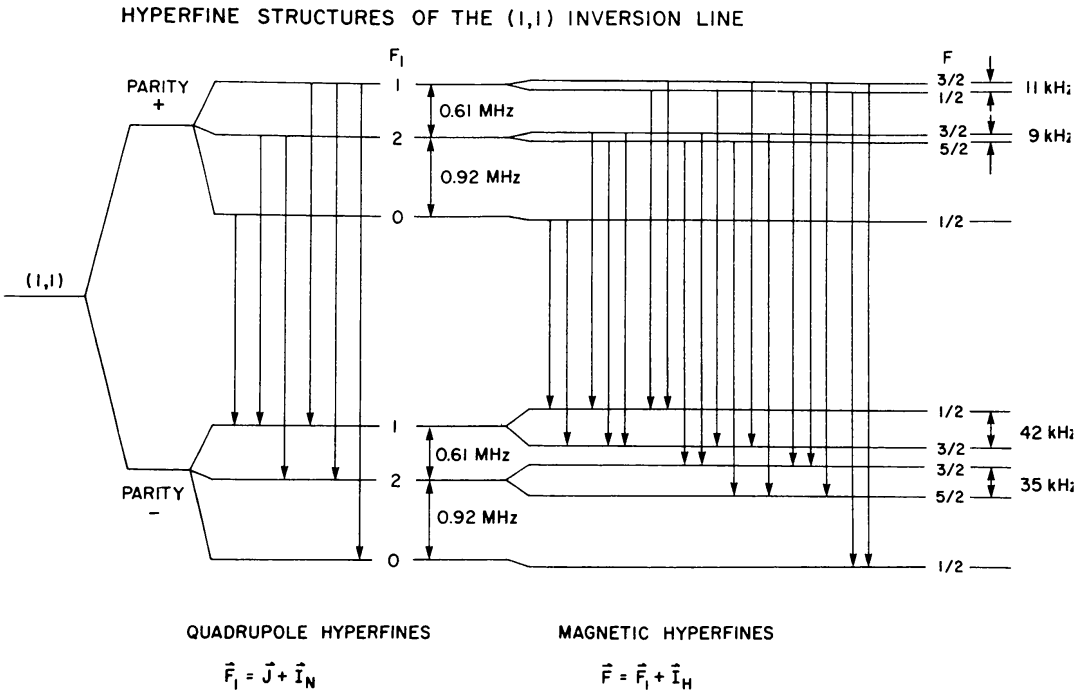

Figure 5.2: Hyperfine splitting of the NH_3 (1, 1) transition indicating the allowed transitions (Fig. from Ho & Townes 1983)

$$N^+ + H_2 \rightarrow NH^+ + H \tag{5.1}$$
$$NH^+ + H_2 \rightarrow NH_2^+ + H \tag{5.2}$$
$$NH_2^+ + H_2 \rightarrow NH_3^+ + H \tag{5.3}$$
$$NH_3^+ + H_2 \rightarrow NH_4^+ + H \quad , \tag{5.4}$$

and then a recombination of NH_4^+ with an electron can form NH_3 as one of the products,

$$NH_4^+ + e^- \rightarrow NH_3 + H \, . \tag{5.5}$$

The principal dissociation mechanism are (Ho & Townes 1983):

$$HCO^+ + NH_3 \rightarrow NH_4^+ + CO \tag{5.6}$$
$$H_3^+ + NH_3 \rightarrow NH_4^+ + H_2 \tag{5.7}$$
$$H_3^+ + NH_3 \rightarrow NH_3^+ + H_2 + H \quad . \tag{5.8}$$

The reactions are temperature dependent. For example, the reaction 5.1 rises at T>100 K, but it is expected to be very slow at a typical temperature of 10 K in cold dense clouds (Ho & Townes 1983; Takano et al. 2002). However, (Dalgarno 1982) reports a rise of the rate coefficient of this reaction at temperatures of 10-20 K. However, there are other effects that can play an important role in the rate coefficient in the reaction 5.1 (see discussion in Takano et al. 2002). NH_3 is more easily produced in the gas phase in high-temperature and/or shocked regions (Takano et al. 2002).

5.2.2 Grain surface reactions

NH_3 can also be efficiently produced on grains and evaporated to the gas phase. High-temperature phenomena accelerate its desorption to the gas phase. The formation on grains is supported by a high abundance of NH_2D in the Orion hot core (Walmsley et al. 1987) and by model calculations containing grain surface reactions (D'Hendecourt et al. 1985; Brown & Charnley 1990). Also, Hiraoka et al. (1995) reported NH_3 formation by reacting H atoms with trapped N atoms in an N_2 matrix at 15 K in a laboratory experiment.

5.2.3 The ortho-to-para ratio

Usually, it is not easy to estimate the contribution of molecules desorbed from dust grains from those formed in the gas phase. The ortho-to-para ratio of NH_3 could provide us such information. The ortho-to-para ratio is expected to be the statistical equilibrium value of 1.0 when the NH_3 molecules are formed at high temperature conditions ($\gtrsim$ 40K, Takano et al. 2002) in the processes of gas-phase reactions or grain surface reactions (Umemoto et al. 1999) on warm gains ($\gtrsim$ 15K, Takano et al. 2002). This is because the reactions that form the NH_3 molecule release large excess energies compared to the energy difference between the lowest ortho and para states, which make the ortho-to-para ratio close to the statistical value. However, the ortho-to-para ratio is larger than 1 when the NH_3 molecules were formed on cold grains ($5 - 10$ K, Takano et al. 2002) surfaces and are released into the gas phase with excess energy for desorption, which is comparable to the energy difference between the ortho and para states (Umemoto et al. 1999). This is because the lowest energy level of the para species is 23 K higher than that of the ortho species; para species require more energy for desorption than ortho species. The timescale of the interconversion between ortho-NH_3 and para-NH_3 is considered to be the order of 10^6 yr in the gas phase Cheung et al. (1969). Therefore, the ortho-to-para ratio provides us valuable information on physical conditions and chemical processes when the NH_3 molecules are released into the gas phase.

Since the lowest energy level of ortho-NH_3, $(J, K) = (0, 0)$, has no inversion doubling, it is necessary to observe the transitions higher than $(J, K) = (3, 3)$ to measure the ortho-to-para ratio. Such high transitions are hardly excited in the dark clouds of low temperature. However, the shocked gas associated with molecular outflows in the dark clouds is heated enough to excite the transitions higher than $(J, K) = (3, 3)$ (e.g., the bipolar outflow in the dark cloud L1157 located at 440 pc from the Sun, Umemoto et al. 1992). Observations have revealed a good morphological coincidence of the NH_3 distribution (Tafalla & Bachiller 1995) with that of the shock tracer SiO (Zhang & Ho

Table 5.1: Intensities of satellite groups relative to the main component (from Wilson et al. 2009b).

(J,K)	(1,1)	(2,2)	(3,3)	(4,4)	(5,5)	(6,6)	(2,1)
I_{inner}	0.295	0.0651	0.0300	0.0174	0.0117	0.0081	0.0651
I_{outer}	0.238	0.0628	0.0296	0.0173	0.0114	0.0081	0.0628

1995; Gueth et al. 1998), in gas associated with molecular outflows in the dark clouds, revealing that the hot ammonia arises from the shocked gas.

Some attempts have been done for measuring the ortho-to-para ratio in the GC. Shocked gas in the GC can excite transitions higher than (6,6) (see e.g., Mauersberger et al. 1986), and several works have derived the ortho-to-para ratio (Hüttemeister et al. 1993a). However, those results are difficult to interpret, because the (3,3) and (6,6) metastable inversion transitions may behave like a maser (Walmsley & Ungerechts 1983a; Mauersberger et al. 1986; Lebrón et al. 2011).

5.3 The NH_3 tracing physical conditions of molecular gas

The inversion transitions of NH_3 give us valuable information about the physical conditions of the molecular gas. They are very close in frequencies, therefore it is possible to observe a large amount of the inversion transitions using only one telescope and receiver.

5.3.1 Optical depth

For the lowest metastable inversion transitions, it is possible to detect and resolve the hyperfine structure in clouds with narrow linewidths. The optical depths can be then derived from the observed relative intensities of the hyperfine transitions, which have known relatives intensities (see Table 5.1).

For the electric quadrupole hyperfine structure of the (J, K) inversion line, one obtains (Ho & Townes 1983):

$$\frac{\Delta T^*(J,K,m)}{\Delta T^*(J,K,s)} = \frac{1 - e^{-\tau(J,K,m)}}{1 - e^{-\alpha\tau(J,K,s)}}\,, \tag{5.9}$$

where ΔT^* is the observed brigtness temperature, m and s refer to the main and satellite hyperfine components, and α is the ratio of the intensity for the satellite compared with the main components. From this relationship it is possible to derive the optical depth. In this formula it is assumed equal filling factor and excitation temperature in the different hyperfine components, which is a reasonable assumption due to the close energy separation and small probability of non-thermal excitation mechanisms between the different hyperfine components.

5.3.2 Kinetic temperature determinations

Observing several NH_3 transitions, it is possible to calculate a rotational temperature, $T_{\rm rot}$ characterizing the distribution of population among the different energy states (see Section 2.9.1). Due to the downward relaxation of the nonmetastable states and the slow collisional coupling between K-ladders, the metastable populations may not resemble a true Boltzmann distribution. It has ben demostrated that $T_{\rm rot}$ determined by NH_3, although underestimates the T_K, is a good indicator of the T_K, as determined by CO emission in a variety of regions (Martin et al. 1982). Walmsley & Ungerechts (1983b) demostrated that after corrections for the depopulation effect, the NH_3 and CO temperatures are in good agreement.

5.4 Kinetic temperatures towards the disk-halo interaction in the Galactic center

In the following, we present a paper submitted to the Astronomy & Astrophysics in October 2011. The paper discusses observations of metastable inversion transitions of the NH_3 molecule (observed with 100m Effelsbeg telescope), to derive kinetic temperature of the molecular gas in the GMLs and the X1 and X2 orbits towards the same positions selected in §4. Using the 30m IRAM telescope, we also observe others molecular tracers such as SiO, HNCO, CS, ^{13}CO, C^{18}O to discuss on the heating mechanism of the molecular gas. I am the first author of the paper, and I was the principal investigator of the project, responsable for the observing proposal, data reduction, data analysis, and writing the paper. The observations and data calibration were done together with Arancha Amo-Baladrón. The procedure to calibrate the Effelsberg data applied to convert the signal from the telescope to $T_{\rm MB}$ is described in Appendix A.

Astronomy & Astrophysics manuscript no. paper˙thesis
December 13, 2011

On the kinetic temperatures of the molecular gas in the disk and halo towards the Galactic center

D. Riquelme[1], M.A. Amo-Baladrón[2], J. Martín-Pintado[2], R. Mauersberger[3], S. Martín[4], and L. Bronfman[5]

[1] Instituto de Radioastronomía Milimétrica (IRAM), Av. Divina Pastora 7, Local 20, E-18012 Granada, Spain
e-mail: riquelme@iram.es
[2] Centro de Astrobiología (CSIC/INTA), Ctra. de Torrejón a Ajalvir km 4, E-28850, Torrejón de Ardoz, Madrid, Spain
[3] Joint ALMA Observatory, Alonso de Córdova 3107, Vitacura, Santiago, Chile
[4] European Southern Observatory, Alonso de Córdova 3107, Vitacura, Casilla 19001, Santiago, Chile
[5] Departamento de Astronomía, Universidad de Chile, Casilla 36-D, Santiago, Chile

ABSTRACT

Context. It is well known that the kinetic temperatures, $T_{\rm kin}$ of the molecular clouds in the Galactic center region are higher than in the disk of the Galaxy. However the T_{kin} of the molecular complexes found at high latitudes ($> 0^\circ.5$) is so far unknown. These high latitude molecular clouds (hereafter refer as halo) are located in the region where it has been proposed that the gas in the disk interacts with the gas in halo.
Aims. To derive $T_{\rm kin}$ in the molecular clouds at high latitude and understand the physical process responsible for the heating of the molecular gas both in the disk and the halo.
Methods. We measured the metastable inversion transitions of NH_3 from $(J, K) = (1, 1)$ to $(6, 6)$ toward six positions selected throughout the Galactic central disk and halo. We use rotational diagrams and LVG modeling to estimate the kinetic temperatures toward all the sources. We also observed other molecules like SiO, HNCO, CS, $C^{34}S$, $C^{18}O$, and ^{13}CO, to derive the densities and to trace different physical processes (shocks, photodissociation, dense gas) which are expected to dominate the heating of the molecular gas
Results. We derive for the first time the $T_{\rm kin}$ of the high latitude clouds interacting with the disk in the Galactic center region. We find high rotational temperatures in all the observed positions. We derive two kinetic temperature components ($\sim$ 200 K and $\sim$ 40 K) for the positions in the Central Molecular Zone and in the disk, and only the warm kinetic temperature component for the clouds at high latitudes. The fractional abundances derived from the different molecules **suggest the shock origin as the main heating mechanism in the Galactic center even at high latitudes.**

Key words. Galaxy: center - ISM: clouds - ISM: molecules

1. Introduction

The interstellar molecular gas in the Galactic center (GC) region (i.e., in the inner $\sim$ 1 kpc of the Galaxy) shows higher kinetic temperatures, $T_{\rm kin}$, than in the disk. There is an extended warm component in the GC of $\sim$ 200 K, which is not coupled with the dust ($T_{\rm dust} < 40$ K, Rodríguez-Fernández et al. 2002; Odenwald & Fazio 1984; Cox & Laureijs 1989). High dust temperatures ($T_{\rm dust} \sim 80$ K) are only seen toward the Sgr B2 molecular cloud, which is claimed to be an anomalous region (Bally et al. 2010), with recent massive star formation. Using metastable inversion transitions of para-NH_3, Güsten et al. (1981) derived kinetic temperatures in the range of 50-120 K towards Sgr A. Morris et al. (1983) found high kinetic temperatures (30-60 K) towards the denser portions of the GC region; mapping the (1,1), (2,2), and (3,3) inversion transitions of NH_3, they derive an analytic relationship between the kinetic temperature and intensity ratios of (3,3)/(1,1) and (2,2)/(1,1). Observing more highly excited NH_3 inversion lines, Mauersberger et al. (1986) and Hüttemeister et al. (1993b) obtained kinetic temperatures $T_{\rm kin} \geq 100$ K in all clouds in the GC including Sgr B2 region. Similarly high temperatures were also found in the central regions of nearby galaxies, (e.g., Mauersberger et al. 2003). From metastable, i.e. $J = K$, inversion transitions of NH_3 toward 36 clouds throughout the GC region, Hüttemeister et al. (1993a) suggested that in addition to a warm component there is also a "cool gas component" with $T_{\rm kin} \sim 20 - 30$ K. So far, to our knowledge, the $T_{\rm kin}$ of molecular clouds has never been determined neither in clouds in the GC region at latitudes $|b| \geq 0^\circ.5$, nor in the forbidden and/or high velocity components, explained by the barred potential model as X1 orbits.

1.1. Heating mechanisms of the molecular gas in the Galactic center

The kinetic temperature of the molecular clouds is given by the thermal balance of the heating and cooling mechanism. While the cooling of the molecular clouds is believed to be understood, the heating source is still under debate. Molecular clouds cool down by the collisional excitation of molecules and atoms followed by the radiative emission of this energy from the cloud (Hollenbach 1988). For the physical conditions present in the GC, the cooling is dominated by H_2 and CO. Hüttemeister et al. (1993a) propose that the dust in the GC region would be an important cooling agent.

To account for the high kinetic temperatures of the molecular interstellar medium throughout the GC and in the central region of external galaxies, several heating mechanism have been proposed. Massive stars can heat up dust in their vicinities, which then heats the surrounding gas. Since the gas is warmer than the

dust, a heating scheme for extended region without dust heating is needed.

1. Heating by a large flux of low energy cosmic rays (Güsten et al. 1981; Morris et al. 1983). This mechanism requires a cosmic ray ionization rate of one or two orders of magnitude larger than the Galactic value of 10^{-17}s^{-1}, which will influence also the gas-phase chemistry, increasing the atomic hydrogen due to the increased cosmic ray dissociation rate of H_2, and also molecular ion emission like HCO^+.
2. Magnetic ion-slipping (Scalo 1977) has been also proposed for the GC region (Hüttemeister et al. 1993a; Nagayama et al. 2007) and for the nucleus of IC342 (Ho et al. 1982).
3. Heating by an extended diffuse source of soft X-ray emission (Watson et al. 1981). This hypothesis is unlikely since the X-ray emission is less extended than the NH_3 emission, and there is no obvious source for the required luminosity in the extended soft X-ray emission (Morris et al. 1983).
4. Heating by an extremely hot plasma emitting X-rays. Nagayama et al. (2007) found that the NH_3 emitting region in the Central Molecular Zone (CMZ, Morris & Serabyn 1996), with $T_{\rm kin} = 20 - 80$ K and $T_{\rm kin} > 80$ K, is surrounded, in the longitude-velocity space, by a high-pressure region (Sawada et al. 2001), where the gas is less dense and hotter ($n(H_2) < 10^3$ cm^{-3}, $T_{\rm kin} > 100$ K). Because the high pressure region is found to be coincident with the hot emitting X-rays, they argue that the thermal energy radiated from the hot plasma emitting X-ray plasma can heat the gas in the high pressure region.
5. Heating by the dissipation of mechanical supersonic turbulence through shocks (Fleck 1981; Wilson et al. 1982; Mauersberger et al. 1986). Due to the large gravitational potential in the GC and the large amount of molecular clouds one expects frequent interactions or collisions between molecular clouds. Such collisions will, however, not lead to a rapid dissipation because the molecular medium tends to be clumpy and the released energy will be used to increase the internal motions within the clouds (Dobbs et al. 2011). These internal motions can then be dissipated via C-shocks on a time scale of several Myrs. The shocks can be produced by several phenomena: supernova or hypernova explosions (Tanaka et al. 2007); response of the gas in a barred potential model (Binney et al. 1991); and when the gas in the "giant molecular loops" (GMLs) flow down their sides along the magnetic field lines, and join with the gas layer of the Galactic plane generating shock front at the "foot points" of the loops (Fukui et al. 2006).

1.2. Kinetic temperatures from ammonia measurements

NH_3 have hyperfine structure, which allow to estimate the optical depth and hence reliable column densities. Observing several metastable inversion transitions one can determinate a rotational temperature, $T_{\rm R}$, which in spite of the fact that it may underestimate the $T_{\rm kin}$, it is a good approximation to it, as determined by CO emission in a variety of regions (Martin et al. 1982; Walmsley & Ungerechts 1983).

Transitions between ortho-NH_3 ($K = 0, 3, 6, 9...$) and para-NH_3 ($K = 1, 2, 4, 5...$) are forbidden since normal radiative and collisional transitions do not change spin orientations. The time scale of convertion between ortho and para species is of 10^6 yrs in gas phase (Cheung et al. 1969). Therefore ortho-NH_3 and para-NH_3 can be almost treated as different species. The spin temperatures between ortho and para-NH_3 may reflect the conditions at the time of the formation of NH_3, while rotational temperature within the same species reflect present conditions (Ho & Townes 1983).

Hot gas associated to the shock fronts may be identified by a kinetic temperature gradient and large NH_3 abundances of the high metastable inversion transitions (e.g., from $(4,4)$, $(5,5)$, $(7,7)$, Mauersberger et al. 1986). The sense of the temperature gradient will help to establish whether the shocks are due to the GML scenario or to the ejection of gas from the disk due to star formation. If the temperature decreases from the galactic disk to the halo, it would indicate that the material is falling from the halo to the galactic disk supporting the GML scenario. This is because the post shocked gas which has cooled down is at larger latitude than the recently heated material at the shock front (see e.g., Fig. 16 of Genzel 1992). The gradient will be in the opposite way if the material is being ejected. Furthermore, the NH_3 abundances in gas phase are enhanced by the sputtering of grain mantles by shocks (see, e.g., Ho & Townes 1983; Takano et al. 2002, and references therein) and decrease in the photodissociation regions as it is easily photodissociated by the UV radiation from stars (Rodríguez-Fernández et al. 2001). Therefore, if the abundance of ammonia in the shocked component traced by SiO is low (below 10^{-9}), all the shock material would be strongly affected by the UV making the scenario of gas ejection driven by galactic winds very likely (as stars from the disk directly illuminate the material).

In this paper, we derive for the first time the kinetic temperatures of the molecular clouds in the disk-halo interaction region (foot point of the GMLs and positions where the X1 orbits intercept X2 orbits in a barred potential). We observe the metastable inversion transitions of NH_3 $(1,1)$, $(2,2)$, $(3,3)$, $(4,4)$, $(5,5)$, and $(6,6)$ to estimate the kinetic temperature, and using other molecular tracer (SiO, HNCO, CS) we discuss the heating mechanism responsible for the high kinetic temperatures of the molecular gas in the GC.

2. Observations

2.1. Effelsberg observations

We observed the metastable inversion transition of NH_3 $(J,K) = (1,1)$, $(2,2)$, $(3,3)$, $(4,4)$, $(5,5)$, and $(6,6)$ using the Effelsberg 100m telescope[1] in April 2010, and April 2011. We used the primary focus $\lambda = 1.3$ cm $(18 - 26$ GHz) receiver, which has 2 linear polarizations, and a Fast Fourier Transform Spectrometer (FFTS) in the "broad IF band" mode with a bandwidth of 500 MHz, providing an effective spectral resolution of 49.133 kHz or 0.386 km s^{-1}. We observed the $(1,1)$, $(2,2)$ and $(3,3)$ line simultaneously, with a band centered at 23.783 GHz, and the $(4,4)$ and $(5,5)$ line in a second setup (centered at 24.336 GHz). The $(6,6)$ was observed in the third setup, centered at 25.056 GHz, using the 100 MHz bandwidth FFTS spectrometer, which provides an effective spectral resolution of 9.827 kHz or 0.073 km s^{-1}. The beam width of the telescope at 23.7 GHz is 42.2". The spectra were observed in position switching mode, with the emission-free reference positions from Riquelme et al. (2010b), which were checked in the first setup, where the most intense lines are detected. Each position was observed for 12 min in the first setup, 24 min in the second setup, and 32 min in the third setup. The calibration in Effelsberg was done by the periodic injection of a constant signal (noise cal). To convert the data to

[1] Based on observations with the 100-m telescope of the Max-Planck-Institut für Radioastronomie at Effelsberg

T_A^* we corrected for the noise-cal (in K), opacity and elevation dependent antenna gain[2]. The uncertainty in the calibration is of the order of 5 – 10%. The main beam temperatures, T_{MB}, were obtained by using $T_{MB} = T_A^* \cdot \frac{1}{Beff}$, where the beam efficiency, Beff, is 0.52 at 24 GHz. The pointing was checked every two hours against the source 1833-212, providing an accuracy of better than 10″.

We observed those positions from Riquelme et al. (2010a) visible from Effelsberg (six out of nine) showed in Fig. 1, one in the footpoint of the GMLs (Halo 1), one in the top of the loop (Halo 4), two in the disk toward the location of the expected interactions between the X1 and X2 orbits (Disk X1-1, Disk X1-2, Disk X2-1, Disk X2-2,) in the barred potential model (Binney et al. 1991) and a pair of positions toward the GC plane (Disk 1, Disk 2)[3] as reference (Table 1).

2.2. Observations with the IRAM 30m telescope

In order to constrain the physical properties of the gas, we also observed the $J = 2 - 1$ rotational transitions of SiO, ^{29}SiO, and ^{30}SiO, the $J = 2 - 1$, $3 - 2$ rotational transitions of CS and the $J = 2 - 1$ of C^{34}S, the $J = 10 - 9$ transition of HNCO, and the $J = 1 - 0$ rotational transition of ^{13}CO and C^{18}O. The observations were carried out with the IRAM-30m telescope[4] at Pico Veleta (Spain) in several periods from June 2009 to October 2010. For the 3mm lines, we used the E090 band of the Eight Mixer Receiver (EMIR)[5], which provides a bandwidth of $\sim$ 8 GHz simultaneously in both polarizations per sideband, and for CS (3 – 2) emission, we use the E150 band of EMIR receiver, which provide a bandwidth of $\sim$ 4 GHz simultaneously in both polarizations. As the backend, we used the Wideband Line Multiple Autocorrelator (WILMA), providing a resolution of 2 MHz or 6.6 km/s at 91 GHz and 4.1 km/s at 146 GHz. We observed the nine selected positions from Riquelme et al. (2010a) that were all observable with the 30m. In this work, we use the antenna temperature scale T_A^*, which can be converted to main beam temperature $T_{MB} = T_A^* \cdot \frac{Feff}{Beff}$, where the forward efficiency Feff is 95% and the main-beam efficiency is Beff = 81% at 86 GHz, and Feff = 93% and Beff = 74% at 145 GHz. The beam width of the telescope is 29″ at 86 GHz, and 16″ at 145 GHz.

3. Results

Fig. 1 shows the spectra taken in each position in all the metastable inversion transitions observed in this work.

[2] http://www.mpifr-bonn.mpg.de/div/effelsberg/calibration/1.3cmpf-.html

[3] Throughout this work, all the positions observed and discussed are in the Galactic center region (in the central kpc of the Galaxy). We denote "Disk" to the positions close to $b = 0°$. When one observed position have components associated to both, the X1 and the X2 orbits in the barred potential model, we called them explicitly as 'Disk X1" and "Disk X2". It is worth to note that the source "Disk 2" which corresponds to Sgr B2, is placed in the X2 orbits, therefore, because this source does not have the velocity components associated to the X1 orbits, we just call to this source as "Disk".

[4] Based on observations carried out with the IRAM 30m telescope. IRAM is supported by INSU/CNRS (France), MPG (Germany), and IGN (Spain).

[5] http://www.iram.es/IRAMES/mainWiki/EmirforAstronomers

3.1. Optical depth and rotational diagrams from NH_3

The NH_3 inversion transition is split into five components: a "main component" and four symmetrically placed "satellites" (the quadrupole hyperfine (HF) structure), spaced by $\geq$ 10 km s^{-1}. Due to the large linewidth of the molecular clouds in the GC, the magnetic splitting cannot be resolved ($<$ 0.2 km s^{-1}). Under the assumption of local thermodynamical equilibrium (LTE) excitation, the relative intensities of the four satellite HF components can be used to estimate the optical depth of the main component of the metastable inversion transitions. If the inversion lines are optically thin, we can estimate the rotational temperature and the column density from the ratios of the peak or integrated intensities.

We use the "NH_3 method" from CLASS[6] to determine the optical depth for the (1, 1), (2, 2) and (3, 3) lines. To define the linewidth (which was used as a fixed parameter in the NH_3 method), we use the (3, 3) transition, because these spectra have the best signal-to-noise ratio in our observations and the HF components are much weaker than those of the (1, 1) and (2, 2) lines. As we can see in Table 11, all the sources observed in this work are optically thin, except in the (1, 1) transition toward Sgr B2. Following the criteria of Hüttemeister et al. (1993a) based on the lower peak intensities in these lines, with respect to the (1, 1), (2, 2) and (3, 3) ones, we assume that the (4, 4) and (5, 5) were also optically thin. Table 11 presents the results from simple Gaussian fits for all the observed positions, allowing all the parameters to be free. We obtained rotational temperatures and column densities from the metastable inversion transition of para-NH_3, and ortho-NH_3, using Boltzmann diagrams (see, Goldsmith & Langer 1999, for detailed explanation and equations of the method). The GC presents extended emission, which fills the beam of the telescope, therefore we take $T_B \sim T_{MB}$. To obtain the rotational diagram we use the MASSA software[7]. The spectroscopic parameters were obtained from JPL catalog (Pickett et al. 1998). Table 2 presents the rotational temperatures, and the NH_3 column densities for each observed position (Fig. 2).

From the LTE analysis, we derived two temperature components for each position. The first one defined from the (1, 1)-(2, 2) transitions, which shows lower temperatures, and the second from the (2, 2)-(4, 4)-(5, 5), with higher temperatures. However, in some positions, a single temperature regime was also a possible solution, and we fit one component to all observed para-NH_3 transitions with a red line in the rotational diagram. We mark in bold face the most likely results consistent with the non-LTE analysis (see Sect. 3.2.2). We also derived the temperature from the ortho-NH_3 (3, 3)-(6, 6) transitions, which is shown with a blue line in the plots (see Fig. 2, and from Fig. 4 to 11). The rotational temperatures from the ortho-NH_3 are close to the ones derived by (2, 2)-(4, 4)-(5, 5) para-NH_3, as shown by the similar slopes fitted on the ortho and para species in Figures mentioned above.

3.2. Physical conditions of the gas from CS and NH_3

To derive the $n(H_2)$ and T_{kin} of the gas, we combine the CS and NH_3 molecular emission, proceeding in a iteratively way. First, we use the rotational temperatures derived from the LTE analysis of NH_3 (Table 2), which is a lower limit of the actual kinetic

[6] http://www.iram.fr/IRAMFR/GILDAS

[7] http://damir.iem.csic.es/mediawiki−1.12.0/index.php/MASSA_Users_Manual

Source name[a]	Associated object	Galactic coordinates l [°]	b [°]	Equatorial coordinates α_{J2000}	δ_{J2000}
Halo 1	M+5.3 − 0.3	5.45	−0.324	$17^h59^m17.8^s$	−24°24′38″
Halo 4	Top Loop	4.75	−0.8	$17^h59^m34.9^s$	−25°15′16″
Disk X1-1, Disk X2-1	1.3 complex	1.28	+0.07	$17^h48^m21.9^s$	−27°48′19″
Disk X1-2, Disk X2-2	Sgr C	359.446	−0.124	$17^h44^m46.9^s$	−29°28′25″
Disk 1	Galactic plane at $l \sim 5°.7$	5.75	0.25	$17^h57^m46.5^s$	−23°51′51″
Disk 2	Sgr B2	0.6932	−0.026	$17^h47^m21.9^s$	−28°21′27″

Table 1. Observed positions in NH_3 lines.

[a] following the notation of Riquelme et al. (2010a)

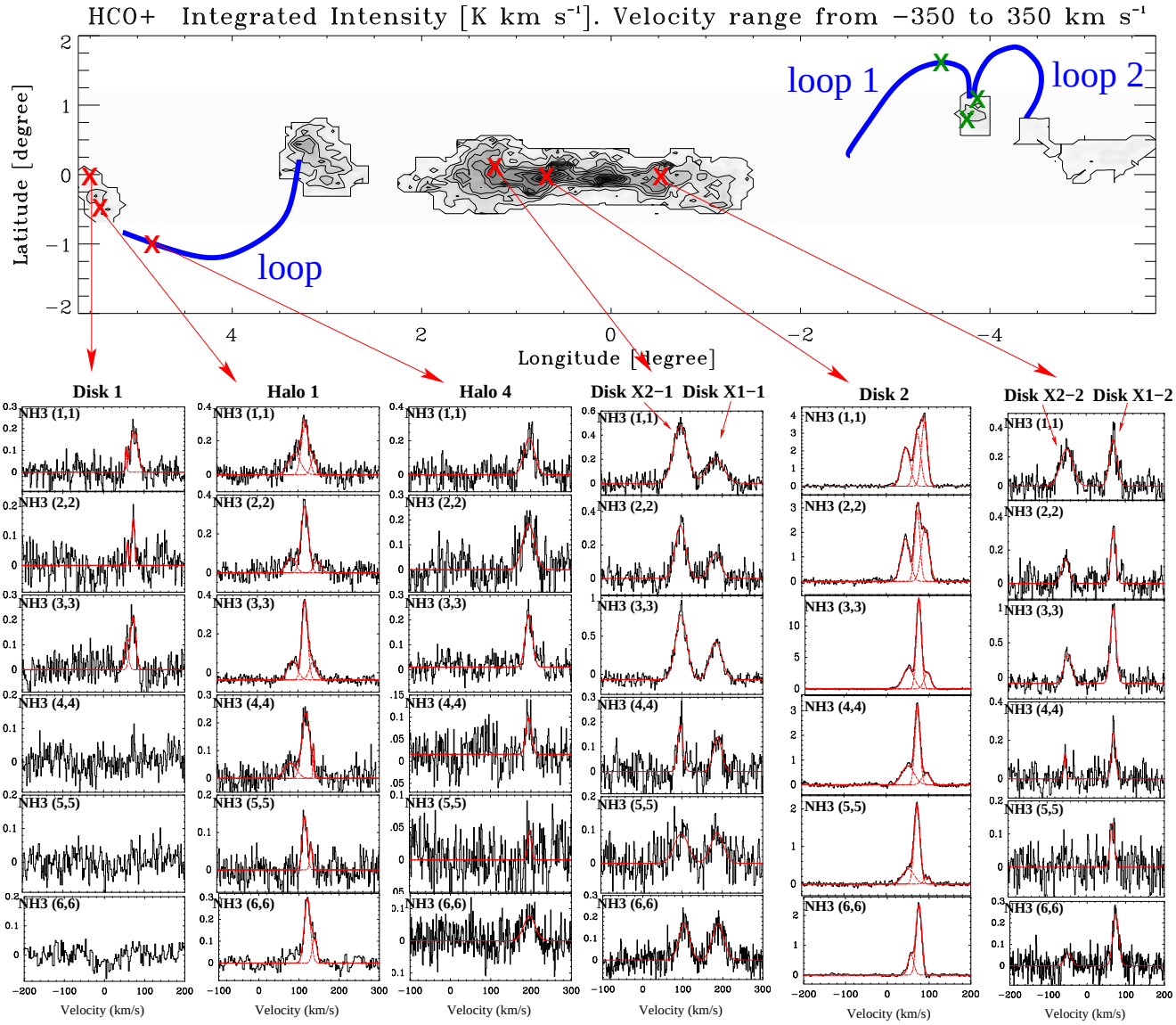

Fig. 1. Spectra toward selected positions in the GC in the metastable inversion transitions from (1,1) to (6,6) of NH_3. The positions are indicated in the HCO^+ integrated intensity map from Riquelme et al. (2010b). The GMLs found by Fukui et al. (2006) are indicated in blue. The positions which could not seen from Effelsberg are indicated with green crosses.

temperature, T_{kin}, as a fixed parameter in RADEX (van der Tak et al. 2007) to derive the $n(H_2)$ and CS column densities. Then, using the $n(H_2)$ obtained from CS, we use RADEX to derive the kinetic temperature from the para-NH_3 transitions (see §3.2.2). With the kinetic temperature, we derive then the final $n(H_2)$ and CS column densities (Table 3).

3.2.1. Density from CS

We used the non-LTE excitation radiative transfer code RADEX to derive the $n(H_2)$ and CS column densities from line intensities of the observed CS lines. The modeling suggests that the CS emission is optically thin with opacities ranging from 0.01 to 0.85 (except for the source "Disk 2" where the optical depth reach a value of 1.2). The results are showen in Table 3. The er-

Table 2. NH_3 physical parameters (rotational temperatures and column densities) derived for each source using MASSA software. Bold faced values indicated the most likely result consistent with the non-LTE analysis.

Source	n^a	$T_{\rm rot}$ (11-22) [K]	$T_{\rm rot}$ (22-44-55) [K]	$T_{\rm rot}$ (11-22-44-55) [K]	$T_{\rm rot}$ (33-66) [K]	$N(NH_3)$ (11-22) 10^{14} cm^{-2}	$N(NH_3)$ (22-44-55) 10^{14} cm^{-2}	$N(NH_3)$ (11-22-44-55) 10^{14} cm^{-2}	N(o-NH_3) (33-66) 10^{14} cm^{-2}
Halo1	1	46.7 ± 0.9	117.5 ± 1.7	**92.7 ± 0.8**	81.0 ± 0.8	2.14 ± 0.07	3.53 ± 0.10	**3.72 ± 0.06**	5.37 ± 1.1
	2	43.2 ± 0.3	131.8 ± 0.9	**96.6 ± 0.3**	156.4 ± 9.6	4.93 ± 0.06	9.09 ± 0.11	**9.49 ± 0.06**	11.1 ± 1.2
	3			80.9 ± 1.1	169 ± 31			2.06 ± 0.06	3.3 ± 1.0
Halo4	1			56.5 ± 2.3	138 ± 10			5.48 ± 0.45	5.39 ± 0.76
DiskX1-1	1	27.2 ± 1.5	156 ± 12		164.1 ± 6.6	4.85 ± 0.53	7.7 ± 1.2		12.07 ± 0.91
DiskX2-1	1	27.4 ± 0.8	91.7 ± 3.6		122.8 ± 3.8	9.75 ± 0.52	9.87 ± 0.78		16.56 ± 0.98
DiskX1-2	1	33.1 ± 2.2	112.7 ± 6.5		138.2 ± 5.1	3.99 ± 0.48	5.75 ± 0.71		10.93 ± 0.80
DiskX2-2	1	22.0 ± 1.4	72.5 ± 6.1		106.9 ± 9.7	4.44 ± 0.55	2.85 ± 0.58		5.09 ± 0.90
Disk1	1	19.1 ± 2.9	154 ± 48		139 ± 26	0.74 ± 0.20	0.66 ± 0.41		0.93 ± 0.39
	2	26.9 ± 2.4	82.9 ± 9.8		100 ± 12	1.41 ± 0.20	1.29 ± 0.34		2.02 ± 0.46
Disk2	1	**38.1 ± 0.6**	**110.3 ± 1.0**	90.6 ± 0.5	95.7 ± 1.5	**31.6 ± 1.0**	**48.1 ± 1.1**	60.3 ± 1.0	61.0 ± 2.0
	2	50.8 ± 1.6	145.6 ± 2.3	**113.8 ± 0.5**	112.9 ± 0.6	42.1 ± 2.1	84.9 ± 3.1	**101.6 ± 1.0**	133.2 ± 1.4
	3	**33.0 ± 0.9**	**63.1 ± 1.2**	51.7 ± 0.5	52.4 ± 3.2	**33.1 ± 1.3**	**32.0 ± 1.7**	47.2 ± 1.0	37.6 ± 6.4

[a] Cloud number defined by the different velocity components (see Table 11)
$N(para-NH_3)$ correspond to the sum of all observed para-NH_3 column densities. When the data is consistent with a two temperature model, $N(para-NH_3)$ correspond to the sum of column 7 and 8. If only one temperature regime is present, the $N(para-NH_3)$ corresponds to column 9.

ror were estimated assuming the 10% calibration error (typical flux calibration uncertainty at the 30m telescope), and we give an upper and lower value based on the minimum and maximum value from the LVG diagrams (see from Fig. 12 to Fig. 22). It is important to note that $n(H_2)$ in some sources are poorly constrained because the line intensity of the LVG model run almost parallel, which translate in large errors shown in the Table 3. If we derive the $n(H_2)$ using the rotational temperature (which is a lower limit to the kinetic temperature), the $n(H_2)$ differ on average in $\sim$ 27%.

3.2.2. LVG analysis from NH_3

As previously mentioned, to better estimate the kinetic temperatures of the gas, we used also a non-LTE excitation and radiative transfer code RADEX. Using the value of $n(H_2)$ derived from the CS LVG analysis (Table 3), and the velocity widths (see Table 11), we can derive the T_{kin} and N_{NH_3}. Fig. 2 shows an example of this procedure, and Table 4 shows the results. In Fig. 2 and from Fig. 4 to Fig. 11, we show in blue the results corresponding to the metastable inversion transitions $(1,1)$-$(2,2)$ (low rotational temperature), and in red, the results corresponding to the metastable inversion transitions $(2,2)$-$(4,4)$-$(5,5)$ (high rotational temperature). For the cases where only one temperature regimen was a possible solution, we plotted the result in red in the LVG plot. When the kinetic temperature defined by the $(1,1)$-$(2,2)$ inversion transitions was also high ($\sim$ 100 K), we assume that there is not low temperature regimen in the source LVG models indicate that the results from one LTE are reliable. When the $(4,4)$ or $(5,5)$ inversion transitions were not detected, the upper limits to their emission were plotted in dashed lines. This upper limit to the emission was obtained as $3\sigma_{rms}$ level, where σ_{rms} is the root mean square per channel of the spectra. The individual fits to all sources are shown in the Online Appendix (Fig.4 to 11). To estimate the uncertainty of the derived parameters, we computed the χ^2 of the line intensities over the grid used for the LVG model. We impose $\Delta\chi^2 = \chi^2 - \chi^2_{\rm min} = 1$ which translate in the 68.3% confidence level projected for each parameter axis (see, e.g., Press et al. 1992, Section §15.6). The black ellipses shows the error in the model (Fig. 2).

3.3. Column densities and relative abundances from other molecules

To shed light into the physical processes that are heating the molecular gas, we derived also relative abundances of NH_3 with respect to the following molecules: SiO, which is a well-known shock tracer (Martín-Pintado et al. 1992), CS which is a high-density gas tracer ($n > 10^4$cm^{-3} Mauersberger & Henkel 1989; Mauersberger et al. 1989), and HNCO which is a shock, and very high density tracer, ($n_{H_2} \geq 10^6$cm^{-3}, Jackson et al. 1984; Martín et al. 2008; Zinchenko et al. 2000) with a high photodissociation rate (Table 7). We also derive the fractional abundances of these molecules with respect to H_2 as traced by ^{13}CO (Table 6). We assumed that they arise from the same volume. This assumption may not be fulfilled for all of our observed position due to the observed differences in the velocity center and linewidth (see Table 12). In all the calculations we assume that the GC sources are extended, therefore we take $T_{\rm B} \sim T_{\rm MB}$.

3.3.1. Column densities of SiO, HNCO, ^{13}CO, and C^{18}O

We used the non-LTE excitation radiative transfer code RADEX to derive the column densities. For the species with only one observed transition (SiO, HNCO, and CO isotopes), we are forced to make some assumption about the physical properties of the gas ($T_{\rm kin}$ and $n(H_2)$). We use the kinetic temperatures derived by NH_3 in Table 2, and the $n(H_2)$ from the CS data. The results are shown in Table 5. We compare the results using LTE approach (Table 12) for a $T_{\rm ex}$ = 10 K (which is consistent with the value derived for SiO by Hüttemeister et al. (1998)) and with our $T_{\rm ex}$ value derived from CS, with the RADEX results, and we found that the column densities agree in a factor of 3-4 with the LVG model. Using $n(H_2) \sim 10^3$ cm^{-3} (because the critical density of CO is lower than for CS) the column densities for the CO isotopes are a factor 2-4 lower than using the $n(H_2) \sim 10^4$ cm^{-3}.

Table 3. Physical parameters derived from CS using non-LTE (RADEX) model. The kinetic temperature used in RADEX is indicated. When more than one $T_{\rm kin}$ regime was present in one position, we derived the physical parameters from each $T_{\rm kin}$. We assumed a 10% calibration error.

Source	Cloud number	T_{kin} [K]	Tex CS(2-1) [K]	Tex CS(3-2) [K]	$\tau_{CS(2-1)}$	$\tau_{CS(3-2)}$	$n(H_2)$ [$\times 10^4$cm^{-3}]	$N(CS)$ [10^{13}cm^{-2}]
Halo1	1	115	< 3.7	< 2.9	> 0.33	> 0.18	< 0.84	> 7.95
	2	90	$10.6^{7.6}_{3.2}$	$7.6^{2.3}_{1.5}$	$0.32^{0.41}_{0.19}$	$0.64^{0.42}_{0.23}$	$6.94^{5.34}_{3.40}$	$18.09^{8.61}_{3.72}$
	3	135	$30.5^{103}_{16.0}$	$10.6^{4.0}_{2.5}$	$0.01^{0.01}_{0.01}$	$0.05^{0.02}_{0.02}$	$13.5^{6.46}_{4.59}$	$1.42^{0.14}_{0.15}$
Halo2	1	113	$4.1^{1.3}_{0.8}$	$4.0^{0.9}_{0.8}$	$0.22^{0.75}_{0.13}$	$0.14^{0.31}_{0.06}$	$1.26^{1.56}_{0.98}$	$5.75^{16.65}_{2.73}$
	2	113	$3.8^{1.3}_{0.8}$	$3.8^{0.9}_{0.9}$	$0.28^{15.3}_{0.18}$	$0.15^{5.81}_{0.07}$	$0.97^{1.54}_{0.96}$	$6.35^{310.21}_{3.44}$
Halo3	1	113	$4.7^{1.8}_{0.0}$	$4.4^{1.1}_{0.0}$	$0.61^{0.10}_{0.38}$	$0.75^{0.12}_{0.35}$	$1.50^{2.05}_{0.09}$	$22.52^{3.55}_{10.64}$
	2	113	$6.1^{3.1}_{1.7}$	$5.2^{1.2}_{1.0}$	$0.07^{0.11}_{0.04}$	$0.05^{0.04}_{0.02}$	$3.55^{2.76}_{1.96}$	$3.71^{3.05}_{1.07}$
Halo4	1	95	$5.4^{2.3}_{1.2}$	$4.7^{1.1}_{0.8}$	$0.21^{0.28}_{0.12}$	$0.17^{0.12}_{0.06}$	$2.75^{2.54}_{1.49}$	$6.18^{5.32}_{2.17}$
Halo5	1	95	$10.4^{8.4}_{3.4}$	$7.0^{2.2}_{1.4}$	$0.11^{0.13}_{0.07}$	$0.21^{0.10}_{0.07}$	$7.47^{5.11}_{3.18}$	$5.29^{1.83}_{0.93}$
Disk-X1-1	1	38	$10.9^{5.6}_{3.1}$	$7.1^{1.9}_{1.2}$	$0.12^{0.10}_{0.06}$	$0.24^{0.09}_{0.07}$	$13.0^{8.21}_{5.05}$	$12.64^{3.33}_{1.91}$
		300	$9.3^{8.3}_{3.0}$	$6.8^{2.2}_{1.4}$	$0.15^{0.20}_{0.09}$	$0.25^{0.14}_{0.09}$	$3.55^{2.56}_{1.66}$	$13.78^{6.31}_{2.82}$
Disk-X2-1	1	38	$6.7^{2.4}_{1.6}$	$5.3^{1.1}_{0.9}$	$0.37^{0.51}_{0.19}$	$0.48^{0.37}_{0.15}$	$5.62^{4.38}_{3.11}$	$19.07^{15.10}_{5.44}$
		100	$5.9^{2.5}_{1.4}$	$5.0^{1.3}_{1.1}$	$0.50^{1.23}_{0.29}$	$0.55^{0.85}_{0.22}$	$2.70^{2.73}_{1.90}$	$22.56^{37.65}_{8.27}$
Disk-X1-2	1	52	$13.7^{8.4}_{4.4}$	$8.5^{2.4}_{1.7}$	$0.16^{0.16}_{0.08}$	$0.42^{0.18}_{0.13}$	$13.3^{8.09}_{5.34}$	$10.60^{2.63}_{1.28}$
		215	$12.9^{15.5}_{4.7}$	$8.4^{2.9}_{1.8}$	$0.18^{0.24}_{0.12}$	$0.43^{0.23}_{0.15}$	$5.62^{3.88}_{2.46}$	$11.03^{3.71}_{1.70}$
Disk-X2-2	1	28	$10.0^{3.8}_{2.5}$	$6.7^{1.6}_{1.2}$	$0.20^{0.18}_{0.09}$	$0.30^{0.13}_{0.08}$	$14.1^{8.88}_{5.98}$	$10.67^{3.49}_{1.73}$
		95	$9.3^{7.1}_{2.8}$	$6.6^{2.1}_{1.3}$	$0.22^{0.28}_{0.14}$	$0.31^{0.17}_{0.11}$	$6.20^{5.02}_{2.95}$	$11.07^{5.26}_{2.48}$
Disk1	1	23	< 3.4	< 3.3	> 0.22	> 0.14	< 1.12	> 2.90
		154	< 3.0	< 3.0	> 0.57	> 0.30	< 0.16	> 7.20
	2	38	$5.5^{2.1}_{1.2}$	$4.7^{1.0}_{0.7}$	$0.17^{0.20}_{0.09}$	$0.17^{0.10}_{0.05}$	$4.57^{3.84}_{2.33}$	$3.89^{2.80}_{1.25}$
		82	$5.0^{1.9}_{1.1}$	$4.5^{1.0}_{0.8}$	$0.21^{0.37}_{0.12}$	$0.19^{0.18}_{0.07}$	$2.51^{2.40}_{1.55}$	$4.54^{5.48}_{1.70}$
Disk2	1	68	$6.8^{3.5}_{1.7}$	$5.4^{1.4}_{0.9}$	$0.16^{0.19}_{0.09}$	$0.21^{0.12}_{0.07}$	$4.97^{3.94}_{2.40}$	$8.98^{5.18}_{2.46}$
		200	$6.1^{2.9}_{1.6}$	$5.3^{1.3}_{1.0}$	$0.20^{0.28}_{0.11}$	$0.23^{0.17}_{0.08}$	$2.47^{2.00}_{1.25}$	$10.03^{8.07}_{3.04}$
	2	145	$6.7^{2.9}_{1.7}$	$5.7^{1.4}_{1.2}$	$0.70^{14.8}_{0.41}$	$0.96^{15.2}_{0.40}$	$2.51^{2.50}_{2.41}$	$25.64^{397.4}_{9.13}$
	3	50	$16.1^{19.2}_{5.6}$	$9.4^{2.7}_{2.1}$	$0.19^{0.22}_{0.09}$	$0.45^{0.23}_{0.13}$	$15.8^{9.27}_{8.94}$	$16.89^{4.31}_{1.86}$
		80	$16.1^{16.2}_{6.2}$	$9.3^{3.5}_{2.2}$	$0.19^{0.27}_{0.12}$	$0.45^{0.26}_{0.16}$	$11.6^{8.32}_{5.32}$	$17.05^{5.18}_{2.08}$

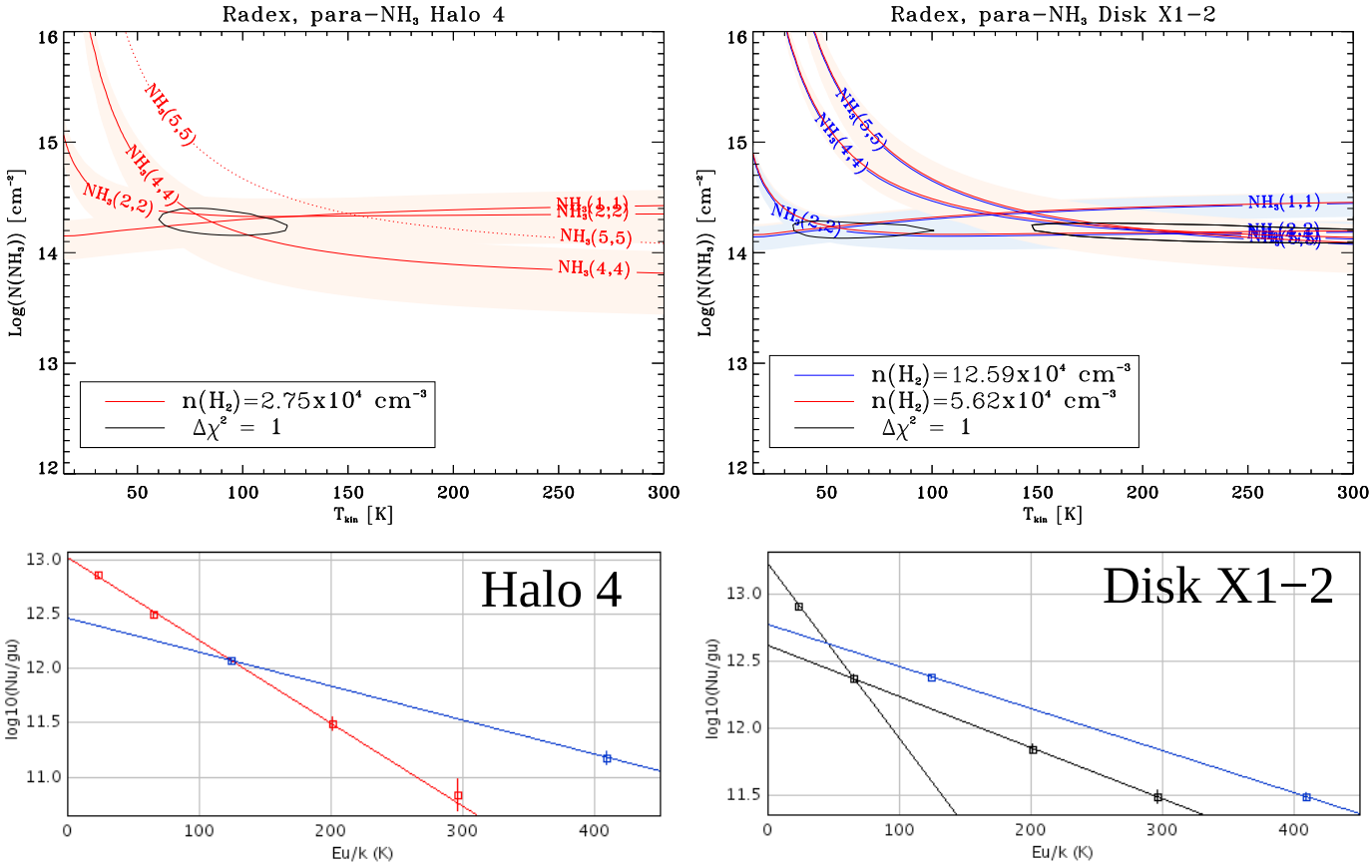

Fig. 2. Example of rotational (bottom) and LVG (top) diagrams of NH_3. Left: Halo 4. Right: Disk X1-2. In the Boltzmann diagram (bottom), para-NH_3 species are fitted with the red line, and the ortho-NH_3 species are fitted with the blue line. In the LVG diagrams (top), we shown the $n(H_2)$ used in the model. The error is shown in the black ellipse, and was computed assuming a 68.3% (1 σ) confidence level (see text for details).

Table 4. Kinetic temperatures derived from LVG calculations

Source	Cloud	low temperature		high temperature		single temperature from p–NH_3	
	number	T_{kin}	$N(NH_3)$	T_{kin}	$N(NH_3)$	T_{kin}	$N(NH_3)$
		[K]	cm^{-2}	[K]	cm^{-2}	[K]	cm^{-2}
Halo1	1					> 115	1.20×10^{14}
	2					> 90	$> 1.99 \times 10^{14}$
	3					> 135	6.6×10^{13}
Halo4	1					90	1.99×10^{14}
DiskX1-1	1	38	1.99×10^{14}	$> 300^a$	1.58×10^{14}		
DiskX2-1	1	38	4.47×10^{14}	100	3.3×10^{14}		
DiskX1-2	1	52	1.66×10^{14}	215	1.51×10^{14}		
DiskX2-2	1	28	1.90×10^{14}	95	1.0×10^{14}		
Disk1	1	23	3.98×10^{13}	$> 154^b$	$> 1.58 \times 10^{13}$		
	2	38	6.31×10^{13}	$> 82^b$	$> 4.47 \times 10^{13}$		
Disk2	1	68	1.41×10^{15}	200	1.41×10^{15}		
	2					> 145	2.00×10^{15}
	3	50	1.41×10^{15}	80	1.41×10^{15}		

[a] LVG gives a T_{kin} greater than 300 K which is the value allowed by the collisional rates given by Danby et al. (1988).
[b] Due that the values for the (4,4)-(5,5) metastable inversion transitions are upper limits to the actual T_{MB}, the modeled curve in the LVG plot is outside the allowed range, and we give a lower limit to the kinetic temperature using the rotational temperature form the LTE plot.

Table 5. Column densities from different molecules derived from RADEX using as a fixed parameter the kinetic temperatures (Table 4), and the $n(H_2)$ from the CS data (Table 3)

Source	Cloud	N(SiO)	N(HNCO)	N($C^{34}S$)	N(^{13}CO)	N($C^{18}O$)	N(H_2)[a]
	number	[$\times 10^{13} cm^{-2}$]	[$\times 10^{13} cm^{-2}$]	[$\times 10^{13} cm^{-2}$]	[$\times 10^{16} cm^{-2}$]	[$\times 10^{16} cm^{-2}$]	[$\times 10^{21} cm^{-2}$]
Halo1	1	$3.01^{0.33}_{0.33}$	$0.79^{0.20}_{0.20}$	–	$4.13^{0.44}_{0.44}$	$0.48^{0.06}_{0.06}$	21.74
	2	$4.64^{2.59}_{1.09}$	$2.77^{0.78}_{0.30}$	$1.26^{0.54}_{0.23}$	$3.96^{0.69}_{0.80}$	$0.94^{0.19}_{0.20}$	20.84
	3	$0.75^{0.12}_{0.08}$	–	–	$3.20^{0.52}_{0.59}$	$0.26^{0.07}_{0.07}$	16.84
Halo2	1	$0.76^{2.45}_{0.38}$	$1.64^{4.83}_{0.75}$	$0.33^{1.67}_{0.21}$	–	–	–
	2	$0.79^{65.0}_{0.45}$	–	$0.45^{43.88}_{0.32}$	–	–	–
Halo3	1	$3.98^{0.59}_{1.99}$	$4.47^{0.55}_{1.74}$	$1.43^{0.36}_{0.70}$	–	–	–
	2	–	$1.27^{0.72}_{0.19}$	$0.29^{0.34}_{0.13}$	–	–	–
Halo4	1	$1.00^{1.00}_{0.38}$	$3.98^{2.69}_{0.80}$	$0.40^{0.42}_{0.18}$	$7.35^{1.83}_{2.07}$	$0.25^{0.08}_{0.08}$	38.68
Halo5	1	$0.99^{0.42}_{0.22}$	$2.58^{0.76}_{0.32}$	$0.47^{0.14}_{0.08}$	–	–	–
Disk-X1-1	1	$3.91^{1.30}_{0.76}$	$3.05^{0.74}_{0.48}$	$0.64^{0.20}_{0.12}$	$8.84^{1.12}_{1.15}$	$0.51^{0.19}_{0.18}$	46.53
		$3.98^{2.00}_{0.90}$	$2.88^{0.67}_{0.33}$	$0.71^{0.35}_{0.18}$	$32.8^{9.39}_{8.73}$	$1.87^{1.08}_{0.87}$	172.58
Disk-X2-1	1	$3.36^{2.95}_{1.12}$	$9.59^{4.00}_{1.02}$	$0.80^{0.64}_{0.24}$	$16.9^{2.45}_{2.94}$	$1.37^{0.23}_{0.27}$	33.78
		$3.60^{6.76}_{1.36}$	$10.6^{13.0}_{2.01}$	$0.98^{1.60}_{0.37}$	$29.2^{7.55}_{11.1}$	$2.51^{0.77}_{0.98}$	58.48
Disk-X1-2	1	$2.09^{0.62}_{0.35}$	$3.19^{0.89}_{0.56}$	$0.71^{0.15}_{0.09}$	$3.10^{0.40}_{0.41}$	$0.32^{0.05}_{0.05}$	16.32
		$2.10^{0.78}_{0.37}$	$2.96^{0.96}_{0.39}$	$0.74^{0.22}_{0.11}$	$8.09^{1.81}_{1.78}$	$0.82^{0.23}_{0.21}$	42.58
Disk-X2-2	1	$0.22^{0.07}_{0.04}$	$2.08^{0.42}_{0.32}$	$0.93^{0.29}_{0.15}$	$12.8^{1.55}_{1.58}$	$1.14^{0.13}_{0.14}$	25.64
		$0.27^{0.19}_{0.08}$	$2.00^{0.57}_{0.25}$	$0.96^{0.48}_{0.19}$	$28.7^{5.26}_{5.83}$	$2.62^{0.52}_{0.53}$	57.42
Disk1	1	$0.71^{65}_{0.46}$	$1.41^{164}_{0.89}$	$0.09^{12.18}_{0.08}$	$1.26^{0.52}_{0.13}$	$0.13^{0.05}_{0.02}$	2.52
		$1.70^{0.14}_{0.27}$	$3.55^{0.54}_{0.73}$	$0.24^{0.16}_{0.15}$	$1.32^{0.15}_{0.10}$	$0.14^{0.02}_{0.02}$	2.64
	2	$0.45^{0.37}_{0.17}$	$1.72^{0.79}_{0.27}$	$0.16^{0.13}_{0.06}$	$2.26^{0.35}_{0.40}$	$0.19^{0.04}_{0.04}$	4.52
		$0.50^{0.62}_{0.22}$	$2.00^{1.99}_{0.52}$	$0.19^{0.26}_{0.08}$	$3.46^{0.85}_{1.08}$	$0.28^{0.09}_{0.10}$	6.92
Disk2	1	$2.98^{2.12}_{0.87}$	–	$3.05^{1.83}_{0.76}$	–	–	–
		$3.16^{2.71}_{1.06}$	–	$3.45^{2.86}_{1.04}$	–	–	–
	2	$9.04^{153}_{3.41}$	$336.1^{4482.8}_{71.7}$	$8.58^{126.96}_{2.91}$	$101.3^{28.5}_{78.3}$	$19.63^{6.48}_{16.39}$	202.56
	3	–	–	–	–	–	–
		–	–	–	–	–	–

[a] Column densities of H_2 derived from ^{13}CO using a conversion factor of 5.0×10^{-6} (Rodríguez-Fernández et al. 2001) for the normal GC gas, and a factor of 1.9×10^{-6} for the gas in the disk-halo interaction regions (see text for details).

It is possible to estimate the total column density of H_2 from the CO isotopologues, which will present lower optical depths than the main isotope, and therefore a more reliable estimation of the column density ($N(H_2) = N(^xC^yO) \times [^xC^yO/H_2]$, where x and y correspond to the isotopic substitution used for the carbon and oxygen atoms). For our calculations, we assume an abundance ratio CO/H_2 of 10^{-4} (see, e.g., Rodríguez-Fernández et al. 2001, and references therein), and we use the ^{13}CO emission. Therefore, we also need the $^{12}C/^{13}C$ isotopic ratio. Recently, Riquelme et al. (2010a) derived a high $^{12}C/^{13}C$ isotopic value (> 40) in some of the sources studied in this work. Such a high isotopic value was found mainly toward the disk-halo interaction

region, therefore, we still use the standard value of 20 (see, e.g., Wilson & Matteucci 1992) in the typical GC gas for the sources "Disk1", "Disk2" and for the sources with kinematic of X2 orbits (Disk X2-1, Disk X2-2). For the sources which are in the disk-halo interaction region, we use the value of 53 corresponding to the typical value found in the 4 kpc molecular ring (Wilson & Rood 1994), which also was used by Torii et al. (2010a) and Kudo et al. (2011) in the GMLs regions. This translate in using a $[^{13}CO/H_2]$ conversion factor of 5.0×10^{-6} for the normal GC gas, and 1.9×10^{-6} for the gas in the disk-halo interaction regions (Table 5) We decide not to use the $C^{18}O$ emission to trace the total column density of H_2, because of the uncertainties in the $^{16}O/^{18}O$ isotopic ratio in the disk-halo interaction region, which could be affected by the unprocessed gas that is being accreted toward the CMZ (Riquelme et al. 2010a).

3.3.2. Fractional abundances

We derived beam averaged fractional abundances with respect to H_2 for all the observed molecules (Table 6), and in Table 7 we show the results of the fractional abundances of NH_3 with respect to the other molecules, and the fractional abundances of SiO and HNCO with respect to CS and $C^{34}S$.

In the following, we do not consider the results for Disk 1, which will be disscused below. X(SiO) varies from $0.06 - 2.23 \times 10^{-9}$ with the largest value toward the foot point of the GMLs. X(HNCO) shows less variation in all the observed sources ranging from 0.27 to 2.18×10^{-9}, except for the Disk 2, where it presents a large abundance of 16.6×10^{-9}. The fractional abundances with respect to H_2 depend on a reliable estimation of the H_2 column density, which depends in a number of assumption (H_2 to CO conversion factor, physical parameters used to derive the column densities of ^{13}CO). Therefore, we also compare the column density of the different molecular tracer (shock, photodissociation) with respect to CS (dense tracer) and its presumably optically thin isotope $C^{34}S$.

Although there are not big differences from source to source in the N(SiO)/N(CS) and N(SiO)/N($C^{34}S$) ratios, we can see that the highest values of are found toward Halo 1 and Disk X1 sources, with a difference up to 1 order of magnitude if we compare the Disk X1-2 with the Disk X2-2 sources. The relative abundance N(HNCO)/N(CS) and N(HNCO)/N($C^{34}S$) in the Disk 2 source shows, by far, the largest values in our sample. The source Disk 2 corresponds to the source Sgr B2M (20",100") from Martín et al. (2008), which is classified as a "typical Galactic center cloud" in their work. They found a large HNCO/^{13}CS abundance ratio of 68 ± 13 in that source.

We exclude from the previous analysis the source Disk 1, because the determination of their physical parameters (kinetic temperature) would be very overestimated. The metastable inversion transitions (4,4) and (5,5) of NH_3 were not detected, therefore the kinetic temperature should no be large. In our radiative transfer calculations we use an upper limit to the rotational temperature (154 K) which was taken as the kinetic temperature of the gas. It is probably that the actual kinetic temperature (if there is a high temperature regimen in this source) could be much lower (similar to the value for the disk X2 positions, which correspond to typical gas in the CMZ). The LVG column density of SiO on this source (Table 5) is a factor of $\sim$ 30 larger than the value from the LTE (Table 12), while the differences for the other positions are only a factor 2-4.

4. Discussion

4.1. Kinetic temperatures in the disk-halo toward the Galactic center

The derived kinetic temperatures for the halo positions are consistent with one high temperature regime (> 90 K), while the clouds placed in the CMZ and in the "normal" gas (Disk 1 position) are consistent with two temperature regimes ($\sim$ 40 and $\sim$ 200 K).

4.1.1. Single temperature regime in the loop region

We derived a single high kinetic temperature regime (> 95 K) for the halo sources (Halo 1 and Halo 4), towards the GML discovered by Fukui et al. (2006). Surprisingly, both the Halo 1 position in the footpoint of the GMLs and Halo 4 in the top of the loop do not show any trace of low kinetic temperatures, which otherwise are present throughout the CMZ as discussed in previous works. Torii et al. (2010a) derived kinetic temperature of 30-100 K or higher, and densities of 10^3 cm^{-3} using multitransitional CO observations toward the foot point of the GML (loop 1 and 2). This foot points correspond to our Halo 2, and Halo 3, which could not be observed with the Effelsberg telescope due to their low elevations. Furthermore, Torii et al. (2010b) made a comparison between the foot points 1 and 2 with the two broad velocity features, the Clump 2 and $l = 5°.5$ complex, finding that they share common properties such as the vertical elongation to the plane and large velocity spans of $50 - 150$ km s^{-1}suggesting that they have a similar origin. Therefore, the physical processes that are occurring in Halo 1 position should be similar to those in the well studied foot point of the loop1 and 2.

Is our Halo 1 position really located at the foot point of the GML? After all, we see the CMZ edge on and the GMLs could be in front of or behind our Halo 1 position. This source is at $l = 5°.5$ and at $\sim$ 790 pc in projection of the GC $(l, b) = (0, 0)$ position assuming a GC distance of 8.3 ± 0.3 kpc (Brunthaler et al. 2011). It was previously observed by several authors (Bitran et al. 1997; Fukui et al. 2006; Sawada et al. 2001; Lee & Lee 2003; Riquelme et al. 2010b); its main velocity component is at 98 km s^{-1}(from the HCO^+ data from Riquelme et al. 2010b), and a large velocity width in all the species is observed in this and previous works, which indicates that this source indeed belong to the GC region. Furthermore, we cannot rule out the possibility that the gas seen in the Halo 1 position has some velocity component belonging to the GC region, but at lower or higher distances due to projection effect. High resolution maps of the foot point region as well as maps of the complete loop are needed to reveal the morphology and kinematic of the complete loop to confirm the association of this position to the GMLs scenario, because this loop is tentatively detected by Fukui et al. (2006). Therefore, the high $^{12}/^{13}$C isotopic ratio found by Riquelme et al. (2010a) toward this position, and towards the well studied foot point of the loop 1 and 2 would provide evidence for the GMLs scenario.

4.1.2. The two components model in the CMZ

In the CMZ (Disk X1-1, Disk X1-2, Disk X2-1, Disk X2-2, and Disk 2) and in the disk (Disk 1), our results are consistent with a two components model, with at least at two different temperatures. Hüttemeister et al. (1993a, 1998) draw a picture in terms of a two components model, where for a typical GC molecular cloud, 25% of the gas has high temperatures (> 100 K), and this

Table 6. Fractional abundances of SiO, HNCO, NH_3, CS, and $C^{34}S$ with respect to H_2

Source	n^a	X(SiO) $\times10^{-9}$	X(HNCO) $\times10^{-9}$	$X(NH_3)^c$ $\times10^{-8}$	X(CS) $\times10^{-9}$	$X(C^{34}S)$ $\times10^{-10}$
Halo1	1	1.38 ± 0.21	0.36 ± 0.10	1.10	3.66 ± 0.39	
	2	2.23 ± 1.32	1.33 ± 0.46	1.91	8.68 ± 4.49	6.05 ± 2.86
	3	0.45 ± 0.11		0.78	0.84 ± 0.18	
Halo2	1					
	2					
Halo3	1					
	2					
Halo4	1	0.26 ± 0.27	1.03 ± 0.75	1.03	1.60 ± 1.45	1.03 ± 1.12
Halo5	1					
DiskX1-1	1	0.36 ± 0.14	0.27 ± 0.08	0.33	1.21 ± 0.42	0.62 ± 0.23
DiskX2-1	1	0.75 ± 0.82	2.18 ± 1.57	1.68	4.51 ± 4.53	1.93 ± 1.93
DiskX1-2	1	0.71 ± 0.21	1.04 ± 0.28	1.08	3.67 ± 0.98	2.46 ± 0.61
DiskX2-2	1	0.06 ± 0.03	0.49 ± 0.11	0.70	2.62 ± 0.85	2.28 ± 0.75
Disk1	1	4.67 ± 1.42	9.61 ± 3.01	2.17	19.6 ± 4.10	6.39 ± 3.72
	2	0.83 ± 0.41	3.25 ± 1.98	1.89	7.37 ± 5.57	3.06 ± 2.61
Disk2	1					
	2	0.45 ± 0.21	16.59 ± 5.85	1.97	1.26 ± 0.57	4.24 ± 1.87
	3					

[a] Cloud number defined by the different velocity components.
[c] Column density of NH_3 correspond to the $N(p-NH_3) + N(o-NH_3) = 2 \times N(p-NH_3)$ assuming a ortho-to-para ratio of 1.

Table 7. Fractional abundances of NH_3 with respect to SiO, HNCO, CS, $C^{34}S$, and of SiO and HNCO with respect to CS and $C^{34}S$

Source		$\frac{N(NH_3)}{N(SiO)}$	$\frac{N(NH_3)}{N(HNCO)}$	$\frac{N(NH_3)}{N(CS)}$	$\frac{N(NH_3)}{N(C^{34}S)}$	$\frac{N(SiO)}{N(CS)}$	$\frac{N(SiO)}{N(C^{34}S)}$	$\frac{N(HNCO)}{N(CS)}$	$\frac{N(HNCO)}{N(C^{34}S)}$	$\frac{N(SiO)}{N(HNCO)}$
Halo1	1	7.97	30.38	3.02		0.38 ± 0.04		0.10 ± 0.03		3.81 ± 1.05
	2	8.58	14.37	2.20	31.59	0.26 ± 0.19	3.68 ± 2.59	0.15 ± 0.08	2.20 ± 1.13	1.68 ± 1.05
	3	17.6		9.30		0.53 ± 0.10				
Halo2	1					0.13 ± 0.43	2.30 ± 13.8	0.29 ± 0.85	4.97 ± 29.1	0.46 ± 2.02
	2					0.12 ± 0.10	1.76 ± 1.60			
Halo3	1					0.18 ± 0.12	2.78 ± 1.95	0.20 ± 0.12	3.13 ± 1.95	0.89 ± 0.56
	2							0.34 ± 0.34	4.38 ± 5.70	
Halo4	1	39.8	10.00	6.44	99.50	0.16 ± 0.21	2.50 ± 3.63	0.64 ± 0.70	9.95 ± 12.4	0.25 ± 0.30
Halo5	1					0.19 ± 0.10	2.11 ± 1.09	0.49 ± 0.22	5.49 ± 2.30	0.38 ± 0.20
DiskX1-1	1	9.05	12.04	2.70	52.89	0.30 ± 0.12	5.84 ± 2.48	0.22 ± 0.07	4.39 ± 1.51	1.33 ± 0.46
DiskX2-1	1	22.3	7.72	3.73	87.30	0.17 ± 0.24	3.91 ± 5.61	0.48 ± 0.57	11.3 ± 13.4	0.35 ± 0.43
DiskX1-2	1	15.1	10.31	2.93	43.72	0.19 ± 0.06	2.89 ± 0.87	0.28 ± 0.09	4.24 ± 1.19	0.68 ± 0.22
DiskX2-2	1	118	14.22	2.67	30.69	0.02 ± 0.01	0.26 ± 0.13	0.19 ± 0.06	2.16 ± 0.74	0.12 ± 0.05
Disk1	1	4.65	2.26	1.11	33.94	0.24 ± 0.05	7.30 ± 4.28	0.49 ± 0.11	15.0 ± 8.86	0.49 ± 0.16
	2	22.7	5.81	2.56	61.71	0.11 ± 0.10	2.71 ± 2.57	0.44 ± 0.41	10.6 ± 10.7	0.26 ± 0.19
Disk2	1	91.86		29.67	86.77	0.32 ± 0.24	0.94 ± 0.72			
	2	44.25	1.19	15.60	46.62	0.35 ± 0.18	1.05 ± 0.53	13.11 ± 5.44	39.2 ± 15.7	0.03 ± 0.01
	3				16.62					

gas has low H_2 density; while the remaining 75% of the total gas mass is cooler ∼ 25 K at densities of ≥ 10^4 cm^{-3}. Both gas components are in pressure equilibrium. We do not confirm the large amount of molecular gas (75%) in the low temperature regime claimed by Hüttemeister et al. (1993a). We derive that the gas in the low temperature component is almost the same amount than the gas in the high temperature component. The positions from Hüttemeister et al. (1993a) are selected as intensity peaks in the CS maps from Bally et al. (1987), therefore the positions correspond to high density regions as CS is a dense tracer. Our sources, on the contrary, correspond to shock positions, therefore expecting that the amount of warm molecular gas will be larger than at the positions from Hüttemeister et al. (1993a).

4.2. On the heating and cooling of the molecular gas in the GMLs and in the CMZ

Although the number of positions observed in the halo is rather limited, a remarkable result obtained in this work, is the single high kinetic temperature regime (> 95 K) for the halo sources, in contrast with the two temperature regimens (cool and warm) present throughout the CMZ. Therefore, the question that naturally arise is if the heating mechanism in the GMLs is so efficient that the molecular gas has no time to be cooled down, or if the cooling in the CMZ is more effective than in the halo positions. In the following, we compute the cooling rates for H_2 and CO emissions, and by the gas-dust coupling.

Goldsmith & Langer (1978) derived the temperature dependence of the total cooling rate for a variety of molecular hydrogen densities and at velocity gradient of 1 km s^{-1} pc^{-1} for the temperature range of 10 to 60 K. For $n(H_2) \leq 10^3$ cm^{-3}

the cooling is dominated by CO, with a total cooling rate of $\Lambda_{\rm total} = 6.8{\times}10^{-27} T^{2.2}$ erg cm^{-3} s^{-1}. For $10^3 \leq n(H_2) \leq 10^5$ cm^3, the isotopic species of CO, CI, and O_2 contribute with the 30% to 70% of the total cooling, and the expression of the cooling rate for $n(H_2) = 4 \times 10^3$ is $\Lambda_{\rm total} = 2.3 \times 10^{-26} T^{2.2}$ erg cm^{-3} s^{-1}. For $n(H_2) \sim 10^4$ cm^3, the cooling rate is $\Lambda_{\rm total} = 1.5 \times 10^{-26} T^{2.7}$, and for $n(H_2) \sim 10^5$ cm^3, the cooling rate is $\Lambda_{\rm total} = 3.8 \times 10^{-26} T^{2.9}$. Taking this formulation with caution because the temperature range for which these expression are valid is below the warm kinetic temperature derived in this work. We estimate the $\Lambda_{\rm total}$ for each source and each temperature-density regime (see Table 8). Later, Le Bourlot et al. (1999) derived the cooling rate by H_2 (Λ_{H_2}) for a wider range of physical parameters ($100 \leq T_{\rm kin} \leq 10^4$ K; $1 \leq n(H_2) \leq 10^8$ cm^{-3}). We use the FORTRAN subroutine provided by them only towards the sources allowed by the parameters range, i.e., for the warm gas (Table 8).

The cooling rate for the coupling of the dust and gas is given by (Goldsmith & Langer 1978)

$$\Lambda_{\rm gd} = 2.4 \times 10^{-33} T_g^{1/2} (T_g - T_d) n^2({\rm H_2})\, {\rm erg\, s^{-1} cm^{-3}} \quad (1)$$

Hüttemeister et al. (1993a) argue that the cold gas component is coupled to the dust temperature at high densities, therefore, the dust in the GC region would be a cooling agent. They propose that the density of the cold gas must be at least an order of magnitude higher than that of the hot gas; otherwise the hot gas would also cooled down. We find that the gas density of the hot component is only slightly lower than in the cold component (a factor $\sim 2-4$ from the CS data in Table 3). Although that the gas-dust coupling becomes significant at $n(H_2) \sim 10^5$ cm^{-3} (Juvela & Ysard 2011), which is reached only in the cool component regime in few positions in the CMZ (Table 3), we estimate this cooling rate for all the positions (Table 8).

In the total cooling rates computed following Goldsmith & Langer (1978), there are two facts that should be taken into account: the depletion of coolant species, and the lack of processed gas in the halo. First, the depletion of the coolant species can increase the gas temperature at low and moderate densities of $n(H_2) \leq 10^4$ cm^{-3}. This effect was studied by Goldsmith (2001) in dark clouds. In the physical conditions of the GC, the depletion of the coolant species is unlikely due to the high densities and low temperatures which are needed to have this effect. Second, as we noted before, in the density range of the GC, the isotopes of CO, CI, and O_2 contribute 30% to 70% of the total cooling. Riquelme et al. (2010a) found a high ^{12}C/^{13}C isotopic ratio towards the disk-halo connection region (halo, disk X1) which they interpreted as non-processed gas being accreted towards the GC. Due to the lack of more processed gas (traced by isotopes of CO), the cooling rate could be decreased in those regions. The drawback of this analysis, is that the high isotopic ratio was also found towards the disk X1 positions, and those positions have indeed a cool temperature regime.

We can see that in total cooling rate derived from Goldsmith & Langer (1978), and also in the H_2 cooling rate derived from Le Bourlot et al. (1999), the X1 orbits positions show a very effective cooling, which could explain the low temperature regime.

Comparing the cooling rates for the halo positions with the ones for the CMZ, it is possible to argue that the lack of the cool component in the halo could be due to the smaller cooling rates in those regions. Therefore the cooling rates estimated for the disk X2 positions are similar with the ones for the halo, and the disk X2 positions still show the low temperature regime. Furthermore, it is necessary to estimate the heating rates affecting the GC region to study if a rise of the heating mechanism should be the responsible of the lack of low temperature regime in the halo sources.

4.3. The heating of the gas in the GC

We find high gas kinetic temperatures for basically all the observed positions of our sample, therefore the heating mechanism responsible for the widespread high temperatures should apply for the gas in the entire GC region, with little effect on the dust. The heating mechanism in the GC should be different from that the heating in the disk, where the molecules are heated by collisions with hot dust, heated by embedded stars.

Several heating mechanisms have been proposed to explain the high kinetic temperatures in the GC region. The dissipation of mechanical turbulence through shocks would offer a compelling answer, because the GC region shows an ubiquitous presence of shocks, as traced by the SiO emission (Martín-Pintado et al. 2000; Riquelme et al. 2010b). The heating rate of the dissipation of turbulence (of velocity v_t on a scale R_c) is given by (Black 1987)

$$\Gamma_{\rm turb} \approx 3.5 \times 10^{-28} v_t^3 n_H \left(\frac{1{\rm pc}}{R_c}\right) {\rm erg\, s^{-1} cm^{-3}} \quad (2)$$

We derive the heating rate of the dissipation of turbulence for each position in Table 8. The origin of this turbulence has several hypothesis. Large scale dynamics in a barred potential (Binney et al. 1991) can explains the shock origin in the CMZ. This is supported by the higher kinetic temperatures found in the disk X1 sources than in the disk X2 sources (Table 4) and by the high ^{12}C/^{13}C isotopic ratio derived in these positions by Riquelme et al. (2010a). Shocks also would be produced by the GMLs scenario toward the foot point of the loops.

We consider that shocks driven by the above mechanisms are heating the gas in the disk-halo interaction regions. Furthermore, the high kinetic temperatures and the large SiO emission are widespread throughout all the GC region. Supernova or hypernova explosions have been proposed to explain the high kinetic temperatures found in the 1.3 complex (Tanaka et al. 2007). The shocks produced by the supernovas in this regions, are associated with the lower velocity components (in our notation, disk X2), could be responsible for the high temperature component found in the gas. For the lower longitudes in the CMZ, Martín-Pintado et al. (1997) propose shocks from interaction with SNRs close to Sgr A, interaction with non-thermal filaments in the radio arc, and cloud cloud collision, and expanding bubbles in the vicinity of Sgr B.

Cloud cloud collisions produced by the Galactic rotation was also proposed in the GC region (Wilson et al. 1982), which is favored by the large linewidth typical in the GC clouds. Güsten et al. (1985) argue that if this mechanism is acting in the molecular gas, the linewidth and the temperatures should be correlated. Mauersberger et al. (1986) found such a correlation for the clouds observed in the GC, which would support this mechanism. Like Hüttemeister et al. (1993a), we do not confirm such clear correlation between the rotational temperature associated with the inversion transitions (2,2), (4,4), and (5,5) (Table 2) and the Doppler width of our sources (see Fig 3). For the few observed positions we can neither confirm nor reject the dissipation of turbulent produced by Galactic rotation as primary heating mechanism in our sources.

We discard the UV heating in the GC region. The high NH_3 abundances in the GC region require effective shielding from UV radiation because the ammonia is easily photodisociated by

ultraviolet radiation (Rodríguez-Fernández et al. 2001). This is also confirmated by the large abundance of HNCO molecule, which is also photodissociated by UV radiation.
The HNCO could be formed via gas phase reactions, but formation in grains seems to be more efficient (see e.g., Martín et al. 2008, and references therein). Presumably this molecule is released to the ISM by grain erosion and/or disruption by shocks (Zinchenko et al. 2000), and is easily photodissociated by UV radiation. The shocks that release the molecule from the grain mantles should be slow enough to not dissociated the molecule. We find that the X(HNCO) is low in the Disk X1-1 source, where we expect shocks, but no UV emission. Also we can see an enhancement toward the Halo 1 source (cloud number 2), and the Disk X2-1 source, which could be due to the shocks present in these regions, are strong enough to evaporate the molecule from the grain mantles but too slow to not dissociate the HNCO. This molecule can be used to trace the shocks properties throughout the GC region.

The GC is pervaded by a magnetic field of few mG (see e.g., Ferrière et al. 2007), and their presence can also influence the heating of the GC. The ion-slip heating has been propose for the molecular clouds in the GC region, where the heating rate depends on the magnetic field B, ionization rate, neutral number density n_n, ion number density n_i, number of collision per second, the reduced mass of the ions and neutrals, and the scale of the cloud R (in pc) (see, Scalo 1977). Because the uncertainty of some on these values for each observed position, it is not possible to estimate the heating rate. However, Larson (1981) showed that $n_n R$ is constant and $B \sim n^{1/2}$ (Troland & Heiles 1986) therefore, $\Gamma_{is} \sim n^2$, this effect is important if the gas is dense (Rodríguez-Fernández 2002).

It is possible that none of the mechanism discussed above would be the responsible of the lack of the low temperature component observed in the halo positions. An extra heating input would be required. Torii et al. (2010a) propose that the gas in the foot point of the GML is heating by C-shocks, and that the warmest region of the foot point (the "U shape") would also be heated by magnetic reconnection or by upward flowing gas bounced by the narrow neck in the foot point. Their estimate that the total available energy (considering the magnetic and gravitational energy) injected to the U shape is $1.8{-}2.6{\times}10^{37}$ergs^{-1} in $\sim 10^6$ years. If we consider a cloud size of 3 pc radius, as estimated by Torii et al. (2010a), the heating rate is $\Gamma \sim 3.9 - 7.8 \times 10^{-21}$ erg cm^{-3} s^{-1}. The kinetic temperature is slightly larger in the foot point than in the top of the loop, which would marginally support the loops scenario.

5. The ammonia ortho-species

As mentioned before, the timescale for a proton spin flip in NH_3 once it has formed is so large that ortho and para ammonia can be regarded as different species. It has been proposed that the spin temperature of ammonia, or the ortho/para ratio, can be used to derive the temperature of the gas at the time ammonia was forming or to give clues on the formation mechanism of NH_3 (see e.g., Umemoto et al. 1999). A ratio of 1.0 would be expected if NH_3 is formed in the gas phase reactions at high temperatures, and a larger value could be explained by a formation on cold dust grains and a subsequent release into the gas phase. For temperatures of about 10 K, the typical temperature of cold dust, the ortho-to-para ratio will be larger than 2.

From the LTE analysis of the ammonia molecule, we derive an ortho-to-para ratio average for all of our sources of 0.99 with a standard deviation of 0.32 (see Table 10) , with small differences

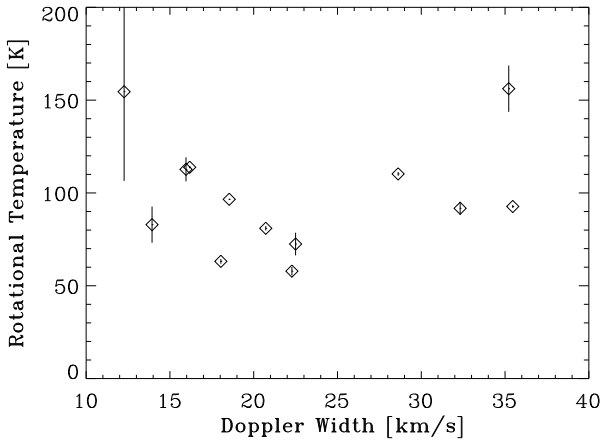

Fig. 3. Plot showing the T_{rot} versus the average velocity linewidth from all the metastable inversion transitions. The T_{rot} correspond to the values in bold from the Table 2

if we consider the halo and disk X1 sources (1.21 ± 0.26), and the normal GC gas, i.e., disk and disk X2 sources (0.80 ± 0.24). This result is consistent with Hüttemeister et al. (1993a) estimation of the $(3,3)$ column density, which do not deviate more than 20% from the LTE averaged over the GC. However, the above ratios assume that NH_3 emission is quasi thermal, which in the case of ortho ammonia may not be always true. Non thermal emission has been predicted for the NH_3 (3,3) line by Walmsley & Ungerechts (1983), and has been observed e.g. by Mauersberger et al. (1986). Also the $(6,6)$ line might be a maser source in some case Lebrón et al. (2011).

The LVG analysis confirms this result if we take into account only the warm component of the para-NH_3 with the ortho-NH_3. While the ortho-NH_3 transitions are probably tracing higher kinetic temperatures than the para-species (see Table 9), the ortho-to-para ratio derived using RADEX for the warm kinetic temperature component approaches to the statistical equilibrium value, possibly suggest that NH_3 has been formed in gas phase and then stick on to the grains or in relatively warm grains.

6. Conclusions

1. We have used the metastable inversion transitions of NH_3 from $(J,K) = (1,1)$ to $(6,6)$ to derive the gas kinetic temperature toward six positions selected in the Galactic central disk and for high latitude molecular clouds. We also observed other molecules like SiO, HNCO, CS, $C^{34}S$, $C^{18}O$, and ^{13}CO, to derive the densities and to trace different physical processes (shocks, photodissociation, dense gas) which was used to reveal the heating mechanisms affecting the molecular gas in these regions.
2. The GC molecular gas consists of roughly two kinetic temperature components in the CMZ. Only the warm kinetic temperature regime is found in the "halo" positions, and in the Disk 2 position, which corresponds to Sgr B2.
3. The kinetic temperatures are high, not only in the typical GC clouds, but also in the high latitude and high velocity clouds observed in this paper. Therefore, the heating mechanism of the molecular clouds are likely to be a general characteristic of the molecular gas in the disk and halo of the GC.
4. Shocks would be a compelling heating mechanism of the molecular clouds in the GC region. This is supported by

the high gas kinetic temperature and by the increased SiO abundance in the location where shock are expected. Due to the fragile nature of the HNCO (enhanced by shock but easily photodissociate by UV radiation and strong shocks), this molecule would be used to reveal the characteristic of the shock. Other heating mechanisms previously proposed for the GC can however not been ruled out.

5. The high kinetic temperature in the X1 orbits and in the foot point of the GMLs seems to support to the large scale dynamics induced by the bar potential and the GMLs scenario as origins for the shocks.

Acknowledgements. D.R. and M.A.A-B. were supported by Radionet during the observations. D.R. was supported by DGI grant AYA 2008-06181-C02-02. J.M-P. and S.M. have been partially supported by the Spanish MICINN under grant numbers ESP2007-65812-C02-01 and AYA2010-21697-C05-01. L.B. acknowledges support from CONICYT projects FONDAP 15010003 and Basal PFB-06.

References

Bally, J., Aguirre, J., Battersby, C., et al. 2010, ApJ, 721, 137
Bally, J., Stark, A. A., Wilson, R. W., & Henkel, C. 1987, ApJS, 65, 13
Binney, J., Gerhard, O. E., Stark, A. A., Bally, J., & Uchida, K. I. 1991, MNRAS, 252, 210
Bitran, M., Alvarez, H., Bronfman, L., May, J., & Thaddeus, P. 1997, A&AS, 125, 99
Black, J. H. 1987, in ASSL Vol. 134: Interstellar Processes, ed. D. J. Hollenbach & H. A. Thronson, Jr., 731–744
Brunthaler, A., Reid, M. J., Menten, K. M., et al. 2011, ArXiv e-prints
Cheung, A. C., Rank, D. M., Townes, C. H., Knowles, S. H., & Sullivan, III, W. T. 1969, ApJ, 157, L13
Cox, P. & Laureijs, R. 1989, in IAU Symp, Vol. 136, The Center of the Galaxy, ed. M. Morris, 121
Danby, G., Flower, D. R., Valiron, P., Schilke, P., & Walmsley, C. M. 1988, MNRAS, 235, 229
Dobbs, C. L., Burkert, A., & Pringle, J. E. 2011, MNRAS, 528
Ferrière, K., Gillard, W., & Jean, P. 2007, A&A, 467, 611
Fleck, Jr., R. C. 1981, ApJ, 246, L151
Fukui, Y., Yamamoto, H., Fujishita, M., et al. 2006, Sci., 314, 106
Genzel, R. 1992, in Saas-Fee Advanced Course 21: The Galactic Interstellar Medium, ed. W. B. Burton, B. G. Elmegreen, & R. Genzel, 275–391
Goldsmith, P. F. 2001, ApJ, 557, 736
Goldsmith, P. F. & Langer, W. D. 1978, ApJ, 222, 881
Goldsmith, P. F. & Langer, W. D. 1999, ApJ, 517, 209
Güsten, R., Walmsley, C. M., & Pauls, T. 1981, A&A, 103, 197
Güsten, R., Walmsley, C. M., Ungerechts, H., & Churchwell, E. 1985, A&A, 142, 381
Ho, P. T. P., Martin, R. N., & Ruf, K. 1982, A&A, 113, 155
Ho, P. T. P. & Townes, C. H. 1983, ARA&A, 21, 239
Hollenbach, D. 1988, Astrophysical Letters Communications, 26, 191
Hüttemeister, S., Dahmen, G., Mauersberger, R., et al. 1998, A&A, 334, 646
Hüttemeister, S., Wilson, T. L., Bania, T. M., & Martin-Pintado, J. 1993a, A&A, 280, 255
Hüttemeister, S., Wilson, T. L., Henkel, C., & Mauersberger, R. 1993b, A&A, 276, 445
Jackson, J. M., Armstrong, J. T., & Barrett, A. H. 1984, ApJ, 280, 608
Juvela, M. & Ysard, N. 2011, ArXiv e-prints
Kudo, N., Torii, K., Machida, M., et al. 2011, PASJ, 63, 171
Larson, R. B. 1981, MNRAS, 194, 809
Le Bourlot, J., Pineau des Forêts, G., & Flower, D. R. 1999, MNRAS, 305, 802
Lebrón, M., Mangum, J. G., Mauersberger, R., et al. 2011, ArXiv e-prints
Lee, C. W. & Lee, H. M. 2003, Journal of Korean Astronomical Society, 36, 271
Martin, R. N., Ruf, K., & Ho, P. T. P. 1982, Nature, 296, 632
Martín, S., Requena-Torres, M. A., Martín-Pintado, J., & Mauersberger, R. 2008, ApJ, 678, 245
Martín-Pintado, J., Bachiller, R., & Fuente, A. 1992, A&A, 254, 315
Martín-Pintado, J., de Vicente, P., Fuente, A., & Planesas, P. 1997, ApJ, 482, L45
Martín-Pintado, J., de Vicente, P., Rodríguez-Fernández, N. J., Fuente, A., & Planesas, P. 2000, A&A, 356, L5
Mauersberger, R. & Henkel, C. 1989, A&A, 223, 79
Mauersberger, R., Henkel, C., Weiß, A., Peck, A. B., & Hagiwara, Y. 2003, A&A, 403, 561
Mauersberger, R., Henkel, C., Wilson, T. L., & Harju, J. 1989, A&A, 226, L5
Mauersberger, R., Henkel, C., Wilson, T. L., & Walmsley, C. M. 1986, A&A, 162, 199
Morris, M., Polish, N., Zuckerman, B., & Kaifu, N. 1983, AJ, 88, 1228
Morris, M. & Serabyn, E. 1996, ARA&A, 34, 645
Nagayama, T., Omodaka, T., Handa, T., et al. 2007, PASJ, 59, 869
Odenwald, S. F. & Fazio, G. G. 1984, ApJ, 283, 601
Pickett, H. M., Poynter, R. L., Cohen, E. A., et al. 1998, J. Quant. Spec. Radiat. Transf., 60, 883
Press, W. H., Teukolsky, S. A., Vetterling, W. T., & Flannery, B. P. 1992, Numerical recipes in C. The art of scientific computing, ed. Press, W. H., Teukolsky, S. A., Vetterling, W. T., & Flannery, B. P.
Riquelme, D., Amo-Baladrón, M. A., Martín-Pintado, J., et al. 2010a, A&A, 523, A51
Riquelme, D., Bronfman, L., Mauersberger, R., May, J., & Wilson, T. L. 2010b, A&A, 523, A45
Rodríguez-Fernández, N. 2002, PhD thesis, Universidad Complutense de Madrid, (2002)
Rodríguez-Fernández, N. J., Martín-Pintado, J., de Vicente, P., & Fuente, A. 2002, Ap&SS, 281, 331
Rodríguez-Fernández, N. J., Martín-Pintado, J., Fuente, A., et al. 2001, A&A, 365, 174
Sawada, T., Hasegawa, T., Handa, T., et al. 2001, ApJS, 136, 189
Scalo, J. M. 1977, ApJ, 213, 705
Takano, S., Nakai, N., & Kawaguchi, K. 2002, PASJ, 54, 195
Tanaka, K., Kamegai, K., Nagai, M., & Oka, T. 2007, PASJ, 59, 323
Torii, K., Kudo, N., Fujishita, M., et al. 2010a, PASJ, 62, 675
Torii, K., Kudo, N., Fujishita, M., et al. 2010b, PASJ, 62, 1307
Troland, T. H. & Heiles, C. 1986, ApJ, 301, 339
Umemoto, T., Mikami, H., Yamamoto, S., & Hirano, N. 1999, ApJ, 525, L105
van der Tak, F. F. S., Black, J. H., Schöier, F. L., Jansen, D. J., & van Dishoeck, E. F. 2007, A&A, 468, 627
Walmsley, C. M. & Ungerechts, H. 1983, A&A, 122, 164
Watson, M. G., Willingale, R., Hertz, P., & Grindlay, J. E. 1981, ApJ, 250, 142
Wilson, T. L. & Matteucci, F. 1992, A&A Rev., 4, 1
Wilson, T. L. & Rood, R. 1994, ARA&A, 32, 191
Wilson, T. L., Ruf, K., Walmsley, C. M., et al. 1982, A&A, 115, 185
Zinchenko, I., Henkel, C., & Mao, R. Q. 2000, A&A, 361, 1079

Table 8. Estimation of heating and cooling rates for each source

Source	T_{kin} [K]	$n(H_2)$ [$\times 10^4 cm^{-3}$]	$\Lambda^{a,c}_{total}$	$\Lambda^{b,c}_{H_2}$	Λ^{c}_{gd}	Γ^{c}_{turb}
Halo1-1	115	0.84	5.5	0.78	0.013	12
Halo1-2	90	6.94	18	4.36	0.58	42
Halo1-3	135	13.5	57	31.4	4.2	81
Halo2-1	113	1.26	5.2	0.015	0.028	19
Halo2-2	113	0.97	5.2	0.82	0.016	10
Halo3-1	113	1.50	5.2	1.3	0.039	39
Halo3-2	113	3.55	5.2	3.1	0.22	112
Halo4	95	2.75	3.3	1.4	0.10	26
Halo5	95	7.47	21	3.9	0.74	32
Disk-X1-1	38	13.0	1.5		0.081	531
	300	3.55	73	261	0.79	145
Disk-X2-1	38	5.62	1.5		0.015	146
	100	2.70	3.8	1.2	0.11	70
Disk-X1-2	52	13.3	3.6		0.51	48
	215	5.62	221	112	1.3	20
Disk-X2-2	28	14.1	0.60		0.57	99
	95	6.20	21	3.3	0.51	43
Disk1-1	23	1.12	0.071		0.005	3.3
	154	0.16	1.5	0.51	0.001	0.47
Disk1-2	38	4.57	0.28		0.010	20
	82	2.51	2.2		0.064	11
Disk2-1	68	4.97	1.3		0.17	156
	200	2.47	25	34	0.23	78
Disk2-2	145	2.51	10	8.1	0.16	20
Disk2-3	50	15.8	3.2		0.60	81
	80	11.6	13		1.3	59

[a] from Goldsmith & Langer (1978).

[b] using program provided by Le Bourlot et al. (1999).

[c] [$\times 10^{-21}$erg s^{-1}cm^{-3}]

Table 9. Column density derived for NH3 (3,3) and NH3 (6,6) using RADEX

Source	n(H2)	T(kin)	N(ortho-NH3)
Halo1-1	0.84×10^4	> 300	1×10^{14}
Halo1-2	6.94×10^4	> 300	1.26×10^{14}
Halo1-3	13.5×10^4	> 300	0.45×10^{14}
Halo4	2.75×10^4	> 170	0.95×10^{14}
DiskX1-1	3.55×10^4	> 300	1.58×10^{14}
DiskX2-1	2.70×10^4	> 200	2.51×10^{14}
DiskX1-2	5.62×10^4	> 280	1.41×10^{14}
DiskX2-2	6.20×10^4	265	0.76×10^{14}
Disk1-1	0.16×10^4	> 300	0.32×10^{14}
Disk1-2	2.51×10^4	> 300	0.32×10^{14}
Disk2-1	2.47×10^4	200	8.32×10^{14}
Disk2-2	2.51×10^4	> 300	12.6×10^{14}
Disk2-3	11.6×10^4	130	4.79×10^{14}

Table 10. Ortho-to-para NH_3 ratio

Source	Cloud number	$N(o-NH_3)/N(p-NH_3)$
Halo1	1	1.44 ± 0.30
	2	1.17 ± 0.13
	3	1.60 ± 0.49
Halo4	1	0.98 ± 0.16
DiskX1-1	1	0.96 ± 0.12
DiskX2-1	1	0.84 ± 0.06
DiskX1-2	1	1.12 ± 0.13
DiskX2-2	1	0.70 ± 0.14
Disk1	1	0.66 ± 0.35
	2	0.75 ± 0.20
Disk2	1	0.76 ± 0.03
	2	1.31 ± 0.02
	3	0.58 ± 0.10

Table 11. Results from Gaussian fit and optical depth from NH_3 method.

Source	Cloud number[f]	Transition (j,k)	v_{LSR} [km s^{-1}]	T_{MB} [K]	$\Delta v_{1/2}$ [km s^{-1}]	Integrated intensity[e] [K km s^{-1}]	rms [mk]	τ
Halo 1	1	(1,1)	85.6 ± 0.4	0.10	29.0 ± 0.4	3.19 ± 0.04	52	0.10 ± 0.30
	2	(1,1)	115.8 ± 0.4	0.32	23.6 ± 0.4	7.91 ± 0.04	52	0.10 ± 0.09
	3	(1,1)	139.3 ± 0.4	0.09	18.8 ± 0.4	1.77 ± 0.04	52	0.10 ± 0.54
	1	(2,2)	83.1 ± 0.4	0.07	37.8 ± 0.4	2.94 ± 0.04	51	0.10 ± 0.76
	2	(2,2)	116.7 ± 0.4	0.35	18.4 ± 0.4	6.77 ± 0.04	51	0.21 ± 0.01
	3	(2,2)	147.1 ± 0.4	0.06	35.5 ± 0.4	2.29 ± 0.04	51	4.9 ± 2.0[d]
	1	(3,3)	87.7 ± 0.4	0.22	38.8 ± 0.4	9.23 ± 0.07	51	0.10 ± 0.03
	2	(3,3)	117.2 ± 0.4	0.85	16.8 ± 0.4	15.16 ± 0.07	51	0.10 ± 0.03
	3	(3,3)	138.6 ± 0.4	0.19	20.8 ± 0.4	4.29 ± 0.07	51	0.16 ± 0.01
	1	(4,4)	82.0 ± 0.4	0.06	32.9 ± 0.4	2.03 ± 0.02	50	
	2	(4,4)	118.7 ± 0.4	0.23	21.5 ± 0.4	5.34 ± 0.02	50	
	3	(4,4)	137.4 ± 0.4	0.05	16.6 ± 0.4	0.91 ± 0.02	50	
	1	(5,5)	87.7[a]	0.12[b]	38.8[a]	0.467[b]	41	
	2	(5,5)	115.7 ± 0.4	0.15	12.4 ± 0.9	1.92 ± 0.13	41	
	3	(5,5)	131.0 ± 0.9	0.06	11.9 ± 3.2	0.74 ± 0.09	41	
	1	(6,6)	87.7[a]	0.13[b]	38.8[a]	0.613[b]	41	
	2	(6,6)	120.5 ± 0.8	0.30	17.3 ± 2.1	5.48 ± 0.61	41	
	3	(6,6)	138.5 ± 1.9	0.12	14.4 ± 2.9	1.78 ± 0.54	41	
Halo 4	1	(1,1)	196.4 ± 0.9	0.22	30.2 ± 2.1	6.99 ± 0.42	83	0.10 ± 0.21
	1	(2,2)	194.7 ± 1.1	0.19	34.1 ± 2.9	6.74 ± 0.47	84	1.72 ± 0.53
	1	(3,3)	195.5 ± 0.5	0.37	20.3 ± 1.2	7.93 ± 0.38	80	0.10 ± 0.21
	1	(4,4)	194.5 ± 1.1	0.09	16.0 ± 2.9	1.44 ± 0.20	49	
	1	(5,5)	195.5[a]	0.15[b]	20.3[a]	0.417	50	
	1	(6,6)	199.4 ± 1.7	0.09	24.3 ± 4.0	2.26 ± 0.32	51	
Disk X1-1	1	(1,1)	183.1 ± 1.0	0.20	48.1 ± 2.2	10.43 ± 0.45	74	0.86 ± 0.27
	1	(2,2)	182.9 ± 1.3	0.15	32.1 ± 2.6	5.10 ± 0.38	71	0.10 ± 0.11
	1	(3,3)	184.1 ± 0.4	0.43	34.8 ± 1.0	15.88 ± 0.39	71	0.10 ± 0.02
	1	(4,4)	188.1 ± 1.1	0.14	24.7 ± 2.2	3.66 ± 0.33	74	
	1	(5,5)	187.1 ± 1.7	0.09	36.4 ± 4.1	3.56 ± 0.34	63	
	1	(6,6)	188.3 ± 1.1	0.17	35.0 ± 2.6	6.25 ± 0.41	59	
Disk X2-1	1	(1,1)	96.4 ± 0.4	0.48	40.8 ± 1.0	20.91 ± 0.42	74	0.10 ± 0.74
	1	(2,2)	96.5 ± 0.5	0.32	30.7 ± 1.4	10.36 ± 0.38	71	0.10 ± 0.02
	1	(3,3)	98.1 ± 0.2	0.74	32.9 ± 0.6	25.95 ± 0.39	71	0.10 ± 0.01
	1	(4,4)	96.0 ± 0.6	0.19	15.7 ± 1.7	3.16 ± 0.28	74	
	1	(5,5)	98.6 ± 2.2	0.09	41.5 ± 4.6	3.91 ± 0.37	63	
	1	(6,6)	103.4 ± 1.1	0.17	30.8 ± 2.6	5.70 ± 0.40	59	
Disk X1-2	1	(1,1)	69.1 ± 0.5	0.32	22.7 ± 1.3	7.77 ± 0.37	78	0.10 ± 0.03
	1	(2,2)	69.4 ± 0.4	0.32	14.5 ± 1.3	4.99 ± 0.33	80	0.10 ± 0.06
	1	(3,3)	69.1 ± 0.2	0.87	17.3 ± 0.6	16.10 ± 0.42	91	0.10 ± 0.04
	1	(4,4)	69.9 ± 0.4	0.25	12.2 ± 1.4	3.23 ± 0.26	71	
	1	(5,5)	67.0 ± 0.7	0.13	13.1 ± 1.4	1.84 ± 0.20	62	
	1	(6,6)	74.1 ± 0.6	0.24	17.8 ± 1.7	4.58 ± 0.33	61	
Disk X2-2	1	(1,1)	−50.2 ± 0.8	0.25	37.9 ± 1.9	10.22 ± 0.46	78	1.00 ± 0.29
	1	(2,2)	−53.0 ± 1.2	0.15	22.1 ± 3.1	3.51 ± 0.39	80	0.10 ± 0.18
	1	(3,3)	−47.1 ± 0.6	0.35	22.9 ± 1.4	8.41 ± 0.45	91	0.10 ± 0.13
	1	(4,4)	−54.1 ± 0.6	0.14	6.7 ± 1.5	0.99 ± 0.18	71	
	1	(5,5)	−47.1[a]	0.19[b]	22.9[a]	0.55[b]	62	
	1	(6,6)	−49.3 ± 2.8	0.07	21.0 ± 4.9	1.31 ± 0.31	61	
Disk 1	1	(1,1)	64.5 ± 0.4	0.08	20.0 ± 0.4	1.73 ± 0.03	61	0.10 ± 1.15
	2	(1,1)	78.2 ± 0.4	0.16	18.4 ± 0.4	3.05 ± 0.03	61	0.10 ± 0.24
	1	(2,2)	59.3 ± 0.8	0.08	5.1 ± 1.6	0.45 ± 0.15	63	0.10 ± 1.25
	2	(2,2)	73.4 ± 0.5	0.16	8.5 ± 1.5	1.47 ± 0.20	63	0.10 ± 0.16
	1	(3,3)	56.5 ± 1.0	0.11	11.7 ± 3.1	1.36 ± 0.27	66	0.10 ± 0.46
	2	(3,3)	72.4 ± 0.6	0.21	14.9 ± 0.5	3.41 ± 0.03	66	0.10 ± 0.22
	1	(4,4)	56[a]	0.16[b]	11.7[a]	0.33[b]	53	
	2	(4,4)	72[a]	0.16[b]	15.0[a]	0.38[b]	53	
	1	(5,5)	56[a]	0.14[b]	11.7[a]	0.29[b]	47	
	2	(5,5)	72[a]	0.14[b]	15.0[a]	0.33[b]	47	
	1	(6,6)	56[a]	0.15[b]	11.7[a]	0.39[b]	50	
	2	(6,6)	72[a]	0.15[b]	15.0[a]	0.44[b]	50	
Disk 2	1	(1,1)	46.1 ± 0.1	2.2	24.1 ± 0.3	56.34 ± 0.65	94	0.10 ± 0.10[c]
	2	(1,1)	73.9 ± 0.1	3.0	18.4 ± 0.2	58.21 ± 0.40	94	3.00 ± 0.10[c]
	3	(1,1)	90.2 ± 0.1	3.6	16.7 ± 0.1	64.73 ± 0.33	94	0.10 ± 0.10[c]
	1	(2,2)	44.9 ± 0.1	1.8	22.6 ± 0.4	42.52 ± 0.58	106	0.10 ± 0.01
	2	(2,2)	74.3 ± 0.2	3.2	17.2 ± 0.3	57.55 ± 1.43	106	0.15 ± 0.01

Table 11. continued.

Source	Cloud number[f]	Transition (j,k)	v_{LSR} [km s^{-1}]	T_{MB} [K]	$\Delta v_{1/2}$ [km s^{-1}]	Integrated intensity[e] [K km s^{-1}]	rms [mk]	τ
	3	(2,2)	94.1 ± 0.3	2.1	18.6 ± 0.5	41.28 ± 1.31	106	0.10 ± 0.01
	1	(3,3)	48.8 ± 0.1	3.4	28.7 ± 0.3	103.6 ± 0.8	98	0.10 ± 0.10[c]
	2	(3,3)	74.5 ± 0.1	14	14.4 ± 0.1	216.2 ± 0.7	98	0.10 ± 0.10[c]
	3	(3,3)	95.8 ± 0.1	2.7	18.6 ± 0.2	52.42 ± 0.51	98	0.10 ± 0.10[c]
	1	(4,4)	50.1 ± 0.6	0.8	32.5 ± 1.3	26.23 ± 0.97	74	
	2	(4,4)	74.0 ± 0.1	3.1	15.0 ± 0.2	49.35 ± 1.03	74	
	3	(4,4)	96.2 ± 0.6	0.48	20.0 ± 1.2	10.24 ± 0.57	74	
	1	(5,5)	53.5 ± 0.1	0.40	35.2 ± 0.5	14.90 ± 0.20	57	
	2	(5,5)	73.0 ± 0.1	2.0	15.9 ± 0.1	33.44 ± 0.28	57	
	3	(5,5)	97.3 ± 0.6	0.18	16.3 ± 1.4	3.10 ± 0.24	57	
	1	(6,6)	56.5 ± 0.3	0.69	15.9 ± 0.8	11.80 ± 0.53	51	
	2	(6,6)	75.7 ± 0.1	2.4	15.2 ± 0.2	38.76 ± 0.48	51	
	3	(6,6)	96[a]	0.15[b]	18.6[a]	0.51[b]	51	

[a] no detected. Value taken as reference from the (3,3) transition.
[b] upper limits.
[c] method NH_3 did not converge properly.
[d] the fit is not good, due to the no convergence of the method.
[e] $\int T_{MB} dv$.
[f] In each source, different velocity components define different clouds.

Table 12. Gaussian fits and column densities for SiO, $C^{34}S$, HNCO

Source	Species	Velocity Center LSR [km s^{-1}]	Δ_v [km s^{-1}]	T_A [K]	$\int T_A dv^c$ [K km s^{-1}]	rms [mK]	N [cm^{-2}]
Halo 1	SiO (2-1)	88.0 ± 0.1	33.5 ± 1.0	0.096	3.41 ± 0.01	4.5	$5.73 \pm 0.01 \times 10^{12}$
		117.8 ± 0.1	17.9 ± 0.1	0.993	18.96 ± 0.08	4.5	$31.82 \pm 0.14 \times 10^{12}$
		133.5 ± 0.3	20.7 ± 0.7	0.174	3.83 ± 0.02	4.5	$6.43 \pm 0.03 \times 10^{12}$
	^{29}SiO(2-1)	119.7 ± 0.6[a]	17.2 ± 1.3	0.085	1.55 ± 0.11	6.3	$2.66 \pm 0.19 \times 10^{12}$
	^{30}SiO (2-1)	120.0 ± 0.8[a]	17.4 ± 1.9	0.063	1.16 ± 0.11	5.9	$2.04 \pm 0.19 \times 10^{12}$
	CS (2-1)	83.8 ± 6.1	25.1 ± 6.1	0.218	5.8 ± 1.8	6.6	
		117.4 ± 6.1	19.2 ± 6.1	1.721	35.1 ± 1.8	6.6	
		136.9 ± 6.1	18.7 ± 6.1	0.168	3.3 ± 1.8	6.6	
	CS (3-2)	83.1 ± 4.1	23.3 ± 4.1	0.075	1.86 ± 0.96	9.6	
		116.5 ± 4.1	15.4 ± 4.1	1.517	24.80 ± 0.96	9.6	
		130.7 ± 4.1	11.2 ± 4.1	0.279	3.34 ± 0.96	9.6	
	$C^{34}S$ (2-1)	–	–	–	–	–	–
		117. ± 0.3	18.8 ± 0.8	0.138	2.75 ± 0.10	5.6	$9.51 \pm 0.34 \times 10^{12}$
		–	–	–	–	–	
	HNCO	83.2 ± 2.0	15.2 ± 4.0	0.023	0.37 ± 0.09	5.2	$10.8 \pm 2.6 \times 10^{12}$
		117.2 ± 0.4	21.7 ± 1.1	0.119	2.75 ± 0.11	5.2	$81.0 \pm 3.4 \times 10^{12}$
		-	-	-	-	-	
	$C^{18}O$(1-0)	89.0 ± 0.9	26.8 ± 1.9	0.057	1.62 ± 0.10	4.7	$1.11 \pm 0.07 \times 10^{15}$
		115.9 ± 0.2	18.8 ± 0.6	0.108	2.17 ± 0.04	4.7	$1.49 \pm 0.03 \times 10^{15}$
		140.7 ± 1.4	16.6 ± 3.8	0.022	0.38 ± 0.07	4.7	$0.26 \pm 0.05 \times 10^{15}$
	^{13}CO(1-0)	85.0 ± 0.4	37.6 ± 1.4	0.344	13.77 ± 0.4	12.0	$0.94 \pm 0.03 \times 10^{15}$
		114.2 ± 0.2	13.3 ± 0.4	0.628	8.92 ± 0.5	12.0	$0.61 \pm 0.03 \times 10^{15}$
		133.7 ± 1.4	27.2 ± 3.1	0.167	4.84 ± 0.6	12.0	$0.33 \pm 0.04 \times 10^{15}$
		169.5 ± 2.3	23.6 ± 6.0	0.049	1.23 ± 0.26	12.0	$0.08 \pm 0.02 \times 10^{15}$
Halo 2	SiO (2-1)	−84.7 ± 1.1	25.5 ± 0.8	0.046	1.25 ± 0.01	4.0	$2.10 \pm 0.01 \times 10^{12}$
		−58.5 ± 1.0	22.6 ± 2.8	0.045	1.07 ± 0.11	4.0	$1.80 \pm 0.19 \times 10^{12}$
	^{29}SiO(2-1)	−85[b]	25[b]	–	< 0.26	6.8	$< 0.453 \times 10^{12}$
		−58[b]	23[b]	–	< 0.26	6.8	$< 0.453 \times 10^{12}$
	^{30}SiO (2-1)	−58.6 ± 2.1[a]	18.9 ± 4.8	0.020	0.40 ± 0.07	3.4	$0.71 \pm 0.13 \times 10^{12}$
	CS (2-1)	−80.2 ± 6.1	25.8 ± 6.1	0.188	5.15 ± 0.30	6.2	
		−51.9 ± 6.1	22.9 ± 6.1	0.192	4.69 ± 0.30	6.2	
	CS (3-2)	−77.6 ± 1.2	22.2 ± 2.7	0.091	2.16 ± 0.30	6.5	
		−51.8 ± 1.5	22.3 ± 2.5	0.078	1.85 ± 0.25	6.5	
	$C^{34}S$ (2-1)	−81.7 ± 13.5	47.8 ± 23.2	0.006	0.47 ± 0.24	3.8	$1.63 \pm 0.84 \times 10^{12}$
		−35.0 ± 14.9	35.6 ± 21.9	0.009	0.24 ± 0.25	3.8	$0.83 \pm 0.85 \times 10^{12}$
	HNCO	−70.4 ± 3.9[a]	30.6 ± 8.2	0.032	1.05 ± 0.26	5.1	$31.0 \pm 7.7 \times 10^{12}$
Halo 3	SiO (2-1)	−62.9 ± 1.2	35.9 ± 3.4	0.194	7.43 ± 0.52	8.4	$12.5 \pm 0.9 \times 10^{12}$
	^{29}SiO(2-1)	−56.6 ± 3.7	23.1 ± 8.6	0.015	0.37 ± 0.11	4.8	$0.64 \pm 0.18 \times 10^{12}$
	^{30}SiO (2-1)	−51.0 ± 8.2	34.3 ± 15.5	0.020	0.73 ± 0.31	3.3	$1.29 \pm 0.55 \times 10^{12}$
	CS (2-1)	−64.7 ± 0.3	31.4 ± 0.8	0.670	22.42 ± 0.46	8.2	
		−13.9 ± 1.1	33.0 ± 2.6	0.186	6.52 ± 0.44	8.2	
	CS (3-2)	−63.6 ± 0.3	18.6 ± 1.1	0.513	10.13 ± 0.57	14.4	
		−21.6 ± 4.5	42.7 ± 9.5	0.077	3.50 ± 0.60	14.4	
	$C^{34}S$ (2-1)	−63.1 ± 1.2	28.8 ± 3.6	0.051	1.58 ± 0.15	6.5	$5.46 \pm 0.52 \times 10^{12}$
		−12.6 ± 2.4	21.4 ± 4.8	0.023	0.52 ± 0.11	6.5	$1.81 \pm 0.39 \times 10^{12}$
	HNCO	−67.3 ± 0.8	35.3 ± 2.0	0.083	3.10 ± 0.15	6.0	$91.5 \pm 4.3 \times 10^{12}$
		−10.6 ± 0.9	21.7 ± 2.2	0.055	1.28 ± 0.11	6.0	$37.7 \pm 3.3 \times 10^{12}$
Halo 4	SiO (2-1)	196.1 ± 0.4	20.6 ± 0.9	0.123	2.69 ± 0.11	3.4	$4.51 \pm 0.19 \times 10^{12}$
	^{29}SiO(2-1)	196[b]	21[b]	–	< 0.14	3.9	$< 0.242 \times 10^{12}$
	^{30}SiO (2-1)	196[b]	21[b]	–	< 0.14	3.9	$< 0.250 \times 10^{12}$
	CS (2-1)	197.1 ± 0.3	21.9 ± 0.6	0.380	8.88 ± 0.21	6.5	
	CS (3-2)	196.7 ± 0.2	22.6 ± 0.4	0.183	4.40 ± 0.07	5.3	
	$C^{34}S$ (2-1)	195.2 ± 2.2	24.8 ± 4.8	0.022	0.57 ± 0.10	4.9	$1.96 \pm 0.34 \times 10^{12}$
	HNCO	196.9 ± 0.2	19.0 ± 0.5	0.178	3.59 ± 0.08	4.7	$106 \pm 2 \times 10^{12}$
	$C^{18}O$	206.1 ± 1.2	7.6 ± 4.0	0.081	0.66 ± 0.18	10.0	$5.2 \pm 2.7 \times 10^{15}$
	^{13}CO	202.3 ± 0.6	25.1 ± 1.4	0.705	18.8 ± 0.9	25.0	$1.28 \pm 0.06 \times 10^{16}$
Halo 5	SiO (2-1)	−62.9 ± 0.1	16.3 ± 0.3	0.254	4.39 ± 0.07	4.6	$7.37 \pm 0.13 \times 10^{12}$
	^{29}SiO(2-1)	−64.8 ± 0.8	11.9 ± 1.4	0.032	0.41 ± 0.05	3.3	$0.70 \pm 0.09 \times 10^{12}$
	^{30}SiO (2-1)	−61.4 ± 2.4	22.1 ± 7.5	0.917	0.40 ± 0.10		$0.71 \pm 0.17 \times 10^{12}$
	CS (2-1)	−62.7 ± 0.1	16.7 ± 0.1	0.646	11.52 ± 0.04	2.9	
	CS (3-2)	−62.7 ± 0.2	14.4 ± 0.4	0.528	8.12 ± 0.18	6.4	
	$C^{34}S$ (2-1)	−62.3 ± 0.3	13.3 ± 0.6	0.074	1.05 ± 0.04	3.0	$3.62 \pm 0.14 \times 10^{12}$
	HNCO	−64.2 ± 0.2	14.6 ± 0.4	0.164	2.54 ± 0.07	4.3	$75.0 \pm 1.9 \times 10^{12}$
Disk X1-1	SiO (2-1)	178.0 ± 0.3	41.3 ± 0.7	0.390	17.1 ± 0.2	9.1	$28.75 \pm 0.39 \times 10^{12}$

Table 12. continued.

Source	Species	Velocity Center LSR [km s^{-1}]	Δ_v [km s^{-1}]	T_A [K]	$\int T_A dv^c$ [K km s^{-1}]	rms [mK]	N [cm^{-2}]
	^{29}SiO(2-1)	179.4 ± 2.5	43.4 ± 5.0	0.031	1.43 ± 0.16	5.4	$2.46 \pm 0.27 \times 10^{12}$
	^{30}SiO (2-1)	188.0 ± 1.0	24.6 ± 2.6	0.039	1.00 ± 0.08	3.3	$1.77 \pm 0.13 \times 10^{12}$
	CS (2-1)	176.2 ± 0.3	36.4 ± 0.7	0.718	27.81 ± 0.41	6.3	
	CS (3-2)	174.3 ± 0.1	31.1 ± 0.3	0.591	19.60 ± 0.16	7.7	
	C^{34}S (2-1)	177.5 ± 1.3	35.1 ± 2.8	0.040	1.51 ± 0.11	5.1	$5.21 \pm 0.38 \times 10^{12}$
	HNCO	187.6 ± 0.6	16.4 ± 1.8	0.170	2.96 ± 0.24	9.3	$87.4 \pm 7.2 \times 10^{12}$
	C^{18}O	177.9 ± 6.4	49.5 ± 13.0	0.040	2.12 ± 0.46	13.3	$1.45 \pm 0.31 \times 10^{15}$
	^{13}CO	175.6 ± 2.6	56.4 ± 6.1	0.603	36.2 ± 3.2	21.2	$2.47 \pm 0.22 \times 10^{16}$
Disk X2-1	SiO (2-1)	99.7 ± 0.3	33.2 ± 0.8	0.282	9.96 ± 0.21	9.1	$16.72 \pm 0.36 \times 10^{12}$
	^{29}SiO(2-1)	95.2 ± 3.3	57.7 ± 19.1	0.021	1.26 ± 0.25	5.4	$2.17 \pm 0.43 \times 10^{12}$
	^{30}SiO (2-1)	94.1 ± 3.3	41.4 ± 9.8	0.013	0.56 ± 0.10	3.3	$0.99 \pm 0.17 \times 10^{12}$
	CS (2-1)	98.1 ± 0.2	30.7 ± 0.4	0.953	31.10 ± 0.37	6.3	
	CS (3-2)	97.1 ± 0.1	26.0 ± 0.3	0.580	16.08 ± 0.16	7.7	
	C^{34}S (2-1)	99.7 ± 0.6	21.0 ± 1.8	0.064	1.43 ± 0.09	5.1	$4.94 \pm 0.33 \times 10^{12}$
	HNCO	96.3 ± 0.5	30.9 ± 1.0	0.293	9.61 ± 0.29	9.3	$283.5 \pm 8.6 \times 10^{12}$
	C^{18}O	94.5 ± 0.8	28.9 ± 1.9	0.194	5.96 ± 0.34	13.3	$4.10 \pm 0.24 \times 10^{15}$
	^{13}CO	95.3 ± 0.5	32.1 ± 1.3	2.056	70.3 ± 2.5	21.2	$4.80 \pm 0.17 \times 10^{16}$
Disk X1-2	SiO (2-1)	69.1 ± 0.1	17.4 ± 0.3	0.522	9.70 ± 0.12	5.7	$16.28 \pm 0.20 \times 10^{12}$
	^{29}SiO(2-1)	68.1 ± 2.4	18.0 ± 5.2	0.020	0.39 ± 0.10	5.5	$0.67 \pm 0.18 \times 10^{12}$
	^{30}SiO (2-1)	72.5 ± 3.3	44.5 ± 7.8	0.018	0.83 ± 0.13	4.7	$1.47 \pm 0.22 \times 10^{12}$
	CS (2-1)	70.0 ± 0.2	16.1 ± 0.5	1.349	23.05 ± 0.66	4.7	
	CS (3-2)	70.6 ± 0.2	12.9 ± 0.4	1.320	18.16 ± 0.45	7.3	
	C^{34}S (2-1)	71.1 ± 0.4	14.8 ± 1.0	0.106	1.67 ± 0.09	4.7	$5.77 \pm 0.32 \times 10^{12}$
	HNCO	68.7 ± 0.4	18.3 ± 0.8	0.151	2.94 ± 0.12	7.0	$86.7 \pm 3.4 \times 10^{12}$
	C^{18}O	68.3 ± 2.8	16.7 ± 5.6	0.058	1.04 ± 0.32	5.6	$0.71 \pm 0.22 \times 10^{15}$
	^{13}CO	68.0 ± 2.2	16.6 ± 5.4	0.567	10.0 ± 2.9	8.0	$0.68 \pm 0.20 \times 10^{16}$
Disk X2-2	SiO (2-1)	−43.5 ± 2.0	29.3 ± 4.5	0.037	1.15 ± 0.16	5.7	$1.92 \pm 0.26 \times 10^{12}$
	^{29}SiO(2-1)	−43^b	29^b	–	< 0.23	5.5	$< 0.402 \times 10^{12}$
	^{30}SiO (2-1)	−51.8 ± 2.8	28.0 ± 4.9	0.018	0.54 ± 0.10	4.7	$0.96 \pm 0.17 \times 10^{12}$
	CS (2-1)	−43.8 ± 0.3	19.6 ± 0.7	1.057	22.09 ± 0.71	4.7	
	CS (3-2)	−43.4 ± 0.4	21.6 ± 1.0	0.648	14.88 ± 0.57	7.3	
	C^{34}S (2-1)	−45.0 ± 0.5	21.0 ± 1.5	0.093	2.07 ± 0.11	4.7	$7.15 \pm 0.39 \times 10^{12}$
	HNCO	−47.1 ± 0.7	21.7 ± 1.7	0.087	2.01 ± 0.13	7.0	$59.2 \pm 3.9 \times 10^{12}$
	C^{18}O	−46.1 ± 0.5	18.2 ± 1.3	0.301	5.81 ± 0.35	5.6	$3.99 \pm 0.24 \times 10^{15}$
	^{13}CO	−44.0 ± 0.4	17.1 ± 1.1	3.312	60.2 ± 3.0	8.0	$4.11 \pm 0.20 \times 10^{16}$
Disk 1	SiO (2-1)	54.1 ± 0.6	11.5 ± 1.8	0.040	0.49 ± 0.07	3.2	$0.82 \pm 0.12 \times 10^{12}$
		73.6 ± 0.5	18.0 ± 1.4	0.062	1.18 ± 0.07	3.2	$1.98 \pm 0.12 \times 10^{12}$
	^{29}SiO(2-1)	54^b	12	–	< 0.06	2.2	$< 0.105 \times 10^{12}$
		74^b	18	–	< 0.07	2.2	$< 0.129 \times 10^{12}$
	^{30}SiO (2-1)	54^b	12	–	< 0.06	2.2	$< 0.106 \times 10^{12}$
		74^b	18	–	< 0.07	2.2	$< 0.130 \times 10^{12}$
	CS (2-1)	56.8 ± 0.3	14.5 ± 0.6	0.087	1.35 ± 0.05	2.2	
		74.9 ± 0.1	17.2 ± 0.2	0.327	5.99 ± 0.07	2.2	
	CS (3-2)	56.3 ± 0.3	9.8 ± 0.8	0.036	0.38 ± 0.03	2.1	
		74.8 ± 0.1	14.8 ± 0.2	0.177	2.78 ± 0.02	2.1	
	C^{34}S (2-1)	50.8 ± 4.5	12.8 ± 7.3	0.003	0.05 ± 0.03	1.9	$0.16 \pm 0.10 \times 10^{12}$
		73.8 ± 0.9	15.2 ± 2.2	0.016	0.26 ± 0.03	1.9	$0.09 \pm 0.11 \times 10^{12}$
	HNCO	55.3 ± 2.8	16.5 ± 6.3	0.024	0.43 ± 0.15	4.2	$12.6 \pm 4.5 \times 10^{12}$
		75.6 ± 0.7	15.7 ± 1.6	0.100	1.66 ± 0.16	4.2	$49.1 \pm 4.7 \times 10^{12}$
	C^{18}O	55.5 ± 0.8	11.5 ± 1.6	0.075	0.92 ± 0.12	9.3	$0.63 \pm 0.09 \times 10^{15}$
		78.6 ± 0.9	11.6 ± 2.3	0.067	0.83 ± 0.13	9.3	$0.57 \pm 0.09 \times 10^{15}$
	^{13}CO	57.3 ± 0.3	12.6 ± 0.8	0.649	9.89 ± 0.48	10.1	$0.59 \pm 0.03 \times 10^{16}$
		77.6 ± 0.3	14.4 ± 0.8	0.647	9.89 ± 0.48	10.1	$0.68 \pm 0.03 \times 10^{16}$
Disk 2	SiO (2-1)	52.3 ± 0.7	18.3 ± 1.8	0.519	10.12 ± 0.92	7.9	$17.0 \pm 1.5 \times 10^{12}$
		76.9 ± 0.3	19.0 ± 0.8	1.233	24.94 ± 0.91	7.9	$41.9 \pm 1.5 \times 10^{12}$
	^{29}SiO(2-1)	69.0 ± 1.0^a	26.2 ± 2.3	0.240	6.67 ± 0.48	5.0	$11.5 \pm 0.8 \times 10^{12}$
	^{30}SiO (2-1)	69.2 ± 1.8^a	26.2 ± 4.4	0.184	5.13 ± 0.73	5.4	$9.0 \pm 1.3 \times 10^{12}$
	CS (2-1)	14.2 ± 6.1	33.0 ± 6.1	0.461	16.2 ± 2.5	12.9	
		55.9 ± 6.1	21.2 ± 6.1	1.544	34.9 ± 2.5	12.9	
		79.0 ± 6.1	17.7 ± 6.1	1.922	36.1 ± 2.5	12.9	
	CS (3-2)	14.7 ± 5.0	26.9 ± 13.4	0.317	9.1 ± 3.5	14.8	
		52.7 ± 1.4	16.4 ± 3.5	1.110	19.3 ± 3.7	14.8	
		76.9 ± 0.9	17.5 ± 2.7	1.640	30.6 ± 3.8	14.8	
	C^{34}S (2-1)	-	-	-	-	-	

Table 12. continued.

Source	Species	Velocity Center LSR [km s^{-1}]	Δ_v [km s^{-1}]	T_A [K]	$\int T_A dv^c$ [K km s^{-1}]	rms [mK]	N [cm^{-2}]
		33.9 ± 2.6	37.5 ± 5.9	0.145	5.79 ± 0.82	2.9	$20.0 \pm 2.8 \times 10^{12}$
		71.6 ± 0.5	23.1 ± 1.2	0.533	13.12 ± 0.75	2.9	$45.4 \pm 2.6 \times 10^{12}$
	HNCO	-	-	-	-	-	
		67.1 ± 0.1	25.1 ± 0.2	8.868	236.8 ± 1.5	11.8	$6982 \pm 44 \times 10^{12}$
		-	-	-	-	-	
	$C^{18}O$	-	-	-	-	-	
		68.0 ± 0.8	23.4 ± 2.0	0.945	23.5 ± 1.6	14.1	$16.2 \pm 1.1 \times 10^{15}$
		-	-	-	-	-	
	^{13}CO	-	-	-	-	-	
		69.1 ± 0.6	28.5 ± 1.5	5.932	179.9 ± 7.6	22.2	$12.3 \pm 0.5 \times 10^{16}$
			-	-	-	-	

[a] only possible to fit one velocity components.
[b] not detected, value for reference taken by the main isotope.
[c] formal errors of a Gaussian fit. The calibration errors may be larger.

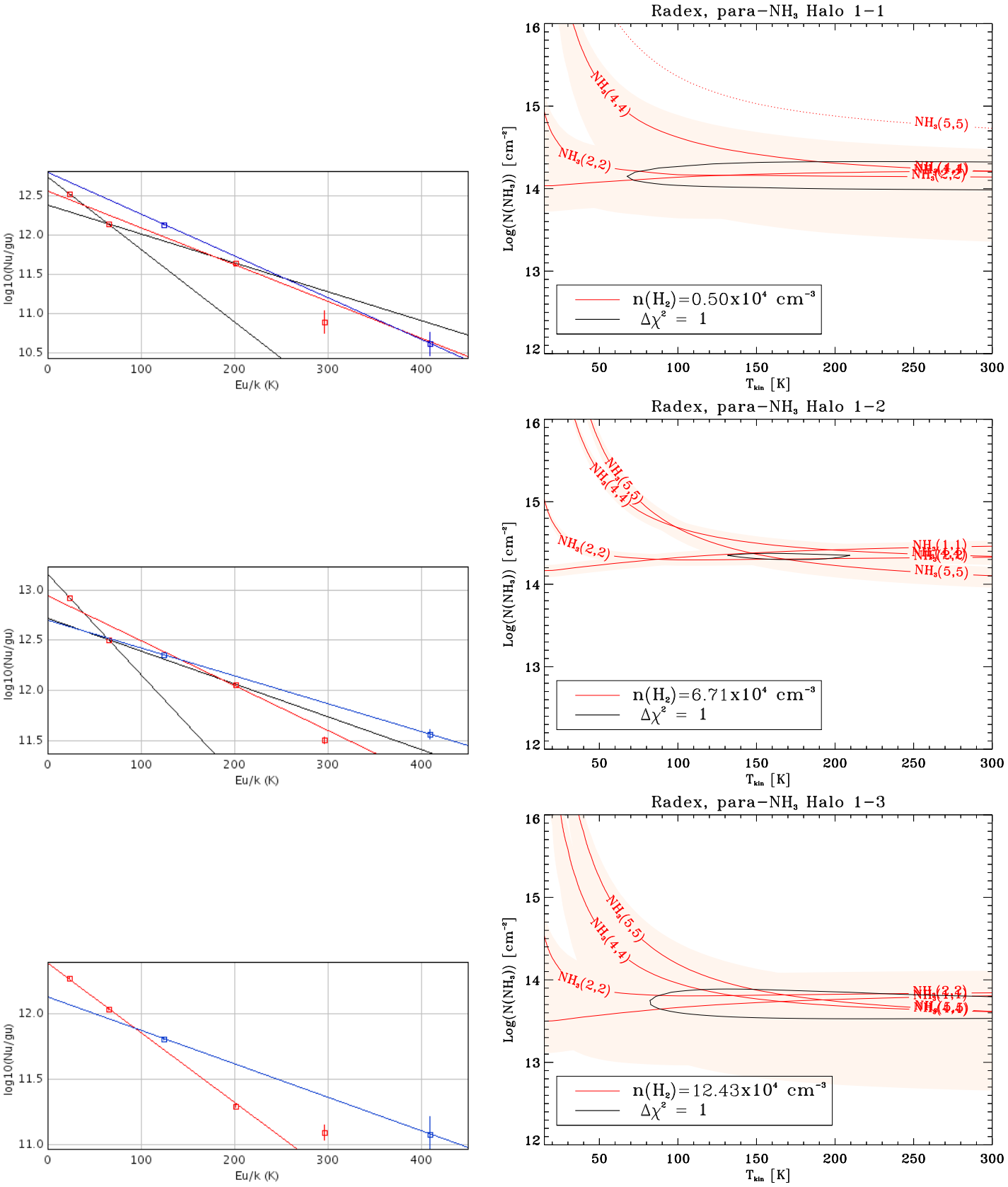

Fig. 4. Rotational (left) and LVG (right) diagrams of NH_3 for each velocity component of Halo 1. In the rotational diagrams, the blue fits correspond to the ortho-NH_3, the black line correspond to the para-NH_3 and when was possible a single fits for all the para-NH_3, was plotted in a red line. In the LVG plot, the blue lines correspond to the low temperature regimen; the red lines to the high temperature regimen; and the black line to the single temperature regimen. Top: 87.7km s^{-1} . Middle: 117.2km s^{-1}. Bottom: 138.6km s^{-1}.

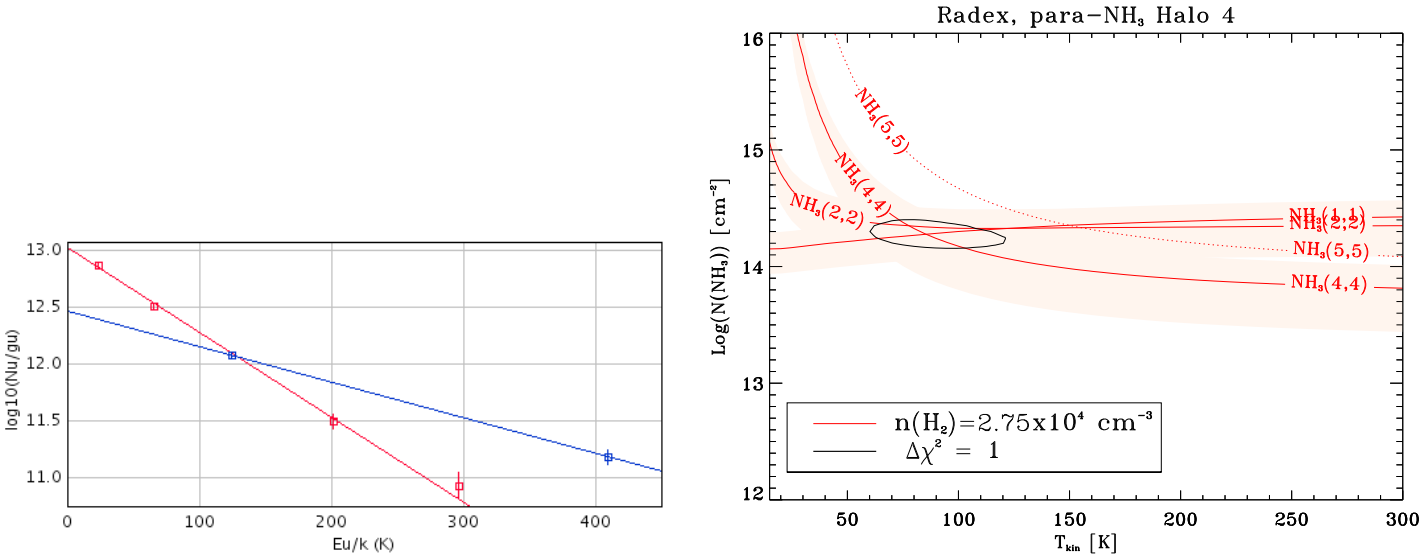

Fig. 5. Rotational (left) and LVG (right) diagrams of NH_3 for each velocity component of Halo 4.

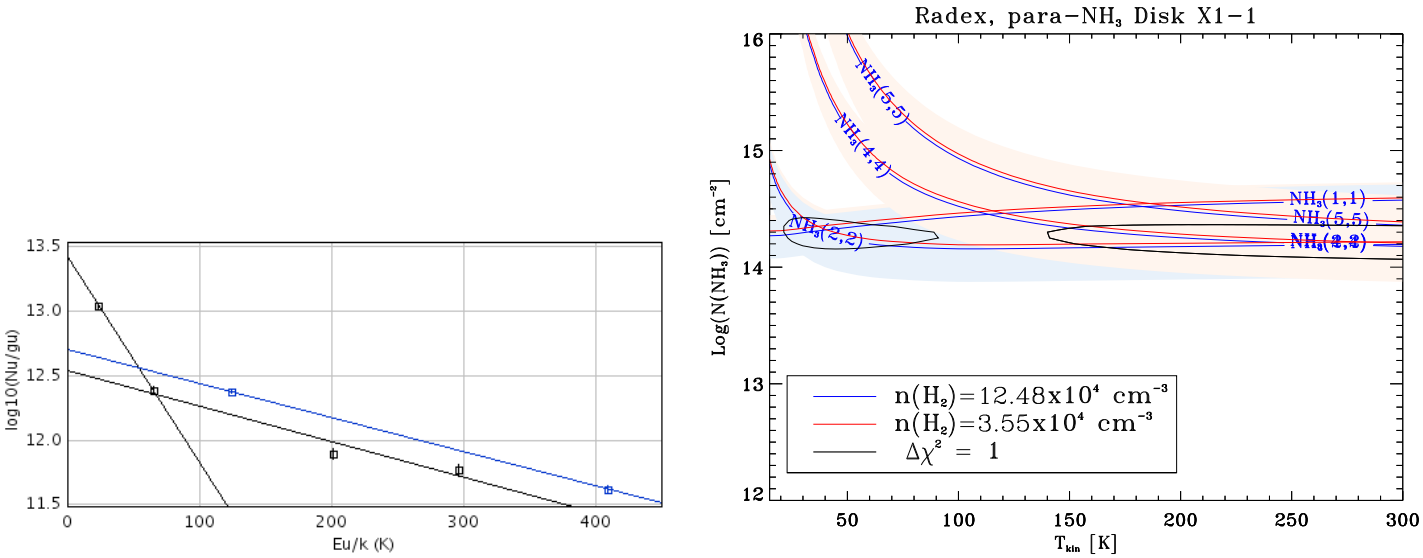

Fig. 6. Rotational (left) and LVG (right) diagrams of NH_3 for each velocity component of Disk X1-1

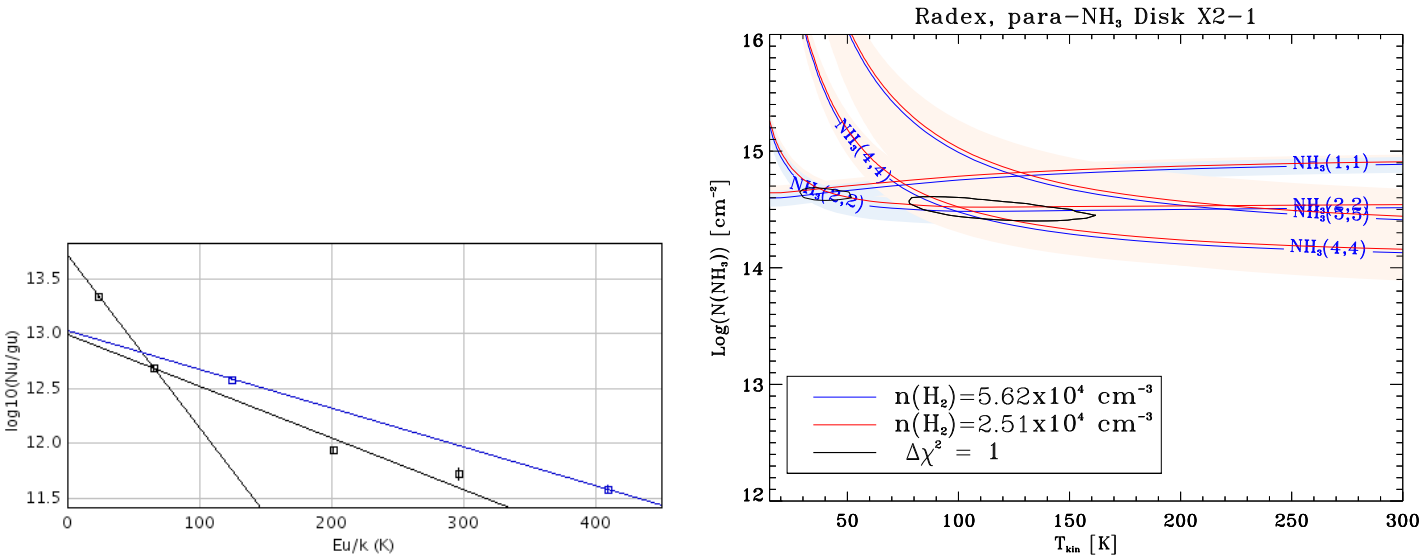

Fig. 7. Rotational (left) and LVG (right) diagrams of NH_3 for each velocity component of Disk X2-1

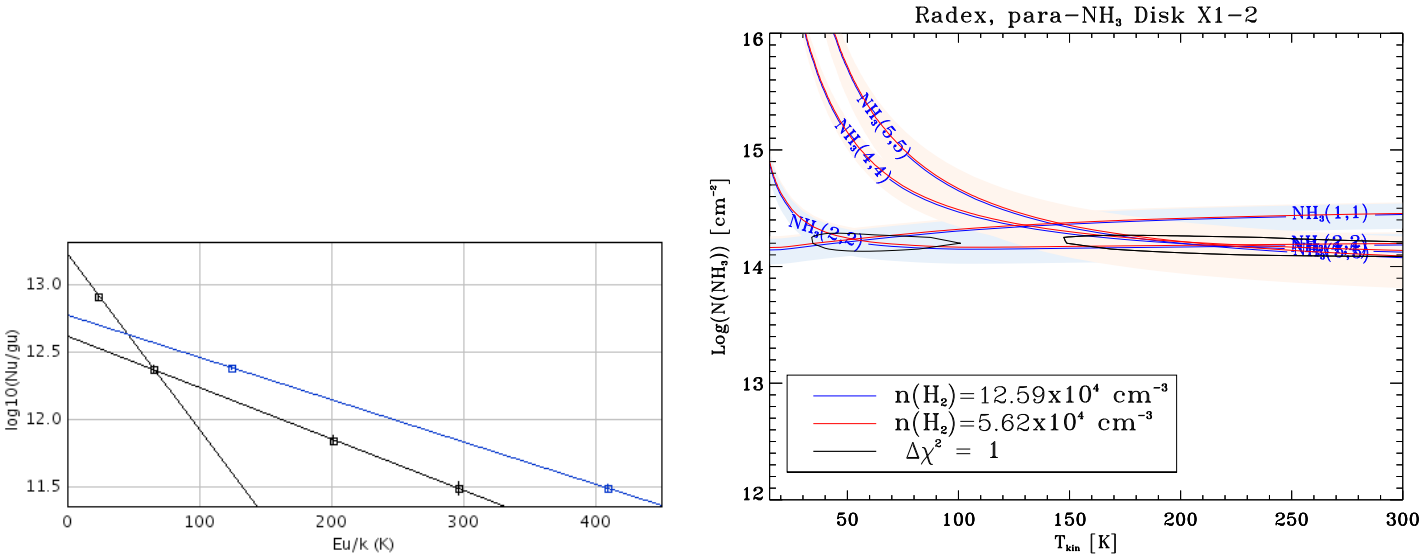

Fig. 8. Rotational (left) and LVG (right) diagrams of NH_3 for each velocity component of Disk X1-2

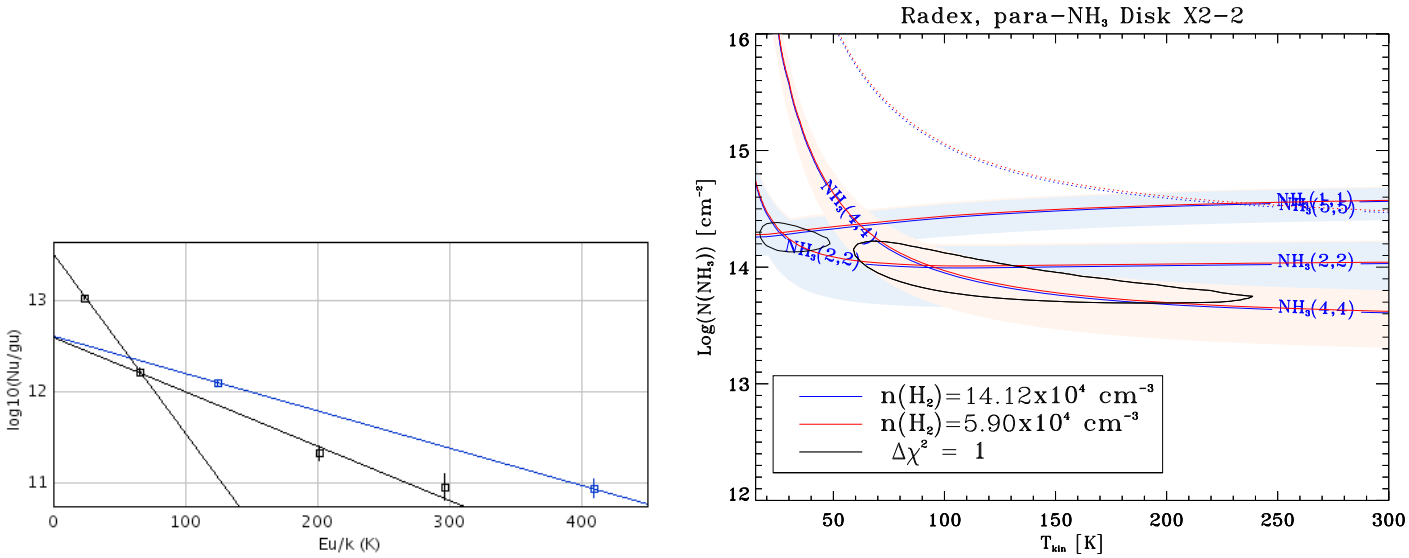

Fig. 9. Rotational (left) and LVG (right) diagrams of NH_3 for each velocity component of Disk X2-2

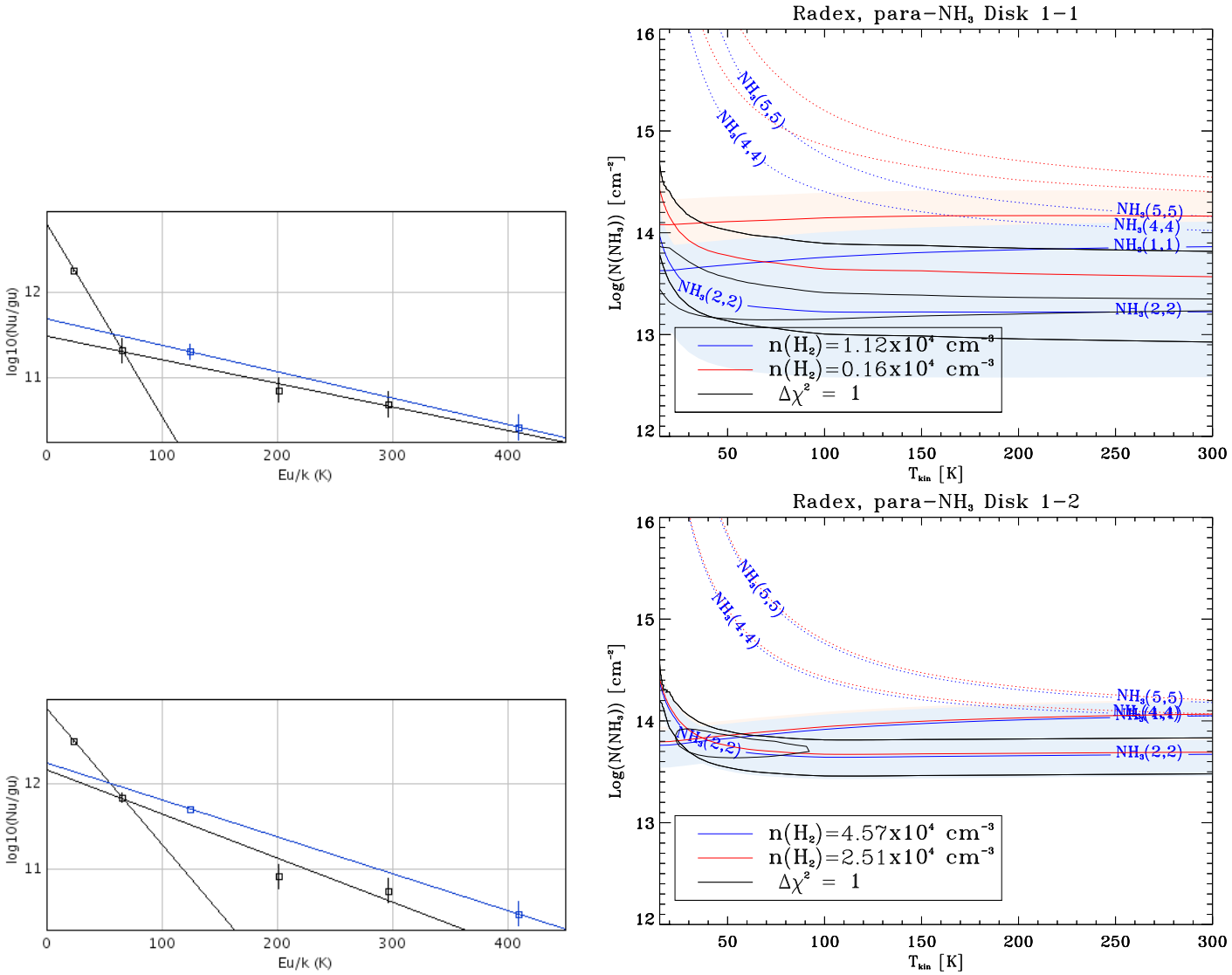

Fig. 10. Rotational (left) and LVG (right) diagrams of NH_3 for each velocity component of Disk 1. Top: 56.5km s^{-1}. Bottom: 72.4km s^{-1}.

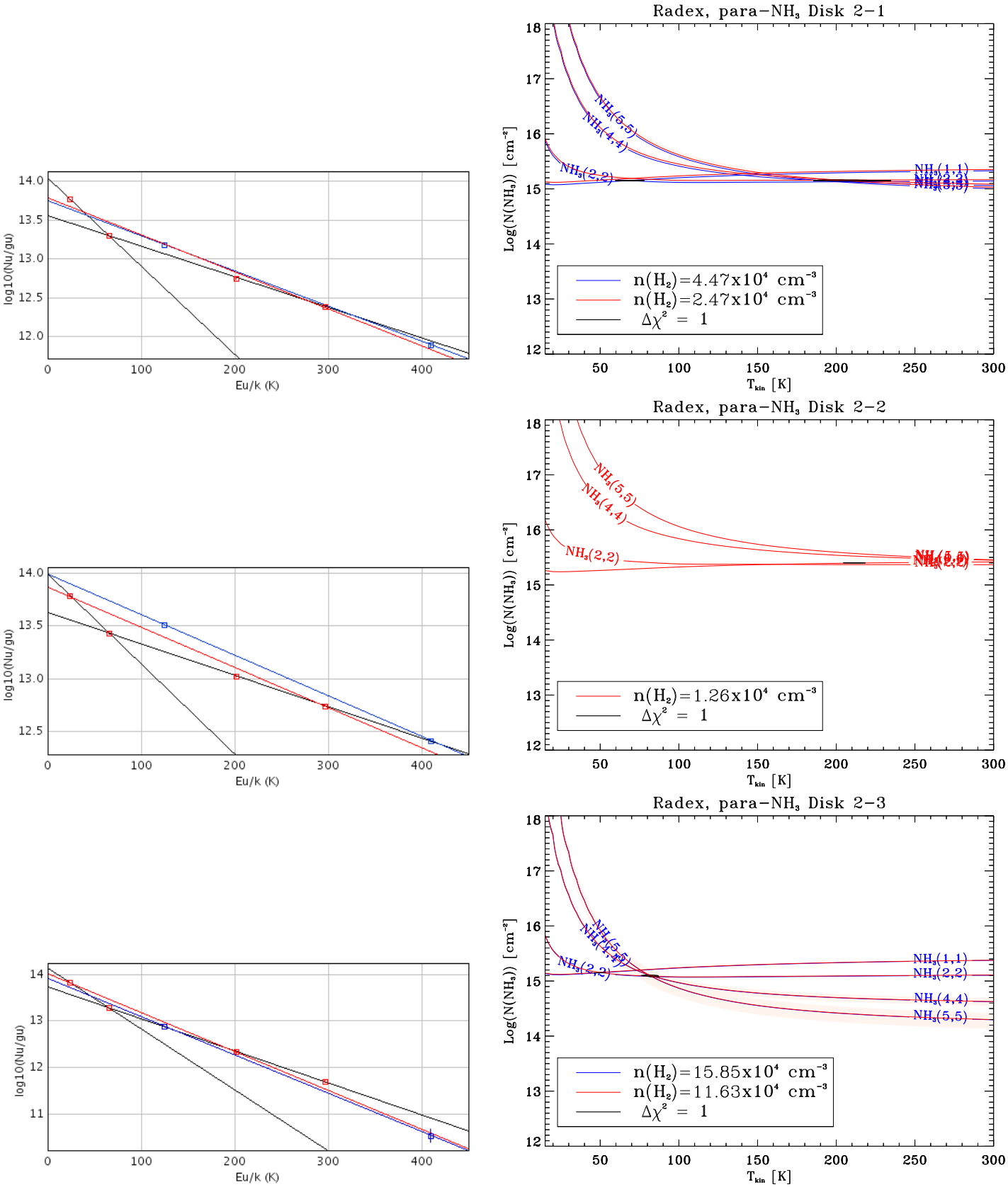

Fig. 11. Rotational (left) and LVG (right) diagrams of NH_3 for each velocity component of Disk 2. Top: 48.8km s^{-1}. Middle: 74.5km s^{-1}. Bottom: 95.8km s^{-1}.

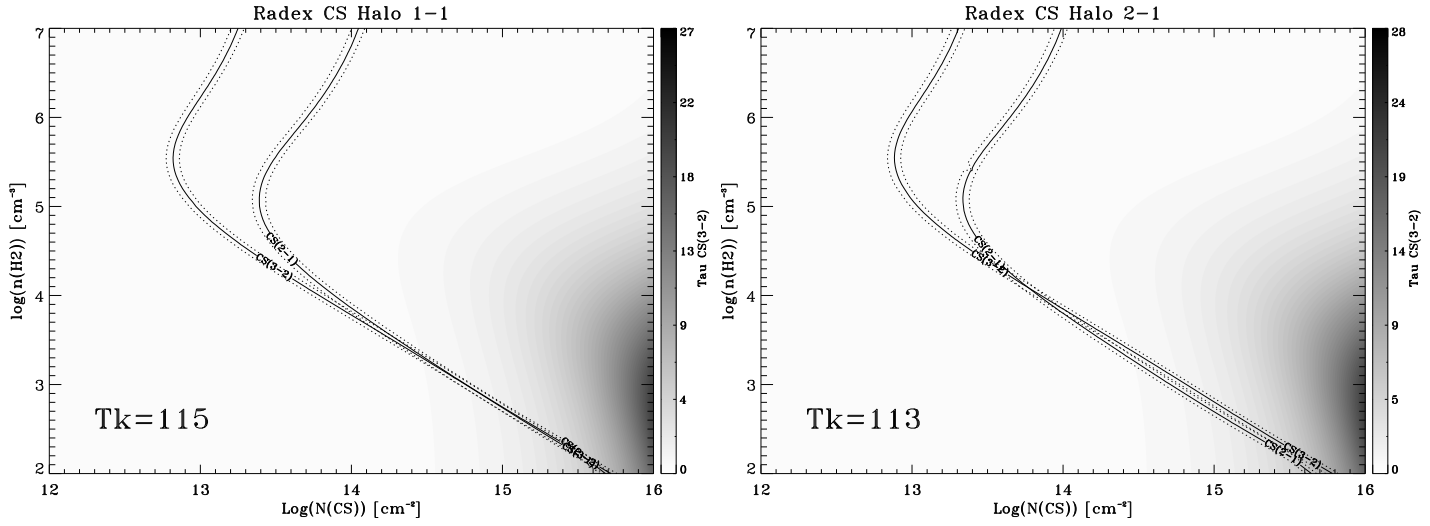

Fig. 13. LVG diagrams of CS for each velocity component of Halo 2. Top:−80km s^{-1}. Bottom: −51.9km s^{-1}.

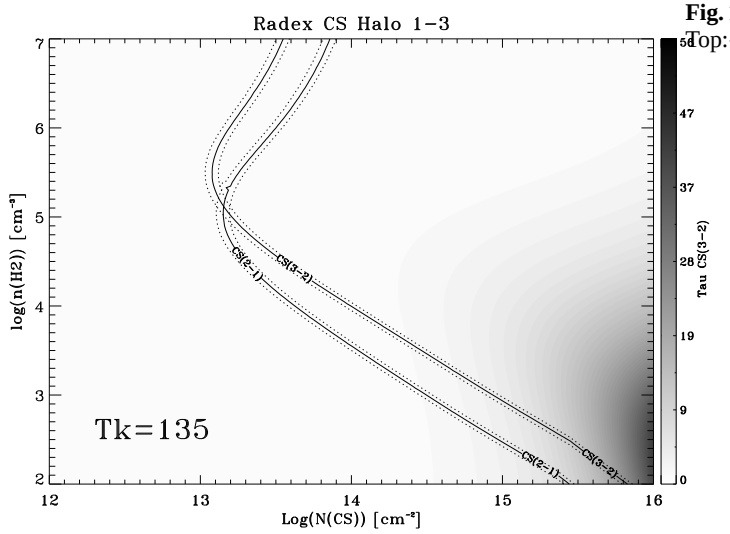

Fig. 12. LVG diagrams of CS for each velocity component (defined by the J=2-1 CS) of Halo 1 (see Table 12) . Top: 83.8 km s^{-1}. Middle: 117.4km s^{-1}. Bottom: 136.9km s^{-1}. The $T_{\rm kin}$ is indicated in the lower left corner in each plot.

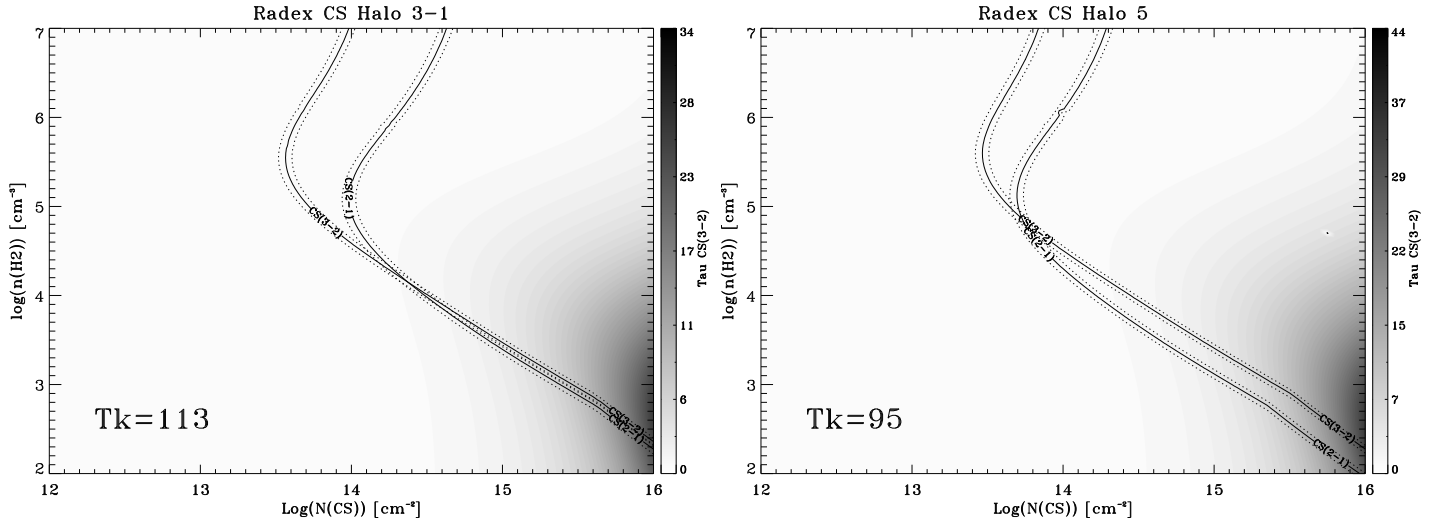

Fig. 16. LVG diagrams of CS for Halo 5.

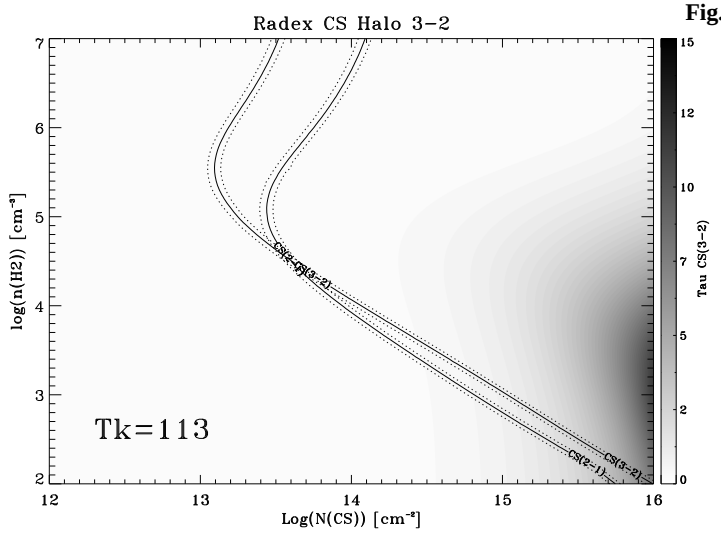

Fig. 14. LVG diagrams of CS for each velocity component of Halo 3. Top: $-64.7\mathrm{km\,s^{-1}}$. Bottom: $-13.9\mathrm{km\,s^{-1}}$.

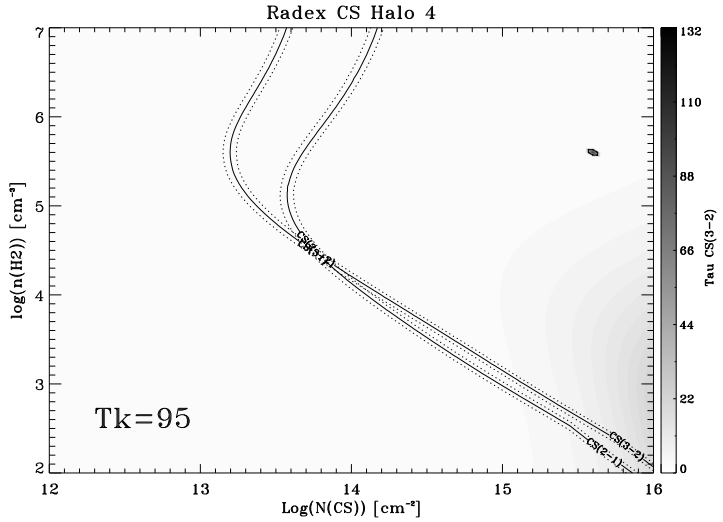

Fig. 15. LVG diagrams of CS for Halo 4.

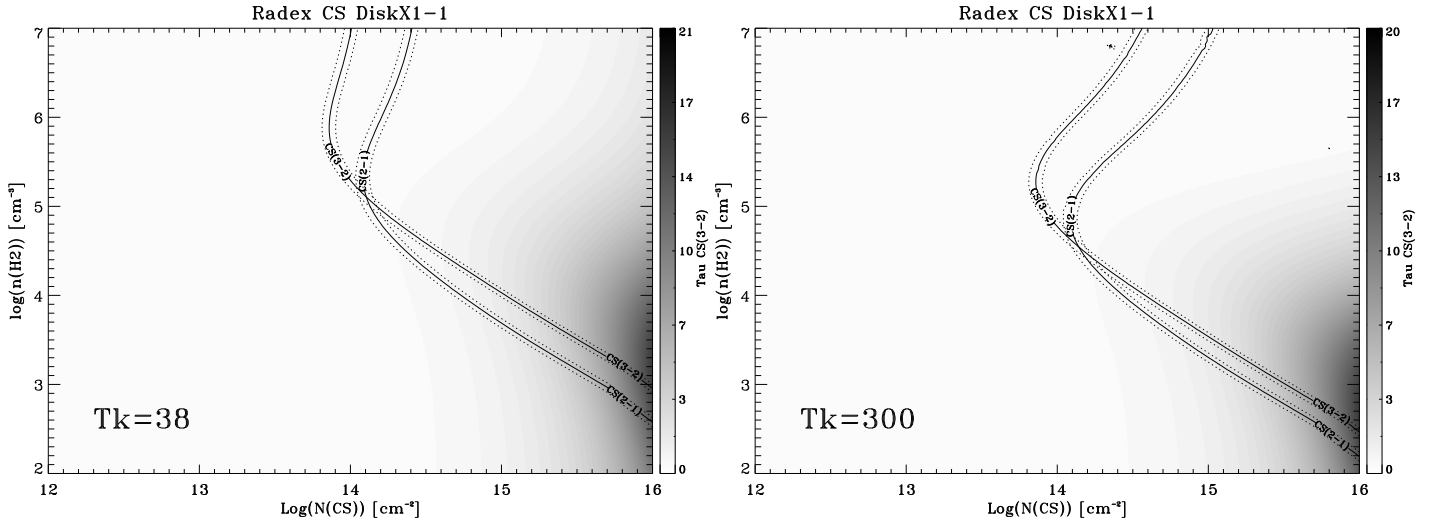

Fig. 17. LVG diagrams of CS for each kinetic temperature regime of Disk X1-1.

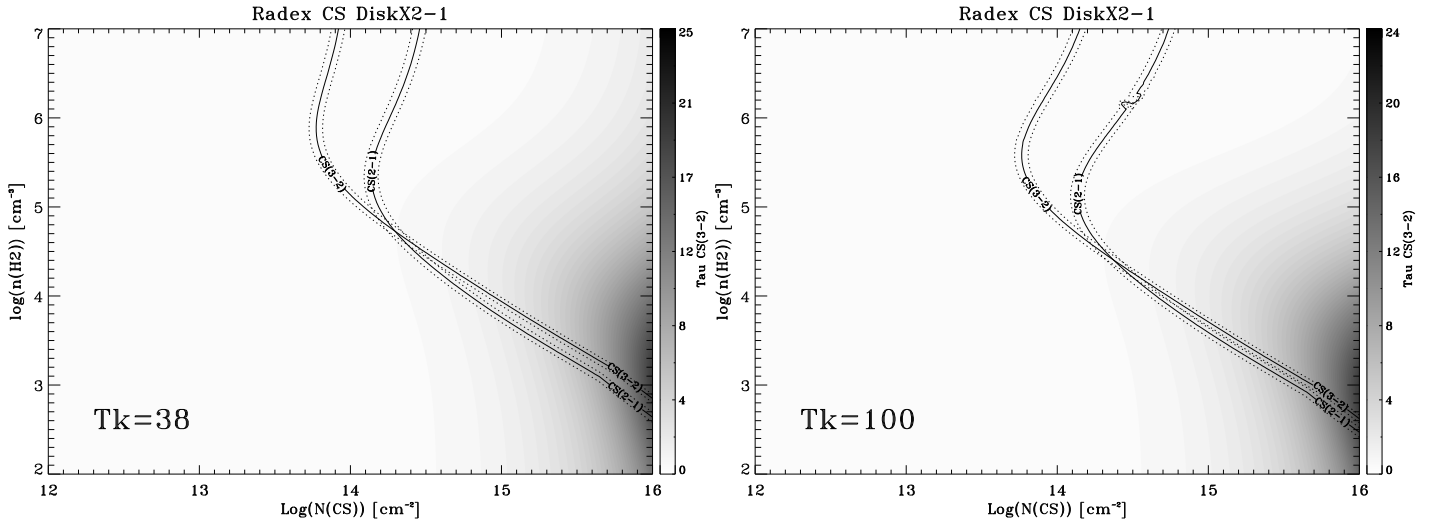

Fig. 18. LVG diagrams of CS for each kinetic temperature regime of Disk X2-1

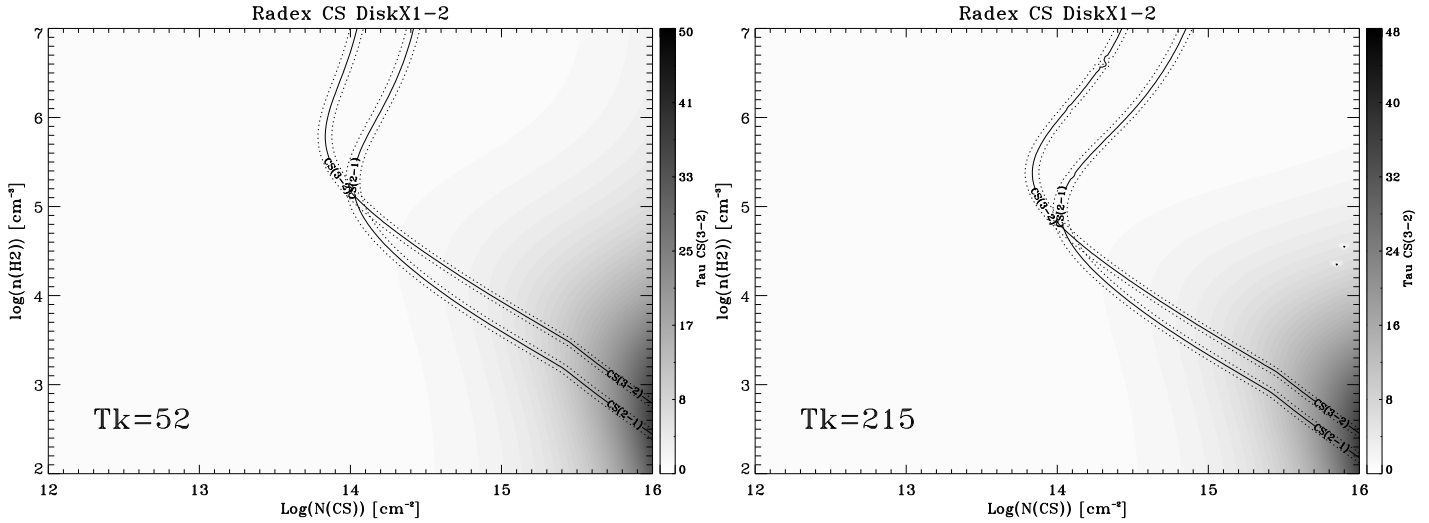

Fig. 19. LVG diagrams of CS for each kinetic temperature regime of Disk X1-2

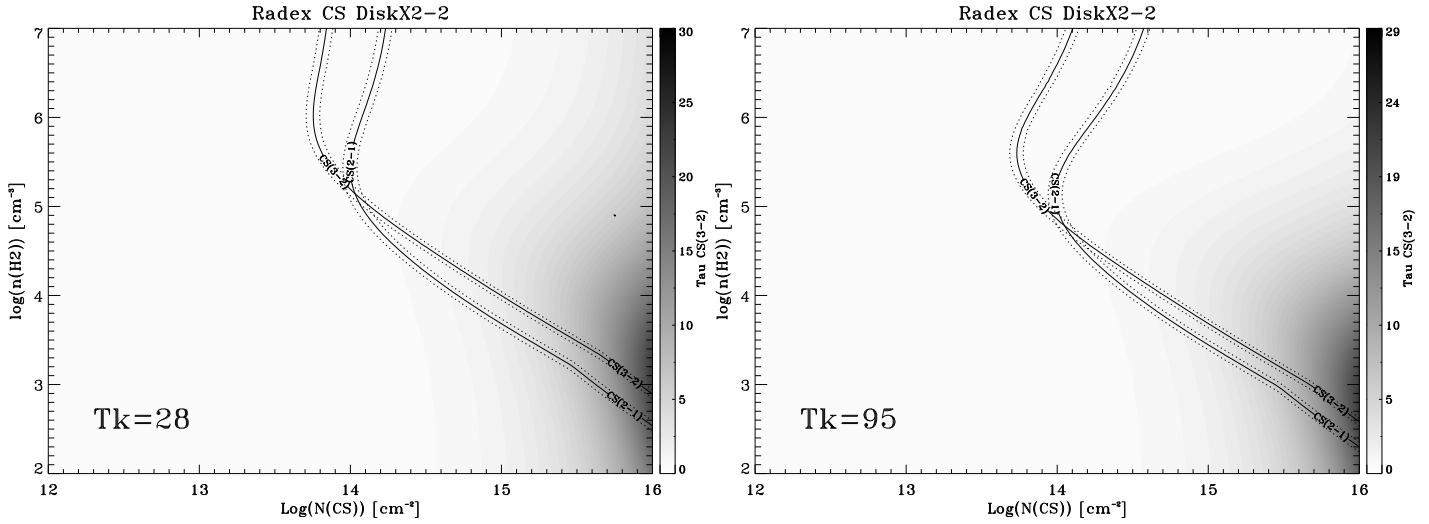

Fig. 20. LVG diagrams of CS for each kinetic temperature regime of Disk X2-2

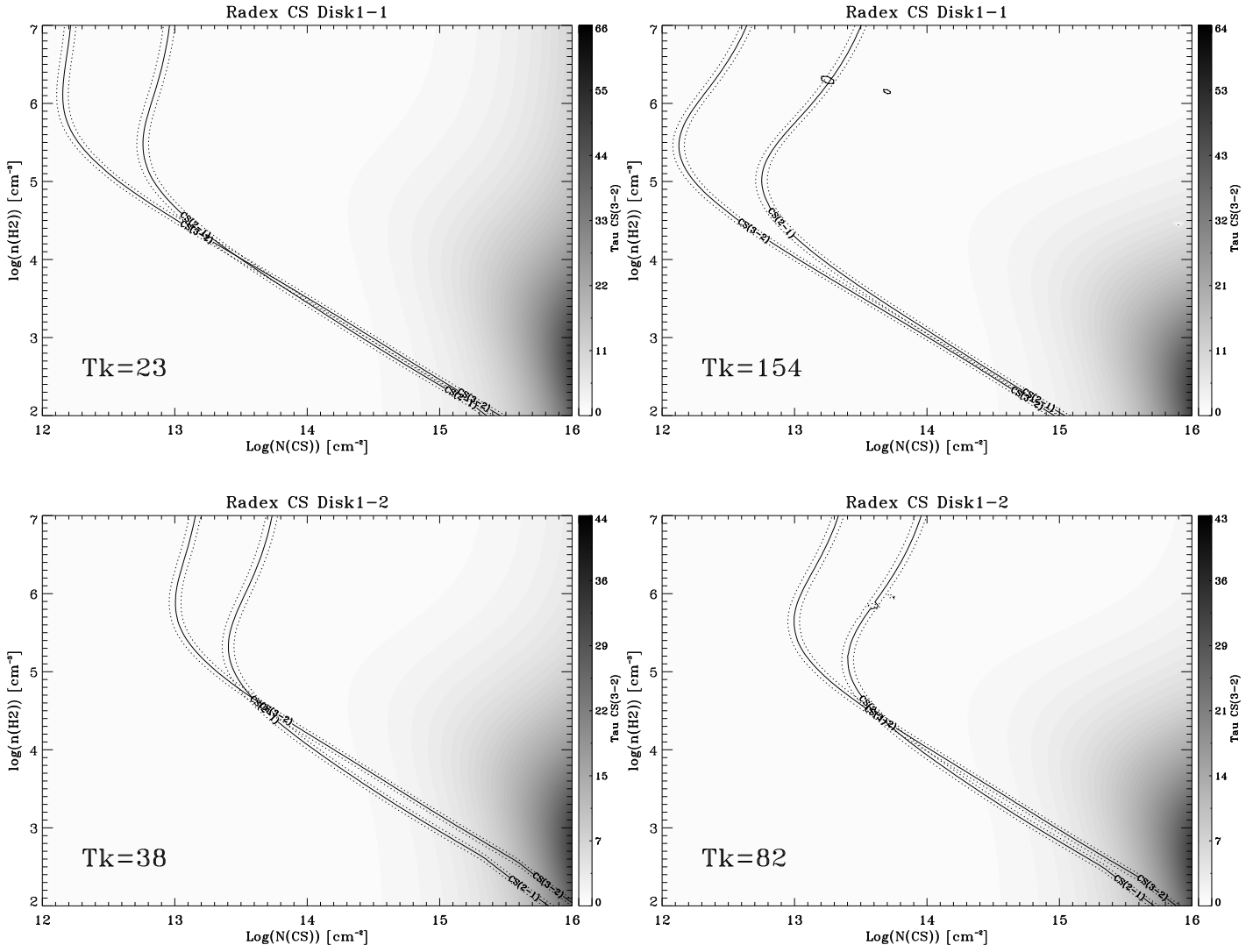

Fig. 21. LVG diagrams of CS for each kinetic temperature regime, for each velocity component of Disk 1. Top: 56.8km s^{-1}. Bottom: 74.9km s^{-1}.

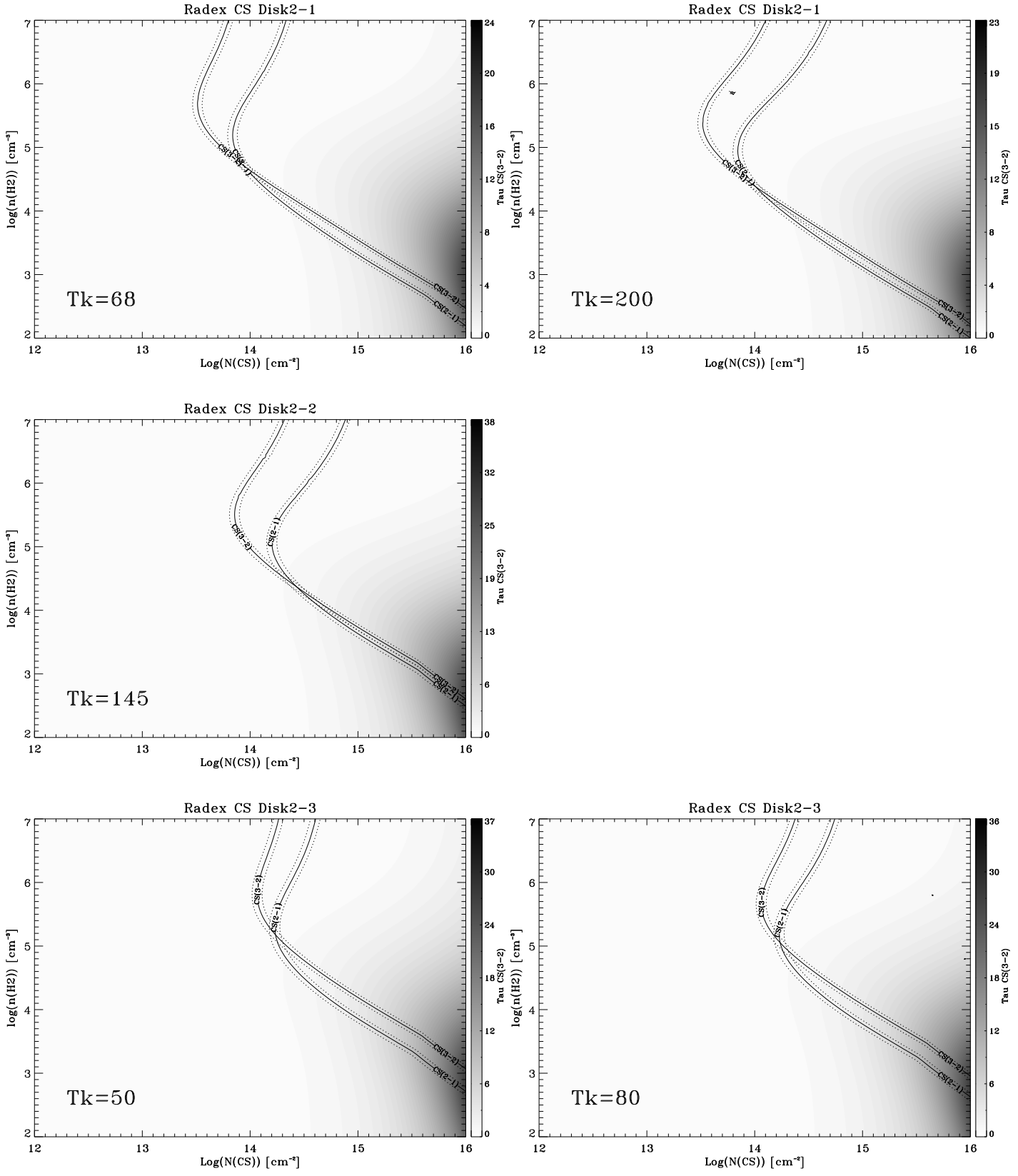

Fig. 22. LVG diagrams of CS for each kinetic temperature regime, for each velocity component of Disk 2. Top: 14.2km s^{-1}. Middle: 55.9km s^{-1}. Bottom: 79.0km s^{-1}.

Chapter 6

Future work: 3 mm line maps of the "foot points" of two Galactic Molecular Loops

In this chapter, we present a 3 mm line observation mapping of a selected region of the $M-3.8+0.9$ molecular cloud, where coexist the foot points of the loops 1 and 2. This is the first mapping of the GMLs in other molecules than CO. The work is on preparation, and only the data and a preliminary analysis is presented.

6.1 The Giant Molecular Loops

As discussed in §1.17, the Giant Molecular Loops (GMLs) are huge structures of dense molecular gas with loop shapes discovered by Fukui et al. (2006) in their CO ($J = 1-0$) maps. They are presumably formed by magnetic flotation caused by a Parker instability. The phenomena is analogous to the solar loops. Alternative explanations for their origin, such as supershells created by multiple massive stellar explosions, have been ruled out by Fukui et al. (2006) and Torii et al. (2010b). Several observational studies and model have been performed in these regions in order of characterize their physical properties. In the following we summarize the results of the recent published studies.

6.1.1 Loop 1 and Loop 2

Torii et al. (2010b) present a detailed observational study determining geometrical parameters and velocities of the loops. Loop 1 ranges from $l = 355^\circ.8 - 358^\circ.0$, $b = 0^\circ.5 - 1^\circ.6$, $v_{\rm LSR} = -180$ to -90 km s^{-1}, and has a total gas mass that ranges from $6.8 - 11.7 \times 10^5 M_\odot$ (total mass estimated from CO emission, $M_{\rm dust}$, and $M_{\rm HI}$). It looks like a filamentary structure of ~ 30 pc width, and ~ 300 pc length (see Fig. 6.1). The foot points are located at $(l, b) \sim (356^\circ, 1^\circ)$ and $(l, b) \sim (357^\circ.4, 0.^\circ 8)$. Loop 2 ranges from $l = 355^\circ.2 - 356^\circ.6$, $b = 0^\circ.6 - 2^\circ.2$, $v_{\rm LSR} = -90$ to -40 km s^{-1}, and has a mass that ranges from $8.2 - 16.1 \times 10^5 M_\odot$. It looks like a structure with a width of ~ 30 pc, and a length of ~ 400 pc, and is elevated by ~ 300 pc from the plane (see Fig. 6.2). The foot points are at $(l, b) \sim (355^\circ.4, 0^\circ.8)$ and $(l, b) \sim (356^\circ.1, 0^\circ.8)$. The feature at $b \sim 1^\circ.4$ is part of

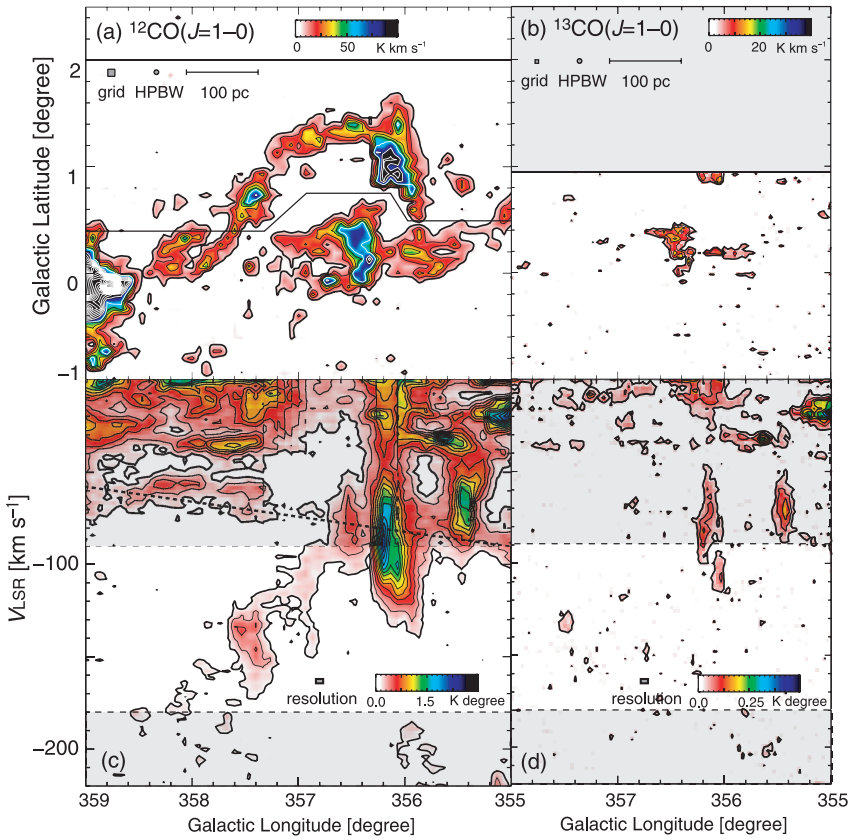

Figure 6.1: Integrated intensity of Loop 1 in ^{12}CO and ^{13}CO(1-0). (a) and (b) Integrated intensity in the velocity range −180 to −90 km s^{-1}. (c) and (d) longiture-velocity plot. Fig. from Torii et al. (2010b)

Loop 1. In this region we selected the position belonging to the top of the loop that we call throughout this thesis "Halo 5". Fig. 6.4 shows the average velocity distribution along the loops by Torii et al. (2010b), who confirmed the velocity gradients derived by Fukui et al. (2006) of ~ 0.2 km s^{-1}pc^{-1} and ~ 0.35 km s^{-1}pc^{-1} along loops 1 and 2, respectively. Fig. 6.5 show the velocity dispersions along the loops. It is clear that the velocity dispersion in the foot points is significantly larger than that in the rest of the loops (Fig. from Torii et al. 2010b).

Fig. 6.3 shows an schematic view of the loops derived from Torii et al. (2010b). The top of the loops show helical features that may be explained by magnetic instabilities (Torii et al. 2010b).

Torii et al. (2010b) also show a comparison of the CO, H I (McClure-Griffiths et al. 2005) and IRAS emission (dust) at 60 μm and 100 μm in the GMLs. They found that the H I emission is similar with the with the CO emission, which indicates an atomic component in the loops, but the H I is more continuously distributed than the CO, with a weaker emission inside the Loop 1, and in the Loop 2 is barely seen. Dust emission is detected in the Loop 1, while in the Loop 2 the dust emission is not clearly seen.

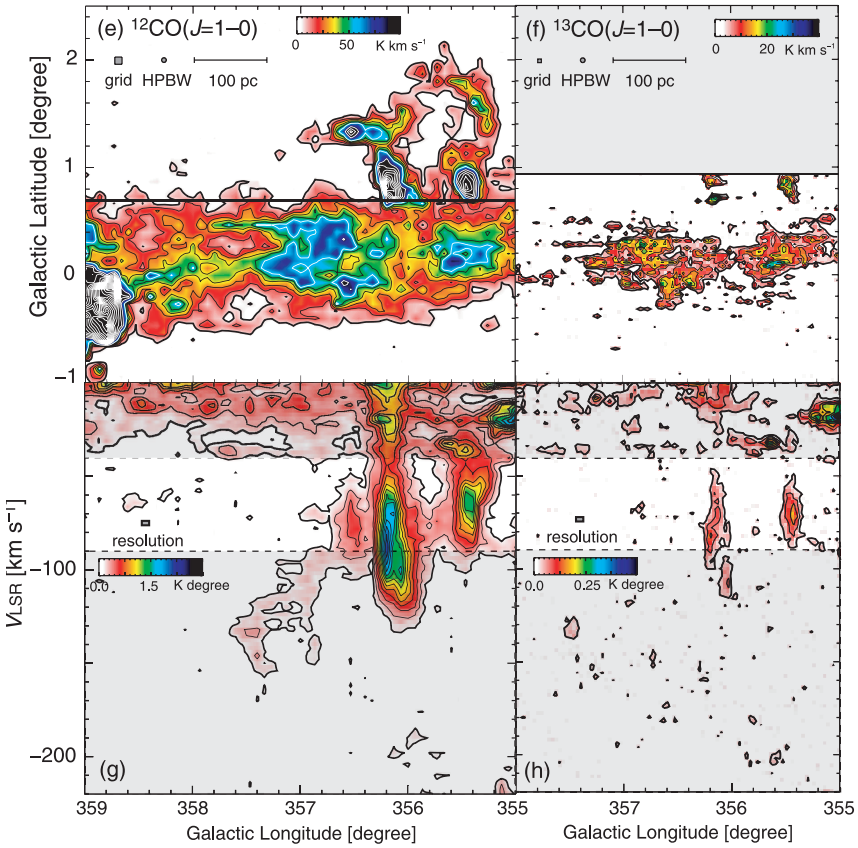

Figure 6.2: Integrated intensity of Loop 2 in ^{12}CO and ^{13}CO(1-0). (a) and (b) Integrated intensity in the velocity range -90 to -40 km s^{-1}. (c) and (d) longiture-velocity plot. Fig. from Torii et al. (2010b)

6.1.1.1 Footpoint of the loops 1 and 2

Torii et al. (2010a) present a multitransitional analysis of ^{12}CO(J=1-0, 3-2, 4-3, 7-6) , ^{13}CO(J=1-0), and C^{18}O(J=1-0) towards the foot points of the GMLs placed towards $l \sim 356°$. In this region, there are two foot points which correspond to loops 1 and 2. They are elongated features vertically to the plane with the most prominent feature from $l = 356°.15 - 356°.25$ and $b = 0°.8 - 1°.0$, and few local maxima at $(l, b) = (356°.17.0°.75), (356°.13, 0°.78), (356°.25, 1°.10)$ (see Fig. 6.6). Their characteristics as sumarized by Torii et al. (2010b) are: the size an the mass of the gas in the foot point are ~ 20 pc and $\sim 10^5$ M$_\odot$, the spatial distribution shows a sharp intensity drop towards the plane, the velocity disperssions are large of $50-60$ km s^{-1}(see Fig. 6.5), the line profiles are of triangle shape with skewness, they show strong velocity gradient towards the plane suggesting shock fronts. They also argue that the high density in the foot points may favours future star formation.

Torii et al. (2010a) identified and analyzed several features. The main part of the loops "main components" (see Fig. 6.7), is distribuited in the velocity range from -150 to -40 km s^{-1}, and there is a weaker emission ("subcomponent") which ranges from

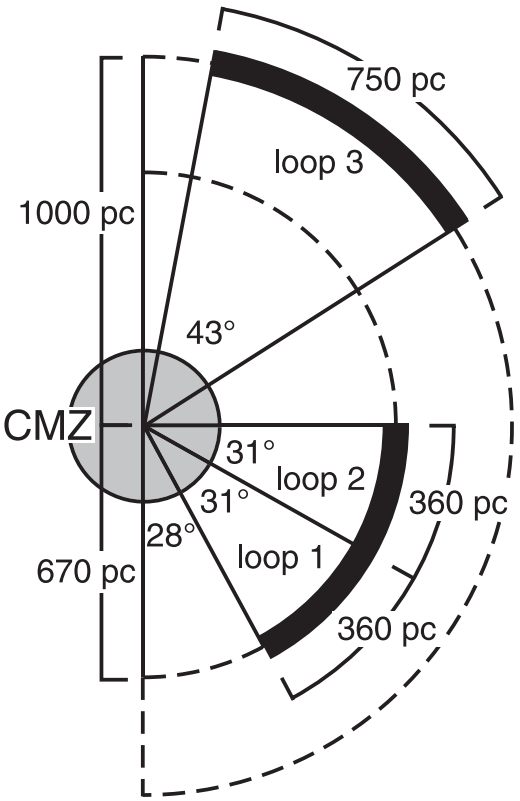

Figure 6.3: Face on view of the shematic position of the GMLs. R is the distance from the Galactic center to the loops, θ is the angle subtended by the arcs between the foot points, and θ_0 is offset (Fig. from Torii et al. (2010b))

-30 to 0 km s^{-1}. They argue that the subcomponent is probably linked to the main components by the connection of broad emission at $b = 0°.8, 0°.88, 0°.94, 1°.0$, and forms two "U" shapes in the $v - b$ diagrams with the main component and the broad emission. They also identified a "protusion" which has an inverse-triangle like shape, placed towards $l = 355°.15 - 356°.20$, $b = 0°.7$, $v = -70$ to -10 km s^{-1}(see Fig. 6.7). They also studied in detail five itensity peak labeled as "A-D" in Fig. 6.6, where the most intense is the peak C which is connected to the bottom of the U shape 1, and peak D which is connected to the protusion, which form the U shape 2. From the multitransition analysis they conclude that the gas in the loop presents high excitation conditions and smaller CO optical depth than local gas, density in the range of $10^3 - 10^4$ cm^{-3} and kinetic temperature $30 - 100$ K or higher, where the peak B shows the highest temperature. They also obtain the CO$(3-2)$/CO$(1-0)$ ratio which indicate that the higer excitation conditions are placed towards the peak B, following by the peak D, but they also found two very narrow velocity width of 1-2 km s^{-1}features which show a high ratio placed at $v \sim -80$ km s^{-1}, $l = 356°.2$, $b = 0°.85 - 1°.05$; and the other at $v \sim -30$ km s^{-1}, $l = 356°.15$, $b = 0°.80 - 0°.95$

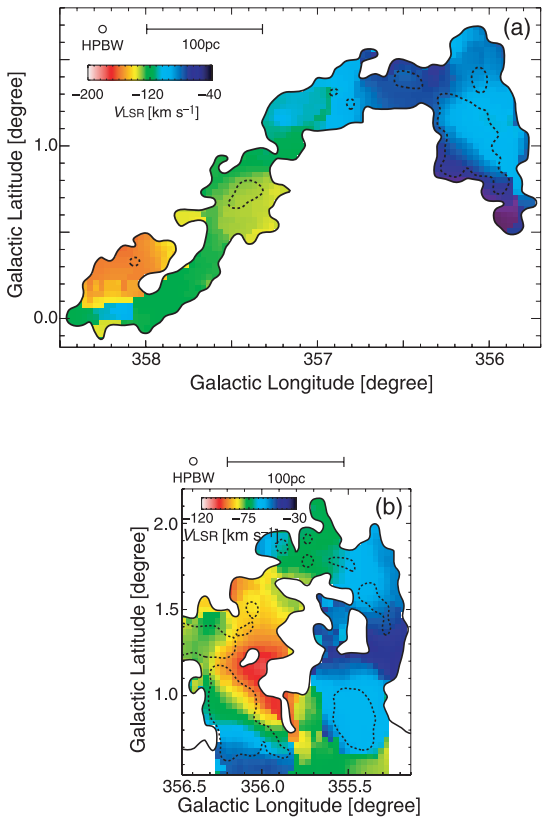

Figure 6.4: Average velocity distribution along the loops. Torii et al. (2010b) derived a velocity gradient along the loops 1 and 2 of ~ 0.2 km s^{-1}pc^{-1} and ~ 0.35 km s^{-1}pc^{-1} respectively (Fig. from Torii et al. (2010b))

Torii et al. (2010a) compared their results with magnetohydrodynamical simulations (Matsumoto et al. 1988; Takahashi et al. 2009) which indicate that the foot point between two loops becomes "U shaped", consisting of the two down flows from the two loops merging at the bottom. They also compare their results with theoretical work on solar activity and argue that the warmest region of the foot point (towards the peak B) may be additionaly heated up by either magnetic reconection (see Fig. 6.8) or by upward flowing gas bounced by the narrow neck in the foot point.

6.1.2 Loop 3

This molecular loops was reported by Fujishita et al. (2009), and it is located towards the same direction as the loops 1 and 2, but at a positive velocity range. Loop 3 ranges from $l = 355°.0 - 359°.0$, $b = 0°.0 - 2°.0$, $v_{\rm LSR} = 30 - 160$ km s^{-1}, and a mass from $1.8 - 21.0 \times 10^5 M_\odot$.

Kudo et al. (2011) studied high excitation molecular gas in the GMLs 1, 2, and 3, from CO(J=2-1), (J=3-2). They covered the complete loops including not only the foot point, but also the top of the loops. They analized four foot points (Fig. 6.9),

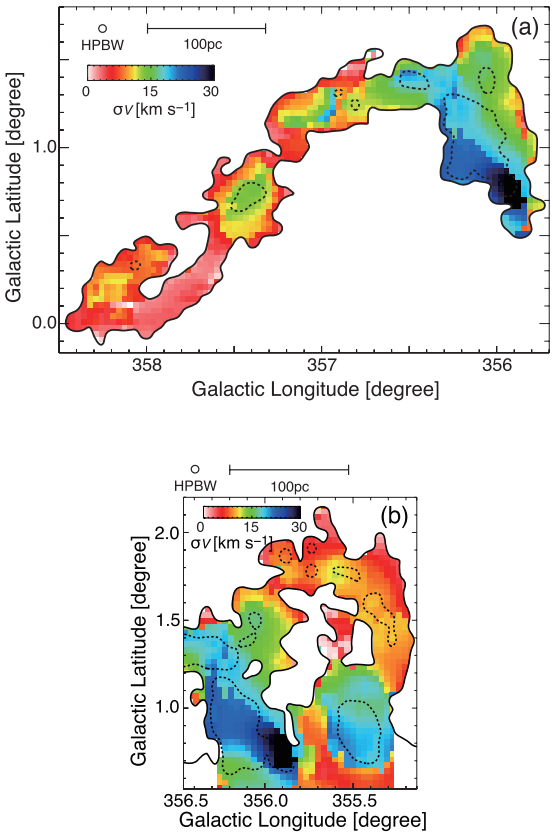

Figure 6.5: Velocity disperssions along the loops (Figure from Torii et al. (2010b))

and explained the U shapes and L shapes using a simple kinematical model that incorporates global rotation and expansion of the loops in addition to falling motion along the loops (see Fig. 6.9).

6.1.3 Loop at $l = 3 - 5^\circ$

This molecular loops is suggested by Fukui et al. (2006), and seems to bridge the M+3.2 − 0.3 and the M5.3 − 0.3 molecular clouds. The bridging components has a large velocity gradient of ∼ 50 km s−1 degree^{-1} in longitude. Fukui et al. (2006) argue (in the supporting online material) that this gradient, and the fact that this bridge is weaker than the others, are characteristics consistent with a magnetic flotation in a later evolutionary stage, where most of the material is down flow and the foot point are enhancement (which is expected by the accumulation of material).

This molecular loops has not received much attention until now. Unfortunately, our mapping of their foot point is not completed (see §8.1), but our studies of the isotopic ratios (see §4) support gas accretion from high latitude, and §5 show a high temperature in this loop.

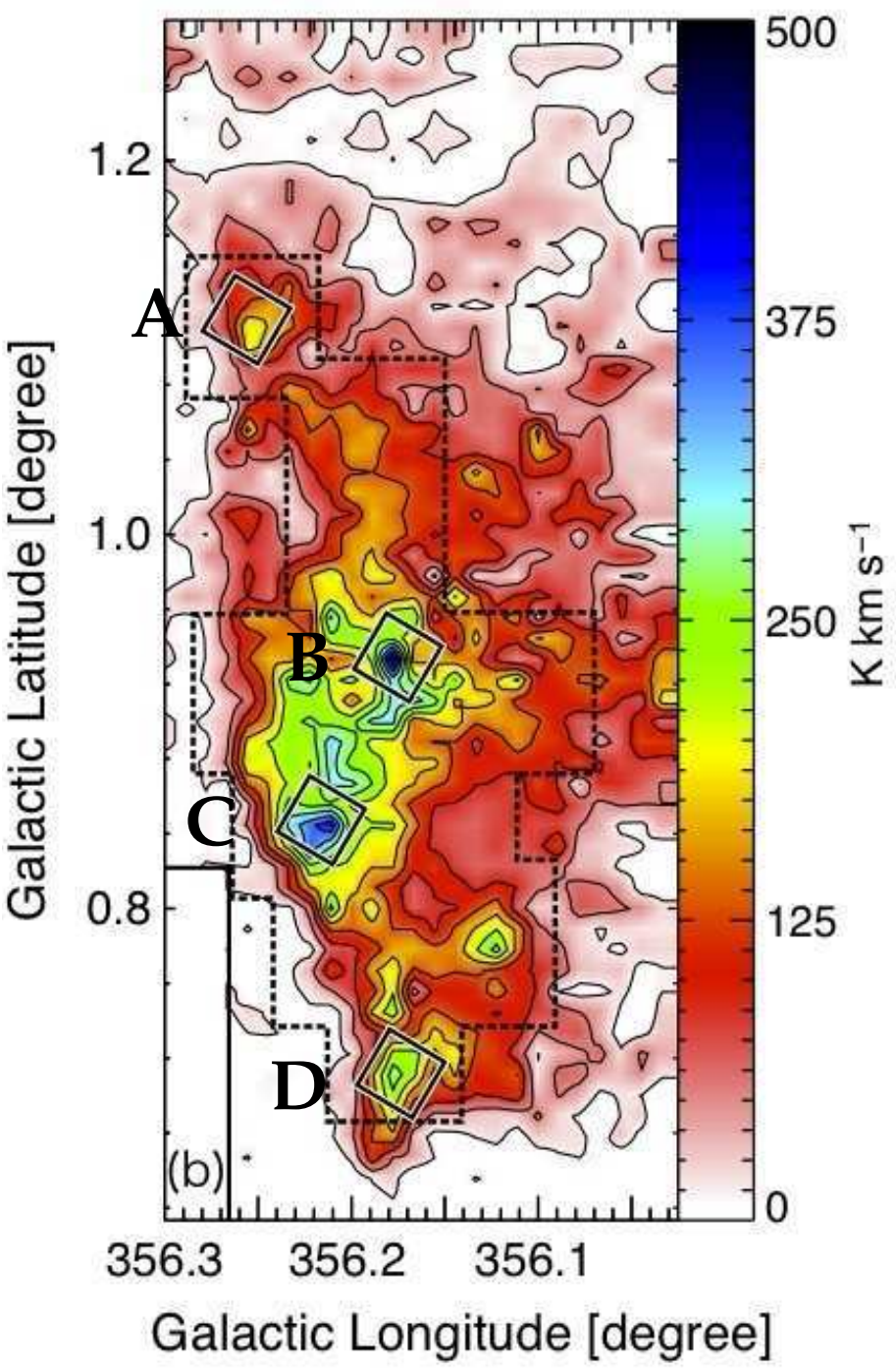

Figure 6.6: Foot point of the GMLs 1 and 2 Torii et al. (2010a)

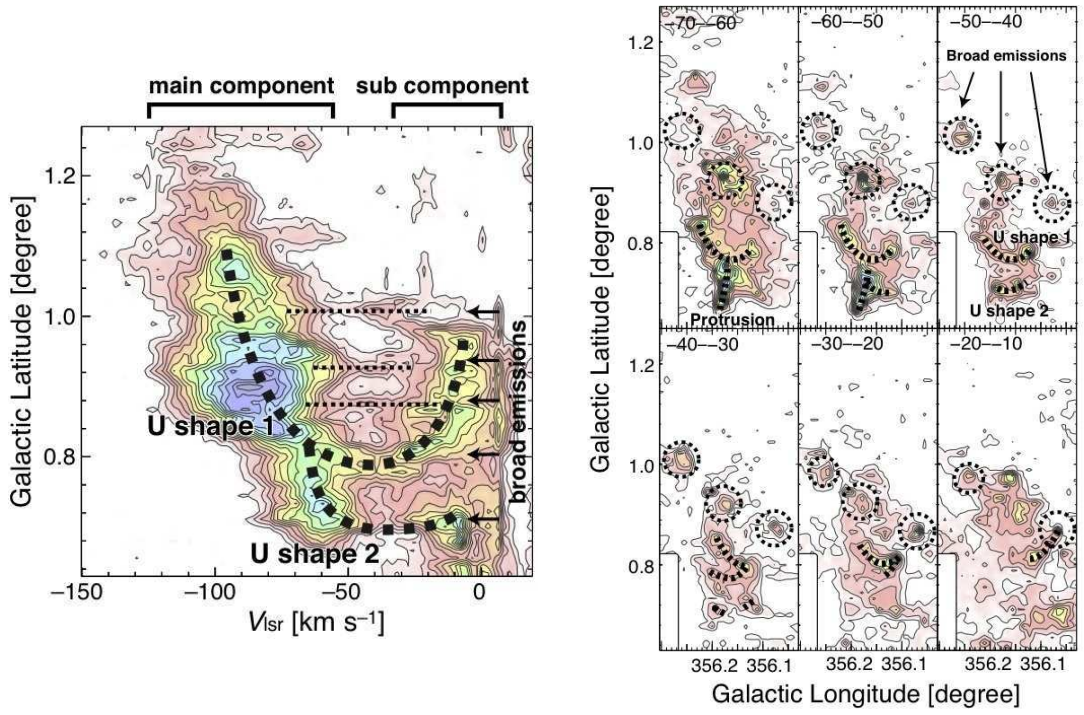

Figure 6.7: Foot point of the GMLs 1 and 2 in the $b - v$ diagram and in channel maps Torii et al. (2010a)

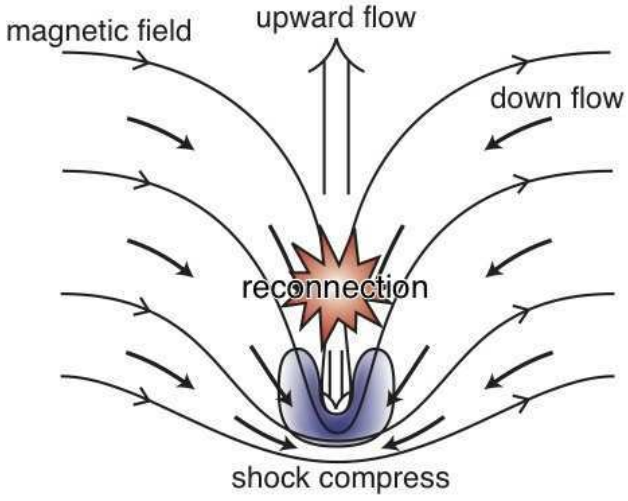

Figure 6.8: Schematic image of reconnection at the foot point between two loops. Fig. from Torii et al. (2010a)

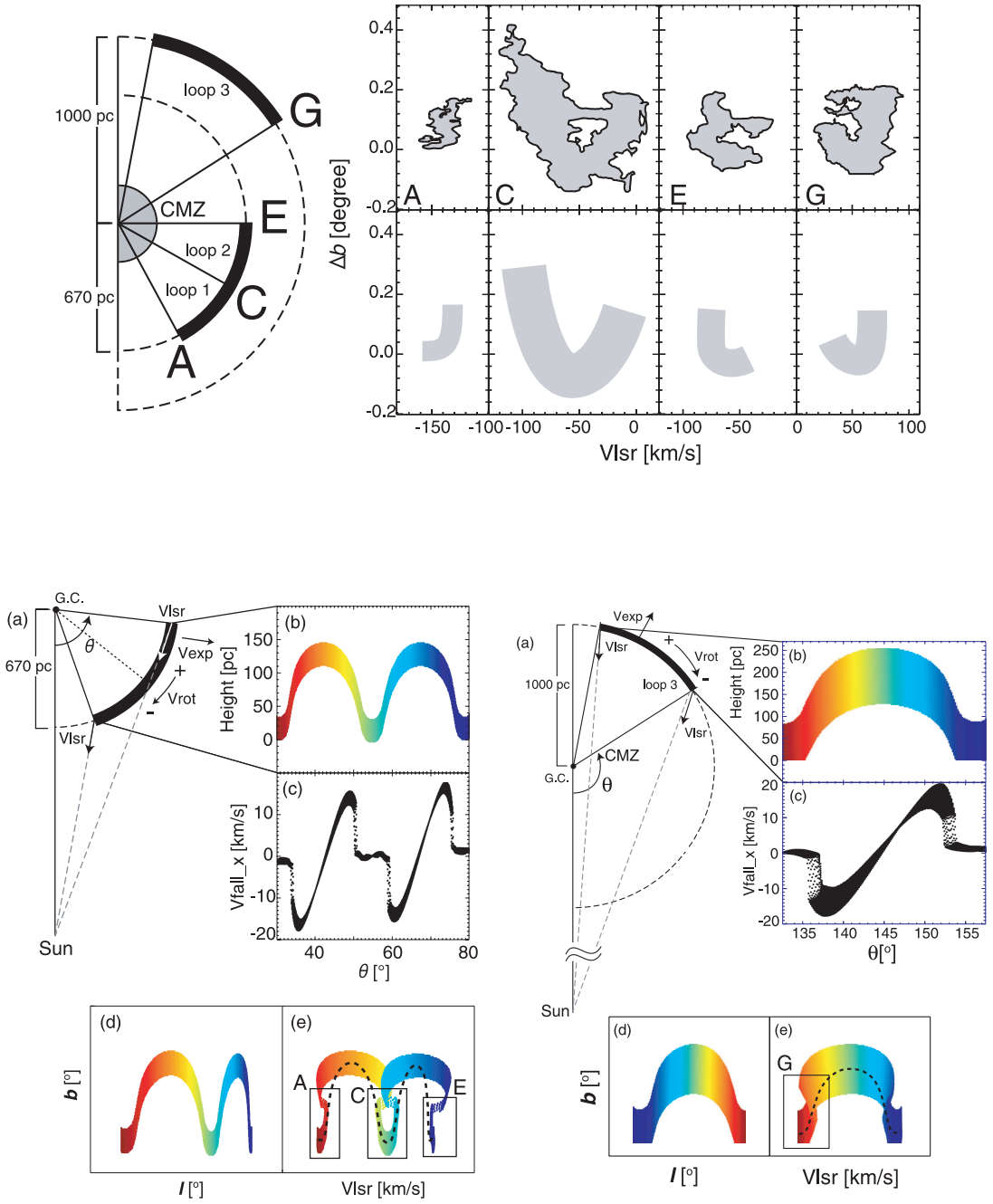

Figure 6.9: Kinematical model of the loops proposed by Kudo et al. (2011). Top: Latitude-velocity plot of the foot point of the loops 1, 2, and 3. Features A, C, E and G correspond to the foot point of the loops plotted in the schema of Torii et al. (2010b). A correspond to the eastern foot point of loop 1. C is the western foot point of loop 1 and eastern foot point of the loop 2. E corresponds to the western foot point of loop 2. G is the western foot point of loop 3. Bottom: Kinematical model of the loops. The model can explain the U shapes and L and mirror-L features showed in the latitude-velocity plots. Fig. from Kudo et al. (2011)

6.2 Kinematic and physical conditions at the foot point of two Galactic Molecular Loops

I am the principal investigator of this project. The observations were done using the 22m Mopra telescope (Australia), and were carried out by Arancha Amo-Baladrón and by me. I am in charge of the proposals preparation, data reduction, data analysis, and writing of the paper. The work is on preparation. For consistency, this chapter is written in the A&A format.

Astronomy & Astrophysics manuscript no. paper˙mopra
December 13, 2011

Kinematic and physical conditions at the foot points of two Galactic Molecular Loops

D. Riquelme[1], M.A. Amo-Baladrón[2], J. Martín-Pintado[2], R. Mauersberger[3], and et al.

[1] Instituto de Radioastronomía Milimétrica (IRAM), Av. Divina Pastora 7, Local 20, E-18012 Granada, Spain
e-mail: riquelme@iram.es
[2] Centro de Astrobiología (CSIC/INTA), Ctra. de Torrejón a Ajalvir km 4, E-28850, Torrejón de Ardoz, Madrid, Spain
[3] Joint ALMA Observatory, Alonso de Córdova 3107, Vitacura, Santiago, Chile

ABSTRACT

Aims. To reveal the morphology, chemical composition and the kinematics of the shocked gas in the foot points of the giant molecular loops (GMLs)
Methods. Using the 22m Mopra telescope, we mapped one molecular cloud placed at the foot points of the GMLs in 3-mm molecular lines.
Results. The data show structures at small scale in SiO emission, with narrower line profiles than those of, e.g, HCO^+ or HCN, which indicate that the shocks are dynamically confined. The data also show clear differences between different molecular tracers, e.g., between the SiO and HCO^+ emission, which would indicate differences in the physical properties and chemistry within the cloud

Key words. Galaxy: center - ISM: clouds - ISM: molecules

1. Introducction

Studies of external edge-on galaxies provide an excellent bird's eye view of galaxy disk-halo interface without some of the confusion which is present in our own Milky Way. Such observations however require high resolution and very good signal-to-noise ratio. Even in the case of the nearest external galaxies, the spatial resolution of the existing telescope does not allow to study the physical processes which dominate the disk-halo interaction. Studies of selected regions of the Milky Way provide the only possibility to study in detail the role of magnetic loops, galactic winds, and gas accretion in the the disk-halo interaction.

There are many molecular surveys of the central 500 pc of the Galactic center (GC) region (see e.g., Jones et al. 2011, which is the latest 3mm molecular lines survey of the central molecular zone (CMZ) (Morris & Serabyn 1996)), but few of them cover the high latitude molecular complexes. Bitran et al. (1997) observed a region of $-12^\circ < l < 12^\circ$ in CO(1 – 0), identifying 5 large velocity width and high CO luminosity clumps outside the CMZ. Fukui et al. (2006) observed a similar region in the same CO transition finding huge loop structures. They proposed that these "giant molecular loops" (GMLs) are formed by a magnetic buoyancy caused by a Parker instability. According to Fukui's model, the gas of the loops would flow down their sides, along the magnetic field lines, and join with the gas layer of the Galactic plane, generating shock fronts at the "foot points" of the loops. This shocked gas is supported by broad velocity features of ~ 40 to 80 km s^{-1} observed by Fukui et al. (2006).

Additional evidence of shocked gas at the "foot points", comes from Riquelme et al. (2010b) complete survey of the GC region in $HCO^+(1-0)$, $H^{13}CO^+(1-0)$, and SiO(2 – 1) lines. The mapped area ($-5^\circ.75 < l < 5^\circ.63$ and $-0^\circ.7 < b < 1^\circ.35$) includes the CMZ and the 5 clumps observed by Bitran et al. (1997). They find an enhancement of the SiO emission at the "foot point" zones with respect to HCO^+, which clearly indicates the presence of shocks, as SiO is one of the prototypical molecular tracer of shocked gas (Martín-Pintado et al. 1992).

Multitransitional CO observations towards both, the foot points and the complete loops have been recently performed, and magnetohydrodynamical simulations support the GMLs scenario. Torii et al. (2010b) presented a detailed observational study determining geometrical parameters and velocities of the loops. Loop 1 ranges from $l = 355^\circ.8$ to $358^\circ.0$, $b = 0^\circ.5$ to $1^\circ.6$, $v_{\rm LSR} = -180$ to -90 km s^{-1}, and has a total gas mass of $6.8 - 11.7 \times 10^5 M_\odot$. The foot points are located at $(l, b) \sim (356^\circ, 1^\circ)$ and $(l, b) \sim (357^\circ.4, 0.^\circ 8)$. Loop 2 ranges from $l = 355^\circ.2$ to $356^\circ.6$, $b = 0^\circ.6$ to $2^\circ.2$, $v_{\rm LSR} = -90$ to -40 km s^{-1}, and has a mass of $8.2 - 16.1 \times 10^5 M_\odot$. The foot points are at $(l, b) \sim (355^\circ.4, 0^\circ.8)$ and $(l, b) \sim (356^\circ.1, 0^\circ.8)$. Both, loops 1 and 2, look like filamentary structures with a width of ~ 30 pc, and a length of ~ 400 pc. Torii et al. (2010a) present a multitransitional analysis of ^{12}CO, ^{13}CO, and C^{18}O towards the foot point of the GMLs placed towards $l \sim 356^\circ$. They identified and analyzed several features including two "U-shapes", which they propose that may be formed by the merging of two down flows between two loops as derived by magneto-hydrodynamics numerical simulations. Fujishita et al. (2009) discovered the "loop 3", placed in the positive-velocity range in $l \simeq 354^\circ - 359^\circ$. Kudo et al. (2011) performed ^{12}CO($J = 2-1$) and ($J = 3-2$) observations toward the complete loops 1 and 2, and a part of the loop 3, revealing detailed distributions of the molecular gas. They compute the line intensity ratio CO($J = 3-2$)/CO($J = 2-1$), which show that gas in the loops presents higher excitation conditions than in the disk. They derive a density of $10^{2.2} - 10^{4.7}$cm^{-3} and temperatures of $15-100$ K or higher. Isotopes studies (Riquelme et al. 2010a) suggest that gas is been accreted towards the foot point of the loops, and metastable inversion transitions observations of ammonia molecule (Riquelme et al., 2012, submitted) revealed high kinetic temperatures in those regions. These works

show the complexity of the zone and the importance of further studies on that regions.

In this paper we present high resolution mapping of 3mm molecular lines toward a molecular cloud placed at the foot point of the molecular loops discovered by Fukui et al. (2006). These observations allow us to derive the morphology, chemistry and the kinematics of the quiescent and shocked gas and to compare with model predictions using different molecular tracers.

2. Observations and data reduction

2.1. Observations

The observations were carried out using 22m Mopra telescope during September 2008, and August 2009. Located in the Southern hemisphere, and due to its high angular resolution and wide-bandwidth spectrometer, the Mopra telescope offers excellent capabilities to establish the physical conditions and chemical abundances of the molecular gas at the foot points of the loops. We used the digital mode filter bank MOPS in broad-band mode, covering 8 GHz of bandwidth simultaneously in four 2.2 GHz subbands, each of them with 8192 channel spaced by 0.27 MHz. Two polarizations are measured simultaneously.

Using on-the-fly (OTF) mapping mode (Ladd et al. 2005), we mapped a selected region of the M−3.8+0.9 molecular cloud (Riquelme et al. 2010b), performing squares of 5×5 arcm^2 to cover the complete region with a overlap of 30″ between them. The complete maps covered a region of $356^\circ.06 < l < 356^\circ.29$ and $0^\circ.645 < b < 1^\circ.1$. We used position switching mode with the off position placed at $(l, b) = (356^\circ.375, 1^\circ.5)$, which was checked to be free of emission, and observed in symmetric mode (one off per OTF scan). The spacing between scan raws was 12″, and each 5×5 arcmin^2 have 25 raws, taking 55 min to complete one map. For pointing correction we observed before each map the SiO maser "AH_Sco". The spectra were read out with 2 seconds of integration time. The system temperature was calibrated with a noise diode, and hot load (paddle) every 30 min. We observed two frequency setup centered at 89.41 GHz and 99.72 GHz which give us a broad-band range of 85.275 to 93.555 GHz and 95.585 to 103.866 GHz respectively.

2.2. Data reduction

The data were reduced using the LIVEDATA and GRIDZILLA packages. LIVEDATA is the processing software used to apply system temperature calibration, bandpass calibration, heliocentric correction, spectral smoothing and to write out the data in sdfits (Garwood 2000) format. GRIDZILLA is a regridding software package to convert the sdfits files to the FITS data cube (Jones et al. 2008). Using LIVEDATA we subtracted a robust first order polynomial baseline. With GRIDZILLA we regridded into data cubes with a Gaussian smoothing interpolation.

The resolution of the data is between 49.8″ and 50.9″ at 115 and 86 GHz respectively, which is obtained after convolution the Mopra beam with 36 arcsec FWHM Gaussian. The beam size of Mopra varies between 33 at 115 GHz to 36 arcsec at 86 GHz (Ladd et al. 2005). The size of the pixel is 15 arcsec in the cube fits. We obtain one data cube per molecule. The data cubes were cleaned using ImageJMadcuba[1] software for FFT and base line subtractions when it was needed.

[1] http://www.cab.inta-csic.es/madcuba

Table 1. RMS noise values for each molecular transition observed for the observed region of M−3.8 + 0.9 molecular cloud.

Molecule	Transition	Rest. Freq. [GHz]	RMS [mK]
SO	$2(2) - 1(1)$	86.093	50
$H^{13}CN$	$1 - 0$*	86.340	56
$H^{13}CO^+$	$1 - 0$	86.754	55
SiO	$2 - 1\ v = 0$	86.847	47
$HN^{13}C$	$1 - 0$*	87.091	50
HNCO	$4(0,4) - 3(0,3)$	87.925	49
HCN	$1 - 0$*	88.632	50
HCO^+	$1 - 0$	89.188	45
HNC	$1 - 0$*	90.664	48
HC_3N	$10 - 9$	90.979	44
CH_3CN	$5 - 4$*	91.979	51
^{13}CS	$2 - 1$	92.494	52
N_2H^+	$1 - 0$*	93.174	49

* have fine or hyperfine structure transitions.

3. Preliminary results and discussion

Following the list of most intense molecular transitions in the 3mm lines observed in Sgr B2 by Jones et al. (see Table 2 in 2008), we made one data cube per molecule. Table 1 shows the RMS noise values reached in each molecular line cube.

3.1. Morphology and kinematics

Fig. 1 presents the integrated intensity map for the observed region of M−3.8 + 0.9 cloud, in the velocity range from −140 to 20 km s^{-1}; the longitude-velocity map integrated in the whole latitude range observed, and the latitude-velocity map integrated in the whole longitude rage observed. In Fig. 2 shows the velocity structure of the molecular cloud in velocity integrated in ranges of 10 km s^{-1}. This has a narrow velocity width emission at positive velocities placed at $(l, b) \sim (356^\circ.25, 0^\circ.70)$, which corresponds to an ultracompact H II region (see Fig. 3), but this source with a radial velocity of $\sim$ 120 km s^{-1}, is not associated to the foot point as noted by Torii et al. (2010a). Therefore this source will not be discussed in this work.

We show the morphology and velocity structure using the HCN molecule, which presents the most intense emission. Fig. 2 shows a velocity gradient from the higher to lower velocities from the north-western to the south-eastern direction. We identified four main velocity components: from −140 to −70 km s^{-1}, from −70 to −40 km s^{-1}, from −40 to −20 km s^{-1}, and from −20 to 20 km s^{-1}. From Fig. 12 to 22 we show the integrated intensity in these velocity ranges in the most intense molecules. In these velocity ranges, we identify five main molecular complexes, which are indicated with green boxes in Fig. 4 on the HCN maps. In the velocity range from −140 to −70 km s^{-1}, the most prominent feature is the complex number 3, which shows an elongated structure with an abrupt sharp intensity decrease towards the eastern edge. In the velocity range from −70 to −40 km s^{-1}, the complexes 1, 2, and 4 appear. It is remarkable that the complex 4 also shows an elongated structure similar to that observed for the complex 3. In the velocity range from −40 to −20 km s^{-1}, we can see the complex 5 which is an elongated feature, perpendicular to the Galactic plane. In the last velocity range, from −20 to 20 km s^{-1}, the emission shows a shell-like structure which appears over the complete molecular cloud and is clearly seen in HCO^+ and HNC maps (Figs. 13 and 18). Fig. 5 shows latitude-velocity maps integrated in longitude steps of

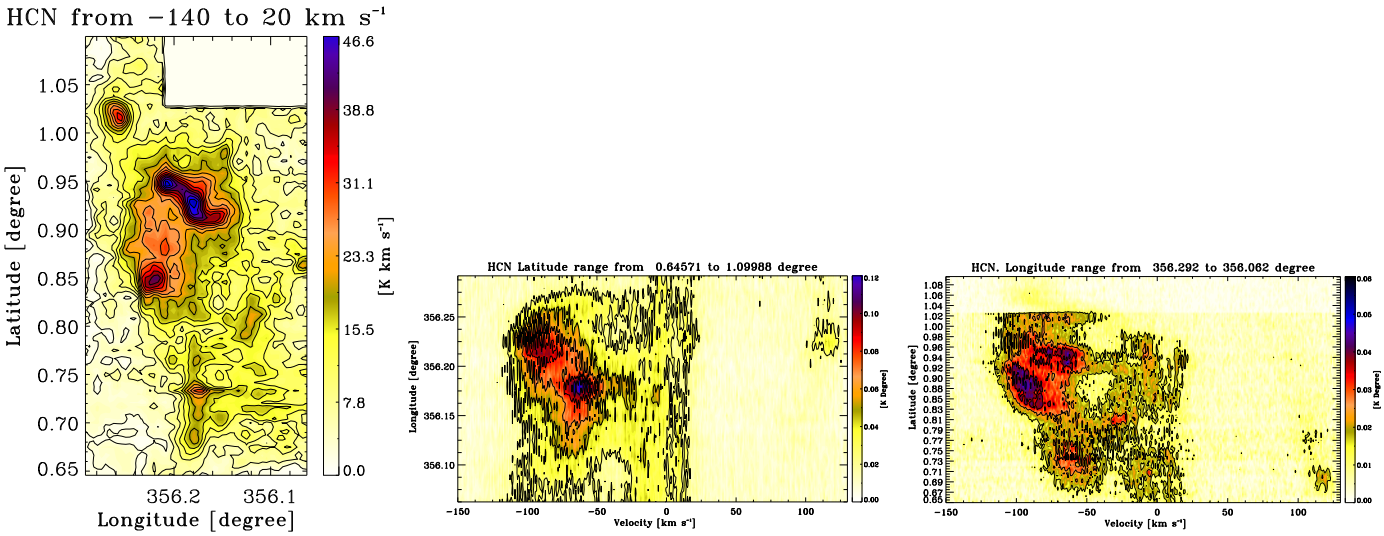

Fig. 1. HCN emission of the M−3.8 + 0.9 cloud: Left. Integrated intensity map in the velocity range from −140 to −20 km s^{-1}. The dashed lines show the mapped region. Center. Longitude-velocity plot integrated over the whole latitude range (from b = 0.64° to b = 1.10°). Right. Latitude-velocity plot integrated over the whole longitude range (from l = 356.29° to 356.06°)

108" in HCO$^+$, HCN, and SiO. In this figure we can see the two "U-shapes" identified by Torii et al. (2010b).

3.2. The SiO emission, an useful tool tracing shocks

We also plot the SiO emission, which is a well known shock tracer (Martín-Pintado et al. 1992), in velocity integrated ranges of 10 km s^{-1} (Fig. 10). The most intense features are the complex 3 and complex 4. The complex 3 is visible from −100 km s^{-1} to −70 km s^{-1}, and the complex 4, which is visible from −70 to −50 km s^{-1}. Both complexes show a filamentary structure perpendicular to the Galactic plane, which indicates that the shocks in this region are confined in a thin layer. It is remarkable that the SiO emission appears preferably elongated perpendicular to the Galactic plane, showing long and thin filaments. In contrast the HCN and HCO$^+$ emission reveal a more extended emission, which is widespread ranging from −110 to 10 km s^{-1}.

In Fig. 6 we show the integrated intensity ratio of the SiO to HCO$^+$ in velocity ranges of 10 km s^{-1}. While it is clear that both, the complex 3 and 4 are intense in both molecules; HCO$^+$ dominates towards the complex 2, showing the lowest ratio, and the SiO dominates in complex 1 (which almost does not present HCO$^+$ emission in comparison with HCN) and in complex 5. There are differences up to a factor 25 between the region where the HCO$^+$ dominate in the complex 2, and where the SiO dominates in the complex 5 and in complex 1. Fig. 11 shows the ratio of the HCO+ to HNC integrated in velocity ranges of 10 km s^{-1}.

3.3. Spectra towards selected regions

We obtain the integrated spectrum (Fig. 8) for the most intense zone of each region, which are indicated with green contours in Fig. 4. We also selected three regions chosen from the four velocity ranges as the places where the differences between the SiO and the HCO$^+$ are more evident. Those small regions are shown in red boxes in Fig. 4. The profiles are shown in Fig. 9. The integrated spectra were obtained using ImageJMadcuba.

Fig. 7 shows the ratio of the integrated intensity of SiO to HCO$^+$ in each of the regions selected in Fig. 4. The velocity range used for the integration is shown in the shadowed rectangle in the Fig. 8 and 9. This plot shows variations for each selected region between both molecular emission, which indicates differences in the chemistry associated to the heating processes throughout this molecular cloud.

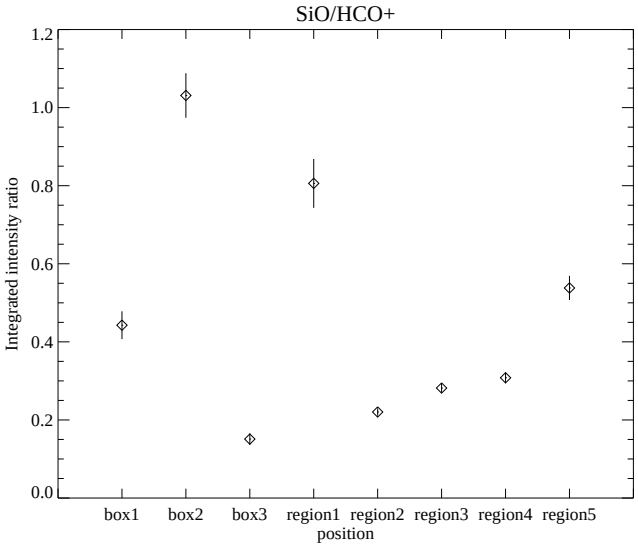

Fig. 7. Integrated intensity ratio of the SiO to HCO$^+$ emission for the selected regions shown in Fig. 4. The figure shows clear differences in the ratio in different regions.

4. Summary

The preliminary analysis of the data shows structures at small scale in SiO emission, with narrower line profiles than those of, e.g, HCO$^+$ or HCN, which indicate that the shocks are dynamically confined. The data also shows clear differences between different molecular tracers, e.g., between the SiO and HCO$^+$ emission, which would indicate differences in the physical properties and chemistry within the cloud.

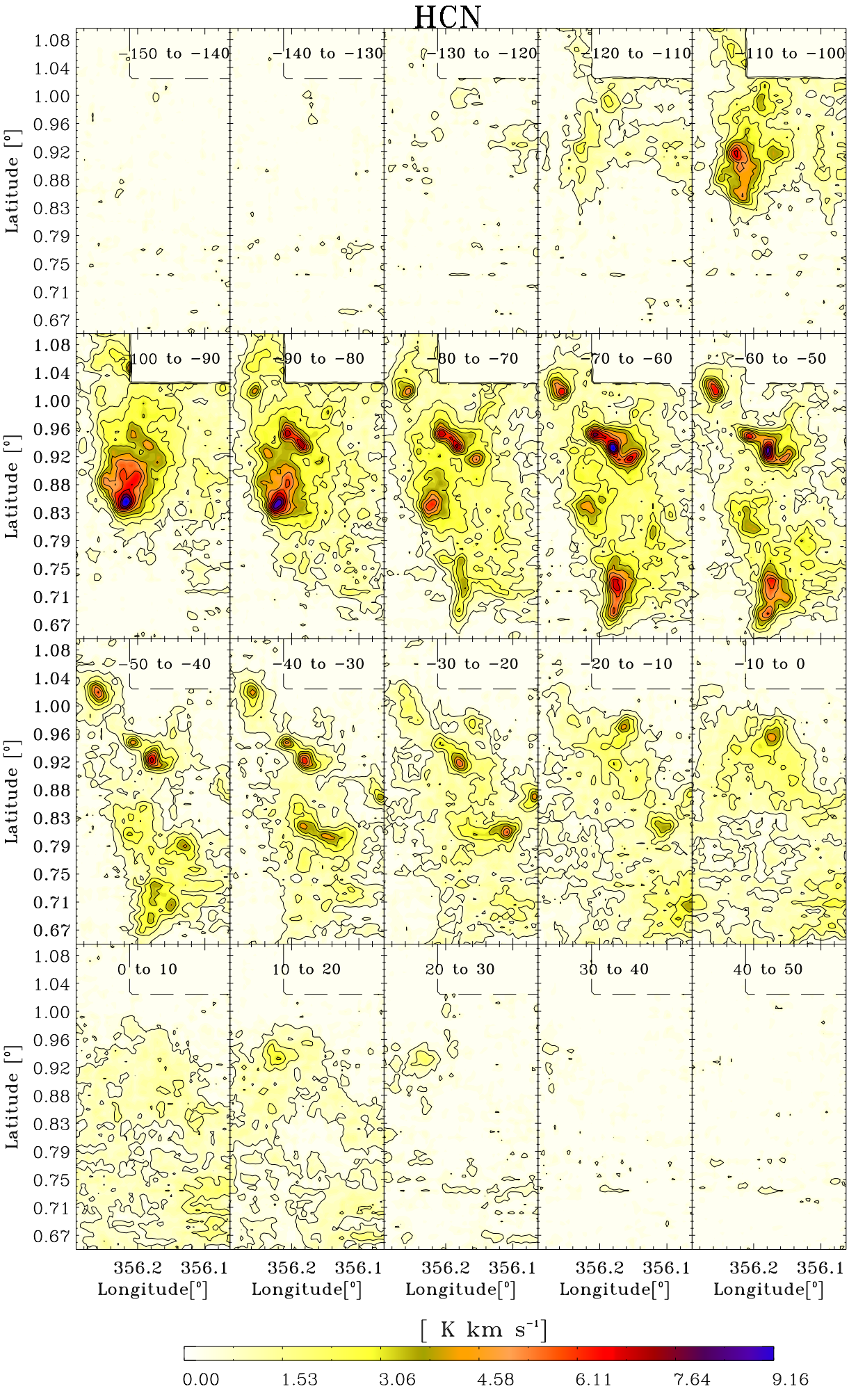

Fig. 2. Integrated intensity of the M−3.8 + 0.9 molecular cloud in HCN (1 − 0) in velocity intervals of 10 km s^{-1}.

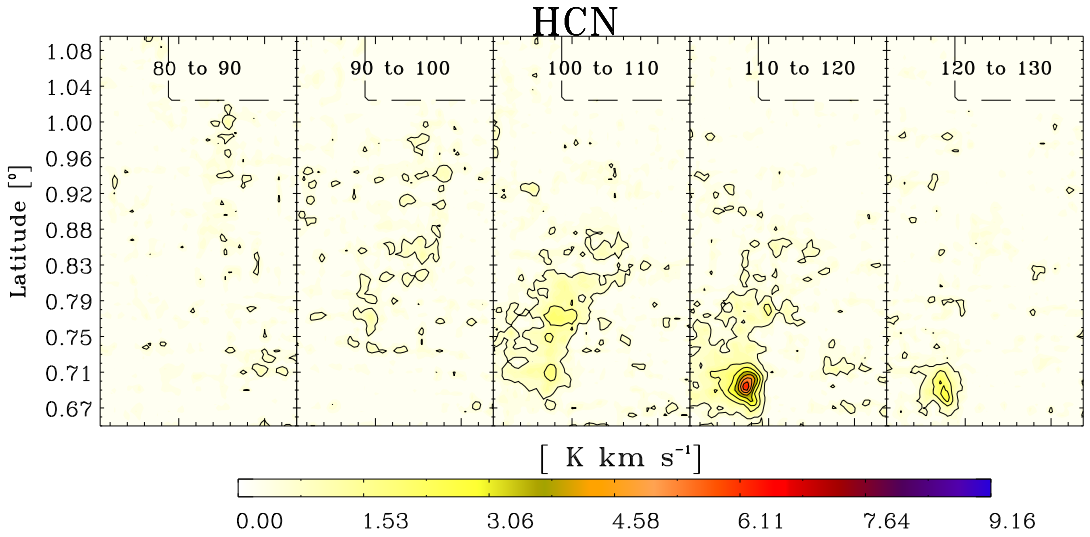

Fig. 3. Integrated intensity of the M−3.8 + 0.9 molecular cloud in HCN (1 – 0) in velocity intervals of 10 km s^{-1}.

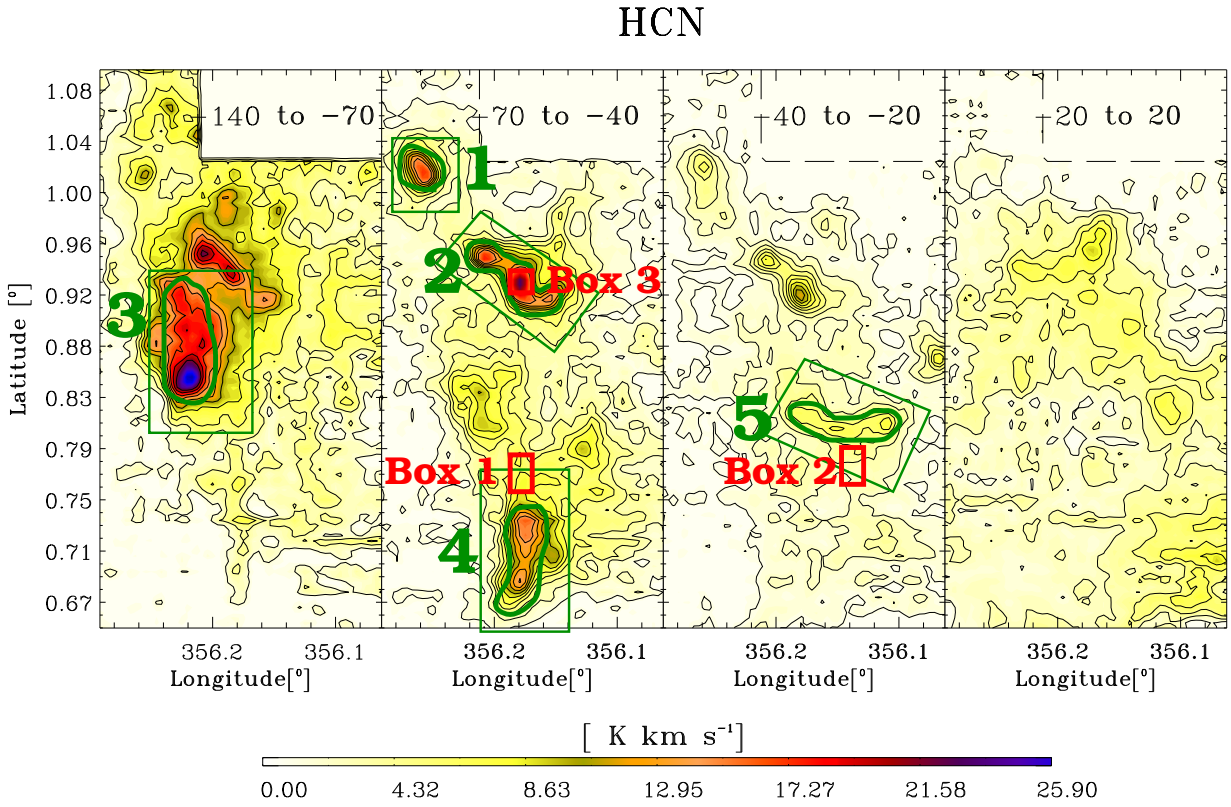

Fig. 4. Position of the five molecular complexes discussed in the text. The green contours show the selected region from where we obtain the integrated spectrum.

Acknowledgements. D.R. was supported by DGI grant AYA 2008-06181-C02-02. J.M-P. and S.M. have been partially supported by the Spanish MICINN under grant number ESP2007-65812-C02-01 and AYA2010-21697-C05-01.

References

Bitran, M., Alvarez, H., Bronfman, L., May, J., & Thaddeus, P. 1997, A&AS, 125, 99
Fujishita, M., Torii, K., Kudo, N., et al. 2009, ArXiv e-prints
Fukui, Y., Yamamoto, H., Fujishita, M., et al. 2006, Sci., 314, 106
Garwood, R. W. 2000, in Astronomical Society of the Pacific Conference Series, Vol. 216, Astronomical Data Analysis Software and Systems IX, ed. N. Manset, C. Veillet, & D. Crabtree, 243
Jones, P. A., Burton, M. G., Cunningham, M. R., et al. 2008, MNRAS, 386, 117
Jones, P. A., Burton, M. G., Cunningham, M. R., et al. 2011, ArXiv e-prints
Kudo, N., Torii, K., Machida, M., et al. 2011, PASJ, 63, 171
Ladd, N., Purcell, C., Wong, T., & Robertson, S. 2005, Publications of the Astronomical Society of Australia, 22, 62
Martín-Pintado, J., Bachiller, R., & Fuente, A. 1992, A&A, 254, 315
Morris, M. & Serabyn, E. 1996, ARA&A, 34, 645
Riquelme, D., Amo-Baladrón, M. A., Martín-Pintado, J., et al. 2010a, A&A, 523, A51
Riquelme, D., Bronfman, L., Mauersberger, R., May, J., & Wilson, T. L. 2010b, A&A, 523, A45
Torii, K., Kudo, N., Fujishita, M., et al. 2010a, PASJ, 62, 675

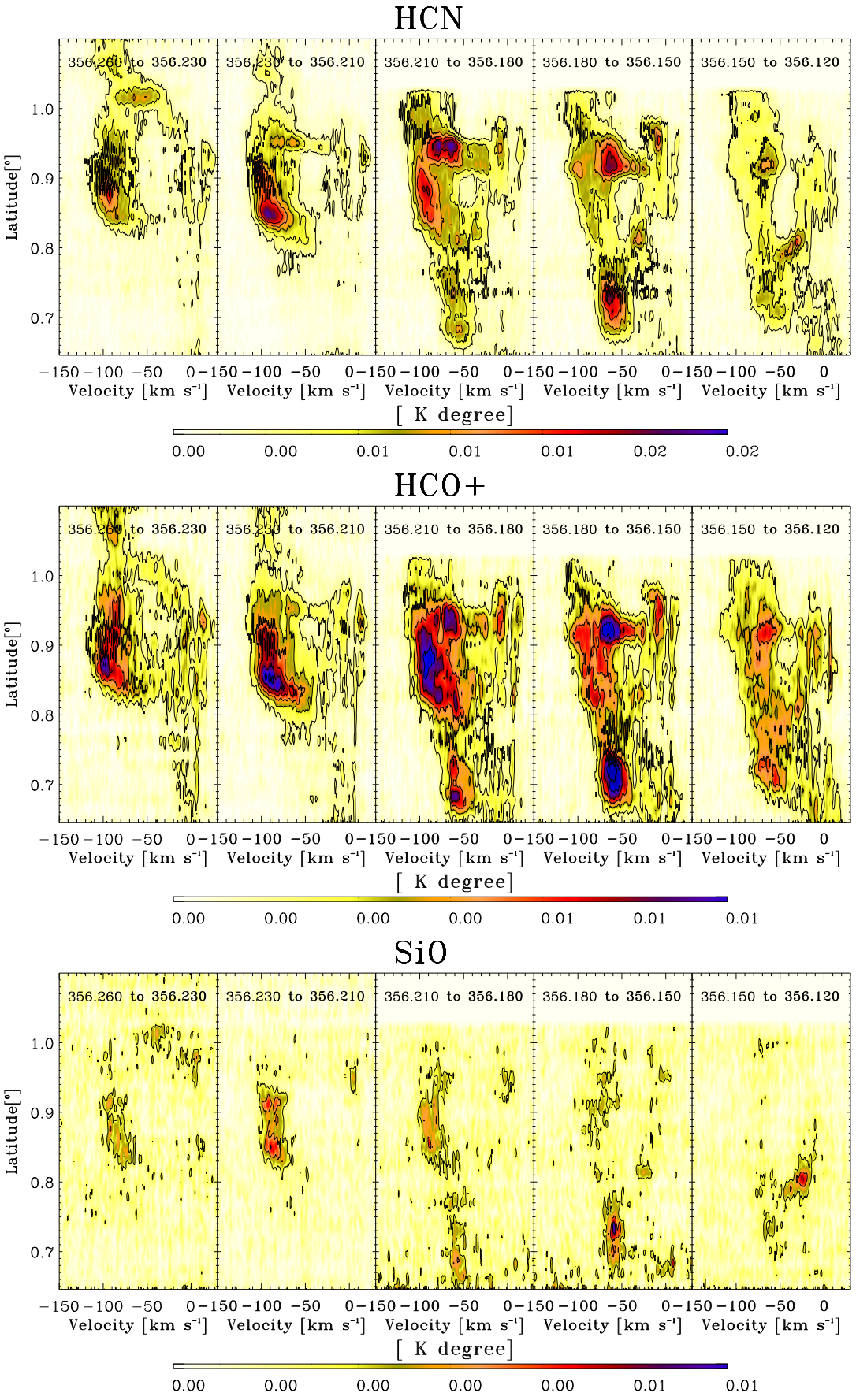

Fig. 5. latitude-velocity maps of the HCN, HCO^+, and SiO emission integrated in longitude steps of 108". It is possible to see the two "U-shapes" discussed by Torii et al. (2010b)

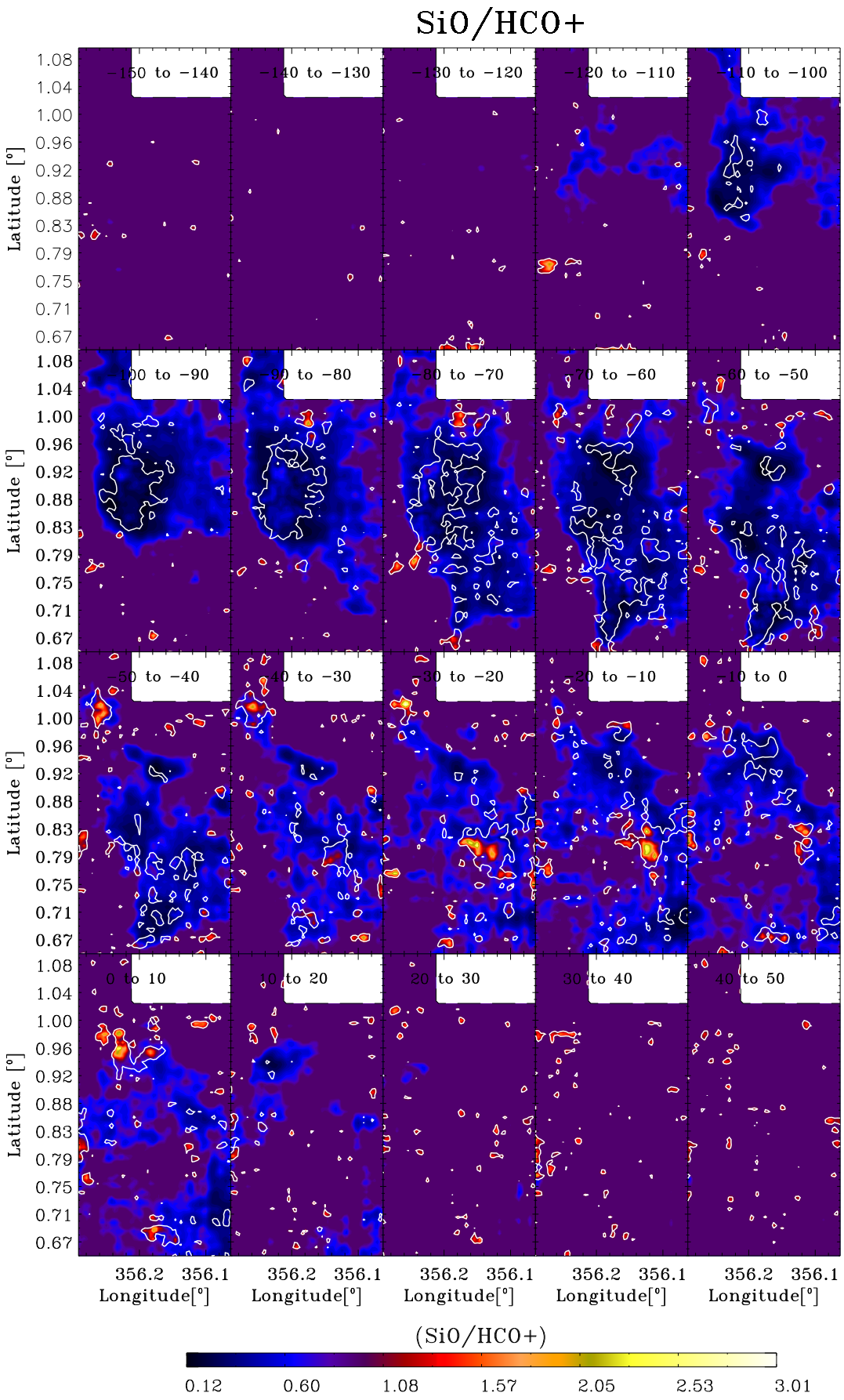

Fig. 6. Ratio of the integrated intensity of SiO(2 – 1) to HCO^+, in velocity intervals of 10 km s^{-1}.

Torii, K., Kudo, N., Fujishita, M., et al. 2010b, PASJ, 62, 1307

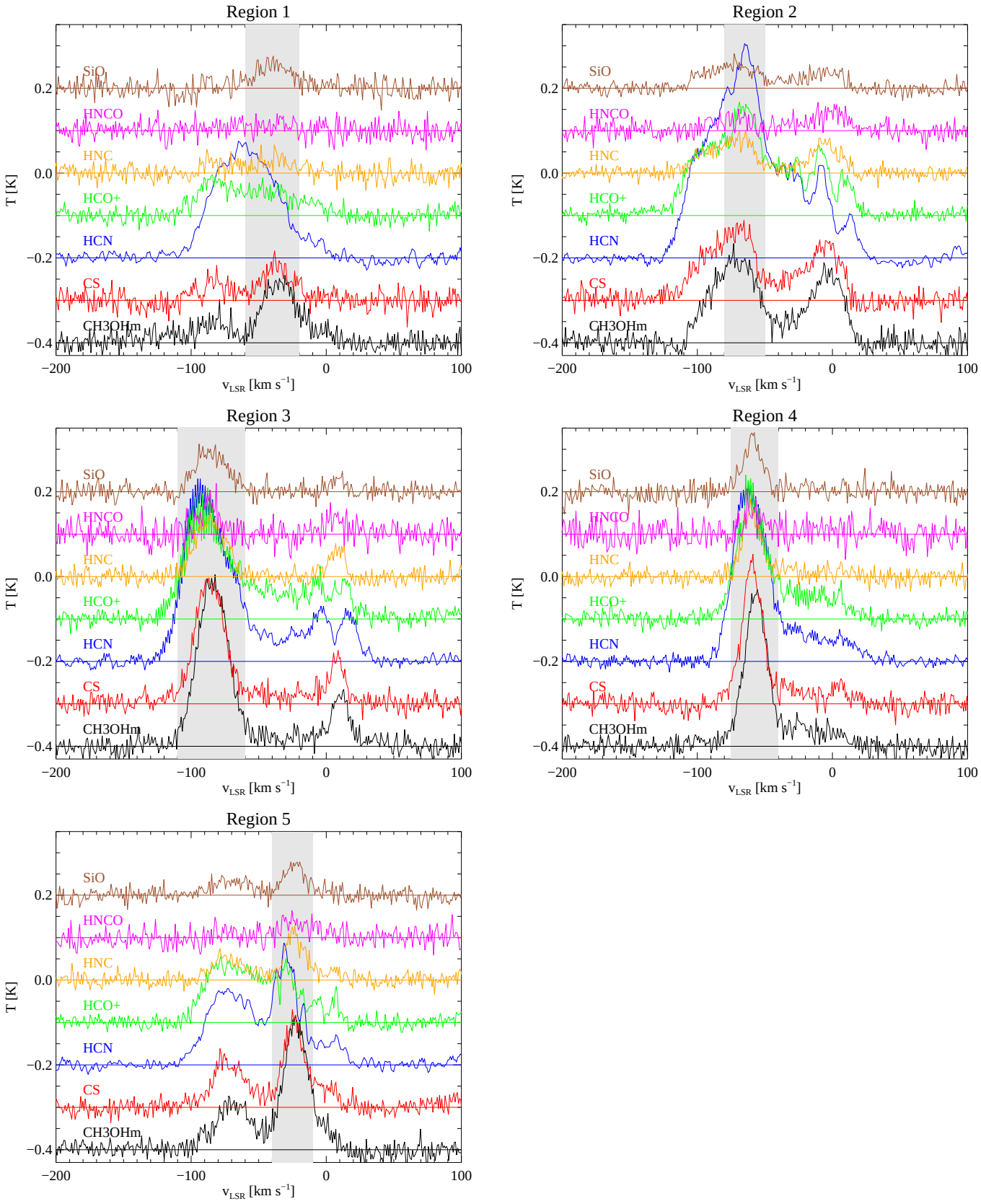

Fig. 8. Integrated spectrum for each selected region. The shadowed region shows the velocity range used.

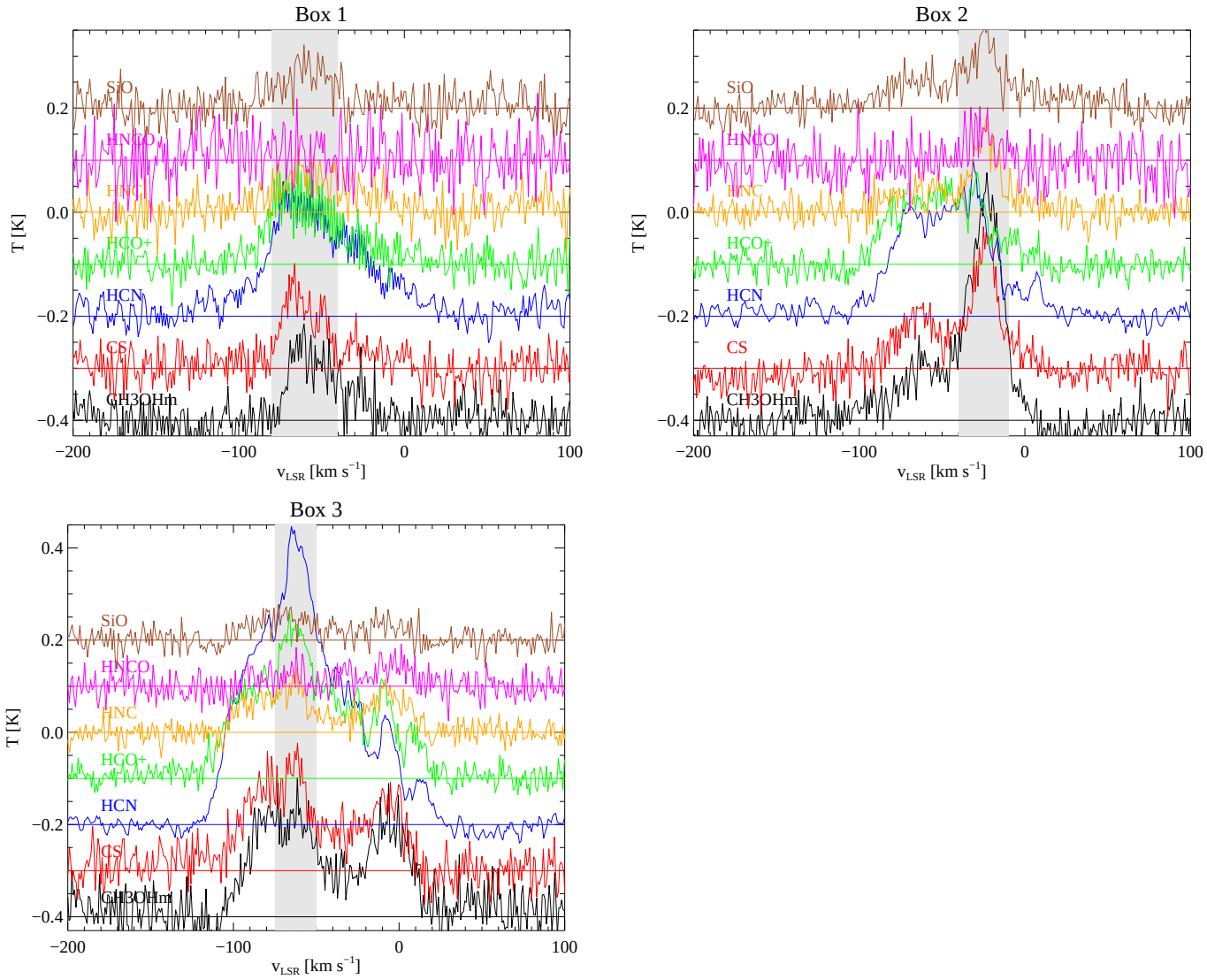

Fig. 9. Integrated spectrum for each selected region showed in red boxs in Fig. 4. The shadowed region shows the velocity range used.

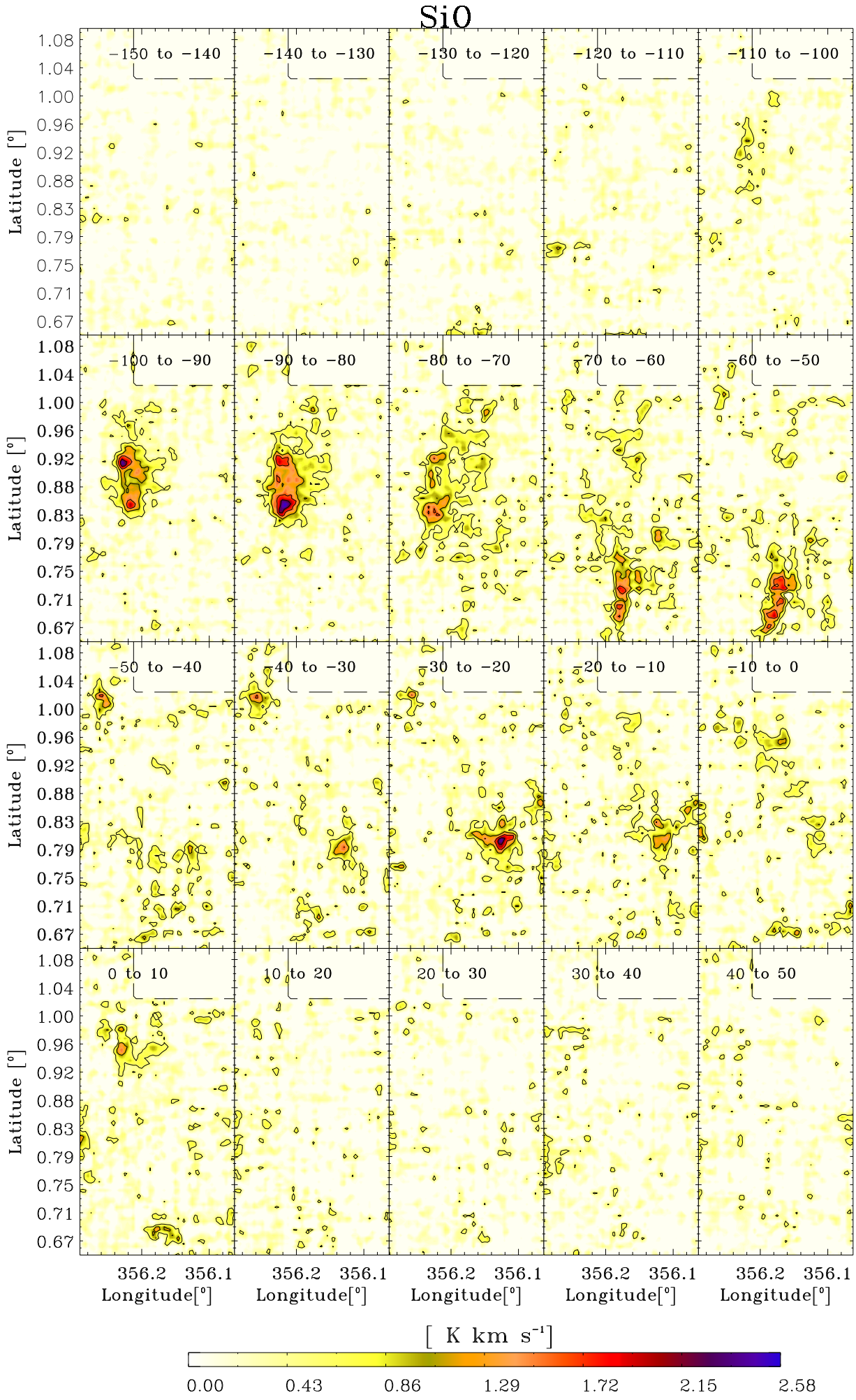

Fig. 10. Integrated intensity of the M−3.8 + 0.9 molecular cloud in SiO (2 − 1) in velocity intervals of 10 km s^{-1}.

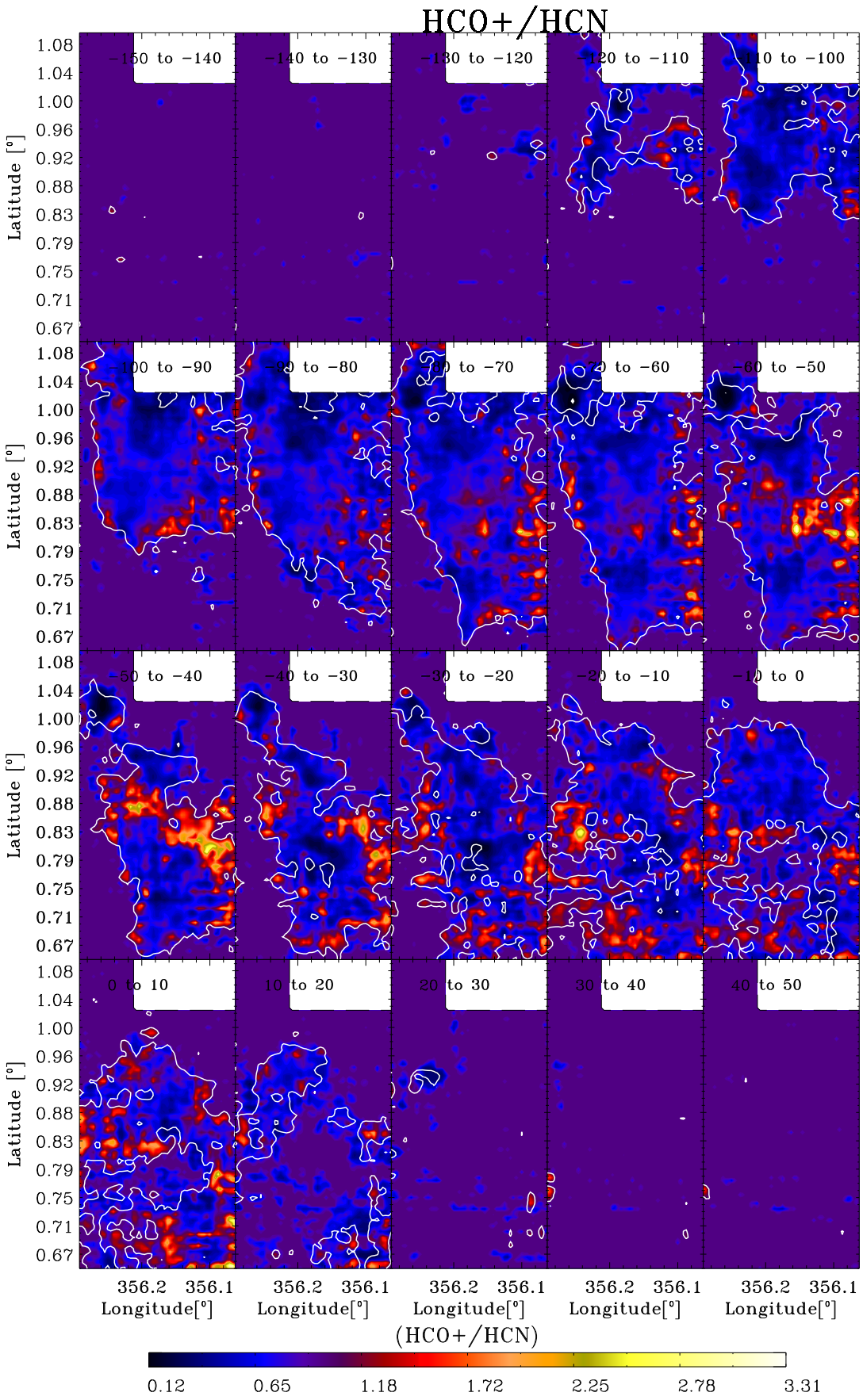

Fig. 11. Ratio of the integrated intensity of HCO^+ to HCN, in velocity intervals of 10 km s^{-1}.

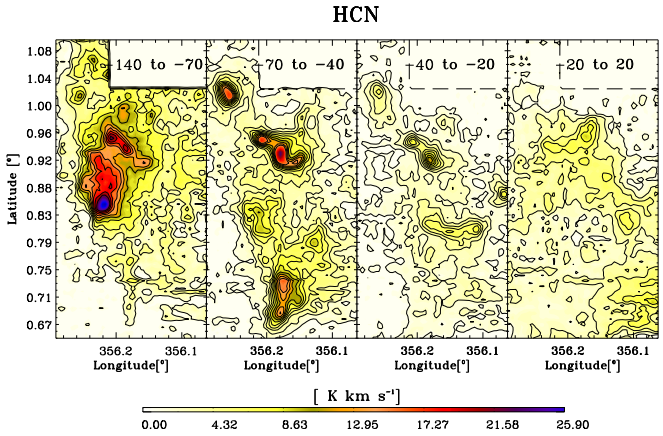

Fig. 12. HCN. From left to rigth: velocity range from -110 to -70 km s^{-1}; -70 to -40 km s^{-1}, -40 to -20 km s^{-1} and -20 to 20 km s^{-1}

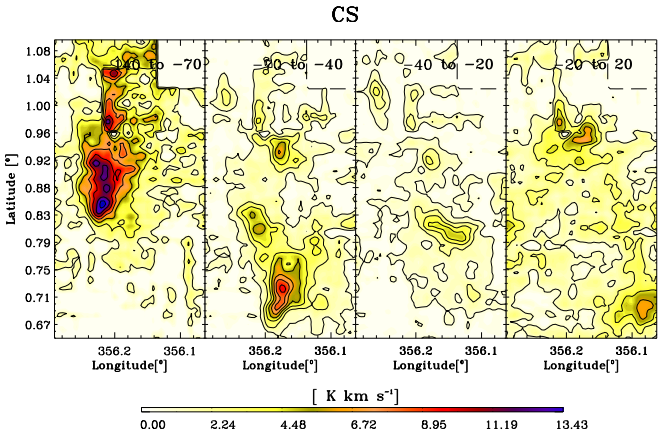

Fig. 15. CS. From left to rigth: velocity range from -110 to -70 km s^{-1}; -70 to -40 km s^{-1}, -40 to -20 km s^{-1} and -20 to 20 km s^{-1}

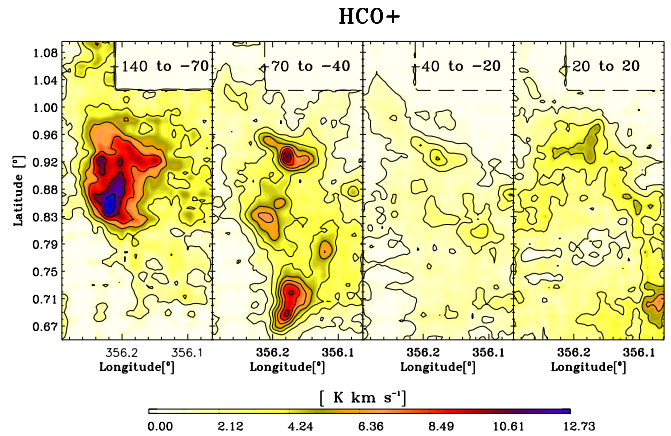

Fig. 13. HCO$^+$. From left to rigth: velocity range from -110 to -70 km s^{-1}; -70 to -40 km s^{-1}, -40 to -20 km s^{-1} and -20 to 20 km s^{-1}

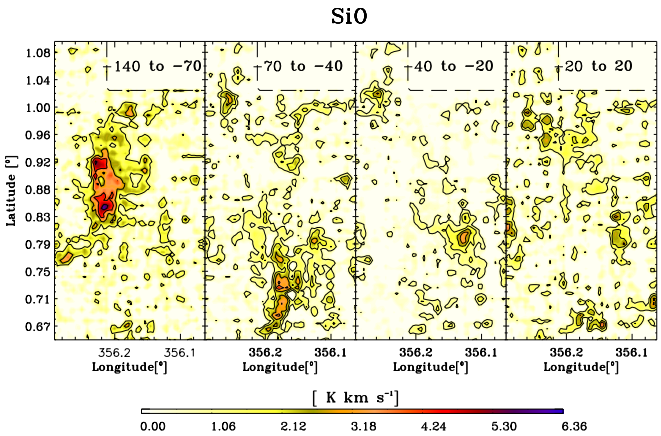

Fig. 16. SiO. From left to rigth: velocity range from -110 to -70 km s^{-1}; -70 to -40 km s^{-1}, -40 to -20 km s^{-1} and -20 to 20 km s^{-1}

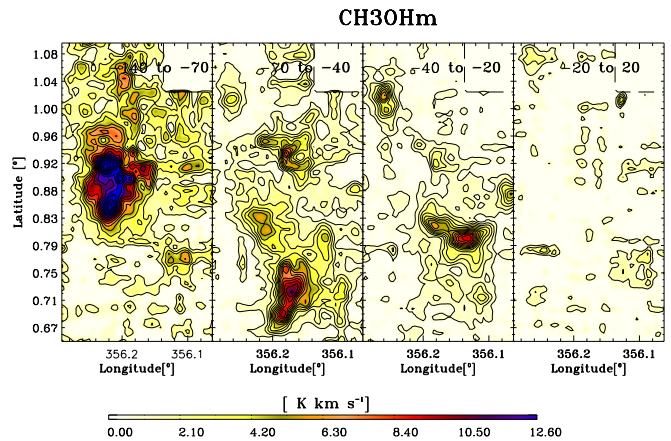

Fig. 14. CH_3OH. From left to rigth: velocity range from -110 to -70 km s^{-1}; -70 to -40 km s^{-1}, -40 to -20 km s^{-1} and -20 to 20 km s^{-1}

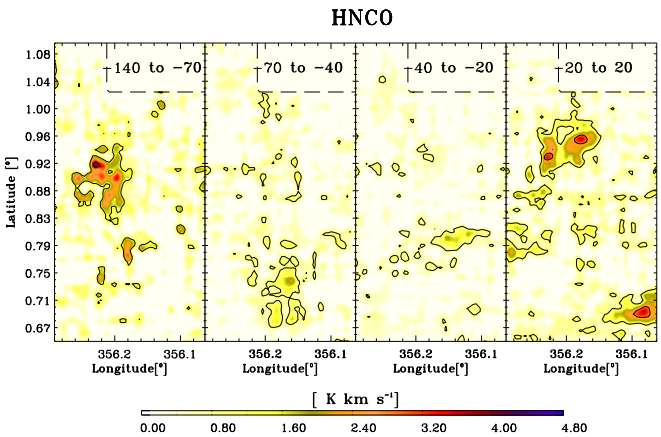

Fig. 17. HNCO. From left to rigth: velocity range from -110 to -70 km s^{-1}; -70 to -40 km s^{-1}, -40 to -20 km s^{-1} and -20 to 20 km s^{-1}

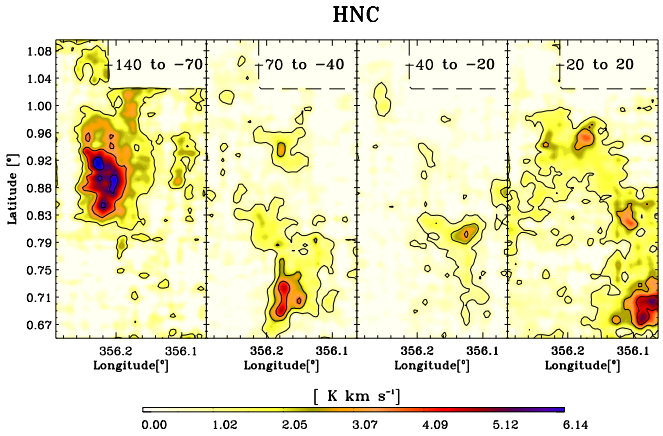

Fig. 18. HNC. From left to rigth: velocity range from -110 to -70 km s^{-1}; -70 to -40 km s^{-1}, -40 to -20 km s^{-1}and -20 to 20 km s^{-1}

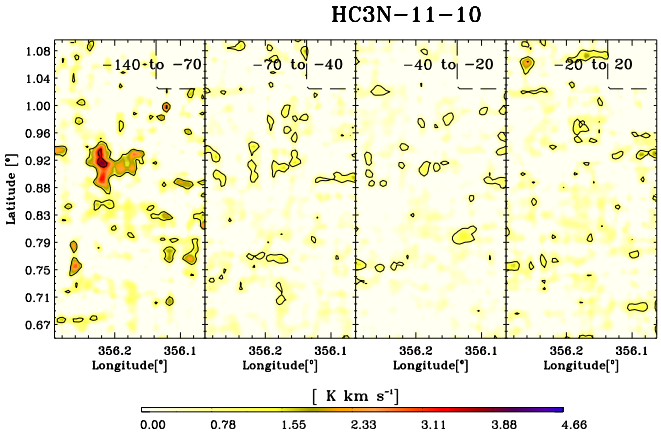

Fig. 21. HC_3N (11-10). From left to rigth: velocity range from -110 to -70 km s^{-1}; -70 to -40 km s^{-1}, -40 to -20 km s^{-1}and -20 to 20 km s^{-1}

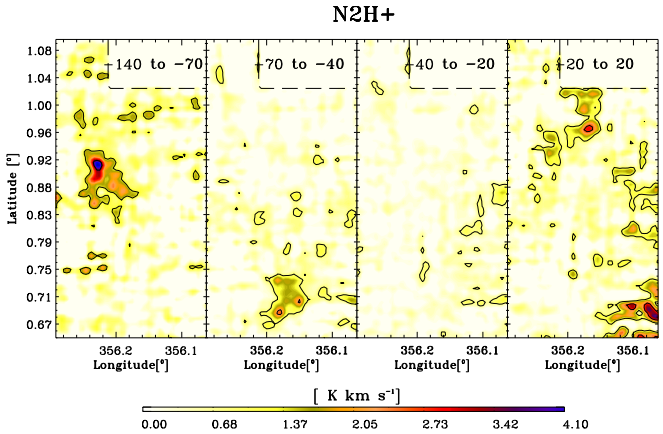

Fig. 19. N_2H^+. From left to rigth: velocity range from -110 to -70 km s^{-1}; -70 to -40 km s^{-1}, -40 to -20 km s^{-1}and -20 to 20 km s^{-1}

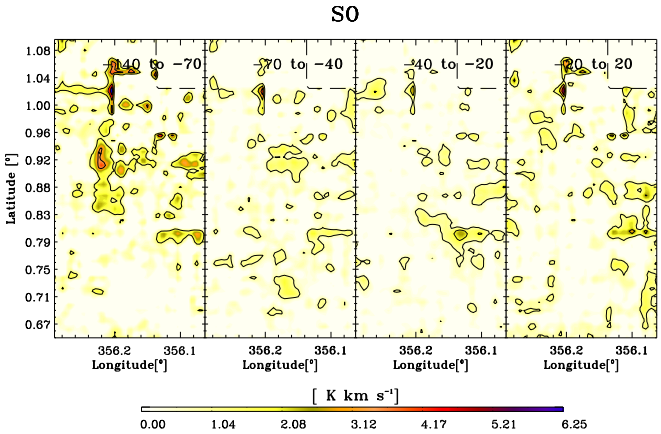

Fig. 22. SO (2-1). From left to rigth: velocity range from -110 to -70 km s^{-1}; -70 to -40 km s^{-1}, -40 to -20 km s^{-1}and -20 to 20 km s^{-1}

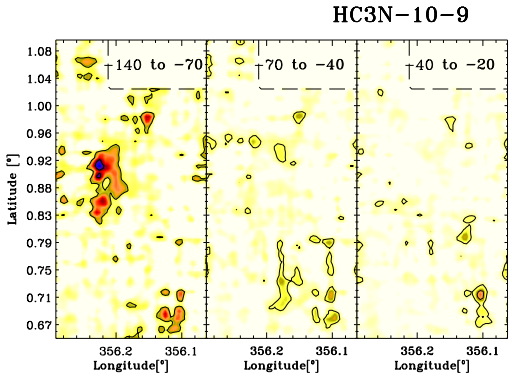

Fig. 20. HC_3N (10-9). From left to rigth: velocity range from -110 to -70 km s^{-1}; -70 to -40 km s^{-1}, -40 to -20 km s^{-1}and -20 to 20 km s^{-1}

Chapter 7

Conclusions

In this thesis we have studied the molecular clouds in the Galactic center region, with special emphasis in the zones where these molecular clouds interact with matter coming from the disk, and from high latitude clouds in the halo of the Galaxy (disk-halo interaction).

First, we performed a large-scale study of the molecular clouds in the GC region in the 3-mm rotational transitions of SiO ($J = 2-1$), HCO^+ ($J = 1-0$), and $H^{13}CO^+$ ($J = 1-0$). All the species were widely detected throughout the Galactic center region, showing the characteristic asymmetry in longitude, with most of the emission toward $l > 0$ and $v > 0$. The main conclusions of this study are the following:

- We identify 51 molecular clouds, where 33 belong to the Galactic center region and 18 to the Galactic disk or local gas.

- For the 51 molecular clouds identified, we derived the luminosity ratios SiO($J = 2 \rightarrow 1$)/CO($J = 1 \rightarrow 0$) and HCO^+($J = 1 \rightarrow 0$)/CO($J = 1 \rightarrow 0$). These luminosity ratios, as well as the velocity widths, are higher for Galactic center clouds than for typical disk clouds. The highest SiO($J = 2 \rightarrow 1$)/CO($J = 1 \rightarrow 0$) luminosity ratios for the Galactic center region correspond, in general, to the highest velocity widths. The average of the luminosity ratio of SiO(J = 2 → 1)/CO(J = 1 → 0) in clouds belonging to the Galactic center region is 0.0049±0.0005 and for disk clouds is 0.0034 ± 0.0009. The luminosity ratio of HCO^+(J = 1 → 0)/CO(J = 1 → 0) in the Galactic center is 0.035 ± 0.003, and for disk clouds is 0.015 ± 0.004.

- The clouds M+3.2+0.3, M-3.8+0.9, M+5.3-0.3, and 1.3° complex show high SiO to HCO^+ ratios, which may indicate that shocks are the main heating sources. Toward the densest regions, the SiO($J = 2 \rightarrow 1$)/HCO^+($J = 1 \rightarrow 0$) ratio is low (Sgr A and Sgr B regions). The SiO emission can be correlated with several phenomena, and we related the SiO predominance over the HCO^+ emission to the molecular loops, formed by a Parker instability, where the shocks are ongoing.

The large-scale survey allowed the identification of shock regions, as traced by the enhancements of the SiO emission with respect to HCO^+. Such shocks are expected in the barred potential model, and in the foot points of the giant molecular loops. This zones where named after "interaction regions". Furthermore we performed detailed

studies using larger and more sensitive telescopes, such as the IRAM 30m, Effelsberg, and Mopra telescopes. We selected 9 positions placed in the "interaction regions": 5 positions are located above or below the plane in the GMLs that were referred by us as "halo", 2 are located in the intersection places where the X1 orbits plunges into the X2 orbits in the barred potential model ("disk X1" and "disk X2"), and 2 positions are tracing normal GC gas which were referred as "disk" sources (one towards Sgr B2, and other at large longitude but close to the plane at $(l, b) \sim (5°.7, 0°)$). We wanted to know whether the shocks were produced by accreted molecular matter towards the Galactic center, or on contrary, whether the shocks were originated by ejection of the material towards high latitude throughout supernova explosions. Using the IRAM 30m telescope, we observed the HCO^+, HCN, HNC and their ^{13}C isotopic substitutions to derive the $^{12}C/^{13}C$ isotopic ratio, which was used as a measure of the processing degree of the gas. The molecular gas at the GC region has a highly processed gas (high metallicity), which is higher than elsewhere in the Galaxy (see e.g., Wilson 1999, and references therein). Therefore, if the isotopic ratios are similar to the typical value derived for the GC ($^{12}C/^{13}C \sim 20 - 25$), it would indicate that the gas was processed by stars and the gas is being ejected from the plane. On contrary, if the isotopic ratio shows a low metallicity, it would indicate that the gas is being accreted by the center of the Milky Way, from a region with less processed by stars. We determined lower limits to the $^{12}C/^{13}C$ isotopic ratio. In contrast to the values found in the disk sources (4 to 30), we found high isotopic ratios toward the halo positions (> 40 to > 70) and X1-X2 orbit interactions (> 42 to > 56). Our results are consistent with a scenario where gas from the halo is accreted toward the disk and with the transfer of gas from the outskirt of the disk to the GC through X1 and X2 orbits, as suggested by the potential bar scenario.

The next step of this thesis was to derive the physical conditions of the gas in the "interaction regions", such as the kinetic temperatures and densities. As we mention in §1.2.1.3, the kinetic temperatures of the molecular clouds in the GC region are relatively high, but they are unknown in the high latitude and large velocity clouds associated with the disk-halo interaction regions studied in this thesis. We have used the metastable inversion transitions of NH_3 from $(J, K) = (1, 1)$ to $(6, 6)$ to derive the gas kinetic temperature toward the six positions visible from the Effelsberg telescope. We also observed, using the IRAM 30m telescope, other molecules like SiO, HNCO, CS, $C^{34}S$, $C^{18}O$, and ^{13}CO, to derive the densities and to trace different physical processes (shocks, photodissociation, dense gas). The abundances of these molecules were used to reveal the heating mechanisms affecting the molecular gas in these regions. The conclusions of this work are summarized as follows:

- The GC molecular gas shows roughly two kinetic temperature components in the CMZ. Only the warm kinetic temperature regime is found in the "halo" positions, and in the Disk 2 position, which corresponds to Sgr B2.

- The kinetic temperatures are high, not only in the typical GC clouds, but also in the high latitude and high velocity clouds. Therefore, the efficient heating mechanism of the molecular clouds seems to be a general characteristic of the gas in the disk and also in the halo of the GC.

- Shocks are a compelling heating mechanism of the molecular clouds in the GC region. This is supported by the high gas kinetic temperature and by the increased SiO abundance in the location where shock are expected. Due to the fragile nature of HNCO (enhanced by shocks, but easily photodissociated by UV radiation and strong shocks), this molecule tells us about the characteristics of the shocks. Other heating mechanisms previously proposed for the GC can however not be ruled out.

- The high kinetic temperature in the X1 orbits and in the foot points of the GMLs is consistent with the bar potential and GMLs scenario as origins for the shocks.

Finally, to reveal the morphology and the kinematics of the shocked gas in the foot points of the GMLs, we use the 22m Mopra telescope to map one molecular cloud in several 3-mm molecular lines. This work is in progress, and the preliminary analysis of the data shows structures at small scale in the SiO emission, with narrower line profiles than those of, e.g, HCO^+ or HCN, which indicate that the shocks are dynamically confined. The data also shows clear differences between different molecular tracers, e.g., between the SiO and HCO^+ emission, which would indicate differences in the physical properties and chemistry within the cloud.

Overall, the results presented and discussed in this thesis give important clues to the undersanding of the nature of the molecular clouds in the Galactic center region. They evidence the presence of shocks and are consistent with the shock origin of the heating mechanisms. Furthermore, this work strongly supports the accretion of the gas towards the GC (through bar potential and GMLs) as the cause of such shocks.

Conclusiones

En esta tesis se realizó un estudio de las nubes moleculares de la región del centro Galáctico (CG), poniendo especial énfasis en las zonas donde estas nubes interaccionan con el gas proveniente del disco, y desde altas latitudes en el halo de nuestra Galaxia (interacción disco-halo).

Primero, se realizó un estudio a gran escala de las nubes moleculares de la región del centro Galáctico en las transiciones rotacionales a longitud de onda de 3 mm de SiO ($J = 2 - 1$), $HCO^+(J = 1 - 0)$, y $H^{13}CO^+(J = 1 - 0)$. Todas las moléculas fueron ampliamente detectadas a lo largo de la región del centro Galáctico, mostrando la asimetría característica en longitud, donde la mayoría de la emisión se encuentra hacia $l > 0$ y $v > 0$. Las principales conclusiones de este trabajo son las siguientes:

- Se identificaron 51 nubes moleculares, de las cuales 33 pertenecen al centro Galáctico y 18 al disco o a gas local en la línea de visión.

- De las 51 nubes moleculares identificadas, se derivaron las razones de luminosidad SiO(J = 2 → 1)/CO(J = 1 → 0) y $HCO^+(J = 1 \rightarrow 0)$/CO($J = 1 \rightarrow 0$). Esas razones de luminosidad, al igual que los anchos en velocidad, son mayores en las nubes del centro Galáctico que en las nubes del disco. Los valores más altos de la razón de luminosidad SiO($J = 2 \rightarrow 1$)/CO($J = 1 \rightarrow 0$) en la región del centro Galáctico, corresponden en general a los mayores anchos de velocidad. El promedio de la razón de luminosidad de SiO($J = 2 \rightarrow 1$)/CO($J = 1 \rightarrow 0$) en nubes pertenecientes al centro Galáctico es de 0.0049 ± 0.0005, y para las nubes del disco es de 0.0034 ± 0.0009. La razón de luminosidad de $HCO^+(J = 1 \rightarrow 0)$/CO($J = 1 \rightarrow 0$) para las nubes del CG es de 0.035 ± 0.003, y para las nubes del disco es de 0.015 ± 0.004.

- Las nubes M+3.2+0.3, M−3.8+0.9, M+5.3−0.3, y el complejo molecular a $l = 1°.3$ tienen una alta razón SiO/HCO^+, lo cual puede indicar que los choques son el principal mecanismo de calentamiento. Esta razón es baja hacia las regiones más densas (hacia las regiones de Sgr A y Sgr B). La emisión de SiO puede ser correlacionada con varios fenómenos. En este trabajo, se relacionó la predominancia de la emisión de SiO sobre la de HCO^+ con los bucles moleculares gigantes formados por una inestabilidad de Parker, donde los choques estarían en curso.

El estudio a gran escala permitió la identificación de las regiones de choques, trazadas mediante el enriquecimiento de la emisión de SiO con respecto a la de HCO^+. Tales choques son esperados en el modelo de potencial barrado Galáctico, y en los pies de los bucles gigantes de gas molecular. Estas zonas fueron llamadas como "regiones

de interacción". Luego se desarrolló un estudio detallado de estas regiones usando telescopios más grandes y más sensibles, tales como IRAM 30-m, Effelsberg y Mopra. Se seleccionaron 9 posiciones ubicadas en las 'regiones de interacción": 5 posiciones ubicadas arriba y abajo del plano en los bucles gigantes de gas molecular que fueron llamadas "halo", 2 posiciones en los lugares de interacción donde las órbitas X1 se intercectan con las órbitas X2 en el potencial barrado ("disco X1" and "disco X2"), y 2 posiciones trazando gas típico del centro Galáctico que fueron llamadas "disco" (una hacia Sgr B2, y otra en el plano de la Galaxia en $(l, b) \sim (5^\circ.7, 0^\circ)$).

Se quiso saber si los choques son producidos debido a acreción de material molecular hacia el CG, o por el contrario, si son producidos por eyección de material hacia altas latitudes mediante explosiones de supernovas. Usando el telescopio de 30 metros de IRAM, se observaron las moléculas de HCO^+, HCN, HNC y sus isótopos ^{13}C para derivar la razón isotópica $^{12}C/^{13}C$, que fue usada para medir el grado de procesamiento del gas. El gas molecular del centro Galáctico tiene un alto grado de procesamiento (alta metalicidad), que es mayor que en cualquier otro lugar de la Galaxia (ver por ejemplo, Wilson 1999, y las referencias de ese trabajo). Por lo tanto, si las razones isotópicas derivadas hacia las regiones de interacción son similares a los valores normales del centro Galactico ($^{12}C/^{13}C \sim 20-25$), indicaría que el gas fue procesado por las estrellas y esta siendo eyectado desde el plano. Por el contrario, si las razones isotópicas mostraran una baja metalicidad, indicaría que el gas esta siendo acretado por el centro de la Vía Láctea desde una región con menos procesamiento por formación estelar. Se determinaron límites inferiores de la razón isotópica $^{12}C/^{13}C$. En contraste con los valores derivados en las posiciones del disco $(4 - 30)$, se encontraron altas razones isotópicas en las posiciones denominadas en este trabajo como "halo" $(> 40- > 70)$ y también en las posiciones de interacción de las órbitas X1-X2 $(> 42- > 56)$. Este resultado es consistente con un escenario donde gas proveniente del halo es acretado hacia el disco, y con la transferencia de gas desde las afueras del disco hacia el CG a través de las órbitas X1 y X2 sugerido por el potencial barrado.

El siguiente paso en esta tesis fue derivar las propiedades físicas del gas en las regiones de interacción, tales como la temperatura cinética y densidades de estas nubes moleculares. Como fue mencionado en §1.2.1.3, las nubes moleculares del centro Galáctico presentan altas temperaturas cinéticas, pero estas temperaturas eran desconocidas en las nubes ubicadas a alta latitud y en las nubes con alta velocidad asociadas con las regiones de interacción estudiadas en esta tesis. Usado las transiciones metaestables de NH_3 desde la $(J, K) = (1, 1)$ hasta la $(6, 6)$ se han derivado las temperaturas cinéticas y densidades en las 6 posiciones observadas con el telescopio Effelsberg. Para derivar densidades y trazar diferentes procesos físicos tales como choques, fotodisociación, y gas denso, se observaron otras emisiones moleculares, tales como SiO, HNCO, CS, $C^{34}S$, $C^{18}O$, y ^{13}CO, usando el telescopio de 30 metros de IRAM, lo cual fue usado para revelar los mecanismos de calentamiento del gas en estas regiones.

Las conclusiones de este trabajo son resumidas a continuación:

- El gas molecular del CG consiste de aproximamente dos temperaturas cinéticas en la zona central molecular. En las posiciones correspondientes al halo y en la posición llamada Disk 2 (que corresponde a Sgr B2) sólo se encuentra la componente de temperatura alta.

- Las temperaturas cinéticas son altas, no sólo en las nubes típicas del centro Galáctico, sino también en las nubes ubicadas a alta latitud y alta velocidad. Por lo tanto, el eficiente mecanismo de calentamiento de las nubes moleculares parece ser una característica general del gas, tanto del disco como del halo del CG.

- Los choques son un mecanismo de calentamiento dominante en las nubes moleculares del CG. Esto es apoyado por las altas temperaturas cinéticas y por la alta abundancia de SiO en los lugares donde se predice su existencia. La molécula de HNCO podría ser usada para revelar las características de estos choques, debido a su frágil naturaleza (enriquecida mediante choques, pero fácilmente fotodisociada por radiación UV y por choques fuertes). Sin embargo, a partir de este trabajo, otros mecanismos de calentamiento propuestos previamente para el CG no pueden descartarse.

- La alta temperatura cinética en las órbitas X1 y en los pies de los bucles gigantes moleculares es consistente con la dinámica a gran escala inducida por el potencial barrado y a los bucles gigantes moleculares como origen de los choques.

Finalmente, para establecer la morfología y cinemática del gas sometido a choques en los pies de los bucles, se realizaron mapas de una nube molecular en varias líneas en la longitud de onda de 3-mm, usando el telescopio Mopra de 22 metros. Este trabajo está en curso, pero el análisis preliminar de los datos muestra estructuras a pequeña escala en la emisión de SiO, con perfiles de línea más delgados que por ejemplo, la molécula de HCO^+ o HCN, lo que indica que los choques están confinados dinámicamente. Los datos también muestran diferencias claras entre distintos trazadores moleculares, como por ejemplo entre el SiO y el HCO^+, lo cual podría indicar diferencias en las propiedades físicas y químicas en la nube.

En terminos generales, los resultados presentados y discutidos en esta tesis proporcionan importantes claves para la comprensión de la naturaleza de las nubes moleculares de la región del centro de la Galaxia. Ellos evidencian la presencia de choques y son consistentes con la hipótesis de los choques como mecanismo de calentamiento. Más aun, este trabajo soporta fuertemente la idea de que la acreción del gas hacia el centro Galáctico es la causa de dichos choques.

Chapter 8

Perspectives

8.1 3mm line maps of the "foot point" of the Molecular loops at $l = 3° - 5°$

Using Mopra 22m telescope, we also started the mapping of the M+5.3 – 0.3 molecular cloud where the eastern foot point of the molecular loop $l = 3° - 5°$ is placed. The mapping is on progress and we mapped a selected region covering the most intense emission, which ranges from $5°.331 < l < 5°.560$ and $-0°.367 < b < -0°.212$. The observations and data reductions are detailed in §6.3. The off position was $(l, b) = (5°.75, 1°.0)$, which was checked to be free of emission. We observe one frequency setup centered in 89.41 GHz, wich give us a broad-band range of 85.275 to 93.555 GHz.

Table 8.1: RMS noise values for each molecule for the observed region of M+5.3 – 0.3 molecular cloud.

Molecule	Transition	Rest. Freq. [GHz]	RMS [mK]
SO	2(2) – 1(1)	86.094	53
$H^{13}CN$	1 – 0*	86.340	51
$H^{13}CO^+$	1 – 0	86.754	56
SiO	2 – 1 $v = 0$	86.847	53
$HN^{13}C$	1 – 0*	87.091	51
HNCO	4(0, 4) – 3(0, 3)	87.925	64
HCN	1 – 0*	88.632	55
HCO^+	1 – 0	89.188	45
HNC	1 – 0*	90.664	48
HC_3N	10 – 9	90.979	51
CH_3CN	5 – 4*	91.979	49
^{13}CS	2 – 1	92.494	48
N_2H^+	1 – 0*	93.174	46

* present fine or hyperfine transitions.

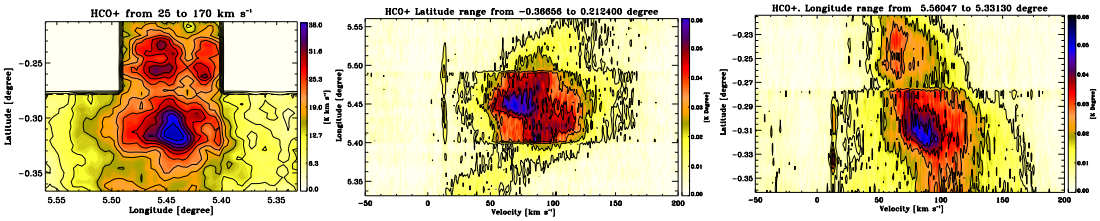

Figure 8.1: M+5.3 − 0.3 cloud: Left. Integrated intensity map in the velocity range from 25 to 170 km s^{-1}. The dashed lines show the mapped region. Center. Longitude-velocity plot integrated over the whole latitude range (from $b = -0°.37$ to $b = -0°.21$). Right. Latitude-velocity plot integrated over the whole longitude range (from $l = 5°.56$ to $5°.33$)

Fig. 8.1 presents the integrated intensity map for the observed region of M+5.3−0.3 cloud, in the velocity range from 25 to 170 km s^{-1}, which is the complete velocity range where there are emission and avoid the local contribution from the galaxy; the longitude-velocity map integrated in the whole latide range observed, and the latitude-velocity map integrated in the whole longitude rage observed. In Fig. 8.2 shows the velocity structure of the molecular cloud in velocity integrated step of 10 km s^{-1} in the HCO^+ emission.

Although of the small region mapped in this molecular cloud, it is possible to distinguish the different velocities structures. From Fig. 8.2 we can see a velocity gradient from the north to the south, identifying mainly three velocities components: from 40 to 70 km s^{-1}, from 70 to 100 km s^{-1}and from 100 to 140 km s^{-1}. The thin velocity width emission in the velocity range from 10 to 20 km s^{-1}in Fig. 8.2 correspond to local gas, which is also seen in the longitude-velocity and latitude-velocity maps in Fig. 8.1. Fig. 8.3 and Fig. 8.4 show the integrated intensity in these velocity ranges for the most intense molecules.

8.2 Isotopic Ratio as an Useful Tool

Motivated by the compelling results recently obtained during my Ph.D. thesis, I am using the $^{12}C/^{13}C$ isotopic ratio approach to map gas accretion in the barred Galactic potential (accepted proposal for this semester in the 30m telescope). The selected region for this task is the 1.3 molecular complex in the GC, where we found clear differences in the gas associated with the X1 and X2 orbits (see Section §1.2.1). We expect to find clouds with high ratio associated to the X1 orbits, and low ratio associated to the X2 orbits, and we will look for the clouds which should have a mixture of material (if any) with different degrees of processing. We plan to observe directly the mixing due to the bar in our Galaxy.

I just observed an accepted project at the 30m telescope for isotopic studies in the galaxy NGC891, which I conduct in collaboration with my thesis advisors and with Dr. Santiago García Burillo (OAN), and Dr. Isabel Pérez (U. de Granada). The main goal of this study is to analyze the transfer of material from the X1 to X2 orbits using the isotopic tools (described above), but in external galaxies, complementing the reseach

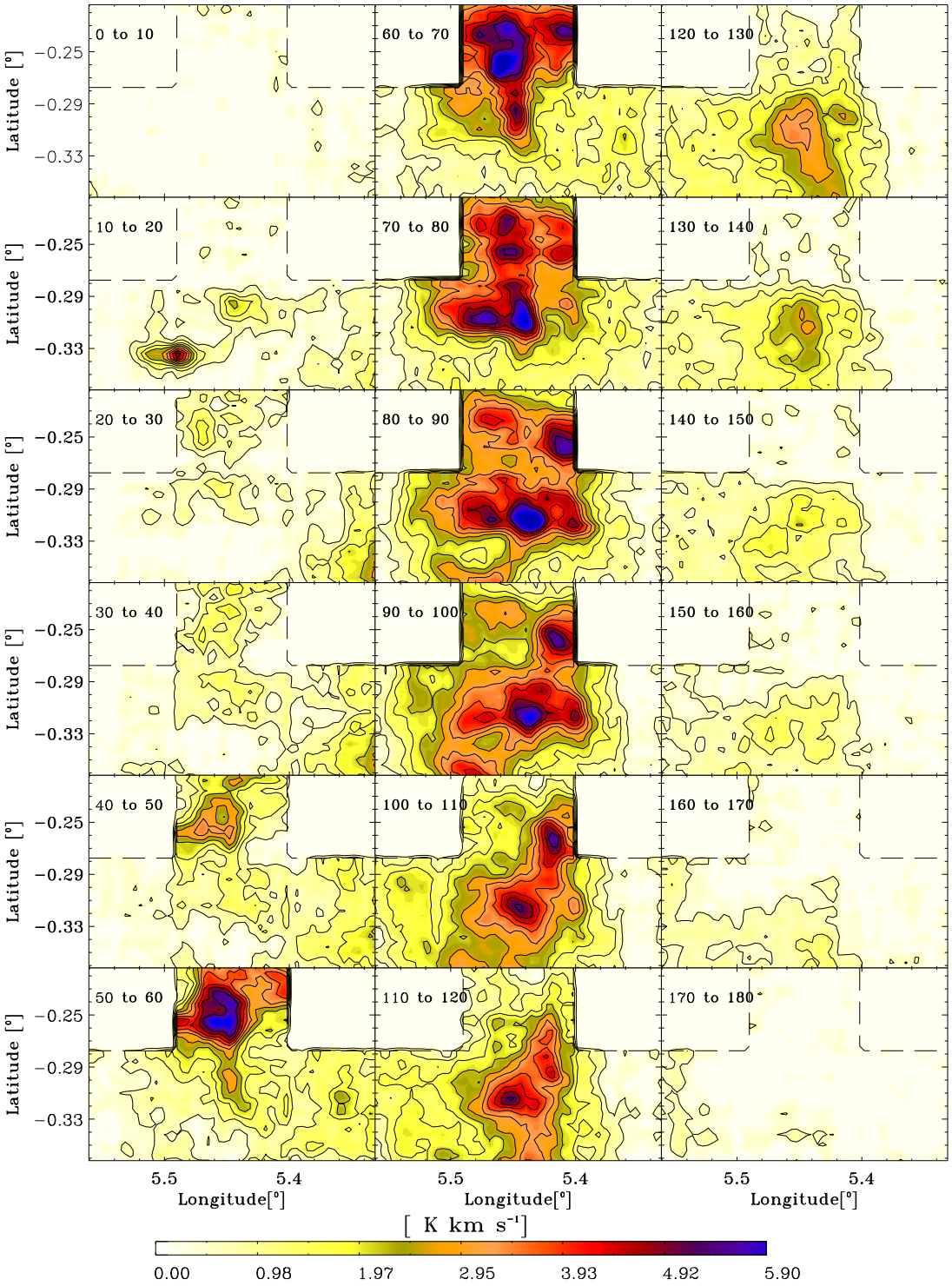

Figure 8.2: Integrated intensity of the M+5.3 − 0.3 molecular cloud in HCO^+ (1 − 0) in velocity intervals of 10 km s^{-1}.

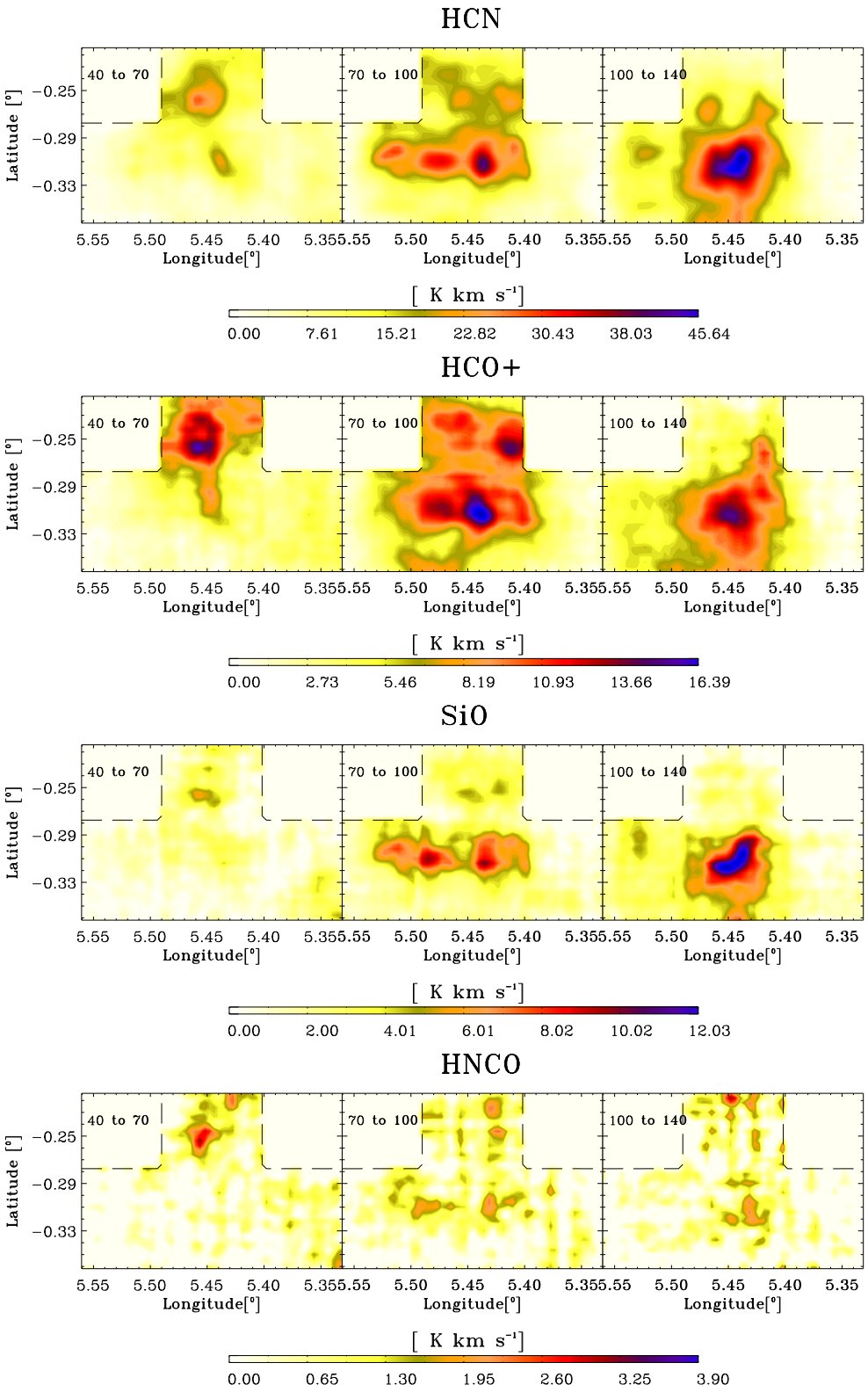

Figure 8.3: Left: velocity range from 40 to 70 km s^{-1}. Center: velocity range from 70 to 100 km s^{-1}. Right: Velocity range from 100 to 140 km s^{-1}

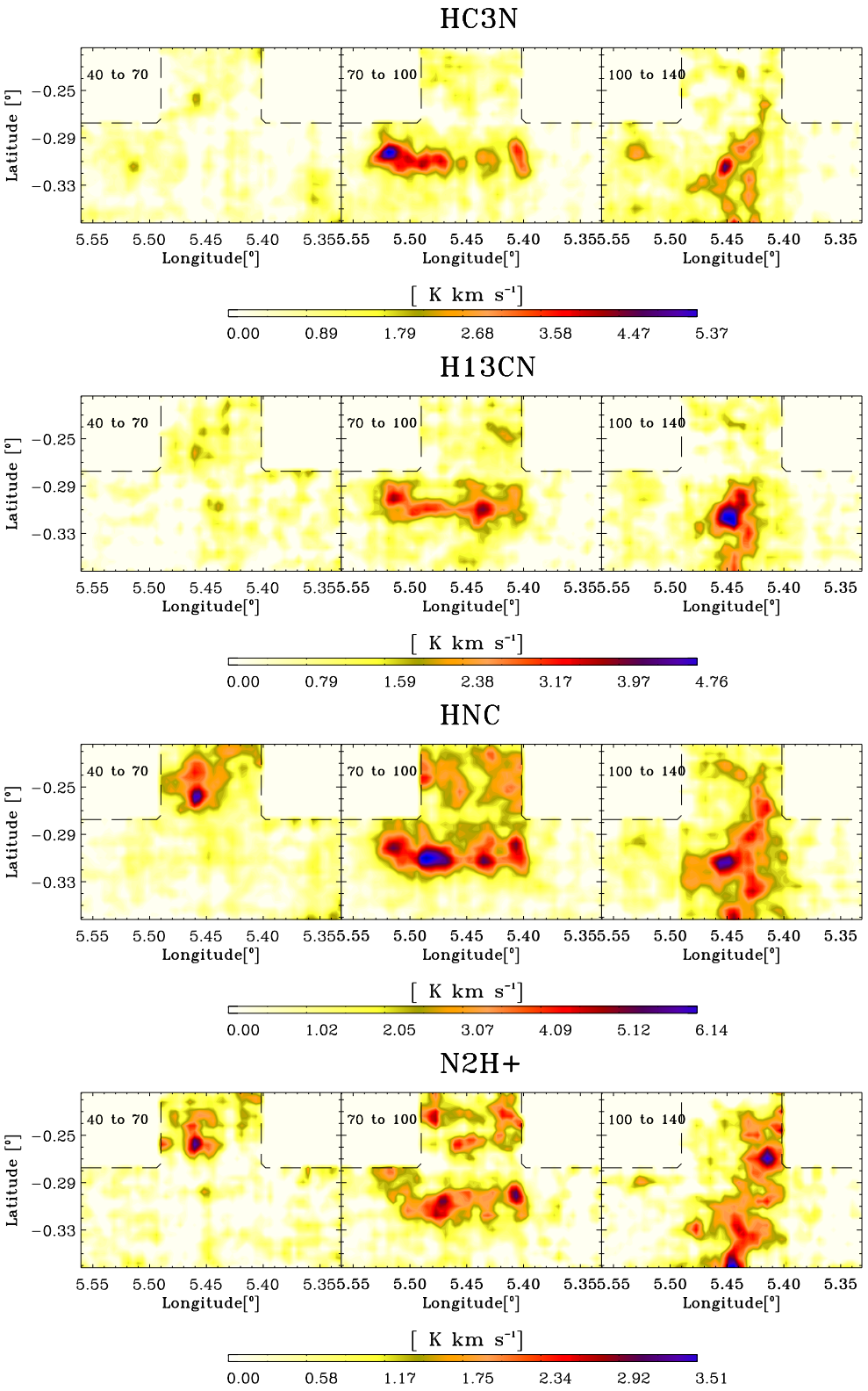

Figure 8.4: Left: velocity range from 40 to 70 km s^{-1}. Center: velocity range from 70 to 100 km s^{-1}. Right: Velocity range from 100 to 140 km s^{-1}

carried out for my Ph.D. project.

8.3 Toward Nearby Galaxies

I am also collaborating with Dr. Rebeca Aladro (UCL; she was my office mate at IRAM) in the project "Chemical Classifications of Galaxies", which is a spectral survey in the 3mm lines, including nearby galaxies and some positions in the GC. The aim of the project is to use the survey as a chemical template for different kinds of nuclear activity (PDRs, shocks, X-ray dominated regions) comparing with the GC sources.

Appendix A

Calibration of the Effelsberg data

A.1 From the measured signal to T_{MB}

A.1.1 Noise tube calibration

The calibration of the Effelsberg data was done following the manual *Calibration of the Effelsberg 100m telescope* by A. Kraus (2009). The calibration in Effelsberg is done by the periodic injection of a constant signal (noise cal) at the very early stage of the receiver. This signal is split into small phases, and in the half of the phases the noise cal is switched on, and in the other half is switched off.

To convert the signal from the telescope in antenna temperature, we need to multiply by the value of the T_{cal} [1]

$$T_A[K] = T_{cal}[K] \times signal[counts] \tag{A.1}$$

In our case, $T_{cal} = 1.8$ K at 24GHz.

A.1.2 Opacity correction

The attenuation due the atmosphere of the observed signal is significant for observations at $\nu \gtrsim 15$ GHz.

$$T_A^{'} = T_A \times e^{\tau_z \cdot AM} \tag{A.2}$$

where τ_z is the zenith opacity (which depends on the frequency) and AM = 1/ sin(Elv) is the airmass.

To derive the τ_z at a given time, we use the "two-step-procedure" suggested in the manual. We use the relation:

$$T_{sys} = T_0 + T_{Atm} \times (1 - e^{-\tau \cdot AM}) \tag{A.3}$$

where the system temperature (T_{sys}) and the airmass is obtained from each observation (from the header of the spectra), and the ambient temperature is assumed to be 270 K. We use all the observations and with a least-square-fit we obtain the T_0 and $\tau_{z,min}$ (lowest zinit opacity). This is done for each polarization and for each setup of observation (see Fig A.1)

[1] see the values for the T_{cal} in http://www.mpifr-bonn.mpg.de/div/effelsberg/calibration/1.3cmpf.html

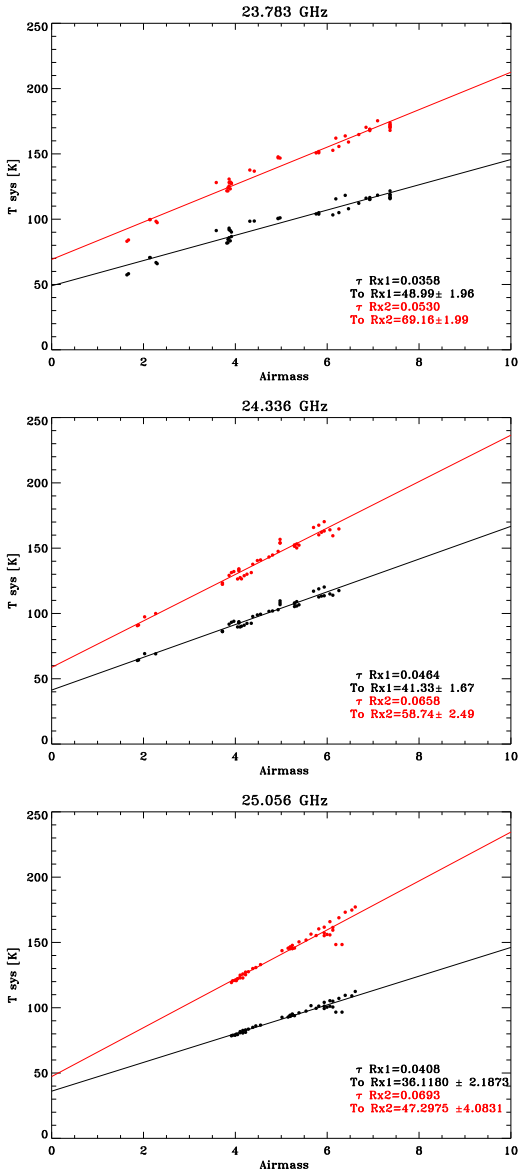

Figure A.1: Least square fit of the observations. Top: for the first setup of frequency (23.783 GHz), we derive T0 = 48.99 ± 1.96 and τ_{min} = 0.0358 for the polarization 1 and T0 = 69.16 ± 1.99 and τ_{min} = 0.0530 for polarization 2. Middle: for the second setup of frequency (24.336 GHz), we derive T0 = 41.33 ± 1.67 and τ_{min} = 0.0464 for the polarization 1 and T0 = 58.74 ± 2.49 and τ_{min} = 0.0658 for polarization 2. Bottom: for the third setup of frequency (25.056 GHz), we derive T0 = 36.12±2.19 and τ_{min} = 0.0408 for the polarization 1 and T0 = 47.30 ± 4.08 and τ_{min} = 0.0693 for polarization 2.

with the value derived for T_0, we obtain the τ for each observation (from A.4),

$$\tau = -\frac{1}{AM} \cdot \ln\left(1 - \frac{T_{sys} - T_0}{T_{Atm}}\right) \tag{A.4}$$

and it is replaced in formula A.2 to obtain the antenna temperature corrected by the opacity for each observation.

A.1.3 Gain-elevation correction

Finally, we need to correct by the small scale deformations of the surface of the telescope when it move to high or low elevations. The surface of the main dish is adjusted by holography measurements using a geo-stationary satellite at an elevation of 32° . When moving to higher or lower elevations (as in this work due the low elevations that the GC reach in this telescope of ∼ 15°), the disk keeps a parabolic form due the principle of homology, and has one well defined focal point. That correction is described by a parabola in elevation (or a higher degree polynomial):

$$T^*_{\rm A} = \frac{T^{'}_{\rm A}}{G(Elv)} = \frac{T^{'}_{\rm A}}{A_0 + A_1 \cdot Elv + A_2 \cdot Elv^2} \tag{A.5}$$

where the coefficient for this normalize curve are: $A_0 = 0.88196$, $A_1 = 6.6278E-3$, $A_2 = -9.2334E-5$, for the receiver at 1.3 cm (it depends to the wavelength), measured in April 2000.

A.1.4 Main beam temperature

The main beam temperatures, TMB, was obtained using $T_{\rm MB} = T^*_{\rm A} \cdot \frac{Feff}{Beff}$, where the forward efficiency Feff = 1, and the beam efficiency is Beff = 52 at 24 GHz. The uncertainty in the calibration is of the order of 5 − 10%.

Bibliography

Aharonian, F., Akhperjanian, A. G., Anton, G., et al. 2009, A&AP, 503, 817 1.2.1.1

Aharonian, F., Akhperjanian, A. G., Aye, K.-M., et al. 2004, A&AP, 425, L13 1.2.1.1

Aharonian, F., Akhperjanian, A. G., Bazer-Bachi, A. R., et al. 2006, Nature, 439, 695 1.2.1.1

Aitken, D. K., Briggs, G. P., Roche, P. F., Bailey, J. A., & Hough, J. H. 1986, MNRAS, 218, 363 1.2.2

Aitken, D. K., Smith, C. H., Gezari, D., McCaughrean, M., & Roche, P. F. 1991, ApJ, 380, 419 1.2.2

Altenhoff, W. J., Downes, D., Pauls, T., & Schraml, J. 1979, AAPS, 35, 23 1.2.1.2

Amo-Baladrón, M. A., Martín-Pintado, J., & Martín, S. 2011, A&AP, 526, A54+ 1.3.1.1, 1.10

An, D., Ramírez, S. V., Sellgren, K., et al. 2011, ApJ, 736, 133 1.2.3

Athanassoula, E. 1992, MNRAS, 259, 345 1.4.1

Bachiller, R., Martin-Pintado, J., & Fuente, A. 1993, ApJL, 417, L45 5.2

Bally, J., Aguirre, J., Battersby, C., et al. 2010, ApJ, 721, 137 3.1

Bally, J., Stark, A. A., Wilson, R. W., & Henkel, C. 1987, APJS, 65, 13 1.1, 1.3.2.2

Bally, J., Stark, A. A., Wilson, R. W., & Henkel, C. 1988, ApJ, 324, 223 1.3.1, 1.3.1.4, 1.3.1.6, 1.3.2.1, 1.3.2.2

Bally, J. & Yusef-Zadeh, F. 1989, ApJ, 336, 173 1.3.1.3

Bania, T. M. 1977, ApJ, 216, 381 1.3.2.1, 1.3.2.2, 1.4.1

Bania, T. M. 1980, ApJ, 242, 95 1.3.2.2

Bania, T. M., Stark, A. A., & Heiligman, G. M. 1986, ApJ, 307, 350 1.3.2.2

Barrett, A. H., Ho, P. T. P., & Myers, P. C. 1977, ApJL, 211, L39 5.1

Becklin, E. E., Gatley, I., & Werner, M. W. 1982, ApJ, 258, 135 1.3.1.1

Bélanger, G., Goldwurm, A., Renaud, M., et al. 2006, ApJ, 636, 275 1.2.1.1

Benjamin, R. A., Churchwell, E., Babler, B. L., et al. 2005, ApJL, 630, L149 1.1

Binney, J., Gerhard, O. E., Stark, A. A., Bally, J., & Uchida, K. I. 1991, MNRAS, 252, 210 (document), 1.4, 1.4.1, 1.13, 1.4.1

Binney, J. & Tremaine, S. 2008, Galactic Dynamics: Second Edition, ed. Binney, J. & Tremaine, S. (Princeton University Press) 1.1

Bissantz, N., Englmaier, P., & Gerhard, O. 2003, MNRAS, 340, 949 1.4.1

Bitran, M., Alvarez, H., Bronfman, L., May, J., & Thaddeus, P. 1997, AAPS, 125, 99 1.1, 1.1, 1.7, 1.3, 1.3, 1.3.2.3, 1.3.2.5, 1.11

Bitran, M. E. 1987, PhD thesis, , University of Florida, (1987) 1.3.2.4

Blitz, L. & Spergel, D. N. 1991, ApJ, 379, 631 1.1

Blum, R. D., Ramírez, S. V., Sellgren, K., & Olsen, K. 2003, ApJ, 597, 323 1.5

Boesgaard, A. M. & Steigman, G. 1985, ARAA, 23, 319 4.1

Boyce, P. J. & Cohen, R. J. 1989, in IAU Symposium, Vol. 136, The Center of the Galaxy, ed. M. Morris, 141–+ 1.3.2.1

Bregman, J. N. 1980, ApJ, 236, 577 (document), 1.5.2, 1.21

Brinch, C. & Hogerheijde, M. R. 2010, A&AP, 523, A25+ 2.9.3

Brown, P. D. & Charnley, S. B. 1990, MNRAS, 244, 432 5.2.2

Burton, W. B. & Liszt, H. S. 1978, ApJ, 225, 815 1.13

Carroll, B. W. & Ostlie, D. A. 2006, An introduction to modern astrophysics and cosmology, ed. Carroll, B. W. & Ostlie, D. A. 1.1

Caswell, J. L. 1996, MNRAS, 283, 606 1.3.1.2

Caswell, J. L. & Haynes, R. F. 1982, ApJL, 254, L31 1.3.2.2

Cheung, A. C., Rank, D. M., Townes, C. H., Knowles, S. H., & Sullivan, III, W. T. 1969, ApJL, 157, L13 5.2.3

Cheung, A. C., Rank, D. M., Townes, C. H., Thornton, D. D., & Welch, W. J. 1968, Physical Review Letters, 21, 1701 5.1

Chin, Y.-N., Henkel, C., Whiteoak, J. B., Langer, N., & Churchwell, E. B. 1996, A&AP, 305, 960 4.1, 4.2

Churchwell, E., Babler, B. L., Meade, M. R., et al. 2009, PASP, 121, 213 1.1, 1.1

Chuss, D. T., Davidson, J. A., Dotson, J. L., et al. 2003, ApJ, 599, 1116 1.2.2

Cohen, R. J. & Dent, W. R. F. 1983, in Astrophysics and Space Science Library, Vol. 105, Surveys of the Southern Galaxy, ed. W. B. Burton & F. P. Israel, 159–164 1.3.2.2

Combes, F. 1996, in IAU Symposium, Vol. 169, Unsolved Problems of the Milky Way, ed. L. Blitz & P. J. Teuben, 133 1.4.1

Contopoulos, G. & Mertzanides, C. 1977, A&AP, 61, 477 1.4.1

Cox, P. & Laureijs, R. 1989, in IAU Symp, Vol. 136, The Center of the Galaxy, ed. M. Morris, 121 1.2.1.2

Crutcher, R. M., Roberts, D. A., Mehringer, D. M., & Troland, T. H. 1996, ApJL, 462, L79 1.2.2

Dahmen, G., Hüttemeister, S., Wilson, T. L., et al. 1997, AAPS, 125, 1 1.1, 1.3.1.4

Dalgarno, A. 1982, in Applied Atomic Collision Physics, Volume 1: Atmospheric Physics and Chemistry, ed. H. S. W. Massey & D. R. Bates, Vol. 1, 427–467 5.2.1

Dame, T. M., Hartmann, D., & Thaddeus, P. 2001, ApJ, 547, 792 1.1

Dame, T. M. & Thaddeus, P. 2008, ApJL, 683, L143 1.1

Das, M. & Jog, C. J. 1995, ApJ, 451, 167 1.2.1.3

Davidson, J. A. 1996, in Astronomical Society of the Pacific Conference Series, Vol. 97, Polarimetry of the Interstellar Medium, ed. W. G. Roberge & D. C. B. Whittet, 504 1.2.2

de Jong, T., Boland, W., & Dalgarno, A. 1980, A&AP, 91, 68 2.9.2.2

de Jong, T., Dalgarno, A., & Chu, S.-I. 1975, ApJ, 199, 69 2.9.2.2

de Vaucouleurs, G. 1964, in IAU Symposium, Vol. 20, The Galaxy and the Magellanic Clouds, ed. F. J. Kerr, 195–+ 1.1

D'Hendecourt, L. B., Allamandola, L. J., & Greenberg, J. M. 1985, A&AP, 152, 130 5.2.2

Diehl, R., Bennett, K., Bloemen, H., et al. 1993, AAPS, 97, 181 1.2.1.1

Downes, D., Genzel, R., Hjalmarson, A., Nyman, L. A., & Ronnang, B. 1982, ApJL, 252, L29 1.2.1.3

Dwek, E., Arendt, R. G., Hauser, M. G., et al. 1995, ApJ, 445, 716 1.1

Elmegreen, B. G. 1982, ApJ, 253, 634 1.4.2.1

Englmaier, P. & Gerhard, O. 1999, MNRAS, 304, 512 1.4.1

Ferrière, K. 2009, A&AP, 505, 1183 1.2.2

Ferrière, K., Gillard, W., & Jean, P. 2007, A&AP, 467, 611 (document), 1.3.1, 1.9

Figer, D. F. 2005, Nature, 434, 192 1.2.3

Figer, D. F. 2009, Massive-star formation in the Galactic center:, ed. Livio, M. & Villaver, E., 40–59 1.2.3, 1.5, 1.2.3, 1.6, 1.3.1.1

Figer, D. F., Kim, S. S., Morris, M., et al. 1999, ApJ, 525, 750 1.2.3, 1.6

Fleck, Jr., R. C. 1980, ApJ, 242, 1019 1.2.1.3

Ford, H. A., Lockman, F. J., & McClure-Griffiths, N. M. 2010, ApJ, 722, 367 1.5.2

Frank, J., King, A., & Raine, D. J. 2002, Accretion Power in Astrophysics: Third Edition, ed. Frank, J., King, A., & Raine, D. J. 1.2.1.1

Freeman, K. 2011, ArXiv e-prints 1.1

Frerking, M. A., Wilson, R. W., Linke, R. A., & Wannier, P. G. 1980, ApJ, 240, 65 4.2

Fujishita, M., Torii, K., Kudo, N., et al. 2009, ArXiv e-prints 1.4.2, 6.1.2

Fukui, Y., Yamamoto, H., Fujishita, M., et al. 2006, Sci., 314, 106 (document), 1.4, 1.4.2, 1.4.2.1, 1.17, 1.6, 6.1, 6.1.1, 6.1.3

Fux, R. 1999, A&AP, 345, 787 1.4.1

Gaume, R. A. & Claussen, M. J. 1990, ApJ, 351, 538 1.3.1.2

Gaume, R. A., Claussen, M. J., de Pree, C. G., Goss, W. M., & Mehringer, D. M. 1995, ApJ, 449, 663 1.3.1.2

Genzel, R., Eisenhauer, F., & Gillessen, S. 2010, Reviews of Modern Physics, 82, 3121 1

Genzel, R., Pichon, C., Eckart, A., Gerhard, O. E., & Ott, T. 2000, MNRAS, 317, 348 1.3.1.1

Genzel, R., Watson, D. M., Townes, C. H., et al. 1984, ApJ, 276, 551 1.2.1.2

Gerhard, O. 2002, in Astronomical Society of the Pacific Conference Series, Vol. 273, The Dynamics, Structure & History of Galaxies: A Workshop in Honour of Professor Ken Freeman, ed. G. S. Da Costa & H. Jerjen, 73–+ 1.1

Gerhard, O. E. 1996, in IAU Symposium, Vol. 169, Unsolved Problems of the Milky Way, ed. L. Blitz & P. J. Teuben, 79 1.4.1

Ghez, A. M., Salim, S., Hornstein, S. D., et al. 2005, ApJ, 620, 744 1.2.3, 1.6, 1.3.1.1

Gilmore, G. & Reid, N. 1983, MNRAS, 202, 1025 1.1

Ginsburg, A., Bally, J., & Williams, J. 2011, ArXiv e-prints 2.8

Goldsmith, P. F. & Langer, W. D. 1999, ApJ, 517, 209 2.9.1

Goldsmith, P. F., Lis, D. C., Lester, D. F., & Harvey, P. M. 1992, ApJ, 389, 338 1.3.1.2

Goldwurm, A. 2011, in Astronomical Society of the Pacific Conference Series, Vol. 439, The Galactic Center: a Window to the Nuclear Environment of Disk Galaxies, ed. M. R. Morris, Q. D. Wang, & F. Yuan, 391–+ 1.2.1.1

Gordon, M. A., Berkermann, U., Mezger, P. G., et al. 1993, A&AP, 280, 208 1.3.1.2

Grebel, E. K. 2001, in Astronomical Society of the Pacific Conference Series, Vol. 239, Microlensing 2000: A New Era of Microlensing Astrophysics, ed. J. W. Menzies & P. D. Sackett, 280–+ 1.18

Guelin, M., Cernicharo, J., & Linke, R. A. 1982, ApJL, 263, L89 4.2

Guesten, R., Genzel, R., Wright, M. C. H., et al. 1987, ApJ, 318, 124 1.3.1.1

Gueth, F., Guilloteau, S., & Bachiller, R. 1998, A&AP, 333, 287 5.2.3

Güsten, R. 1989, in IAU Symposium, Vol. 136, The Center of the Galaxy, ed. M. Morris, 89–+ 1.2.1.3, 1.2.3

Güsten, R. & Downes, D. 1980, A&AP, 87, 6 1.2.1.3, 1.2.3

Güsten, R., Walmsley, C. M., & Pauls, T. 1981, A&AP, 103, 197 1.2.1.3

Handa, T., Sofue, Y., Nakai, N., Hirabayashi, H., & Inoue, M. 1987, PASJ, 39, 709 1.2.1.2

Hartwick, F. D. A. 1987, in NATO ASIC Proc. 207: The Galaxy, ed. G. Gilmore & B. Carswell, 281–290 1.1

Heiligman, G. M. 1987, ApJ, 314, 747 1.1, 1.3.1

Henkel, C., Güsten, R., & Gardner, F. F. 1985, A&AP, 143, 148 4.1

Henkel, C., Walmsley, C. M., & Wilson, T. L. 1980, A&AP, 82, 41 4.1

Herbst, E. & Klemperer, W. 1973, ApJ, 185, 505 5.2.1

Herbst, E., Millar, T. J., Wlodek, S., & Bohme, D. K. 1989, A&AP, 222, 205 1.2.1.3

Hiraoka, K., Yamashita, A., Yachi, Y., et al. 1995, ApJ, 443, 363 5.2.2

Ho, P. T. P., Martin, R. N., Myers, P. C., & Barrett, A. H. 1977, ApJL, 215, L29 5.1

Ho, P. T. P. & Townes, C. H. 1983, ARAA, 21, 239 (document), 5.1, 5.2, 5.2.1, 5.2.1, 5.3.1

Hogerheijde, M. R. & van der Tak, F. F. S. 2000, A&AP, 362, 697 2.9.3

Hüttemeister, S., Dahmen, G., Mauersberger, R., et al. 1998, A&AP, 334, 646 1.2.1.3, 1.3.1.6, 1.4.1

Hüttemeister, S., Wilson, T. L., Bania, T. M., & Martin-Pintado, J. 1993a, A&AP, 280, 255 1.2, 1.2.1.3, 5.2, 5.2.3

Hüttemeister, S., Wilson, T. L., Henkel, C., & Mauersberger, R. 1993b, A&AP, 276, 445 5.2

Ibata, R. A., Gilmore, G., & Irwin, M. J. 1994, Nature, 370, 194 1.5.1

Ibata, R. A. & Lewis, G. F. 1998, ApJ, 500, 575 (document), 1.5.1, 1.19

Ibata, R. A., Wyse, R. F. G., Gilmore, G., Irwin, M. J., & Suntzeff, N. B. 1997, AJ, 113, 634 1.5.1

Iglesias, E. R. & Silk, J. 1978, ApJ, 226, 851 1.2.1.3

Immer, K., Schuller, F., Omont, A., & Menten, K. M. 2011, ArXiv e-prints 1.2.3

Jackson, J. M., Heyer, M. H., Paglione, T. A. D., & Bolatto, A. D. 1996, ApJL, 456, L91 1.1, 1.2.1.3

Jenkins, A. & Binney, J. 1994, MNRAS, 270, 703 1.4.1, 1.4.1

Jones, P. A., Burton, M. G., Cunningham, M. R., et al. 2008, MNRAS, 386, 117 1.3.1.2

Jones, P. A., Burton, M. G., Cunningham, M. R., et al. 2011, ArXiv e-prints 3.1

Kaifu, N., Kato, T., & Iguchi, T. 1972, Nature, 238, 105 1.4.1

Kerr, F. J. & Lynden-Bell, D. 1986, MNRAS, 221, 1023 1

Koyama, K., Maeda, Y., Sonobe, T., et al. 1996, PASJ, 48, 249 1.2.1.1

Koyama, K., Takikawa, Y., Hyodo, Y., et al. 2009, PASJ, 61, 255 1.2.1.1

Krabbe, A., Genzel, R., Eckart, A., et al. 1995, ApJL, 447, L95+ 1.3.1.1

Kraus, J. D. 1986, Radio astronomy, ed. Kraus, J. D. 2.1

Krivonos, R., Revnivtsev, M., Churazov, E., et al. 2007, A&AP, 463, 957 1.2.1.1

Kroupa, P. 2001, MNRAS, 322, 231 1.2.3

Kudo, N., Torii, K., Machida, M., et al. 2011, PASJ, 63, 171 (document), 6.1.2, 6.9

Lacy, J. H., Townes, C. H., Geballe, T. R., & Hollenbach, D. J. 1980, ApJ, 241, 132 1.2.1.2

Langer, W. D. & Glassgold, A. E. 1990, ApJ, 352, 123 1.2.1.3

LaRosa, T. N., Brogan, C. L., Shore, S. N., et al. 2005, ApJL, 626, L23 1.2.2

LaRosa, T. N., Kassim, N. E., Lazio, T. J. W., & Hyman, S. D. 2000, AJ, 119, 207 1.3.1, 1.8

Lebrón, M., Mangum, J. G., Mauersberger, R., et al. 2011, ArXiv e-prints 5.2.3

Lee, C. W. 1996, APJS, 105, 129 1.3.2.5

Lee, C. W. & Lee, H. M. 2003, Journal of Korean Astronomical Society, 36, 271 1.3.2.1

Lee, C. W., Lee, H. M., Ann, H. B., & Kwon, K. H. 1999, ApJ, 513, 242 1.3.2.2

Lis, D. C. & Carlstrom, J. E. 1994, ApJ, 424, 189 1.2.1.2, 1.3.1.3

Lis, D. C. & Goldsmith, P. F. 1990, ApJ, 356, 195 1.3.1.2

Liszt, H. S. 1992, APJS, 82, 495 1.3.1.4

Liszt, H. S. 2006, A&AP, 447, 533 1.3.1.5

Liszt, H. S. & Spiker, R. W. 1995, APJS, 98, 259 1.3.1.3

Lo, K. Y. & Claussen, M. J. 1983, Nature, 306, 647 1.3.1.1

Lockman, F. J. 2011, ArXiv e-prints 1.5.2

Lockman, F. J. & Gordon, M. A. 1973, ApJ, 182, 25 1.2.1.2

López-Corredoira, M., Cabrera-Lavers, A., Mahoney, T. J., et al. 2007, AJ, 133, 154 1.1

López-Corredoira, M., Hammersley, P. L., Garzón, F., et al. 2001, A&AP, 373, 139 1.1

Machida, M., Matsumoto, R., Nozawa, S., et al. 2009, PASJ, 61, 411 1.4.2.1

Marinacci, F., Fraternali, F., Binney, J., et al. 2011, ArXiv e-prints 1.5.2

Marshall, J., Lasenby, A. N., & Yusef-Zadeh, F. 1995, MNRAS, 274, 519 1.2.2

Martin, R. N., Ruf, K., & Ho, P. T. P. 1982, Nature, 296, 632 5.3.2

Martín, S., Aladro, R., Martín-Pintado, J., & Mauersberger, R. 2010, A&AP, 522, A62+ 4.2

Martín, S., Requena-Torres, M. A., Martín-Pintado, J., & Mauersberger, R. 2008, ApJ, 678, 245 4.2

Martín-Pintado, J., Bachiller, R., & Fuente, A. 1992, A&AP, 254, 315 (document), 1.2.1.3

Martín-Pintado, J., de Vicente, P., Fuente, A., & Planesas, P. 1997, ApJL, 482, L45 (document), 1.2, 1.2.1.3

Matsumoto, R., Horiuchi, T., Shibata, K., & Hanawa, T. 1988, PASJ, 40, 171 6.1.1.1

Mauersberger, R., Henkel, C., Wilson, T. L., & Walmsley, C. M. 1986, A&AP, 162, 199 5.2.3

Mayer-Hasselwander, H. A., Bertsch, D. L., Dingus, B. L., et al. 1998, A&AP, 335, 161 1.2.1.1

McClure-Griffiths, N. M., Dickey, J. M., Gaensler, B. M., et al. 2005, APJS, 158, 178 6.1.1

McGee, R. X. 1970, Australian Journal of Physics, 23, 541 1.3.2.1

McGrath, E. J., Goss, W. M., & De Pree, C. G. 2004, APJS, 155, 577 1.3.1.2

Mehringer, D. M., Goss, W. M., Lis, D. C., Palmer, P., & Menten, K. M. 1998, ApJ, 493, 274 1.3.1.4

Mehringer, D. M., Goss, W. M., & Palmer, P. 1994, ApJ, 434, 237 1.3.1.2

Mehringer, D. M. & Menten, K. M. 1997, ApJ, 474, 346 1.3.1.2

Mehringer, D. M., Palmer, P., & Goss, W. M. 1993a, ApJL, 402, L69 1.3.1.2

Mehringer, D. M., Palmer, P., Goss, W. M., & Yusef-Zadeh, F. 1993b, ApJ, 412, 684 1.3.1.2

Mehringer, D. M., Yusef-Zadeh, F., Palmer, P., & Goss, W. M. 1995, Astronomy Data Image Library, 1 1.3.1.2

Meyer, B. S. 1994, ARAA, 32, 153 4.1, 4.1

Mezger, P. G., Duschl, W. J., & Zylka, R. 1996, A&ARv, 7, 289 1.1

Mezger, P. G. & Pauls, T. 1979, in IAU Symposium, Vol. 84, The Large-Scale Characteristics of the Galaxy, ed. W. B. Burton, 357–365 1.2.1.2

Mihalas, D. 1978, Stellar atmospheres /2nd edition/, ed. Hevelius, J. 2.9.2.2

Molinari, S., Bally, J., Noriega-Crespo, A., et al. 2011, ApJL, 735, L33 (document), 1.4.1, 1.16

Morris, M. 1990, in IAU Symposium, Vol. 140, Galactic and Intergalactic Magnetic Fields, ed. R. Beck, R. Wielebinski, & P. P. Kronberg, 361–367 1.2.2

Morris, M., Polish, N., Zuckerman, B., & Kaifu, N. 1983, AJ, 88, 1228 1.2.1.3

Morris, M. & Serabyn, E. 1996, ARAA, 34, 645 (document), 1.1, 1.2, 1.2.1.1, 1.2.1.2, 1.2.1.3, 1.2.1.4, 1.2.3, 1.3, 1.3.1, 1.4, 1.4.1, 1.14, 8

Morris, M. & Yusef-Zadeh, F. 1985, AJ, 90, 2511 1.2.2

Morris, M. R. 2006, Sci., 314, 70 1.2.2, 1.4.2.1

Muno, M. P., Arabadjis, J. S., Baganoff, F. K., et al. 2004, ApJ, 613, 1179 1.2.1.1

Muno, M. P., Bauer, F. E., Baganoff, F. K., et al. 2009, APJS, 181, 110 1.2.1.1, 1.2

Nakagawa, T., Doi, Y., Yui, Y. Y., et al. 1996, ApJL, 457, L121+ 1.2.1.2

Nishiyama, S., Hatano, H., Tamura, M., et al. 2010, ApJL, 722, L23 (document), 1.2.2, 1.4

Nishiyama, S., Tamura, M., Hatano, H., et al. 2009, ApJ, 690, 1648 1.2.2

Novak, G., Dotson, J. L., Dowell, C. D., et al. 2000, ApJ, 529, 241 1.2.2

Odenwald, S. F. & Fazio, G. G. 1984, ApJ, 283, 601 1.2, 1.2.1.2

Oka, T., Hasegawa, T., Sato, F., et al. 2001, ApJ, 562, 348 1.3.1.6

Ossenkopf, V. 1997, New Astronomy, 2, 365 2.9.2

Osterbrock & Ferland. 2006, Mercury, 35, 010000 2.9.2.2

Park, S., Muno, M. P., Baganoff, F. K., et al. 2004, ApJ, 603, 548 1.2.1.1

Parker, E. N. 1966, ApJ, 145, 811 1.4.2.1

Pauls, T. & Mezger, P. G. 1975, A&AP, 44, 259 1.2.1.2

Penzias, A. A. 1981, ApJ, 249, 518 4.2

Picaud, S., Cabrera-Lavers, A., & Garzón, F. 2003, A&AP, 408, 141 1.1

Pidopryhora, Y., Lockman, F. J., & Shields, J. C. 2007, ApJ, 656, 928 1.5.2

Pierce-Price, D., Richer, J. S., Greaves, J. S., et al. 2000, ApJL, 545, L121 1.2.1.3, 1.3.1.2, 3.1

Ponti, G., Terrier, R., Goldwurm, A., Belanger, G., & Trap, G. 2010, ApJ, 714, 732 1.2.1.1

Portegies Zwart, S. F., McMillan, S. L. W., & Gerhard, O. 2003, ApJ, 593, 352 1.2.3

Prantzos, N., Aubert, O., & Audouze, J. 1996, A&AP, 309, 760 4.1

Purcell, C. W., Bullock, J. S., Tollerud, E. J., Rocha, M., & Chakrabarti, S. 2011, Nature, 477, 301 (document), 1.20

Reid, M. J. 1993, ARAA, 31, 345 1

Requena-Torres, M. A., Martín-Pintado, J., Martín, S., & Morris, M. R. 2008, ApJ, 672, 352 1.2.1.3

Requena-Torres, M. A., Martín-Pintado, J., Rodríguez-Franco, A., et al. 2006, A&AP, 455, 971 1.2.1.3

Roberts, D. A. & Goss, W. M. 1993, APJS, 86, 133 1.3.1.1

Rodriguez-Fernandez, N. J. & Combes, F. 2008, A&AP, 489, 115 1.1, 1.4.1

Rodriguez-Fernandez, N. J., Combes, F., Martin-Pintado, J., Wilson, T. L., & Apponi, A. 2006, A&AP, 455, 963 (document), 1.4.1, 1.4.1, 1.15

Rodríguez-Fernández, N. J. & Martín-Pintado, J. 2005, A&AP, 429, 923 1.2.1.2

Romano, D. & Matteucci, F. 2003, MNRAS, 342, 185 4.1

Rougoor, G. W. 1964, Bull. Astr. Inst. Netherlands, 17, 381 1.3.2.2

Rougoor, G. W. & Oort, J. H. 1960, Proceedings of the National Academy of Science, 46, 1 1.3.2.2

Sanders, R. H. & Prendergast, K. H. 1974, ApJ, 188, 489 1.1

Sato, F., Hasegawa, T., Whiteoak, J. B., & Miyawaki, R. 2000, ApJ, 535, 857 1.2.3

Sawada, T., Hasegawa, T., Handa, T., & Cohen, R. J. 2004, MNRAS, 349, 1167 1.2.1.4

Sawada, T., Hasegawa, T., Handa, T., et al. 2001, APJS, 136, 189 1.2.1.4

Schödel, R., Ott, T., Genzel, R., et al. 2003, ApJ, 596, 1015 1.2.3

Schuller, F., Menten, K. M., Contreras, Y., et al. 2009, A&AP, 504, 415 3.1

Schwarz, U. J. & Lasenby, J. 1990, in IAU Symposium, Vol. 140, Galactic and Intergalactic Magnetic Fields, ed. R. Beck, R. Wielebinski, & P. P. Kronberg, 383 1.2.2

Scoville, N. Z. 1972, ApJL, 175, L127+ 1.4.1, 1.12

Seab, C. G. & Shull, J. M. 1983, ApJ, 275, 652 1.2.1.3

Serabyn, E. & Guesten, R. 1991, A&AP, 242, 376 1.3.1.1

Serabyn, E. & Morris, M. 1994, ApJL, 424, L91 1.3.1.1

Simpson, J. P., Colgan, S. W. J., Cotera, A. S., et al. 1997, ApJ, 487, 689 1.2.1.2

Sobolev, V. V. 1960, Moving envelopes of stars, ed. Sobolev, V. V. 2.9.2, 2.9.2.2

Sofue, Y. 1990, PASJ, 42, 827 1.3.1.2

Sofue, Y. 1995, PASJ, 47, 551 1.2.1.4, 1.4.1, 1.12

Spergel, D. N. & Blitz, L. 1992, Nature, 357, 665 1.2.1.4

Stark, A. A. & Bania, T. M. 1986, ApJL, 306, L17 1.3.2.1

Stolte, A., Brandner, W., Grebel, E. K., Lenzen, R., & Lagrange, A.-M. 2005, ApJL, 628, L113 1.2.3

Stolte, A., Grebel, E. K., Brandner, W., & Figer, D. F. 2003, in Astronomical Society of the Pacific Conference Series, Vol. 287, Galactic Star Formation Across the Stellar Mass Spectrum, ed. J. M. De Buizer & N. S. van der Bliek, 433–438 1.2.3

Sunyaev, R. A., Markevitch, M., & Pavlinsky, M. 1993, ApJ, 407, 606 1.2.1.1

Suzuki, H., Yamamoto, S., Ohishi, M., et al. 1992, ApJ, 392, 551 5.2

Tafalla, M. & Bachiller, R. 1995, ApJL, 443, L37 5.2, 5.2.3

Takahashi, K., Nozawa, S., Matsumoto, R., et al. 2009, PASJ, 61, 957 6.1.1.1

Takano, S., Nakai, N., & Kawaguchi, K. 2002, PASJ, 54, 195 5.2, 5.2.1, 5.2.3

Tanaka, K., Kamegai, K., Nagai, M., & Oka, T. 2007, PASJ, 59, 323 1.3.1.6

Terrier, R., Bélanger, G., Ponti, G., et al. 2009, in American Institute of Physics Conference Series, Vol. 1126, American Institute of Physics Conference Series, ed. J. Rodriguez & P. Ferrando, 355–358 1.2.1.1

Terrier, R., Ponti, G., Bélanger, G., et al. 2010, ApJ, 719, 143 1.2.1.1, 1.2

Torii, K., Kudo, N., Fujishita, M., et al. 2010a, PASJ, 62, 675 (document), 6.1.1.1, 6.1.1.1, 6.6, 6.7, 6.8

Torii, K., Kudo, N., Fujishita, M., et al. 2010b, PASJ, 62, 1307 (document), 6.1, 6.1.1, 6.1, 6.2, 6.1.1.1, 6.3, 6.4, 6.5, 6.9

Townes, C. H. & Schawlow, A. L. 1955, Microwave Spectroscopy, ed. Townes, C. H. & Schawlow, A. L. 5.1

Tsuboi, M., Handa, T., & Ukita, N. 1999, APJS, 120, 1 1.2.1.3, 1.2.2, 1.16

Tsuboi, M., Inoue, M., Handa, T., Tabara, H., & Kato, T. 1985, PASJ, 37, 359 1.2.2

Tsuboi, M., Inoue, M., Handa, T., et al. 1986, AJ, 92, 818 1.2.2

Tuthill, P., Monnier, J., Tanner, A., et al. 2006, Science, 313, 935 1.2.3

Uchida, K. I. & Guesten, R. 1995, A&AP, 298, 473 1.2.2

Uchida, K. I., Morris, M., & Bally, J. 1994a, in NATO ASIC Proc. 445: The Nuclei of Normal Galaxies: Lessons from the Galactic Center, ed. R. Genzel & A. I. Harris, 99 1.4.1

Uchida, K. I., Morris, M. R., Serabyn, E., & Bally, J. 1994b, ApJ, 421, 505 1.4.1

Umemoto, T., Iwata, T., Fukui, Y., et al. 1992, ApJL, 392, L83 5.2, 5.2.3

Umemoto, T., Mikami, H., Yamamoto, S., & Hirano, N. 1999, ApJL, 525, L105 5.1, 5.2, 5.2.3

van den Bergh, S. 2000, Cambridge Astrophysics Series, 35 1.5

van der Kruit, P. C. 1971, A&AP, 13, 405 1.1

van der Tak, F., Neufeld, D., Yates, J., et al. 2005, in ESA Special Publication, Vol. 577, ESA Special Publication, ed. A. Wilson, 431–432 2.9.3

van der Tak, F. F. S., Black, J. H., Schöier, F. L., Jansen, D. J., & van Dishoeck, E. F. 2007, A&AP, 468, 627 2.9

van Woerden, H., Rougoor, G. W., & Oort, J. H. 1957, Academie des Sciences Paris Comptes Rendus, 244, 1691 1.1

van Zadelhoff, G.-J., Dullemond, C. P., van der Tak, F. F. S., et al. 2002, A&AP, 395, 373 2.9.3

Walmsley, C. M., Hermsen, W., Henkel, C., Mauersberger, R., & Wilson, T. L. 1987, A&AP, 172, 311 5.2.2

Walmsley, C. M. & Ungerechts, H. 1983a, A&AP, 122, 164 5.2.3

Walmsley, C. M. & Ungerechts, H. 1983b, A&AP, 122, 164 5.3.2

Wannier, P. G. 1980, ARAA, 18, 399 4.1

Wannier, P. G. & Linke, R. A. 1978, ApJ, 226, 817 4.1

Wannier, P. G., Penzias, A. A., Linke, R. A., & Wilson, R. W. 1976, ApJ, 204, 26 4.1

Wilson, T. L. 1999, Rep. Progr. Phys., 62, 143 (document), 4.1, 4.2, 7, 7

Wilson, T. L. & Matteucci, F. 1992, A&ARv, 4, 1 4.1, 4.1

Wilson, T. L., Rohlfs, K., & Hüttemeister, S. 2009a, Tools of Radio Astronomy (Springer-Verlag) (document), 1.2.1.3, 5.1, 5.1

Wilson, T. L., Rohlfs, K., & Hüttemeister, S. 2009b, Tools of Radio Astronomy, ed. Wilson, T. L., Rohlfs, K., Huttemeister, S. (Springer-Verlag) (document), 2.1, 5.1

Wilson, T. L. & Rood, R. 1994, ARAA, 32, 191 4.1, 1

Wouterloot, J. G. A., Henkel, C., Brand, J., & Davis, G. R. 2008, A&AP, 487, 237 4.1, 4.2

Yamauchi, S., Kawada, M., Koyama, K., Kunieda, H., & Tawara, Y. 1990, ApJ, 365, 532 1.2.1.1

Yusef-Zadeh, F., Hewitt, J. W., Arendt, R. G., et al. 2009, ApJ, 702, 178 1.2.3

Yusef-Zadeh, F., Hewitt, J. W., & Cotton, W. 2004, APJS, 155, 421 (document), 1.2.2, 1.3

Yusef-Zadeh, F. & Morris, M. 1987a, ApJ, 320, 545 1.2.2, 1.6, 1.3.1.1

Yusef-Zadeh, F. & Morris, M. 1987b, ApJ, 322, 721 1.3.1.1

Yusef-Zadeh, F., Morris, M., & Chance, D. 1984, Nature, 310, 557 1.2.2, 1.3.1.1

Zhang, Q. & Ho, P. T. P. 1995, ApJL, 450, L63 5.2.3

Ziurys, L. M., Snell, R. L., & Dickman, R. L. 1989, ApJ, 341, 857 1.2.1.3

Zolotov, A., Willman, B., Brooks, A. M., et al. 2009, ApJ, 702, 1058 1.1

Zylka, R., Güsten, R., Henkel, C., & Batrla, W. 1992, AAPS, 96, 525 1.3.2.1